Using Living Crystallization-Driven Self-Assembly to Form Functional π-Conjugated Nanostructures for Potential Optoelectronic Device Applications

Marcus A. Vespa

Bachelor of Science (Hon.), University of Calgary, 2018

A Dissertation Submitted for Fulfilment of the Requirements the Degree of

DOCTOR OF PHILOSOPHY

in the Department of Chemistry

University of Victoria

Victoria, British Columbia, Canada

Supervisory Committee

Using Living Crystallization-Driven Self-Assembly to Form Functional π-Conjugated Nanostructures for Potential Optoelectronic Device Applications

Marcus A. Vespa

Supervisory Committee:

Prof. Ian Manners, Department of Chemistry

Supervisor (deceased)

Prof. David Leitch, Department of Chemistry

Interim Supervisor and Departmental Member

Prof. J. Scott McIndoe, Department of Chemistry

Departmental Member

Prof. Arthur Blackburn, Department of Physics and Astronomy

Outside Member

Abstract

At the micro- and nanoscale, mimicking the level of complex organization observed in nature is difficult, and reproduction of these materials has been a key challenge in the fields of materials science and synthetic chemistry. Solution self-assembly of amphiphilic block copolymers (BCPs) is a promising route towards the construction of nanoscale assemblies with various sizes, morphologies, and material properties. Living crystallization-driven self-assembly (CDSA) of polymers with a crystallizable core-forming block has emerged as a valuable method to exert control over the dimensions of one- and two-dimensional (1D and 2D) nanostructures. This method reliably produces nanostructures with predictable sizes and low size distributions.

Due to the variety of BCPs capable of crystallization, a wide array of hierarchically organized nanostructures have been fabricated which show promising potential for application to a broad assortment of fields such as optoelectronics, biomedicine, and catalysis. The work presented in this thesis focuses on expanding the library of materials known to be compatible with living CDSA by introducing a new crystallizable π-conjugated core-forming block. This work also seeks to extend controlled self-assembly techniques in systems where precise nanoscale control is highly sought-after and deepen our understanding of the processes that govern π-conjugated block copolymer self-assembly by establishing structure-property relationships; the practical realization of which are all key goals in modern energy, materials, and nanoscience research.

Table of Contents

List of Figures

List of Schemes

List of Tables

List of Abbreviations

1D	One dimensional
^{1}H NMR	Proton nuclear magnetic resonance
^{31}P NMR	Phosphorus-31 nuclear magnetic resonance
2D	Two dimensional
Å	Angstroms
AFM	Atomic force microscopy
AIBN	Azobisisobutyronitrile
A_n	Number-average area
A_w	Weight-average area
-*b*-	Block
BCP	Block copolymer
BPh_4	Tetraphenylborate anion
ca.	Circa
$CDCl_3$	Deuterated chloroform
CDSA	Crystallization-driven self-assembly
CMC	Critical micelle concentration
CPNPs	π-Conjugated polymer nanoparticles
CuAAC	Copper-catalyzed azide-alkyne cycloaddition
Da	Daltons
DMF	Dimethylformamide
DNA	Deoxyribonucleic acid
$Đ_A$	Area dispersity
$Đ_L$	Length dispersity
$Đ_M$	Molar mass dispersity
DP_n	Number-average degree of polymerization
dppe	1,3-Bis(diphenylphosphino)ethane
dppp	1,3-Bis(diphenylphosphino)propane
DSC	Differential scanning calorimetry
equiv.	Equivalents
eV	Electron volts
FRET	Förster resonance energy transfer
g	Grams
GPC	Gel permeation chromatography
GRIM	Grignard Metathesis
h	Hours
HOMO	Highest occupied molecular orbital
*i*PrMgCl•LiCl	Isopropylmagnesium chloride - lithium chloride
*i*PrOH	Isopropanol
IR	Infrared
J	Joules

KCTP	Kumada catalyst transfer polycondensation
kDa	Kilodaltons
LCSM	Laser scanning confocal microscopy
L_n	Number-average length
LUMO	Lowest unoccupied molecular orbital
L_w	Weight-average length
L_w/L_n	Nanofiber length dispersity
-m-	Micelle segment
M	Meter
Me	Methyl
MeOH	Methanol
mg	Milligram
min.	Minutes
mL	Millilitre
mmol	Millimoles
M_n	Number-average molar mass
m_{unimer}/m_{seed}	Unimer-to-seed mass ratio
M_w	Weight-average molar mass
n	Number counted
*n*BuAc	*n*-Butyl acetate
*n*BuOH	*n*-Butyl alcohol
nm	Nanometer
OFET	Organic field-effect transistor
OLED	Organic light emitting diode
OPV	Organic photovoltaic
o-tolyl	*Ortho*-tolyl
P2VP	Poly(2-vinylpyridine)
P3EHT	Poly(3-(2'-ethylhexyl)thiophene)
P3HT	Poly(3-hexylthiophene)
PAA	Poly(acrylic acid)
PCL	Poly(ε-caprolactone)
PD	Photodetector
PDHF	Poly(di-*n*-hexylfluorene)
PDMS	Poly(dimethylsiloxane)
PE	Polyethylene
PEG	Poly(ethylene glycol)
PFAAs	Perfluoroalkyl acids
PFG	Poly(ferrocenyldimethylgermane)
PFS	Poly(ferrocenyldimethylsilane)
PFTMC	Poly(fluorenyltrimethylcarbonate)
Ph	Phenyl
PI	Poly(isoprene)
PLLA	Poly(L-lactic acid)
PMDETA	*N,N,N′,N′,N″*-Pentamethyldiethylenetriamine

PMMA	Poly(methyl methacrylate)
PPP	Poly(2,5-bis(2-ethylhexyloxy)phenylene)
PPV	Poly(*p*-phenylene vinylene)
PS	Polystyrene
QPT	Quaternized polythiophene
R^2	Coefficient of determination
RNA	Ribonucleic acid
rr	Regioregular
rs	Regiosymmetric
s	Second
SEM	Scanning electron microscopy
T_c	Crystallization temperature
TEM	Transmission electron microscopy
THF	Tetrahydrofuran
T_m	Melt temperature
TMV	Tobacco mosaic virus
UV	Ultraviolet
UV/Vis	Ultraviolet-visible
VT-UV/Vis	Variable-temperature ultraviolet-visible
WAXS	Wide angle X-ray scattering
ε	Molar extinction coefficient
W	Watts
W_n	Number-average micelle width
λ_{abs}	Absorbance wavelength
μm	Micrometer
σ	Standard deviation
χ_{AB}	Flory-Huggins parameter

Dedication

This dissertation is dedicated to Prof. Ian Manners, a man who made me a better person and scientist, always believed in me even in times when I didn't believe in myself, and someone who always encouraged me to see the bright side of life. This thesis is equally dedicated to my grandmother, Emma, my mother, Sylvia, and my sister, Lea, for all their love and support.

Acknowledgements

There are many people that supported me and contributed to my life in unique ways to make my journey through my PhD special, and I can't give enough gratitude for the impact they have had. Firstly, I would like to thank my professor, Ian Manners, for giving me the opportunity to learn from him on how to be an ever-inquisitive scientist. I would also like to thank Deborah O'Hanlon-Manners for all her support over the years, her diligence with group affairs, her kind encouragement, and dedication to the group.

I want to sincerely thank the people outside the Manners group that helped shape my graduate school experience in Victoria including Cody E, Stefania M, Charlie K, Alejandro F, Nick R, and L. Bi. I would also like to thank my entire friend group in Calgary that made life easier for me when I was struggling during my PhD.

I thank all my group members, past and present, including Harrison Y, S. Lei, Ayesha N, Diego H, Charlotte E, Hill C, Hayley P, Hannah S, Harvey M, Matt B, Matt W, Mitch N, Chen L, Jiandong C, Liam M, Steve S, Tomoya F, Yifan Z, John F, Horatio H, and Nikki O, as well as the many professors I learned from during my undergraduate degree and PhD. I deeply thank Dr. Etienne LaPierre who taught me many invaluable things during my undergraduate degree and PhD, as well as being a good friend and mentor. I would also like to acknowledge my committee Prof. David Leitch, Prof. J. Scott McIndoe, Prof. Arthur Blackburn, and Prof. Dwight Seferos.

I thank my grandmother, Emma, who always wanted to see me graduate but unfortunately passed away before I did, as well as my aunt, Anna, her partner, Todd, and my cousin, Julian, for their unwavering, incredible support. Finally, I thank my mother, Sylvia, and my sister, Lea, for supporting and encouraging me every step of the way.

Chapter 1

Introduction

1.1 The role of hierarchical self-assembly in nature

The natural world is replete with organic and inorganic examples of hierarchically assembled structures that span from the nano- to the macroscale with a range of complexities. Hierarchical assembly involves the organization and integration of smaller subunits into larger and more complex ordered assemblies to produce a range of diverse materials with useful structures and functions. Their functionality is often dependent on the nature of their constituent subunits and how they are arranged (Figure 1.1). The range of materials produced in nature that exhibit precise organization and the variability of their functionality highlights the utility and versatility of hierarchical self-assembly.

The structure of proteins provides an excellent example of complex and multidimensional organization.[1] The primary structure of a protein is composed of a specifically sequenced amino acid chain which twists and folds to form the secondary structure, α-helices or β-sheets, that mainly form due to hydrogen bonding (Figure 1.1).[1] The helices and sheets fold into tertiary 3-dimensional structures which form as a result of steric and geometric constraints, hydrophobic interactions, electrostatic interactions, dipole-dipole interactions, and hydrogen bonding.[1,2] Finally, multiple folded protein subunits can further assemble into higher-order quaternary structures to form multi-subunit complexes. The hierarchically assembled structure of proteins makes them useful for a broad range of purposes as they can be used to convey mechanical strength to tissues such as collagen or fibrin, signalling purposes such as actin filaments,[3] or chemical purposes such as in enzymes.[4]

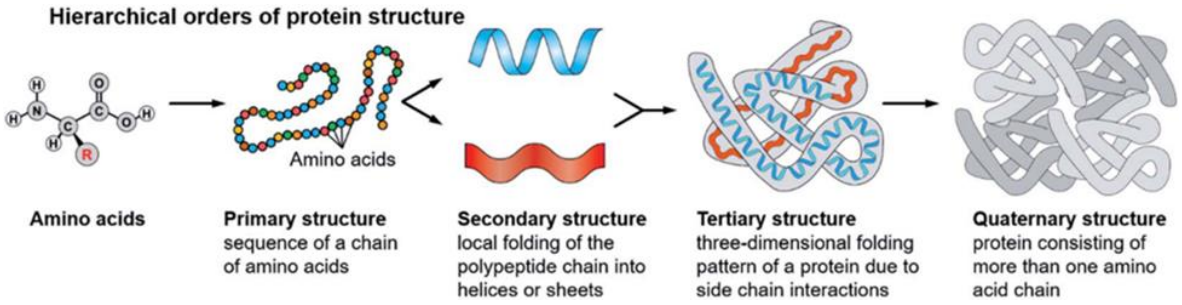

Figure 1.1. The hierarchical structural organization of proteins. An amino acid sequence composes the primary structure which fold into α-helices or β-sheets (secondary structure). The helices/sheets fold into 3-dimensional architectures which can further assemble to form a protein with distinct compartments (quaternary structure). Reproduced with permission from ref 1.[1]

Mollusks, such as clams and abalone, are aquatic organisms with soft internal bodies that are shielded from predators and the environment by a hard outer shell. These lightweight shells have high strength, toughness, and an exceptional ability to dissipate mechanical stress which are directly related to the precise hierarchical structuring of their organic and inorganic components. In general, there are three layers to the shell: the outermost periostracum composed of hardened proteins, the middle prismatic layer composed of columnar calcite, and the inner nacreous layer (Figure 1.2a).[5] The inner nacre layer is a heterogeneous, anisotropic organic-inorganic composite with a "brick-and-mortar" structure wherein the inorganic phase, composed of 95 wt% mineralized calcium carbonate (aragonite), behaves as hard bricks while the organic matrix, composing the other 5 wt%, is a matrix of viscoelastic polysaccharides and fibrous proteins that behaves as mortar (Figure 1.2b-d).[5–7] The organic matrix templates nucleation and growth of the aragonite platelets and creates a patterned composite that is tough yet elastic.[6] The multiscale hard/soft motif of nacre and the layered platelet hierarchy gives it the rigidity to withstand impacts while also allowing for some degree of elastic deformation to effectively resist mechanical stress and prevent fracturing of the shell. The ability of this composite to be lightweight and have high mechanical toughness has inspired many efforts to fabricate synthetic nacre-like materials.[6,8]

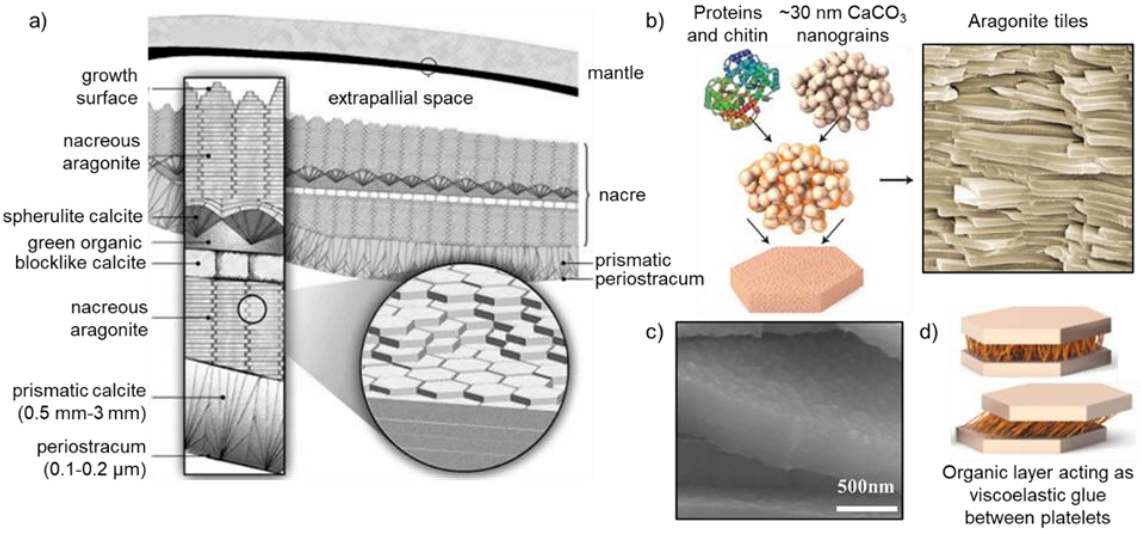

Figure 1.2. The multidimensional and hierarchical structure of nacre from the shell of a red abalone. **(a)** Depiction of the structure of a red abalone shell highlighting the layered composite nature of nacre. Reproduced with permission from ref 5.[5] **(b)** (Left) $CaCO_3$ nanograins (bricks) bound together with a protein/chitin matrix (mortar) to form tiled brick-and-mortar aragonite layers (right). **(c)** Scanning electron micrograph image of the polysaccharide/protein "mortar" matrix on the platelet of nacre. **(d)** Cartoon schematic of organic protein layer in between aragonite tiles that acts as glue to bind tiles together. Figures reproduced and adapted with permission from refs 5, 9, and 10.[5,9,10]

The term "self-assembly" has been used broadly and extensively in the literature, which has generated many varying definitions and interpretations.[3] In this dissertation, the definition of self-assembly will be restricted to "the spontaneous and hierarchical organization of smaller, disordered pre-existing units into a larger distinct arrangement or structure as a consequence of specific, local interactions without external direction".[3,11] Ordering smaller components into lower entropy complex structures *via* self-assembly is not restricted to atomic and molecular examples as this process also extends to larger structures which appear in nature such as the formation of mammalian cells,[3,12] weather systems,[12] and galaxies.[12] Within the context of atomic and molecular assemblies such as nucleic acids and proteins, their assembly into larger structures is typically governed by non-covalent interactions such as π-π stacking, hydrogen bonding,

electrostatic forces, van der Waals forces, hydrophobic effects, and host-guest interactions.[13] The relative strength of these interactions is outlined in Table 1.1 and when their strengths are viewed individually, these interactions are relatively weak compared to covalent bond energies but their cumulative effects collectively stabilize the supramolecular assembly.[13]

Table 1.1. Strengths of several non-covalent interactions involved in self-assembly[13,14]

Interaction	Strength (kJ/mol)
Covalent bond	100-400
Coulombic force	250
Hydrogen bonding	10-65
Dipole-dipole	5-50
π-π stacking	0-50
van der Waals forces	< 5
Hydrophobic effects	Difficult to assess

The tobacco mosaic virus (TMV) offers a sophisticated demonstration of viral self-assembly. The genetic material of TMV is composed of a single-stranded RNA molecule encased by a protective protein capsid that provides environmental stability by preventing degradation of the coiled RNA strand by cellular enzymes (Figure 1.3a). The capsid is formed by the hierarchical organization of 2,130 identical protein subunits that assemble to produce monodisperse structures that are 300 nm long and 18 nm wide (Figure 1.3b).[15] The regularity of the resulting structures is due to a templating effect by the RNA molecule caused by the specific length and sequence of its nucleotides.[16] Under physiological conditions, formation of this protective capsid is initialized by assembly of the protein subunits into a cylindrical disk-like structure. Upon binding to a specific hairpin-like RNA sequence and incorporation of the RNA into the central hole of the disk, the disk undergoes a screw dislocation transformation.[17] This allows additional disks to add to the protein

capsid until construction of the assembly is completed. This is akin to a "nucleation-growth" self-assembly mechanism wherein disk dislocation can be thought of as the nucleation step while the subsequent association of protein disks and assembly of the remaining protein capsid can be thought of as the growth phase. Nature repeatedly uses the directed supramolecular assembly of pre-formed subunits to form higher complexity structures with remarkable reproducibility.

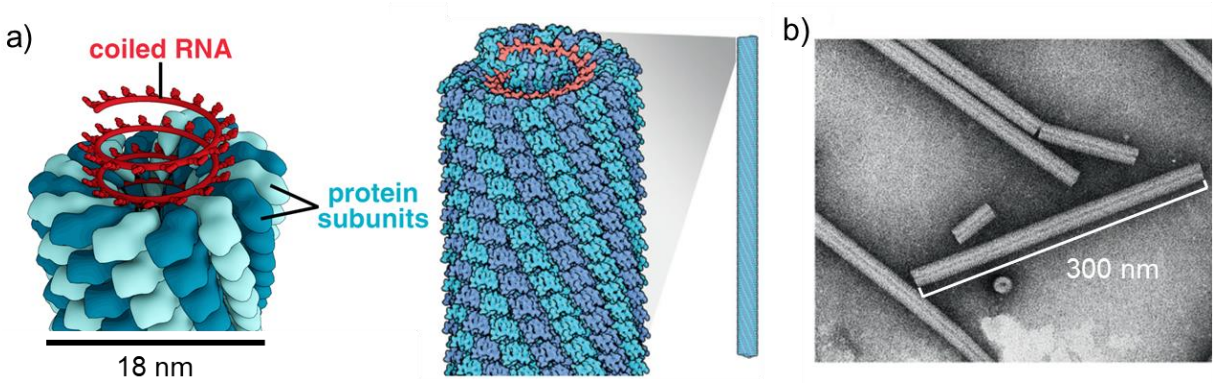

Figure 1.3. (a) Cartoon schematic and **(b)** transmission electron microscopy (TEM) micrograph of the tobacco mosaic virus. Reproduced and adapted with permission from refs 4 and 18.[4,18]

1.2 Supramolecular chemistry & nanoscale self-assembly *via* non-covalent interactions

As explored in the preceding section, nature has achieved synthesis across multiple length scales in a remarkably impressive manner (Figure 1.4a). Despite the incredible ability of nature to fabricate materials with well-defined dimension, functionality, and structural hierarchy at length scales down to 10^{-10} m, synthetic manufacturing from the nano- to micrometer scale remains a formidable challenge.[19] There are two main strategies for nanoscale fabrication: top-down and bottom-up (Figure 1.4b). Top-down manufacturing is a subtractive process wherein material is removed from a substrate to give a specific shape and size with a small-scale example including nanolithography that uses X-rays, extreme UV light, or electron beams to etch away material.[20,21]

Conversely, bottom-up manufacturing is an additive process whereby smaller subunits are assembled to form larger structures. At the nanoscale, bottom-up fabrication is exemplified by the field of supramolecular chemistry and self-assembly of atomic and molecular-scale objects into nano- and micromaterials with a specific pattern and structure.[22] Self-assembly of macromolecular building blocks such as block copolymers (BCPs) has emerged as a useful tool for nanoscopic manufacturing with tailored functionality; conveniently filling the current gap in our synthetic fabrication capabilities. BCPs can organize into a wide array of intricate nanostructures with tailorable structure and multifunctionality. These nano- and micrometer scale (10^{-9} to 10^{-6} m) materials have shown great promise in a wide range of applications such as therapeutic drug delivery, nanopatterning, composite material fabrication, and energy generation, and this thesis primarily focuses on the emerging optoelectronic applications of nanomaterials.[23,24]

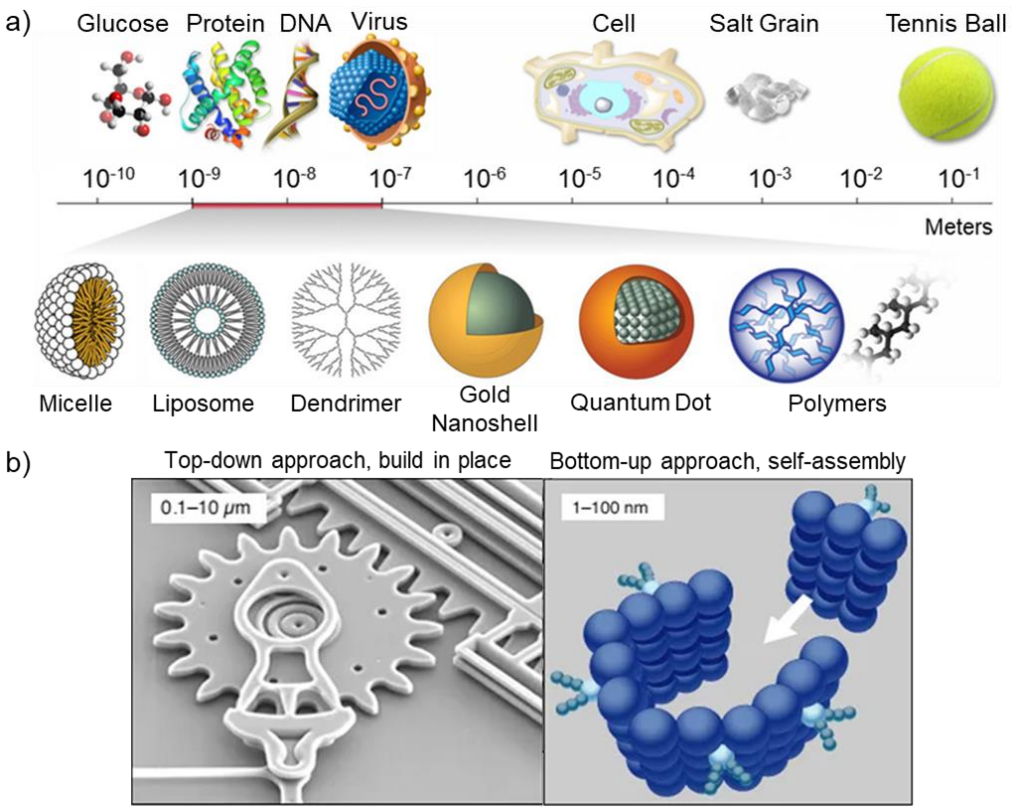

Figure 1.4. (a) Scale comparison of various natural and synthetic structures. Reproduced with permission from ref 25.[25] **(b)** Schematic showing the differences between "top-down" fabrication (left, scanning electron micrograph of a gear system formed by electron beam nanolithography) and "bottom-up" fabrication (right, organization of pre-existing subunits into a larger nanostructure). Reproduced with permission from ref 26.[26]

The fields of supramolecular chemistry and nanotechnology have a rich history. In 1959, the renowned physicist Richard Feynman presented a lecture to the American Physical Society entitled "There's Plenty of Room at the Bottom" where he proposed the ability to construct molecules through the direct manipulation of single atoms, enabling tailored chemical syntheses on an atom-by-atom basis.[27] He theorized about creating nanoscopic machines that autonomously assemble through the organized arrangement of atoms and imagined that they could directly move matter.[27] With these propositions, he laid the ideological groundwork for bottom-up assembly at the nanoscale wherein small pre-existing subunits arrange to form more complex structures in a

controlled fashion. Following this in the 1970's, the term supramolecular chemistry was introduced by Jean-Marie Lehn which was described as the "chemistry of molecular assemblies and of the intermolecular bond.[28] Lehn's work, along with pioneering investigations focusing on the development and use of molecules with highly selective structure-specific interactions by Cram and Pedersen was awarded the Nobel Prize in Chemistry in 1987. Coordinated self-assembly and molecular recognition in host-guest systems has resulted in a variety of novel supramolecular architectures with a wide range of applications including photocatalysis,[1] asymmetric synthesis,[1,29] explosives/nerve agent detection,[30–32] and photothermal/photodynamic therapies (Figure 1.5a-d).[33–36]

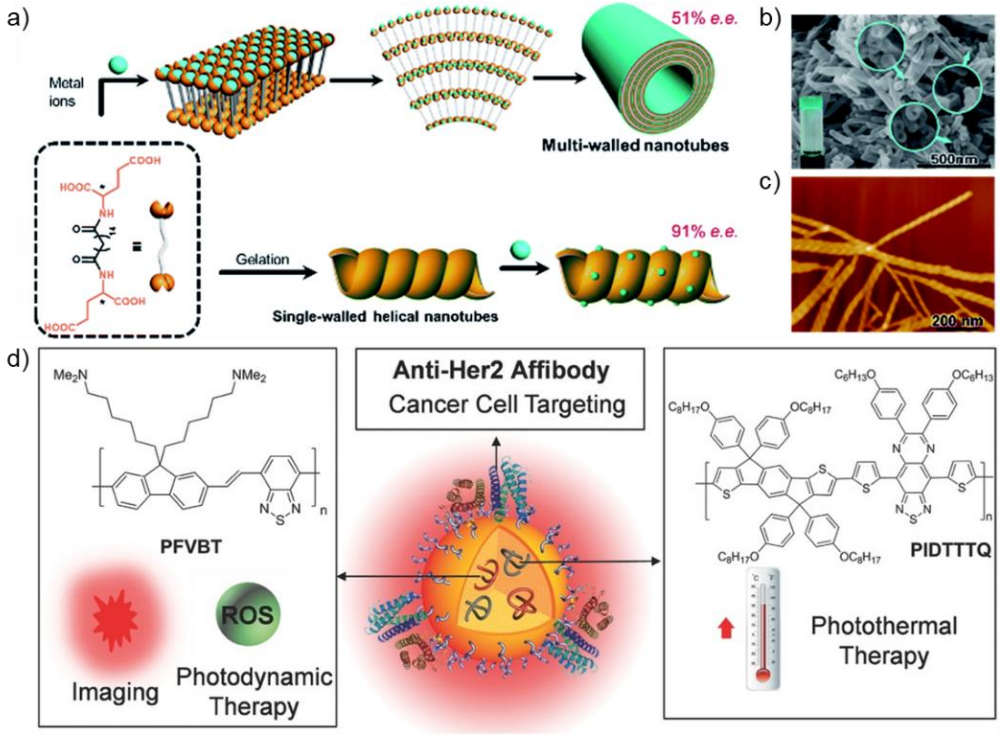

Figure 1.5. (a) Schematic illustration showing nanostructure morphology difference during hierarchical self-assembly of multi-walled nanotubes (top) and single-walled helical nanotubes (bottom).[1] **(b)** Scanning electron microscopy (SEM) image of multi-walled nanotubes and **(c)** atomic force microscopy (AFM) image of single-walled helical nanotubes. Figures (a-c) reproduced with permission from ref 1.[1] **(d)** Schematic illustration of π-conjugated polymer nanoparticles (CPNPs) decorated with anti-Her2 affibodies used for cancer call targeting and photodynamic/photothermal therapy. Reproduced with permission from ref 36.[36]

1.3 Self-assembly of small molecules

When considering the self-assembly of carbon-based molecular species into supramolecular assemblies, there are two main categories of building blocks: the first category comprises "head-and-tail" amphiphiles, while the second category consists of polymeric amphiphiles such as block copolymers (BCPs).[13] Two common examples of low molecular weight "head-and-tail" amphiphiles are lipids and surfactants. These molecules contain a solvophilic, polar "head" group, and a solvophobic, non-polar "tail" group typically consisting of a hydrocarbon chain (Figure 1.6a). When placed in polar solvents such as water, these amphiphiles spontaneously assemble into nanostructures provided that the concentration is above a specific equilibrium concentration known as the critical micelle concentration (CMC). Water selectively solvates the solvophilic head group and the hydrophobicity of the hydrocarbon tails drives their aggregation to form core-shell micelles with an inner hydrophobic core and an outer solvated shell or corona through a process known as micellization. Micellization of molecular amphiphiles in water is mainly driven by the increase in entropy associated with the expulsion of solvating molecules.[37] Aggregation of the hydrophobic tails to form the micelle core minimizes enthalpically unfavorable hydrophobe−water interactions and the solvophilic head groups forms the micelle corona which maximizes solvent contact by pointing outward towards the solvent. Exposure of the hydrophilic head groups toward the water and sequestration of the hydrophobic tails in the micelle core prevents disruption of hydrogen bonding between water molecules, leading to a further reduction in the total free energy of the system.[37,38] It is important to note that these are equilibrium structures at the thermodynamic energy minimum where dynamic exchange of surfactants between the micelles and solution occurs and amphiphiles can escape the assemblies and dissolved amphiphiles can enter assemblies at equal rates with no net flow of energy or matter.[39]

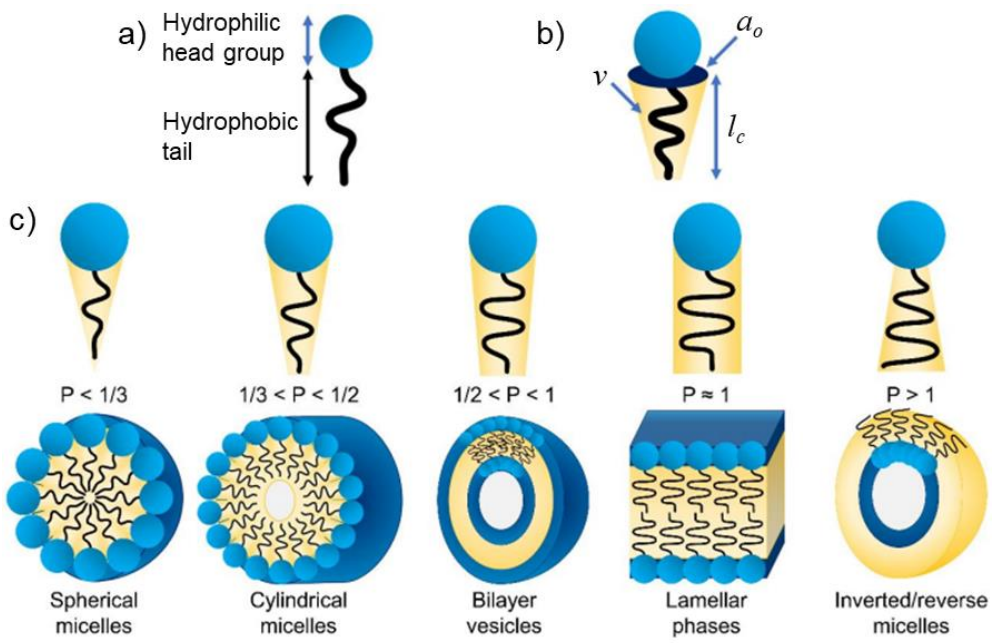

Figure 1.6. (a) General structure of "head-and-tail" amphiphiles with a hydrophobic head (blue) and a hydrophobic tail (black/yellow). **(b)** Schematic showing the general factors affecting the packing parameter (*P*). **(c)** Schematic showing the dependence of thermodynamic micelle morphology on the packing parameter, *P*. Reproduced and adapted with permission from ref 42.[42]

Above the CMC, a multitude of diverse nanostructure morphologies are obtainable including spherical micelles, cylindrical micelles, bicontinuous structures, vesicles, and lamellar structures.[40,41] One metric used to characterize these structures is the degree of interfacial curvature at the core-corona interface. The micelle morphology can be predicted using the packing parameter (*P*) (Equation 1.1) where v is the volume of the solvophobic core segment, a_o is the contact area of the head group at the aggregate interface, and l_c is the length of the core segment (Figure 1.6b). The resulting micellar morphologies are a direct consequence of the molecular amphiphile structure and what the optimal packing of these structures are with respect to the minimization of thermodynamically or entropically unfavorable interactions. In general, as the packing parameter increases, the interfacial curvature decreases. High curvature spherical micelles are preferred if $P \leq \frac{1}{3}$, cylindrical worm-like micelles are preferred if $\frac{1}{3} < P \leq \frac{1}{2}$, and low curvature bilayers, vesicles,

and planar lamellae are preferred if $P \geq \frac{1}{2}$. If P is larger than 1, inverted or reverse micelles form where the interfacial curvature becomes negative (Figure 1.6c).

$$\boldsymbol{P = \frac{v}{a_0 l_c}} \qquad \textbf{Equation 1.1}$$

1.4 Self-assembly of block copolymers in the solid state

Next, we will consider the other main class of carbon-based molecular amphiphiles capable of supramolecular assembly, polymeric amphiphiles. Diblock copolymers are polymeric amphiphiles with two chemically different blocks that are typically covalently linked. In the solid state, BCPs with two immiscible blocks microphase separate into various self-assembled nanostructures. The unfavorable mixing enthalpy between the two blocks combined with a small mixing entropy drive self-assembly while the covalent linkage between the blocks prevents macroscale phase separation.[41]

In the case of A-B diblock copolymers where A≠B, the phase separation and resulting nanostructure morphology is a consequence of many factors such as: the volume fraction of the A and B blocks (f_A and f_B, where $f_A + f_B = 1$), the total degree of polymerization (DP_n) of the BCP ($DP_n = DP_{n(A)} + DP_{n(B)}$), the chemical composition of each block, and the degree of incompatibility between the A and B blocks.[41] The degree of incompatibility between blocks arises from their immiscibility which drives self-assembly in bulk and is described by the Flory-Huggins parameter (χ_{AB}). Modification of the size of each block or the introduction of multiple blocks (such as in the case of triblock copolymers or miktoarm copolymers) can be used for further structural tailoring and facilitates the production of other distinct morphologies.

1.5 Solution self-assembly of block copolymers with an amorphous core-forming block

Similar to molecular surfactants, BCPs can self-assemble in solution by adding a solvent that selectively solvates one of the blocks, known as a selective solvent. The result is colloidally stable core-shell micellar nanoparticles, where the core consists of an insoluble, solvophobic block, and the shell consists of a soluble, solvophilic block. This provides access to a range of novel and exotic structures including "crew-cut" micelles, large compound micelles, and baroclinic tubules (Figure 1.7).[41] However, unlike solution self-assembly of small molecule surfactants or solid-state BCP self-assembly, solution-phase BCP self-assembly involves interactions between a solvent and a given BCP with considerably more thermodynamic and kinetic factors, making prediction of the final morphology more difficult. These kinetic and thermodynamic factors are discussed below.

The packing parameter (Equation 1.1) can be used to estimate the final micelle morphology, but this equation purely involves thermodynamic considerations and has limitations when applied to BCP solution self-assembly. In particular, solvent-induced swelling of the corona can increase the effective volume fraction of the corona-forming block such that the a_0 term in the packing parameter equation (P) does not accurately describe the area of the head group at the aggregate interface.

In the case of solution self-assembly of BCPs with an amorphous core-forming block, the thermodynamically preferred morphology is primarily governed by three factors: 1) the degree of chain-stretching of the core-forming block, 2) the degree of interfacial energy between the core-forming block and the solvent, and 3) repulsive interchain interactions between coronal blocks. The morphology can be further modified by changing the BCP concentration, the length of each

BCP block, composition of the solvent system, temperature, processing method, or through the addition of additives (such as ions or homopolymers).[43–46]

One key difference between solution self-assembly of molecular amphiphiles and polymeric amphiphiles is that nanostructure formation in polymeric amphiphiles is typically kinetically controlled. Exchange of BCPs between the formed micelles and solution occurs very slowly or is non-existent due to the high energetic barrier that needs to be overcome to reach the global potential energy minimum. These structures are kinetically trapped in a local energetic minimum meaning that different structures can arise from the same BCP depending on the self-assembly conditions, which is known as non-ergodicity.[41,47] The kinetically trapped nature of structures formed by amorphous-core BCP self-assembly also contributes to the difficulty predicting the final micelle morphology compared to equilibrium surfactant self-assembly.

In amorphous core BCP solution self-assembly, the final micelle morphology results from a balance between enthalpic and entropic factors. Because the two blocks are immiscible, and therefore mixing is unfavorable, the structures seek to reduce the interfacial area between the blocks which lowers enthalpy, causing chain stretching away from the ideal chain conformation. They form the structure with the lowest possible amount of core chain stretching which is an entropic contribution. To reduce enthalpy and increase entropy, the system balances the lowest interfacial energy and the least amount of chain stretching. High curvature structures are favoured with BCPs that have corona-forming blocks with a large volume fraction as this reduces the core-corona interfacial area and chain stretching. Typically, for a given BCP, solution-phase self assembly results in the formation of higher core-corona interfacial curvature assemblies like spheres when compared to solid state self-assembly due to increased repulsive interactions between swollen solvated coronal chains and an increased effective coronal volume fraction. Phase

space maps depict the different possible nanostructure morphologies accessible by a given BCP and helps predict which structure will form under specific conditions. The region of phase space occupied by low interfacial curvature structures like 1D nanofibers and 2D platelets is generally small when using amorphous BCPs so it is typically difficult to access morphologically pure samples of these assemblies, and mixtures of different morphologies are usually obtained.[40]

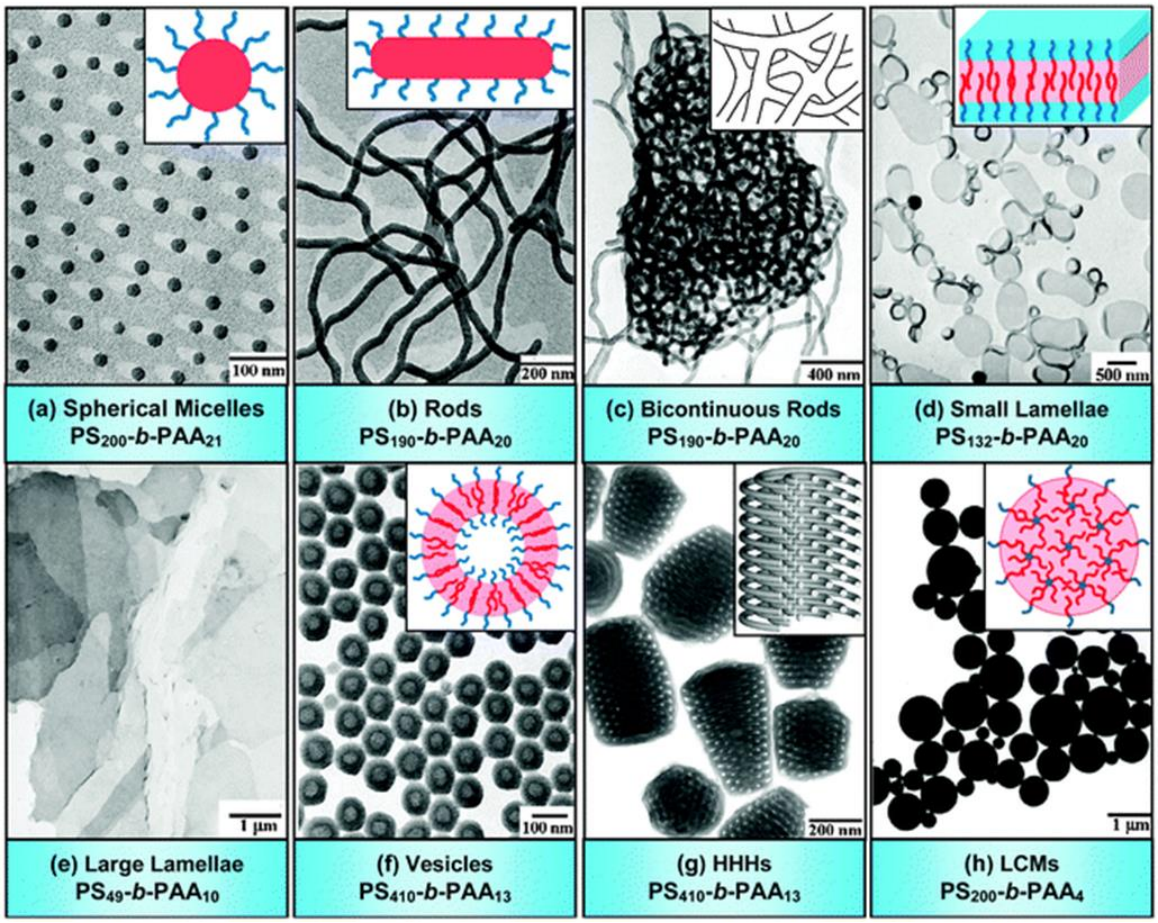

Figure 1.7. TEM micrographs and corresponding cartoon schematics of various morphologies produced by self-assembly of amphiphilic polystyrene-*b*-poly(acrylic acid) (PS_m-*b*-PAA_n) BCPs in dioxane:water mixtures. m and n represent the degrees of polymerization (DP_n) of PS and PAA, respectively. In schematics, red portions depict hydrophobic PS segment and blue portions depict hydrophilic PAA segment. HHHs: hexagonally packed hollow hoops. LCMs: large compound micelles. Reproduced with permission from ref 41.[41]

1.6 Solution self-assembly of block copolymers with a crystalline core-forming block

During solution self-assembly of amphiphilic BCPs with a crystallizable core-forming block in a corona-selective solvent, crystallization occurs which produces micelles with a crystalline core.[48] Crystalline-core BCPs exhibit a strong preference toward generating non-spherical, low-interfacial curvature nanoparticles such as cylinders and platelets because core-crystallization provides an additional enthalpic contribution, as opposed to solely solvophobic interactions which dominate amorphous core BCP self-assembly. Crystallization has such a key influence in determining the structure and organization of the resulting micelle that this class of self-assembly is referred to as "crystallization-driven self-assembly" (CDSA).[49] Crystalline-core BCP self-assembly drastically expands the phase space occupied by low-interfacial curvature assemblies and provides access to numerous 1D and 2D morphologies which are difficult to obtain using amorphous BCPs. Until recently, access to morphologically pure samples of these structures has been restricted which has hampered their practical investigation and application.

CDSA has two distinct phases: nucleation and elongation.[50] First, homogeneous, or self-, nucleation occurs by aggregation of the BCP core-forming block to form a crystallite. Established methods to achieve this include: 1) dissolving the BCP in a solvent that is suitable for both blocks (common solvent) and adding solvent which selectively solvates the corona-forming block (corona-selective solvent) or 2) by heating the BCP in a temperature-dependent selective solvent that acts as a common solvent at high temperatures and a corona-selective solvent at ambient temperature. Crystallization is an exothermic process that lowers energy by forming a more stable, ordered structure with minimized potential energy and strong bonding interactions, despite a decrease in entropy. The CMC for BCPs is significantly lower than for molecular surfactants and

this, combined with the energetic stabilization gained by crystallization makes the CMC negligible for crystalline-coil BCPs.[47] However, rearranging solvated BCPs (unimer) into configurations that permit crystallization still requires an input of energy and this energetic barrier prevents spontaneous formation of nuclei from unimer aggregation (Figure 1.8). When the conditions for nucleation are met, nucleation occurs stochastically, generating nuclei at different times and locations in a solution so growth from each nucleus is not initiated simultaneously which results in micelles with varying lengths or areas (polydisperse).[51] Once nuclei form, the thermodynamic energy barrier has been overcome and elongation becomes significantly more favorable which occurs when more unimer adds to the nucleus through epitaxial crystallization resulting in the growth of larger micelles (Figure 1.8).[50]

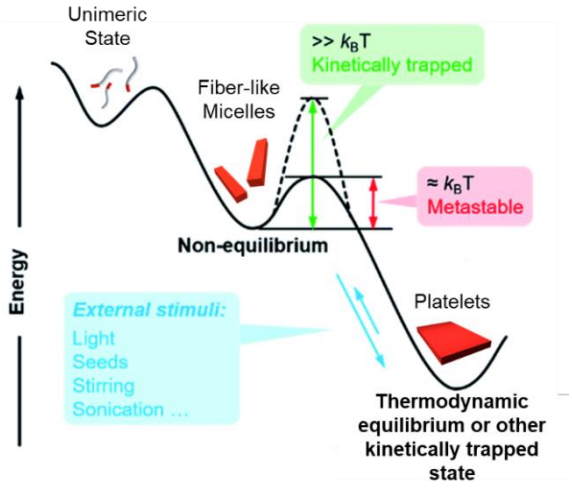

Figure 1.8. Thermodynamic potential energy diagram showing formation of 1D micelles from unimer nucleation and subsequent elongation. The potential formation of 2D micelles from 1D fibers is also shown. k_BT= Boltzmann constant multiplied by temperature which equals the thermodynamic energy according to $E=k_BT$. Reproduced and adapted with permission from ref 1.[1]

As with amorphous core BCP self assembly, crystalline core BCP self-assembly is a complex process with contributions from many factors that dictate the final micelle morphology. In general, chain repulsion between adjacent coronal units induces formation of high interfacial

curvature structures while introduction of a crystallizable core-forming block counteracts these effects by producing a lattice energy that favors formation of an interface with zero curvature. The effect of BCP crystallization on micelle morphology was first described by Keller *et. al.* which showed that self-assembly of poly(ethylene glycol)-*b*-poly(styrene) (PEG-*b*-PS) in ethylbenzene, a solvent selective for PS, resulted in 2D platelets with a PEG core.[52] Crystal diffraction studies revealed that the PEG platelet core exhibited the same unit cell as that of PEG homopolymer and crystallization of the PEG core forms a nucleation site that can initiate further crystal growth.[52]

While core-crystallization plays a dominant role in determining morphology in crystalline-coil BCP self-assembly, the coronal block size, nature of the polymer backbone, relative core:corona block ratio, temperature, and self-assembly solvent system also play important roles. These factors all impact whether 1D fibers or 2D platelets are the experimentally observed morphology. Generally, a shorter coronal block occupies less volume, thereby reducing intercoronal repulsion, leading to lower interfacial curvature structures like 2D platelets. For example, terminating poly(ferrocenyldimethylsilane) (PFS) or poly(L-lactic acid) (PLLA) crystalline homopolymers with a positively-charged phosphonium group, which occupies a smaller volume compared to a coronal chain, resulted in the formation of colloidally-stable 2D platelets. However, when poly(3-hexylthiophene) (P3HT) or poly(fluorenyltrimethylcarbonate) (PFTMC) homopolymers were terminated using the same phosphonium end-group, the formation of 1D nanofibers was preferred over 2D platelets which was postulated to be the result of strong π–π stacking interactions between polymer chains within the micelle core, highlighting how BCP chemical composition affects nanostructure morphology.[53–55] Even though reducing the corona-forming block volume fraction generally favors the formation of 2D platelets, self-assembly of BCPs with higher corona block content relative to the core-forming block can also result in 2D

platelets through a core plasticization mechanism. In a study comparing nanostructure morphologies resulting from self-assembly of PFS-*b*-poly(2-vinylpyridine) (P2VP) BCPs with core:corona block ratios of either 5:1 or 1:1 in various THF/isopropanol (*i*PrOH) mixtures, the authors found that spheres preferentially formed at low THF content (10%) but the spheres slowly transformed into 2D lenticular platelets.[56] Platelet formation was slower for the BCP with a 5:1 core:corona ratio compared to the BCP with a 1:1 ratio even though it had less corona block content. This was attributed to the fact that the core-forming block was larger and had a slower crystallization rate arising from the relatively increased molecular motions necessary for it to crystallize. Core-crystallization and the resulting preferred morphology can also be modified by manipulating self-assembly solvent conditions. A study investigating PFS-*b*-P2VP BCPs with the same core:corona block ratios of 1:6 but different overall molar masses found that increasing the THF fraction (a good solvent for both blocks) in THF:*i*PrOH mixtures caused a transition from spheres to platelets.[57] By adding more common solvent, unimer solubility is increased which results in slower crystallization and plasticization of the micelle core, leading to a more thermodynamically favored morphology.

CDSA has been performed using a wide variety of crystallizable core BCPs including PFS,[50,58,59] poly(ferrocenyldimethylgermane) (PFG),[60–62] polyethylene (PE),[63] PLLA,[24,64,65] poly(ε-caprolactone) (PCL),[66,67] polycarbonate,[68,69] P3HT,[70–72] poly(tellurophene),[73] poly(di-*n*-hexylfluorene),[74,75] and poly(*p*-phenylene vinylene).[76,77] CDSA is a convenient methodology for the fabrication of morphologically pure samples of low interfacial curvature cylinders and platelets which are desirable for a myriad of advanced applications.[23,49] Unfortunately, control over the distribution of micelle lengths or areas is challenging because nucleation occurs at random locations in solution and has a slow rate compared to epitaxial growth.[51]

1.7 Living crystallization-driven self-assembly and emerging applications

Living crystallization-driven self-assembly (CDSA) of BCPs with a crystallizable core-forming block has emerged as a useful method to generate low length dispersity ($Đ_L$<1.1, where $Đ_L = L_w/L_n$) samples of 1D nanofibers with controlled size and dimensions.[23,34,59,65,71,77–80] Two main self-assembly methods exist under the umbrella term "living CDSA": the seeded growth method and the self-seeding method. Formation of length-controlled 1D micelles will be used for the following general examples but the same processes apply to 2D micelles. The first approach is the seeded growth method which begins with the formation of long polydisperse nanofibers through homogeneous nucleation described in Section 1.6.[50,59] The long fibers are subsequently fragmented using ultrasonication to generate "seed" micelle fragments with relatively short average lengths (L_n).[50,59] Unimer, in a solvent suitable for both blocks, is added to the seed solution and preferentially crystallizes on the seed termini (as opposed to self-nucleating), resulting in controlled-length micelles which are near monodisperse ($Đ_L$ < 1.1). A linear relationship between the unimer-to-seed mass ratio (m_{unimer}/m_{seed}) and micelle length exists, offering a substantial degree of fine control over the size and production of fibers with predictable lengths (Figure 1.9, 1.10). This method also provides the ability to fabricate coronally segmented B-A-B triblock comicelles by adding unimer with the same core-forming block but a chemically distinct corona-forming block from the BCP used for the seed.

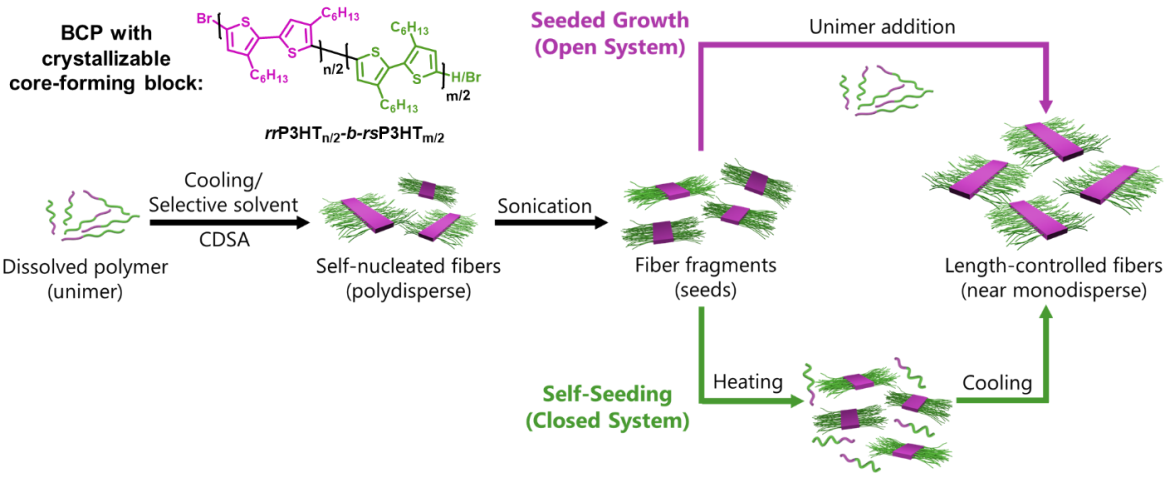

Figure 1.9. Schematic depiction of the living CDSA seeded growth method (top, purple pathway) and the living CDSA self-seeding method (bottom, green pathway). P3HT = poly(3-hexylthiophene), *rr*: regioregular, *rs*: regiosymmetric, n/m: degrees of polymerization.

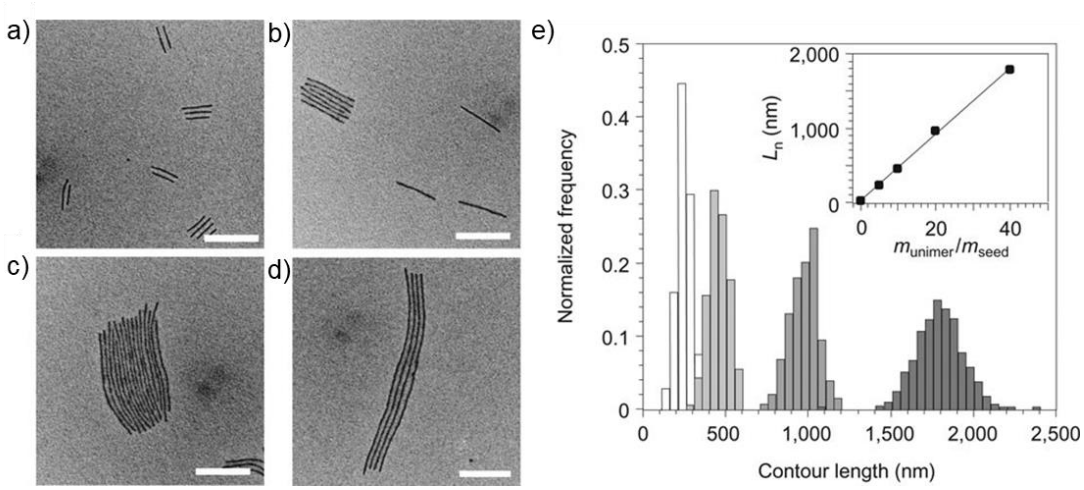

Figure 1.10. TEM images of 1D cylindrical nanofibers made by living CDSA seeded growth by treating seed micelles with varying equivalents of unimer equal to unimer-to-seed ratios (m_{unimer}/m_{seed}) = **(a)** 5, **(b)** 10, **(c)** 20, and **(d)** 40. Scale bars: 500 nm. **(e)** Contour length distribution histograms of samples a–d. Inset shows linear dependence of micelle length on unimer-to-seed ratio (m_{unimer}/m_{seed}). Reproduced with permission from ref 59.[59]

The second living CDSA approach is thermal self-seeding and this method involves generating seeds *in situ* by heating seeds in a selective solvent to induce dissolution of the less crystalline regions of the seeds (Figure 1.9).[52,58,81–83] Seed dissolution generates free unimer which,

upon cooling, crystallizes epitaxially onto the termini of the surviving seeds resulting in length-controlled nanofibers. The nanofiber lengths are dependent on the unimer-to-seed ratio which itself strongly depends on the self-seeding temperature. As the temperature is increased, the number of surviving seeds decreases and the amount of unimer released into solution increases, resulting in longer nanofibers. Small modulations of the self-seeding temperature can result in large nanofiber length differences which makes prediction of the final lengths more challenging compared to seeded growth. The exponential nature of the length versus self-seeding temperature curve also makes it difficult to obtain short nanofibers (Figure 1.11).[58,81] Furthermore, the temperature at which polymer crystals melt depends on their thermal history and sample crystallinity, implying that the self-seeding temperatures are batch-dependent.[81,84–86] Although these are potential disadvantages, self-seeding typically produces longer nanofibers because of the exponential relationship between self-seeding temperature and micelle length and a proposed thermal annealing effect that the heating process has on the polymer chains.

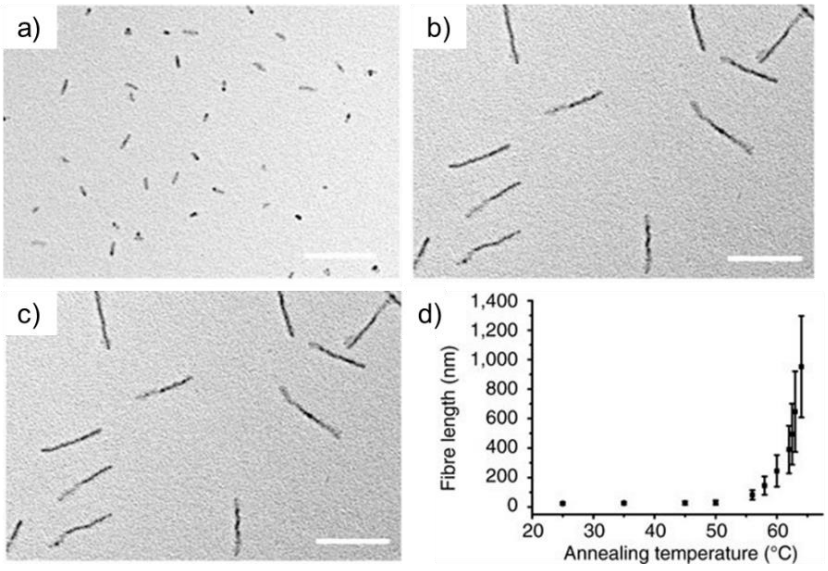

Figure 1.11. TEM micrographs of 1D cylindrical nanofibers made by living CDSA self-seeding by heating seed micelles to **(a)** 56 °C, **(b)** 62.5 °C, and **(c)** 64 °C for 30 min. and then cooling to 23 °C over 6 h. Scale bars: 500 nm. **(d)** Plot showing exponential relationship between nanofiber length and the self-seeding temperature. Reproduced with permission from ref 83.[83]

When living CDSA is performed by seeded growth or self-seeding, formation of new seed nuclei instead of epitaxial growth from existing seeds is a persistent issue. Self-nucleation consumes available unimer causing deviations from predicted lengths and formation of short micelle fragments, thereby increasing sample dispersity ($Đ_L$). Self-nucleation is particularly prevalent when using P3HT-based BCPs because of strong intermolecular π-π stacking interactions that drive P3HT crystallization.[87–89] Recently, a method that effectively suppresses unimer self-nucleation was developed and reported by our group termed "self-nucleation suppression".[86] The method involves firstly heating a nanofiber solution to a temperature where the nanofibers fully dissolve and the BCP is in the fully unimeric state. The solution is then cooled to the lowest temperature at which a supersaturated solution forms, but nucleation does not occur. Seed nuclei are added to the supersaturated solution at this self-nucleation suppression temperature, which results in efficient epitaxial growth from the seed termini. Because the solution is held at a temperature where homogeneous nucleation is suppressed, growth from the added seeds is favored over the generation of new nuclei. This also consumes available unimer so that when the solution is cooled from the self-nucleation suppression temperature to ambient temperature, there is a lower concentration of unimer present in solution capable of self-nucleation, resulting in longer fibers and a lower incidence of small self-nucleated fiber fragments, thereby reducing $Đ_L$. Self-nucleation suppressed seeded growth of the BCP *rr*P3HT-*b*-*rs*P3HT (*rr* = regioregular and *rs* = regiosymmetric, respectively) allowed for the formation of length-controlled nanofibers with lengths up to 4 μm with $Đ_L < 1.09$; the first example of length-controlled P3HT BCP nanofibers made by seeded growth with lengths over 2 μm.[86] Use of this method to form long, well-defined polythiophene-based fibers, as well as a deeper discussion on the nucleation/growth process is found in Chapter 2.

An extensive variety of crystallizable core-forming block BCPs with different coronal chemistries have been investigated to precisely create a vast range of novel and bespoke architectures with varying shapes and functions. Nanostructures assembled from PFS-based macromolecules include fluorescent barcode nanofibers utilized to encode information,[90] hollow platelet micelles,[91] rectangular platelets,[53,92] quasi-hexagonal discs,[53] homogeneous and heterogeneous lenticular platelets,[56,57,93] double-headed spear-like micelles,[93] and dendritic structures with controlled branching that can be used for hazardous anion detection (Figure 1.12).[62] The higher-order hierarchical assembly of PFS-based nanostructures has resulted in the formation of multidimensional "cross" and "windmill" supermicelles,[94] surface-confined micellar brushes,[95,96] and 3D supermicellar networks/lattices (Figure 1.12).[97]

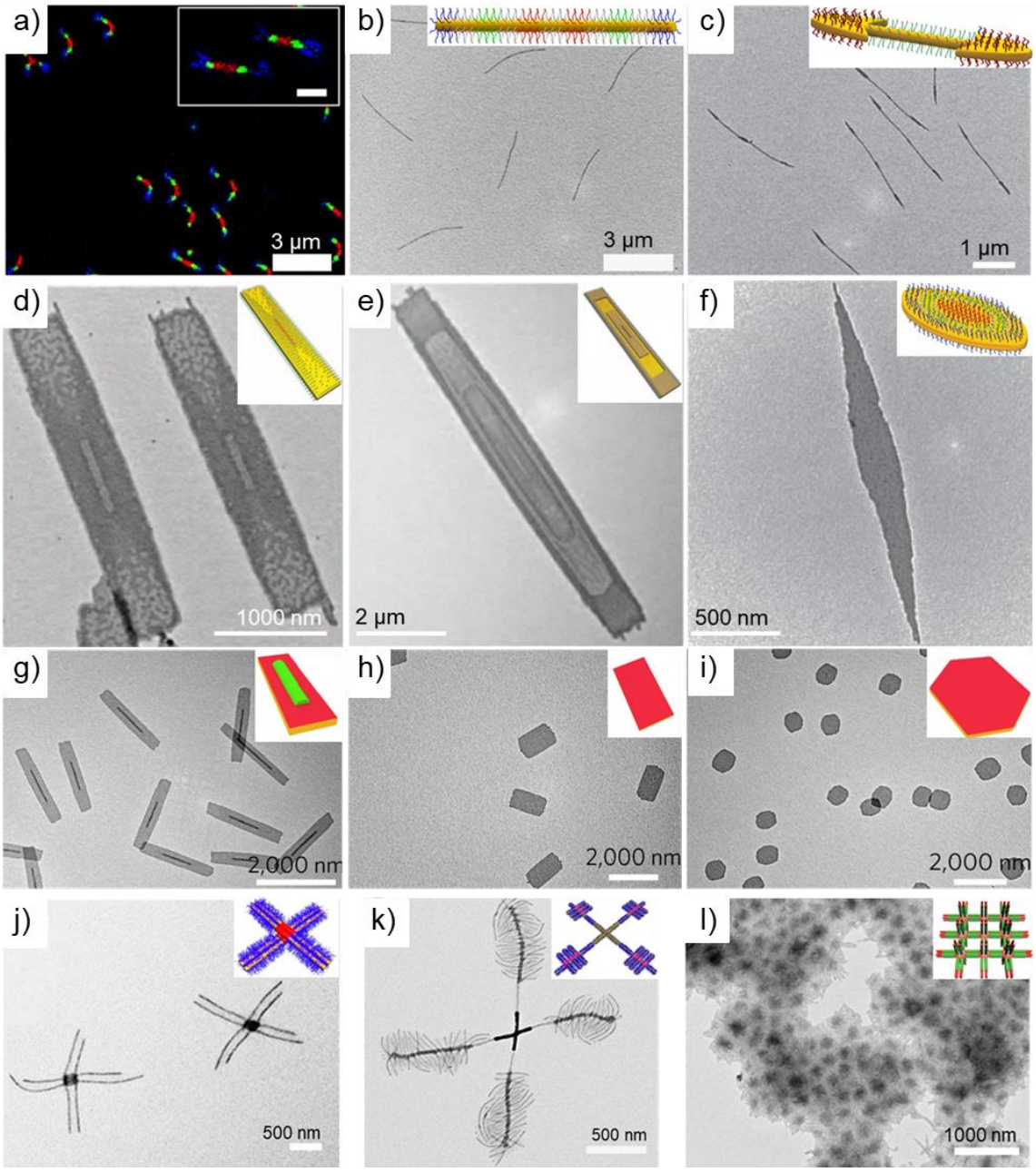

Figure 1.12. Examples of PFS-based nanostructures assembled *via* living CDSA with cartoon schematics representative of the structures in each TEM micrograph (top corners). **(a)** Laser scanning confocal microscopy (LCSM) micrograph of fluorescent, color tunable 11-block comicelles.[90] **(b)** TEM micrograph of multiblock fluorescent micelles.[90] **(c)** TEM micrograph of double-headed spear-like micelles.[93] **(d)** TEM micrograph of "patchy" 2D nanoplatelet micelles.[91] **(e)** TEM micrograph of "patchy" rectangular platelet multiblock comicelles.[91] **(f)** TEM micrograph of 2D concentric lenticular block comicelles.[93] **(g, h)** TEM micrographs of rectangular 2D platelets.[53] **(i)** TEM micrograph of quasi-hexagonal 2D platelets.[53] **(j, k)** TEM micrograph of "cross" and "windmill" supermicelles.[94,98] **(l)** TEM micrograph of 3D supermicellar networks.[97] All TEM micrographs and cartoons reproduced with permission from their respective publishers.

Nanostructures made by living CDSA of biocompatible polymers such as PCL, PLLA, PFTMC, and other polycarbonates have demonstrated utility in a wide variety of biomedically relevant applications ranging from drug[99] and DNA delivery,[100,101] cell targeting,[102] as adhesive hydrogels,[24] emulsifiers,[64] and antimicrobials.[103,104] As an example, size-controlled diamond 2D platelets with a PLLA core were used to analyze the structure-property relationship between platelet surface area and emulsion stabilization.[64] This emphasizes that tuning the dimensionality of 2D platelets allows for custom design and realization of effective interfacial stabilizers for application in water-in-water emulsions.

1.8 π-Conjugated polymers

π-Conjugated polymers are macromolecules with monomeric units that are formally connected by continuous σ-bonds and alternating π-bonds along their backbone (Figure 1.13a). Specifically, the π-overlap of p_z atomic orbitals perpendicular to the polymer backbone creates a conjugated chain of delocalized electrons (Figure 1.13b), resulting in materials that absorb light in the ultraviolet (UV) to infrared (IR) range.[105–108] Organic polymeric semiconductors are solution-processable, have inexpensive manufacturing processes, and can be printed on large-area flexible substrates.[109–112] Synthetic modification of the conjugated scaffold with side chains and functional groups can tune their solubility, charge transport capabilities, molecular packing, and optical properties. Their modular optical and semiconducting properties make them excellent candidates for application to a variety of useful optoelectronic devices such as organic field-effect transistors (OFETs), organic light-emitting diodes (OLEDs), organic photovoltaics (OPVs), and stretchable electronics.[109,113–115]

Exploration of their electronic properties was largely facilitated by significant advances made in their synthesis. The first known conductive polymer was polyacetylene (Figure 1.13a), described in 1977 by Shirakawa, MacDiarmid, and Heeger, which earned them the Nobel Prize in Chemistry in 2000. Since then, an extensive library of conjugated polymers have been synthesized which include examples such as poly(aniline), poly(thiophene), poly(fluorene), and poly(*p*-phenylene vinylene) (PPV) (Figure 1.13a). In particular, regioregular P3HT (*rr*-P3HT) is the most used conductive polymer in organic electronics due to its high molar extinction coefficient, charge carrier mobility, and solution processability.[116,117] The first synthesis of low dispersity *rr*-P3HT was reported by McCollough *et al*. in 1999[118] using a Kumada-type polycondensation and then in 2004, the groups of Yokozawa[119] and McCollough[120] independently reported that the synthesis exhibited features of a controlled, or living, chain-growth mechanism which affords polymers with predictable molecular masses that are linearly dependant on the monomer/catalyst ratio and narrow dispersity. The reaction type is now known as Grignard Metathesis (GRIM) or a Kumada catalyst-transfer polycondensation (KCTP). Since its description, the scope of CTP reactions has been drastically expanded beyond thiophenes to include an expansive array of monomers.[105,121–125] KCTP has been utilized extensively to create many well-defined π-conjugated polymers with interesting electronic properties, as well as allowing for one-pot syntheses of block and gradient copolymers.[105,125,126]

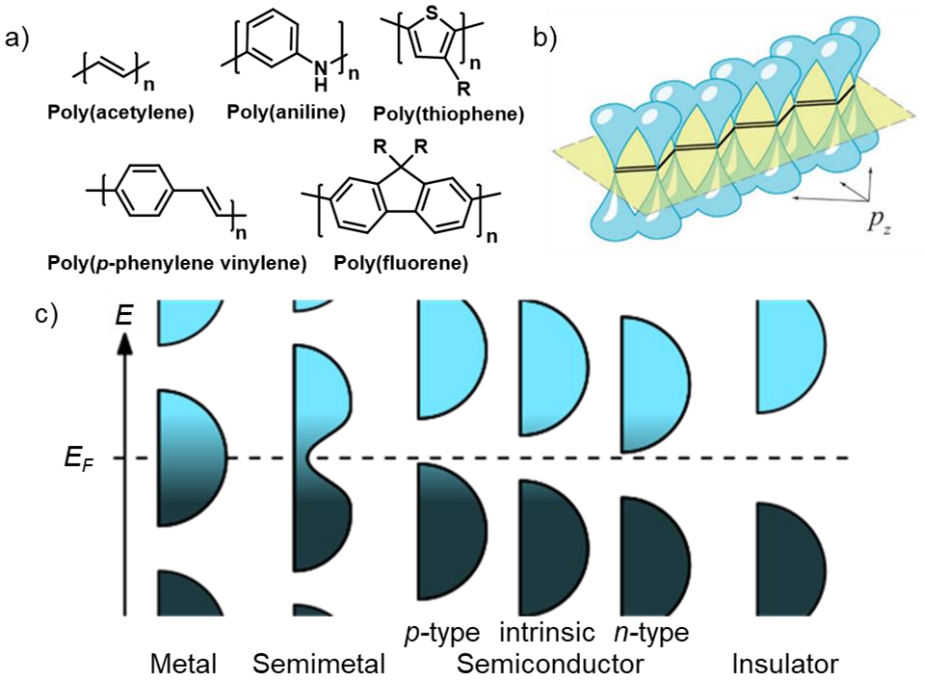

Figure 1.13. (a) Chemical structures of commonly used π-conjugated polymers. **(b)** Conjugated backbone of polyacetylene with overlapping p_z orbitals that are oriented perpendicular to the molecular plane. Reproduced with permission from ref 108.[108] **(c)** Energy level diagram comparing bandlike structures and bandgaps of metals, semimetals (such as graphite with bandgap = 0 eV), semiconductors, and insulators. Grey = valence band; blue = conduction band. E_F: Fermi level. Reproduced and adapted with permission from ref 127.[127]

π-Conjugated polymers generally adopt a planar conformation in the solid state and this planarity, along with favorable π-π-stacking interactions, drives self-assembly to form semicrystalline ordered domains. Efficient intra- and inter-chain π-orbital overlap establishes effective avenues for the flow of charges through the material. Their semiconductive and optoelectronic properties can be explained through band theory (Figure 1.13c). As the number of orbitals in a material increase, the energy differences between the discrete levels becomes smaller. Eventually, the orbitals become so abundant and close in energy that they can be viewed as continuous "bands". The energetically highest occupied molecular orbitals (HOMOs) of the repeat units form the valence band and the energetically lowest unoccupied molecular orbitals (LUMOs)

form the conduction band (Figure 1.13c), with the energy difference between both bands referred to as the "bandgap". Electrons can be promoted from the valence band into the conduction band if sufficient energy is provided, where they can then participate in conduction. In insulating materials, the energy bandgap is large meaning that there is no or very little movement of electrons from the valence band to the conduction band without the absorption of large amounts of energy. In conductive materials such as metals, the valence and conduction bands overlap meaning that there is free movement of charge carriers at ambient temperature. In intrinsically semiconductive materials like π-conjugated polymers, the bandgap size is such that electrons can be promoted into the conduction band if given enough energy, usually through the absorption of light that falls somewhere in the UV-IR range (1.5 - 3.5 eV).[108] Chemical dopants can be added to conjugated polymers to create *p*-type or *n*-type semiconductors that increase conductivity, photostability, and molar extinction coefficients, depending on the identity of the dopant.[106]

Promoting a negatively charged electron from the valence to the conduction band leaves behind a positively charged electron hole in its original position, and the coulombically bound electron-hole pair creates a quasiparticle known as an exciton. Because the hole and electron have an electrostatic attraction, the electron can relax back down to the original state, with a loss of the absorbed energy usually in the form of light emission or vibration-induced heat radiation, and this is known as exciton recombination. Prior to recombination, the pair can travel through the semiconductor, a process known as exciton diffusion, but organic semiconductors exhibit notoriously short exciton diffusion lengths of 5-10 nm.[108] It is not fully understood why such a broad range of materials exhibit similarly low exciton diffusion lengths but some factors thought to be involved are the fast intrinsic decay rates of photoexcited polymer chains back to their ground state, strong exciton-phonon coupling, and high exciton transfer energy barriers.[108,128] Recent

research also suggests that low exciton diffusion lengths in organic polymeric films occur due to the energetic and structural disorder inherent to commonly used film fabrication methods such as spin-coating or thermal evaporation and weak electronic couplings between chromophores.[128]

There is profound interest in furthering our understanding of the physical processes that underly photon absorption, exciton diffusion, and energy transfer in π-conjugated polymers as well as using capitalizing on that understanding to improve their electronic performance.[129] In OPVs, increased exciton diffusion lengths allows for thicker active layers to be used which increases the number of photons absorbed and maximizes the number of excitons generated *via* the photoelectric effect. Significant efforts have also been put towards increasing exciton generation by using low-bandgap polymers with alternating electron-rich donor moieties next to electron-poor acceptor moieties because a smaller bandgap requires lower energy radiation to cause electronic excitation and delocalization of π-electrons is easier.[130–132] Increasing exciton diffusion lengths and gaining a deeper understanding of the physical processes that underly exciton diffusion in organic semiconductors is also an area of intensive research.

1.9 Preparation and applications of functional π-conjugated polymer nanoparticles (CPNPs)

Many recent reports detail the utility of 1D and 2D nanostructures formed by the living CDSA of crystalline-core BCPs to a range of fields including optoelectronic devices, photocatalysis, and stimuli-responsive materials.[23,24,37,49,64,77,85,133] π-Conjugated polymers represent an attractive class of materials that are promising for a range of electronic applications with properties that are difficult to achieve with their currently available inorganic counterparts.[134]

Effective combination of the beneficial properties of length- and area-controlled nanostructures and π-conjugated polymers can be achieved through solution self-assembly of conjugated polymers into π-conjugated nanoparticles (CPNPs). There are many methods used to fabricate CPNPs but two primary approaches prevail in the literature: reprecipitation[33,135,136] and mini-emulsion formation,[137,138] which typically afford 20-500 nm diameter spherical nanoparticles.[23] Formation of dimensionally-controlled non-spherical 1D and 2D morphologies can also be achieved using solution self-assembly (CDSA and living CDSA) and microfluidic approaches.[79]

In the field of optoelectronics, commonly used film processing and post-processing methods such as drop-casting, spin-coating, and solvent-vapour annealing results in films with a microstructural order that is difficult to accurately reproduce. Most polymers are semicrystalline, with ordered crystalline regions surrounded by disordered amorphous regions and the intrinsic structural disorder associated with polymer crystallization has dramatic impacts on electronic performance. Establishing much of the order necessary to optimize optoelectronic performance prior to device fabrication remains an attractive approach and can be achieved through solution self-assembly of π-conjugated polymers into CPNPs. Segmented 1D nanofibers with a crystalline poly(di-*n*-hexylfluorene) (PDHF) core made by living CDSA facilitate exciton diffusion lengths of 200 nm (~20x the typical length for films of organic polymeric semiconductors) and are capable of efficient Förster resonance energy transfer (FRET) to inorganic quantum dots in hybrid nanowires.[80,108,139] 1D nanofibers with a P3HT core displayed even higher exciton diffusion lengths of 350 nm (Figure 1.14a).[140] The crystallization mechanism inherent to living CDSA creates fibers with a highly ordered crystalline core, forming a uniform energetic landscape upon which long-range exciton diffusion can occur. Other length-controlled P3HT-based fibers made by living CDSA were integrated into an organic field-effect transistor (OFET) that showed a

superlinear dependence of charge carrier mobility on nanofiber length and core-block DP_n.[83] Critically, these fibers exhibited superior performance compared to an analogous thin film P3HT-based OFET.

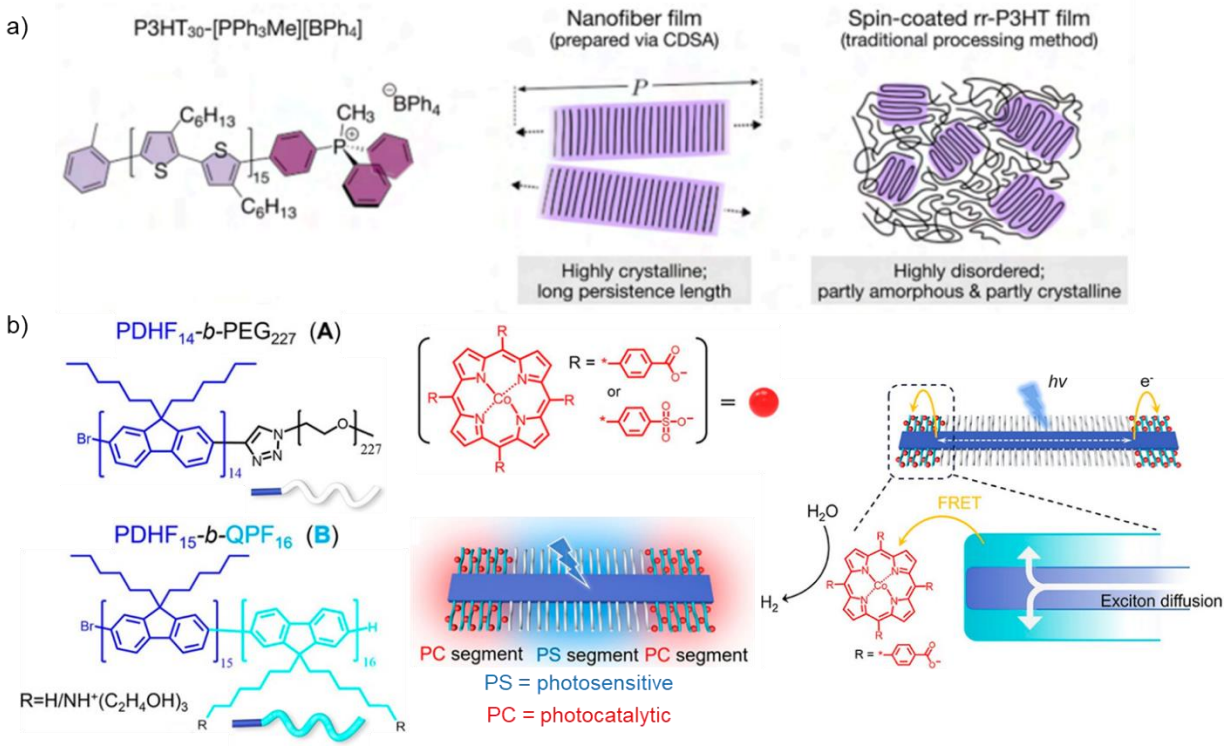

Figure 1.14. High exciton diffusion lengths in CPNPs and application to an artificial light-harvesting antennae for photocatalytic water splitting. **(a)** Chemical structure of a phosphonium-terminated P3HT homopolymer with a tetraphenylborate counterion ([$P3HT_{30}$-PPh_3Me][BPh_4]). Schematic comparison between the microstructure of films from well-defined nanofibers and spin-coated *rr*-P3HT. High polymer chain alignment and order within the core of nanofibers made by living CDSA show superior organization compared to disordered films with both crystalline and amorphous domains made by spin coating. Reproduced and adapted with permission from ref 140.[140] **(b)** Efficient energy funnelling from segmented PDHF-based nanofibers with cobalt(II) porphyrin catalysts at the termini. Upon excitation, excitons generated within the nanofiber core diffuse towards the catalysts and transfer energy *via* FRET, allowing for hydrogen production from water splitting. Reproduced and adapted with permission from ref 141.[141]

Naturally occurring photosynthetic organelles use a highly organized system of proteins for light absorption and conversion to chemical energy.[29] CPNPs made by living CDSA have high absorption cross sections, chromophore density, and exciton diffusion lengths, making them ideal models for synthetic light-harvesting systems.[80,106,129,141] Visible-light harvesting antennae were fabricated from photocatalytic CPNPs decorated with photosensitized cobalt(II) porphyrin catalysts that effectively produced hydrogen gas from water (Figure 1.14b).[141] Optimization of the catalyst turnover number and hydrogen production rate were accomplished by tuning the length of the π-conjugated crystalline core *via* living CDSA. Precise control over the hierarchical assembly produced modular architectures that provide a proof-of-concept scaffold for future application in other fields such as small molecular synthesis or CO_2 reduction.

Thermo-responsive, pH-responsive, chemo-responsive, or light-responsive materials are attractive synthetic targets due to their potential in detecting local environment changes and separation science.[142] Living CDSA has been expanded to include stimuli-sensitive formation of supramolecular assemblies. Choi and coworkers reported using *cis*-to-*trans* photoisomerization of PPV-based BCPs to trigger living CDSA and fabricate length-controlled homogeneous and heterogenous 1D nanofibers (Figure 1.15a).[77] Predictable monomer isomerization under light irradiation led to seeded growth that could be activated and deactivated using "on-off" light modulation (Figure 1.15b). The stimuli-induced self-assembly concept was further exemplified by Seferos *et al.* wherein they used selective oxidation of BCPs with blocks that had different oxidation potentials to promote self-assembly.[73]

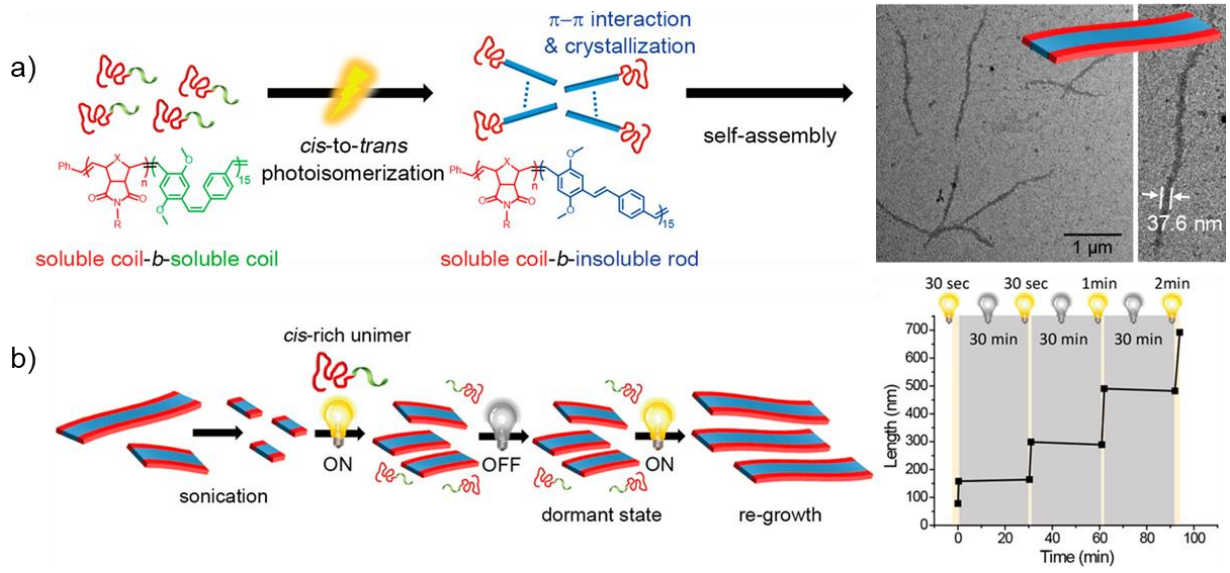

Figure 1.15. Example of a stimuli-responsive living CDSA system. **(a)** Chemical structures of PPV-based BCPs that undergo photoisomerization-induced self-assembly into 1D nanofibers. **(b)** Schematic showing the "on-off" nature of this isomerization and how light modulation can be utilized to form nanofibers of varying lengths over time. Figures **(a)** and **(b)** reproduced and adapted with permission from ref 77.[77]

2-Dimensional semiconducting nanomaterials such as graphene have gained enormous attention due to their flat morphology[143] and large surface area.[144] Controlled growth of 2D CPNPs remains challenging because strong intermolecular π-π stacking leads to anisotropic growth primarily in the π-π stacking direction resulting in a preference to form fibers over 2D platelets. Recently, considerable progress has been made on fabricating 2D nanostructures using BCPs with a π-conjugated core, with some examples achieving dimensional control.[70,145,146] For instance, conductive 2D rhombic micelles were made from a PPV BCP and incorporated into nanoscale pressure sensors (Figure 1.16a).[146] The sensor displayed high on-state current density and a high sensitivity which were modified by changing the platelet thickness.[146] In addition, a P3HT derivative bearing oligomeric ethylene glycol (OTT) side chains and a PEG corona-forming block (PTOTT-*b*-PEG) was self-assembled into tape-like nanoribbons (Figure 1.16b). Mixed assembly

of PTOTT-*b*-PEG and PTOTT functionalized with an oligonucleotide strand (DNA) as the corona-forming block (PTOTT-*b*-DNA) resulted in DNA-functionalized nanoribbons capable of sequence-specific binding to DNA-modified gold nanoparticles.[147]

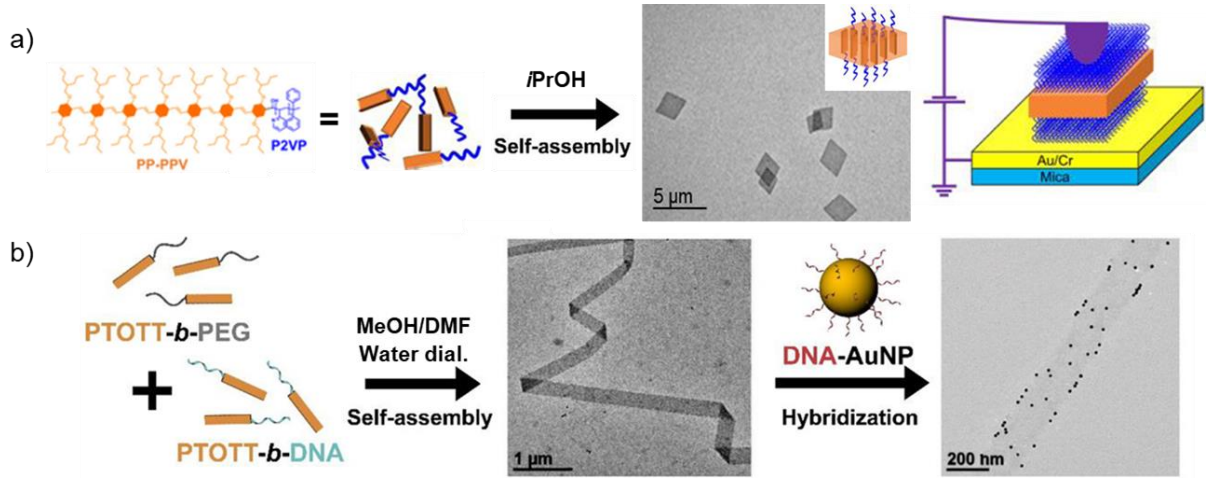

Figure 1.16. Formation and functionalization of 2D CPNPs. **(a)** Self-assembly of poly((*i*-propylpentyloxy)phenylene vinylene)-*b*-P2VP (PP-PPV-*b*-P2VP) in *i*PrOH to form area-controlled rhombic micelles. Micelles were subsequently incorporated into a flexible pressure sensor nanodevice. Au = gold; Cr = chromium. Reproduced and adapted with permission from ref 146.[146] **(b)** Co-assembly of PTOTT-*b*-PEG and PTOTT-*b*-DNA in a methanol/dimethylformamide (MeOH/DMF) mixture dialyzed against water (water dial.) to induce self-assembly into DNA-functionalized nanoribbons that were decorated using DNA-modified gold nanoparticles (DNA-AuNP). Reproduced with permission from ref 148.[148]

Despite recent progress in creating functional CPNPs, many formidable challenges remain. Particularly in the case of polythiophene-based BCP self-assembly, reports of long, low-dispersity (L_n >1 μm, $Đ_L$<1.1) nanofibers are confined to a limited number of reports and BCP systems.[83,86,149,150] Further control needs to be exerted over polythiophene crystallization to fully realize its potential as a semiconducting material. Additionally, 2D and 3D CPNPs may possess unique properties that provide exciting opportunities for application in optoelectronics; however, the controlled growth of these structures is largely elusive. Methods to equalize multidirectional growth kinetics must be introduced to fabricate these structures and analyze their structure-

property relationships. Finally, living CDSA is typically done in small batches at low concentration which presents issues with scalability, reproducibility of results, and practical utilization of these assemblies. One approach that promisingly addresses these factors is the formation of CPNPs using flow chemistry.

1.10 Thesis objectives

The work presented in this thesis is a compilation of research projects focusing on exploring the CDSA of block copolymer materials containing π-conjugated core-forming blocks, with a primary focus on polythiophene-based materials, to fabricate novel 1D and 2D nanostructures. The research objectives are outlined as 3 key goals below:

(a) Investigation of structure-property relationships in polythiophene self-assembly. Despite the ubiquity of polythiophenes as polymeric semiconducting materials, efficient control over their self-assembly has scarcely been reported due to the strong tendency of unimer to self-nucleate which causes deviations from predicted lengths and increased sample dispersity. One aim of this thesis is to investigate if small structural changes in the polythiophene alkyl chain identity reduces this tendency and results in advanced control over the self-assembly behaviour. This will be the topic of Chapter 2. Further, previous investigations into solution CDSA have primarily involved using BCPs with a crystallizable, rigid rod-like core-forming block and a coiled corona-forming block, with few reports investigating CDSA of BCPs where both the core and corona blocks are rigid. This thesis aims to provide a deeper understanding of how corona rigidity affects the ability of BCPs to undergo living CDSA and the resulting nanostructures and this will be described in Chapter 3.

(b) Extend the utilization of controlled self-assembly techniques in systems where precise nanoscale control is highly sought-after. To date, the self-nucleation suppression method is only known to be successful with one polythiophene-based block copolymer. This thesis aims to further generalize this method by providing other examples of π-conjugated block copolymers that benefit from its utilization. This creates a fundamental and experimental basis to investigate if other BCPs behave similarly and allows for the fabrication of uniform nanofiber samples with lengths and dispersities that were previously unachievable. This will be described in Chapters 2 and 3.

(c) Expand the library of conjugated materials known to be compatible with living CDSA and fabricate more complex architectures such as 2D CPNPs and surface-confined nanofibers. By investigating the self-assembly of BCPs with a new core-forming block, poly(3-(2'-ethylhexyl)thiophene) (P3EHT), the work in this thesis aims to expand the library of conjugated materials known to be compatible with living CDSA thereby providing opportunities for further discovery of potential applications. The reduced crystallization rate of P3EHT compared to P3HT and the recent success using self-assembly of polymeric amphiphiles containing a terminal charged group instead of a coronal chain permits access to form conjugated 2D CPNPs, which have remained an attractive yet largely elusive target. This will be the topic of Chapter 4. Surface-confined nanofiber growth has been shown to be a promising method to form specifically patterned surfaces with various functionalities. Self-assembly of PDHF and P3EHT BCPs can be used to explore the self-assembly of surface-confined π-conjugated micellar brushes towards energy-funnelling CPNP-silicon devices which will be described in Chapter 5.

1.11 Thesis summary

This thesis comprises four results chapters in addition to a final summary, conclusions, and outlook chapter, highlighting the impact of this work and possible future research directions.

Chapter 2 outlines the synthesis and living CDSA of poly(3-(2'-ethylhexyl)thiophene)-based block copolymers to produce precisely-defined nanofibers and segmented triblock comicelles. This chapter expands the scope of living CDSA and the self-nucleation suppression method to include new block copolymers, highlighting the utility of these methods in the controlled formation of electroactive nanostructures.

Chapter 3 focuses on investigations of the self-assembly behaviour of two fully-rigid poly(3-hexylthiophene)-*b*-poly(*para*-phenylene) BCPs with different molecular masses.

Chapter 4 describes results involving the formation of 2D platelets from charge-terminated poly(3-(2'-ethylhexyl)thiophene) species. It also outlines the controlled self-assembly of well-defined B-A-B and B-C-B triblock comicelles.

Chapter 5 outlines the surface-confined growth of poly(di-*n*-hexylfluorene) and poly(3-(2'-ethylhexyl)thiophene) BCPs into micellar brushes which are potentially capable of energy transfer to a substrate with the final objective of fabricating a photodetection device. Investigations into the surface morphology and growth characteristics of the brush layers are described.

In accordance with previous theses from Professor Ian Manners' research group, each chapter of this thesis has been written in a self-contained fashion such that it may be published in a peer-reviewed scientific journal. The work in this thesis was often performed in collaboration with colleagues within the Manners research group, as well as members of other research groups. Major contributions to each project are outlined at the beginning of each chapter.

1.12 References

(1) Sang, Y.; Liu, M. Hierarchical Self-Assembly into Chiral Nanostructures. *Chem. Sci.* **2022**, *13*, 633–656. https://doi.org/10.1039/d1sc03561d.

(2) Philp, D.; Stoddart, J. F. Self-Assembly in Natural and Unnatural Systems. *Angew. Chem. Int. Ed.* **1996**, *35*, 1154–1196.

(3) Whitesides, G. M.; Grzybowski, B. Self-Assembly at All Scales. *Science* **2002**, *295* (5564), 2418–2421. https://doi.org/10.1126/science.1070821.

(4) Burrell, C. J.; Howard, C. R.; Murphy, F. A. *Virion Structure and Composition*; 2017. https://doi.org/10.1016/b978-0-12-375156-0.00003-5.

(5) Sun, J.; Bhushan, B. Hierarchical Structure and Mechanical Properties of Nacre: A Review. *RSC Adv.* **2012**, *2*, 7617–7632. https://doi.org/10.1039/c2ra20218b.

(6) Mao, L. B.; Yao, H. Bin; Liu, L.; Colfen, H.; Liu, G.; Chen, S. M.; Li, S. K.; Yan, Y. X.; Liu, Y. Y.; Yu, S. H. Synthetic Nacre by Predesigned Matrix-Directed Mineralization. *Science* **2016**, *354* (6308), 107–110. https://doi.org/https://dx.doi.org/10.1126/science.aaf8991.

(7) Jinmei, S.; Wanlin, G. Chemical-Mechanical Stability of the Hierarchical Structure of Shell Nacre. *Sci. China Phys. Mech. Astron.* **2010**, *53* (2), 380–388. https://doi.org/10.1007/s11433-010-0134-x.

(8) Wang, J.; Tang, Z. Layered Nanocomposites Inspired by the Structure and Mechanical Properties of Nacre Ship between Their Structure And. *Chem. Soc. Rev* **2012**, *41*, 1111–1129. https://doi.org/10.1039/c1cs15106a.

(9) Zhao, H.; Yang, Z.; Guo, L. Nacre-Inspired Composites with Different Macroscopic Dimensions: Strategies for Improved Mechanical Performance and Applications. *NPG Asia Mater.* **2018**, *10* (4), 1–22. https://doi.org/10.1038/s41427-018-0009-6.

(10) Yang, H. M.; Jo, S.; Oh, J. H.; Choi, B. H.; Woo, J. Y.; Han, C. S. Strong and Tough Nacre-Inspired Graphene Oxide Composite with Hierarchically Similar Structure. *ACS Nano* **2022**, *16* (7), 10509–10516. https://doi.org/10.1021/acsnano.2c01667.

(11) Winkler, D. A.; Halley, J. D.; David, A. Consistent Concepts of Self-Organization and Self-Assembly. *Complexity* **2008**, *14* (2), 10–17. https://doi.org/10.1002/cplx.

(12) Whitesides, G. M.; Boncheva, M. Beyond Molecules : Self-Assembly of Mesoscopic and Macroscopic Components. *Proc. Natl. Acad. Sci.* **2002**, *99* (8), 4769–4774. https://doi.org/10.1073/pnas.082065899.

(13) Lombardo, D.; Calandra, P.; Pasqua, L.; Magazù, S. Self-Assembly of Organic Nanomaterials and Biomaterials: The Bottom-up Approach for Functional Nanostructures Formation and Advanced Applications. *Materials* **2020**, *13* (5). https://doi.org/10.3390/ma13051048.

(14) Hoeben, F. J. M.; Jonkheijm, P.; Meijer, E. W.; Schenning, A. P. H. J. About Supramolecular Assemblies of π-Conjugated Systems. *Chem. Rev.* **2005**, *105* (4), 1491–1546. https://doi.org/10.1021/cr030070z.

(15) Gulati, N. M.; Pitek, A. S.; Steinmetz, N. F.; Stewart, P. L. Cryo-Electron Tomography Investigation of Serum Albumin-Camouflaged Tobacco Mosaic Virus Nanoparticles. *Nanoscale* **2017**, *9* (10), 3408–3415. https://doi.org/10.1039/c6nr06948g.

(16) Caspar, D. L. D. Assembly and Stability of the Tobacco Mosaic Virus Particle. *Adv. Protein Chem.* **1964**, *18* (C), 37–121. https://doi.org/10.1016/S0065-3233(08)60268-5.

(17) Klug, A. The Tobacco Mosaic Virus Particle: Structure and Assembly. *Phil. Trans. R. Soc. Lond. B* **1999**, No. 354, 1–6.

(18) Splettstoesser, T. *TMV_structure_simple*. https://upload.wikimedia.org/wikipedia/commons/8/8e/TMV_structure_simple.png (accessed 2023-12-06).

(19) Macfarlane, L. Application of Living Crystallization-Driven Self-Assembly to π-Conjugated and Peptidic Materials, University of Bristol, 2018.

(20) Naderi, A.; Bhattacharjee, N.; Folch, A. Digital Manufacturing for Microfluidics. *Annu. Rev. Biomed. Eng.* **2019**, *21*, 325–364. https://doi.org/10.1146/annurev-bioeng-092618-020341.

(21) Zandi Shafagh, R.; Vastesson, A.; Guo, W.; Van Der Wijngaart, W.; Haraldsson, T. E-Beam Nanostructuring and Direct Click Biofunctionalization of Thiol-Ene Resist. *ACS Nano* **2018**, *12* (10), 9940–9946. https://doi.org/10.1021/acsnano.8b03709.

(22) Biswas, A.; Bayer, I. S.; Biris, A. S.; Wang, T.; Dervishi, E.; Faupel, F. Advances in Top-down and Bottom-up Surface Nanofabrication: Techniques, Applications & Future Prospects. *Adv. Colloid Interface Sci.* **2012**, *170* (1–2), 2–27. https://doi.org/10.1016/j.cis.2011.11.001.

(23) MacFarlane, L. R.; Shaikh, H.; Garcia-Hernandez, J. D.; Vespa, M.; Fukui, T.; Manners, I. Functional Nanoparticles through π-Conjugated Polymer Self-Assembly. *Nat. Rev. Mater.* **2021**, *6* (1), 7–26. https://doi.org/10.1038/s41578-020-00233-4.

(24) Arno, M. C.; Inam, M.; Weems, A. C.; Li, Z.; Binch, A. L. A.; Platt, C. I.; Richardson, S. M.; Hoyland, J. A.; Dove, A. P.; O'Reilly, R. K. Exploiting the Role of Nanoparticle Shape in Enhancing Hydrogel Adhesive and Mechanical Properties. *Nat. Commun.* **2020**, *11* (1), 1–9. https://doi.org/10.1038/s41467-020-15206-y.

(25) Tunçsoy, M. Impacts of Metal Nanoparticles on Fish. *Handb. Green Sustain. Nanotechnol.* **2023**, 2645–2662. https://doi.org/10.1007/978-3-031-16101-8_39.

(26) Picraux, S. T. *Nanotechnology*. Encyclopedia Britannica. https://www.britannica.com/technology/nanotechnology/Nanofabrication (accessed 2024-01-17).

(27) Feynman, R. There' s Plenty of Room at the Bottom, 1959, 1–10.

(28) Lehn, J.-M. Cryptates: The Chemistry of Macropolycyclic Inclusion Complexes. *Acc. Chem. Res.* **1978**, *174* (2), 49–57.

(29) Liu, A.; Tai, C. W.; Holá, K.; Tian, H. Hollow Polymer Dots: Nature-Mimicking Architecture for Efficient Photocatalytic Hydrogen Evolution Reaction. *J. Mater. Chem. A* **2019**, *7* (9), 4797–4803. https://doi.org/10.1039/c8ta12146j.

(30) Zhu, Q.; Xiong, W.; Gong, Y.; Zheng, Y.; Che, Y.; Zhao, J. Discrimination of Five Classes of Explosives by a Fluorescence Array Sensor Composed of Two Tricarbazole-Nanostructures. *Anal. Chem.* **2017**, *89* (22), 11908–11912. https://doi.org/10.1021/acs.analchem.7b04083.

(31) Xiong, W.; Zhu, Q.; Gong, Y.; Wang, C.; Che, Y.; Zhao, J. Interpenetrated Binary Supramolecular Nanofibers for Sensitive Fluorescence Detection of Six Classes of Explosives. *Anal. Chem.* **2018**, *90* (7), 4273–4276. https://doi.org/10.1021/acs.analchem.8b00556.

(32) Xiong, W.; Gong, Y.; Che, Y.; Zhao, J. Sensitive Discrimination of Nerve Agent and Sulfur Mustard Simulants Using Fluorescent Coassembled Nanofibers with Förster Resonance Energy Transfer-Enhanced Photostability and Emission. *Anal. Chem.* **2019**, *91* (3), 1711–1714. https://doi.org/10.1021/acs.analchem.8b05225.

(33) Zhang, B.; Wang, F.; Zhou, H.; Gao, D.; Yuan, Z.; Wu, C.; Zhang, X. Polymer Dots Compartmentalized in Liposomes as a Photocatalyst for In Situ Hydrogen Therapy. *Angew. Chem. Int. Ed.* **2019**, *58* (9), 2744–2748. https://doi.org/10.1002/anie.201813066.

(34) Ma, J.; Hao, B.; Zhang, S.; Huang, X.; Lu, G.; Feng, C. Uniform π-Conjugated-Co-Oligomer-Based Nanofibers of Controlled Length with Near-Infrared Emission, Photodynamic and Photothermal Activities. *Adv. Mater. Interfaces* **2022**, *9* (33), 2201823. https://doi.org/10.1002/admi.202201823.

(35) Vines, J.; Lim, D.-J.; Park, H.; Vines, J. B.; Lim, D.-J.; Park, H. Contemporary Polymer-Based Nanoparticle Systems for Photothermal Therapy. *Polymers.* **2018**, *10*, 1357. https://doi.org/10.3390/polym10121357.

(36) Feng, G.; Fang, Y.; Liu, J.; Geng, J.; Ding, D.; Liu, B. Multifunctional Conjugated Polymer Nanoparticles for Image-Guided Photodynamic and Photothermal Therapy. *Small* **2017**, *13* (3), 1602807. https://doi.org/10.1002/smll.201602807.

(37) Tritschler, U.; Pearce, S.; Gwyther, J.; Whittell, G. R.; Manners, I. 50th Anniversary Perspective: Functional Nanoparticles from the Solution Self-Assembly of Block Copolymers. *Macromolecules* **2017**, *50* (9), 3439–3463. https://doi.org/10.1021/acs.macromol.6b02767.

(38) Hamley, I. W. Nanotechnology with Soft Materials. *Angew. Chemie* **2003**, *115* (15), 1730–1752. https://doi.org/10.1002/ange.200200546.

(39) Van Rossum, S. A. P.; Tena-Solsona, M.; Van Esch, J. H.; Eelkema, R.; Boekhoven, J. Dissipative Out-of-Equilibrium Assembly of Man-Made Supramolecular Materials. *Chem. Soc. Rev.* **2017**, *46* (18), 5519–5535. https://doi.org/10.1039/c7cs00246g.

(40) Blanazs, A.; Armes, S. P.; Ryan, A. J. Self-Assembled Block Copolymer Aggregates: From Micelles to Vesicles and Their Biological Applications. *Macromol. Rapid Commun.* **2009**, *30* (4–5), 267–277. https://doi.org/10.1002/marc.200800713.

(41) Mai, Y.; Eisenberg, A. Self-Assembly of Block Copolymers. *Chem. Soc. Rev.* **2012**, *41* (18), 5969. https://doi.org/10.1039/c2cs35115c.

(42) Lei, S. Fundamental Studies and Potential Optoelectronic Applications of Living Crystallization-Driven Self-Assembly, University of Victoria, 2023.

(43) Arno, M. C.; Inam, M.; Coe, Z.; Cambridge, G.; Macdougall, L. J.; Keogh, R.; Dove, A. P.; O'Reilly, R. K. Precision Epitaxy for Aqueous 1D and 2D Poly(ϵ-Caprolactone) Assemblies. *J. Am. Chem. Soc.* **2017**, *139* (46), 16980–16985. https://doi.org/10.1021/jacs.7b10199.

(44) Wang, J.; Lu, Y.; Chen, Y. Fabrication of 2D Surface-Functional Polymer Platelets via Crystallization-Driven Self-Assembly of Poly(ε-Caprolactone)-Contained Block Copolymers. *Polymer.* **2019**, *160* (November 2018), 196–203. https://doi.org/10.1016/j.polymer.2018.11.053.

(45) Cao, L.; Manners, I.; Winnik, M. A. Influence of the Interplay of Crystallization and Chain Stretching on Micellar Morphologies: Solution Self-Assembly of Coil-Crystalline Poly(Isoprene-Block-Ferrocenylsilane). *Macromolecules* **2002**, *35* (22), 8258–8260.

(46) Hicks, G. E. J.; Cranston, R. R.; Lotocki, V.; Manion, J. G.; Lessard, B. H.; Seferos, D. S. Dopant-Stabilized Assembly of Poly(3-Hexylthiophene). *J. Am. Chem. Soc.* **2022**, *144* (36), 16456–16470. https://doi.org/10.1021/jacs.2c04984.

(47) Hayward, R. C.; Pochan, D. J. Tailored Assemblies of Block Copolymers in Solution: It Is All about the Process. *Macromolecules* **2010**, *43* (8), 3577–3584. https://doi.org/10.1021/ma9026806.

(48) Schacher, F. H.; Rupar, P. A.; Manners, I. Functional Block Copolymers: Nanostructured Materials with Emerging Applications. *Angew. Chem. Int. Ed.* **2012**, *51* (32), 7898–7921. https://doi.org/10.1002/anie.201200310.

(49) Ganda, S.; Stenzel, M. H. Concepts, Fabrication Methods and Applications of Living Crystallization-Driven Self-Assembly of Block Copolymers. *Prog. Polym. Sci.* **2020**, *101*, 101195. https://doi.org/10.1016/j.progpolymsci.2019.101195.

(50) Wang, X.; Guerin, G.; Wang, H.; Wang, Y.; Manners, I.; Winnik, M. A. Cylindrical Block Copolymer Micelles and Co-Micelles of Controlled Length and Architecture. *Science* **2007**, *317* (5838), 644–647. https://doi.org/10.1126/science.1141382.

(51) Sear, R. P. Quantitative Studies of Crystal Nucleation at Constant Supersaturation: Experimental Data and Models. *CrystEngComm* **2014**, *16* (29), 6506–6522. https://doi.org/10.1039/c4ce00344f.

(52) Lotz, B.; Kovacs, A. J.; Bassett, G. A.; Keller, A. Properties of Copolymers Composed of One Poly-Ethylene-Oxide and One Polystyrene Block - II. Morphology of Single Crystals. *Kolloid-Zeitschrift Zeitschrift für Polym.* **1966**, *209* (2), 115–128. https://doi.org/10.1007/BF01500629.

(53) He, X.; Hsiao, M. S.; Boott, C. E.; Harniman, R. L.; Nazemi, A.; Li, X.; Winnik, M. A.; Manners, I. Two-Dimensional Assemblies from Crystallizable Homopolymers with Charged Termini. *Nat. Mater.* **2017**, *16* (4), 481–488. https://doi.org/10.1038/NMAT4837.

(54) Fukui, T.; Garcia-Hernandez, J. D.; MacFarlane, L. R.; Lei, S.; Whittell, G. R.; Manners, I. Seeded Self-Assembly of Charge-Terminated Poly(3-Hexylthiophene) Amphiphiles Based on the Energy Landscape. *J. Am. Chem. Soc.* **2020**, *142* (35), 15038–15048. https://doi.org/10.1021/jacs.0c06185.

(55) He, X.; Finnegan, J. R.; Hayward, D. W.; MacFarlane, L. R.; Harniman, R. L.; Manners, I.

Living Crystallization-Driven Self-Assembly of Polymeric Amphiphiles: Low-Dispersity Fiber-like Micelles from Crystallizable Phosphonium-Capped Polycarbonate Homopolymers. *Macromolecules* **2020**, *53* (23), 10591–10600. https://doi.org/10.1021/acs.macromol.0c02075.

(56) Yusoff, S. F. M.; Hsiao, M. S.; Schacher, F. H.; Winnik, M. A.; Manners, I. Formation of Lenticular Platelet Micelles via the Interplay of Crystallization and Chain Stretching: Solution Self-Assembly of Poly(Ferrocenyldimethylsilane)-Block-Poly(2-Vinylpyridine) with a Crystallizable Core-Forming Metalloblock. *Macromolecules* **2012**, *45* (9), 3883–3891. https://doi.org/10.1021/ma2027726.

(57) Hsiao, M. S.; Yusoff, S. F. M.; Winnik, M. A.; Manners, I. Crystallization-Driven Self-Assembly of Block Copolymers with a Short Crystallizable Core-Forming Segment: Controlling Micelle Morphology through the Influence of Molar Mass and Solvent Selectivity. *Macromolecules* **2014**, *47* (7), 2361–2372. https://doi.org/10.1021/ma402429d.

(58) Qian, J.; Guerin, G.; Lu, Y.; Cambridge, G.; Manners, I.; Winnik, M. A. Self-Seeding in One Dimension: An Approach to Control the Length of Fiberlike Polyisoprene-Polyferrocenylsilane Block Copolymer Micelles. *Angew. Chem. Int. Ed.* **2011**, *50* (7), 1622–1625. https://doi.org/10.1002/anie.201006223.

(59) Gilroy, J. B.; Gädt, T.; Whittell, G. R.; Chabanne, L.; Mitchels, J. M.; Richardson, R. M.; Winnik, M. A.; Manners, I. Monodisperse Cylindrical Micelles by Crystallization-Driven Living Self-Assembly. *Nat. Chem.* **2010**, *2* (7), 566–570. https://doi.org/10.1038/nchem.664.

(60) Nazemi, A.; He, X.; Macfarlane, L. R.; Harniman, R. L.; Hsiao, M. S.; Winnik, M. A.; Faul, C. F. J.; Manners, I. Uniform "Patchy" Platelets by Seeded Heteroepitaxial Growth of Crystallizable Polymer Blends in Two Dimensions. *J. Am. Chem. Soc.* **2017**, *139* (12), 4409–4417. https://doi.org/10.1021/jacs.6b12503.

(61) Gädt, T.; Ieong, N. S.; Cambridge, G.; Winnik, M. A.; Manners, I. Complex and Hierarchical Micelle Architectures from Diblock Copolymers Using Living, Crystallization-Driven Polymerizations. *Nat. Mater.* **2009**, *8* (2), 144–150. https://doi.org/10.1038/nmat2356.

(62) Zhang, Y.; Pearce, S.; Eloi, J. C.; Harniman, R. L.; Tian, J.; Cordoba, C.; Kang, Y.; Fukui, T.; Qiu, H.; Blackburn, A.; Richardson, R. M.; Manners, I. Dendritic Micelles with Controlled Branching and Sensor Applications. *J. Am. Chem. Soc.* **2021**, *143* (15), 5805–5814. https://doi.org/10.1021/jacs.1c00770.

(63) Schmelz, J.; Schedl, A. E.; Steinlein, C.; Manners, I.; Schmalz, H. Length Control and Block-Type Architectures in Worm-like Micelles with Polyethylene Cores. *J. Am. Chem. Soc.* **2012**, *134* (34), 14217–14225. https://doi.org/10.1021/ja306264d.

(64) Inam, M.; Jones, J. R.; Pérez-Madrigal, M. M.; Arno, M. C.; Dove, A. P.; O'Reilly, R. K. Controlling the Size of Two-Dimensional Polymer Platelets for Water-in-Water Emulsifiers. *ACS Cent. Sci.* **2018**, *4* (1), 63–70. https://doi.org/10.1021/acscentsci.7b00436.

(65) Petzetakis, N.; Dove, A. P.; O'Reilly, R. K. Cylindrical Micelles from the Living Crystallization-Driven Self-Assembly of Poly(Lactide)-Containing Block Copolymers. *Chem. Sci.* **2011**, *2* (5), 955–960. https://doi.org/10.1039/c0sc00596g.

(66) Ganda, S.; Dulle, M.; Drechsler, M.; Förster, B.; Förster, S.; Stenzel, M. H. Two-Dimensional Self-Assembled Structures of Highly Ordered Bioactive Crystalline-Based Block Copolymers. *Macromolecules* **2017**, *50* (21), 8544–8553. https://doi.org/10.1021/acs.macromol.7b01453.

(67) Cha, Y.; Jarrett-Wilkins, C.; Rahman, M. A.; Zhu, T.; Sha, Y.; Manners, I.; Tang, C. Crystallization-Driven Self-Assembly of Metallo-Polyelectrolyte Block Copolymers with a Polycaprolactone Core-Forming Segment. *ACS Macro Lett.* **2019**, *8* (7), 835–840. https://doi.org/10.1021/acsmacrolett.9b00335.

(68) Ellis, C. E.; Garcia-Hernandez, J. D.; Manners, I. Scalable and Uniform Length-Tunable Biodegradable Block Copolymer Nanofibers with a Polycarbonate Core via Living Polymerization-Induced Crystallization-Driven Self-Assembly. *J. Am. Chem. Soc.* **2022**, *144* (44), 20525–20538. https://doi.org/10.1021/jacs.2c09715.

(69) Finnegan, J. R.; He, X.; Street, S. T. G.; Garcia-Hernandez, J. D.; Hayward, D. W.; Harniman, R. L.; Richardson, R. M.; Whittell, G. R.; Manners, I. Extending the Scope of "Living" Crystallization-Driven Self-Assembly: Well-Defined 1D Micelles and Block Comicelles from Crystallizable Polycarbonate Block Copolymers. *J. Am. Chem. Soc.* **2018**, *140* (49), 17127–17140. https://doi.org/10.1021/jacs.8b09861.

(70) Qi, R.; Zhu, Y.; Han, L.; Wang, M.; He, F. Rectangular Platelet Micelles with Controlled Aspect Ratio by Hierarchical Self-Assembly of Poly(3-Hexylthiophene)-b-Poly(Ethylene Glycol). *Macromolecules* **2020**, *53* (15), 6555–6565. https://doi.org/10.1021/acs.macromol.0c01092.

(71) Hwang, S.-H.; Kang, S.-Y.; Yang, S.; Lee, J.; Choi, T.-L. Synchronous Preparation of Length-Controllable 1D Nanoparticles via Crystallization-Driven in Situ Nanoparticlization of Conjugated Polymers. *J. Am. Chem. Soc.* **2022**, *144* (13), 5921–5929. https://doi.org/10.1021/jacs.1c13385.

(72) Kim, Y. J.; Cho, C. H.; Paek, K.; Jo, M.; Park, M. K.; Lee, N. E.; Kim, Y. J.; Kim, B. J.; Lee, E. Precise Control of Quantum Dot Location within the P3HT-b-P2VP/QD Nanowires Formed by Crystallization-Driven 1D Growth of Hybrid Dimeric Seeds. *J. Am. Chem. Soc.* **2014**, *136* (7), 2767–2774. https://doi.org/10.1021/ja410165f.

(73) Hicks, G. E. J.; Jarrett-Wilkins, C. N.; Panchuk, J. R.; Manion, J. G.; Seferos, D. S. Oxidation Promoted Self-Assembly of π-Conjugated Polymers. *Chem. Sci.* **2020**, *11* (25), 6383–6392. https://doi.org/10.1039/d0sc00806k.

(74) Street, S. T. G.; He, Y.; Jin, X. H.; Hodgson, L.; Verkade, P.; Manners, I. Cellular Uptake and Targeting of Low Dispersity, Dual Emissive, Segmented Block Copolymer Nanofibers. *Chem. Sci.* **2020**, *11* (32), 8394–8408. https://doi.org/10.1039/d0sc02593c.

(75) Lin, C.; Tung, Y.; Ruokolainen, J.; Mezzenga, R.; Chen, W. Poly[2,7-(9,9-Dihexylfluorene)]-Block-Poly(2-Vinylpyridine) Rod-Coil and Coil-Rod-Coil Block Copolymers: Synthesis, Morphology and Photophysical Properties in Methanol/THF Mixed Solvents. *Macromolecules* **2008**, *41*, 8759–8769.

(76) Zhu, Y.; Han, L.; Fan, H.; Wang, M.; Qi, R.; Zhao, Y.; He, F. Three-Dimensional Spirals of Conjugated Block Copolymers Driven by Screw Dislocation. *Macromolecules* **2020**, *53*, 3217–3223. https://doi.org/10.1021/acs.macromol.0c00071.

(77) Shin, S.; Menk, F.; Kim, Y.; Lim, J.; Char, K.; Zentel, R.; Choi, T. L. Living Light-Induced Crystallization-Driven Self-Assembly for Rapid Preparation of Semiconducting Nanofibers. *J. Am. Chem. Soc.* **2018**, *140* (19), 6088–6094. https://doi.org/10.1021/jacs.8b01954.

(78) Xu, L.; Wang, C.; Li, Y.-X.; Xu, X.; Zhou, L.; Liu, N.; Wu, Z.-Q. Crystallization-Driven Asymmetric Helical Assembly of Conjugated Block Copolymers and the Aggregation Induced White-Light Emission and Circularly Polarized Luminescence. *Angew. Chem. Int. Ed.* **2020**, *59* (38), 16675–16682. https://doi.org/10.1002/anie.202006561.

(79) Ma, J.; Lu, G.; Huang, X.; Feng, C. π-Conjugated-Polymer-Based Nanofibers through Living Crystallization-Driven Self-Assembly: Preparation, Properties and Applications. *Chem. Commun.* **2021**, *57* (98), 13259–13274. https://doi.org/10.1039/d1cc04825b.

(80) Jin, X.-H.; Price, M. B.; Finnegan, J. R.; Boott, C. E.; Richter, J. M.; Rao, A.; Menke, S. M.; Friend, R. H.; Whittell, G. R.; Manners, I. Long-Range Exciton Transport in Conjugated Polymer Nanofibers Prepared by Seeded Growth. *Science* **2018**, *360* (3691), 897–900. https://doi.org/10.1126/science.aar8104.

(81) Qian, J.; Lu, Y.; Chia, A.; Zhang, M.; Rupar, P. A.; Gunari, N.; Walker, G. C.; Cambridge, G.; He, F.; Guerin, G.; Manners, I.; Winnik, M. A. Self-Seeding in One Dimension: A Route to Uniform Fiber-like Nanostructures from Block Copolymers with a Crystallizable Core-Forming Block. *ACS Nano* **2013**, *7* (5), 3754–3766. https://doi.org/10.1021/nn400124x.

(82) Xu, J.; Ma, Y.; Hu, W.; Rehahn, M.; Reiter, G. Cloning Polymer Single Crystals through Self-Seeding. *Nat. Mater.* **2009**, *8* (4), 348–353. https://doi.org/10.1038/nmat2405.

(83) Li, X.; Wolanin, P. J.; MacFarlane, L. R.; Harniman, R. L.; Qian, J.; Gould, O. E. C. C.; Dane, T. G.; Rudin, J.; Cryan, M. J.; Schmaltz, T.; Frauenrath, H.; Winnik, M. A.; Faul, C. F. J. J.; Manners, I. Uniform Electroactive Fibre-like Micelle Nanowires for Organic Electronics. *Nat. Commun.* **2017**, *8* (1), 15909. https://doi.org/10.1038/ncomms15909.

(84) Strobl, G. Crystallization and Melting of Bulk Polymers: New Observations, Conclusions and a Thermodynamic Scheme. *Prog. Polym. Sci.* **2006**, *31* (4), 398–442. https://doi.org/10.1016/j.progpolymsci.2006.01.001.

(85) MacFarlane, L.; Zhao, C.; Cai, J.; Qiu, H.; Manners, I. Emerging Applications for Living Crystallization-Driven Self-Assembly. *Chem. Sci.* **2021**, *12* (13), 4661–4682. https://doi.org/10.1039/d0sc06878k.

(86) MacFarlane, L. R.; Li, X.; Faul, C. F. J.; Manners, I. Efficient and Controlled Seeded Growth of Poly(3-Hexylthiophene) Block Copolymer Nanofibers through Suppression of Homogeneous Nucleation. *Macromolecules* **2021**, *54* (24), 11269–11280. https://doi.org/10.1021/acs.macromol.1c02005.

(87) Gilroy, J. B.; Lunn, D. J.; Patra, S. K.; Whittell, G. R.; Winnik, M. A.; Manners, I. Fiber-like Micelles via the Crystallization-Driven Solution Self-Assembly of Poly(3-Hexylthiophene)-Block-Poly(Methyl Methacrylate) Copolymers. *Macromolecules* **2012**, *45* (14), 5806–5815. https://doi.org/10.1021/ma3008114.

(88) Gwyther, J.; Gilroy, J. B.; Rupar, P. A.; Lunn, D. J.; Kynaston, E.; Patra, S. K.; Whittell, G. R.; Winnik, M. A.; Manners, I. Dimensional Control of Block Copolymer Nanofibers with a π-Conjugated Core: Crystallization-Driven Solution Self-Assembly of Amphiphilic

Poly(3-Hexylthiophene)-b-Poly(2-Vinylpyridine). *Chem. Eur. J.* **2013**, *19* (28), 9186–9197. https://doi.org/10.1002/chem.201300463.

(89) Hayward, D. W.; Lunn, D. J.; Seddon, A.; Finnegan, J. R.; Gould, O. E. C.; Magdysyuk, O.; Manners, I.; Whittell, G. R.; Richardson, R. M. Structure of the Crystalline Core of Fiber-like Polythiophene Block Copolymer Micelles. *Macromolecules* **2018**, *51* (8), 3097–3106. https://doi.org/10.1021/acs.macromol.7b02552.

(90) Hudson, Z. M.; Lunn, D. J.; Winnik, M. A.; Manners, I. Colour-Tunable Fluorescent Multiblock Micelles. *Nat. Commun.* **2014**, *5*. https://doi.org/10.1038/ncomms4372.

(91) Qiu, H.; Gao, Y.; Boott, C. E.; Gould, O. E. C.; Harniman, R. L.; Miles, M. J.; Webb, S. E. D.; Winnik, M. A.; Manners, I. Uniform Patchy and Hollow Rectangular Platelet Micelles from Crystallizable Polymer Blends. *Science* **2016**, *352* (6286), 697–702.

(92) Lei, S.; Tian, J.; Kang, Y.; Zhang, Y.; Manners, I. AIE-Active, Stimuli-Responsive Fluorescent 2D Block Copolymer Nanoplatelets Based on Corona Chain Compression. *J. Am. Chem. Soc.* **2022**, *144* (38), 17630–17641. https://doi.org/10.1021/jacs.2c07133.

(93) Hudson, Z. M.; Boott, C. E.; Robinson, M. E.; Rupar, P. A.; Winnik, M. A.; Manners, I. Tailored Hierarchical Micelle Architectures Using Living Crystallization-Driven Self-Assembly in Two Dimensions. *Nat. Chem.* **2014**, *6* (10), 893–898. https://doi.org/10.1038/nchem.2038.

(94) Li, X.; Gao, Y.; Boott, C. E.; Hayward, D. W.; Harniman, R.; Whittell, G. R.; Richardson, R. M.; Winnik, M. A.; Manners, I. "Cross" Supermicelles via the Hierarchical Assembly of Amphiphilic Cylindrical Triblock Comicelles. *J. Am. Chem. Soc.* **2016**, *138* (12), 4087–4095. https://doi.org/10.1021/jacs.5b12735.

(95) Cai, J.; Li, C.; Kong, N.; Lu, Y.; Lin, G.; Wang, X.; Yao, Y.; Manners, I.; Qiu, H. Tailored Multifunctional Micellar Brushes via Crystallization-Driven Growth from a Surface. *Science* **2019**, *366* (6469), 1095–1098. https://doi.org/10.1126/science.aax9075.

(96) Lin, G.; Cai, J.; Sun, Y.; Cui, Y.; Liu, Q.; Manners, I.; Qiu, H. Capillary-Bound Dense Micelle Brush Supports for Continuous Flow Catalysis. *Angew. Chem. Int. Ed.* **2021**, *60* (46), 24637–24643. https://doi.org/10.1002/anie.202110206.

(97) Qiu, H.; Hudson, Z. M.; Winnik, M. A.; Manners, I. Multidimensional Hierarchical Self-Assembly of Amphiphilic Cylindrical Block Comicelles. *Science* **2015**, *347* (6228), 1329–1332. https://doi.org/10.1126/science.1261816.

(98) Li, X.; Gao, Y.; Boott, C. E.; Winnik, M. A.; Manners, I. Non-Covalent Synthesis of Supermicelles with Complex Architectures Using Spatially Confined Hydrogen-Bonding Interactions. *Nat. Commun.* **2015**, *6*, 1–8. https://doi.org/10.1038/ncomms9127.

(99) Garcia-Hernandez, J. D.; Parkin, H. C.; Ren, Y.; Zhang, Y.; Manners, I. Hydrophobic Cargo Loading at the Core–Corona Interface of Uniform, Length-Tunable Aqueous Diblock Copolymer Nanofibers with a Crystalline Polycarbonate Core. *Polym. Chem.* **2022**, *13*, 4100–4110. https://doi.org/10.1039/d2py00395c.

(100) Zhang, X.; Chen, G.; Zheng, B.; Wan, Z.; Liu, L.; Zhu, L.; Xie, Y.; Tong, Z. Uniform Two-Dimensional Crystalline Platelets with Tailored Compositions for PH Stimulus-Responsive Drug Release. *Biomacromolecules* **2023**, *24* (2), 1032–1041.

https://doi.org/10.1021/acs.biomac.2c01481.

(101) Street, S. T. G.; Chrenek, J.; Harniman, R. L.; Letwin, K.; Mantell, J. M.; Borucu, U.; Willerth, S. M.; Manners, I. Length-Controlled Nanofiber Micelleplexes as Efficient Nucleic Acid Delivery Vehicles. *J. Am. Chem. Soc.* **2022**, *144* (43), 19799–19812. https://doi.org/10.1021/jacs.2c06695.

(102) Ganda, S.; Wong, C. K.; Biazik, J.; Raveendran, R.; Zhang, L.; Chen, F.; Ariotti, N.; Stenzel, M. H. Macrophage-Targeting and Complete Lysosomal Degradation of Self-Assembled Two-Dimensional Poly(ϵ-Caprolactone) Platelet Particles. *ACS Appl. Mater. Interfaces* **2022**, *14* (31), 35333–35343. https://doi.org/10.1021/acsami.2c06555.

(103) Song, Y.; Elsabahy, M.; Collins, C. A.; Khan, S.; Li, R.; Hreha, T. N.; Shen, Y.; Lin, Y. N.; Letteri, R. A.; Su, L.; Dong, M.; Zhang, F.; Hunstad, D. A.; Wooley, K. L. Morphologic Design of Silver-Bearing Sugar-Based Polymer Nanoparticles for Uroepithelial Cell Binding and Antimicrobial Delivery. *Nano Lett.* **2021**, *21* (12), 4990–4998. https://doi.org/10.1021/acs.nanolett.1c00776.

(104) Parkin, H. C.; Garcia-Hernandez, J. D.; Street, S. T. G.; Hof, R.; Manners, I. Uniform, Length-Tunable Antibacterial 1D Diblock Copolymer Nanofibers. *Polym. Chem.* **2022**, *13*, 2941–2949. https://doi.org/10.1039/d2py00262k.

(105) Bryan, Z. J.; McNeil, A. J. Conjugated Polymer Synthesis via Catalyst-Transfer Polycondensation (CTP): Mechanism, Scope, and Applications. *Macromolecules* **2013**, *46* (21), 8395–8405. https://doi.org/10.1021/ma401314x.

(106) Tuncel, D. π-Conjugated Nanostructured Materials: Preparation, Properties and Photonic Applications. *Nanoscale Adv.* **2019**, *1* (1), 19–33. https://doi.org/10.1039/c8na00108a.

(107) Woods, E. F.; Berl, A. J.; Kalow, J. A. Advances in the Synthesis of π-Conjugated Polymers by Photopolymerization. *ChemPhotoChem* **2021**, *5* (1), 4–11. https://doi.org/10.1002/cptc.202000212.

(108) Mikhnenko, O. V.; Blom, P. W. M.; Nguyen, T. Q. Exciton Diffusion in Organic Semiconductors. *Energy Environ. Sci.* **2015**, *8* (7), 1867–1888. https://doi.org/10.1039/c5ee00925a.

(109) Duan, L.; Hou, L.; Lee, T. W.; Qiao, J.; Zhang, D.; Dong, G.; Wang, L.; Qiu, Y. Solution Processable Small Molecules for Organic Light-Emitting Diodes. *J. Mater. Chem.* **2010**, *20* (31), 6392–6407. https://doi.org/10.1039/b926348a.

(110) Jiang, J. M.; Yuan, M. C.; Dinakaran, K.; Hariharan, A.; Wei, K. H. Crystalline Donor-Acceptor Conjugated Polymers for Bulk Heterojunction Photovoltaics. *J. Mater. Chem. A* **2013**, *1* (14), 4415–4422. https://doi.org/10.1039/c2ta00965j.

(111) Schmatz, B.; Yuan, Z.; Lang, A. W.; Hernandez, J. L.; Reichmanis, E.; Reynolds, J. R. Aqueous Processing for Printed Organic Electronics: Conjugated Polymers with Multistage Cleavable Side Chains. *ACS Cent. Sci.* **2017**, *3* (9), 961–967. https://doi.org/10.1021/acscentsci.7b00232.

(112) Stolar, M.; Baumgartner, T. Organic N-Type Materials for Charge Transport and Charge Storage Applications. *Phys. Chem. Chem. Phys.* **2013**, *15* (23), 9007–9024. https://doi.org/10.1039/c3cp51379c.

(113) Mazzio, K. A.; Luscombe, C. K. The Future of Organic Photovoltaics. *Chem. Soc. Rev.* **2015**, *44* (1), 78–90. https://doi.org/10.1039/c4cs00227j.

(114) Guo, X.; Baumgarten, M.; Müllen, K. Designing-Conjugated Polymers for Organic Electronics. *Prog. Polym. Sci.* **2013**, *38*, 1832–1908. https://doi.org/10.1016/j.progpolymsci.2013.09.005.

(115) Kiriy, A.; Pötzsch, R.; Wei, Q.; Voit, B. High-Tech Functional Polymers Designed for Applications in Organic Electronics. *Polym. Degrad. Stab.* **2017**, *145*, 150–156. https://doi.org/10.1016/j.polymdegradstab.2017.06.009.

(116) Kamps, A. C.; Fryd, M.; Park, S. J. Hierarchical Self-Assembly of Amphiphilic Semiconducting Polymers into Isolated, Bundled, and Branched Nanofibers. *ACS Nano* **2012**, *6* (3), 2844–2852. https://doi.org/10.1021/nn300385p.

(117) Sirringhaus, H.; Brown, P. J.; Friend, R. H.; Nielsen, M. M.; Bechgaard, K.; Langeveld-Voss, B. M. W.; Spiering, A. J. H.; Janssen, R. A. J.; Meijer, E. W.; Herwig, P.; de Leeuw, D. M. Two-Dimensional Charge Transport in Self-Organized, High-Mobility Conjugated Polymers. *Nature* **1999**, *401*, 685–688.

(118) Loewe, B. R. S.; Khersonsky, S. M.; Mccullough, R. D. A Simple Method to Prepare Head-to-Tail Coupled, Regioregular Poly(3-Alkylthiophenes) Using Grignard Metathesis. *Adv. Mater.* **1999**, No. 3, 250–253.

(119) Yokoyama, A.; Miyakoshi, R.; Yokozawa, T. Chain-Growth Polymerization for Poly(3-Hexylthiophene) with a Defined Molecular Weight and a Low Polydispersity. *Macromolecules* **2004**, *37*, 1169–1171. https://doi.org/10.1021/ja01211a087.

(120) Sheina, E. E.; Liu, J.; Lovu, M. C.; Laird, D. W.; McCullough, R. D. Chain Growth Mechanism for Regioregular Nickel-Initiated Cross-Coupling Polymerizations. *Macromolecules* **2004**, *37* (10), 3526–3528. https://doi.org/10.1021/ma0357063.

(121) Kiriy, A.; Senkovskyy, V.; Sommer, M. Kumada Catalyst-Transfer Polycondensation: Mechanism, Opportunities, and Challenges. *Macromol. Rapid Commun.* **2011**, *32* (19), 1503–1517. https://doi.org/10.1002/marc.201100316.

(122) Govaerts, S.; Verstappen, P.; Penxten, H.; Defour, M.; Van Mele, B.; Lutsen, L.; Vanderzande, D.; Maes, W. Synthesis of Highly Fluorescent All-Conjugated Alternating Donor–Acceptor (Block) Copolymers via GRIM Polymerization. *Macromolecules* **2016**, *49* (17), 6411–6419. https://doi.org/10.1021/acs.macromol.6b01389.

(123) Schroot, R.; Schubert, U. S.; Jäger, M. Poly(*N* -Alkyl-3,6-Carbazole)s via Kumada Catalyst Transfer Polymerization: Impact of Metal–Halogen Exchange. *Macromolecules* **2016**, *49* (23), 8801–8811. https://doi.org/10.1021/acs.macromol.6b02088.

(124) Kynaston, E. L.; Nazemi, A.; MacFarlane, L. R.; Whittell, G. R.; Faul, C. F. J. J.; Manners, I. Uniform Polyselenophene Block Copolymer Fiberlike Micelles and Block Co-Micelles via Living Crystallization-Driven Self-Assembly. *Macromolecules* **2018**, *51* (3), 1002–1010. https://doi.org/10.1021/acs.macromol.7b02317.

(125) Stefan, M. C.; Javier, A. E.; Osaka, I.; McCullough, R. D. Grignard Metathesis Method (GRIM): Toward a Universal Method for the Synthesis of Conjugated Polymers. *Macromolecules* **2009**, *42* (1), 30–32. https://doi.org/10.1021/ma8020823.

(126) Ono, R. J.; Todd, A. D.; Hu, Z.; Vanden Bout, D. A.; Bielawski, C. W. Synthesis of a Donor-Acceptor Diblock Copolymer via Two Mechanistically Distinct, Sequential Polymerizations Using a Single Catalyst. *Macromol. Rapid Commun.* **2014**, *35* (2), 204–209. https://doi.org/10.1002/marc.201300440.

(127) Nanite. *Band Structure Diagrams for Metal, Etc*. Wikipedia. https://commons.wikimedia.org/wiki/File:Band_filling_diagram.svg (accessed 2024-01-17).

(128) Sneyd, A. J.; Beljonne, D.; Rao, A. A New Frontier in Exciton Transport: Transient Delocalization. *J. Phys. Chem. Lett.* **2022**, *13* (29), 6820–6830. https://doi.org/10.1021/acs.jpclett.2c01133.

(129) Jiang, Y.; McNeill, J. Light-Harvesting and Amplified Energy Transfer in Conjugated Polymer Nanoparticles. *Chem. Rev.* **2017**, *117* (2), 838–859. https://doi.org/10.1021/acs.chemrev.6b00419.

(130) Liu, C.; Wang, K.; Gong, X.; Heeger, A. J. Low Bandgap Semiconducting Polymers for Polymeric Photovoltaics. *Chem. Soc. Rev.* **2016**, *45* (17), 4825–4846. https://doi.org/10.1039/C5CS00650C.

(131) Dou, L.; Liu, Y.; Hong, Z.; Li, G.; Yang, Y. Low-Bandgap Near-IR Conjugated Polymers/Molecules for Organic Electronics. *Chem. Rev.* **2015**, *115* (23), 12633–12665. https://doi.org/10.1021/acs.chemrev.5b00165.

(132) Pirotte, G.; Verstappen, P.; Vanderzande, D.; Maes, W. On the "True" Structure of Push-Pull-Type Low-Bandgap Polymers for Organic Electronics. *Adv. Electron. Mater.* **2018**, *4* (10), 1700481. https://doi.org/10.1002/aelm.201700481.

(133) Tian, J.; Zhang, Y.; Du, L.; He, Y.; Jin, X. H.; Pearce, S.; Eloi, J. C.; Harniman, R. L.; Alibhai, D.; Ye, R.; Phillips, D. L.; Manners, I. Tailored Self-Assembled Photocatalytic Nanofibres for Visible-Light-Driven Hydrogen Production. *Nat. Chem.* **2020**, *12* (12), 1150–1156. https://doi.org/10.1038/s41557-020-00580-3.

(134) Wang, Y.; Michinobu, T. Benzothiadiazole and Its π-Extended, Heteroannulated Derivatives: Useful Acceptor Building Blocks for High-Performance Donor-Acceptor Polymers in Organic Electronics. *J. Mater. Chem. C* **2016**, *4* (26), 6200–6214. https://doi.org/10.1039/c6tc01860b.

(135) Wu, C.; Szymanski, C.; McNeill, J. Preparation and Encapsulation of Highly Fluorescent Conjugated Polymer Nanoparticles. *Langmuir* **2006**, *22* (7), 2956–2960. https://doi.org/10.1021/la060188l.

(136) Tian, Z.; Yu, J.; Wu, C.; Szymanski, C.; McNeill, J. Amplified Energy Transfer in Conjugated Polymer Nanoparticle Tags and Sensors. *Nanoscale* **2010**, *2* (10), 1999–2011. https://doi.org/10.1039/c0nr00322k.

(137) Hicks, G. E. J.; Li, S.; Obhi, N. K.; Jarrett-Wilkins, C. N.; Seferos, D. S. Programmable Assembly of π-Conjugated Polymers. *Adv. Mater.* **2021**, *33* (46), 1–21. https://doi.org/10.1002/adma.202006287.

(138) Baier, M. C.; Huber, J.; Mecking, S. Fluorescent Conjugated Polymer Nanoparticles by Polymerization in Miniemulsion. *J. Am. Chem. Soc.* **2009**, *131* (40), 14267–14273.

https://doi.org/10.1021/ja905077c.

(139) Zhang, Y.; Shaikh, H.; Sneyd, A. J.; Tian, J.; Xiao, J.; Blackburn, A.; Rao, A.; Friend, R. H.; Manners, I. Efficient Energy Funneling in Spatially Tailored Segmented Conjugated Block Copolymer Nanofiber-Quantum Dot or Rod Conjugates. *J. Am. Chem. Soc.* **2021**, *143* (18), 7032–7041. https://doi.org/10.1021/jacs.1c01571.

(140) Sneyd, A. J.; Fukui, T.; Paleček, D.; Prodhan, S.; Wagner, I.; Zhang, Y.; Sung, J.; Collins, S. M.; Slater, T. J. A.; Andaji-Garmaroudi, Z.; MacFarlane, L. R.; Garcia-Hernandez, J. D.; Wang, L.; Whittell, G. R.; Hodgkiss, J. M.; Chen, K.; Beljonne, D.; Manners, I.; Friend, R. H.; Rao, A. Efficient Energy Transport in an Organic Semiconductor Mediated by Transient Exciton Delocalization. *Sci. Adv.* **2021**, *7* (32). https://doi.org/10.1126/sciadv.abh4232.

(141) Zhang, Y.; Tian, J.; Shaikh, H.; MacKenzie, H. K.; He, Y.; Zhao, C.; Lei, S.; Ren, Y.; Manners, I. Tailored Energy Funneling in Photocatalytic π-Conjugated Polymer Nanofibers for High-Performance Hydrogen Production. *J. Am. Chem. Soc.* **2023**, *145* (41), 22539–22547. https://doi.org/10.1021/jacs.3c07443.

(142) Musarurwa, H.; Tavengwa, N. T. Stimuli-Responsive Polymers and Their Applications in Separation Science. *React. Funct. Polym.* **2022**, *175* (April), 105282. https://doi.org/10.1016/j.reactfunctpolym.2022.105282.

(143) Yang, S.; Kang, S. Y.; Choi, T. L. Semi-Conducting 2D Rectangles with Tunable Length via Uniaxial Living Crystallization-Driven Self-Assembly of Homopolymer. *Nat. Commun.* **2021**, *12* (1), 6–13. https://doi.org/10.1038/s41467-021-22879-6.

(144) Xia, T.; Tong, Z.; Xie, Y.; Arno, M. C.; Lei, S.; Xiao, L.; Rho, J. Y.; Ferguson, C. T. J.; Manners, I.; Dove, A. P.; O'Reilly, R. K. Tuning the Functionality of Self-Assembled 2D Platelets in the Third Dimension. *J. Am. Chem. Soc.* **2023**, *145* (46), 25274–25282. https://doi.org/10.1021/jacs.3c08770.

(145) Guo, X. S.; Zhang, Z. K.; Zhang, T. Y.; Tong, Z. Z.; Xu, J. T.; Fan, Z. Q. Interfacial Self-Assembly of Amphiphilic Conjugated Block Copolymer into 2D Nanotapes. *Soft Matter* **2019**, *15* (43), 8790–8799. https://doi.org/10.1039/c9sm01503e.

(146) Han, L.; Fan, H.; Zhu, Y.; Wang, M.; Pan, F.; Yu, D.; Zhao, Y.; He, F. Precisely Controlled Two-Dimensional Rhombic Copolymer Micelles for Sensitive Flexible Tunneling Devices. *CCS Chem.* **2021**, *3* (5), 1399–1409. https://doi.org/10.31635/ccschem.020.202000297.

(147) Kamps, A. C.; Cativo, M. H. M.; Chen, X. J.; Park, S. J. Self-Assembly of DNA-Coupled Semiconducting Block Copolymers. *Macromolecules* **2014**, *47* (11), 3720–3726. https://doi.org/10.1021/ma500509u.

(148) Kang, S.; Kim, G. H.; Park, S. J. Conjugated Block Copolymers for Functional Nanostructures. *Acc. Chem. Res.* **2022**, *55* (16), 2224–2234. https://doi.org/10.1021/acs.accounts.2c00244.

(149) Vespa, M.; Hudson, Z. M.; Manners, I. Homogeneous and Segmented Nanofibers with a Conjugated Poly[3-(2′-Ethylhexyl)Thiophene] Core via Living Crystallization-Driven Self-Assembly. *Macromolecules* **2024**, *57* (4), 1509–1520. https://doi.org/10.1021/acs.macromol.3c02357.

(150) Liu, N.; Gao, R.; Wu, Z. Helix-Induced Asymmetric Self-Assembly of Π-Conjugated Block

Copolymers: From Controlled Syntheses to Distinct Properties. *Acc. Chem. Res.* **2023**, *56*, 2954–2967. https://doi.org/10.1021/acs.accounts.3c00425.

Chapter 2

Homogeneous and Segmented Nanofibers with a Conjugated Poly(3-(2´-ethylhexyl)thiophene) Core *via* Living Crystallization-Driven Self-Assembly

This chapter has been adapted from:

Marcus Vespa, Zachary M. Hudson, and Ian Manners. *Macromolecules* **2024**, *57*(4), 1509-1520. https://doi.org/10.1021/acs.macromol.3c02357.

Contributions:

This work was conceived by Prof. Ian Manners and Marcus Vespa. Marcus Vespa performed the synthesis, self-assembly experiments, and characterizations. Prof. Ian Manners, Dr. Shixing Lei, and Dr. Juan Diego Garcia Hernandez contributed to data discussions. Marcus Vespa wrote the manuscript with input from Prof. Ian Manners and Prof. Zachary Hudson. AFM images made use of the 4D LABS core facility at Simon Fraser University (SFU) and were obtained by Ayesha Nadeem.

2.1 Abstract

The ambient temperature living crystallization-driven self-assembly (CDSA) seeded growth method for polymeric amphiphiles with a crystallizable core-forming block has emerged as a promising approach to morphologically pure samples of uniform, length-controlled 1D nanofibers as well as more complex architectures such as segmented assemblies. Access to nanofibers with poly(3-hexylthiophene) (P3HT) as the core-forming block is highly desirable as a result of their optoelectronic properties. However, application of the living CDSA method to P3HT diblock copolymers has proven to be a challenge due to rapid P3HT crystallization. This causes uncontrolled homogenous nucleation and defect formation, resulting in a loss of length control and increased nanofiber length dispersity. Herein we have explored the replacement of the P3HT core-forming block with a more soluble poly(3-(2'-ethylhexyl)thiophene) (P3EHT) core, and demonstrate improved control over nanofiber formation. Specifically, we have studied two P3EHT-containing diblock copolymers, $P3EHT_{23}$-*b*-PEG_{113} (PEG = poly(ethylene glycol)) and $P3EHT_{19}$-*b*-$P2VP_{138}$ (P2VP = poly(2-vinylpyridine). Seeded growth of $P3EHT_{19}$-*b*-$P2VP_{138}$ nanofibers at 22 °C produced low dispersity nanofibers with length control up to ~1 μm while $P3EHT_{23}$-*b*-PEG_{113} only provided length control up to ~300 nm under similar conditions. Self-nucleation was postulated to impair efficient seeded growth of $P3EHT_{23}$-*b*-PEG_{113} and solution-state variable-temperature UV-Vis spectroscopy was used to locate temperatures where self-nucleation was suppressed. These studies revealed that homogenous nucleation is suppressed for at least 24 h at or above 30 °C for $P3EHT_{23}$-*b*-PEG_{113} in a 1:1 *n*-butanol:methanol solution. In the case of $P3EHT_{23}$-*b*-PEG_{113}, this allowed us to efficiently perform seeded growth under conditions (≥30 °C) that resulted in the formation of near-uniform nanofibers with controlled lengths of up to ~1 μm. Self-nucleation suppression was also successfully utilized during thermal self-seeding

experiments wherein P3EHT$_{23}$-*b*-PEG$_{113}$ nanofibers with controlled lengths up to 2.8 μm and low length dispersities were formed. Seeded growth of P3EHT$_{19}$-*b*-P2VP$_{138}$ from the termini of P3EHT$_{23}$-*b*-PEG$_{113}$ seeds at 22 °C provided access to well-defined B-A-B triblock comicelles with a segmented coronal structure.

2.2 Introduction

Self-assembly of conjugated, semiconducting organic polymers is of intense current interest due to their ability to form functional 1D nanofibers for optoelectronic applications.[1–9] Conjugated polymers have large absorption cross sections and can exhibit highly efficient energy transfer which makes them excellent candidates for light harvesting, light-emitting, photovoltaic, and photodetection applications.[10–12] Nanofiber properties are dependent on their length and chemical composition, and exerting control over these factors is crucial for maximizing optoelectronic performance.[13,14]

Living crystallization-driven self-assembly (CDSA) of block copolymers (BCPs) with a crystallizable core-forming block has emerged as a useful method to generate low length dispersity ($Đ_L < 1.1$, where $Đ_L = L_w/L_n$) samples of 1D nanofibers with controlled size and dimensions.[3,4,7,14–19] Two main self-assembly methods exist under the umbrella term “living CDSA”. The first approach is the seeded growth method using pre-existing, externally added seeds that begins with the formation of long polydisperse nanofibers through homogeneous nucleation.[16,20] This is achieved by: 1) dissolving the BCP in a solvent that is suitable for both blocks (common solvent) and adding solvent which selectively solvates the corona-forming block, inducing crystallization of the insoluble core-forming block or 2) by heating the BCP in a temperature-dependent selective

solvent that acts as a common solvent at high temperatures and a corona-selective solvent at room temperature. The long fibers are subsequently fragmented using ultrasonication to generate "seed" micelle fragments with relatively low average lengths.[16,20] The seeds dispersed in a selective solvent remain active towards the addition of molecularly dissolved BCP (unimer) in a good solvent for both blocks. This leads to epitaxial crystallization at the seed termini at ambient temperature and creates nanofibers with final lengths that are linearly correlated to the unimer-to-seed mass ratio (m_{unimer}/m_{seed}), allowing for the fabrication of nanofibers with varying and predictable lengths. This method also provides the ability to fabricate modular, segmented B-A-B triblock comicelles by adding unimer with the same core-forming block, but with a corona-forming block that is chemically distinct from that of the BCP used for the seed.

The second living CDSA method is termed thermal self-seeding and in this approach the BCP is heated in a selective solvent to induce dissolution of the less crystalline regions of the seeds.[13,21–24] Dissolution generates free unimer which, upon cooling, crystallizes epitaxially *in situ* onto the termini of the surviving seeds resulting in length-controlled nanofibers. The nanofiber lengths are dependent on the unimer-to-seed ratio which itself strongly depends on the self-seeding temperature. As the temperature is increased, the number of surviving seeds decreases and the amount of unimer released into solution increases, resulting in longer nanofibers. Small modulations of the self-seeding temperature result in large nanofiber length differences which makes prediction of the final lengths more challenging compared to when seeded growth is used. The exponential nature of the length versus self-seeding temperature curve makes it difficult to obtain short nanofibers.[22,23] Furthermore, the temperature at which polymer crystals melt depends on their thermal history and sample crystallinity, implying that the self-seeding temperatures are batch-dependent.[23,25–27]

Previous investigations into ambient temperature seeded growth of conjugated BCPs such as P3HT-*b*-PDMS (PDMS = poly(dimethylsiloxane), P3HT-*b*-PMMA (PMMA = poly(methyl methacrylate), and P3HT-*b*-P2VP have shown that the generation of new nuclei through unimer homogeneous (or self-) nucleation (as opposed to growth from existing seeds or nanofibers) makes control over nanofiber length challenging and results in large dispersities.[28–30] Suppression of this process is critical to fabricate uniform samples of polythiophene nanofibers and a method that effectively inhibits unimer homogenous nucleation termed self-nucleation suppression was developed and reported by our group.[27] The method involves heating a nanofiber solution to a temperature where the nanofibers fully dissolve and the BCP is in the fully unimeric state then cooling the solution to the lowest temperature where a supersaturated solution forms, but nucleation does not occur. Seed nuclei are added to the supersaturated solution at the self-nucleation suppression temperature resulting in efficient epitaxial growth from the seed termini. Because the solution is held at a temperature where homogeneous nucleation is suppressed, growth from existing nuclei (i.e. the externally added seeds) is favored over the generation of new nuclei. Self-nucleation suppressed seeded growth of the BCP *rr*P3HT-*b*-*rs*P3HT (*rr* = regioregular and *rs* = regiosymmetric, respectively) allowed for the formation of length-controlled nanofibers that reached lengths up to 4 μm with $Đ_L$ under 1.09; the first example of length-controlled P3HT BCP nanofibers made by seeded growth over 2 μm.[27]

During self-assembly studies of the P3HT BCPs we also found evidence that rapid unimer crystallization onto seed termini creates crystalline defects in the micelle core that prevent epitaxial growth and only provide length control over a low range of lengths (< 300 nm).[28–30] Replacement of the aliphatic *n*-hexyl side chains for more solubilizing *n*-octyl groups led to a significant improvement in length control with values up to ca. 600 nm and $Đ_L$ = 1.1-1.3.[31] This work

indicated that the presence of a larger, more solubilizing side group promotes nanofiber elongation and hinders homogenous nucleation. Introducing a larger steric barrier to crystallization into the polythiophene repeat unit is proposed to slow down face-to-face packing of the polymer chains while the increased solubility promotes structural rearrangement of the polythiophene chains and decreases the amount of defects during the self-assembly process.[31] It has also been previously established that poly(3-(2'-ethylhexyl)thiophene) (P3EHT) exhibits slower crystallization kinetics relative to P3HT which is a consequence of the stereocenter at the C_2 position of the branched hexyl side chain, which prevents side chains from fully interdigitating.[32] We have previously used the higher solubility of P3EHT to create the outer core of nanofibers with an inner crystalline polyfluorene core domain, which function as coaxial heterojunction nanowires.[33] These features encouraged us to investigate if BCPs with a P3EHT core-forming block offered improvements in the length control for nanofibers assembled using living CDSA.

Herein, we detail the synthesis, characterization, and self-assembly behaviour of two P3EHT BCPs, P3EHT$_{23}$-*b*-PEG$_{113}$ and P3EHT$_{19}$-*b*-P2VP$_{138}$, and further develop the library of conjugated BCPs that are available for self-assembly using living CDSA. We also extend the previously described self-nucleation suppression method[27] to these BCPs and show that this approach can be expanded to include polythiophene BCP systems other than the previously reported P3HT. Self-nucleation suppression was used during seeded growth and self-seeding experiments to fabricate nanofibers with lengths up to ca. 3 μm and we successfully fabricated B-A-B (P3EHT$_{19}$-*b*-P2VP$_{138}$-*m*-P3EHT$_{23}$-*b*-PEG$_{113}$-*m*-P3EHT$_{19}$-*b*-P2VP$_{138}$) (PEG = polyethylene glycol, *m* = micelle segment) block comicelle structures, the first reported examples of well-defined and modular block structures utilizing a P3EHT core.

2.3 Results and Discussion

2.3.1 Block copolymer synthesis and characterization

Alkyne-terminated P3EHT homopolymers were formed by Grignard Metathesis Polymerization. Addition of an *ortho*-tolyl-functionalized nickel(II) catalyst to a solution of dibrominated thiophene monomer resulted in the formation of the $P3EHT_{23}$ homopolymer with a living chain end. Subscripts denote the polymer degree of polymerization (DP_n). *In situ* termination of the $P3EHT_{23}$ chain with an alkyne end group was achieved through the addition of excess ethynylmagnesium bromide (Scheme S2.3).[34] The DP_n of $P3EHT_{23}$ was determined by relative integration of ^{1}H NMR spectrum resonances (Figure S2.3) corresponding to the *ortho*-tolyl methyl group at 2.51 ppm and the proton in the 4-position on the thiophene rings at 6.94 ppm. The terminal hydroxy group on a PEG-methyl ether homopolymer was initially converted to a tosyl group followed by azidation using sodium azide (Scheme S2.4). The azide-functionalized-PEG (PEG_{113}-N_3) was suitable for block copolymerization using copper-mediated azide-alkyne cycloaddition click chemistry (CuAAC). A CuAAC-mediated click reaction was performed between the azide-functionalized-PEG_{113} and the alkyne-terminated-$P3EHT_{23}$ to form $P3EHT_{23}$-*b*-PEG_{113} (Figure 2.1, Scheme S2.6). Following $P3EHT_{23}$-*b*-PEG_{113} synthesis, remaining PEG_{113}-N_3 homopolymer was removed using water washes followed by successive precipitation into methanol (MeOH) and acetone and final purification using preparatory gel permeation chromatography (GPC). The resulting product was then analyzed using GPC and the $P3EHT_{23}$-*b*-PEG_{113} trace had a relatively lower retention volume suggesting that the cycloaddition reaction was successful and a species with higher molecular mass was formed when compared to the constituent homopolymers (Figure S2.1). BCP analysis using ^{1}H NMR spectroscopy showed broadened P3EHT signals compared to the alkyne-P3EHT homopolymer, which is consistent with block copolymerization (Figure S2.5).

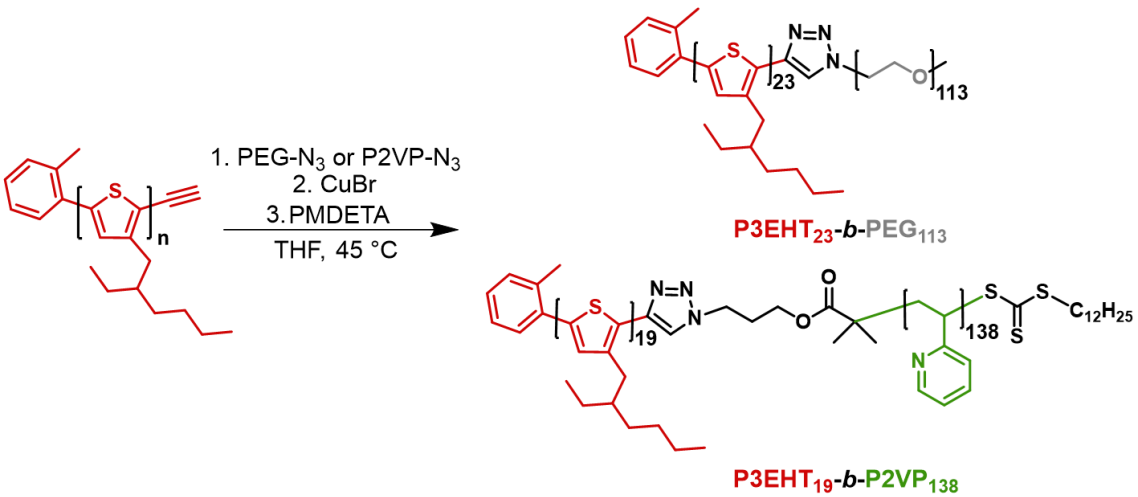

Polymer	M_n (Da)	M_w (Da)	$Đ_M$[a]
P3EHT$_{23}$-*b*-PEG$_{113}$	11,900[a]; 9,600[b]	12,600[a], 10,200[b]	1.06
P3EHT$_{19}$-*b*-P2VP$_{138}$	18,300[a];18,800[b]	20,000[a], 22,100[b]	1.14

Figure 2.1. Chemical structures and molar mass characterization of the synthesized BCPs analyzed by GPC and integration of proton nuclear magnetic resonance (^{1}H NMR) spectra. [a]Determined by GPC. [b]Determined by relative integration of ^{1}H NMR spectrum signals. M_w[b] values from ^{1}H NMR signals were estimated by using the $Đ_M$[a] obtained from GPC data and multiplying it by M_n[b] values obtained by ^{1}H NMR spectroscopy according to the equation $(Đ_M^a)(M_n^b) = M_w^b$. For alkynyl-P3EHT, relative integration was performed between ^{1}H NMR signals at 2.51 ppm (s, *o*-tolyl CH_3 = 3H) and 6.97 ppm (s, thiophene CH = 1H). For P2VP-N_3, relative integration was performed between ^{1}H NMR signals at 3.25 ppm (bs, RAFT CH_2, 2H) and 8.27 (bm, pyridine CH, 1H). CuBr = copper(I) bromide, PMDETA = *N,N,N′,N″,N″*-pentamethyldiethylenetriamine, THF = tetrahydrofuran.

The azide-terminated P2VP (P2VP$_{138}$-N_3) corona-forming block was synthesized through reversible addition-fragmentation chain-transfer polymerization (RAFT) using an azide-terminated trithiocarbonate chain-transfer agent (Scheme S2.5). The DP_n of the P2VP$_{138}$-N_3 homopolymer was determined by relative integration of ^{1}H NMR spectrum resonances (Figure S2.4) corresponding to the methylene group on the trithiocarbonate RAFT agent at 3.20 ppm and the proton in the 6-position on the pyridine rings from 8.02-8.60 ppm. The CuAAC click reaction was then performed between alkynyl-P3EHT$_{19}$ and P2VP$_{138}$-N_3 to form P3EHT$_{19}$-*b*-P2VP$_{138}$

(Figure 2.1, Scheme S2.7). Following precipitation into hexanes, excess P2VP-N_3 was removed by repetitive acidification of the P2VP block, removal of the P3EHT homopolymer using THF, basification of the P2VP block and precipitation into acetone several times to remove any P2VP homopolymer. Following this process, the material was analyzed using GPC which also showed the formation of a species with a higher molecular mass than the alkynyl-P3EHT$_{19}$ and P2VP$_{138}$-N_3 homopolymers (Figure S2.2). ^{1}H NMR analysis of the final product showed the presence of signals belonging to both the P3EHT block as well as the P2VP block. Further, a signal at 7.60 ppm representing the proton on the triazole ring is present, indicating successful formation of the triazole ring, and there is an absence of the peak at 3.51 ppm representing removal of the alkynyl proton on the P3EHT terminus (Figure S2.6). The polymer molar mass dispersity ($Đ_M$, where $Đ_M = M_w/M_n$) and purity of the homopolymer precursors and final BCPs were determined by GPC analysis using triple detection calibration methods (Figure S2.1, S2.2) and thin layer chromatography, respectively. The characterization details of the resultant BCPs are summarized in Figure 2.1. Both BCPs were isolated as red solids in overall yields of 16% for P3EHT$_{23}$-*b*-PEG$_{113}$ and 4% for P3EHT$_{19}$-*b*-P2VP$_{138}$ and possessed low molar mass dispersities of $Đ_M$ = ~1.1.

2.3.2 Solution self-assembly of P3EHT$_{23}$-*b*-PEG$_{113}$ and P3EHT$_{19}$-*b*-P2VP$_{138}$

Polydisperse fiber-like micelles (nanofibers) of P3EHT$_{23}$-*b*-PEG$_{113}$ were formed in two steps. First, the solid material was heated in *n*-butanol (*n*BuOH) to 90 °C for 30 min. to ensure the BCP was fully dissolved. Next, the solution was cooled to ambient temperature (22 °C) slowly (over ca. 4 h) and aged for 24 h. Heating the solution to 90 °C resulted in the formation of a clear, yellow solution and cooling the solution from 90 °C to 22 °C followed by aging led to a red solution, consistent with planarization of the polymer backbone and extension of the π-conjugation

of the core-forming block during self-assembly (Figure S2.10a, b).[5,35,36] MeOH was then added to form a 1:1 v/v *n*BuOH:MeOH mixture (0.1 mg/mL) which was drop-cast onto a carbon-coated copper grid and imaged using bright-field transmission electron microscopy (TEM) (Figure 2.2a, b, S2.15a, b). The long-term colloidal stability of the P3EHT$_{23}$-*b*-PEG$_{113}$ nanofibers was confirmed as no precipitation was observed when the 1:1 *n*BuOH:MeOH nanofiber solution was allowed to stand at 22 °C for 16 months (Figure S2.7b). Polydisperse P3EHT$_{19}$-*b*-P2VP$_{138}$ nanofibers were also fabricated by heating the solid material in *n*BuOH to 90 °C for 30 min., and then cooling to ambient temperature (22 °C) slowly (over ca. 4 h) and aging for 24 h (Figure 2.2c, d, S2.16a, b). The addition of MeOH was not necessary to maintain the colloidal stability in this case as the P3EHT$_{19}$-*b*-P2VP$_{138}$ fibers were stable in pure *n*BuOH over 8 months. Stabilization of this BCP with only *n*BuOH is likely a result of the lower relative polarity of P2VP$_{138}$ compared to PEG$_{113}$.

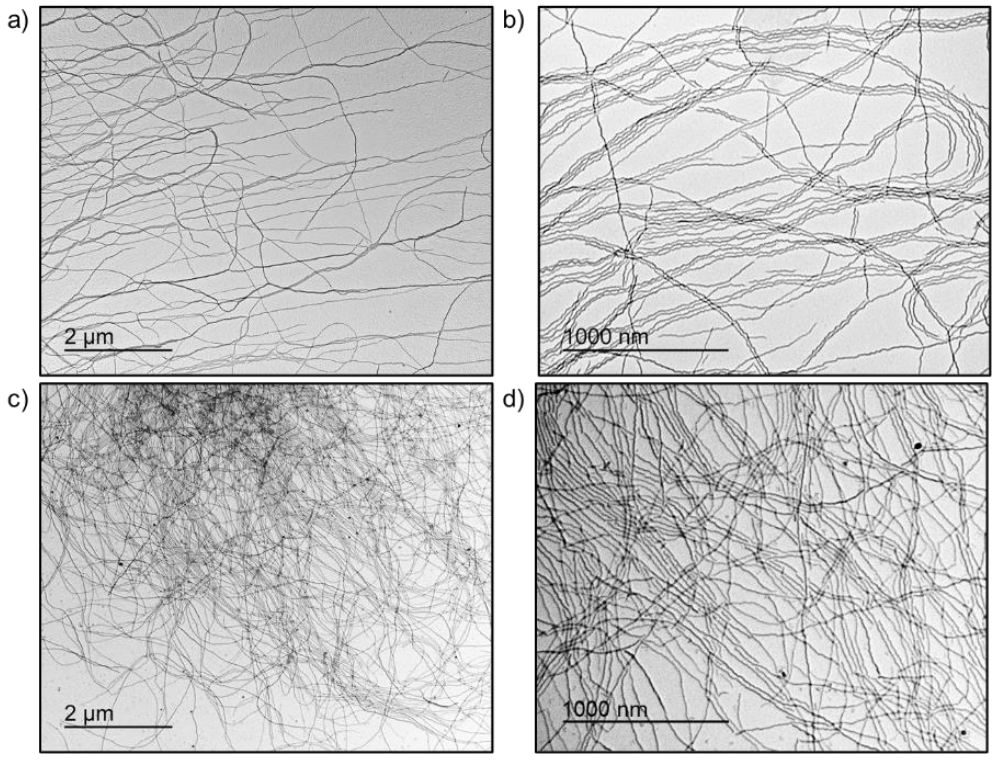

Figure 2.2. TEM images at different degrees of magnification of polydisperse **(a, b)** P3EHT$_{23}$-*b*-PEG$_{113}$ and **(c, d)** P3EHT$_{19}$-*b*-P2VP$_{138}$ nanofibers following solvent evaporation.

To gain more insight into the internal crystalline order of the nanofiber core, wide-angle X-ray scattering (WAXS) was performed on a film of polydisperse P3EHT$_{23}$-*b*-PEG$_{113}$ nanofibers that was formed by drop-casting a 5 mg/mL 1:1 *n*BuOH:MeOH solution onto a crystalline silicon substrate. A sharp Bragg peak at a q value of q = 0.42 Å^{-1} (d = 1.51 nm) was clearly observed (Figure S2.12a) which corresponds to the (100) plane associated with the alkyl side chain stacking distance,[37] with a higher-order broad reflection of this peak visible at q = 0.84 Å^{-1} (d = 0.75 nm) (Figure S2.14). The peak at q = 1.30 Å^{-1} (d = 0.49 nm) corresponds to the reflection caused by π-π stacking between adjacent polymer chains within the micelle core (010 plane), which experimentally has a slightly shorter distance of 0.49 nm compared to a simulated P3EHT crystal (d = 0.51 nm).[38] These diffraction peaks demonstrate the crystalline nature of the P3EHT core-forming block in the P3EHT$_{23}$-*b*-PEG$_{113}$ nanofibers. Another prominent peak at q = 1.35 Å^{-1} matches the Bragg reflection associated with crystalline PEG domains formed upon drying of the P3EHT$_{23}$-*b*-PEG$_{113}$ nanofiber solution.[39] WAXS analysis was performed on a film of polydisperse P3EHT$_{19}$-*b*-P2VP$_{138}$ nanofibers that was formed by drop-casting a 5 mg/mL *n*BuOH solution onto a crystalline silicon substrate (Figure S2.12b). As was in the case of the P3EHT$_{23}$-*b*-PEG$_{113}$ film WAXS spectrum, a sharp Bragg peak at q = 0.42 Å^{-1} (d = 1.51 nm) associated with alkyl chain interdigitation was observed, with a sharp higher order peak at q = 0.86 Å^{-1} (d = 0.73 nm). The peak associated with π-π stacking was found at q = 1.25 Å^{-1} (d = 0.51 nm), suggesting that the π-π stacking distance between the thiophene rings in adjacent P3EHT chains in nanofibers formed from P3EHT$_{19}$-*b*-P2VP$_{138}$ is slightly larger than in P3EHT$_{23}$-*b*-PEG$_{113}$ nanofibers. There are two sharp peaks at q = 1.49 Å^{-1} and 1.72 Å^{-1} which have been previously identified as belonging to the (320) and (410) planes of P3EHT crystals.[37]

To provide further characterization of the P3EHT$_{23}$-*b*-PEG$_{113}$ nanofiber dimensions, a 1:1 *n*BuOH:MeOH solution (0.05 mg/mL) of ~800 nm nanofibers prepared by seeded growth (Figure S2.30e) was drop cast onto a glow discharged silicon substrate and analyzed using atomic force microscopy (AFM) (Figure S2.13a). The average height was found to be 7.3 nm ± 0.7 nm when measurements were made perpendicular to the long axis of the nanofiber (Figure S2.13b). Crystal simulation models and diffraction data from other reports have been used to determine that the height of a P3EHT crystal along the alkyl-stacking direction is 1.45 – 1.52 nm[38,40] and when this is taken together with the alkyl chain stacking distance of 1.51 nm found above, a nanofiber height of 7.3 nm suggests that ~6 lamellae of P3EHT chains interdigitate in this direction to constitute the nanofiber height (Figure S2.14). The heights are similar to the nanofiber heights found using AFM when analyzing nanofibers with a P3HT core-forming block made by living CDSA which were shown to range from 1.6–7 nm depending on the corona-forming block used.[41] Measurements of the nanofiber core width were also extracted from the TEM data which showed an average width (W_n) value of W_n = 9.8 ± 1.4 nm. The P3EHT unit cell contains a 3-(2'-ethylhexyl)thiophene dimer and the width of this unit along the polymer chain backbone is 7.72 Å.[38] Considering this, a P3EHT polymer with a DP_n = 23 would have a nanofiber core width of 8.9 nm, which is in very good agreement with the widths measured by TEM. Regioregular P3HT chain-folding occurs at a molecular mass of roughly 10 kDa (DP_n = ~60).[13] Because the DPs of the P3EHT core-forming blocks are well below that limit, we infer that chain-folding has not taken place; however, we cannot fully exclude this possibility, nor can we exclude that the chains may be stacking in a different way.

A solution of ~400 nm P3EHT$_{19}$-*b*-P2VP$_{138}$ nanofibers prepared by seeded growth (Figure S2.27e) was also analyzed using AFM by drop casting the solution (0.05 mg/mL in *n*BuOH) onto

a glow discharged silicon substrate (Figure S2.13c). The average height was found to be 5.9 ± 0.2 nm when measurements were made perpendicular to the long axis of the nanofiber (Figure S2.13d). When considering the alkyl chain stacking distance of 1.51 nm, a nanofiber height of 5.9 nm suggests that 5 lamellae of P3EHT chains interdigitate in this direction to constitute the nanofiber height. The difference between the number of lamellae which interdigitate to comprise the height of P3EHT$_{19}$-*b*-P2VP$_{138}$ nanofibers (5) compared to P3EHT$_{23}$-*b*-PEG$_{113}$ nanofibers (6) may be due to the relatively higher volume fraction of the P2VP block relative to the PEG block, resulting in higher coronal steric repulsion and preventing further lamellae from interdigitating. The nanofiber core widths were also measured using the TEM data and showed an average nanofiber width (W_n) of W_n = 12.0 ±1.9 nm. A P3EHT polymer with a DP_n = 19 would have a nanofiber core width of 7.4 nm, which is smaller than the width measured by TEM. This discrepancy may be resultant of the fact that the electron density of the P2VP corona is significantly higher than the electron density of the PEG corona, causing darkening of the regions around the core and the appearance of relatively thicker nanofibers which makes accurate determination of the width by TEM difficult in this case.

2.3.3 Attempted length-control of homogenous nanofibers by seeded growth at ambient temperature (22 °C)

a) P3EHT$_{23}$-*b*-PEG$_{113}$

Small nanofiber fragments that function as seeds were produced by sonication of a solution of polydisperse P3EHT$_{23}$-*b*-PEG$_{113}$ nanofibers (Figure S2.15a, b) in 1:1 *n*BuOH:MeOH at 0 °C for 3 h (L_n = 42 nm, $Đ_L$ = 1.28) (Figure S2.17a, b). Seeded growth of length-controlled P3EHT$_{23}$-*b*-PEG$_{113}$ nanofibers at 22 °C was attempted by adding increasing volumes of unimeric P3EHT$_{23}$-

b-PEG$_{113}$ (2 mg/mL) in tetrahydrofuran (THF) to seed solutions in 1:1 *n*BuOH:MeOH. Nanofibers with lengths ranging from L_n = 168 nm (m_{unimer}/m_{seed} = 4) to L_n = 1058 nm (m_{unimer}/m_{seed} = 20) and dispersities from $Đ_L$ = 1.29-1.57 were fabricated (Figure S2.21a-f, S2.22, S2.23a-f, Table S2.1). The experimental nanofiber lengths are close to the theoretically predicted values within one standard deviation (σ); however, this is likely a consequence of the large standard deviation in the length values. Theoretically predicted values are based on the equation $L_{n(theory)} = L_{n(seed)}[(m_{unimer}/m_{seed}) +1]$.[27] As an example, at m_{unimer}/m_{seed} = 12, $L_{n(theory)}$ is 546 nm and the experimental value is 609 nm. Annealing of polythiophene crystals has previously been shown to improve molecular packing in crystallites,[42,43] and so seeded growth experiments using the same protocol were performed with seeds from the same batch which had been annealed in *n*BuOH at 30 °C for 18 h (Figure S2.18a). Upon annealing in *n*BuOH at 30 °C for 18 h and cooling to 22 °C, no significant seed dissolution occurred as evidenced by the lack of significant changes in the average length or dispersity of the seeds (L_n = 44 nm, $Đ_L$ = 1.26) (Figure S2.18b). Seeded growth using annealed P3EHT$_{23}$-*b*-PEG$_{113}$ seeds resulted in nanofibers with lengths ranging from L_n = 131 nm (m_{unimer}/m_{seed} = 4) to L_n = 1528 nm (m_{unimer}/m_{seed} = 20) and dispersities from $Đ_L$ = 1.22-1.30 (Figure S2.24a-f, S2.25, S2.26a-f, Table S2.2). The resulting nanofiber dispersities were up to $Đ_L$ = ~1.3 as opposed to when the seeds were not annealed ($Đ_L$ = ~1.5). The lowered dispersity values provide indirect experimental evidence that there are defects in the seeds caused by sonication and that annealing creates a more defect-free crystalline nanofiber core. Unfortunately, discrepancies between the experimental values of L_n and theoretical length values still exist at m_{unimer}/m_{seed} ratios ≥ 12 which has been observed with seeded growth of previous poly(3-alkylthiophene) BCPs.[28–30] Increased nanofiber dispersity and deviations from theoretically predicted lengths at higher equivalents in these experiments are postulated to be the result of unimer self-nucleation.

b) P3EHT$_{19}$-*b*-P2VP$_{138}$

P3EHT$_{19}$-*b*-P2VP$_{138}$ seeds were produced by ultrasonication of a solution of polydisperse P3EHT$_{19}$-*b*-P2VP$_{138}$ nanofibers (Figure 2.2c, d) in *n*BuOH at 0 °C for 3 h (L_n = 23 nm, $Đ_L$ = 1.07) (Figure S2.20a, b). The seeds were annealed at 30 °C for 18 h prior to use. Seeded growth of length-controlled P3EHT$_{19}$-*b*-P2VP$_{138}$ nanofibers at 22 °C was attempted by adding increasing volumes of unimeric P3EHT$_{19}$-*b*-P2VP$_{138}$ (2 mg/mL in $CHCl_3$) to seed solutions in *n*BuOH. Nanofibers with lengths ranging from L_n = 107 nm (m_{unimer}/m_{seed} = 4) to L_n = 912 nm (m_{unimer}/m_{seed} = 40) and low dispersities ($Đ_L$ = 1.07 - 1.09) were fabricated (Figure 2.3a-e, S2.27a-h, S2.29a-h, Table S2.3). The experimental nanofiber lengths align exceptionally well to the theoretically predicted values. Compared to seeded growth of length-controlled P3EHT$_{23}$-*b*-PEG$_{113}$ nanofibers at 22 °C, the experimental lengths of P3EHT$_{19}$-*b*-P2VP$_{138}$ nanofibers prepared by seeded growth at 22 °C are longer and are much closer to theoretically predicted values (Figure 2.3e). This is proposed to be a consequence of the core:corona block ratio difference between P3EHT$_{23}$-*b*-PEG$_{113}$ (~1:5) and P3EHT$_{19}$-*b*-P2VP$_{138}$ (~1:7). The comparatively higher solubility of P3EHT$_{19}$-*b*-P2VP$_{138}$ suggests that self-nucleation is less likely to occur during seeded growth. It is also possible that the chemical identity differences between P2VP and PEG plays a role that affects their ability to act as solubilizing shell blocks.

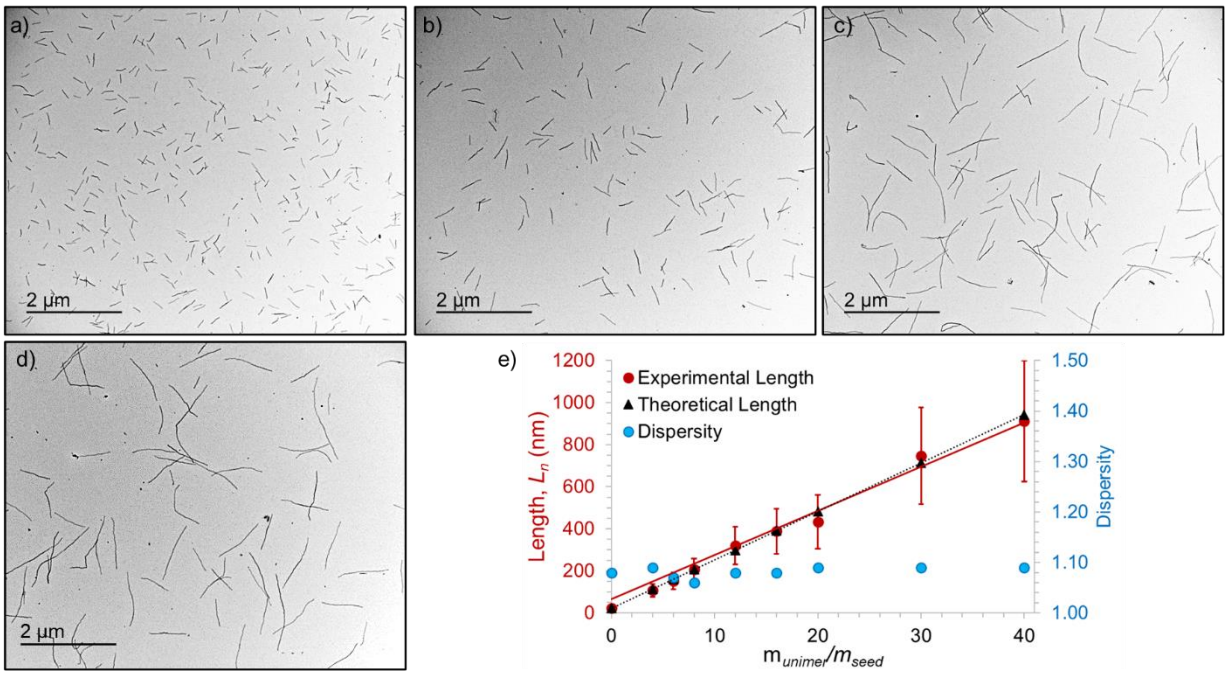

Figure 2.3. TEM images of length-controlled P3EHT$_{19}$-*b*-P2VP$_{138}$ nanofibers; unimer to seed ratio m_{unimer}/m_{seed} = **(a)** 10, **(b)** 20, **(c)** 30, and **(d)** 40. **(e)** Plot showing the dependence of P3EHT$_{19}$-*b*-P2VP$_{138}$ nanofiber length (L_n) on unimer-to-seed ratio (m_{unimer}/m_{seed}). Seeds (L_n = 23 nm, $Đ_L$ = 1.07) that were annealed at 30 °C for 18 h prior were used for seeded growth experiments at 22 °C. Error bars represent standard deviation.

2.3.4 Evaluation of a self-nucleation suppression temperature for P3EHT$_{23}$-*b*-PEG$_{113}$ by variable-temperature UV-Vis spectroscopy

Due to the difficulties obtaining P3EHT$_{23}$-*b*-PEG$_{113}$ nanofibers with low D_L and lengths which match theoretically predicted values *via* seeded growth at 22 °C, variable-temperature UV-Vis spectroscopy was used to find temperatures where self-nucleation is suppressed following heating of the P3EHT$_{23}$-*b*-PEG$_{113}$ nanofibers in a temperature-dependant selective solvent mixture. At 20 °C and in the self-assembled state, P3EHT$_{23}$-*b*-PEG$_{113}$ polydisperse nanofibers in a 1:1 *n*BuOH:MeOH solution (0.05 mg/mL) exhibit an absorbance shoulder at 440 nm representing an intrachain π-π* transition,[5] a maximum absorption (λ_{max}) at 480 nm as well as vibronic absorbances at 520 nm and 570 nm associated with the crystalline P3EHT core (Figure

2.4a, S2.7). The ratio between the amplitudes of the vibronic $A_{0\text{-}0}$ (570 nm) and the $A_{0\text{-}1}$ (520 nm) peaks is < 1 which is characteristic for partially ordered H-aggregate-like chains coexisting with non-aggregated chain sequences.[44] Heating the solution from 20 °C to 90 °C resulted in a red-to-orange/yellow color transition associated with a lower conjugation length caused by the onset of free rotation of the thiophene rings that are mainly planar in the solid state (Figure 2.4a, Figure S2.10a, b).[35,36,45] Nanofiber dissociation and the emergence of unimeric BCP was detected by the disappearance of the vibronic peaks associated with the P3EHT core at 520 nm and 570 nm (Figure 2.4a, b) and blue-shifting of the λ_{max} from 480 nm to 440 nm. Thompson and coworkers found a similar UV-Vis absorption maximum at 445 nm when analyzing a chlorobenzene solution of P3EHT homopolymer where the P3EHT is fully solubilized.[46] A P3EHT thin film that was spin-cast from the chlorobenzene solution and annealed under N_2 at 150 °C for 30 min. caused red-shifting of the absorbance at 445 nm by ~40 nm to a new absorption maximum at 485 nm as well as vibronic features at higher wavelengths, suggesting solid state crystalline order.[46] From these experiments, it is clear that the fibers have been fully dissolved at 90 °C and only unimeric BCP exists at this temperature. When the 1:1 *n*BuOH:MeOH $P3EHT_{23}$-*b*-PEG_{113} polydisperse nanofiber solution was cooled from 90 °C to 20 °C over 3.5 h, a slight increase in the absorbance at 570 nm was observed (Figure 2.4b), indicating the slow formation of vibronic structures characteristic of a crystalline P3EHT core. A thermal hysteresis exists between solutions that were heated from 20 °C to 90 °C and those that were cooled from 90 °C to 20 °C (Figure 2.4b). This has been observed previously in other P3HT-based systems due to the crystal lattice energy that needs to be overcome for dissolution to occur.[27,45]

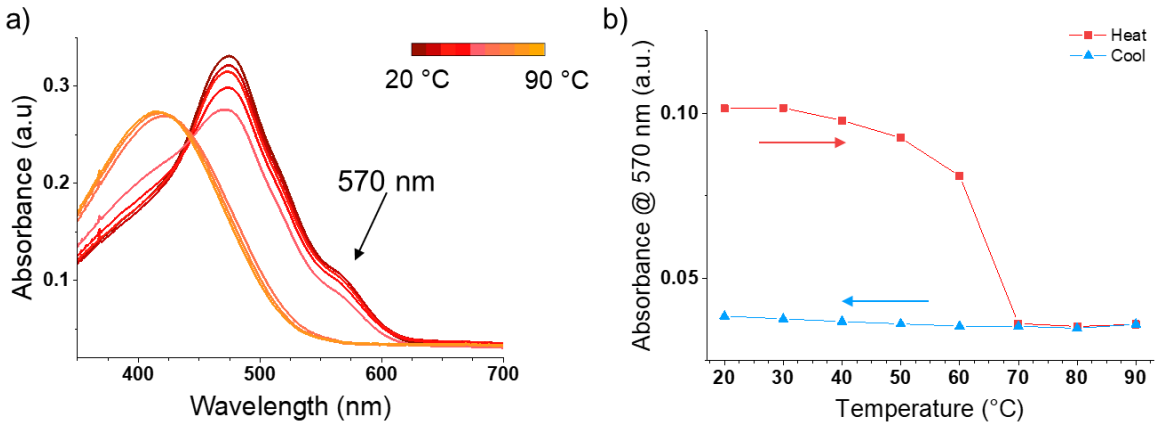

Figure 2.4. (a) Overlayed UV-Vis absorbance spectra of a P3EHT$_{23}$-*b*-PEG$_{113}$ polydisperse nanofiber solution (0.05 mg/mL) in 1:1 *n*BuOH:MeOH that was heated from 20 °C to 90 °C (10 °C/min) with scans taken every 10 °C increment at a heating rate of 10 °C/min. **(b)** Absorbance plot at 570 nm of a P3EHT$_{23}$-*b*-PEG$_{113}$ polydisperse nanofiber solution (0.05 mg/mL) in 1:1 *n*BuOH:MeOH that was heated from 20 °C to 90 °C and then cooled from 90 °C to 20 °C using 10 °C increments at a rate of 10 °C/min. Solutions were allowed to equilibrate at the target temperatures for 30 min. prior to each scan being taken.

To find a suitable self-nucleation suppression temperature for P3EHT$_{23}$-*b*-PEG$_{113}$, the following procedure was completed for all the temperatures listed in Figure 2.5 with 35 °C being used as a representative example. A P3EHT$_{23}$-*b*-PEG$_{113}$ polydisperse nanofiber solution (0.05 mg/mL) was heated to 90 °C for 1 h to ensure the BCP was in the unimeric state and then quickly cooled to 35 °C where the solution was left for 24 h. The solution was then transferred into a UV-Vis spectrometer at 35 °C and analyzed. This was done to ensure that no self-assembly occurred during the transfer process or the analysis. It was found that all temperatures ≥30 °C suppressed nanofiber formation and the only temperature where nucleation and nanofiber growth occurred after 24 h was 20 °C. This is evidenced by the absence of the peaks at 480 nm, 520 nm, and 570 nm at temperatures ≥30 °C.

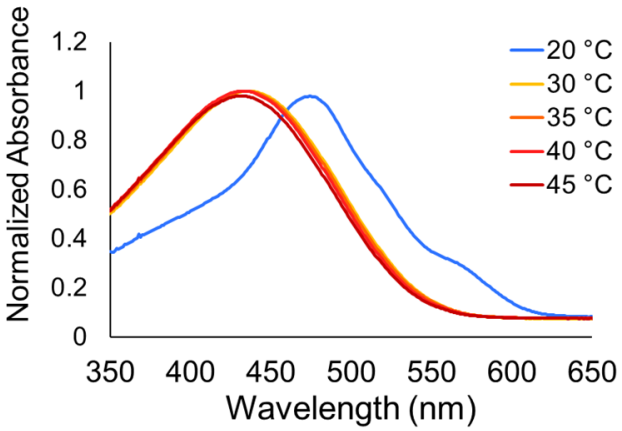

Figure 2.5. Overlayed UV-Vis absorbance spectra of P3EHT$_{23}$-*b*-PEG$_{113}$ polydisperse nanofiber solutions (0.05 mg/mL) in 1:1 *n*BuOH:MeOH for elucidation of a self-nucleation suppression temperature. Separate vials containing P3EHT$_{23}$-*b*-PEG$_{113}$ polydisperse nanofiber solutions (0.05 mg/mL) were heated to 90 °C for 1 h and then cooled from 90 °C to 20 °C, 30 °C, 35 °C, 40 °C, or 45 °C. The solutions were left at these temperatures for 24 h. The solutions were then quickly transferred into a UV-Vis spectrometer that was at these temperatures and analyzed.

2.3.5 Attempted length control of homogenous P3EHT$_{23}$-*b*-PEG$_{113}$ nanofibers by seeded growth using self-nucleation suppression at 30 °C and 50 °C

Self-nucleation suppressed seeded growth begins by heating polydisperse nanofibers in a temperature dependant selective solvent to 90 °C, so all of the BCP is in the unimeric state (Figure 2.6).[27] The solution is then cooled to a temperature where a supersaturated solution is formed but nucleation has not occurred (≥30 °C) (Figure 2.5). To that solution, nuclei (in the form of seeds) are introduced, causing spontaneous and rapid growth from the seed termini. Finally, the solution is maintained at the self-nucleation suppression temperature for 24 h prior to cooling to 22 °C to disfavor the formation of new nuclei and instead promote growth from the added seeds. According to the UV-Vis studies described in Section 2.3.4, cooling a nanofiber solution from 90 °C to any temperature above 30 °C creates a supersaturated solution where self-nucleation is suppressed for at least 24 h. It is critical that the seeds do not melt at the self-nucleation suppression temperature

upon addition, so seeded growth experiments were initially conducted at the lowest tested temperature where self-nucleation was suppressed (30 °C) to reduce this possibility.

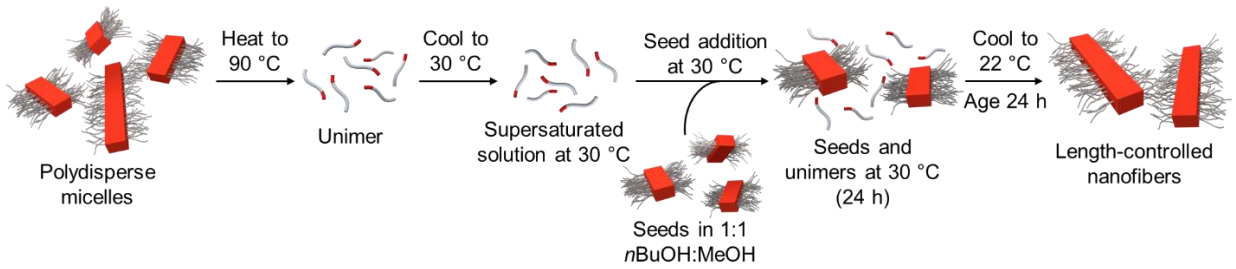

Figure 2.6. Cartoon schematic diagram showing self-nucleation suppressed seeded growth using 30 °C as a self-nucleation suppression temperature.

Various volumes of P3EHT$_{23}$-*b*-PEG$_{113}$ polydisperse nanofiber solution (0.05 mg/mL, 1:1 *n*BuOH:MeOH) were placed in separate vials and heated to 90 °C for 1 h and then allowed to cool to 30 °C and maintained at 30 °C for 2 h. Equal amounts of seed solution (L_n = 44 nm, $Đ_L$ = 1.26, annealed), also at 30 °C (1:1 *n*BuOH:MeOH, 0.1 mg/mL), were added to achieve different m_{unimer}/m_{seed} ratios. After seed addition and mixing, the vials were left at 30 °C for 24 h and then aged at 22 °C for 24 h. Length analysis of the resultant P3EHT$_{23}$-*b*-PEG$_{113}$ nanofibers from self-nucleation suppressed seeded growth experiments at 30 °C showed a linear correlation between the unimer-to-seed ratio and nanofiber length (Figure 2.7e). Fiber lengths ranging from L_n = 290 nm (m_{unimer}/m_{seed} = 4) up to L_n = 913 nm (m_{unimer}/m_{seed} = 20) were achieved with low dispersities ($Đ_L$ = 1.08-1.15), with an average value of $Đ_L$ = 1.10 (Figure 2.7a-e, S2.30a-f, S2.31a-f, Table S2.4). Since all temperatures at or above 30 °C suppress self-nucleation, seeded growth using a higher temperature (50 °C) was also performed to investigate if cooling to this temperature following heating to 90 °C provides improved results compared to cooling to 30 °C. P3EHT$_{23}$-*b*-PEG$_{113}$ nanofibers with lengths ranging from L_n = 292 nm (m_{unimer}/m_{seed} = 4) up to L_n = 579 nm (m_{unimer}/m_{seed} = 20) were obtained with dispersities ranging from $Đ_L$ = 1.08-1.17 with an average

value of $Đ_L$ = 1.13 (Figure S2.32a-f, S2.32, S2.34a-f, Table S2.5). At the highest unimer-to-seed ratio (m_{unimer}/m_{seed} = 20), the average lengths were roughly half of the lengths achieved when 30 °C was used as a self-nucleation suppression temperature. Although the lengths achievable using 50 °C as a self-nucleation suppression temperature are close to theoretically predicted values, at higher equivalents, the lengths reach a maximum value (~700 nm) and then plateau and begin to decrease which has been observed for other polythiophene BCPs.[30] Considering these results, self-seeding and self-nucleation suppressed self-seeding was utilized in the following experiments to investigate if length control could be achieved at lengths higher than 1 µm.

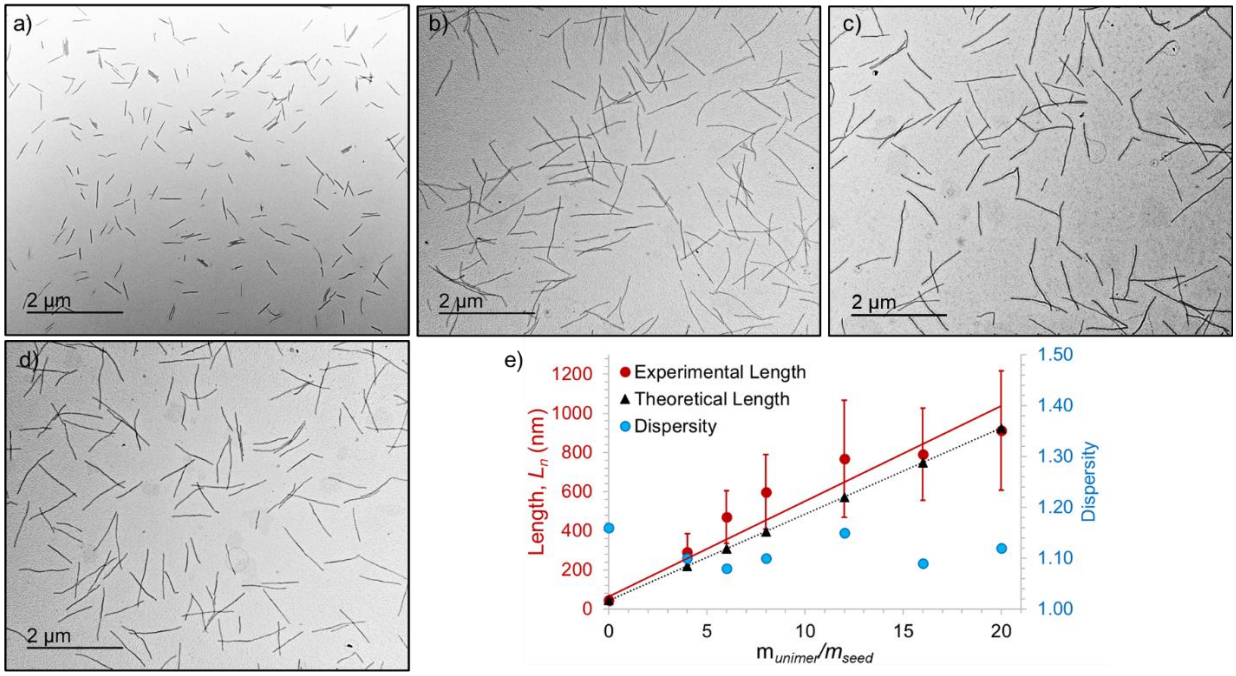

Figure 2.7. TEM images of length-controlled P3EHT$_{23}$-*b*-PEG$_{113}$ nanofibers formed by self-nucleation suppressed seeded growth at 30 °C; unimer to seed ratio m_{unimer}/m_{seed} = **(a)** 4, **(b)** 12, **(c)** 16, and **(d)** 20. **(e)** Plot showing the dependence of P3EHT$_{23}$-*b*-PEG$_{113}$ nanofiber length (L_n) on unimer-to-seed ratio (m_{unimer}/m_{seed}) when self-nucleation suppressed seeded growth at 30 °C was used. Error bars represent standard deviation.

2.3.6 Homogenous length-controlled P3EHT$_{23}$-*b*-PEG$_{113}$ nanofibers by self-seeding with cooling directly to ambient temperature (22 °C) or to the lowest self-nucleation suppression temperature (30 °C) and then 22 °C

Self-seeding experiments, where seeds are thermally generated *in situ*, were conducted as this method typically produces higher length nanofibers when using conjugated BCPs (Figure 2.8a). P3EHT$_{23}$-*b*-PEG$_{113}$ seeds (L_n = 65 nm, $Đ_L$ = 1.16) (Figure S2.19a, b) were heated to self-seeding temperatures for 1 h to create free unimer and then cooled directly to 22 °C. No change in nanofiber length was observed from temperatures 66 °C – 69 ° C but when the solutions were heated to 70 °C – 72 °C, nanofiber lengths increased exponentially from L_n = 215 nm (70 °C, $Đ_L$ =1.15) to L_n = 2.7 µm (72 °C, $Đ_L$ =1.10) (Figure 2.8a, 2.9a-c, 2.10, S2.35a-f, Table S2.6). Heating to 73 °C apparently led to complete dissolution of seeds as only polydisperse nanofibers were formed under these conditions.

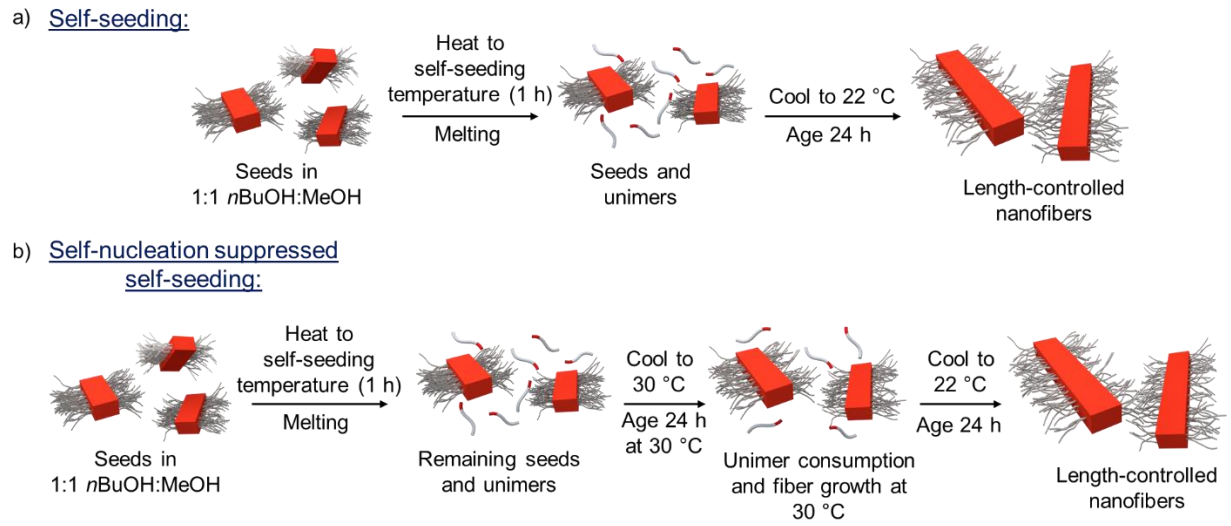

Figure 2.8. Cartoon schematics showing P3EHT$_{23}$-*b*-PEG$_{113}$ nanofiber growth using **(a)** self-seeding and **(b)** self-nucleation suppressed self-seeding with 30 °C as a self-nucleation suppression temperature.

Next, self-nucleation suppressed self-seeding experiments using 30 °C as a self-nucleation suppression temperature were conducted to determine if P3EHT$_{23}$-*b*-PEG$_{113}$ nanofibers with lengths > 2.7 μm could be obtained while maintaining a low dispersity (Figure 2.8b). P3EHT$_{23}$-*b*-PEG$_{113}$ seeds (L_n = 65 nm, $Đ_L$ = 1.16) (Figure S2.19a, b) from the same batch that were used during the previous self-seeding experiments were heated to self-seeding temperatures for 1 h and then cooled to 30 °C for 24 h before being brought to ambient temperature (22 °C) and aged for 24 h. As observed in the previous self-seeding experiments, the seed length did not change from 66 – 69 °C within standard error (Figure 2.10, Table S2.6). Heating to 70 – 72 °C resulted in P3EHT$_{23}$-*b*-PEG$_{113}$ nanofibers with L_n = 781 nm (70 °C, $Đ_L$ = 1.04) to L_n = 2.8 μm (72 °C, $Đ_L$ = 1.08) (Figure 2.9e-f, 2.10, S2.36a-f, Table S2.6). Critically, in all cases where self-nucleation suppression was used during self-seeding, the resultant P3EHT$_{23}$-*b*-PEG$_{113}$ nanofibers were higher in length (781 nm - 2.8 μm) and exhibited lower dispersities ($Đ_L$ =1.04 – 1.08) compared to when the solution was cooled directly to 22 °C (Figure 2.10, Table S2.6). Because cooling to 30 °C and maintaining the solution at 30 °C for 24 h suppresses the self-nucleation pathway, unimer does not have the possibility to self-nucleate and therefore can only epitaxially crystallize on the termini of the existing seeds. This consumes available unimer so that when the solution is cooled from 30 °C to 22 °C, there is a lower concentration present in solution capable of self-nucleation. This results in longer fibers and a lower incidence of small self-nucleated fiber fragments, thereby reducing $Đ_L$. This method allowed us to exert substantial length control, allowing for very high length conjugated nanofibers of 2.8 μm to be fabricated with a low dispersity (average $Đ_L$ when growth occurred = 1.05). This result confirms the benefits of suppressing homogenous nucleation during the self-seeded growth of P3EHT$_{23}$-*b*-PEG$_{113}$ fibers. Further, it expands the previously reported self-nucleation suppression method[27] to a conjugated BCP system that does not include a poly(3-

hexylthiophene) core-forming block. The irregularity of the 2-ethylhexyl side chain has been shown to cause more distant face-to-face packing in the polythiophene crystal compared to P3HT[32,38]; however, it is currently unclear if the reduced rate of P3EHT crystallization in solution provides additional time for reorganization into a more ordered crystalline core. This would have obvious benefits for optoelectronic properties such as exciton diffusion lengths and further investigations into this are pending.

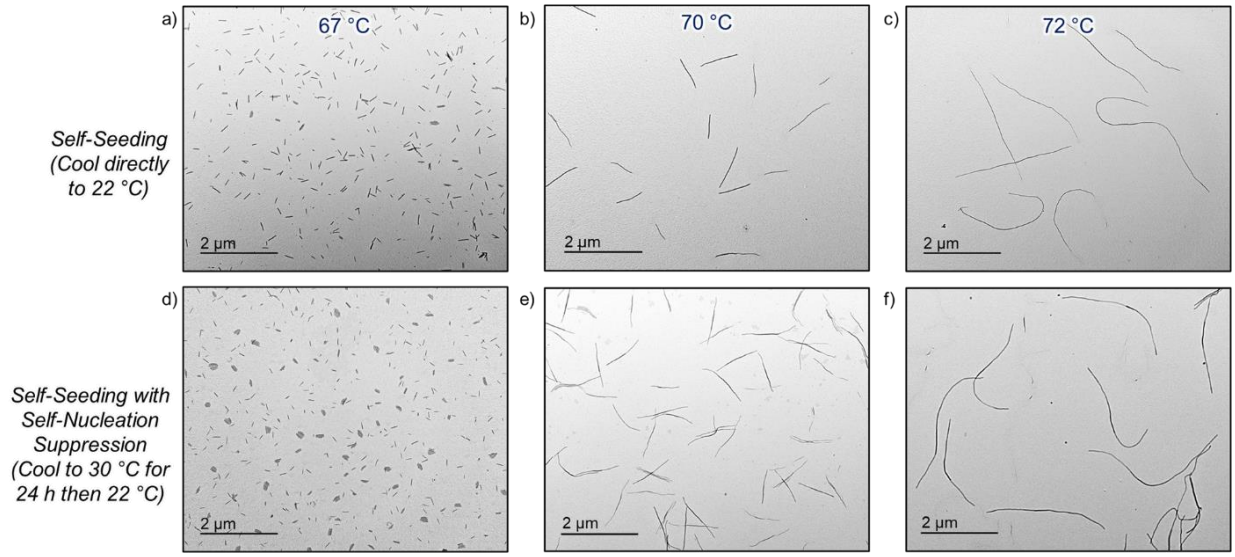

Figure 2.9. TEM images of P3EHT$_{23}$-*b*-PEG$_{113}$ nanofibers generated using self-seeding in 1:1 *n*BuOH:MeOH when solutions were cooled from **(a)** 67 °C, **(b)** 70 °C, **(c)** 72 °C directly to 22 °C and aged at 22 °C for 24 h. TEM images of P3EHT$_{23}$-*b*-PEG$_{113}$ nanofibers generated using self-nucleation suppressed self-seeding in 1:1 *n*BuOH:MeOH when solutions were cooled from **(d)** 67 °C, **(e)** 70 °C, **(f)** 72 °C to 30 °C, aged at 30 °C for 24 h prior to being cooled to 22 °C and aged at 22 °C for 24 h.

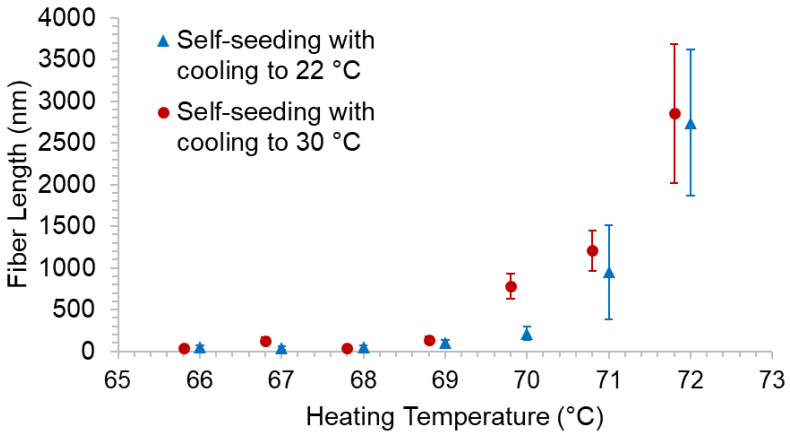

Figure 2.10. Contour length plot of P3EHT$_{23}$-*b*-PEG$_{113}$ nanofibers formed by self-seeding by cooling from the self-seeding temperatures directly to 22 °C (blue trace) and from the self-seeding temperatures to 30 °C and then to 22 °C (self-nucleation suppressed self-seeding) (red trace). Red points are slightly offset by 0.2 °C for clarity.

2.3.7 Formation of length-controlled B-A-B (P3EHT$_{19}$-*b*-P2VP$_{138}$-*m*-P3EHT$_{23}$-*b*-PEG$_{113}$-*m*-P3EHT$_{19}$-*b*-P2VP$_{138}$) triblock comicelles by seeded growth at 22 °C

Finally, we aimed to extend the living CDSA of BCPs with a P3EHT core-forming block to include the formation of B-A-B triblock comicelles that possess a segmented coronal structure by preparing nanofibers with a continuous P3EHT core and a PEG corona located in the central "A" block and a P2VP corona located on the terminal "B" regions. B-A-B block comicelles (P3EHT$_{19}$-*b*-P2VP$_{138}$-*m*-P3EHT$_{23}$-*b*-PEG$_{113}$-*m*-P3EHT$_{19}$-*b*-P2VP$_{138}$) (*m* = micelle segment) were fabricated by seeded growth at 22 °C by adding increasing amounts of P3EHT$_{19}$-*b*-P2VP$_{138}$ unimer solution (2 mg/mL in $CHCl_3$) to P3EHT$_{23}$-*b*-PEG$_{113}$ seeds (L_n = 44 nm, $Đ_L$ = 1.26, annealed) (Figure S2.18a) in *n*BuOH (Figure 2.11a). The triblock comicelle lengths increased linearly with the unimer-to-seed ratio (m_{unimer}/m_{seed} = 5 – 20) with lengths ranging from L_n = 320 nm to L_n = 934 nm and $Đ_L \leq 1.06$ (Figure 2.11b-e, 2.11g, S2.37, Table S2.7). This can be increased to ~1500 nm by using self-nucleation suppressed seeded growth (see Figure S2.38-S2.41). The experimental lengths are identical to theoretically predicted lengths. The difference between the electron density

of the P2VP corona-forming block and the PEG corona-forming block and the ensuing contrast in electron density allows for clear visualization of the block structures (Figure 2.11f). The P2VP block, which is comparatively more electron dense, appears grey in color and diffuse while the PEG corona is not apparent. To our knowledge, these are the first reported examples of length-controlled triblock comicelle nanostructures which contain a P3EHT core.

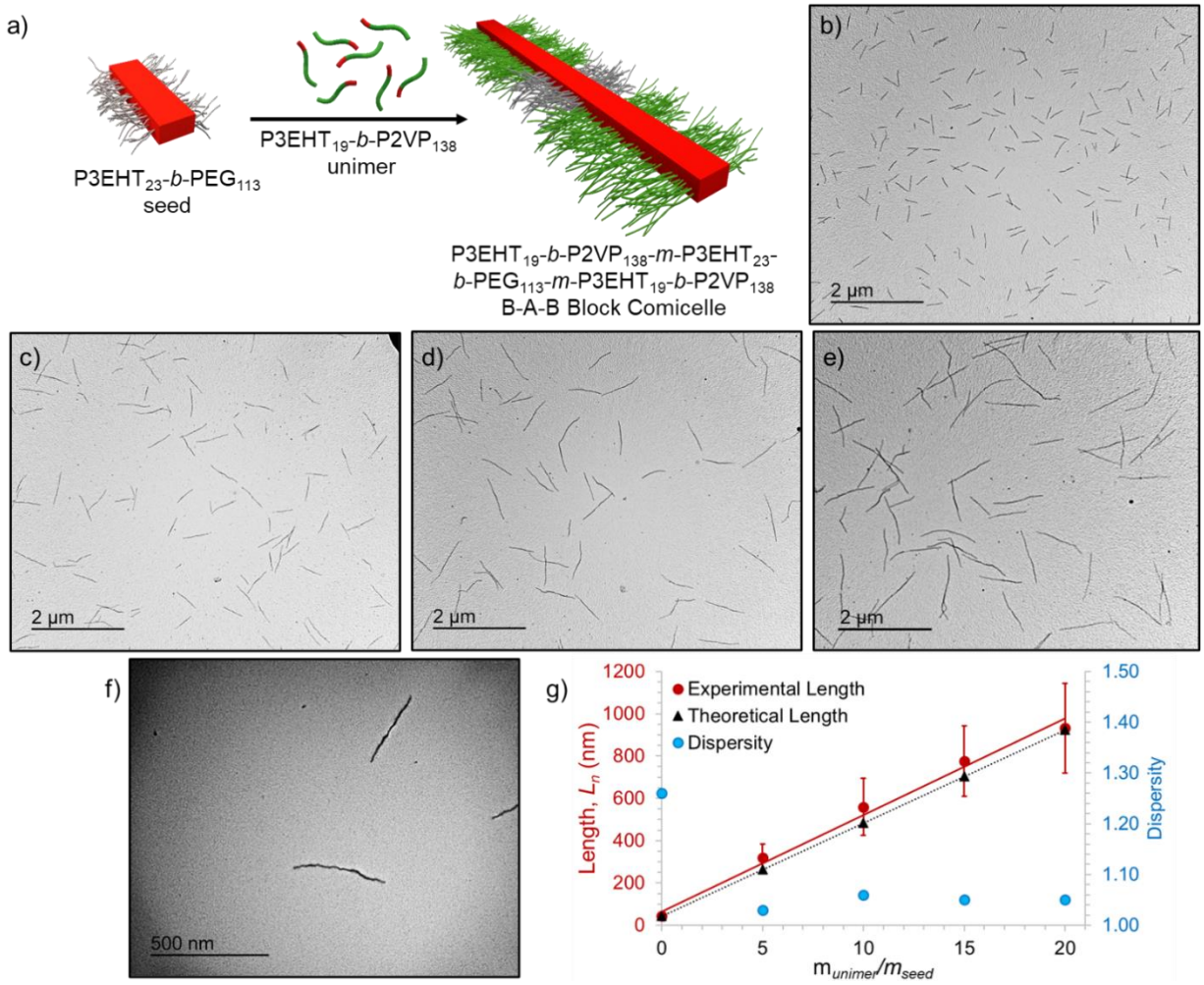

Figure 2.11. (a) Schematic showing B-A-B ($P3EHT_{19}$-*b*-$P2VP_{138}$-*m*-$P3EHT_{23}$-*b*-PEG_{113}-*m*-$P3EHT_{19}$-*b*-$P2VP_{138}$) block comicelles. *m* = micelle segment. TEM images of length-controlled B-A-B nanofibers. m_{unimer}/m_{seed} = **(b)** 5, **(c)** 10, **(d)** 15, and **(e)** 20. **(f)** Zoomed in TEM image of ~500 nm long B-A-B ($P3EHT_{19}$-*b*-$P2VP_{138}$-*m*-$P3EHT_{23}$-*b*-PEG_{113}-*m*-$P3EHT_{19}$-*b*-$P2VP_{138}$) nanofibers (m_{unimer}/m_{seed} = 10) showing electron density differences between the central PEG corona and the terminal P2VP coronas. **(g)** Plot showing the dependence of B-A-B nanofiber length (L_n) on unimer-to-seed ratio (m_{unimer}/m_{seed}).

2.4 Conclusions and Summary

This chapter details the synthesis and characterization of two P3EHT-containing BCPs, P3EHT$_{23}$-*b*-PEG$_{113}$ and P3EHT$_{19}$-*b*-P2VP$_{138}$, and their self-assembly into length-controlled 1D nanofibers. As with other polythiophene-based BCP systems, seeded growth experiments at 22 °C using P3EHT$_{23}$-*b*-PEG$_{113}$ seeds which were not annealed and P3EHT$_{23}$-*b*-PEG$_{113}$ seeds that had been annealed at 30 °C for 18 h prior to growth experiments resulted in modest success. Despite the lack of control over nanofiber lengths when higher equivalents were used, the generally lower dispersity of nanofibers obtained from growth experiments using annealed seeds ($Đ_L$ = ~ 1.3) compared to unannealed seeds ($Đ_L$ = ~ 1.5) provides compelling direct evidence that annealing reduces crystalline defects in the micelle core generated during sonication. Seeded growth of P3EHT$_{19}$-*b*-P2VP$_{138}$ at 22 °C from annealed seeds resulted in low dispersity fibers with controlled lengths and low dispersities. In the case of P3EHT$_{23}$-*b*-PEG$_{113}$, heating the solution to 90 °C and cooling to temperatures ≥30 °C resulted in the formation of a supersaturated solution where the rate of homogenous nucleation was significantly suppressed. This finding allowed us to exert greater fine control over the length and dispersity of the resultant nanofibers. Self-nucleation suppressed seeded growth experiments using P3EHT$_{23}$-*b*-PEG$_{113}$ performed at 30 °C resulted in nanofibers up to ca. 1 μm with $Đ_L$ = ~ 1.1, with lengths closely matching theoretical values. Conversely, self-seeding experiments using P3EHT$_{23}$-*b*-PEG$_{113}$ allowed for exceptionally long homogeneous nanofibers of ~2.7 μm to be obtained with a dispersity $Đ_L$ = 1.10. These results were improved upon when self-nucleation suppressed self-seeding of P3EHT$_{23}$-*b*-PEG$_{113}$ was used, which allowed for the fabrication of ~2.8 μm fibers with an average dispersity $Đ_L$ = 1.05. To our knowledge, this is the first example of length-controlled nanofibers that utilize a P3EHT core-forming block.

Finally, we successfully formed length-controlled coronally segmented B-A-B block comicelle structures using living CDSA of BCPs containing a π-conjugated P3EHT core-forming block. By addition of P3EHT$_{19}$-*b*-P2VP$_{138}$ unimer to P3EHT$_{23}$-*b*-PEG$_{113}$ seeds (to form P3EHT$_{19}$-*b*-P2VP$_{138}$-*m*-P3EHT$_{23}$-*b*-PEG$_{113}$-*m*-P3EHT$_{19}$-*b*-P2VP$_{138}$), we also achieved the first example of length-controlled triblock comicelle nanostructures which contain a P3EHT core. The modularity of this nanofiber system provides promising opportunities for energy-funneling applications and analysis of the exciton diffusion lengths through the fiber core. The hydrogen bonding capability of the PEG and P2VP coronas also provide us with the opportunity to conduct surface-confined nanofiber growth experiments, which are currently underway.

2.5 Supporting Information

2.5.1 Methods

Materials

All reagents used for polymers synthesis were of reagent grade and were used as received unless otherwise stated. All air-free chemistry was performed in a dinitrogen-filled (N_2) MBraun 200B glovebox equipped with a cold-well or using a dinitrogen Schlenk line using standard techniques. 3-bromothiophene (97%), poly(ethylene glycol) methyl ether (PEG) (average M_n = 5000 Da), (2-ethylhexyl)magnesium bromide (1.0 M in diethyl ether), ethynylmagnesium bromide (0.5M in THF), 2-vinylpyridine (97%), azobisisobutyronitrile (AIBN) (98%), (2-(dodecylthiocarbonothioylthio)-2-methylpropionic acid 3-azido-1-propanol ester (CTA) (HPLC, 98%), isopropylmagnesium chloride – lithium chloride (*i*PrMgCl•LiCl) (1.3 M in THF), *p*-toluenesulfonyl chloride (99%), sodium azide, and 1,2-bis(diphenylphosphino)propane dichloronickel(II) (Ni(dppp)Cl_2) were purchased from Millipore Sigma. *N*-Bromosuccinimide (NBS) was recrystallized from boiling water prior to use[47] and Ni(*o*-tolyl)(dppe)Cl was synthesized as previously reported.[48] 3-(2'-ethylhexyl)thiophene and 2,5-dibromo-3-(2'-ethylhexyl)thiophene were synthesized as previously reported.[32] Copper(I) bromide (CuBr) was purified by suspending in glacial acetic acid, filtering and washing with copious amounts of absolute ethyl alcohol then anhydrous ethyl ether followed by drying in a vacuum oven at 80 °C for three days and storing under nitrogen.[49] *N,N,N′,N′,N″*-pentamethyldiethylenetriamine (PMDETA) was degassed prior to use using 3 freeze-pump-thaw cycles and stored under an N_2 atmosphere. Solvents were dried and deoxygenated using a Solvent Purification System (SPS).[50] Self-assembly experiments were performed using HPLC grade solvents and the solvents were filtered through a 0.2 μm poly(tetrafluoroethylene) membrane.

Nuclear Magnetic Resonance (NMR)

^{1}H NMR spectra were taken with a Bruker 500 MHz spectrometer; chemical shifts were referenced to the residual proteosolvent peak ($CHCl_3$, δ = 7.26 ppm).

Gel Permeation Chromatography (GPC)

GPC was conducted using a Malvern Omnisec Resolve/Reveal equipped with an automatic sampler, pump, injector, inline degasser column oven (set at 35 °C), elution columns consisting of styrene/divinylbenzene gels (of pore size 500–5,000 Å), refractometer, four capillary differential viscometer, UV/Vis detector (λ = 440 nm) and dual angle laser light scattering detector (7° and 90°). GPC grade THF with 1 wt% triethylamine was used as the mobile phase, with a set flow rate of 1 mL/min. Samples were dissolved in THF at 1 mg/mL and filtered through a 0.2 µm poly(tetrafluoroethylene) membrane prior to analysis.

Preparatory GPC

Preparatory gel permeation chromatography was performed on a Shimadzu Prep GPC equipped with a CBM-20A communications bus module, LC-20AP solvent delivery unit, SIL-10AP autosampler, CTO-40C column oven, SPD-40 UV-Vis detector, RID-20A refractive index detector, and FRC-10A fraction collector. An initial injection of polymer in THF (1 mL, 10 mg/mL) at a flow rate of 3 mL/min using HPLC grade THF as mobile phase was used to gather the retention times of the species in solution. Using this data, the fraction collector was calibrated to separate the desired peaks into separate vials. Subsequent injections (3 mL, 10 mg/mL, 3 mL/min) were repeated until the desired volume was collected. The resulting solutions were concentrated *in vacuo* to yield the final polymers. Removal of homopolymers was assessed using UV-detection on the Malvern Omnisec GPC and thin layer chromatography.

Transmission Electron Microscopy (TEM)

Carbon films were deposited onto freshly cleaved mica sheets using a Leica EM ACE600 sputter/carbon coater instrument. Carbon films were deposited onto copper grids (500 mesh) purchased from Ted Pella, Inc. by floatation on water and allowed to dry over 24 h. Samples for electron microscopy were prepared by drop-casting 10 μL of a colloidal nanofiber solution onto a TEM grid placed on filter paper to absorb the excess solution. Bright field TEM images were obtained using a JEOL JEM 1011 microscope operating at 80 kV, equipped with a Gatan Orius SC1000 CCD camera.

Sonication

Sonication was carried out using a Fisherbrand FB11203 sonication bath (37 kHz sonication frequency, 100% power) with the sweep function on and a bath temperature of 0 °C.

Variable-temperature UV/Vis absorption spectroscopy (VT-UV/Vis)

VT-UV/vis data was obtained on a Cary 100 spectrometer equipped with a Peltier temperature controller employing quartz cells (1 cm x 0.1 cm) from 200 to 800 nm. Experiments were conducted at a concentration of 0.05 mg/mL to allow for convenient monitoring of fiber-like micelle formation and dissolution.

Wide-Angle X-ray Scattering (WAXS)

Reciprocal space maps were collected with a Pixcel 3D detector on an Empyrean diffractometer (Panalytical) equipped with a Cu Kα1 ($\lambda = 1.5406$ Å) source powered at 45 kV and 40 mA.

Atomic Force Microscopy (AFM)

Atomic force microscopy (AFM) height images were taken at ambient temperature in air using a Bruker Multimode VIII atomic force microscope equipped with a ScanAsyst-HR fast scanning module and ScanAsyst-Air-HR probe (tip radius of 2 nm), utilising peak force feedback control. Samples for AFM were drop-cast onto a glow discharged silicon wafer (1 x 1 cm) and allowed to dry in air before imaging. The spring constant for the AFM tip used was 5 N/m.

2.5.2 Statistical Analysis

Nanofiber lengths and widths were analysed using ImageJ, an open source software package developed at the US National Institute of Health.[51] Approximately 150 micelles were traced by hand to determine contour lengths that were then used to calculate the number-averaged length (L_n) and weight-average length (L_w) was calculated by using supplementary equations S2.1 and S2.2 from the measurements of the contour length (L_i) of individual micelles, where N_i is the number of the micelles of length L_i, and n is the number of micelles examined in each sample.

$$(Equation\ S2.1)\ L_n = \frac{\sum_{i=1}^{n} N_i L_i}{\sum_{i=1}^{n} N_i} \qquad (Equation\ S2.2)\ \ L_w = \frac{\sum_{i=1}^{n} N_i L_i^2}{\sum_{i=1}^{n} N_i L_i}$$

Number-averaged width (W_n) was calculated according to equation S2.3 where W_i = object width and N_i = number of micelles of length W_i.

$$(Equation\ S2.3)\quad W_n = \frac{\sum_{i}^{n} N_i W_i}{\sum_{i}^{n} N_i}$$

The polydispersity index ($Đ_L$) and standard deviations (σ) of the measured lengths were related through the following expressions (Eq. S2.4 and S2.5)

$$(Equation\ S2.4)\quad Đ_L = \frac{L_w}{L_n} \qquad (Equation\ S2.5)\quad \frac{L_w}{L_n} - 1 = \left(\frac{\sigma}{L_n}\right)^2$$

2.5.3 Synthesis and Characterization

Scheme S2.1. Synthesis of 3-(2'-ethylhexyl)thiophene

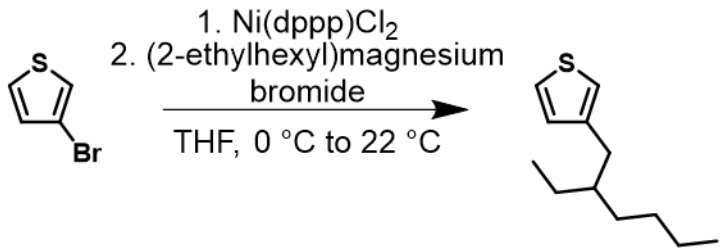

This product was synthesized using a modified procedure from ref 32.[32] The reaction was performed under an N_2 atmosphere using a Schlenk line. A commercial Grignard reagent was used in place of Mg turnings and 2-ethylhexylbromide. The final compound was purified by concentrating the yellow solution on a vacuum line equipped with an external liquid nitrogen trap. The solution was placed under dynamic vacuum (~2 x 10^{-2} millibar) while stirring and heating to 65 °C for 24 h to remove remaining starting materials. (11.11 g, 62% yield).^{1}H NMR spectrum matches what was previously reported in the literature.[32]

Scheme S2.2. Synthesis of 2,5-dibromo-3-(2'-ethylhexyl)thiophene

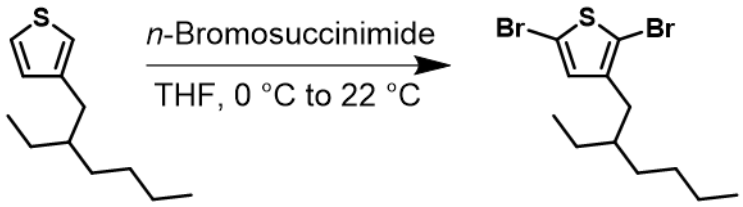

This product was synthesized using a previously published procedure from ref 32.[32] The reaction was performed on the benchtop in air. (11.30 g, 83% yield).

Scheme S2.3. Synthesis of alkynyl-terminated P3EHT$_{23}$

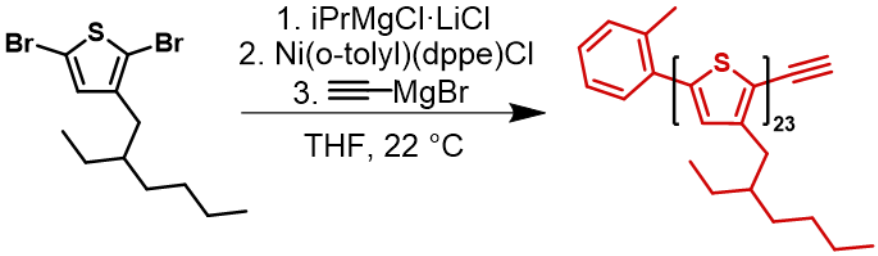

The following procedure was conducted in oven dried glassware, under inert N_2 atmosphere in a glove box. To a 500 mL round-bottomed Schlenk flask equipped with a stir bar, 2,5-dibromo-3-(2'-ethylhexyl)thiophene (400 mg, 1.13 mmol, 35 equiv.) was added and dissolved in SPS THF (200 mL). iPrMgCl•LiCl (1.3 M in THF, 0.84 mL, 34 equiv.) was added dropwise with vigorous stirring and the solution was stirred at room temperature for 1 h causing the colourless solution to become light yellow. (*o*-tolyl)Ni(dppe)Cl (19 mg, 0.032 mmol, 1 equiv.) was weighed into a vial and dissolved in SPS THF (2 mL) then added to the monomer solution in one swift injection with vigorous stirring. The yellow solution immediately became dark orange/red. The polymerization was left for 10 min. before ethynylmagnesium bromide (0.5 M in THF, 1.6 mL, 25 equiv.) was added in one swift injection. The reaction was allowed to stir for 15 min. before being removed from the glovebox and quenched using cold MeOH (200 mL) followed by stirring for 25 min. The red solution was collected by centrifugation and then dissolved in $CHCl_3$ (100 mL) before being washed with water (2 x 150 mL) and then brine (1 x 150 mL). The $CHCl_3$ fractions were combined, dried using $MgSO_4$, filtered and concentrated using a rotary evaporator. The residue was taken up in $CHCl_3$ (min. amount), precipitated into acetone and collected by centrifugation which yielded the product as a red solid (123 mg, 85% yield, M_n = 4, 600 Da, $Đ_M$ = 1.08). The synthesis of alkynyl-P3EHT$_{19}$ was carried out using the same procedure as detailed above. ^{1}H NMR ($CDCl_3$ = 7.26 ppm, 500 MHz): 7.49–7.44 (m, tolyl), 7.27–7.24 (m,

tolyl), 6.97 (s, thiophene), 3.53 (s, alkyne) 2.76 (d, J = 7.0 Hz, thiophene-CH_2-), 2.51 (s, -CH_3), 1.78–1.66 (m, -CH-), 1.46–1.26 (m, -CH_2-), 0.92 (m, -CH_3).

Scheme S2.4. Synthesis of azide-terminated poly(ethylene glycol) (PEG_{113}-N_3)

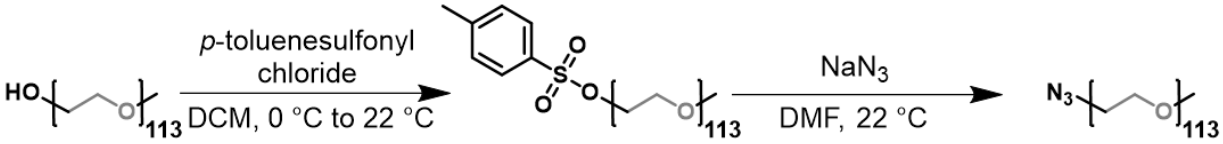

This product was synthesized using a previously published procedure from ref 52.[52] Tosylation was performed on a Schlenk line under N_2 atmosphere (5.45 g, 88% yield). Azidation was performed on a Schlenk line under N_2 atmosphere (2.02 g, 69% yield). ^{1}H NMR spectra match what was previously reported in the literature.[52] (M_n = 5, 000 Da, $Đ_M$ = 1.16).

Scheme S2.5. Synthesis of azide-terminated poly(2-vinylpyridine) ($P2VP_{138}$-N_3)

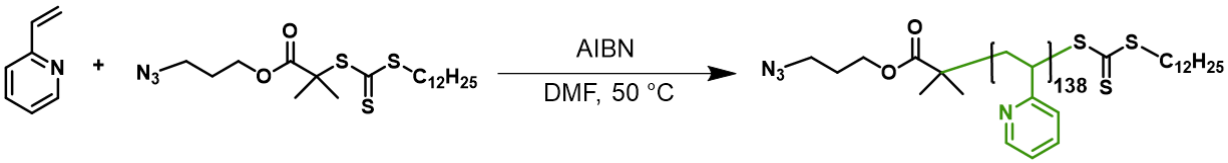

This product was synthesized using a previously published procedure from ref 53.[53] Reaction was performed using a Schlenk line under N_2 atmosphere (757 mg, 49% yield, M_n = 14, 800 Da, $Đ_M$ = 1.23).

Scheme S2.6. Synthesis of P3EHT$_{23}$-*b*-PEG$_{113}$

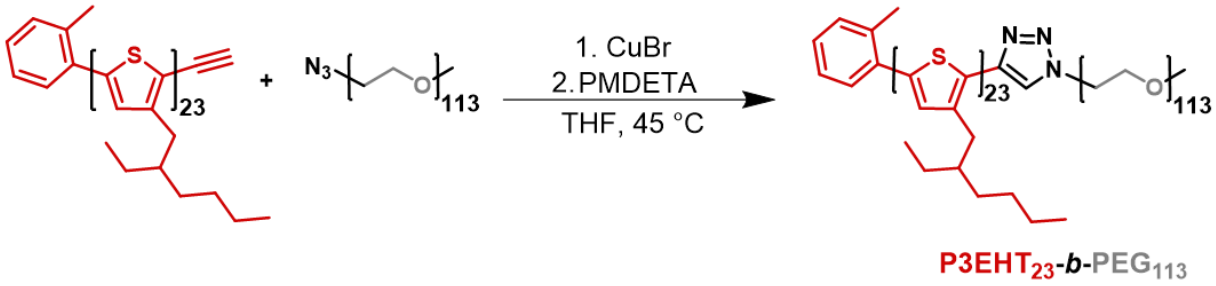

Alkynyl terminated-P3EHT$_{23}$ (123 mg, 0.03 mmol, 1.0 equiv.), PEG$_{113}$-N$_3$ (184 mg, 0.04 mmol, 1.5 equiv.), and CuBr (23 mg, 0.16 mmol, 6.0 equiv.) were added to a Schlenk flask equipped with a stir bar and attached to a Schlenk line. The flask was evacuated and backfilled three times with nitrogen gas before dry THF (20 mL) was added. PMDETA (28 mg, 33 µl, 0.16 mmol, 6 equiv.) was added to the flask. The solution was degassed using 3 freeze-pump-thaw cycles, the flask was backfilled with nitrogen gas and then stirred at 45 °C for 3 days. To the orange, clear solution was added $CHCl_3$ (50 mL), and the mixture was passed through a basic alumina plug to remove the copper catalyst. The solution was washed with water (3 x 50 mL) and brine (1 x 50 mL), dried over magnesium sulfate, gravity filtered, and concentrated using a rotary evaporator. The solid was taken up in $CHCl_3$ (min. amount) and precipitated into pentane. The crude solid was purified further using preparatory GPC with THF as a mobile phase and purity was checked using thin layer chromatography with $CHCl_3$ as a mobile phase which showed no evidence of remaining homopolymers. The final product was a red solid (42 mg, 16% yield). ^{1}H NMR ($CDCl_3$, 500 MHz): 7.53–7.41 (m, aromatic), 7.27–7.21 (m, aromatic), 6.94 (s, 23H, thiophene), 3.64 (s, 529H, O-CH_2-CH_2-O), 3.55 (m, O-CH_3), 2.73 (d, 56H, thiophene-CH_2), 2.51 (s, 3H, -CH_3), 1.97–1.52 (m, -CH-), 1.44–1.16 (m, -CH_2-), 0.94-0.77 (m, -CH_3).

GPC: M_n = 11,900 Da, $Đ_M$ = 1.06

Scheme S2.7. Synthesis of P3EHT$_{19}$-*b*-P2VP$_{138}$

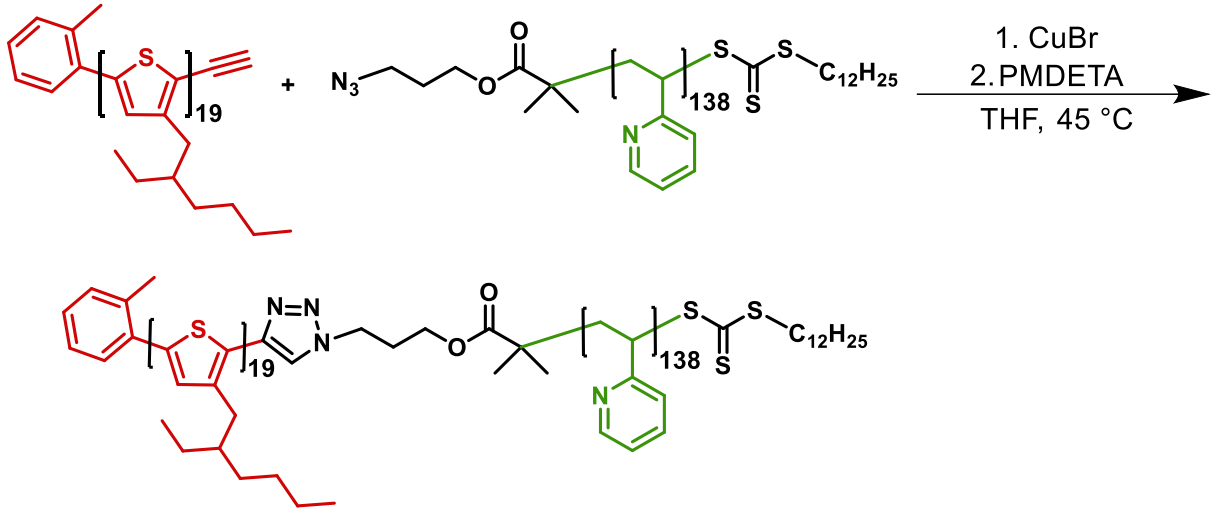

Alkynyl terminated-P3EHT$_{19}$ (167 mg, 0.04 mmol, 1.0 equiv.), P2VP$_{138}$-N$_3$ (757 mg, 0.05 mmol, 1.2 equiv.), and CuBr (34 mg, 0.24 mmol, 6 equiv.) were added to a Schlenk flask equipped with a stir bar. The flask was evacuated and backfilled three times with nitrogen gas before dry THF (20 mL) and PMDETA (42 mg, 50 µl, 0.24 mmol, 6 equiv.) were added to the flask. The solution was degassed using 3 freeze-pump-thaw cycles, the flask was backfilled with nitrogen gas, sealed, and then stirred at 45 °C for 3 days. To the orange, clear solution was added $CHCl_3$ (50 mL), and the mixture was passed through a basic alumina plug to remove the copper catalyst. The solution was washed with deionized water (3 x 50 mL) and brine (1 x 50 mL), dried over magnesium sulfate, gravity filtered, and concentrated using a rotary evaporator. The solid was taken up in $CHCl_3$ (min. amount) and precipitated into hexanes. Following precipitation, excess P2VP-N$_3$ was removed by precipitation into a solution of THF containing dilute HCl. This resulted in protonation of the nitrogen atoms in the pyridine rings, causing precipitation of the BCP and any P2VP homopolymer and leaving P3EHT homopolymer impurities in the THF/HCl supernatant. The precipitate was then redissolved in $CHCl_3$/triethylamine and reprecipitated into

hexanes. The polymer was then precipitated into acetone several times to remove any P2VP homopolymer. The solid was taken up in $CHCl_3$ and washed using 1M NaOH solution (3 x 100 mL) to remove any triethylamine hydrochloride, dried over magnesium sulfate, filtered, and concentrated on a rotary evaporator before being dried overnight at 40 °C in a vacuum oven. Purity was assessed using thin layer chromatography using chloroform followed by pyridine as mobile phases which showed no evidence of remaining homopolymers. The final product was a red solid (31 mg, 4% yield). The low yield was due to a low ethynyl capping percentage on the P3EHT homopolymer as well as material loss during the repetitive acidification, precipitation, and washing process. ^{1}H NMR ($CDCl_3$, 500 MHz): 8.52–8.01 (m, 139H, pyridine N-CH), 7.60 (s, 1H, triazole H), 7.45–6.01 (bm, 417H, pyridine Hs), 6.94 (s, 19H, thiophene), 3.55 (m, O-CH_3), 2.73 (d, 56H, thiophene-CH_2), 2.49 (s, 3H, *o*-tolyl-CH_3), 1.80–1.66 (bm, ethylhexyl -CH- and pyridine), 1.46–1.26 (m, -CH_2-), 0.99–0.70 (m, -CH_3). GPC: M_n = 18, 300 Da, $Đ_M$ = 1.14

2.5.4 Gel Permeation Chromatography

Alkynyl-P3EHT$_{23}$, PEG$_{113}$-N$_3$, and P3EHT$_{23}$-*b*-PEG$_{113}$

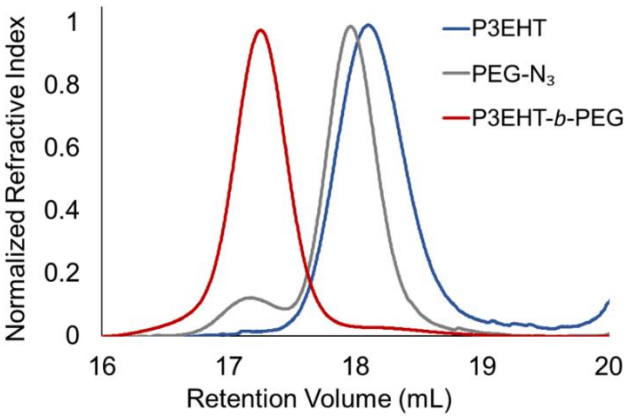

Figure S2.1. Overlaid GPC chromatograms of alkynyl-P3EHT$_{23}$ (blue trace), PEG$_{113}$-N$_3$ (grey trace), and P3EHT$_{23}$-*b*-PEG$_{113}$ (red trace). Sample concentrations were 1 mg/mL in THF.

Alkynyl-P3EHT$_{19}$, P2VP$_{138}$-N$_3$, and P3EHT$_{19}$-*b*-P2VP$_{138}$

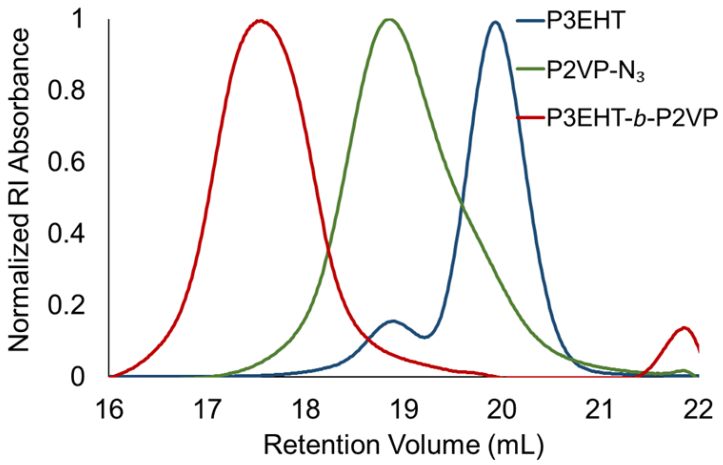

Figure S2.2. Overlaid GPC chromatograms of alkynyl-P3EHT$_{19}$ (blue trace), P2VP$_{138}$-N$_3$ (green trace), and P3EHT$_{19}$-*b*-P2VP$_{138}$ (red trace). Sample concentrations were 1 mg/mL in THF.

2.5.5 ^{1}H NMR Spectroscopy

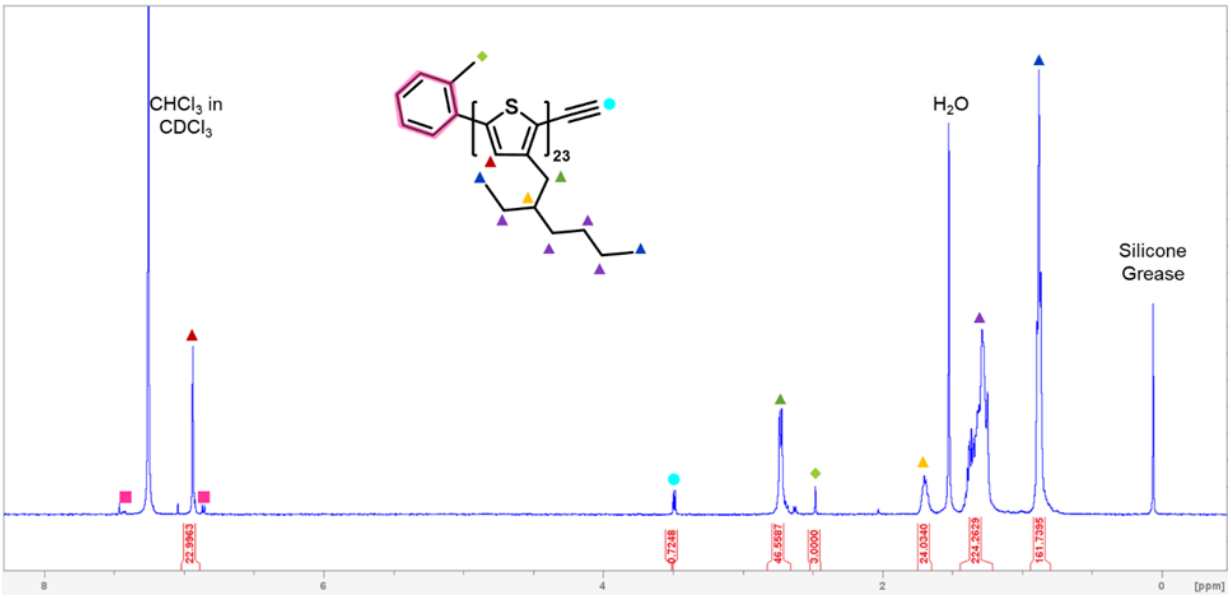

Figure S2.3. ^{1}H NMR spectrum of alkyne-terminated P3EHT$_{23}$ homopolymer (500 MHz, $CDCl_3$).

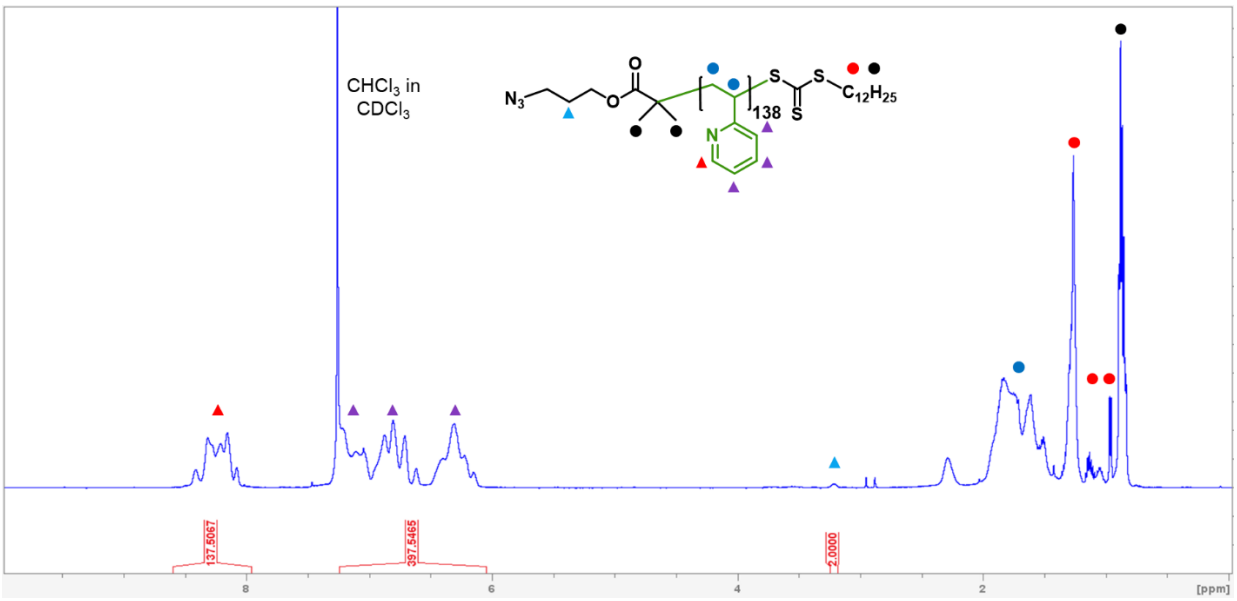

Figure S2.4. ^{1}H NMR spectrum of azide-terminated P2VP$_{138}$ homopolymer (500 MHz, $CDCl_3$).

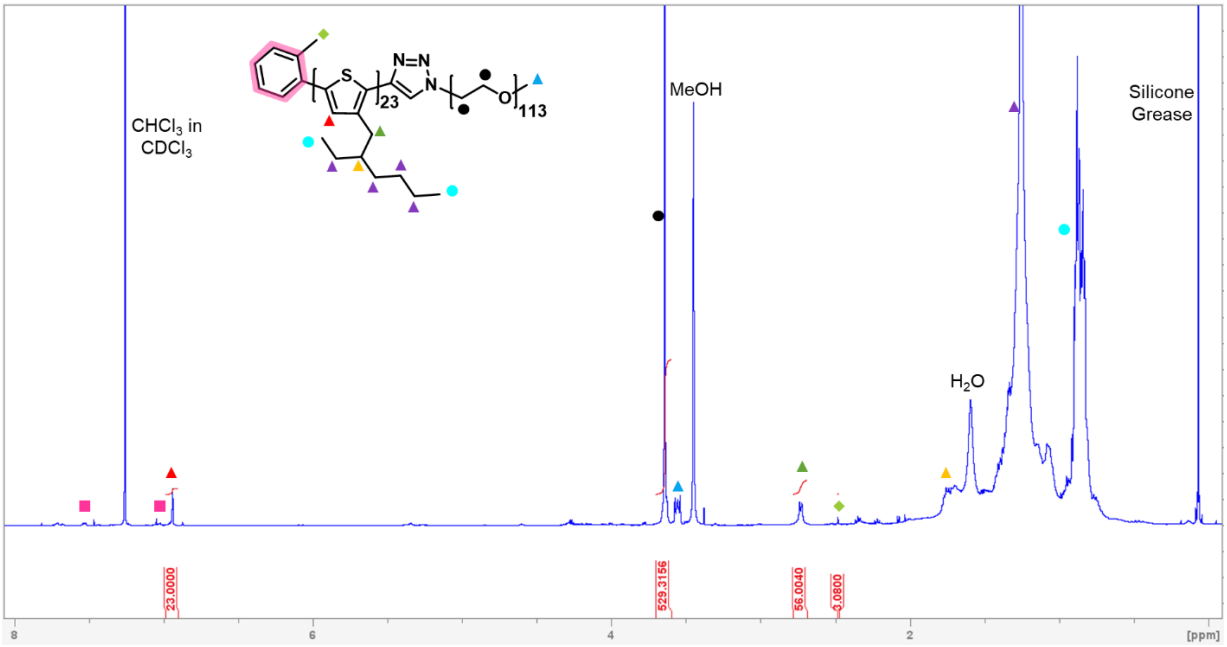

Figure S2.5. ^{1}H NMR spectrum of P3EHT$_{23}$-*b*-PEG$_{113}$ block copolymer (500 MHz, $CDCl_3$). Small unassigned peaks in the spectrum arise from the fact a 500 MHz spectrometer was used, with long acquisition times and a high number of scans so that integration of the polymer peaks was achievable. This results in the appearance of impurity signals from species that are in a reasonably low concentration and do not affect the polymer self-assembly behaviour.

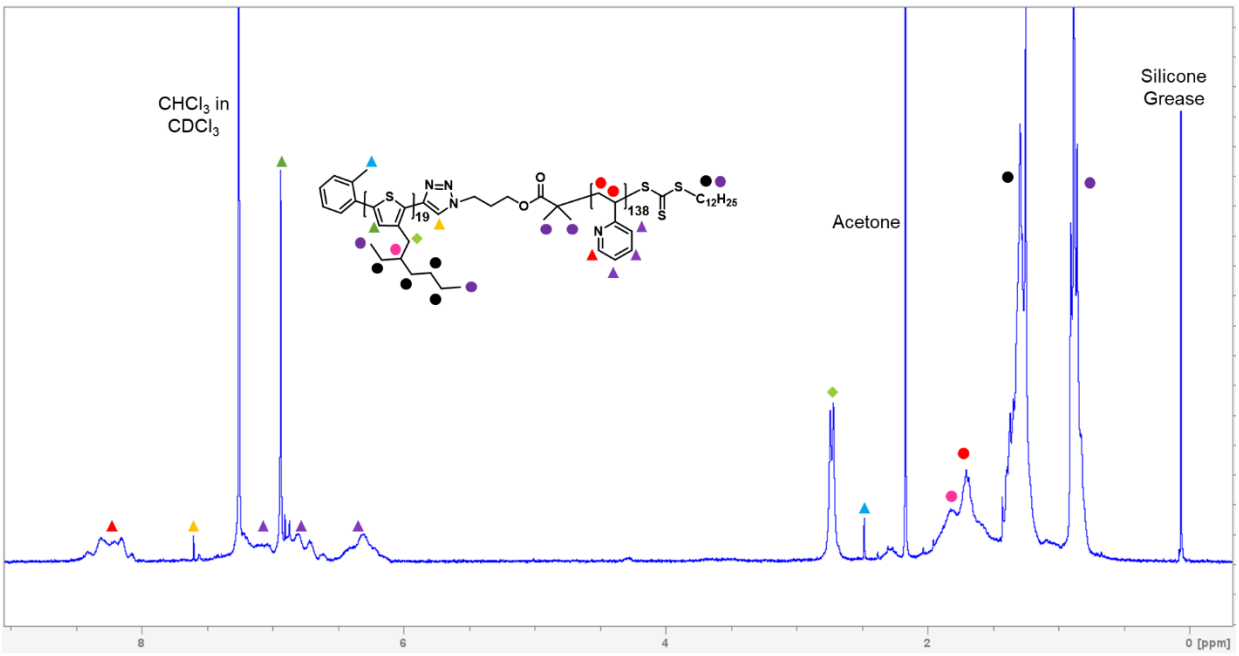

Figure S2.6. ^{1}H NMR spectrum of P3EHT$_{19}$-*b*-P2VP$_{138}$ block copolymer (500 MHz, $CDCl_3$).

2.5.6 Crystallization-Driven Self-Assembly Procedures

General self-assembly procedure for polydisperse fibers of P3EHT$_{23}$-*b*-PEG$_{113}$ or P3EHT$_{19}$-*b*-P2VP$_{138}$ and seed production

10 mL of deoxygenated *n*BuOH was added to a vial containing 2 mg of solid P3EHT$_{23}$-*b*-PEG$_{113}$ or P3EHT$_{19}$-*b*-P2VP$_{138}$ which was then heated to 90 °C in a metal heating block for 30 min. The 0.2 mg/mL solution was allowed to cool to 22 °C slowly (ca. 4 h) followed by aging for 24 h. After aging, 10 mL of deoxygenated MeOH was added to form a solution with a final concentration of 0.1 mg/mL (only for P3EHT$_{23}$-*b*-PEG$_{113}$). The vial was then placed in a 0 °C ultrasonic cleaning bath and sonicated for 3 h to give seed micelles (37 kHz, 100% power). Seeds were then annealed at 30 °C for 18 h prior to use.

It should be noted that polydisperse nanofibers can be grown successfully in the temperature-dependent selective solvent *n*BuOH alone when heated to 90 °C for 30 min. and

subsequently cooled to 22 °C, but nanofiber precipitation was observed if the solution was allowed to stand at 22 °C undisturbed for 96 h or more (only in the case of P3EHT$_{23}$-*b*-PEG$_{113}$). The results suggested that *n*BuOH is not sufficiently selective for the PEG corona-forming block at 22 °C and the more hydrophilic solvent MeOH was added to provide long-term colloidal stability. Deoxygenated solvents are necessary for long-term stability of P3EHT$_{23}$-*b*-PEG$_{113}$ and P3EHT$_{19}$-*b*-P2VP$_{138}$ in solution because these materials, like other poly(3-alkylthiophenes), undergo oxidative photodegradation through simultaneous cross-linking and alkyl chain scission events, causing eventual conversion of the red nanofiber solution to an orange/yellow solution.[54–57] The observed conversion over time from red to orange/yellow is likely the result of decreasing conjugation length in the P3EHT core-forming block as chain scission occurs.

General self-assembly procedure for seeded growth of length-controlled nanofibers at 22 °C

P3EHT$_{23}$-*b*-PEG$_{113}$ seed micelle solution (1:1 *n*BuOH:MeOH, 0.1 mg/mL) was added to a vial and diluted with a deoxygenated 1:1 *n*BuOH:MeOH solution such that the final concentration will be 0.05 mg/mL following unimer addition. P3EHT$_{23}$-*b*-PEG$_{113}$ unimer solution (2 mg/mL in deoxygenated THF) was added quickly, the solutions were vortexed for 10 s and then aged at 22 °C for 24 h prior to imaging by TEM.

General self-assembly procedure for self-nucleation suppressed seeded growth of length-controlled nanofibers using self-nucleation suppression temperatures of 30 °C or 50 °C

Six vials were filled with increasing amounts of P3EHT$_{23}$-*b*-PEG$_{113}$ polydisperse micelle solution (1:1 *n*BuOH:MeOH, 0.1 mg/mL), and diluted using a deoxygenated 1:1 *n*BuOH:MeOH mixture such that the final concentration after seed addition will be 0.05 mg/mL. The solutions were heated to 90 °C for 1 h and then cooled to 30 °C (or 50 °C) over ~2 h by placing in a preheated metal block. Equal amounts of seed micelle solution at 30 °C (or 50 °C) (1:1 *n*BuOH:MeOH, 0.1

mg/mL) correlating to m_{unimer}/m_{seed} = 4, 6, 8, 12, 16 and 20 were added quickly, the solutions were vortexed for 10 s and then placed back in the 30 °C (or 50 °C) heating block for 24 h. After 24 h, the solutions were cooled to ambient temperature (22 °C) and aged for 24 h prior to TEM imaging.

General self-assembly procedure for self-seeding of length-controlled P3EHT$_{23}$-*b*-PEG$_{113}$ nanofibers using cooling directly to 22 °C from self-seeding temperature

P3EHT$_{23}$-*b*-PEG$_{113}$ seed micelle solution (1:1 *n*BuOH:MeOH, 0.05 mg/mL) was heated to self-seeding temperatures (66 - 72 °C) for 1 h and then cooled slowly (ca. 4 h) to 22 °C. After reaching 22 °C and aging for 24 h, the samples were imaged by TEM following solvent evaporation.

General self-assembly procedure for self-seeding of length-controlled P3EHT$_{23}$-*b*-PEG$_{113}$ nanofibers using 30 °C as a self-nucleation suppression temperature

P3EHT$_{23}$-*b*-PEG$_{113}$ seed micelle solution (1:1 *n*BuOH:MeOH, 0.05 mg/mL) was heated to self-seeding temperatures (66 - 72 °C) for 1 h and then placed into a preheated 30 °C metal block for 24 h. After 24 h, the solutions were cooled to ambient temperature (22 °C) and aged 24 h prior to imaging by TEM following solvent evaporation.

General self-assembly for formation of B-A-B (P3EHT$_{19}$-*b*-P2VP$_{138}$-*m*-P3EHT$_{23}$-*b*-PEG$_{113}$-*m*-P3EHT$_{19}$-*b*-P2VP$_{138}$ P3EHT$_{23}$-*b*-PEG$_{113}$) triblock comicelles at 22 °C

P3EHT$_{23}$-*b*-PEG$_{113}$ seed micelle solution (1:1 *n*BuOH:MeOH, 0.1 mg/mL) was added to a vial and diluted with deoxygenated 1:1 *n*BuOH:MeOH solution such that the final concentration after P3EHT$_{19}$-*b*-P2VP$_{138}$ unimer addition will be 0.05 mg/mL. P3EHT$_{19}$-*b*-P2VP$_{138}$ unimer solution (2 mg/mL in deoxygenated $CHCl_3$) was added quickly, the solutions were vortexed for 10 s and then aged at ambient temperature (22 °C) for 24 h prior to imaging by TEM.

General self-assembly for formation of B-A-B (P3EHT$_{19}$-*b*-P2VP$_{138}$-*m*-P3EHT$_{23}$-*b*-PEG$_{113}$-*m*-P3EHT$_{19}$-*b*-P2VP$_{138}$ P3EHT$_{23}$-*b*-PEG$_{113}$) triblock comicelles using self-nucleation suppressed seeded growth at 55 °C

Various volumes of P3EHT$_{19}$-*b*-P2VP$_{138}$ polydisperse nanofiber solution (0.05 mg/mL, *n*BuOH) were placed in separate vials and heated to 90 °C for 1 h and then allowed to cool to 55 °C and maintained at 55 °C for 2 h. Equal amounts of P3EHT$_{23}$-*b*-PEG$_{113}$ seed solution (L_n = 44 nm, $Đ_L$ = 1.26, annealed), also at 55 °C (1:1 *n*BuOH:MeOH, 0.1 mg/mL), were added to achieve different m_{unimer}/m_{seed} ratios. After seed addition and mixing, the vials were left at 55 °C for 24 h and then aged at 22 °C for 24 h prior to imaging by TEM.

2.5.7 UV-Vis Spectroscopy and Variable-Temperature UV/Vis Spectroscopy

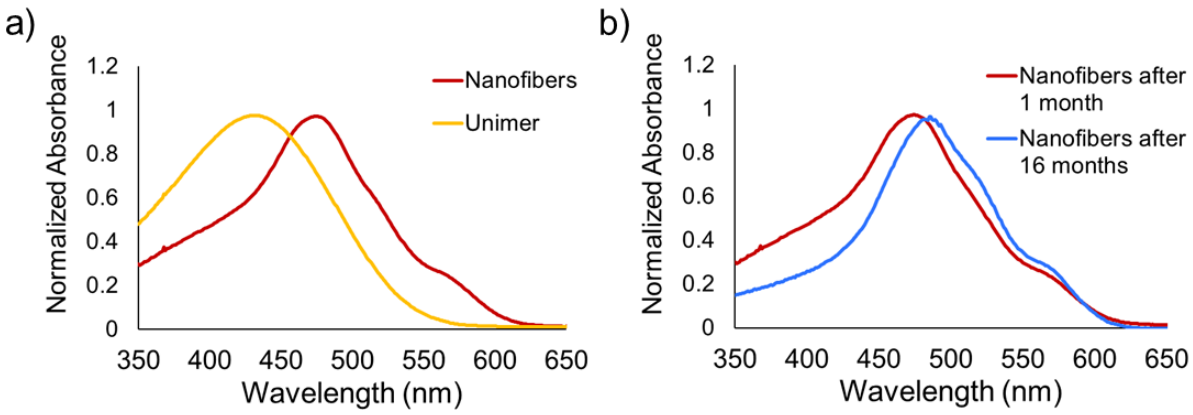

Figure S2.7. (a) Overlayed solution-phase UV-Vis absorbance plots from polydisperse P3EHT$_{23}$-*b*-PEG$_{113}$ nanofiber solution in 1:1 *n*BuOH:MeOH (0.05 mg/mL) (red trace) and P3EHT$_{23}$-*b*-PEG$_{113}$ unimer in THF (0.1 mg/mL) (orange trace) at 22 °C. **(b)** Overlayed solution-phase UV-Vis absorbance plots of polydisperse P3EHT$_{23}$-*b*-PEG$_{113}$ nanofiber solutions in 1:1 *n*BuOH:MeOH (0.05 mg/mL) at 22 °C. Red trace spectrum was obtained 1 month after self-assembly was performed and blue trace spectrum was obtained from the same sample 16 months after self-assembly was performed. Small differences in the spectra are likely due to minor annealing of the crystal structure ($\lambda_{max,\ blue\ trace}$ = 487 nm).

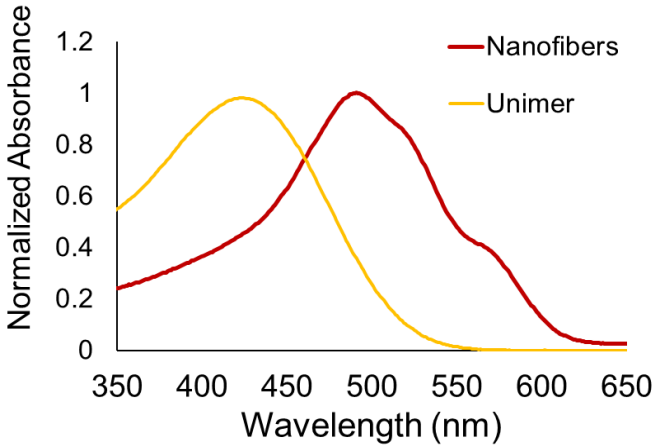

Figure S2.8. Overlayed solution-phase UV-Vis absorbance plots from polydisperse P3EHT$_{19}$-*b*-P2VP$_{138}$ nanofiber solution in *n*BuOH (0.05 mg/mL) (red trace) and P3EHT$_{19}$-*b*-P2VP$_{138}$ unimer in $CHCl_3$ (0.1 mg/mL) (orange trace) at 22 °C.

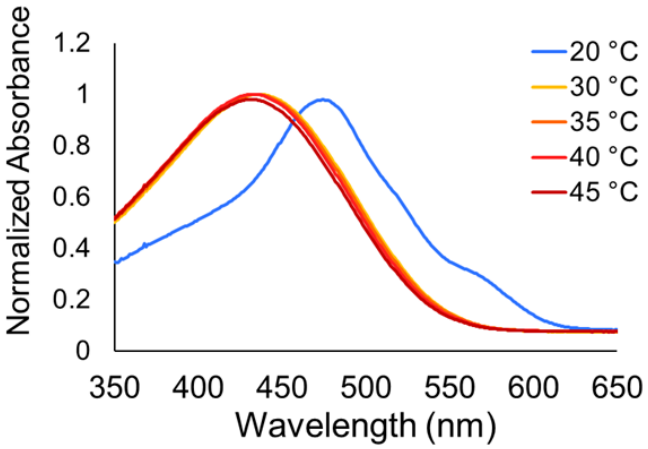

Figure S2.9. Overlayed solution-phase UV-Vis absorbance plots from polydisperse P3EHT$_{23}$-*b*-PEG$_{113}$ nanofiber solutions in 1:1 *n*BuOH:MeOH (0.05 mg/mL) used to investigate self-nucleation suppression temperatures (where a supersaturated solution has formed after heating and cooling). The following procedure was completed for all the temperatures listed in Figure S2.9 with 35 °C being used as a representative example. A polydisperse P3EHT$_{23}$-*b*-PEG$_{113}$ nanofiber solution (0.05 mg/mL) was heated to 90 °C for 1 h to ensure it was in the unimeric state and then quickly transferred to a preheated metal block at 35 °C where it was left at 35 °C for 24 h. The solution was then quickly transferred into a quartz cuvette placed in a UV-Vis spectrometer equipped with a heating block that was set to 35 °C and analyzed.

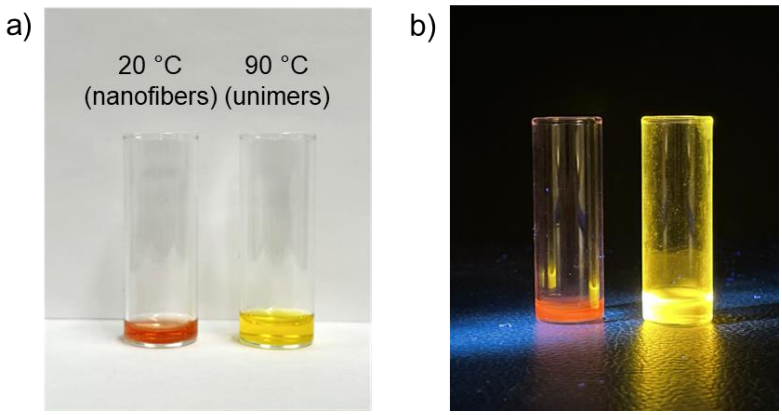

Figure S2.10. (a) Left vial – Polydisperse P3EHT$_{23}$-*b*-PEG$_{113}$ nanofiber solution (1:1 *n*BuOH:MeOH, 0.05 mg/mL) at 20 °C after self-assembly (red, self-assembled). Right vial – Solution (1:1 *n*BuOH:MeOH, 0.05 mg/mL) of polydisperse P3EHT$_{23}$-*b*-PEG$_{113}$ nanofibers that was heated to 90 °C (yellow/orange, unimeric). **(b)** Left vial – Self-assembled P3EHT$_{23}$-*b*-PEG$_{113}$ polydisperse nanofiber solution (1:1 *n*BuOH:MeOH, 0.05 mg/mL) at 20 °C while being irradiated with 365 nm light. Right vial – Solution (1:1 *n*BuOH:MeOH, 0.05 mg/mL) of polydisperse P3EHT$_{23}$-*b*-PEG$_{113}$ nanofibers that was heated to 90 °C (yellow/orange, unimeric) while being irradiated with 365 nm light.

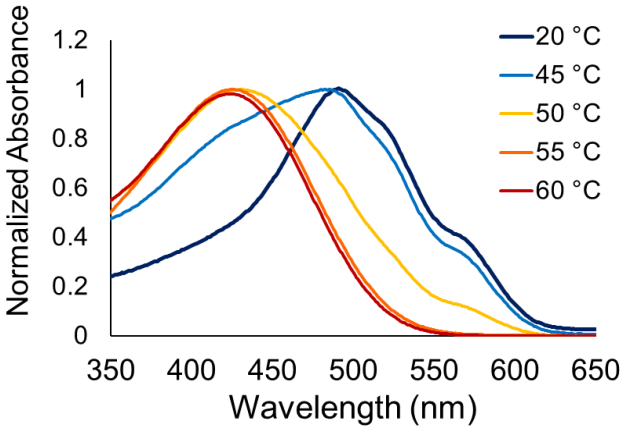

Figure S2.11. Overlayed solution-phase UV-Vis absorbance plots from polydisperse P3EHT$_{19}$-*b*-P2VP$_{138}$ nanofiber solutions in *n*BuOH (0.05 mg/mL) used to investigate self-nucleation suppression temperatures (where a supersaturated solution has formed after heating and cooling). The following procedure was completed for all the temperatures listed in Figure S2.11 with 55 °C being used as a representative example. A polydisperse P3EHT$_{19}$-*b*-P2VP$_{138}$ nanofiber solution (0.05 mg/mL) was heated to 90 °C for 1 h to ensure it was in the unimeric state and then quickly transferred to a preheated metal block at 55 °C where it was left at 55 °C for 24 h. The solution was then quickly transferred into a quartz cuvette placed in a UV-Vis spectrometer equipped with a heating block that was set to 55 °C and analyzed.

2.5.8 Wide Angle X-Ray Scattering

a)

Peak	q (Å^{-1})	Assignment	d (nm)
1	0.42	100 (alkyl stacking)	1.51
2	0.84	200	0.75
3	1.30	010 (π-π stack)	0.49
4	1.35	PEG	0.46
5	1.86	420	0.34

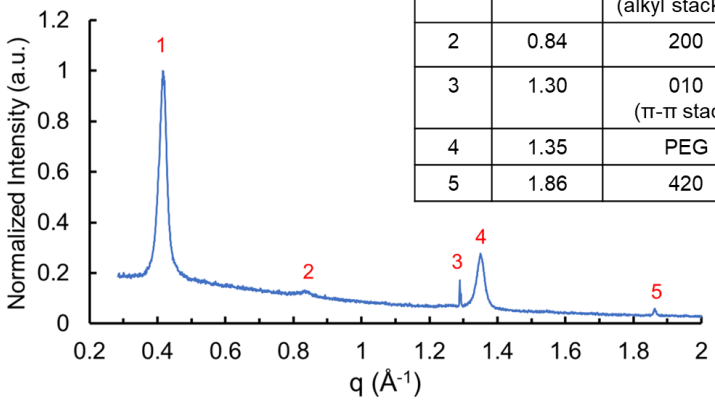

b)

Peak	q (Å^{-1})	Assignment	d (nm)
1	0.42	100 (alkyl stacking)	1.51
2	0.86	200	0.73
3	1.25	010 (π-π stack)	0.51
4	1.49	320	0.42
5	1.72	410	0.36

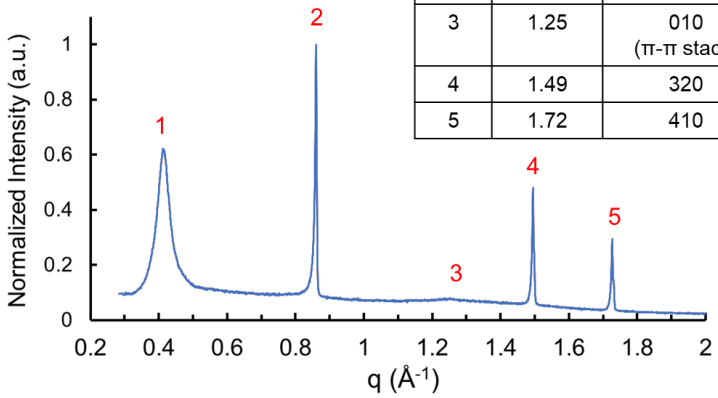

Figure S2.12. (a) Solid-state WAXS pattern of a film of polydisperse P3EHT$_{23}$-*b*-PEG$_{113}$ nanofibers after background subtraction. The film was formed by drop-casting a polydisperse nanofiber solution (5 mg/mL) in 1:1 *n*BuOH:MeOH onto a crystalline silicon substrate. **(b)** Solid-state WAXS pattern of a film of polydisperse P3EHT$_{19}$-*b*-P2VP$_{138}$ nanofibers after background subtraction. The film was formed by drop-casting a polydisperse nanofiber solution (5 mg/mL) in *n*BuOH onto a crystalline silicon substrate.

2.5.9 Atomic Force Microscopy

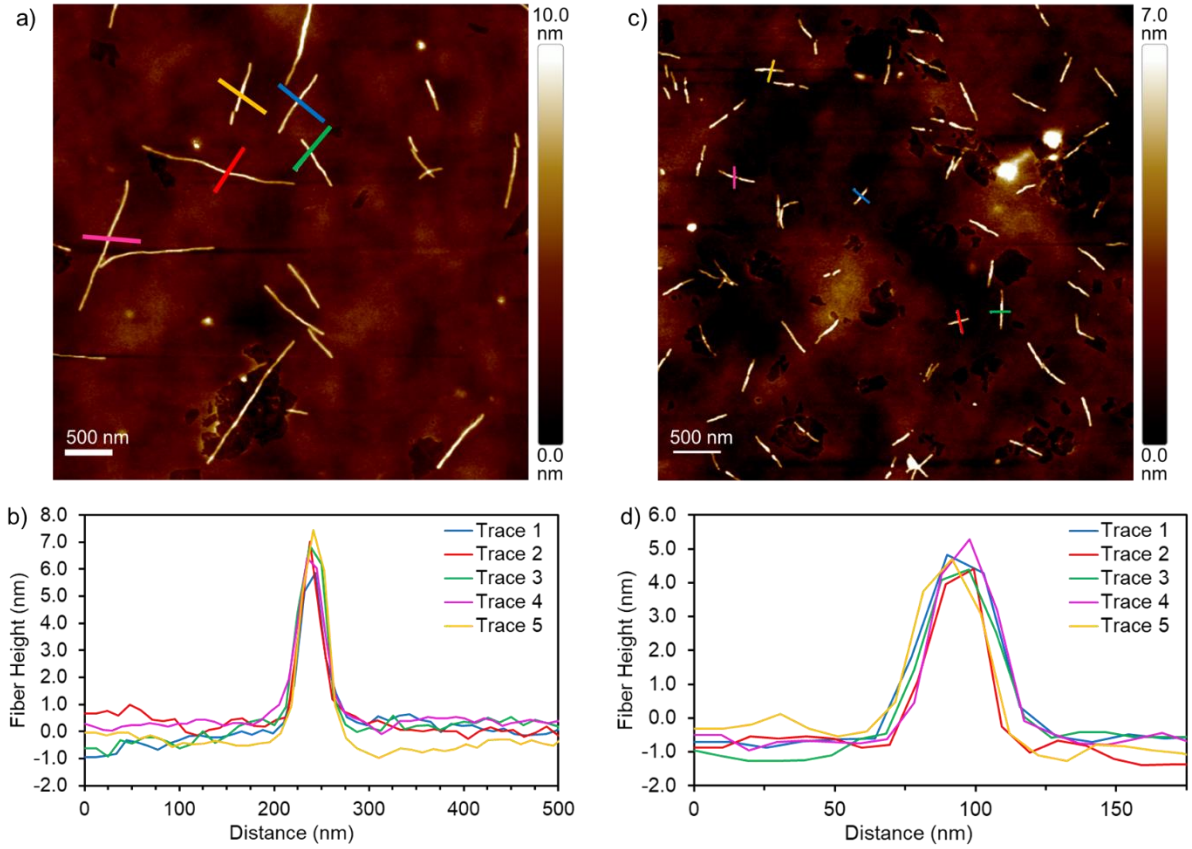

Figure S2.13. (a) AFM height image of ~800 nm homogenous P3EHT$_{23}$-*b*-PEG$_{113}$ fibers (made by self-nucleation suppressed seeded growth at 30 °C, m_{unimer}/m_{seed} = 16) in 1:1 *n*BuOH:MeOH (0.05 mg/mL) drop-cast onto a glow discharged silicon wafer. Coloured lines indicate height profile shown in **(b)** drawn perpendicular to the long axis of the nanofibers. Series 1 - height: 6.8 nm; Series 2 - height: 7.3 nm; Series 3 - height: 7.8 nm; Series 4 - height: 6.4 nm; Series 5 - height: 8.0 nm. Average height: 7.3 nm ± 0.7 nm. **(c)** AFM height image of ~400 nm homogenous P3EHT$_{19}$-*b*-P2VP$_{138}$ fibers (made by seeded growth, m_{unimer}/m_{seed} = 16) in *n*BuOH (0.05 mg/mL) drop-cast onto a glow discharged silicon wafer. Coloured lines indicate height profile shown in **(d)** drawn perpendicular to the long axis of the nanofibers. Series 1 - height: 5.7 nm; Series 2 - height: 6.0 nm; Series 3 - height: 5.7 nm; Series 4 - height: 6.2 nm; Series 5 - height: 6.0 nm. Average height = 5.9 nm ± 0.2 nm.

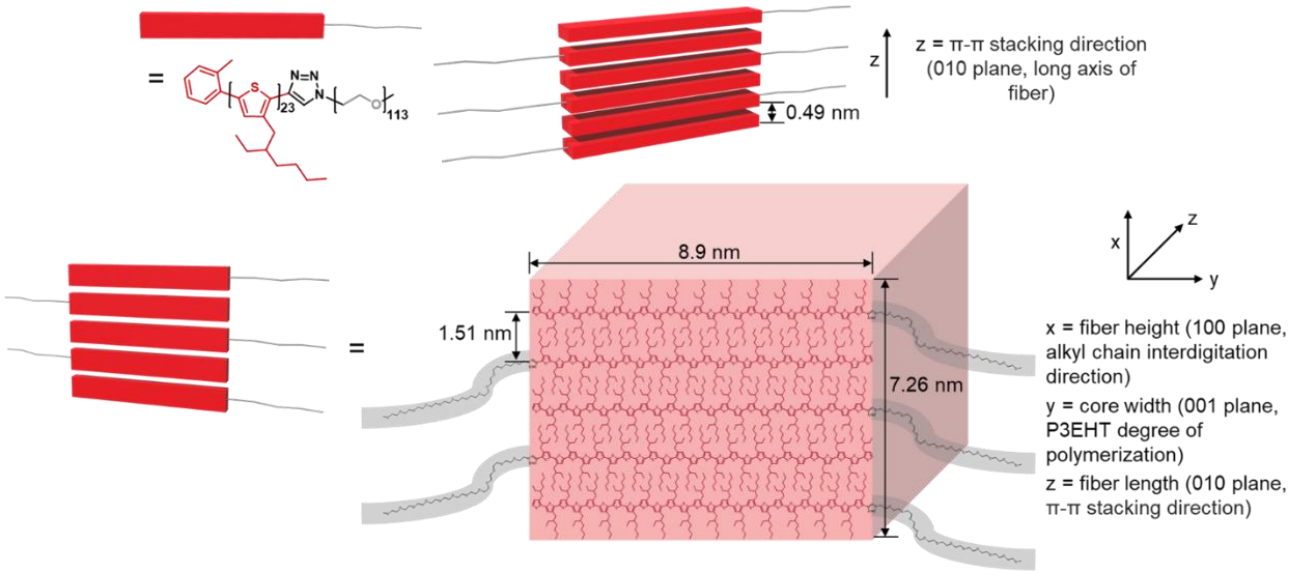

Figure S2.14. Cartoon schematic showing the chain packing geometry (not drawn to scale) and dimensions of a P3EHT$_{23}$-*b*-PEG$_{113}$ fiber.

2.5.10 Transmission Electron Microscopy

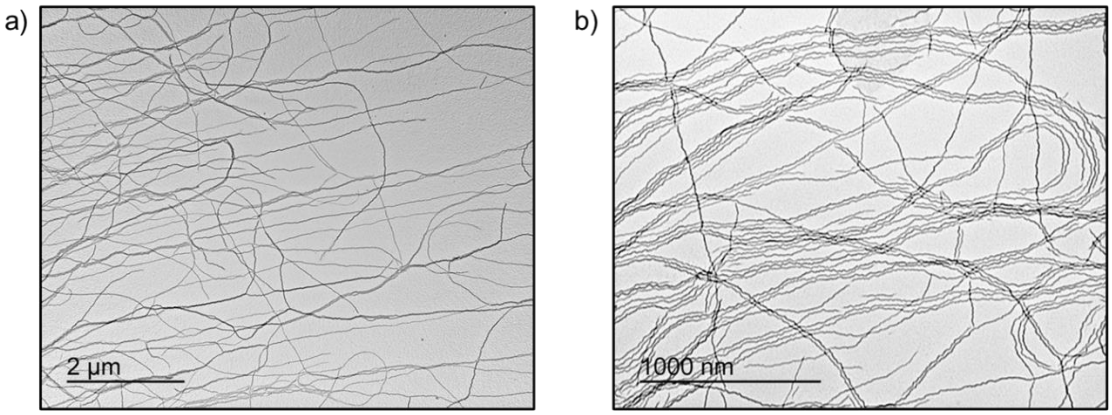

Figure S2.15. (a, b) TEM images of polydisperse P3EHT$_{23}$-*b*-PEG$_{113}$ nanofibers made by heating solid P3EHT$_{23}$-*b*-PEG$_{113}$ in deoxygenated *n*BuOH to 90 °C for 30 min. and then cooling the 0.2 mg/mL solution to 22 °C and aging 24 h. After aging, an equivalent amount of deoxygenated MeOH was added to form a solution with a final concentration of 0.1 mg/mL. The samples were then drop-cast onto a carbon-coated copper TEM grid and imaged by TEM following solvent evaporation.

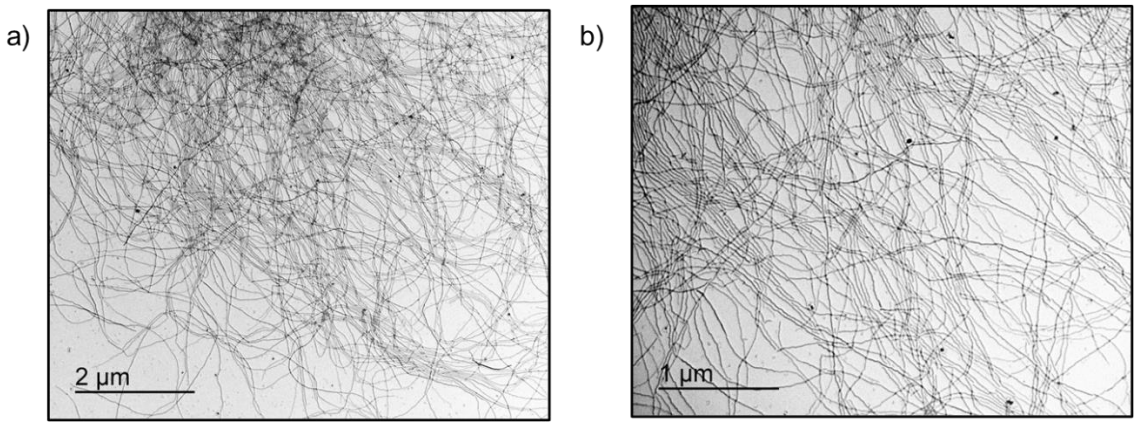

Figure S2.16. (a, b) TEM images of polydisperse P3EHT$_{19}$-*b*-P2VP$_{138}$ nanofibers made by heating solid P3EHT$_{19}$-*b*-P2VP$_{138}$ in deoxygenated *n*BuOH to 90 °C for 30 min. and then cooling the solution (0.1 mg/mL) to 22 °C and aging at 22 °C for 24 h. The samples were then drop-cast onto a carbon-coated copper TEM grid and imaged following solvent evaporation.

Seed Fabrication

Batch 1 – Not Annealed

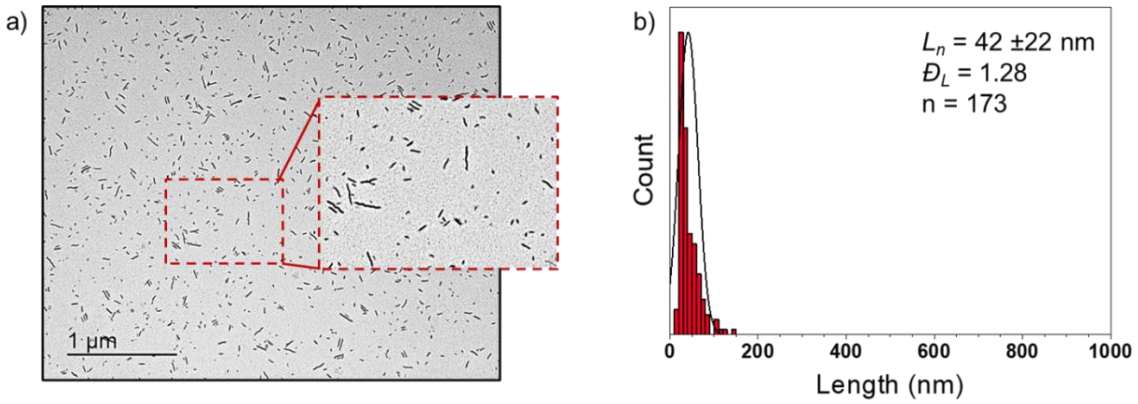

Figure S2.17. (a) TEM image of seeds formed by ultrasonication of a P3EHT$_{23}$-*b*-PEG$_{113}$ polydisperse nanofiber solution (1:1 *n*BuOH:MeOH, 0.1 mg/mL) at 0 °C for 3 h. **(b)** Histogram showing the fiber length distribution of P3EHT$_{23}$-*b*-PEG$_{113}$ seeds (L_n = 42 nm, L_w = 54 nm, $Đ_L$ = 1.28, σ = ± 22 nm, n = 173).

Batch 1 – Annealed

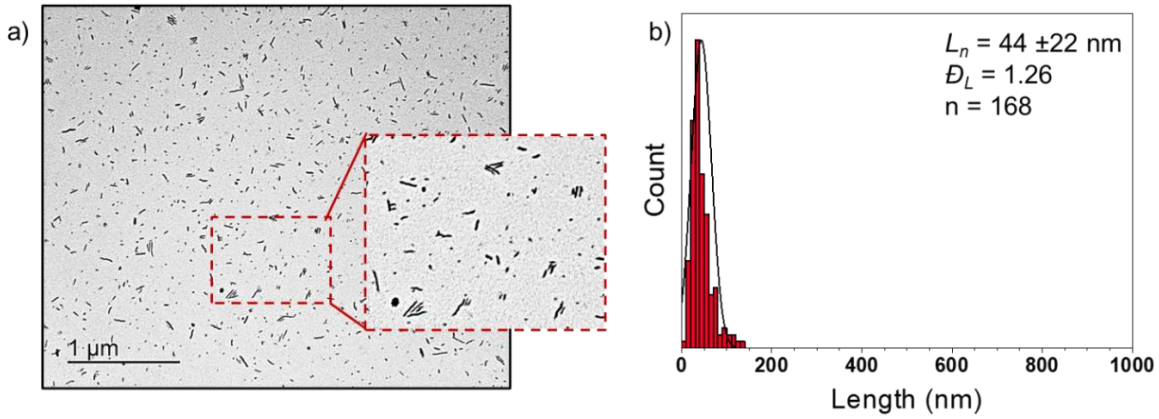

Figure S2.18. (a) TEM image of seeds formed by ultrasonication of a P3EHT$_{23}$-*b*-PEG$_{113}$ polydisperse nanofiber solution (1:1 *n*BuOH:MeOH, 0.1 mg/mL) at 0 °C for 3 h. Seeds were annealed at 30 °C for 18 h and then cooled to 22 °C and imaged following solvent evaporation. **(b)** Histogram showing the fiber length distribution of annealed P3EHT$_{23}$-*b*-PEG$_{113}$ seeds (L_n = 44 nm, L_w = 55 nm, $Đ_L$ = 1.26, σ = ± 22 nm, n = 168).

Batch 2 - Annealed

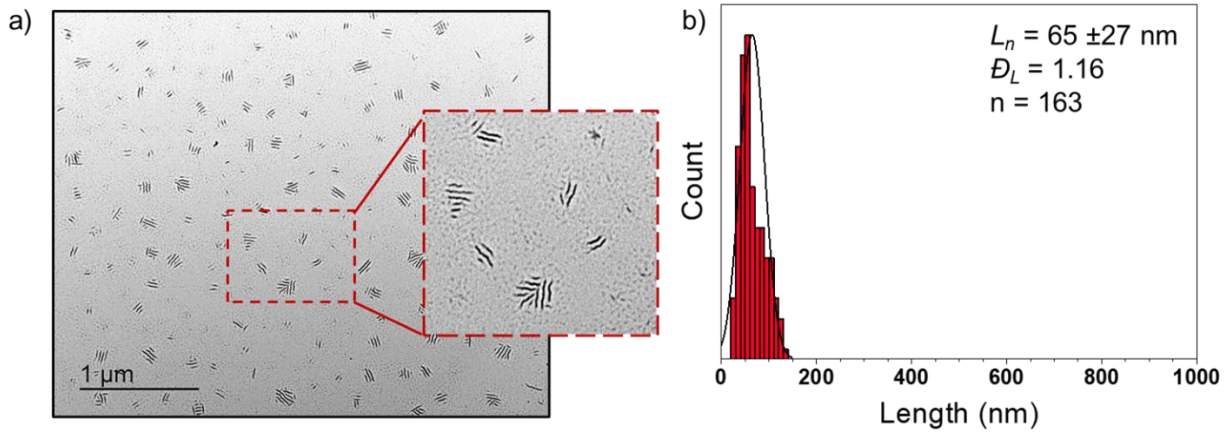

Figure S2.19. (a) TEM image of seeds formed by ultrasonication of a P3EHT$_{23}$-*b*-PEG$_{113}$ polydisperse nanofiber solution (1:1 *n*BuOH:MeOH, 0.1 mg/mL) at 0 °C for 3 h. Seeds were annealed at 30 °C for 18 h and then cooled to 22 °C and imaged following solvent evaporation. **(b)** Histogram showing the fiber length distribution of P3EHT$_{23}$-*b*-PEG$_{113}$ seeds (L_n = 65 nm, L_w = 75 nm, $Đ_L$ = 1.16, σ = ± 27 nm, n = 163).

P3EHT$_{19}$-*b*-P2VP$_{138}$ - Annealed

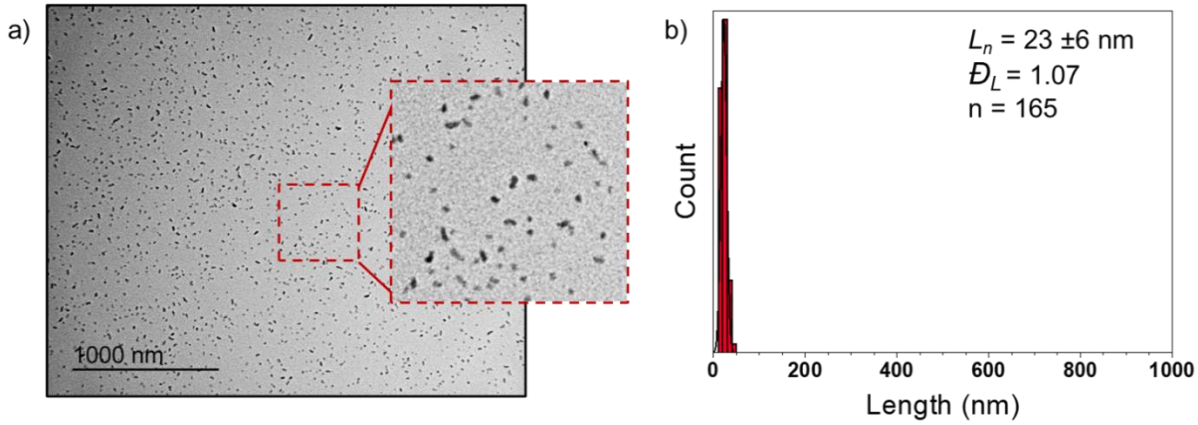

Figure S2.20. (a) TEM image of seeds formed by ultrasonication of a P3EHT$_{19}$-*b*-P2VP$_{138}$ polydisperse nanofiber solution (*n*BuOH, 0.1 mg/mL) at 0 °C for 3 h. Seeds were annealed at 30 °C for 18 h prior to use then cooled to 22 °C and imaged following solvent evaporation. **(b)** Histogram showing the fiber length distribution of P3EHT$_{19}$-*b*-P2VP$_{138}$ seeds (L_n = 23 nm, L_w = 25 nm, $Đ_L$ = 1.07, σ = ± 6 nm, n = 165).

Attempted length-control of nanofibers formed using seeded growth at 22 °C

Seeded growth at 22 °C with P3EHT$_{23}$-*b*-PEG$_{113}$ seeds which were not annealed

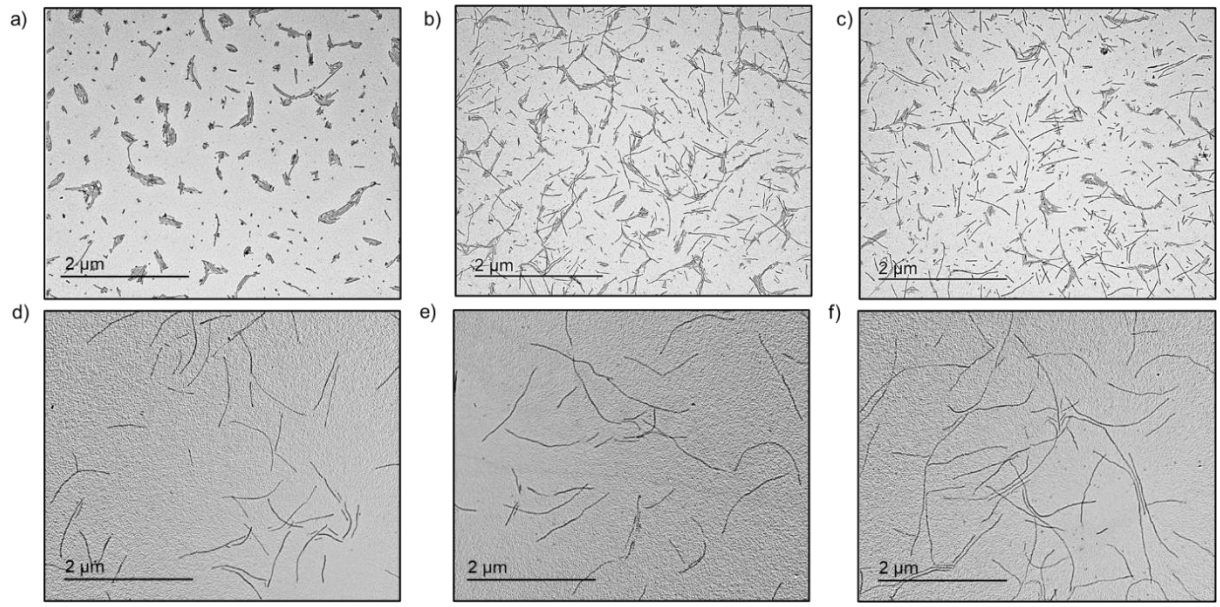

Figure S2.21. TEM images of P3EHT$_{23}$-*b*-PEG$_{113}$ nanofibers in 1:1 *n*BuOH:MeOH (0.05 mg/mL) formed by living CDSA seeded growth using seed micelles (1:1 *n*BuOH:MeOH, 0.1 mg/mL) which were not annealed prior to use. P3EHT$_{23}$-*b*-PEG$_{113}$ seed micelles (1:1 *n*BuOH:MeOH, 0.1 mg/mL) were treated with **(a)** 4, **(b)** 6, **(c)** 8, **(d)** 12, **(e)** 16, and **(f)** 20 equivalents of P3EHT$_{23}$-*b*-PEG$_{113}$ unimer (THF, 2 mg/mL) at 22 °C. Solutions were aged at 22 °C for 24 h followed by solvent evaporation prior to TEM imaging.

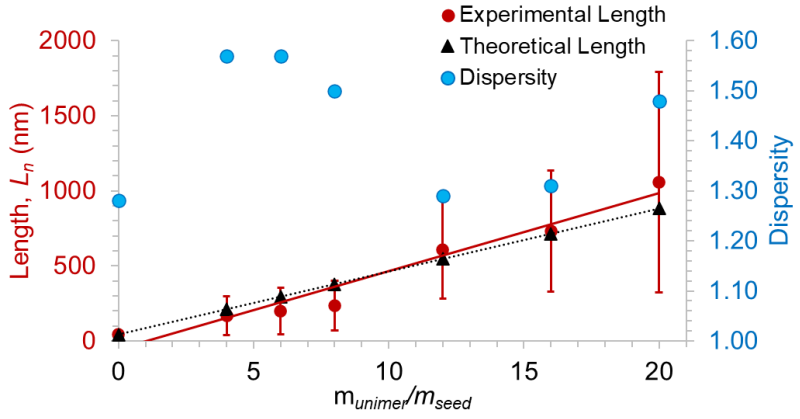

Figure S2.22. Plot showing the dependence of fiber length (L_n) on unimer to seed mass ratio when using P3EHT$_{23}$-*b*-PEG$_{113}$ seeds (L_n = 42 nm, $Đ_L$ = 1.28) that were not annealed prior to seeded growth experiments at 22 °C. Error bars represent standard deviation.

Table S2.1. Summary of data from seeded growth experiments with P3EHT$_{23}$-*b*-PEG$_{113}$ seed micelles which were not annealed. σ is standard deviation in L_n measurements.

m_{unimer}/m_{seed}	L_n	L_w	$Đ_L$	σ
Seeds	42	54	1.28	22
4	168	264	1.57	124
6	200	314	1.57	156
8	236	354	1.50	167
12	609	786	1.29	328
16	731	403	1.31	403
20	1058	1568	1.48	734

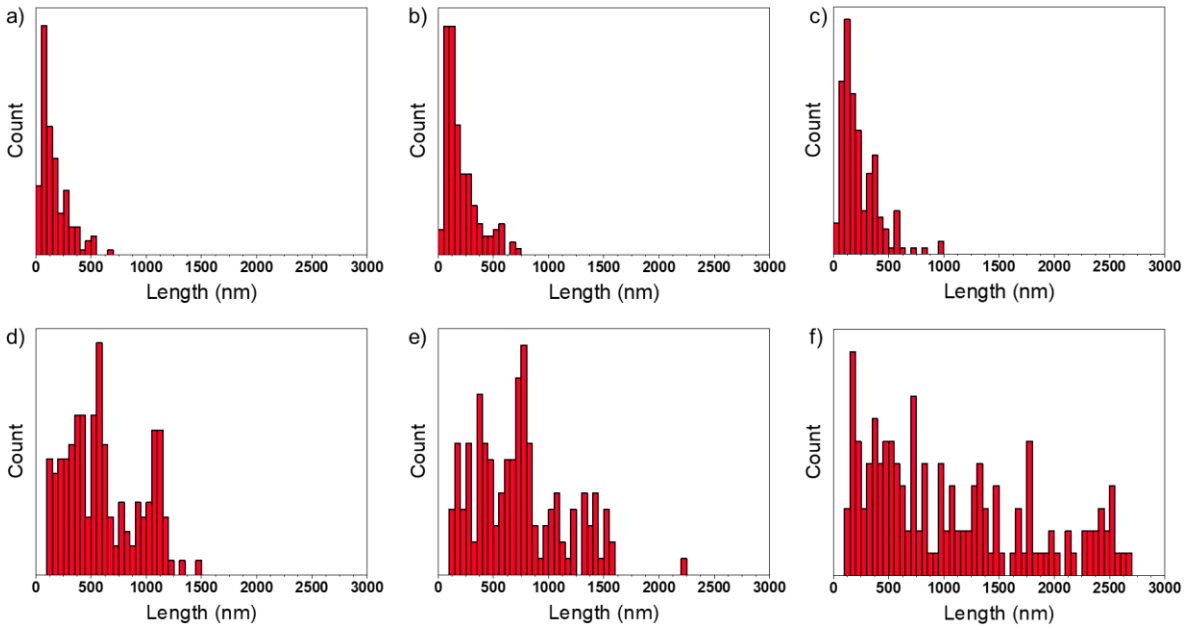

Figure S2.23. Histograms showing the nanofiber length distribution of P3EHT$_{23}$-*b*-PEG$_{113}$ seed micelles (not annealed) that were treated with **(a)** 4, **(b)** 6, **(c)** 8, **(d)** 12, **(e)** 16, and **(f)** 20 equivalents of P3EHT$_{23}$-*b*-PEG$_{113}$ unimer in THF at 22 °C.

Seeded growth at 22 ° C with P3EHT$_{23}$-*b*-PEG$_{113}$ seeds that were annealed at 30 °C for 18 h

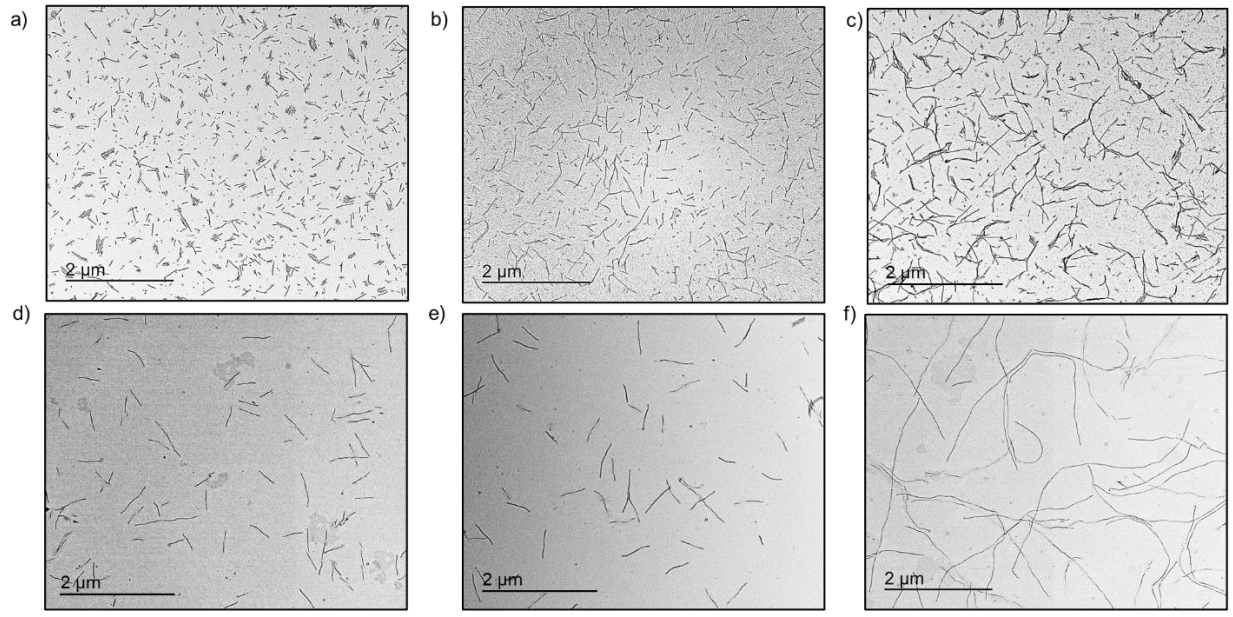

Figure S2.24. TEM images of P3EHT$_{23}$-*b*-PEG$_{113}$ nanofibers in 1:1 *n*BuOH:MeOH (0.05 mg/mL) formed by living CDSA seeded growth using seed micelles (1:1 *n*BuOH:MeOH, 0.1 mg/mL) which were annealed at 30 °C for 18 h prior to use. Annealed P3EHT$_{23}$-*b*-PEG$_{113}$ seed micelles (0.1 mg/mL, 1:1 *n*BuOH:MeOH) were treated with **(a)** 4, **(b)** 6, **(c)** 8, **(d)** 12, **(e)** 16, and **(f)** 20 equivalents of P3EHT$_{23}$-*b*-PEG$_{113}$ unimer (THF, 2 mg/mL) at 22 °C. Solutions were aged at 22 °C for 24 h followed by solvent evaporation prior to TEM imaging.

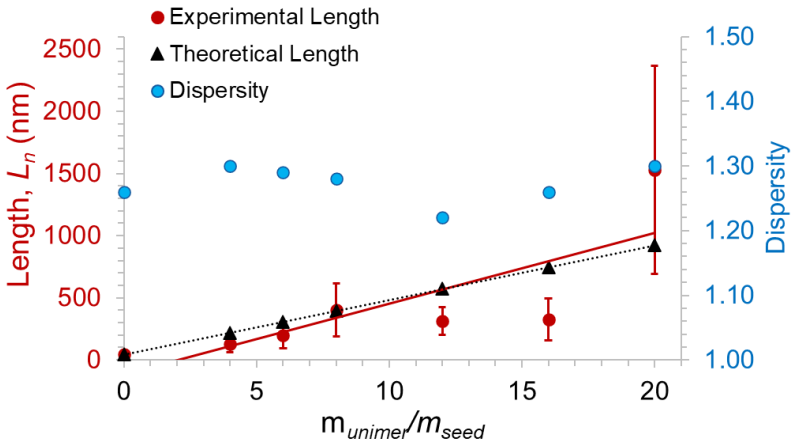

Figure S2.25. Plot showing the dependence of fiber length (L_n) on unimer to seed mass ratio when using seeds (L_n = 44 nm, $Đ_L$ = 1.26) that were annealed at 30 °C for 18 h prior to conducting seeded growth experiments at 22 °C. Error bars represent standard deviation.

Table S2.2. Summary of data from seeded growth experiments at 22 °C with P3EHT$_{23}$-*b*-PEG$_{113}$ seed micelles (1:1 *n*BuOH:MeOH, 0.05 mg/mL) which were annealed at 30 °C for 18 h. σ is standard deviation in L_n measurements.

m_{unimer}/m_{seed}	L_n	L_w	$Đ_L$	σ
Seeds	44	55	1.26	22
4	131	170	1.30	72
6	200	258	1.29	156
8	403	516	1.28	215
12	313	382	1.22	109
16	326	411	1.26	168
20	1528	1986	1.30	839

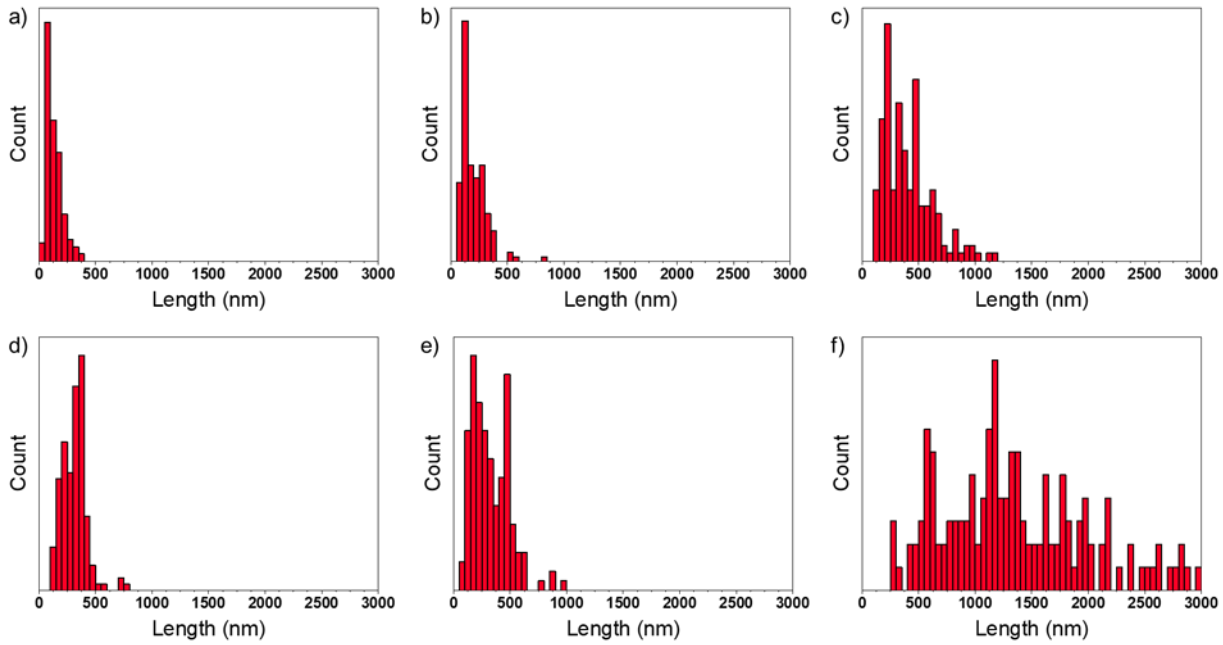

Figure S2.26. Histograms showing the nanofiber length distribution of annealed (30 °C, 18 h) P3EHT$_{23}$-*b*-PEG$_{113}$ seed micelles (1:1 *n*BuOH:MeOH, 0.1 mg/mL) that were treated with **(a)** 4, **(b)** 6, **(c)** 8, **(d)** 12, **(e)** 16, and **(f)** 20 equivalents of P3EHT$_{23}$-*b*-PEG$_{113}$ unimer (THF, 2 mg/mL) at 22 °C. Final concentrations were 0.05 mg/mL.

Seeded growth at 22 °C with P3EHT$_{19}$-*b*-P2VP$_{138}$ seeds which were annealed at 30 °C for 18 h prior to use

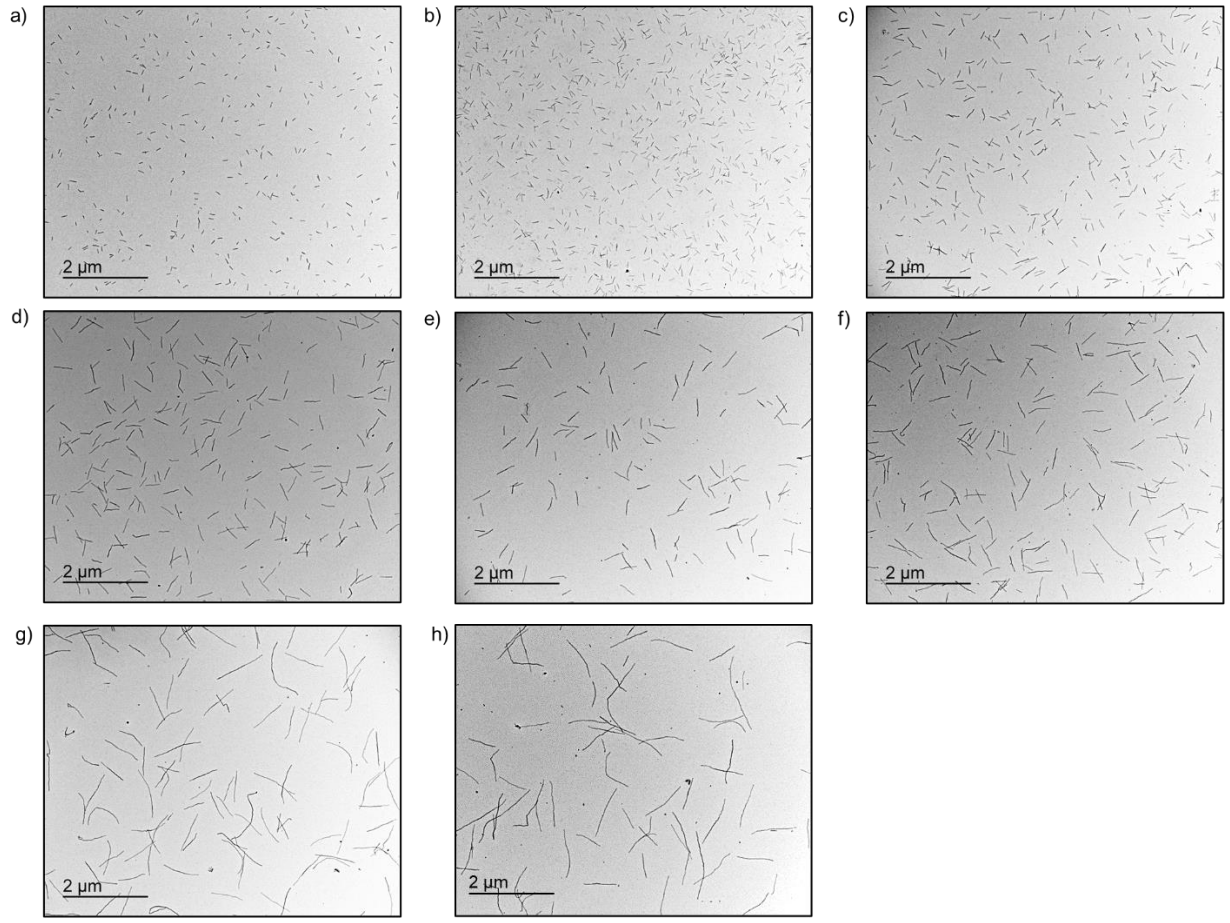

Figure S2.27. TEM images of P3EHT$_{19}$-*b*-P2VP$_{138}$ nanofibers in *n*BuOH (0.05 mg/mL) formed by living CDSA seeded growth using seed micelles (23 nm, 0.1 mg/mL, *n*BuOH) which were annealed at 30 °C prior to use. P3EHT$_{19}$-*b*-P2VP$_{138}$ seed micelles (0.1 mg/mL, *n*BuOH) were treated with **(a)** 4, **(b)** 6, **(c)** 8, **(d)** 12, **(e)** 16, **(f)** 20, **(g)** 30, and **(h)** 40 equivalents of P3EHT$_{19}$-*b*-P2VP$_{138}$ unimer (2 mg/mL, $CHCl_3$) at 22 °C. Solutions were aged at 22 °C for 24 h followed by solvent evaporation prior to TEM imaging**.**

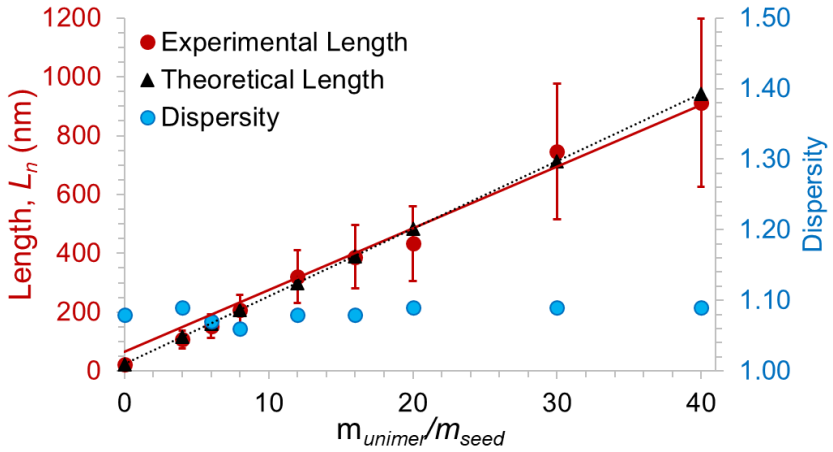

Figure S2.28. Plot showing the dependence of fiber length (L_n) on unimer-to-seed mass ratio when using P3EHT$_{19}$-*b*-P2VP$_{138}$ seeds (L_n = 23 nm, $Đ_L$ = 1.08) that were annealed at 30 °C for 18 h prior to seeded growth experiments at 22 °C. Error bars represent standard deviation.

Table S2.3. Summary of data from seeded growth experiments at 22 °C with P3EHT$_{19}$-*b*-P2VP$_{138}$ seed micelles which were annealed at 30 °C for 18 h prior to use. σ is standard deviation in L_n measurements.

m_{unimer}/m_{seed}	L_n	L_w	$Đ_L$	σ
Seeds	23	25	1.07	6
4	107	116	1.09	31
6	152	163	1.07	40
8	207	219	1.06	51
12	321	347	1.08	90
16	388	419	1.08	108
20	433	472	1.09	127
30	746	813	1.09	230
40	912	994	1.09	287

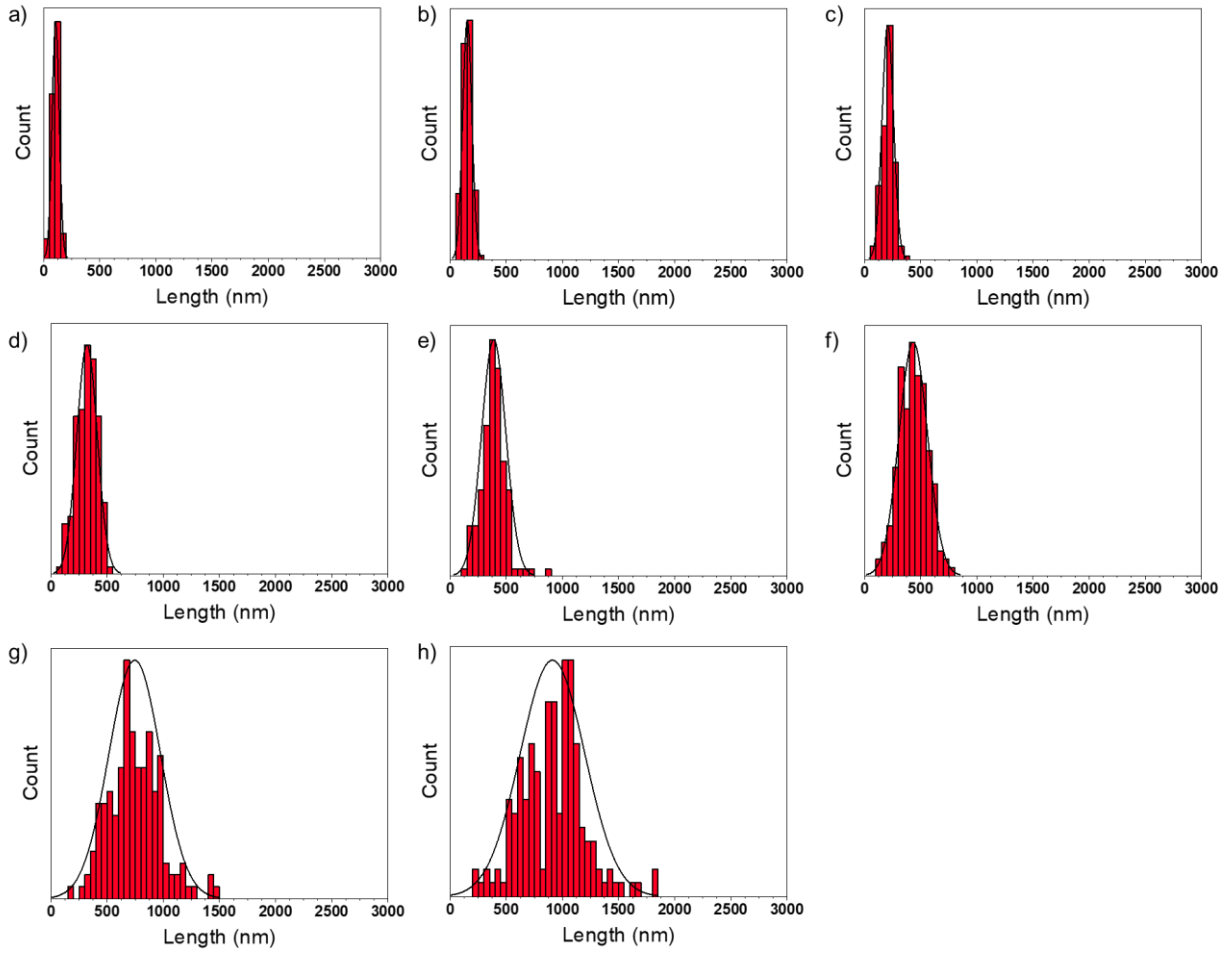

Figure S2.29. Histograms showing the nanofiber length distribution of P3EHT$_{19}$-*b*-P2VP$_{138}$ seed micelles that were treated with **(a)** 4, **(b)** 6, **(c)** 8, **(d)** 12, **(e)** 16, **(f)** 20, **(g)** 30, and **(h)** 40 equivalents of P3EHT$_{19}$-*b*-P2VP$_{138}$ unimer in $CHCl_3$ at 22 °C.

Self-nucleation suppressed seeded growth of length-controlled P3EHT$_{23}$-*b*-PEG$_{113}$ nanofibers at 30 °C using annealed P3EHT$_{23}$-*b*-PEG$_{113}$ seeds (Batch 1)

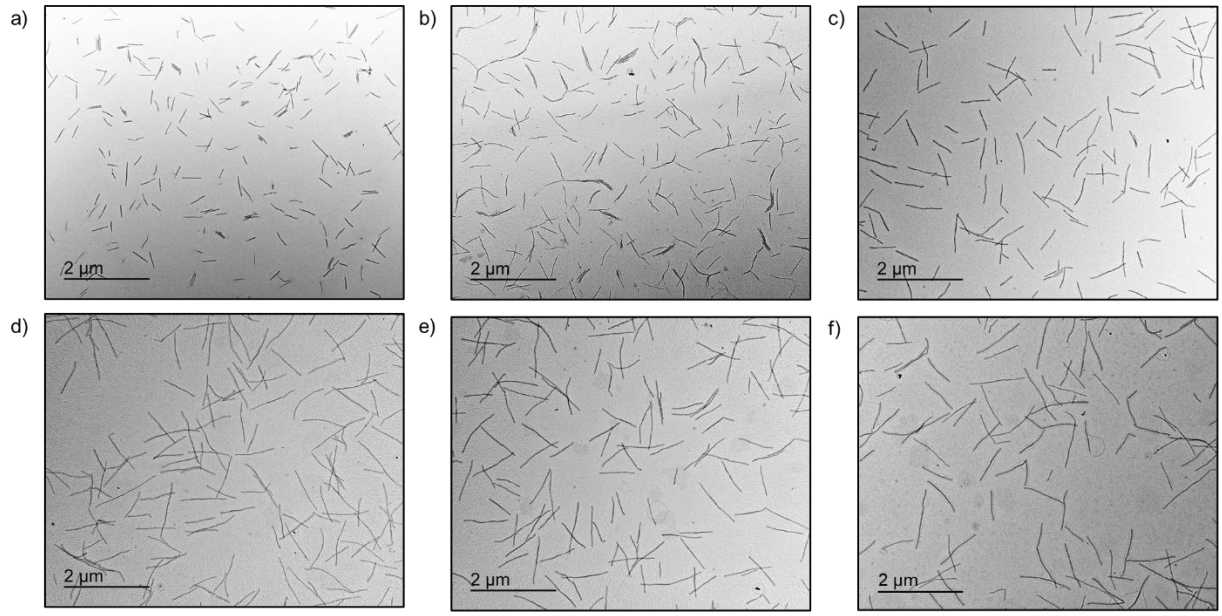

Figure S2.30. TEM images of P3EHT$_{23}$-*b*-PEG$_{113}$ nanofibers formed in 1:1 *n*BuOH:MeOH (0.05 mg/mL) by self-nucleation suppressed seeded growth (30 °C) following solvent evaporation. Unimer-to-seed ratio m_{unimer}/m_{seed} = **(a)** 4, **(b)** 6, **(c)** 8, **(d)** 12, **(e)** 16, and **(f)** 20. Fibers are formed through the addition of P3EHT$_{23}$-*b*-PEG$_{113}$ seed micelles in (1:1 *n*BuOH:MeOH, 0.1 mg/mL) to polydisperse nanofiber solutions (1:1 *n*BuOH:MeOH, 0.1 mg/mL) which were heated to 90 °C for 1 h and then cooled to 30 °C over the course of 2 h. Following seed addition at 30 °C, solutions were maintained at 30 ° C for 24 h before being cooled to 22 °C and aged at 22 °C for 24 h.

Table S2.4. Summary of data from self-nucleation suppressed seeded growth experiments of P3EHT$_{23}$-*b*-PEG$_{113}$ nanofibers at 30 °C. σ is standard deviation in L_n measurements.

m_{unimer}/m_{seed}	L_n	L_w	$Đ_L$	σ
Seeds	44	55	1.26	22
4	290	319	1.10	94
6	471	509	1.08	134
8	396	436	1.10	190
12	768	883	1.15	300
16	791	862	1.09	236
20	913	1023	1.12	305

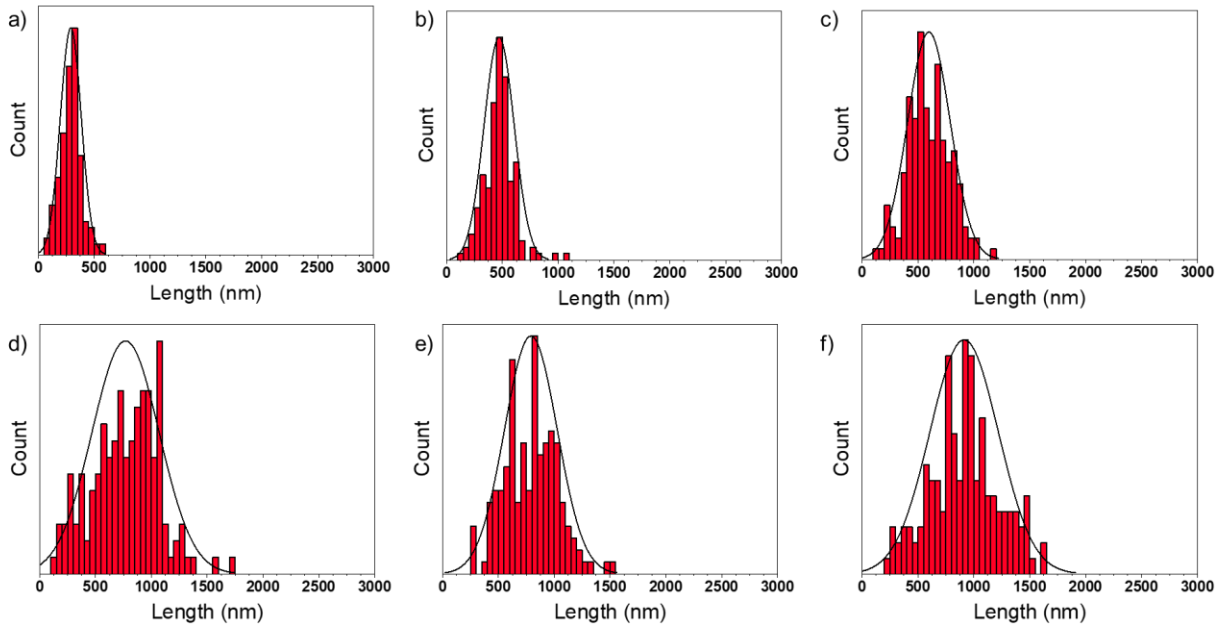

Figure S2.31. Histograms showing the nanofiber length distribution of P3EHT$_{23}$-*b*-PEG$_{113}$ fibers formed using self-nucleation suppressed seeded growth at 30 °C. Unimer-to-seed ratio m_{unimer}/m_{seed} = **(a)** 4, **(b)** 6, **(c)** 8, **(d)** 12, **(e)** 16, and **(f)** 20.

Self-nucleation suppressed seeded growth of length-controlled P3EHT$_{23}$-*b*-PEG$_{113}$ nanofibers at 50 °C using annealed P3EHT$_{23}$-*b*-PEG$_{113}$ seeds (Batch 1)

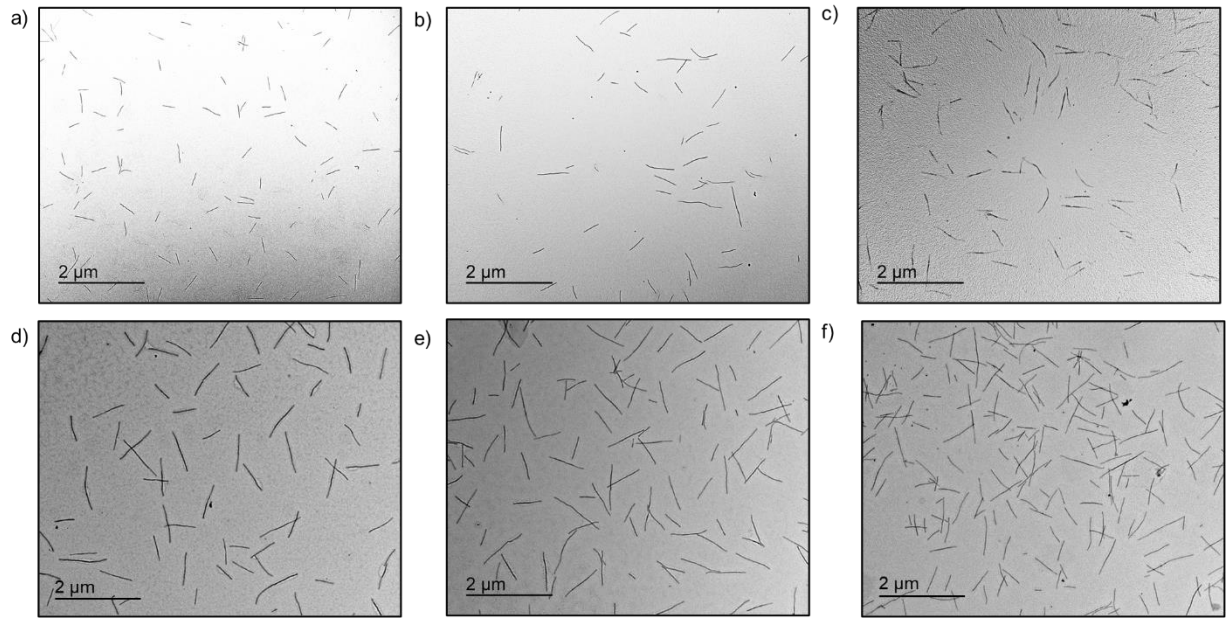

Figure S2.32. TEM images of P3EHT$_{23}$-*b*-PEG$_{113}$ nanofibers formed in 1:1 *n*BuOH:MeOH (0.05 mg/mL) by self-nucleation suppressed seeded growth (50 °C) following solvent evaporation. Unimer-to-seed ratio m_{unimer}/m_{seed} = **(a)** 4, **(b)** 6, **(c)** 8, **(d)** 12, **(e)** 16, and **(f)** 20. Fibers are formed through the addition of P3EHT$_{23}$-*b*-PEG$_{113}$ seed micelles (0.1 mg/mL, 1:1 *n*BuOH:MeOH) to polydisperse nanofiber solutions (0.1 mg/mL, 1:1 *n*BuOH:MeOH) which were heated to 90 °C for 1 h and then cooled to 50 °C over the course of 2 h. Following seed addition at 50 °C, the solutions were maintained at 50 ° C for an additional 24 h before being cooled to 22 °C and aged at 22 °C for 24 h.

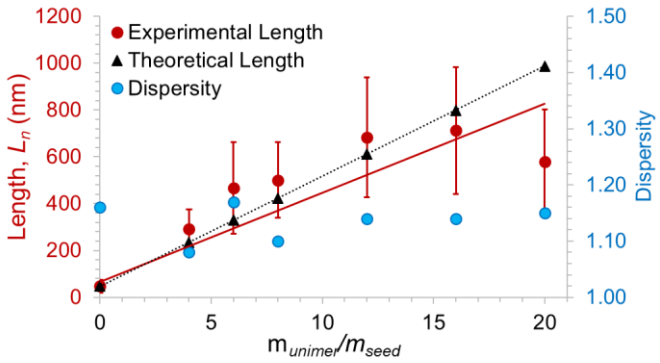

Figure S2.33. Plot showing the dependence of P3EHT$_{23}$-*b*-PEG$_{113}$ fiber length (L_n) on unimer to seed mass ratio when using using self-nucleation suppressed seeded growth at 50 °C.

Table S2.5. Summary of data from self-nucleation suppressed seeded growth experiments of P3EHT$_{23}$-*b*-PEG$_{113}$ nanofibers at 50 °C. σ is standard deviation in L_n measurements.

m_{unimer}/m_{seed}	L_n	L_w	$Đ_L$	σ
Seeds	44	55	1.26	22
4	292	315	1.08	84
6	467	546	1.17	195
8	501	551	1.10	162
12	683	779	1.14	257
16	712	812	1.14	270
20	579	666	1.15	223

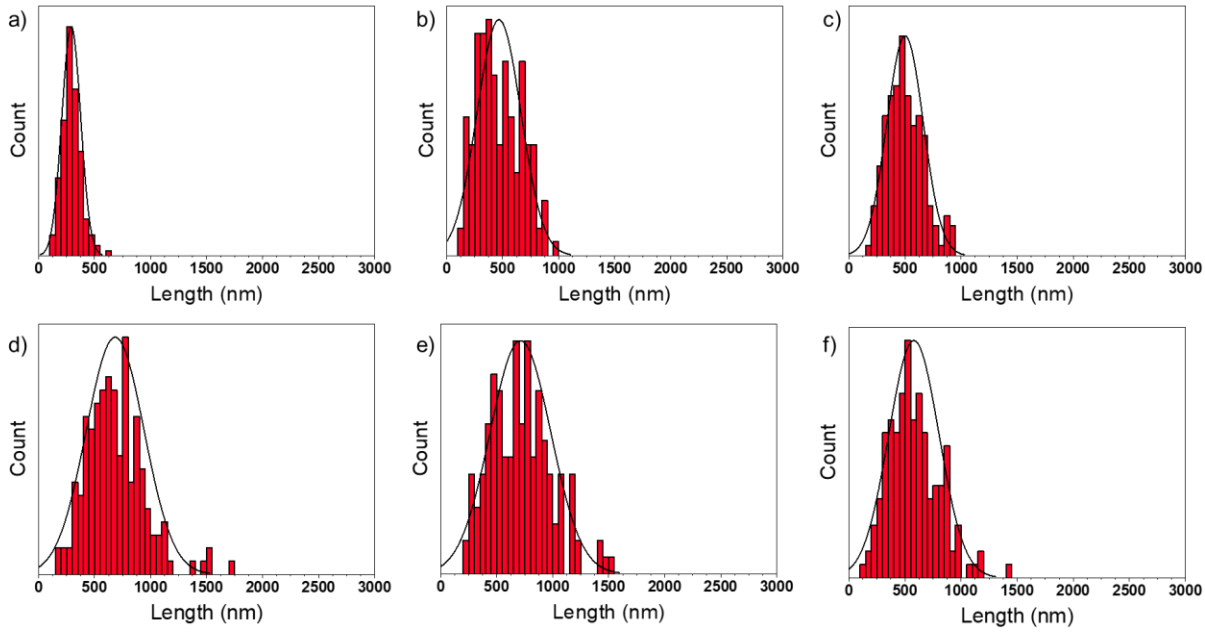

Figure S2.34. Histograms showing the nanofiber length distribution of P3EHT$_{23}$-*b*-PEG$_{113}$ fibers formed using self-nucleation suppressed seeded growth at 50 °C. unimer-to-seed ratio m_{unimer}/m_{seed} = **(a)** 4, **(b)** 6, **(c)** 8, **(d)** 12, **(e)** 16, and **(f)** 20.

Length-controlled P3EHT$_{23}$-*b*-PEG$_{113}$ nanofibers by self-seeding and self-nucleation suppressed self-seeding

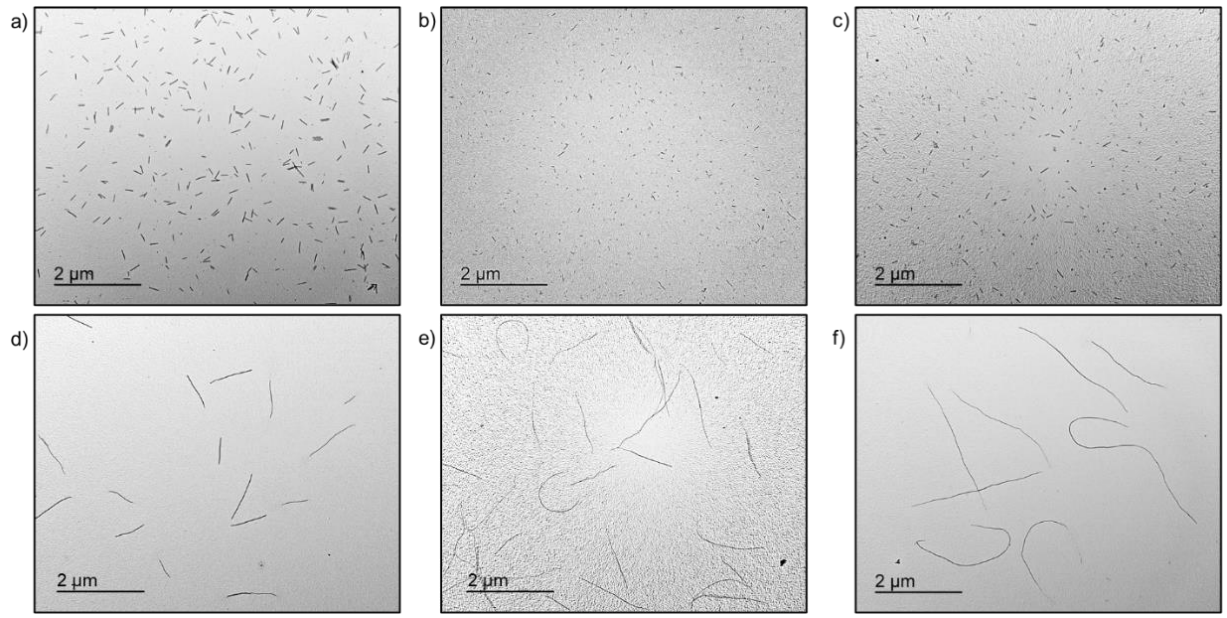

Figure S2.35. TEM images of P3EHT$_{23}$-*b*-PEG$_{113}$ nanofibers formed through self-seeding by heating annealed seed solutions (1:1 *n*BuOH:MeOH, 0.05 mg/mL, batch 2, 65 nm) to the self-seeding temperatures for 1 h and then cooling directly to 22 °C slowly (ca. 4 h) followed by aging 24 h and solvent evaporation. Self-seeding temperatures **(a)** 67 °C, **(b)** 68 °C, **(c)** 69 °C, **(d)** 70 °C, **(e)** 71 °C, and **(f)** 72 °C.

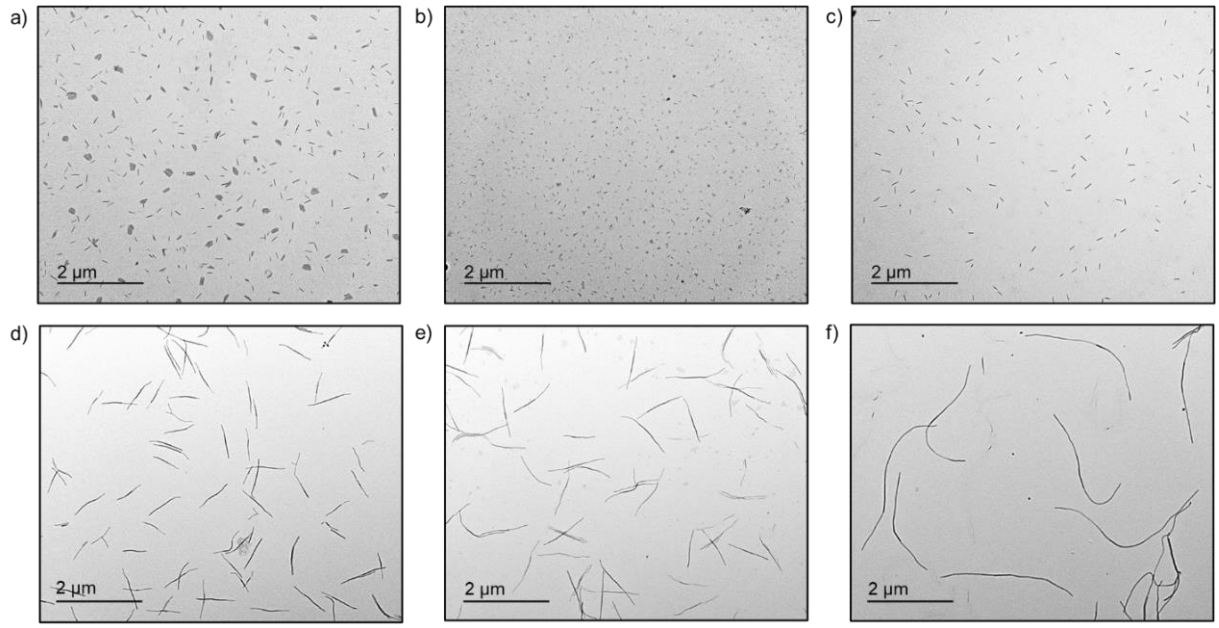

Figure S2.36. TEM images of P3EHT$_{23}$-*b*-PEG$_{113}$ nanofibers formed through self-seeding by heating annealed seed solutions (1:1 *n*BuOH:MeOH 0.05 mg/mL, batch 2, 65 nm) to the self-seeding temperatures for 1 h and then cooling to 30 °C slowly (ca. 4 h) and aging at 30 °C for 24 h. Solutions were then cooled to 22 °C and aged 24 h followed by solvent evaporation. Self-seeding temperatures **(a)** 67 °C, **(b)** 68 °C, **(c)** 69 °C, **(d)** 70 °C, **(e)** 71 °C, and **(f)** 72 °C.

Table S2.6. Summary of contour length data from 1) heating annealed seed solutions (1:1 *n*BuOH:MeOH, 0.05 mg/mL, batch 2, 65 nm) to self-seeding temperatures and then directly cooling to 22 °C followed by aging at 22 °C for 24 h prior to TEM imaging and measurement and 2) self-nucleation suppressed self-seeding experiments where annealed seed solutions (1:1 *n*BuOH:MeOH, 0.05 mg/mL, batch 2, 65 nm) were heated to self-seeding temperatures, cooled to 30 °C and aged at 30 °C for 24 h before being cooled to 22° and aged at 22 °C for 24 h prior to TEM imaging and measurement.

	Cooled directly to 22 °C				Cooled to 30 °C and then 22 °C			
Self-Seeding T (°C)	L_n	L_w	$Đ_L$	σ	L_n	L_w	$Đ_L$	σ
Seeds	65	75	1.16	27	65	75	1.16	27
66	45	58	1.28	24	40	49	1.23	19
67	42	54	1.29	23	130	140	1.08	38
68	48	62	1.30	26	40	46	1.16	16
69	100	114	1.14	37	135	147	1.09	40
70	215	245	1.15	82	781	812	1.04	147
71	950	1283	1.35	564	1210	1258	1.04	241
72	2743	3017	1.10	878	2852	3080	1.08	832

Length-controlled B-A-B triblock comicelles by seeded growth of P3EHT$_{19}$-*b*-P2VP$_{138}$ from P3EHT$_{23}$-*b*-PEG$_{113}$ seeds (P3EHT$_{19}$-*b*-P2VP$_{138}$-*m*-P3EHT$_{23}$-*b*-PEG$_{113}$-*m*-P3EHT$_{19}$-*b*-P2VP$_{138}$) at 22 °C

Table S2.7. Summary of data from seeded growth experiments at 22 °C to form B-A-B (P3EHT$_{19}$-*b*-P2VP$_{138}$-*m*-P3EHT$_{23}$-*b*-PEG$_{113}$-*m*-P3EHT$_{19}$-*b*-P2VP$_{138}$) triblock comicelles with a central P3EHT$_{23}$-*b*-PEG$_{113}$ block and terminal P3EHT$_{19}$-*b*-P2VP$_{138}$ blocks. σ is standard deviation in L_n.

m_{unimer}/m_{seed}	L_n	L_w	$Đ_L$	σ
Seeds	44	75	1.26	22
5	320	330	1.03	63
10	560	594	1.06	134
15	777	816	1.05	166
20	932	979	1.05	212

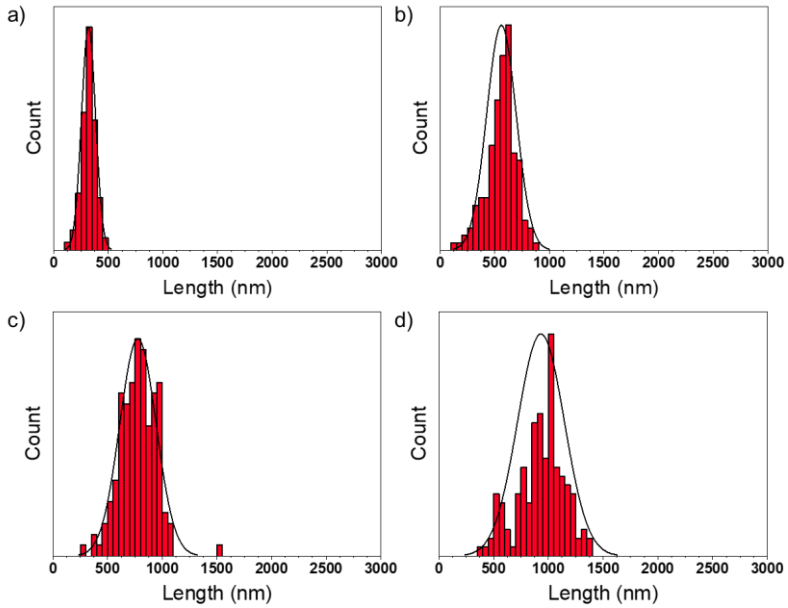

Figure S2.37. Histograms showing nanofiber length distribution of B-A-B (P3EHT$_{19}$-*b*-P2VP$_{138}$-*m*-P3EHT$_{23}$-*b*-PEG$_{113}$-*m*-P3EHT$_{19}$-*b*-P2VP$_{138}$) triblock comicelle seeded growth experiments. Annealed P3EHT$_{23}$-*b*-PEG$_{113}$ seed micelles (1:1 *n*BuOH:MeOH, 0.1 mg/mL, batch 1, 44 nm) were treated with **(a)** 5, **(b)** 10, **(c)** 15 and **(d)** 20 equivalents of P3EHT$_{19}$-*b*-P2VP$_{138}$ unimer in $CHCl_3$ (2 mg/mL) at 22 °C. Final concentrations were 0.05 mg/mL.

Length-controlled B-A-B triblock comicelles by self-nucleation suppressed seeded growth of P3EHT$_{19}$-*b*-P2VP$_{138}$ from P3EHT$_{23}$-*b*-PEG$_{113}$ seeds (P3EHT$_{19}$-*b*-P2VP$_{138}$-*m*-P3EHT$_{23}$-*b*-PEG$_{113}$-*m*-P3EHT$_{19}$-*b*-P2VP$_{138}$) at 55 °C

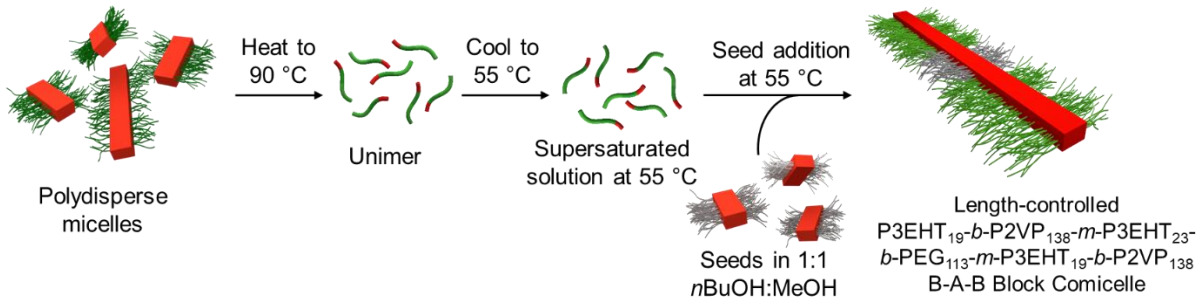

Figure S2.38. Cartoon schematic showing self-nucleation suppressed growth of B-A-B (P3EHT$_{19}$-*b*-P2VP$_{138}$-*m*-P3EHT$_{23}$-*b*-PEG$_{113}$-*m*-P3EHT$_{19}$-*b*-P2VP$_{138}$) block comicelles prepared by the addition of P3EHT$_{23}$-*b*-PEG$_{113}$ seeds to P3EHT$_{19}$-*b*-P2VP$_{138}$ unimer in *n*BuOH at 55 °C.

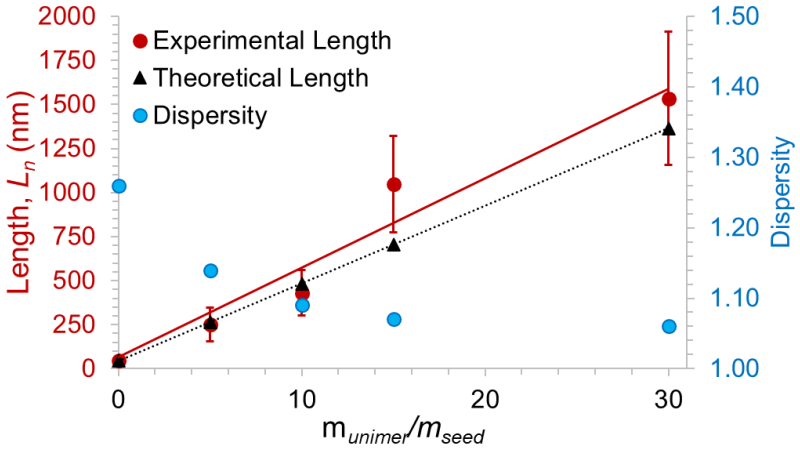

Figure S2.39. Plot showing the dependence of B-A-B (P3EHT$_{19}$-*b*-P2VP$_{138}$-*m*-P3EHT$_{23}$-*b*-PEG$_{113}$-*m*-P3EHT$_{19}$-*b*-P2VP$_{138}$) fiber length (L_n) on unimer to seed mass ratio when using using self-nucleation suppressed seeded growth at 55 °C.

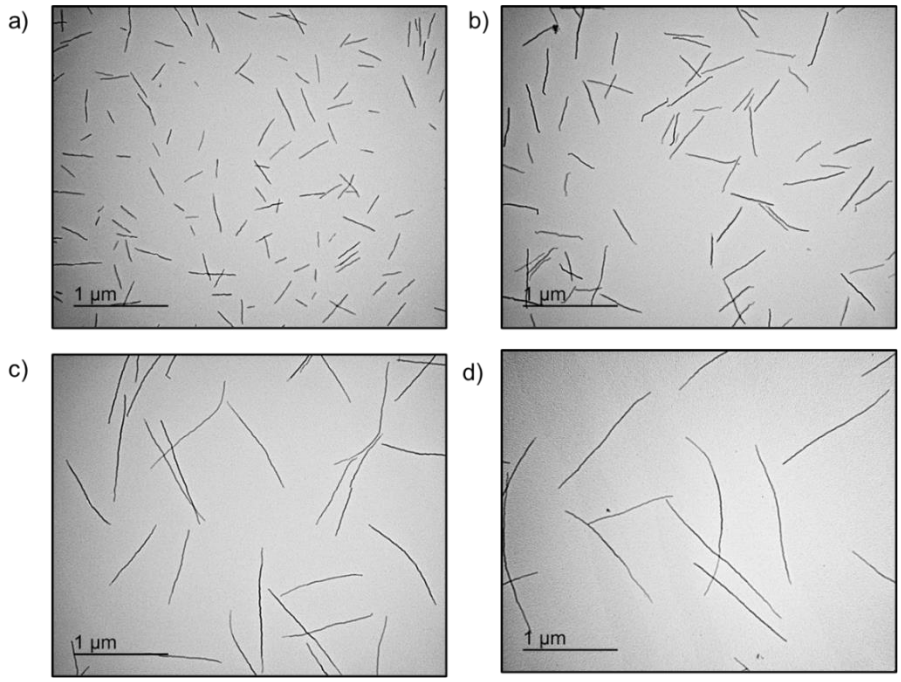

Figure S2.40. TEM images of B-A-B (P3EHT$_{19}$-*b*-P2VP$_{138}$-*m*-P3EHT$_{23}$-*b*-PEG$_{113}$-*m*-P3EHT$_{19}$-*b*-P2VP$_{138}$ P3EHT$_{23}$-*b*-PEG$_{113}$) nanofibers formed in *n*BuOH (0.05 mg/mL) by self-nucleation suppressed seeded growth (55 °C) following solvent evaporation. Unimer-to-seed ratio m_{unimer}/m_{seed} = **(a)** 5, **(b)** 10, **(c)** 15, and **(d)** 30.

Table S2.8. Summary of data from self-nucleation suppressed seeded growth experiments at 55 °C to form B-A-B (P3EHT$_{19}$-*b*-P2VP$_{138}$-*m*-P3EHT$_{23}$-*b*-PEG$_{113}$-*m*-P3EHT$_{19}$-*b*-P2VP$_{138}$) triblock comicelles with a central P3EHT$_{23}$-*b*-PEG$_{113}$ block and terminal P3EHT$_{19}$-*b*-P2VP$_{138}$ blocks. σ is standard deviation in L_n measurements.

m_{unimer}/m_{seed}	L_n	L_w	$Đ_L$	σ
Seeds	44	55	1.26	22
5	251	286	1.14	94
10	431	470	1.09	131
15	1049	1122	1.07	273
30	1535	1627	1.06	378

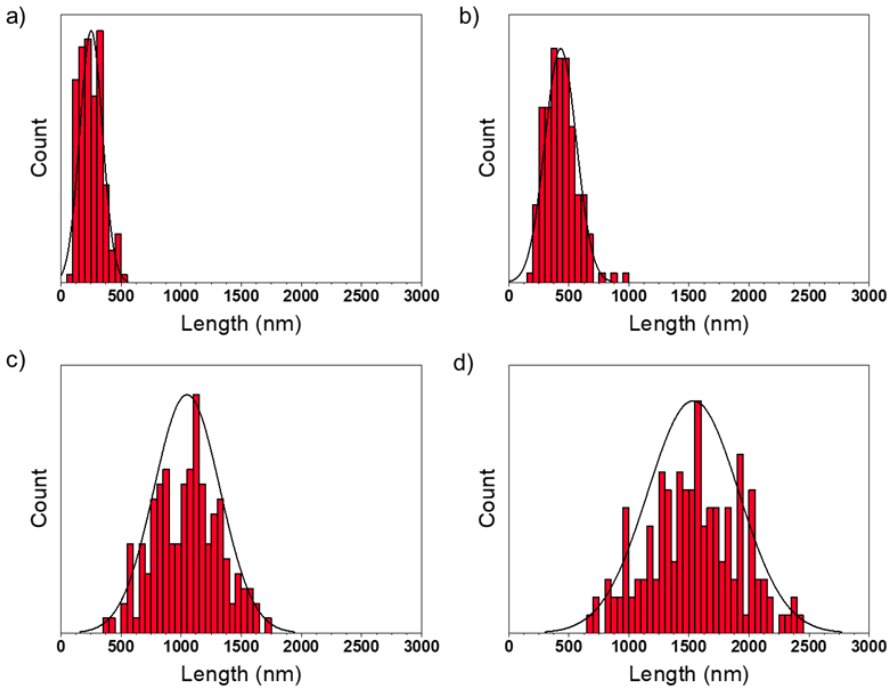

Figure S2.41. Histograms showing the nanofiber length distribution of B-A-B ($P3EHT_{19}$-*b*-$P2VP_{138}$-*m*-$P3EHT_{23}$-*b*-PEG_{113}-*m*-$P3EHT_{19}$-*b*-$P2VP_{138}$) triblock comicelle self-nucleation suppressed seeded growth experiments with a central $P3EHT_{23}$-*b*-PEG_{113} block and terminal $P3EHT_{19}$-*b*-$P2VP_{138}$ blocks at 55 °C. Unimer-to-seed ratio m_{unimer}/m_{seed} = **(a)** 5, **(b)** 10, **(c)** 15, and **(d)** 30. Final concentrations were 0.05 mg/mL.

2.6 References

(1) Kim, J.; Chung, W.; Kim, D.; Kang, J.; Grandes Reyes, C. F.; Jeong, J.; Kim, K. T. Semi-Conductive Micellar Networks of All-Conjugated Diblock and Triblock Copolymer Blends. *Chem. Commun.* **2023**, *59* (24), 3578–3581. https://doi.org/10.1039/d3cc00081h.

(2) Narasimha, K.; Albert, S. K.; Kim, J.; Kang, H.; Kang, S.; Park, J.; Park, J. H.; Park, S. J. Charge-Transfer-Induced Self-Assembly of Doped Conjugated Block Copolymer Nanofibers. *ACS Macro Lett.* **2023**, *12*, 382–388. https://doi.org/10.1021/acsmacrolett.2c00752.

(3) MacFarlane, L. R.; Shaikh, H.; Garcia-Hernandez, J. D.; Vespa, M.; Fukui, T.; Manners, I. Functional Nanoparticles through π-Conjugated Polymer Self-Assembly. *Nat. Rev. Mater.* **2021**, *6* (1), 7–26. https://doi.org/10.1038/s41578-020-00233-4.

(4) Shin, S.; Menk, F.; Kim, Y.; Lim, J.; Char, K.; Zentel, R.; Choi, T. L. Living Light-Induced Crystallization-Driven Self-Assembly for Rapid Preparation of Semiconducting Nanofibers. *J. Am. Chem. Soc.* **2018**, *140* (19), 6088–6094. https://doi.org/10.1021/jacs.8b01954.

(5) Jo, G.; Jung, J.; Chang, M. Controlled Self-Assembly of Conjugated Polymers via a Solvent Vapor Pre-Treatment for Use in Organic Field-Effect Transistors. *Polymers.* **2019**, *11* (2), 332. https://doi.org/10.3390/polym11020332.

(6) Zhu, Y.-Y.; Yin, T.-T.; Yin, J.; Liu, N.; Yu, Z.-P.; Zhu, Y.-W.; Ding, Y.-S.; Yin, J.; Wu, Z.-Q. Poly(3-Hexylthiophene)-Block-Poly(5,8-Di-p-Tolylquinoxaline-2,3-Diyl) Conjugated Rod-Rod Copolymers: One Pot Synthesis, Self-Assembly and Highly Selective Sensing of Cobalt. *RSC Adv.* **2014**, *4* (76), 40241–40250. https://doi.org/10.1039/c4ra06571a.

(7) Xu, L.; Wang, C.; Li, Y.-X.; Xu, X.; Zhou, L.; Liu, N.; Wu, Z.-Q. Crystallization-Driven Asymmetric Helical Assembly of Conjugated Block Copolymers and the Aggregation Induced White-Light Emission and Circularly Polarized Luminescence. *Angew. Chem. Int. Ed.* **2020**, *59* (38), 16675–16682. https://doi.org/10.1002/anie.202006561.

(8) Hicks, G. E. J.; Jarrett-Wilkins, C. N.; Panchuk, J. R.; Manion, J. G.; Seferos, D. S. Oxidation Promoted Self-Assembly of π-Conjugated Polymers. *Chem. Sci.* **2020**, *11* (25), 6383–6392. https://doi.org/10.1039/d0sc00806k.

(9) Kang, S.; Kim, G. H.; Park, S. J. Conjugated Block Copolymers for Functional Nanostructures. *Acc. Chem. Res.* **2022**, *55* (16), 2224–2234. https://doi.org/10.1021/acs.accounts.2c00244.

(10) Tuncel, D. π-Conjugated Nanostructured Materials: Preparation, Properties and Photonic Applications. *Nanoscale Adv.* **2019**, *1* (1), 19–33. https://doi.org/10.1039/c8na00108a.

(11) Jiang, Y.; McNeill, J. Light-Harvesting and Amplified Energy Transfer in Conjugated Polymer Nanoparticles. *Chem. Rev.* **2017**, *117* (2), 838–859. https://doi.org/10.1021/acs.chemrev.6b00419.

(12) Kundu, S.; Patra, A. Nanoscale Strategies for Light Harvesting. *Chem. Rev.* **2017**, *117* (2), 712–757. https://doi.org/10.1021/acs.chemrev.6b00036.

(13) Li, X.; Wolanin, P. J.; MacFarlane, L. R.; Harniman, R. L.; Qian, J.; Gould, O. E. C. C.; Dane, T. G.; Rudin, J.; Cryan, M. J.; Schmaltz, T.; Frauenrath, H.; Winnik, M. A.; Faul, C. F. J. J.; Manners, I. Uniform Electroactive Fibre-like Micelle Nanowires for Organic Electronics. *Nat. Commun.* **2017**, *8* (1), 15909. https://doi.org/10.1038/ncomms15909.

(14) Jin, X.-H.; Price, M. B.; Finnegan, J. R.; Boott, C. E.; Richter, J. M.; Rao, A.; Menke, S. M.; Friend, R. H.; Whittell, G. R.; Manners, I. Long-Range Exciton Transport in Conjugated Polymer Nanofibers Prepared by Seeded Growth. *Science* **2018**, *360* (3691), 897–900. https://doi.org/10.1126/science.aar8104.

(15) Ma, J.; Hao, B.; Zhang, S.; Huang, X.; Lu, G.; Feng, C. Uniform π-Conjugated-Co-Oligomer-Based Nanofibers of Controlled Length with Near-Infrared Emission, Photodynamic and Photothermal Activities. *Adv. Mater. Interfaces* **2022**, *9* (33), 2201823. https://doi.org/10.1002/admi.202201823.

(16) Gilroy, J. B.; Gädt, T.; Whittell, G. R.; Chabanne, L.; Mitchels, J. M.; Richardson, R. M.; Winnik, M. A.; Manners, I. Monodisperse Cylindrical Micelles by Crystallization-Driven Living Self-Assembly. *Nat. Chem.* **2010**, *2* (7), 566–570. https://doi.org/10.1038/nchem.664.

(17) Petzetakis, N.; Dove, A. P.; O'Reilly, R. K. Cylindrical Micelles from the Living Crystallization-Driven Self-Assembly of Poly(Lactide)-Containing Block Copolymers. *Chem. Sci.* **2011**, *2* (5), 955–960. https://doi.org/10.1039/c0sc00596g.

(18) Hwang, S.-H.; Kang, S.-Y.; Yang, S.; Lee, J.; Choi, T.-L. Synchronous Preparation of Length-Controllable 1D Nanoparticles via Crystallization-Driven in Situ Nanoparticlization of Conjugated Polymers. *J. Am. Chem. Soc.* **2022**, *144* (13), 5921–5929. https://doi.org/10.1021/jacs.1c13385.

(19) Ma, J.; Lu, G.; Huang, X.; Feng, C. π-Conjugated-Polymer-Based Nanofibers through Living Crystallization-Driven Self-Assembly: Preparation, Properties and Applications. *Chem. Commun.* **2021**, *57* (98), 13259–13274. https://doi.org/10.1039/d1cc04825b.

(20) Wang, X.; Guerin, G.; Wang, H.; Wang, Y.; Manners, I.; Winnik, M. A. Cylindrical Block Copolymer Micelles and Co-Micelles of Controlled Length and Architecture. *Science* **2007**, *317* (5838), 644–647. https://doi.org/10.1126/science.1141382.

(21) Lotz, B.; Kovacs, A. J.; Bassett, G. A.; Keller, A. Properties of Copolymers Composed of One Poly-Ethylene-Oxide and One Polystyrene Block - II. Morphology of Single Crystals. *Kolloid-Zeitschrift Zeitschrift für Polym.* **1966**, *209* (2), 115–128. https://doi.org/10.1007/BF01500629.

(22) Qian, J.; Guerin, G.; Lu, Y.; Cambridge, G.; Manners, I.; Winnik, M. A. Self-Seeding in One Dimension: An Approach to Control the Length of Fiberlike Polyisoprene-Polyferrocenylsilane Block Copolymer Micelles. *Angew. Chem. Int. Ed.* **2011**, *50* (7), 1622–1625. https://doi.org/10.1002/anie.201006223.

(23) Qian, J.; Lu, Y.; Chia, A.; Zhang, M.; Rupar, P. A.; Gunari, N.; Walker, G. C.; Cambridge, G.; He, F.; Guerin, G.; Manners, I.; Winnik, M. A. Self-Seeding in One Dimension: A Route to Uniform Fiber-like Nanostructures from Block Copolymers with a Crystallizable Core-Forming Block. *ACS Nano* **2013**, *7* (5), 3754–3766. https://doi.org/10.1021/nn400124x.

(24) Xu, J.; Ma, Y.; Hu, W.; Rehahn, M.; Reiter, G. Cloning Polymer Single Crystals through Self-Seeding. *Nat. Mater.* **2009**, *8* (4), 348–353. https://doi.org/10.1038/nmat2405.

(25) Strobl, G. Crystallization and Melting of Bulk Polymers: New Observations, Conclusions and a Thermodynamic Scheme. *Prog. Polym. Sci.* **2006**, *31* (4), 398–442. https://doi.org/10.1016/j.progpolymsci.2006.01.001.

(26) MacFarlane, L.; Zhao, C.; Cai, J.; Qiu, H.; Manners, I. Emerging Applications for Living Crystallization-Driven Self-Assembly. *Chem. Sci.* **2021**, *12* (13), 4661–4682. https://doi.org/10.1039/d0sc06878k.

(27) MacFarlane, L. R.; Li, X.; Faul, C. F. J.; Manners, I. Efficient and Controlled Seeded Growth of Poly(3-Hexylthiophene) Block Copolymer Nanofibers through Suppression of Homogeneous Nucleation. *Macromolecules* **2021**, *54* (24), 11269–11280. https://doi.org/10.1021/acs.macromol.1c02005.

(28) Patra, S. K.; Ahmed, R.; Whittell, G. R.; Lunn, D. J.; Dunphy, E. L.; Winnik, M. A.; Manners, I. Cylindrical Micelles of Controlled Length with a π-Conjugated Polythiophene Core via Crystallization-Driven Self-Assembly. *J. Am. Chem. Soc.* **2011**, *133* (23), 8842–8845. https://doi.org/10.1021/ja202408w.

(29) Gilroy, J. B.; Lunn, D. J.; Patra, S. K.; Whittell, G. R.; Winnik, M. A.; Manners, I. Fiber-like Micelles via the Crystallization-Driven Solution Self-Assembly of Poly(3-Hexylthiophene)-Block-Poly(Methyl Methacrylate) Copolymers. *Macromolecules* **2012**, *45* (14), 5806–5815. https://doi.org/10.1021/ma3008114.

(30) Gwyther, J.; Gilroy, J. B.; Rupar, P. A.; Lunn, D. J.; Kynaston, E.; Patra, S. K.; Whittell, G. R.; Winnik, M. A.; Manners, I. Dimensional Control of Block Copolymer Nanofibers with a π-Conjugated Core: Crystallization-Driven Solution Self-Assembly of Amphiphilic Poly(3-Hexylthiophene)-b-Poly(2-Vinylpyridine). *Chem. - Eur. J.* **2013**, *19* (28), 9186–9197. https://doi.org/10.1002/chem.201300463.

(31) Tritschler, U.; Gwyther, J.; Harniman, R. L.; Whittell, G. R.; Winnik, M. A.; Manners, I. Toward Uniform Nanofibers with a π-Conjugated Core: Optimizing the "Living" Crystallization-Driven Self-Assembly of Diblock Copolymers with a Poly(3-Octylthiophene) Core-Forming Block. *Macromolecules* **2018**, *51* (14), 5101–5113. https://doi.org/10.1021/acs.macromol.8b00488.

(32) Ho, V.; Boudouris, B. W.; Segalman, R. A. Tuning Polythiophene Crystallization through Systematic Side Chain Functionalization. *Macromolecules* **2010**, *43* (19), 7895–7899. https://doi.org/10.1021/ma101697m.

(33) Shaikh, H.; Jin, X. H.; Harniman, R. L.; Richardson, R. M.; Whittell, G. R.; Manners, I. Solid-State Donor-Acceptor Coaxial Heterojunction Nanowires via Living Crystallization-Driven Self-Assembly. *J. Am. Chem. Soc.* **2020**, *142* (31), 13469–13480. https://doi.org/10.1021/jacs.0c04975.

(34) Jeffries-El, M.; Sauvé, G.; McCullough, R. D. In-Situ End-Group Functionalization of Regioregular Poly(3-Alkylthiophene) Using the Grignard Metathesis Polymerization Method. *Adv. Mater.* **2004**, *16* (12), 1017–1019. https://doi.org/10.1002/adma.200400137.

(35) Kleinhenz, N.; Persson, N.; Xue, Z.; Chu, P. H.; Wang, G.; Yuan, Z.; McBride, M. A.; Choi, D.; Grover, M. A.; Reichmanis, E. Ordering of Poly(3-Hexylthiophene) in Solutions and Films: Effects of Fiber Length and Grain Boundaries on Anisotropy and Mobility. *Chem. Mater.* **2016**, *28* (11), 3905–3913. https://doi.org/10.1021/acs.chemmater.6b01163.

(36) Kleinhenz, N.; Rosu, C.; Chatterjee, S.; Chang, M.; Nayani, K.; Xue, Z.; Kim, E.; Middlebrooks, J.; Russo, P. S.; Park, J. O.; Srinivasarao, M.; Reichmanis, E. Liquid Crystalline Poly(3-Hexylthiophene) Solutions Revisited: Role of Time-Dependent Self-Assembly. *Chem. Mater.* **2015**, *27* (7), 2687–2694. https://doi.org/10.1021/acs.chemmater.5b00635.

(37) Davidson, E. C.; Beckingham, B. S.; Ho, V.; Segalman, R. A. Confined Crystallization in Lamellae Forming Poly(3-(2′-Ethyl)Hexylthiophene) (P3EHT) Block Copolymers. *J. Polym. Sci. Part B Polym. Phys.* **2016**, *54* (2), 205–215. https://doi.org/10.1002/polb.23904.

(38) Himmelberger, S.; Duong, D. T.; Northrup, J. E.; Rivnay, J.; Koch, F. P. V.; Beckingham, B. S.; Stingelin, N.; Segalman, R. A.; Mannsfeld, S. C. B.; Salleo, A. Role of Side-Chain Branching on Thin-Film Structure and Electronic Properties of Polythiophenes. *Adv. Funct. Mater.* **2015**, *25* (17), 2616–2624. https://doi.org/10.1002/adfm.201500101.

(39) Zhang, C.; Easteal, A. J. Thermoanalytical, Spectroscopic, and Morphological Study of Poly(Ethylene Glycol)/Poly(2-Acrylamido-2-Methylpropanesulfonic Acid-Co-N-

Isopropylacrylamide) Semi-Interpenetrating Network Gels. *J. Appl. Polym. Sci.* **2007**, *104*, 1723–1731. https://doi.org/10.1002/app.25812.

(40) C. Faria, G.; Duong, D. T.; Da Cunha, G. P.; Selter, P.; Strassø, L. A.; Davidson, E. C.; Segalman, R. A.; Hansen, M. R.; Deazevedo, E. R.; Salleo, A. On the Growth, Structure and Dynamics of P3EHT Crystals. *J. Mater. Chem. C* **2020**, *8* (24), 8155–8170. https://doi.org/10.1039/d0tc00704h.

(41) Hayward, D. W.; Lunn, D. J.; Seddon, A.; Finnegan, J. R.; Gould, O. E. C.; Magdysyuk, O.; Manners, I.; Whittell, G. R.; Richardson, R. M. Structure of the Crystalline Core of Fiber-like Polythiophene Block Copolymer Micelles. *Macromolecules* **2018**, *51* (8), 3097–3106. https://doi.org/10.1021/acs.macromol.7b02552.

(42) Erb, T.; Zhokhavets, U.; Gobsch, G.; Raleva, S.; Stühn, B.; Schilinsky, P.; Waldauf, C.; Brabec, C. J. Correlation between Structural and Optical Properties of Composite Polymer/Fullerene Films for Organic Solar Cells. *Adv. Funct. Mater.* **2005**, *15* (7), 1193–1196. https://doi.org/10.1002/adfm.200400521.

(43) Peng, R.; Zhu, J.; Pang, W.; Cui, Q.; Wu, F.; Liu, K.; Wang, M.; Pan, G. Thermal Annealing Effects on the Absorption and Structural Properties of Regioregular Poly(3-Hexylthiophene) Films. *J. Macromol. Sci. Part B* **2011**, *50* (3), 624–636. https://doi.org/10.1080/00222341003784741.

(44) Rahimi, K.; Botiz, I.; Agumba, J. O.; Motamen, S.; Stingelin, N.; Reiter, G. Light Absorption of Poly(3-Hexylthiophene) Single Crystals. *RSC Adv.* **2014**, *4* (22), 11121–11123. https://doi.org/10.1039/c3ra47064d.

(45) Fukui, T.; Garcia-Hernandez, J. D.; MacFarlane, L. R.; Lei, S.; Whittell, G. R.; Manners, I. Seeded Self-Assembly of Charge-Terminated Poly(3-Hexylthiophene) Amphiphiles Based on the Energy Landscape. *J. Am. Chem. Soc.* **2020**, *142* (35), 15038–15048. https://doi.org/10.1021/jacs.0c06185.

(46) Burkhart, B.; Khlyabich, P. P.; Thompson, B. C. Influence of the Ethylhexyl Side-Chain Content on the Open-Circuit Voltage in Rr-Poly(3-Hexylthiophene-Co-3-(2-Ethylhexyl)Thiophene) Copolymers. *Macromolecules* **2012**, *45* (9), 3740–3748. https://doi.org/10.1021/ma300263a.

(47) Dauben, B. H. J.; Mccoy, L. L. N-Bromosuccinimide. I. Allylic Bromination, a General Survey of Reaction Variables. *J. Am. Chem. Soc* **1959**, *81* (18), 4863–4873. https://doi.org/https://doi.org/10.1021/ja01527a027.

(48) Standley, E. A.; Smith, S. J.; Müller, P.; Jamison, T. F. A Broadly Applicable Strategy for Entry into Homogeneous Nickel(0) Catalysts from Air-Stable Nickel(II) Complexes. *Organometallics* **2014**, *33* (8), 2012–2018. https://doi.org/10.1021/om500156q.

(49) Azzam, T.; Eisenberg, A. Control of Vesicular Morphologies through Hydrophobic Block Length. *Angew. Chem. Int. Ed.* **2006**, *45* (44), 7443–7447. https://doi.org/10.1002/anie.200602897.

(50) Pangborn, A. B.; Giardello, M. A.; Grubbs, R. H.; Rosen, R. K.; Timmers, F. J. Safe and Convenient Procedure for Solvent Purification. *Organometallics* **1996**, *15* (5), 1518–1520. https://doi.org/10.1021/om9503712.

(51) Schneider, C. A.; Rasband, W. S.; Eliceiri, K. W. NIH Image to ImageJ: 25 Years of Image Analysis. *Nat. Methods* **2012**, *9* (7), 671–675. https://doi.org/10.1038/nmeth.2089.

(52) Deng, J.; Luo, Y.; Zhang, L. M. PEGylated Polyamidoamine Dendron-Assisted Encapsulation of Plasmid DNA into in Situ Forming Supramolecular Hydrogel. *Soft Matter* **2011**, *7* (13), 5944–5947. https://doi.org/10.1039/c1sm05259d.

(53) Zhang, Y.; Shaikh, H.; Sneyd, A. J.; Tian, J.; Xiao, J.; Blackburn, A.; Rao, A.; Friend, R. H.; Manners, I. Efficient Energy Funneling in Spatially Tailored Segmented Conjugated Block Copolymer Nanofiber-Quantum Dot or Rod Conjugates. *J. Am. Chem. Soc.* **2021**, *143* (18), 7032–7041. https://doi.org/10.1021/jacs.1c01571.

(54) Manceau, M.; Rivaton, A.; Gardette, J. L.; Guillerez, S.; Lemaître, N. The Mechanism of Photo- and Thermooxidation of Poly(3-Hexylthiophene) (P3HT) Reconsidered. *Polym. Degrad. Stab.* **2009**, *94* (6), 898–907. https://doi.org/10.1016/j.polymdegradstab.2009.03.005.

(55) Ohta, H.; Koizumi, H. Mechanisms of Photo-Induced Degradation of Polythiophene Derivatives: Re-Examination of the Role of Singlet Oxygen. *Polym. Bull.* **2017**, *74* (6), 2319–2330. https://doi.org/10.1007/s00289-016-1837-6.

(56) Hintz, H.; Egelhaaf, H. J.; Lüer, L.; Hauch, J.; Peisert, H.; Chassé, T. Photodegradation of P3HT - A Systematic Study of Environmental Factors. *Chem. Mater.* **2011**, *23* (2), 145–154. https://doi.org/10.1021/cm102373k.

(57) Hintz, H.; Sessler, C.; Peisert, H.; Egelhaaf, H.; Chasse, T. Wavelength-Dependent Pathways of Poly-3-Hexylthiophene Photo- Oxidation. *Chem. Mater.* **2012**, *24*, 2739−2743.

Chapter 3

Crystallization-Driven Self-Assembly of Poly(3-hexylthiophene)-*b*-poly(2,5-bis(2-ethylhexyloxy)*p*-phenylene), a π-Conjugated Diblock Copolymer with a Rigid Rod Corona-Forming Block

This chapter has been adapted from:

Marcus Vespa, Liam R. MacFarlane, Zachary M. Hudson, and Ian Manners. *Polym. Chem.* **2024**, 15, 1839-1850. https://doi.org/10.1039/D4PY00154K

Contributions:

The project was conceived by Marcus Vespa and discussed intensively with Prof. Ian Manners and Dr. Liam MacFarlane. Marcus Vespa performed the synthesis, self-assembly experiments, and characterization. Marcus Vespa wrote the manuscript with input from Prof. Ian Manners and Prof. Zachary Hudson.

3.1 Abstract

Crystallization-driven self-assembly (CDSA) of polymeric amphiphiles with a crystallizable core-forming block has emerged as a powerful method to create morphologically pure samples of 1-dimensional (1D) nanofibers with a wide array of potential applications. Many previous investigations into solution phase π-conjugated block copolymer (BCP) CDSA have focused on BCPs with a crystalline rod-like core-forming block and amorphous, coil-like corona-forming block. Reports on the solution-phase CDSA of BCPs where both the core- and corona-forming blocks are rigid are comparatively rare. Here, we report studies of the synthesis and self-assembly of two all-conjugated poly(3-hexylthiophene)-*b*-poly(2,5-bis(2-ethylhexyloxy)*p*-phenylene) BCPs ($P3HT_{60}$-*b*-PPP_{30} and $P3HT_{35}$-*b*-PPP_{15}) with crystallizable P3HT core-forming blocks and different overall molar masses but similar core:corona block ratios (~2:1). Previous self-assembly studies using similar materials only produced short nanofibers (~120 nm) while we were able to fabricate long (>5 μm) polydisperse nanofibers from both materials here, which are desirable for optoelectronic applications. WAXS and AFM were used to characterize the internal nanofiber core crystallinity and the nanoscale morphology, respectively, and UV/Visible spectroscopy was used to probe the temperature-dependent crystallization behaviour, including temperatures where self-nucleation was supressed upon cooling (≥50°C). This work provides a method for forming long polydisperse nanofibers with well-connected core domains for potential applications involving energy transfer.

3.2 Introduction

1D core-shell nanofibers formed by self-assembly of amphiphilic BCPs with a π-conjugated core-forming segment are candidates for applications in optoelectronic devices and energy funnelling.[1–4] These nanostructures can exhibit many desirable characteristics for application in these fields, such as high absorptivity, photostability, charge carrier mobility, and fluorescent quantum yields.[3,5,6] Efficient intra- and inter-chain π-orbital overlap leads to charge delocalization throughout the nanofiber core, creating conductive networks for effective energy transfer. These structures can also be made solution-processable through facile modification of the conjugated backbone, a practical advantage for device fabrication.[7]

Crystallization-driven self-assembly (CDSA) has emerged as a convenient methodology to fabricate morphologically pure samples of well-defined structures such as 1D nanofibers and 2D platelets from BCPs with a crystallizable conjugated core-forming block.[8,9] Crystallization is an exothermic process that lowers energy by forming a more stable, ordered structure with minimized potential energy. The self-assembly of BCPs with a crystallizable core-forming segment is driven by solvophobic interactions between the core-forming block and the solvent and the lattice energy contribution from core crystallization to produce structures with low core:corona interfacial curvature.[8–10] CDSA is compatible with a variety of crystalline-core BCPs, including π-conjugated materials such as oligo- and poly(*p*-phenylene vinylene)s,[11–14] poly(chalcogenophene)s,[15–20] and polyfluorenes.[21,22] These materials have been used for photocatalytic hydrogen production,[2] as the active layer in organic field effect transistors,[3] and for flexible pressure sensors[23]; however, exerting control over the length and dimensions of these nanostructures remains challenging.[8,24,25]

Living CDSA is a useful seeded growth technique to generate low length dispersity (D_L) (< 1.1) samples of 1D micelles with controlled size and dimensions.[11,26–29] The living CDSA

seeded growth method begins with the formation of long polydisperse nanofibers that are subsequently fragmented by sonication to generate short "seed" micelles with low length differences.[10,27] The seeds remain active towards the addition of molecularly dissolved BCP (unimer) in a good solvent for both blocks. Epitaxial crystallization of unimer on the seed termini creates nanofibers with final lengths that are linearly correlated to the unimer-to-seed mass ratio (m_{unimer}/m_{seed}) providing that the added unimer only adds to the seed termini and does not create new nuclei by self- (or homogeneous) nucleation. This produces uniform samples of nanofibers that possess a highly ordered nanofiber core, facilitating processes such as energy transfer.[2,6,22]

Despite the prevalence of polymeric functional materials in organic photovoltaics, short exciton diffusion lengths of 5-10 nm continue to limit their practical use.[30] It is not fully understood why such a broad range of materials exhibit similarly low exciton diffusion lengths, but some factors thought to be involved are the fast intrinsic decay rates of photoexcited polymer chains back to their ground state, strong exciton-phonon coupling, and high energy barriers to exciton transfer.[30,31] Recent research also suggests that low exciton diffusion lengths in organic solar cell films occur due to the energetic and structural disorder inherent to commonly used film fabrication methods such as spin-coating or thermal evaporation, resulting in weak electronic coupling between chromophores.[31] In this context, in collaboration with Rao and Friend we recently reported the living CDSA of a poly(di-*n*-hexylfluorene)-*b*-poly(ethylene glycol) and a poly(di-*n*-hexylfluorene)-*b*-quaternized-P3HT block copolymer system to form modular B-A-B block comicelles that exhibited high exciton diffusion lengths of ~200 nm in solution.[22] Living CDSA seeded growth has also been utilized with charged, phosphonium terminated-P3HT amphiphiles to produce length-controlled nanofibers that allowed for even higher exciton diffusion lengths of ~350 nm in thin films.[6] The long diffusion lengths in these materials are believed to arise from a

transient delocalization mechanism in which exciton coupling to vibronic states occurs.[31] This is made possible by the uniform energy landscape in the core, generated by the living CDSA process through epitaxial growth.

Previous investigations into self-assembled, π-conjugated nanofibers made using solution-phase CDSA have primarily involved using BCPs with a crystallizable, rigid rod-like core-forming block and a corona-forming block that adopts an amorphous, coiled confirmation in solution.[32–34] Reports investigating the solution-phase CDSA of BCPs in which both the core and corona blocks are rigid are however comparatively scarce.[35–41] All-conjugated BCPs are an attractive target from a photophysical perspective as they combine the absorbance profiles of both blocks to cover a larger area of the UV/visible/NIR spectrum, with obvious benefits for applications in light-harvesting devices.[4] From a synthetic perspective, the synthesis and purification of all-conjugated BCPs is relatively straightforward compared to approaches such as copper-catalyzed azide-alkyne or ”thiol-ene” click chemistry or macroinitiated block copolymerization that are commonly used to prepare rod-coil BCPs. All-conjugated BCPs can instead be prepared by Kumada catalyst transfer polycondensation (KCTP), a one-pot strategy that eliminates the need for synthesis and purification of separate blocks that gives BCPs in high yield with low dispersity.[42]

A study by Choi and coworkers on the solution self-assembly of polythiophene-*b*-PPP BCPs with linear *n*-hexyloxy substituents on the PPP corona-forming block showed that BCPs with a low core:corona block ratio (1:2) exhibited a preference for forming nanospheres and short nanorods over longer nanofibers.[35] When a BCP with a higher core:corona block ratio of 1:1 was used, thereby increasing the volume fraction of the polythiophene core-block, a larger area of the solvophobic core becomes exposed to the solvent. To minimize this unfavorable interaction, the nanospheres with exposed cores cling to one another to form longer nanofibers with oscillating

heights, referred to as "nanocaterpillars".[35] Choi *et al.* state that even though the nanospheres associate with one another, the sterically large, diffuse corona-forming block limits the contact between the spheres.[35] This results in a discontinuous fiber with a non-uniform core, which would impair the flow of charges within the fiber if it were used for electronic applications. This suggests that further reduction of the corona-forming block volume fraction would reduce steric interactions between adjacent coronal units, thereby exposing more of the solvophobic polythiophene core and promoting the growth of longer, better connected nanofibers. Based on this hypothesis, P3HT-*b*-PPP BCPs with a comparatively high ratio of core to corona were used in this study (~2:1) to promote growth of 1D nanofibers with high lengths and well-connected core domains. While Choi *et al.* demonstrated nanofibers with lengths of ~120 nm,[35] longer (>1 μm) nanofibers are more desirable for optoelectronic applications because intra-fiber energy transfer between P3HT chains within the micelle core is more efficient than inter-fiber transfer.[3] Charge carrier mobility increases as fiber length increases due to the decreased incidence of grain boundaries, as well as an effective increase in grain size.[3] Additionally, having a well-connected fiber core creates a uniform energetic landscape across which charges can efficiently flow. For these reasons, maximizing nanofiber length and producing highly crystalline, homogeneous fibers can improve electronic performance in conductive nanofiber-based devices. A follow-up report by Choi and coworkers using branched 2-ethylhexyloxy substituents on the PPP moieties and monomethylated thiophene rings found that long (>2 μm) nanocaterpillars could be formed when using BCPs with core:corona ratios of 1:2 and ~1:1.[43] It is proposed that the higher core:corona block ratios used here, along with the increased relative solubility of *n*-hexyl substituted thiophenes relative to methyl-substituted thiophenes, will have cooperative effects to slow down face-to-face packing of the core forming block leading to better connected cores, optimal crystal packing and longer nanofibers. To this

end, this report describes the synthesis of two fully conjugated BCPs, P3HT$_{60}$-*b*-PPP$_{30}$ and P3HT$_{35}$-*b*-PPP$_{15}$, and investigates their crystallization behaviour and their self-assembly into long (>5 μm) nanofibers.

3.3 Results and Discussion

3.3.1 Synthesis and characterization of P3HT$_n$-*b*-PPP$_m$ BCPs

A KCTP polymerization involving sequential addition of Grignard-activated monomers to an *ortho*-tolyl-functionalized nickel(II) catalyst was used to synthesize P3HT$_{60}$-*b*-PPP$_{30}$ and P3HT$_{35}$-*b*-PPP$_{15}$ (Figure 3.1), where the subscripts denote the number-average degree of polymerization of the respective blocks (DP$_n$).[44] Poly(*para*-phenylene) (PPP) bearing two asymmetrically branched 2-ethylhexyloxy substituents in the 2- and 5- positions of the phenylene rings was chosen as the coronal block as these side chains hinder efficient crystal packing in the corona to render it amorphous. Since the thiophene monomer is a comparatively stronger π-donor than the phenylene monomer, the order of addition to the nickel catalyst is critical to reaction success.[45–47] As such, the PPP monomer was polymerized first by adding iPrMgCl•LiCl to a THF solution of 1,4-dibromo-2,5-bis(2-ethylhexyloxy)benzene followed by addition of Ni(*o*-tolyl)(dppe)Cl which resulted in formation of the PPP homopolymers with a living chain end (Scheme S3.2, S3.3). Grignard-activated 2,5-dibromo-3-hexylthiophene monomer was then added to the living PPP solution to afford P3HT-*b*-PPP BCPs. PPP homopolymer aliquots were purified by washing the precipitated solid with copious amounts of methanol (MeOH) and BCPs were purified by precipitation into ice-cold MeOH followed by acetone. Low dispersity BCPs were obtained following fractionation of the crude product using preparatory GPC. This resulted in P3HT$_{60}$-*b*-PPP$_{30}$ and P3HT$_{35}$-*b*-PPP$_{15}$ polymer samples in yields of 38% and 69%, respectively.

The number-average molar mass (M_n) and dispersity ($Đ_M$, where $Đ_M = M_w/M_n$) of the PPP_m homopolymers and $P3HT_n$-*b*-PPP_m BCPs were determined by GPC (Figure 3.1, S3.1, S3.2). $Đ_M$ values obtained from GPC were low (≤ 1.14) and are considered to be accurate; however, end-group analysis by ^{1}H NMR spectroscopy was used for an alternative, absolute measurement of M_n due to the probable mass overestimation expected for rod-type polymers.[48,49] Relative integration between signals belonging to the methyl group on the *ortho*-tolyl catalyst at 2.25 ppm and signals belonging to the phenylene protons at 7.08 – 7.00 ppm and the thiophene protons at 7.00 - 6.97 ppm gave absolute determination of DP_n values for the polymers and, subsequently, segments present in the BCPs. This revealed their structures to be as follows: PPP_{30} and $P3HT_{60}$-*b*-PPP_{30} (Figure 3.1, S3.6-S3.8) and PPP_{15} and $P3HT_{35}$-*b*-PPP_{15} (Figure 3.1, S3.9, S3.10), respectively.

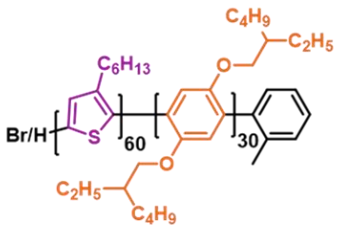

P3HT$_{60}$-*b*-PPP$_{30}$

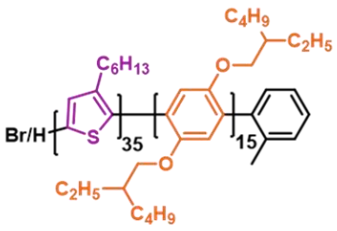

P3HT$_{35}$-*b*-PPP$_{15}$

Polymer	M_n (Da)	M_w (Da)	$Đ_M{}^a$	DP_n
PPP_{30}	10,800[a]; 11,000[b]	12,000[a], 12,200[b]	1.11	32[a], 30[b]
P3HT$_{60}$-*b*-PPP$_{30}$	18,200[a]; 20,100[b]	20,000[a], 22,100[b]	1.10	-
PPP_{15}	5,500[a]; 5,200[b]	6,300[a], 5,900[b]	1.14	17[a], 15[b]
P3HT$_{35}$-*b*-PPP$_{15}$	12,000[a]; 11,000[b]	13,000[a], 11,900[b]	1.08	-

Figure 3.1. Chemical structures and molar mass characterization of synthesized polymers analyzed by GPC and integration of proton nuclear magnetic resonance (^{1}H NMR) spectra. [a]Determined by GPC. [b]Determined by relative integration of ^{1}H NMR spectrum signals. $M_w{}^b$ values from ^{1}H NMR signals were estimated by using $Đ_M{}^a$ obtained from GPC data and multiplying it by $M_n{}^b$ values obtained by ^{1}H NMR spectroscopy according to the equation $(Đ_M{}^a)(M_n{}^b) = M_w{}^b$. For PPP_m, relative integration was performed between ^{1}H NMR signals at 2.25 ppm (s, *o*-tolyl CH_3 = 3H) and 7.08-7.00 ppm (bs, phenylene-H, = 2H). For $P3HT_n$, relative integration was performed between ^{1}H NMR spectrum signals at 2.25 ppm (s, *o*-tolyl CH_3 = 3H) and 7.00-6.97 ppm (bs, thiophene CH = 1H).

Unsymmetrically branched 2-ethylhexyloxy substituents on the phenylene rings were selected to prevent ordered packing of the PPP segments through the induction of a high torsion angle between repeat units due to steric repulsion. This was anticipated to lead to an amorphous corona-forming PPP segment. To provide evidence for the amorphous nature of this material, the thermal transition behavior of the PPP_{30} homopolymer was probed using differential scanning calorimetry (DSC) (Figure S3.3). No apparent peaks characteristic of a crystallization temperature (T_c) or a melt temperature (T_m) were observed in the temperature range (0 °C – 250 °C) suggesting that the material is amorphous. $P3HT_{60}$-*b*-PPP_{30} BCP crystallization was examined in the solid state by DSC (scan rate of 10 °C/min) which revealed a melting transition at T_m = 231 °C with a melting enthalpy of 13.0 J/g during the heating scan (Figure S3.4). During the cooling scan of the BCP, a crystallization peak was observed at T_c = 180 °C with an enthalpy of crystallization of 12.0 J/g. Crystallization of the $P3HT_{35}$-*b*-PPP_{15} BCP was also examined in the solid state by DSC (scan rate of 10 °C/min) which revealed a melting transition at T_m = 186 °C with a melting enthalpy of 8.2 J/g during the heating scan and a crystallization peak was observed at T_c = 153 °C with an enthalpy of crystallization of 9.9 J/g during the cooling scan (Figure S3.5). Notably, the heating and cooling traces of both BCPs show distinct melt and crystallization transitions which come from the melting and crystallization of the P3HT core-forming block and there are no visible transitions associated with the PPP block which reinforce that the 2-ethylhexyl chains render it amorphous, as these are typically found in the 0-100 °C range when *n*-hexyl substituents are used.[35,46] The observed peak traces and melt/crystallization temperatures are comparable to some previously reported P3HT-based block copolymers;[33,50] however, the T_m and T_c temperatures differ from previously reported P3HT-*b*-PPP materials, even with similar block ratios.[35,51,52] Potential reasons for this include the overall BCP molecular mass differences between the materials reported

here and ones reported by others. Reported P3HT-*b*-PPP materials vary widely in their overall molecular mass and so direct comparison of the T_m and T_c values is challenging as the molecular mass differences have a large influence on crystallization and melt temperatures. Additionally, the inclusion of 2-ethylhexyl substituents as opposed to linear *n*-hexyl substituents on the phenylene rings could result in differences in the observed T_m and T_c temperatures.

3.3.2 Solution self-assembly of P3HT$_{60}$-*b*-PPP$_{30}$ and P3HT$_{35}$-*b*-PPP$_{15}$ and nanofiber characterization

Polydisperse fiber-like micelles (nanofibers) of P3HT$_{60}$-*b*-PPP$_{30}$ were formed in two steps. We found that *n*-butyl acetate (*n*BuAc) functions as a selective solvent for the PPP corona-forming block at ambient temperature but becomes a good solvent for both blocks when the temperature is elevated. Heating solid P3HT$_{60}$-*b*-PPP$_{30}$ to 80 °C in *n*BuAc led to complete dissolution of the material, yielding a clear, orange solution (1 mg/mL). Allowing this solution to cool from 80 °C to ambient temperature (22 °C) over ca. 4 h causes crystallization of the core-forming P3HT block, leading to the formation of a purple solution of polydisperse multi-micron long nanofibers. The solution of polydisperse P3HT$_{60}$-*b*-PPP$_{30}$ nanofibers was drop-cast onto a carbon-coated copper grid and imaged using bright-field transmission electron microscopy (TEM) following solvent evaporation (Figure 3.2a, b). P3HT possesses a fully-extended chain conformation up to molar masses of ~10 kDa (DP_n = ca. 60), above which chain-folding can occur, so the nanofiber widths were analyzed to determine if the P3HT core-forming block was folding within the core.[32] TEM width analysis revealed that the number-average micelle width (W_n) was 21.8 ± 5.7 nm (Figure S3.14a, b). In the solid-state, the length of one 3-hexylthiophene repeat unit is 0.38 - 0.39 nm,[50,53,54] indicating that for a core-forming block with DP_n = 60 a width of 23.1 nm would be expected if

the chains were in their fully extended conformation. This value is in good agreement with the length of a fully extended P3HT chain conformation in the nanofiber core and so the existence of chain-folding is unlikely within the core of $P3HT_{60}$-*b*-PPP_{30} nanofibers.

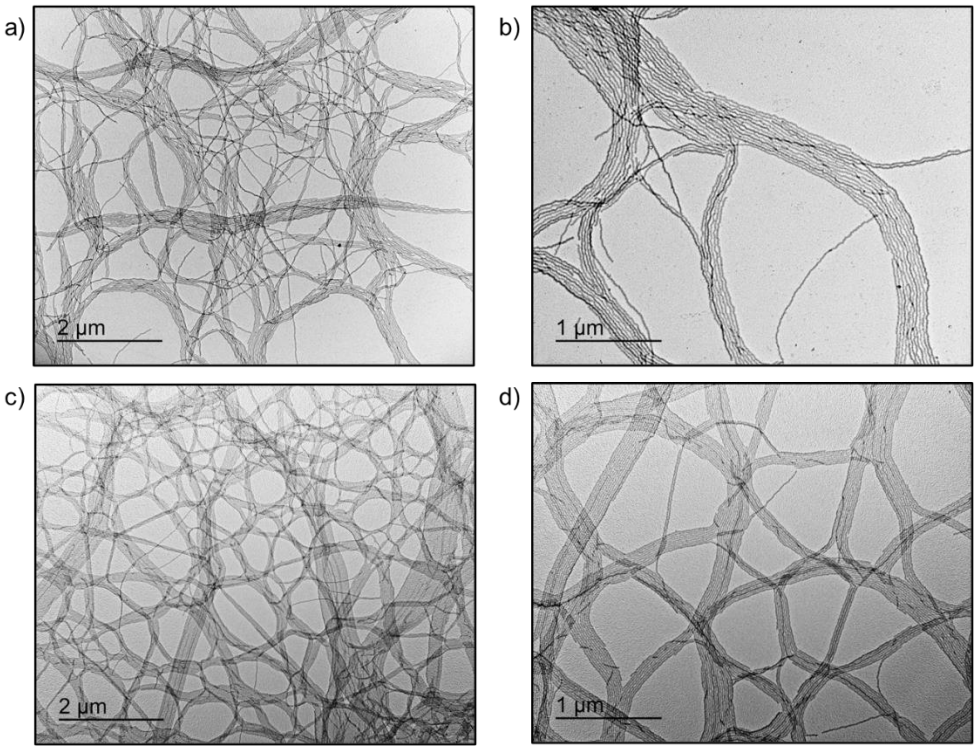

Figure 3.2. (a, b) TEM images of polydisperse $P3HT_{60}$-*b*-PPP_{30} nanofibers following solvent evaporation. **(c, d)** TEM images of polydisperse $P3HT_{35}$-*b*-PPP_{15} nanofibers following solvent evaporation.

Next, polydisperse $P3HT_{35}$-*b*-PPP_{15} nanofibers were obtained by heating solid $P3HT_{35}$-*b*-PPP_{15} in *n*BuAc to 90 °C, again producing a clear, orange solution (1 mg/mL). Subsequent cooling of the solution from 90 °C to 22 °C over ca. 4 h followed by aging for 24 h resulted in the formation of a mahogany solution. This solution was then drop-cast onto a carbon-coated copper grid and analyzed using TEM following solvent evaporation, revealing multi-micron long polydisperse fibers (Figure 3.2c, d, S3.15a, b). Heating $P3HT_{35}$-*b*-PPP_{15} in *n*BuAc caused a mahogany-to-orange color change, which is also attributed to increased rotational

freedom of the thiophene rings in the P3HT core-forming block.[55–57] TEM width analysis of polydisperse P3HT$_{35}$-*b*-PPP$_{15}$ fibers showed that the W_n was 12.7 ± 2.4 nm (Figure S3.15a, b). Based on the repeat unit length (0.39 nm) for a P3HT core with a DP_n = 35, a width of 13.5 nm would be anticipated, in good agreement with the observed value and indicative of a lack of chain folding within the core.

Solution-phase UV/vis spectroscopy was used to analyze the color difference observed when P3HT$_{60}$-*b*-PPP$_{30}$ is fully solvated compared to when it has undergone self-assembly. After heating to 80 °C and cooling to 22 °C, the polydisperse P3HT$_{60}$-*b*-PPP$_{30}$ nanofiber solution (*n*BuAc, 0.05 mg/mL) exhibits a peak at λ = 335 nm which corresponds to absorption from the solvated PPP block (Figure 3.3a). Wu and coworkers reported a similar absorbance wavelength corresponding to the PPP block when solution state UV/Vis was performed on P3HT$_{40}$-*b*-PPP$_{30}$ in chlorobenzene (λ = 340 nm).[46] The UV/Vis spectrum of the polydisperse P3HT$_{60}$-*b*-PPP$_{30}$ nanofiber solution also shows a small absorbance shoulder at 444 nm representing an intrachain π-π* transition,[57,58] a maximum absorption (λ_{max}) at 521 nm, as well as vibronic absorbances at 552 nm and 601 nm associated with the crystalline P3HT core (Figure 3.3a). The ratio between the amplitudes of the vibronic $A_{0\text{-}0}$ (601 nm) and the $A_{0\text{-}1}$ (552 nm) peaks is < 1, which is characteristic for partially ordered H-aggregate-like chains coexisting with non-aggregated chain sequences.[59] When a P3HT$_{60}$-*b*-PPP$_{30}$ unimer solution (THF, 0.05 mg/mL) was analyzed, disappearance of all vibronic peaks is observed as well as hypsochromic shifting of the λ_{max} from 521 nm to 444 nm caused by the onset of free rotation of the thiophene rings that are mainly planar in the solid state (Figure 3.3a).[55,56,60] The absorbance values closely match what has been previously reported for P3HT$_n$-*b*-PPP$_m$ materials.[46] Similar to the solution-phase UV/Vis spectrum of P3HT$_{60}$-*b*-PPP$_{30}$, the spectrum of a P3HT$_{35}$-*b*-PPP$_{15}$ unimer solution (THF, 0.05 mg/mL)

exhibits two peaks, one at λ = 334 nm corresponding to the maximum absorption of the PPP block and another at λ_{max} = 442 nm corresponding to the maximum absorption of the P3HT block (Figure 3.3c). The P3HT$_{35}$-*b*-PPP$_{15}$ nanofiber solution (*n*BuAc, 0.05 mg/mL) exhibits the same peak at λ = 334 nm corresponding to the solvated PPP block but absorbance shoulders at λ = 425 nm and 483 nm are also visible, with λ_{max} at 510 nm (Figure 3.3c). The A_{0-1} and A_{0-0} peaks are present at 545 and 597 nm, respectively.

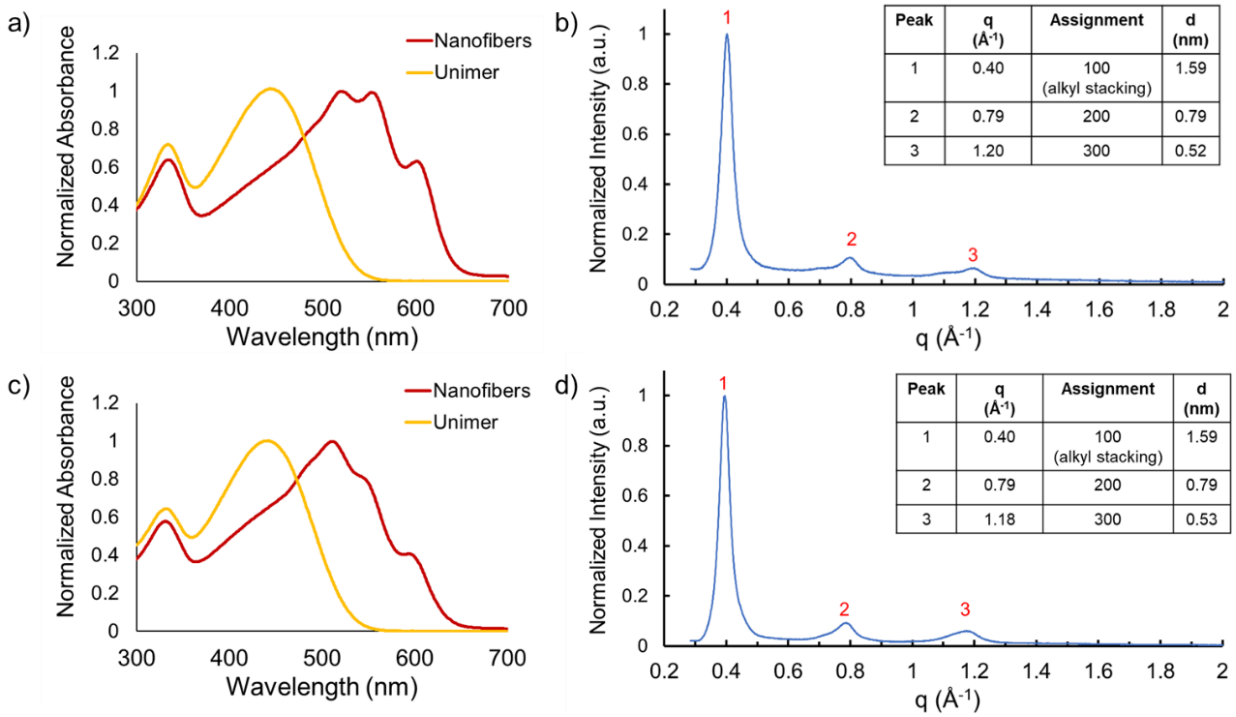

Figure 3.3. (a) Overlayed solution-phase UV/Vis absorbance plots from polydisperse P3HT$_{60}$-*b*-PPP$_{30}$ nanofiber solution in *n*BuAc (0.05 mg/mL) (red trace) and P3HT$_{60}$-*b*-PPP$_{30}$ unimer in THF (0.05 mg/mL) (orange trace) at 22 °C. **(b)** Solid-state WAXS pattern of a film of polydisperse P3HT$_{60}$-*b*-PPP$_{30}$ nanofibers. The film was formed by drop-casting a polydisperse nanofiber solution (2 mg/mL) in *n*BuAc onto a crystalline silicon substrate. **(c)** Overlayed solution-phase UV/Vis absorbance plots from polydisperse P3HT$_{35}$-*b*-PPP$_{15}$ nanofiber solution in *n*BuAc (0.05 mg/mL) (red trace) and P3HT$_{35}$-*b*-PPP$_{15}$ unimer in THF (0.05 mg/mL) (orange trace) at 22 °C. **(d)** Solid-state WAXS pattern of a film of polydisperse P3HT$_{35}$-*b*-PPP$_{15}$ nanofibers.

To gain more insight into the internal crystalline order of the nanofiber core, solid-state wide-angle X-ray scattering (WAXS) was performed on a film of polydisperse $P3HT_{60}$-*b*-PPP_{30} nanofibers that was formed by drop-casting a 2 mg/mL *n*BuAc solution onto a crystalline silicon substrate and allowing the solvent to evaporate (Figure 3.3b). A sharp Bragg peak at a q value of q = 0.40 $Å^{-1}$ (d = 1.59 nm) was clearly observed which corresponds to the (100) plane associated with the P3HT alkyl side chain stacking distance,[33,61] with higher order reflections of this peak visible as broad signals at q = 0.79 $Å^{-1}$ (200 plane, d = 0.79 nm) and q = 1.20 $Å^{-1}$ (300 plane, d = 0.52 nm). When considering previously reported P3HT alkyl chain stacking distances of 1.61-1.72 nm,[33,50,53,62] the distance between interdigitated hexyl side chains on the polythiophene core-forming block found here is slightly smaller (d =1.59 nm) but reasonably close to prior measurements. Reflections representing π-π stacking between thiophene rings on adjacent chains that commonly appear at q = ~ 1.63 $Å^{-1}$ (d = 0.38 nm, 010 plane)[33,53,54] were not readily visible. Solid-state WAXS was similarly performed on a film of polydisperse $P3HT_{35}$-*b*-PPP_{15} nanofibers (Figure 3.3d). Like the WAXS spectrum of $P3HT_{60}$-*b*-PPP_{30}, Bragg peaks at q = 0.40 $Å^{-1}$ (d = 1.59 nm), q = 0.79 $Å^{-1}$ (d = 0.79 nm), and q = 1.18 $Å^{-1}$ (d = 0.53 nm) corresponding to P3HT lamellar stacking in the (100), (200), and (300) planes, respectively, are visible with no apparent reflections for π-π stacking (010 plane). One notable difference is that the $P3HT_{60}$-*b*-PPP_{30} spectrum signals are sharper compared to the signals visible in the $P3HT_{35}$-*b*-PPP_{15} spectrum. It has been shown previously with P3HT-*b*-PPP BCP nanostructures that decreasing the DP_n of the polythiophene block causes broadening of the spectrum and a reduction in the intensity of second- and third-order diffractions.[51] In general, the WAXS spectrum and the d-spacing values described here closely match with previously obtained spectra and values for P3HT-*b*-PPP BCPs.[63]

Characterization of the P3HT$_{60}$-*b*-PPP$_{30}$ nanofiber dimensions was provided by drop-casting a polydisperse nanofiber solution (*n*BuAc, 0.05 mg/mL) (Figure 3.2c, d) onto a glow-discharged silicon wafer and analyzing the film following evaporation using atomic force microscopy (AFM) (Figure S3.11a). The average fiber height was found to be 3.5 ± 0.3 nm when measurements were made perpendicular to the long axis of the nanofibers (Figure S3.11b). When considering the P3HT alkyl chain stacking distance of 1.61-1.72 nm,[33,50,53,62] a fiber height of 3.5 nm suggests that ~3 lamellae of P3HT chains interdigitate in this direction to constitute the nanofiber height. The heights found here are similar to values found when analyzing nanofibers with a P3HT core-forming block made by CDSA using AFM which range from 1.6 – 7 nm depending on the corona-forming block.[50] Width measurements were extracted from the AFM data which showed that the nanofibers had an average width of W_n = 94.7 ± 4.7 nm (Figure S3.11b). P3HT$_{35}$-*b*-PPP$_{15}$ nanofiber dimensions were also analyzed using AFM characterization (Figure S3.12a) and the average fiber height was found to be 5.4 ± 0.3 nm when measurements were made perpendicular to the long axis of the nanofibers (Figure S3.12b). A height of 5.4 nm suggests that ~4 lamellae of P3HT chains interdigitate to constitute the P3HT$_{35}$-*b*-PPP$_{15}$ nanofiber height implying interdigitation of an additional lamella when compared to a P3HT$_{60}$-*b*-PPP$_{30}$ fiber (4 lamellae versus 3). This is proposed to be the caused by the reduced steric bulk associated with a shorter PPP block as the bulky ethylhexyloxy chains could sterically obstruct further lamella from adding in P3HT$_{60}$-*b*-PPP$_{30}$ fibers. Width measurements were extracted from the AFM data which showed that the P3HT$_{35}$-*b*-PPP$_{15}$ nanofibers had a W_n = 49.7 ± 3.1 nm which is approximately half the width found when analyzing P3HT$_{60}$-*b*-PPP$_{30}$ nanofibers (W_n = 94.7 nm). This result is expected, as the DP$_n$ of both the core- and corona-forming blocks in P3HT$_{35}$-*b*-PPP$_{15}$ are nearly half the DP$_n$ of P3HT$_{60}$-*b*-PPP$_{30}$. Crucially, the standard deviation in the fiber height measurements

described for both $P3HT_{60}$-*b*-PPP_{30} and $P3HT_{35}$-*b*-PPP_{15} are 0.3 and 0.3 nm, respectively, suggesting the nanofibers have roughly equal heights and do not oscillate to the same degree as fibers reported by Choi *et al.*, which had height standard deviations of 0.6 – 1.1 nm.[35] This emphasizes that reducing the corona-forming block volume fraction results in a more morphologically uniform nanofiber. It should be noted that the nanofiber widths found using AFM are considerably larger than those found when using TEM because AFM measurements include the PPP corona-forming block width, whereas only the P3HT core-forming block is visible by TEM.

3.3.3 Attempted length-control of homogenous nanofibers by seeded growth at ambient temperature (22 °C)

a) $P3HT_{60}$-*b*-PPP_{30}

Small nanofiber micelle fragments that function as seeds were prepared by sonicating a solution of polydisperse $P3HT_{60}$-*b*-PPP_{30} nanofibers (Figure S3.14a, b) in *n*BuAc at 0 °C for 4 h using a sonication bath (L_n = 103 nm, $Đ_L$ = 1.14) (Figure S3.16a, b). Sonication may introduce crystalline defects in the micelle core that propagate and multiply in the epitaxially grown layers, ultimately leading to unfavorable epitaxial growth.[32] Thermal annealing is a well-established way to improve crystal packing in polycrystalline systems like P3HT by removing potential defects.[64,65] To find a suitable annealing temperature, 3 aliquots of a seed solution (*n*BuAc, 0.1 mg/mL) from the same batch (L_n = 103 nm, $Đ_L$ = 1.14) were placed in separate vials and the vials were heated to 30 °C, 35 °C and 40 °C, respectively, for 18 h and then cooled to 22 °C slowly (ca. 4 h). These samples were drop-cast onto carbon-coated copper grids and imaged using bright-field TEM following solvent evaporation. Length analysis of the sample that was heated to 30 °C displayed

no change in length within standard error (30 °C: L_n = 81 nm, $Đ_L$ = 1.33, σ = ± 47) (Figure S3.17a, b) while heating to temperatures ≥35 °C caused seed dissolution and recrystallization of dissolved unimers on existing seed termini upon cooling (self-seeding) as the recovered nanofibers had increased L_n and $Đ_L$ (35 °C: L_n = 153 nm, $Đ_L$ = 1.35, σ = ± 90) (Figure S3.18b, S3.19b); 40 °C: L_n = 417 nm, $Đ_L$ = 1.98, σ = ± 412 (Figure S3.18c, S3.19c).[66–68] In light of these results, seeds annealed at 30 °C were used for seeded growth studies wherein rapid injection of increasing volumes of unimeric P3HT$_{60}$-*b*-PPP$_{30}$ (THF, 1 mg/mL) to annealed seed solutions (*n*BuAc, 0.1 mg/mL) followed by aging 24 h at 22 °C was performed. TEM analysis showed that this method yielded elongated fibers that were polydisperse in length (Figure S3.22a-d). We propose that the seeded growth at 22 °C was unsuccessful using this BCP because of self-nucleation upon unimer addition which caused uncontrolled formation of nuclei and sporadic growth from seeds. While *n*-butyl acetate serves as a sufficient solvent for both blocks at elevated temperatures and allows for slow addition of unimer to nuclei upon cooling, the addition of unimer to room temperature *n*-butyl acetate could cause rapid aggregate formation. It is possible that the relatively large DP_n of the P3HT and PPP blocks makes the material largely insoluble in *n*BuAc at 22 °C. Because of the complications in achieving length-controlled fibers with this material, P3HT$_{35}$-*b*-PPP$_{15}$ was used in the following seeded growth investigations.

b) P3HT$_{35}$-*b*-PPP$_{15}$

When polydisperse nanofibers of P3HT$_{35}$-*b*-PPP$_{15}$ were sonicated using the same regime described for P3HT$_{60}$-*b*-PPP$_{30}$ (4 h at 0 °C), low dispersity seeds were not recovered and increasing sonication time to 7 h also failed to produce suitable seeds (L_n = 238 nm, $Đ_L$ = 1.52) (Figure S3.20a, b). The solution temperature was decreased to -45 °C to increase the fragility of the fibers, and a titanium sonotrode placed directly inside the micelle solution was used instead of a sonication

bath. Polydisperse P3HT$_{35}$-*b*-PPP$_{15}$ fibers (*n*BuAc, 1 mg/mL) were sonicated for 7 h at –45 °C using this method, and then the seeds were annealed at 30 °C for 18 h prior to use. This resulted in seeds with low average lengths and low dispersity (L_n = 49 nm, $Đ_L$ = 1.20) (Figure S3.21a, b). The fibers were observed to have unusually high mechanical robustness compared to previous conjugated polymer nanofibers, which typically fragment much more rapidly (≤ 3 h) when subjected to ultrasonication-induced stress.[21,69,70] It is not immediately clear why fibers made from P3HT-*b*-PPP materials are apparently able to dissipate induced stress without fracturing better than other conjugated polymer nanofibers.[35] This resilience towards shear stress would make them good candidates for potential use as reinforcing components of nanofiber-based composites.[71–73]

Seeded growth of length-controlled P3HT$_{35}$-*b*-PPP$_{15}$ nanofibers at 22 °C was attempted by rapid injection of increasing volumes of unimeric P3HT$_{35}$-*b*-PPP$_{15}$ (THF, 1 mg/mL) to annealed seed solutions (*n*BuAc, 0.1 mg/mL, L_n = 49 nm, $Đ_L$ = 1.20). Length analysis of the resulting nanofibers that were imaged using TEM revealed the presence of elongated micelles with average lengths that had a linear correlation (R^2 = 0.9995) with the unimer-to-seed ratio from equivalents 1 – 3 (Figure 3.4, S3.23a-c, S3.24a-c, Table S3.1) and dispersities ranging from $Đ_L$ =1.21-1.33. Despite this, the nanofibers had L_n substantially higher than theoretically predicted values, suggesting that the number of active seeds was fewer than expected. Addition of 4 mass equivalents caused significant deviation from the linear correlated fit with lower average lengths (L_n = 1126 nm) and higher dispersity ($Đ_L$ = 1.39) than when 3 equivalents were added, suggesting that self-nucleation was occurring instead of epitaxial growth in this trial (Figure S3.23d, S3.24d, Table S3.1). The preference for self-nucleation to occur over epitaxial growth when higher mass equivalents of unimer are added has been previously identified in seeded growth experiments involving P3HT-based BCPs as well as structurally similar poly(3-alkylselenophene)-based

BCPs.[74,75] Since unimer self-nucleation at 22 °C is proposed to cause deviations from theoretically predicted nanofiber lengths and higher than expected dispersities, variable-temperature UV/Vis (VT-UV/Vis) spectroscopy experiments were conducted to find conditions where self-nucleation would be suppressed.[70]

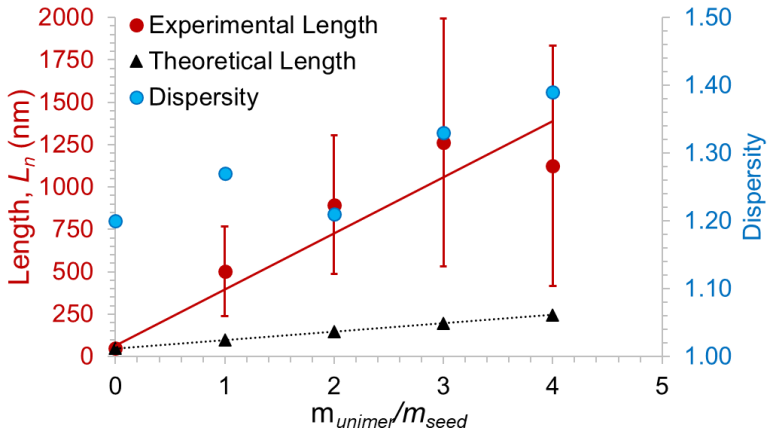

Figure 3.4. Plot showing the dependence of P3HT$_{35}$-*b*-PPP$_{15}$ nanofiber length (L_n) on unimer-to-seed ratio (m_{unimer}/m_{seed}). Error bars represent standard deviation in L_n measurements.

3.3.4 Evaluation of a self-nucleation suppression temperature for P3HT$_{35}$-*b*-PPP$_{15}$ by variable-temperature UV/Vis spectroscopy and attempted living CDSA *via* self-nucleation suppressed seeded growth

When an *n*BuAc solution of polydisperse P3HT$_{35}$-*b*-PPP$_{15}$ nanofibers (0.05 mg/mL) was heated from 20 °C to 90 °C, dissociation into the unimeric state was detected by the disappearance of the peak at 540 nm (Figure 3.5a). The absorbance peak intensity at 540 nm is higher than the peak intensity at 610 nm so this wavelength was chosen to monitor self-assembly progress (Figure 3.5a, red arrow).

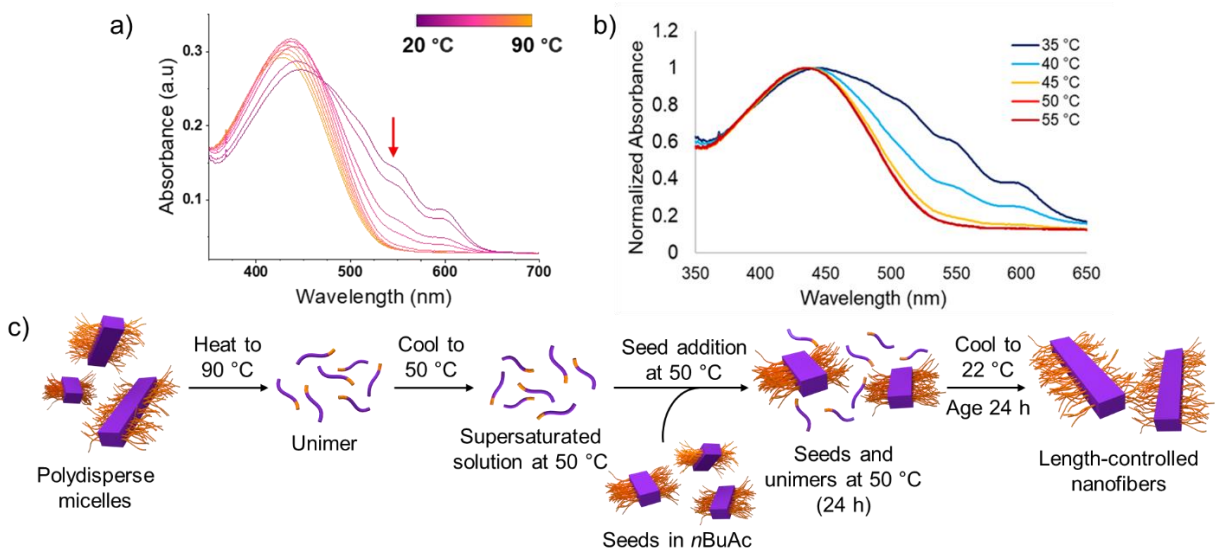

Figure 3.5. (a) Overlayed absorbance spectra of *n*BuAc P3HT$_{35}$-*b*-PPP$_{15}$ polydisperse micelle solution (0.05 mg/mL) heated from 20 °C to 90 °C at a rate of 10 °C/min with scans taken at 5 °C increments from 20 - 40 °C and 10 °C increments from 40 – 90 °C. **(b)** Overlayed solution-phase UV/Vis absorbance plots from polydisperse P3HT$_{35}$-*b*-PPP$_{15}$ nanofiber solutions in *n*BuAc (0.05 mg/mL) used to investigate self-nucleation suppression temperatures (where a supersaturated solution has formed after heating and cooling). **(c)** Cartoon schematic diagram showing self-nucleation suppressed seeded growth using 50 °C as a self-nucleation suppression temperature.

To identify a temperature where self-nucleation was suppressed when solutions were heated to 90 °C and then cooled, vials containing polydisperse P3HT$_{35}$-*b*-PPP$_{15}$ nanofiber solutions (*n*BuAc, 0.05 mg/mL) were first heated to 90 °C for 1 h to ensure that P3HT$_{35}$-*b*-PPP$_{15}$ was in the unimeric state (fully solvated) (Figure 3.5b) and then cooled from 90 °C to temperatures ranging from 35 – 55 °C with 5 °C increments and aged at these temperatures for 24 h. The solutions were quickly transferred to a UV/Vis spectrometer equipped with a heating element at the same temperature. We found that vibronic bands characteristic of crystallized P3HT were only visible at temperatures ≤ 45 °C, confirming that 50 °C is a suitable self-nucleation temperature (Figure 3.5b). Self-nucleation suppressed seeded growth follows the same process except after cooling to 50 °C, nuclei in the form of seeds are added, causing spontaneous and rapid growth from the seed

termini (Figure 3.5c).[70,76] The solution is then maintained at 50 °C for 24 h prior to cooling to 22 °C to disfavor formation of new nuclei and promote growth from the added seeds. Equal amounts of seed solution (L_n = 49 nm, $Đ_L$ = 1.20), also at 50 °C (*n*BuAc, 0.1 mg/mL), were added to achieve different m_{unimer}/m_{seed} ratios. After seed addition and mixing, the vials were left at 50 °C for 24 h and aged at 22 °C for 24 h. Length analysis of the resultant P3HT$_{35}$-*b*-PPP$_{15}$ nanofibers (0.05 mg/mL) from self-nucleation suppressed seeded growth experiments at 50 °C showed high polydispersity ($Đ_L$ = 1.52-1.92) and experimental nanofiber lengths that are close to theoretically predicted values within one standard deviation (σ); however, this is likely a consequence of the large standard deviation in the length values (Figure S3.25 – S3.27, Table S3.2). One potential reason for the higher-than-expected experimental lengths and high $Đ_L$ is that the aggressive sonication regime necessary to generate seeds created nuclei with low crystallinity, which melted upon heating and the free unimer crystallized on the surviving seed termini upon cooling. This finding shows that even though self-nucleation suppressed seeded growth has been successfully used for poly(alkylthiophene)-based BCPs before, the living CDSA behaviour is specific to the system used.

3.4 Conclusions and Summary

Here we have reported the synthesis and characterization of two rigid rod-rod P3HT-*b*-PPP BCPs with different molar masses using KCTP. Multi-micron long polydisperse nanofibers of P3HT$_{60}$-*b*-PPP$_{30}$ and P3HT$_{35}$-*b*-PPP$_{15}$ were successfully fabricated using a heat-cool cycle in the temperature-dependent selective solvent *n*-butyl acetate. Fiber characterization was completed using WAXS which showed that nanofibers composed of both materials had an ordered, crystalline core. AFM was performed on P3HT$_{35}$-*b*-PPP$_{15}$ fibers, demonstrating that there was little variation

in the fiber heights and suggesting that they have a continuous core, in contrast to the previously described “nanocaterpillar” system. This supports the hypothesis that reducing corona-forming block volume fraction can lead to more well-connected core domains and produce more uniform nanofibers, with potential benefits for optoelectronic applications. Following this, seeds with low contour lengths and relatively low dispersities were made, albeit using relatively aggressive sonication protocols. The surprising resilience of the polydisperse fibers to sonication-induced shear stress makes them good candidates for investigation in nanofiber-based reinforced composites. Seeds of $P3HT_{60}$-*b*-PPP_{30} and $P3HT_{35}$-*b*-PPP_{15} were used in attempts to form length-controlled nanofibers using living CDSA seeded growth, which did not produce length-controlled fibers. Variable-temperature UV/Vis spectroscopy was used to gain a deeper understanding of $P3HT_{35}$-*b*-PPP_{15} self-assembly and find temperatures where self-nucleation is suppressed, which was found to be ≥50 °C. Self-nucleation suppressed seeded growth experiments produced nanofibers with L_n closer to theoretically predicted values, but with higher $Đ_L$. This article reports an initial investigation into the solution self-assembly of rigid rod-rod BCPs into nanofibers, but further investigation is needed to achieve control over fiber length. Nonetheless, we have reported methods for the fabrication of multi-micron long nanofibers made by CDSA of all-conjugated BCPs with well-connected cores and high mechanical resistance to shear.

3.5 Supporting Information

3.5.1 Methods

Materials

All reagents used for polymer synthesis were of reagent grade and used as received unless otherwise stated. All the air-free chemistry was performed in a dinitrogen-filled (N_2) MBraun 200B glovebox equipped with a cold-well or on a dinitrogen Schlenk line using standard Schlenk techniques. Isopropylmagnesium chloride – lithium chloride (*i*PrMgCl•LiCl) (1.3M in THF), potassium carbonate, and 2,5-dibromohydroquinone (97%) were purchased from Millipore Sigma. 2,5-dibromo-3-hexylthiophene was purchased from Combiblocks and distilled under reduced pressure before use. Solvents were dried and deoxygenated using a Solvent Purification System (SPS).[77] Ni(*o*-tolyl)(dppe)Cl was synthesized as previously reported.[78] Self-assembly experiments were performed using HPLC grade solvents and solvents were filtered through a 0.2 μm polytetrafluoroethylene membrane.

Nuclear magnetic resonance (NMR)

^{1}H NMR spectra were taken with a Bruker 500 MHz spectrometer; chemical shifts were referenced to the residual proteosolvent peak ($CHCl_3$, δ = 7.26 ppm).

Gel Permeation Chromatography (GPC)

GPC was conducted using a Malvern Omnisec Resolve/Reveal equipped with an automatic sampler, pump, injector, inline degasser column oven (set at 35 °C), elution columns consisting of styrene/divinylbenzene gels (of pore size 500–5,000 Å), refractometer, four capillary differential viscometer, UV/Vis detector (λ = 440 nm) and dual angle laser light scattering detector (7° and 90°). GPC grade THF with 1 wt% triethylamine was used as the eluent, with a set flow rate of 1

mL/min. BCP samples were dissolved in THF at 1 mg/mL and filtered through a 0.2 μm poly(tetrafluoroethylene) membrane prior to analysis. Homopolymer concentration was 2 mg/mL in THF and filtered through a 0.2 μm poly(tetrafluoroethylene) membrane prior to analysis.

Preparatory GPC

Preparatory gel permeation chromatography was performed on a Shimadzu Prep GPC equipped with a CBM-20A communications bus module, LC-20AP solvent delivery unit, SIL-10AP autosampler, CTO-40C column oven, SPD-40 UV/Vis detector, RID-20A refractive index detector, and FRC-10A fraction collector. An initial injection of polymer in THF (1 mL, 10 mg/mL) at a flow rate of 3 mL/min using HPLC grade THF as eluent was used to gather the retention times of the species in solution. Using this data, the fraction collector was calibrated to separate the desired peaks into separate vials. Subsequent injections (3 mL, 10 mg/mL, 3 mL/min) were repeated until the desired volume was collected. The resulting solutions were concentrated *in vacuo* to yield the final polymers. Removal of homopolymers was assessed using UV-detection on the Malvern Omnisec GPC and thin layer chromatography.

Transmission Electron Microscopy (TEM)

Carbon films were deposited onto freshly cleaved mica sheets using a Leica EM ACE600 sputter/carbon coater instrument. Carbon films were deposited onto copper grids (500 mesh) purchased from Ted Pella, Inc. by floatation on water and allowed to dry over 24 h. TEM samples were prepared by drop-casting 10 μL of a colloidal nanofiber solution onto a TEM grid placed on filter paper to absorb the excess solution. Bright field TEM images were obtained using a JEOL JEM 1011 microscope operating at 80 kV, equipped with a Gatan Orius SC1000 CCD camera.

Sonication

Sonication bath: Nanofiber sonication was carried out using a Fisherbrand FB11203 sonication bath (37 kHz sonication frequency and 100% power) with the sweep function on and a bath temperature of 0 °C.

Sonotrode: Nanofiber sonication was carried out using a Heischler UP100H ultrasonic processor affixed with a titanium sonotrode probe at 100% power.

Variable-temperature UV/Vis absorption spectroscopy (VT-UV/Vis)

VT-UV/vis data was obtained on a Cary 100 spectrometer equipped with a Peltier temperature controller employing quartz cells (1 cm x 0.1 cm) from 200 to 800 nm. Experiments were conducted at a concentration of 0.05 mg/mL to allow for convenient monitoring of fiber-like micelle formation and dissolution.

Wide-Angle X-ray Scattering (WAXS)

Reciprocal space maps were collected with a Pixcel 3D detector on an Empyrean diffractometer (Panalytical) equipped with a Cu Kα1 (λ = 1.5406 Å) source powered at 45 kV and 40 mA.

Atomic Force Microscopy (AFM)

AFM analysis was obtained using a 5500 Atomic Force Microscope (Agilent Technologies). The images were recorded in AC mode with a scanning speed of 1.0 μm/s in an area of 4.0 μm^2 at 1024 × 1024 resolution. The tips employed (Tap150Al-G, Budget Sensors) consisted of a conical silicon tip with aluminum reflective coating and a resonance frequency and spring force constant of 150 kHz and 5 N/m, respectively. The samples for AFM were prepared on a silicon wafer by drop-casting the nanofiber solution (in 100 % *n*BuAc, 20 μL, 0.05 mg/mL)

onto the clean silicon wafer. The silicon wafer was gently dried from the sides with a filter paper and dried *via* vacuum desiccation.

3.5.2 Statistical Analysis

Nanofiber lengths and widths were analysed using ImageJ, an open source software package developed at the US National Institute of Health.[79] Approximately 150 micelles were traced by hand to determine contour lengths that were then used to calculate the number-averaged length (L_n) and weight-average length (L_w) was calculated by using supplementary equations S3.1 and S3.2 from the measurements of the contour length (L_i) of individual micelles, where N_i is the number of the micelles of length L_i, and n is the number of micelles examined in each sample.

$$(Equation\ S3.1)\ L_n = \frac{\sum_{i=1}^{n} N_i L_i}{\sum_{i=1}^{n} N_i} \qquad (Equation\ S3.2)\ \ L_w = \frac{\sum_{i=1}^{n} N_i L_i^2}{\sum_{i=1}^{n} N_i L_i}$$

Number-averaged width (W_n) was calculated according to equation S3.3 where W_i = object width and N_i = number of micelles of length W_i.

$$(Equation\ S3.3)\quad W_n = \frac{\sum_{i}^{n} N_i W_i}{\sum_{i}^{n} N_i}$$

The polydispersity index ($Đ_L$) and standard deviations (σ) of the measured lengths were related through the following expressions (Eq. S3.4 and S3.5).

$$(Equation\ S3.4)\quad Đ_L = \frac{L_w}{L_n} \qquad (Equation\ S3.5)\quad \frac{L_w}{L_n} - 1 = \left(\frac{\sigma}{L_n}\right)^2$$

3.5.3 Experimental Procedures

Scheme S3.1. Synthesis of 1,4-dibromo-2,5-bis(2-ethylhexyloxy)benzene

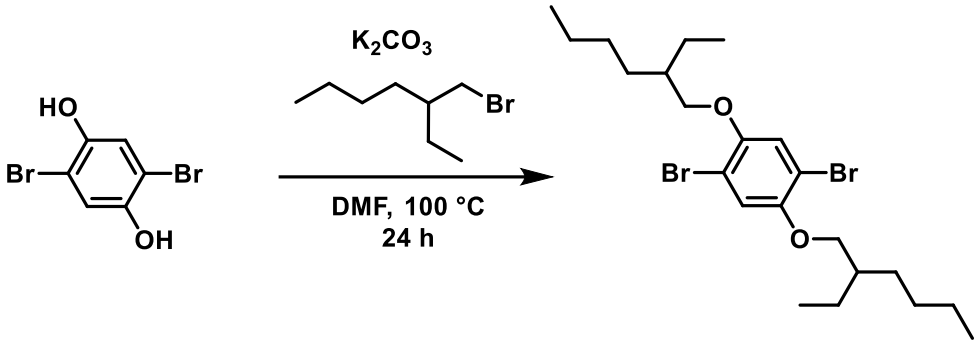

This product was synthesized using a previously published procedure from ref 80.[80] (6.73 g, 91% yield).

Scheme S3.2. Synthesis of P3HT$_{35}$-*b*-PPP$_{15}$

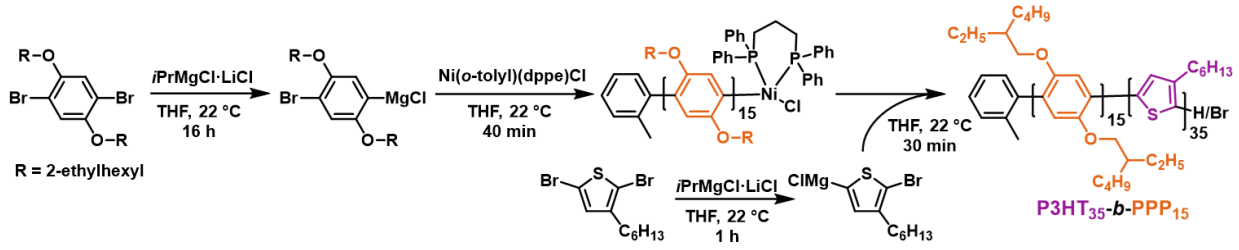

In a N_2-filled glovebox, a dry 100-mL Schlenk flask affixed with a stir bar was charged with 1,4-dibromo-2,5-bis(2-ethylhexyloxy)benzene (1.02 g, 2.05 mmol, 45 equiv.) and dry tetrahydrofuran (THF) (10 mL) was added. iPrMgCl•LiCl (1.3 M in THF, 1.62 mL, 2.11 mmol, 46 equiv.) was added dropwise and the solution was stirred for 16 h resulting in a faint yellow solution. In a separate dry 100-mL Schlenk flask affixed with a stir bar, 2,5-dibromo-3-hexylthiophene (0.448g, 1.37 mmol, 30 equiv.) was dissolved in dry THF (10 mL). iPrMgCl•LiCl (1.3 M in THF, 1.07 mL, 1.39 mmol, 31 equiv.) was added dropwise and the solution was stirred for 1 h resulting in a yellow solution. Ni(*o*-tolyl)(dppe)Cl (27 mg, 0.046 mmol, 1 equiv.) was

dissolved in dry THF (2 mL) and injected quickly into the 1,4-dibromo-2,5-bis(2-ethylhexyloxy)benzene solution causing a deep yellow color to immediately evolve. This was stirred for 40 min. and after such time a small aliquot (1.5 mL) was removed from the flask and quenched with 5M HCl prior to analysis by GPC. The thiophene monomer solution was injected quickly into the 1,4-dibromo-2,5-bis(2-ethylhexyloxy)benzene solution causing a dark orange color to evolve. The solution was stirred for 30 min, a septum was affixed, the flask was removed from the glove box and then quenched using 5M HCl (12 mL) followed by stirring for an additional 15 min. $CHCl_3$ (100 mL) was added, the solution was washed using distilled water (3 x 100 mL), dried using $MgSO_4$, gravity filtered and then concentrated *in vacuo* to yield a reddish-purple solid. The crude product was dissolved in $CHCl_3$ and precipitated into ice-cold MeOH followed by acetone which yielded a reddish-purple solid. The crude solid was purified further using preparatory GPC with THF as the eluent (380 mg, 69% yield). Diblock Copolymer: GPC: M_n = 12, 000 Da, $Đ_M$ = 1.08

^{1}H NMR (500 MHz, $CDCl_3$) (ppm): 7.44 (d, 2H, phenyl-H, **Ha**), 7.17 (d, 2H, phenyl-H, **Hb**) 7.08-7.04 (bs, 30H, phenylene-H, **Hc**), 7.00-6.97 (bs, 35H, thiophene-H, **Hd**) 3.80-3.71 (bm, 60H, phenylene-O-CH_2-CH, **He**), 2.84-2.79 (bt, 70H, thiophene-CH_2-C_5H_{11}, **Hf**) 2.25 (s, 3H, *o*-tolyl-CH_3, **Hg**) 1.76-1.68 (bm, 30H, O-CH_2-CH, **Hh**), 1.47-1.20 (m, 520H, -CH_2-, **Hi**) 0.95-0.90 (bt, 105H, thiophene-C_5H_{10}-CH_3, **Hj**), 0.87-0.80 (bm, 180H, O-C_3H_5-CH_3 and O-C_5H_9-CH_3, **Hk**)

Work-up of PPP_{15} homopolymer aliquot: $CHCl_3$ (25 mL) was added to the 5M HCl solution and the mixture was washed using distilled water (3 x 50 mL). The organic phase was dried over $MgSO_4$, gravity filtered, and concentrated *in vacuo* to a yellow oil. MeOH (50 mL) was added, and the solution was shaken vigorously and sonicated using a sonication bath. The yellow solid was collected by vacuum filtration and washed thoroughly with MeOH to yield the homopolymer

as a yellow, gum-like residue. PPP Homopolymer: GPC: M_n = 5, 500 Da, $Đ_M$ = 1.14, $DP_{n,\ GPC}$ = 17; $DP_{n,\ H\ NMR}$ = 15

^{1}H NMR (500 MHz, $CDCl_3$) (ppm): 7.44 (d, 2H, phenyl-H, **Ha**), 7.17 (d, 2H, phenyl-H, **Hb**) 7.08-7.00 (bs, 2H, phenylene-H, **Hc**) 3.85-3.68 (bm, 4H, phenylene-O-CH_2-CH, **Hd**), 2.25 (s, o-tolyl-CH_3, **He**) 1.80-1.70 (m, 2H, O-CH_2-CH, **Hf**), 1.40-1.07 (m, 16H, -CH_2-, **Hg**) 0.90-0.79 (bm, 12H, -CH_3, **Hh**)

Scheme S3.3. Synthesis of P3HT$_{60}$-*b*-PPP$_{30}$

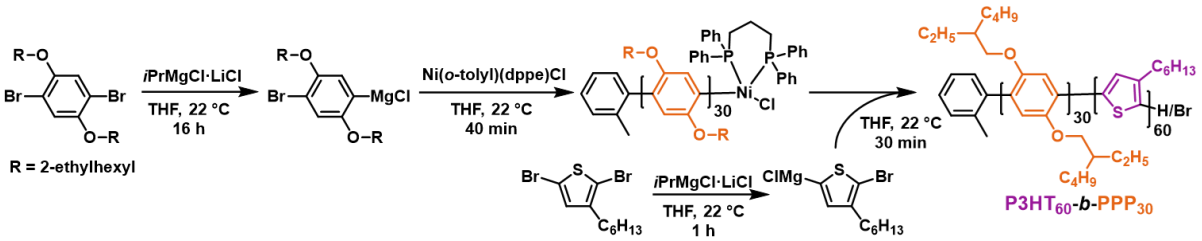

The synthesis of **P3HT$_{60}$-*b*-PPP$_{30}$** was carried out using the same procedure for **P3HT$_{35}$-*b*-PPP$_{15}$** detailed above. (180 mg, 38% yield). Diblock Copolymer: GPC: M_n = 18, 200 Da, $Đ_M$ = 1.10

^{1}H NMR (500 MHz, $CDCl_3$) (ppm): 7.44 (d, 2H, phenyl-H, **Ha**), 7.17 (d, 2H, phenyl-H, **Hb**) 7.08-7.04 (bs, 60H, phenylene-H, **Hc**), 7.00-6-97 (bs, 60H, thiophene-H, **Hd**) 3.80-3.71 (bm, 120H, phenylene-O-CH_2-CH, **He**), 2.84-2.79 (bt, 120H, thiophene-CH_2-C_5H_{11}, **Hf**) 2.25 (s, 3H, *o*-tolyl-CH_3, **Hg**) 1.76-1.68 (bm, 60H, O-CH_2-CH, **Hh**), 1.47-1.20 (m, 960H, -CH_2-, **Hi**) 0.95-0.90 (bt, 180H, thiophene-C_5H_{10}-CH_3, **Hj**), 0.87-0.80 (bm, 360H, O-C_3H_5-CH_3 and O-C_5H_9-CH_3, **Hk**)

PPP_{30} Homopolymer: GPC: M_n = 10, 800 Da, $Đ_M$ = 1.11, $DP_{n,\ GPC}$ = 32; $DP_{n,\ H\ NMR}$ = 30

^{1}H NMR (500 MHz, $CDCl_3$) (ppm): 7.36 (d, 2H, phenyl-H, **Ha**), 7.12 (d, 2H, phenyl-H, **Hb**) 7.08-

7.00 (bs, 60H, phenyl-H, **Hc**) 3.85-3.68 (bm, 4H, phenyl-O-CH_2-CH, **Hd**), 2.25 (s, *o*-tolyl-CH_3, **He**) 1.65-1.57 (m, 60H, O-CH_2-CH, **Hf**), 1.40-1.07 (m, 480H, -CH_2-, **Hg**) 0.90-0.79 (bm, 12H, -CH_3, **Hh**).

3.5.4 Gel Permeation Chromatography

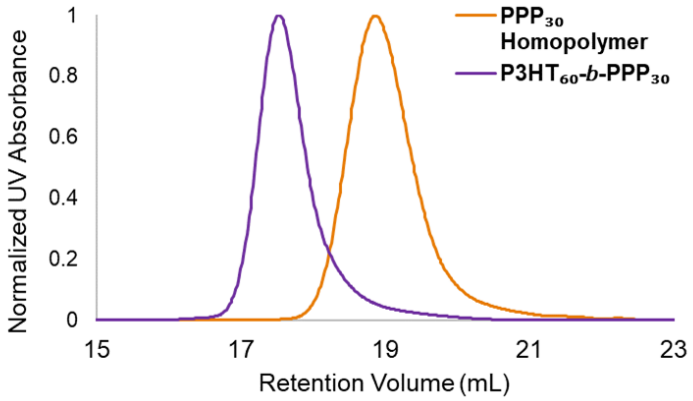

Figure S3.1 Overlaid GPC chromatograms of P3HT$_{60}$-*b*-PPP$_{30}$ BCP (purple trace) and its corresponding coronal-block PPP$_{30}$ homopolymer (orange trace) using UV/Vis detection at an absorbance wavelength of 330 nm.

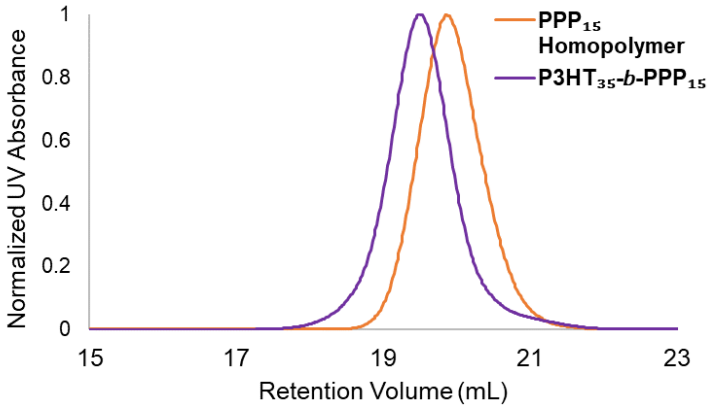

Figure S3.2. Overlaid GPC chromatograms of P3HT$_{35}$-*b*-PPP$_{15}$ BCP (purple trace) and its corresponding coronal-block PPP$_{15}$ homopolymer (orange trace) using UV/Vis detection at an absorbance wavelength of 330 nm.

3.5.5 Differential Scanning Calorimetry

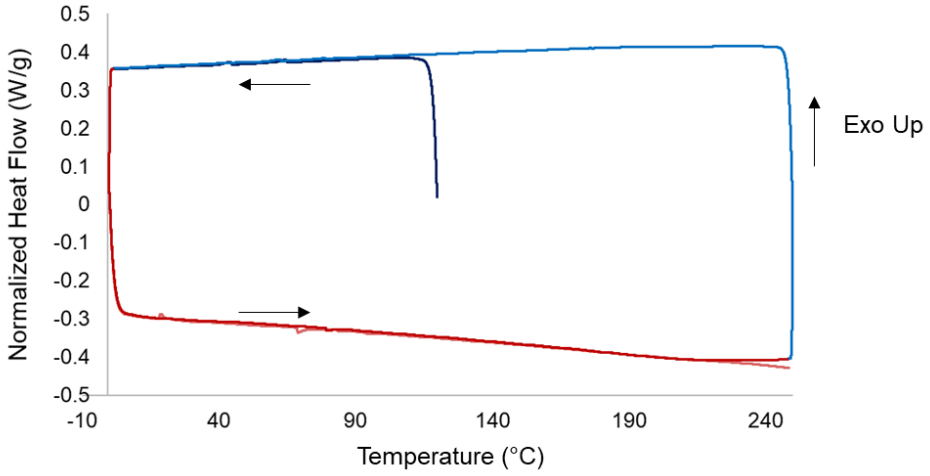

Figure S3.3. DSC thermogram of PPP_{30} heated at a temperature ramp rate of 10 °C/min under N_2 showing no T_c or T_m. Arrows denote the direction of heating and cooling cycles. The thermal history of the material was removed by annealing at 120 °C for 3 h under N_2 flow prior to being subjected to two cool-heat cycles from 0 °C to 250 °C, at a temperature ramp rate of 10 °C/min. 120 °C was chosen as the annealing temperature as this is ~25 °C above the reported T_m of PPP homopolymer.[46]

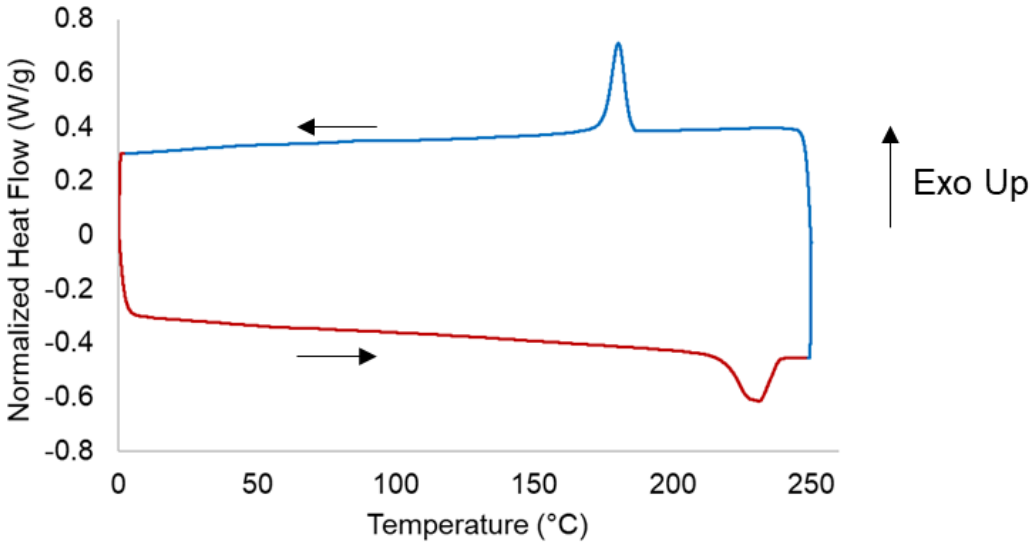

Figure S3.4. DSC thermogram of $P3HT_{60}$-*b*-PPP_{30} heated at a temperature ramp rate of 10 °C/min under N_2. Arrows denote the direction of heating and cooling cycles. T_m peak temperature = 231 °C with a melting enthalpy of 13.0 J/g. T_c = 180 °C with an enthalpy of crystallization of 12.0 J/g.

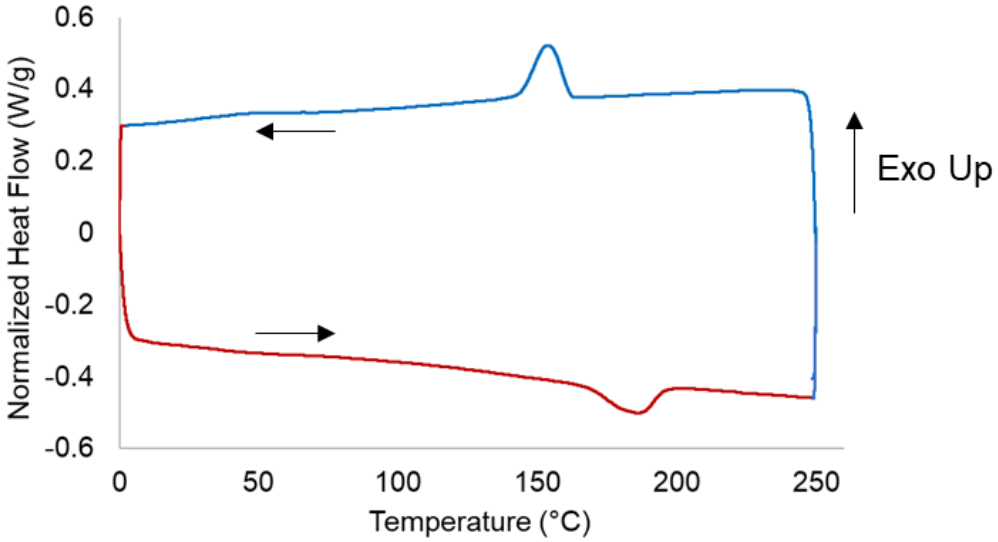

Figure S3.5. DSC thermogram of P3HT$_{35}$-*b*-PPP$_{15}$ heated at a temperature ramp rate of 10 °C/min under N_2. Arrows denote the direction of heating and cooling cycles. T_m peak temperature = 186 °C with a melting enthalpy of 8.2 J/g. T_c = 153 °C with an enthalpy of crystallization of 9.9 J/g.

3.5.6 ^{1}H NMR Spectroscopy

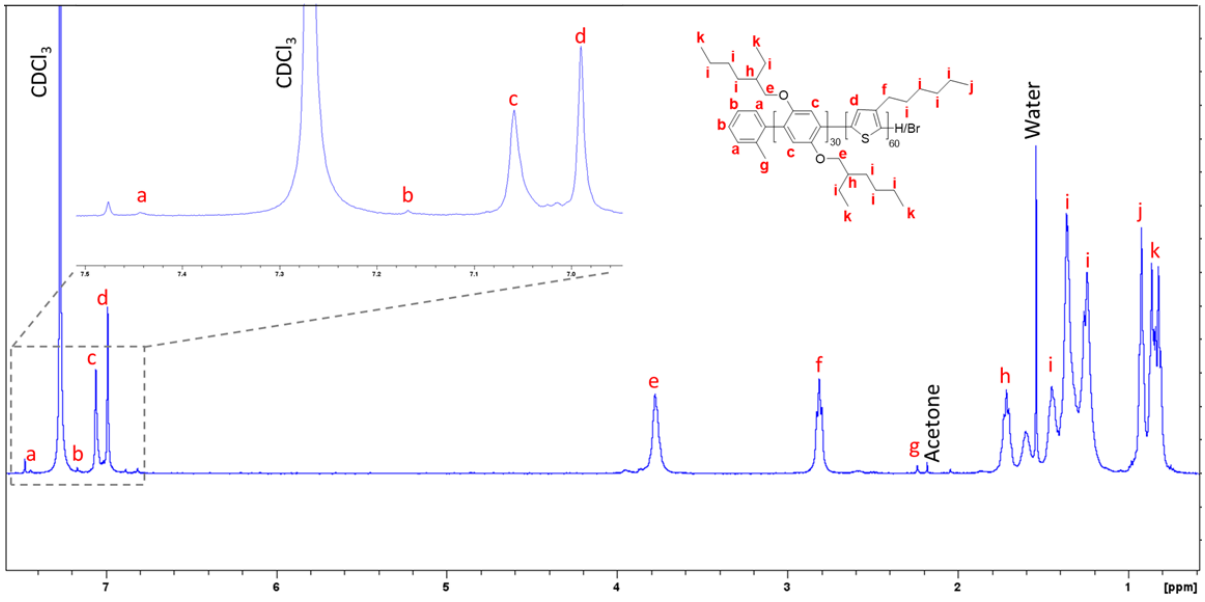

Figure S3.6. ^{1}H NMR spectrum of P3HT$_{60}$-*b*-PPP$_{30}$ (500 MHz, $CDCl_3$).

PPP_{30} Homopolymer

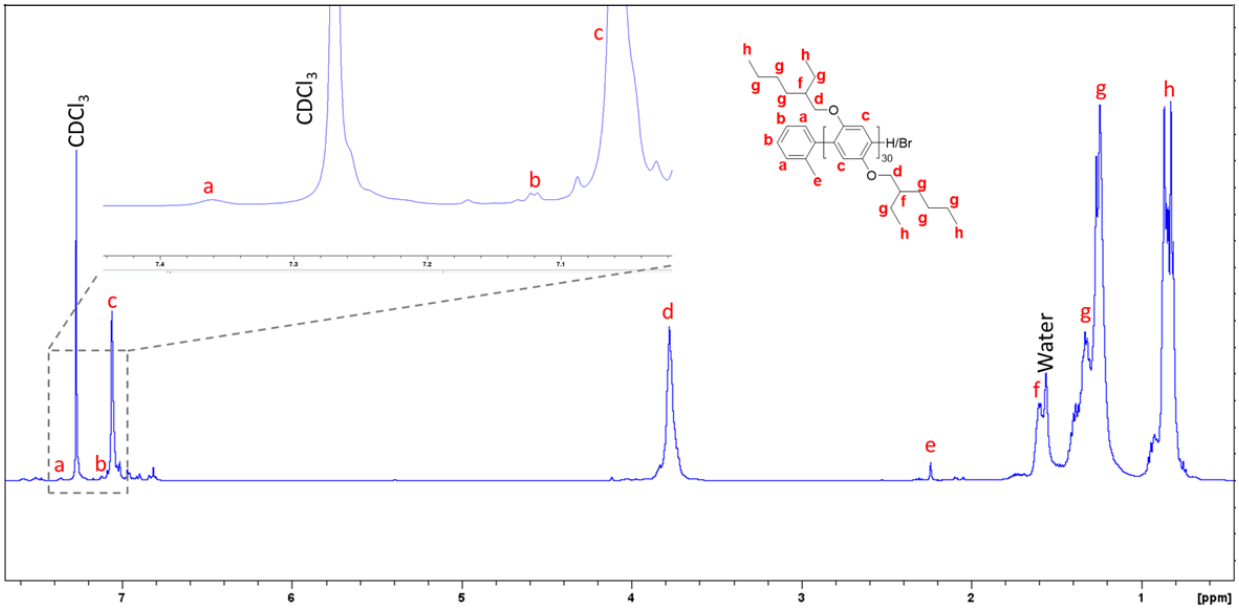

Figure S3.7. ^{1}H NMR spectrum of PPP_{30} homopolymer (500 MHz, $CDCl_3$).

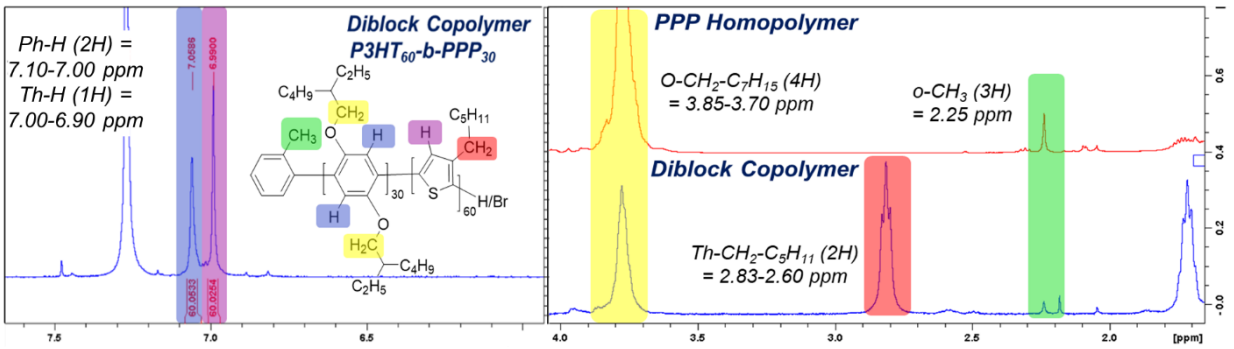

Figure S3.8. ^{1}H NMR spectra of PPP_{30} homopolymer and $P3HT_{60}$-*b*-PPP_{30} in $CDCl_3$ highlighting how relative integrations are used to determine degree of polymerization. The spectrum exhibits a small singlet at 2.25 ppm corresponding to the *ortho*-tolyl methyl group. The spectrum exhibits a singlet corresponding to the two protons in the 3- and 6- positions on the phenyl rings (denoted in blue) that can be used for relative integration; however, this signal can overlap with the singlet peak from 7.00-6.90 ppm corresponding to the vinylic proton in the 4- position on the thiophene rings (denoted in purple). The vinylic proton signal can be used to determine the P3HT core-block DP_n which was found to be 60 in this example. In the case of overlap between the two signals around 7.00 ppm, the broad signal from 3.85-3.70 ppm (denoted in yellow) corresponding to the methylene protons adjacent to the oxygen atoms at the 2- and 5- positions on the phenyl rings can be used. The relative integration ratio of this signal to the *o*-tolyl methyl resonance was 120:3, giving a DP_n of the PPP block of 30.

P3HT$_{35}$-*b*-PPP$_{15}$

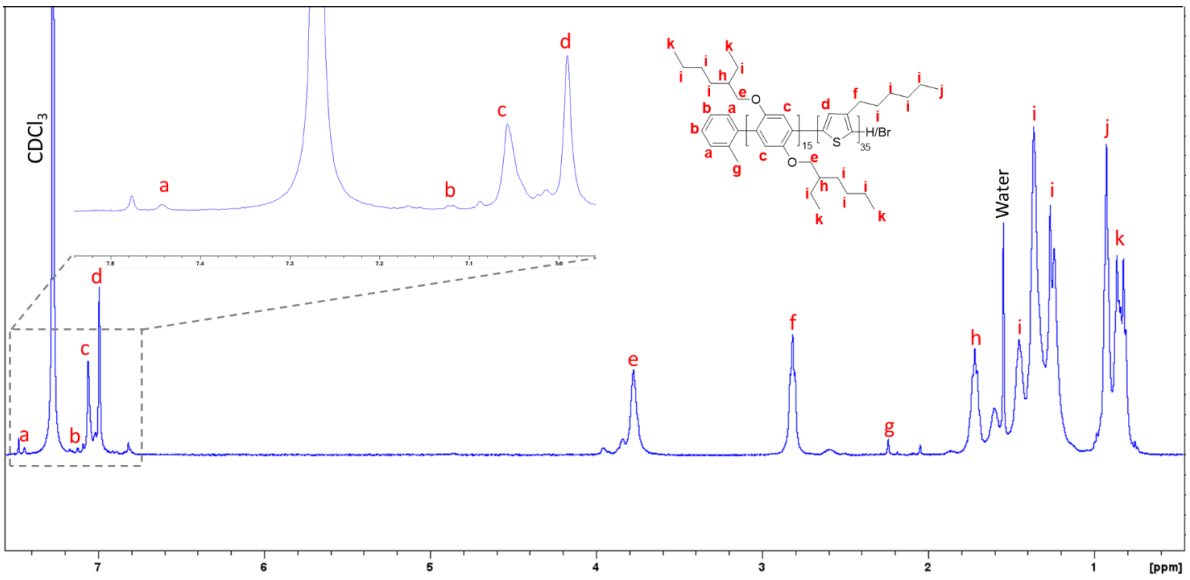

Figure S3.9. ^{1}H NMR spectrum of P3HT$_{35}$-*b*-PPP$_{15}$ (500 MHz, $CDCl_3$).

PPP$_{15}$ Homopolymer

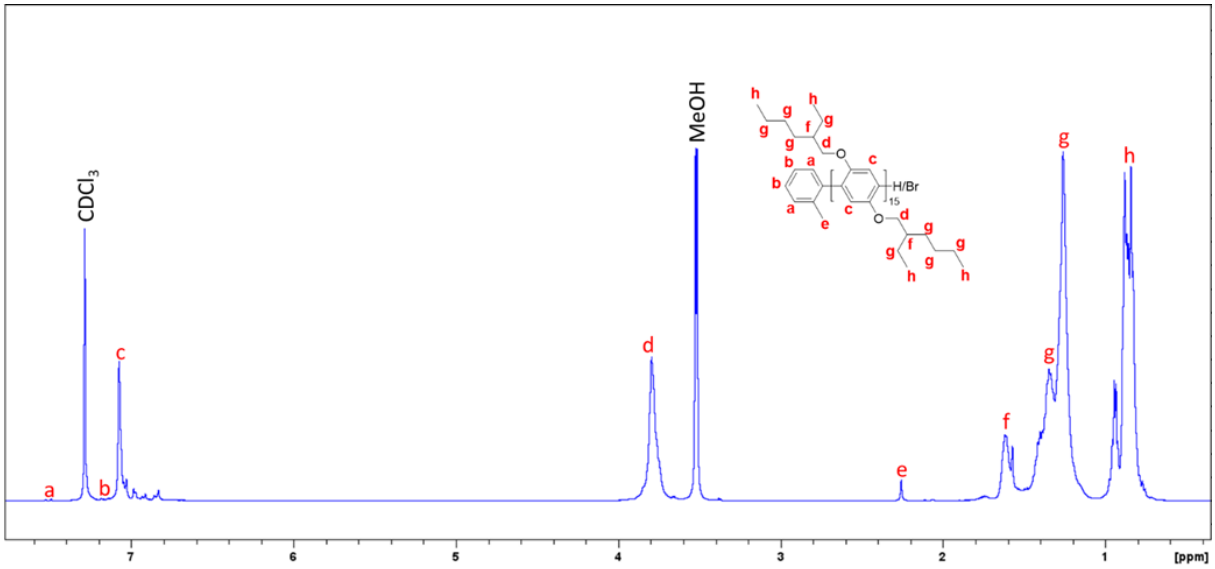

Figure S3.10. ^{1}H NMR spectrum of PPP$_{15}$ homopolymer (500 MHz, $CDCl_3$).

3.5.7 Crystallization-Driven Self-Assembly Procedures

General self-assembly procedure for fabrication of polydisperse fibers and seed micelles

P3HT$_{60}$-*b*-PPP$_{30}$

Self-assembly of P3HT$_{60}$-*b*-PPP$_{30}$ into polydisperse fiber-like micelles was achieved by adding 4 mL of *n*BuAc to a vial containing 4 mg of P3HT$_{60}$-*b*-PPP$_{30}$ (1 mg/mL). The vial was then placed in a metal heating block at 80 °C and heated for 30 min. The 1 mg/mL solution was allowed to cool to 22 °C slowly (ca. 4 h) followed by aging for 24 h. The vial was then placed in a 0 °C ultrasonic cleaning bath and sonicated for 4 h to give seed micelles (37 kHz, 100% power). Seeds were then annealed at 30 °C for 18 h prior to use.

P3HT$_{35}$-*b*-PPP$_{15}$

Self-assembly of P3HT$_{35}$-*b*-PPP$_{15}$ into polydisperse fiber-like micelles was achieved by adding 4 mL of *n*BuAc to a vial containing 4 mg of P3HT$_{35}$-*b*-PPP$_{15}$ (1 mg/mL). The vial was then placed in a metal heating block at 90 °C and heated for 30 min. The 1 mg/mL solution was allowed to cool to 22 °C slowly (ca. 4 h) followed by aging for 24 h. A sonotrode affixed with a titanium probe was placed in an *n*BuAc solution (1 mg/mL) of polydisperse P3HT$_{35}$-*b*-PPP$_{15}$ micelles at -45 °C and sonicated for 7 h at 100% power. Seeds were then annealed at 30 °C for 18 h prior to use.

General self-assembly procedure for attempted length-control of P3HT$_{35}$-*b*-PPP$_{15}$ nanofibers *via* seeded growth at 22 °C

P3HT$_{35}$-*b*-PPP$_{15}$ seed micelle solution (*n*BuAc, 0.1 mg/mL) was added to a vial and diluted with *n*BuAc such that the final concentration will be 0.05 mg/mL following unimer addition. P3HT$_{35}$-*b*-PPP$_{15}$ unimer solution (1 mg/mL in THF) was added in one aliquot, the solutions were

vortexed for 10 s and then aged at 22 °C for 24 h prior to imaging by TEM.

General self-assembly procedure for attempted length-control of P3HT$_{35}$-*b*-PPP$_{15}$ nanofibers *via* self-nucleation suppressed seeded growth at 50 °C

Four vials were filled with increasing amounts of polydisperse P3HT$_{35}$-*b*-PPP$_{15}$ nanofiber solution (*n*BuAc, 0.1 mg/mL) and diluted using *n*BuAc such that the final concentration after seed addition will be 0.05 mg/mL. The solutions were heated to 90 °C for 1 h and then cooled to 50 °C over ~2 h by placing in a preheated metal block. Equal amounts of seed micelle solution at 50 °C (*n*BuAc, 0.1 mg/mL) correlating to m_{unimer}/m_{seed} = 1, 2, 3, and 4 were added in one aliquot, the solutions were vortexed for 10 s, and then placed back in the 50 °C heating block for 24 h before cooling to 22 °C slowly (ca. 2 h) and aged 24 h prior to imaging by TEM.

3.5.8 Atomic Force Microscopy

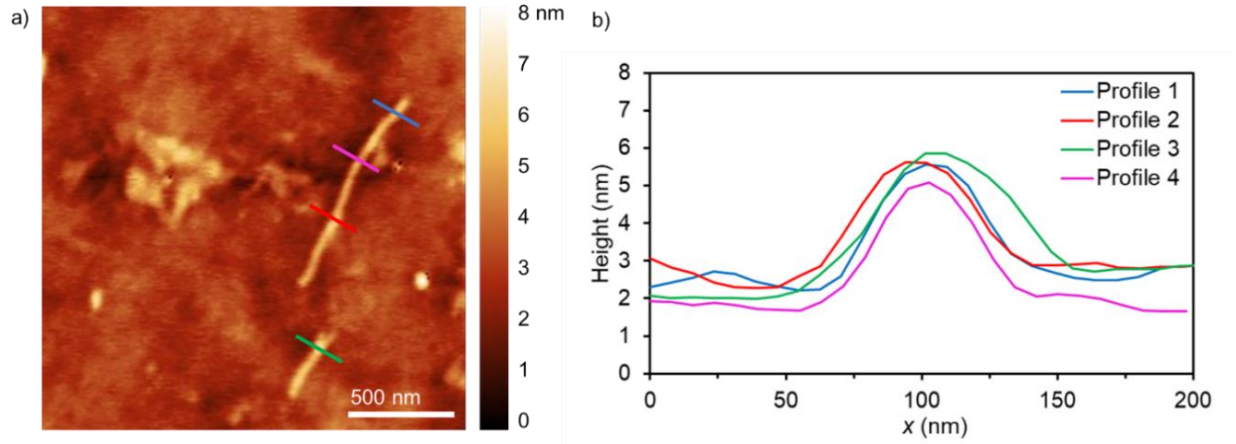

Figure S3.11. (a) AFM height image of polydisperse P3HT$_{60}$-*b*-PPP$_{30}$ nanofibers in *n*BuAc (0.05 mg/mL) drop-cast onto a glow discharged silicon wafer. Coloured lines indicate height profile shown in **(b)** drawn perpendicular to the long axis of the fibers. Series 1 - height: 3.3 nm, width: 93.7 nm; Series 2 - height: 3.3 nm, width: 94.0 nm; Series 3 - height: 3.4 nm, width: 101.1 nm; Series 4 - height: 3.4 nm, width: 89.9 nm. Average height: 3.5 nm ± 0.3 nm. Average width: (W_n = 94.7 nm ± 4.7 nm).

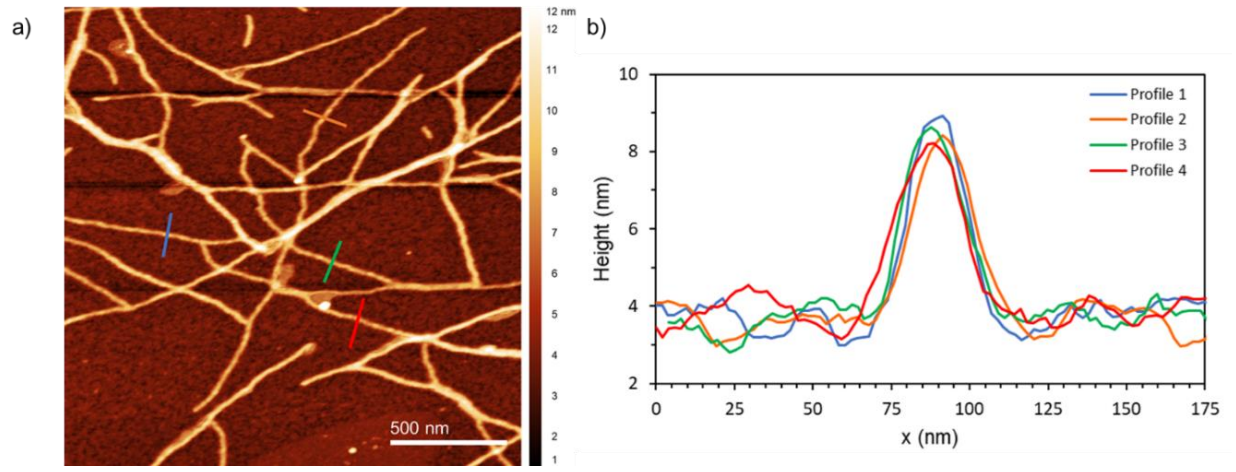

Figure S3.12. (a) AFM height image of polydisperse P3HT$_{35}$-*b*-PPP$_{15}$ nanofibers in *n*BuAc (0.05 mg/mL) drop-cast onto a glow discharged silicon wafer. Coloured lines indicate height profile shown in **(b)** drawn perpendicular to the long axis of the fibers. Series 1 - height: 5.7 nm, width: 48.5 nm; Series 2 - height: 5.2 nm, width: 52.5 nm; Series 3 - height: 5.4 nm, width: 45.2 nm; Series 4 - height: 5.0 nm, width: 52.6 nm. Average height: 5.4 nm ± 0.3 nm. Average width: (W_n = 49.7 nm ± 3.1 nm).

3.5.9 Variable-Temperature UV/Vis Spectroscopy

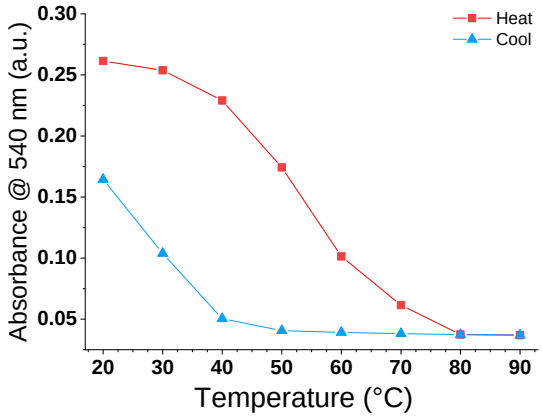

Figure S3.13. Absorbance plot showing a thermal hysteresis during heating and cooling of a *n*BuAc P3HT$_{35}$-*b*-PPP$_{15}$ polydisperse micelle solution (0.05 mg/mL) heated from 20 °C to 90 °C and then cooled from 90 °C to 20 °C using 10 °C increments at a rate of 10 °C/min. Solutions were allowed to equilibrate at the target temperatures for 30 min. prior to each scan. 540 nm was the absorbance wavelength chosen to monitor the self-assembly. Upon cooling, the absorbance peak at 540 nm became visible below 50 °C suggesting that above this temperature, nucleation had not occurred or was occurring at a very slow rate. This has been observed in other P3HT-based systems, due to the crystal lattice energy that needs to be overcome for dissolution to occur.[60,70]

3.5.10 Transmission Electron Microscopy

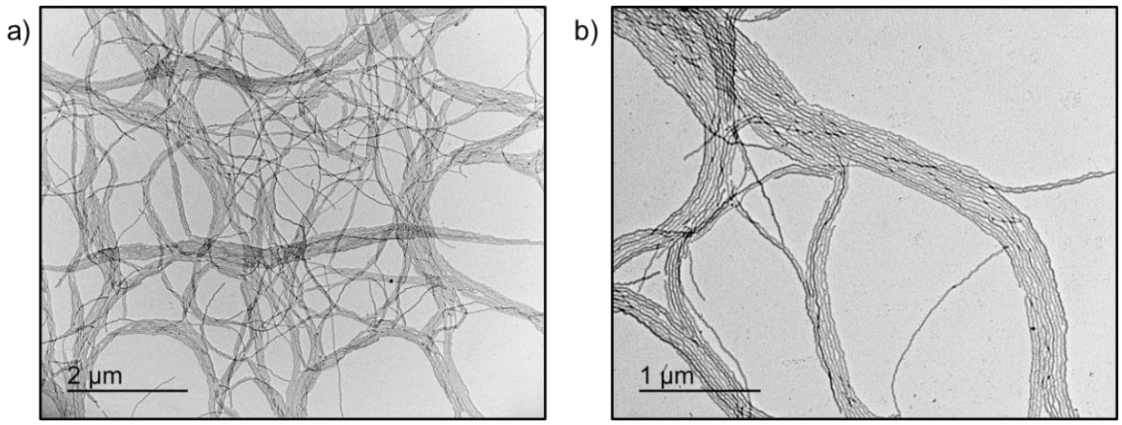

Figure S3.14. (a, b) TEM images of polydisperse P3HT$_{60}$-*b*-PPP$_{30}$ fibers. Samples were drop-cast onto a carbon-coated copper TEM grid and imaged following solvent evaporation. Width analysis of polydisperse nanofibers imaged using TEM showed W_n = 21.8 ± 5.7 nm (number counted = 8).

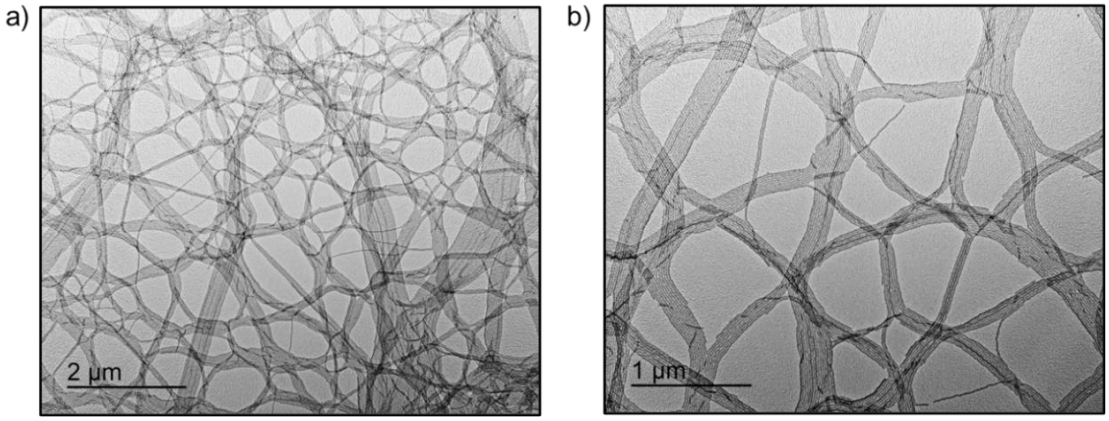

Figure S3.15. (a, b) TEM images of polydisperse P3HT$_{35}$-*b*-PPP$_{15}$ fibers. Samples were drop-cast onto a carbon-coated copper TEM grid and imaged following solvent evaporation. Width analysis of polydisperse nanofibers imaged using TEM showed W_n = 12.7 ± 2.4 nm (number counted = 8).

Seed Fabrication

P3HT$_{60}$-*b*-PPP$_{30}$ - Sonication Bath: Not annealed

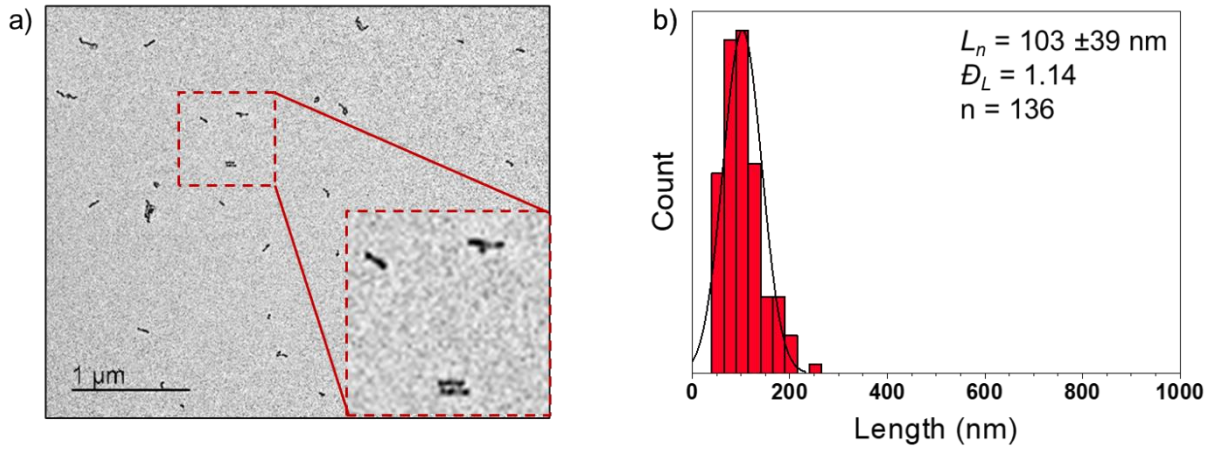

Figure S3.16. (a) TEM image of seeds formed by ultrasonication of a P3HT$_{60}$-*b*-PPP$_{30}$ polydisperse micelle solution (*n*BuAc, 1 mg/mL) in a 0 °C bath for 4 h (37 kHz, 100% power) which were not annealed prior to use. **(b)** Histogram showing the fiber length distribution of P3HT$_{60}$-*b*-PPP$_{30}$ seeds (L_n = 103 nm, L_w = 118 nm, $Đ_L$ = 1.14, σ = ± 39 nm, n = 136).

P3HT$_{60}$-*b*-PPP$_{30}$ - Sonication Bath: Annealed at 30 °C

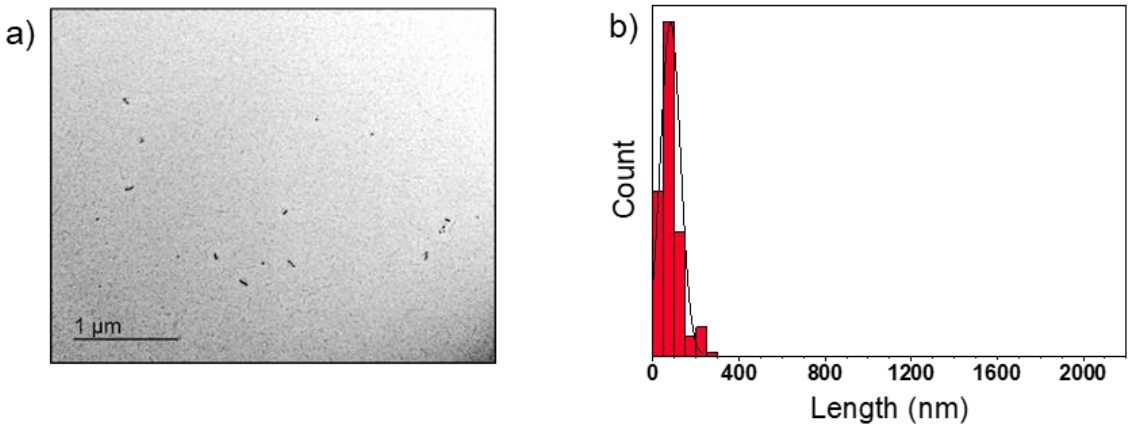

Figure S3.17. (a) TEM image of P3HT$_{60}$-*b*-PPP$_{30}$ seeds that were diluted to 0.1 mg/mL using *n*BuAc and annealed for 18 h at 30 °C before being brought to 22 °C (ca. 2 h). **(b)** Histogram showing the fiber length distribution of P3HT$_{60}$-*b*-PPP$_{30}$ seeds (L_n = 81 nm, L_w = 108 nm, $Đ_L$ = 1.33, σ = ± 47 nm, n = 163).

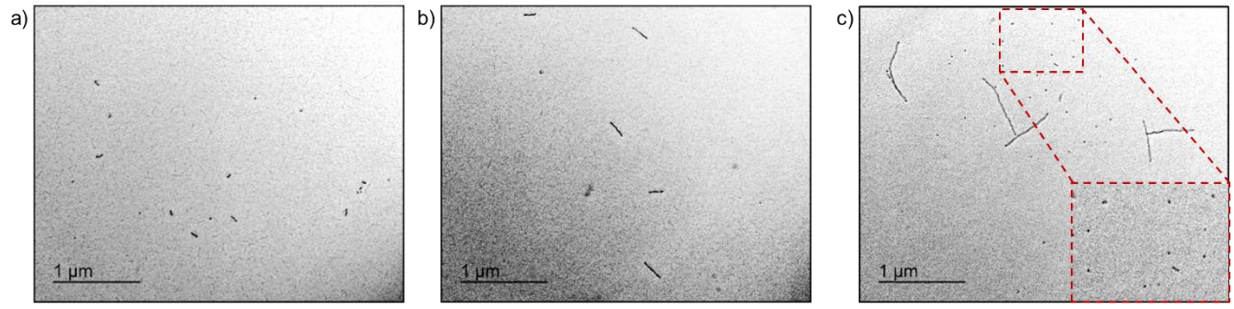

Figure S3.18. TEM images of P3HT$_{60}$-*b*-PPP$_{30}$ seeds that were diluted to 0.1 mg/mL using *n*BuAc and annealed at **(a)** 30 °C, **(b)** 35 °C and **(c)** 40 °C for 18 h at before being brought to 22 °C and aged at 22 °C for 24 h. **(c)** Inset shows small nanofiber fragments amongst elongated fibers.

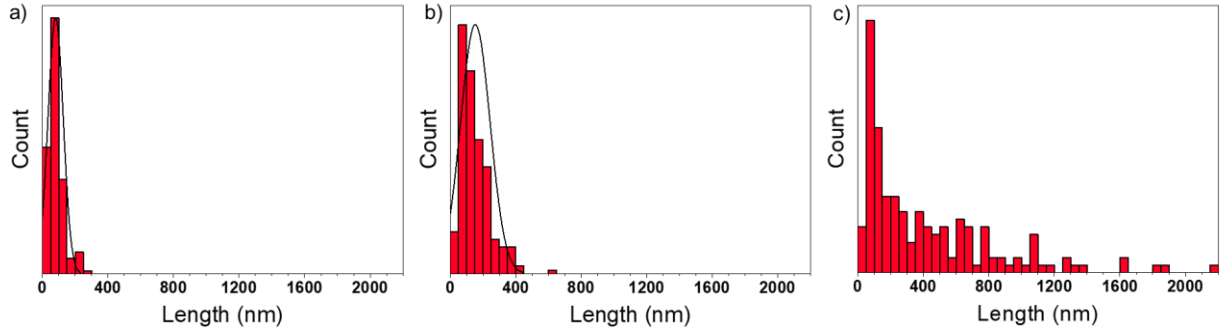

Figure S3.19. Histograms showing P3HT$_{60}$-*b*-PPP$_{30}$ nanofiber contour length distributions after annealing seeds at **(a)** 30 °C, **(b)** 35 °C and **(c)** 40 °C for 18 h and then cooled to 22 °C and aged at 22 °C for 24 h. **(a)** 30 °C: L_n = 81 nm, $Đ_L$ = 1.33, σ = ± 47. **(b)** 35 °C: L_n = 153 nm, $Đ_L$ = 1.35, σ = ± 90) (**c**) 40 °C: L_n = 417 nm, $Đ_L$ = 1.98, σ = ± 412.

P3HT$_{35}$-*b*-PPP$_{15}$ – Sonication Bath

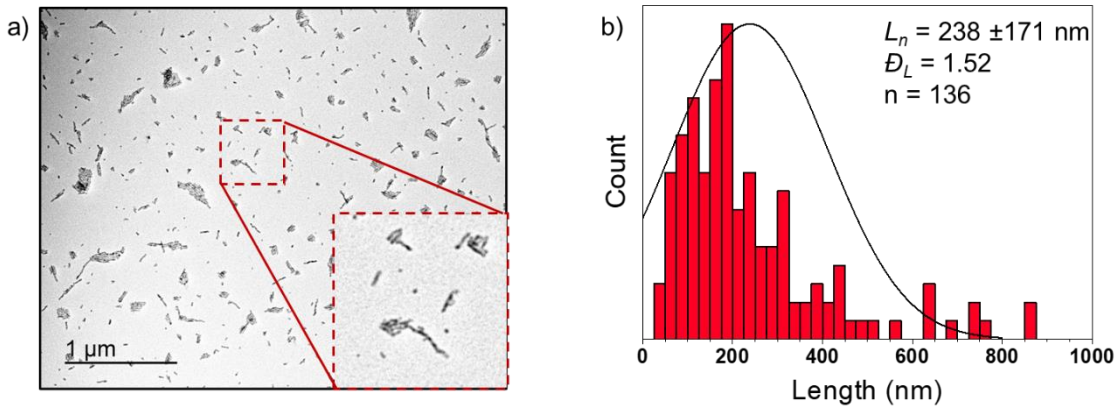

Figure S3.20. (a) TEM image of seeds formed from ultrasonication of a P3HT$_{35}$-*b*-PPP$_{15}$ polydisperse nanofiber solution (*n*BuAc, 1 mg/mL) in a 0 °C bath for 7 h (100% power). **(b)** Histogram showing the fiber length distribution of P3HT$_{35}$-*b*-PPP$_{15}$ seeds (L_n = 238 nm, L_w = 362 nm, $Đ_L$ = 1.52, σ = ± 171 nm, n = 136).

P3HT$_{35}$-*b*-PPP$_{15}$ – Sonotrode Probe: Annealed

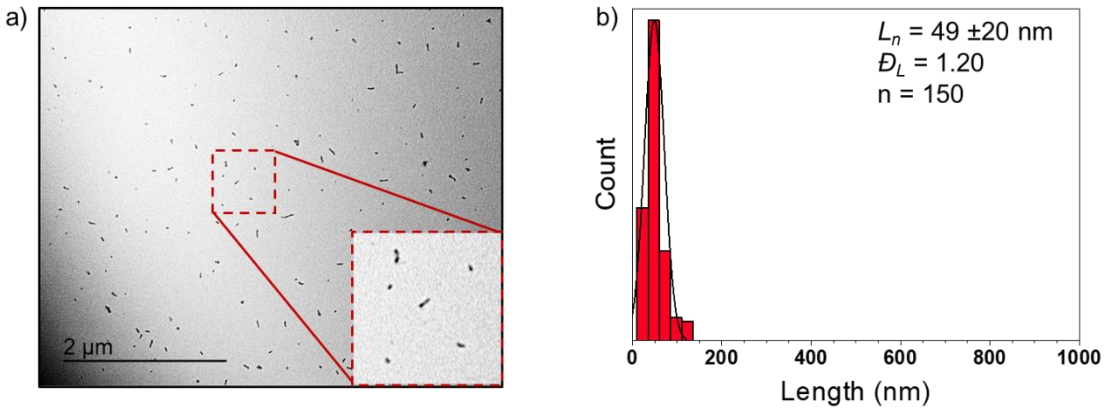

Figure S3.21. (a) TEM image of seeds formed from ultrasonication of a P3HT$_{35}$-*b*-PPP$_{15}$ polydisperse nanofiber solution (*n*BuAc, 1 mg/mL) at -45 °C using a sonotrode probe for 7 h (100% power). Seeds were annealed at 30 °C for 18 h prior to use. **(b)** Histogram showing the fiber length distribution of P3HT$_{35}$-*b*-PPP$_{15}$ seeds (L_n = 49 nm, L_w = 59 nm, $Đ_L$ = 1.20, σ = ± 20 nm, n = 150).

Attempted seeded growth of length-controlled P3HT$_{60}$-*b*-PPP$_{30}$ nanofibers at 22 °C using annealed seeds

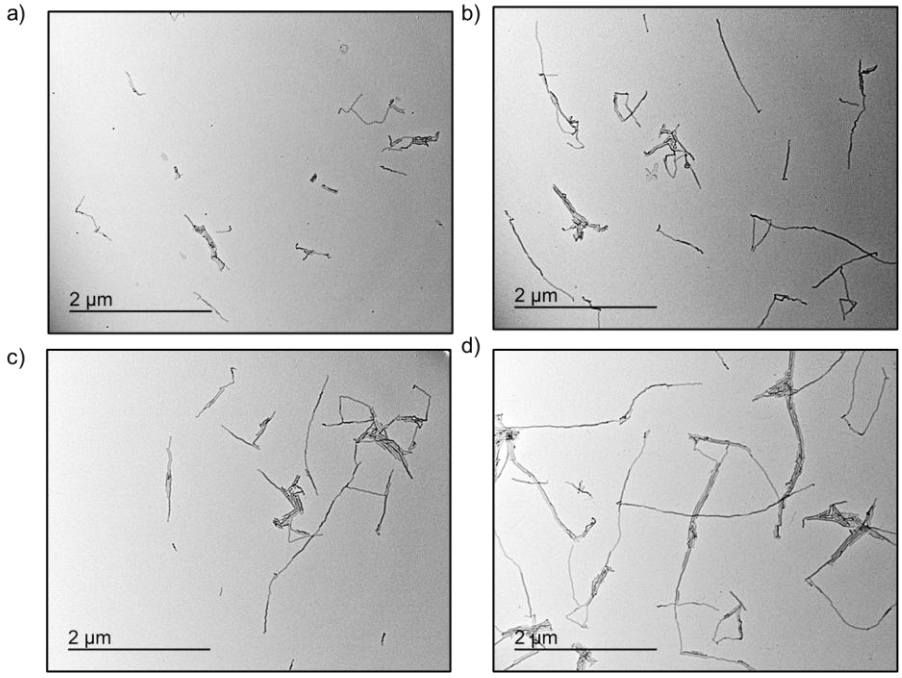

Figure S3.22. TEM images of P3HT$_{60}$-*b*-PPP$_{30}$ nanofibers in (*n*BuAc, 0.05 mg/mL) formed by living CDSA seeded growth using addition of **(a)** 1, **(b)** 2, **(c)** 3, and **(d)** 4 equivalents of P3HT$_{60}$-*b*-PPP$_{30}$ unimer solution (THF, 1 mg/mL) to P3HT$_{60}$-*b*-PPP$_{30}$ seeds (annealed, 30 °C, *n*BuAc, 0.1 mg/mL) at 22 °C. Solutions were aged at 22 °C for 24 h followed by solvent evaporation prior to TEM imaging.

Attempted seeded growth of length-controlled P3HT$_{35}$-*b*-PPP$_{15}$ nanofibers at 22 °C using annealed seeds

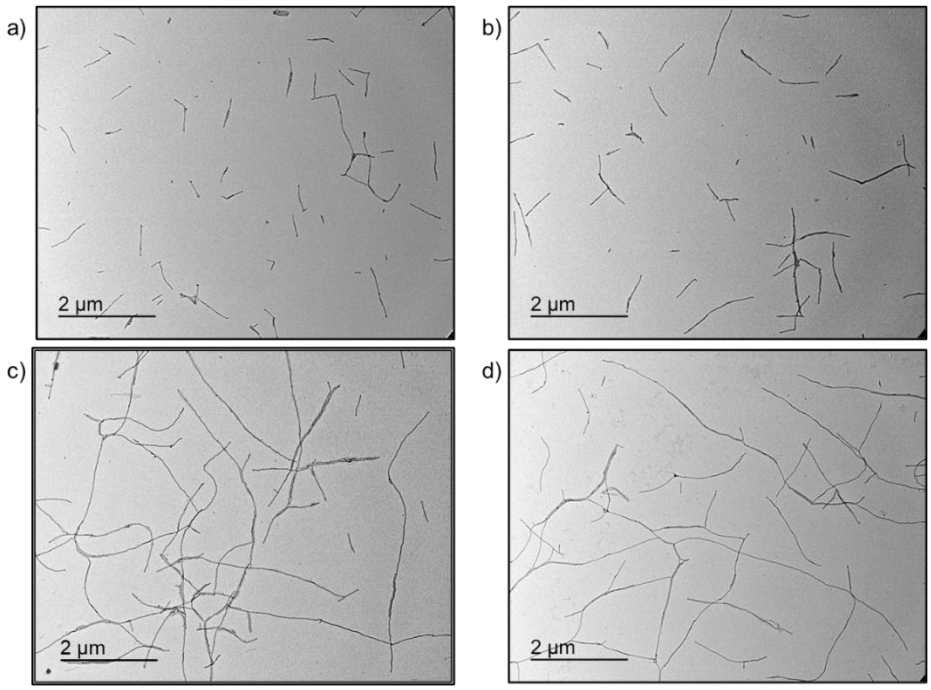

Figure S3.23. TEM images of P3HT$_{35}$-*b*-PPP$_{15}$ nanofibers in (*n*BuAc, 0.05 mg/mL) formed by living CDSA seeded growth using addition of **(a)** 1, **(b)** 2, **(c)** 3, and **(d)** 4 equivalents of P3HT$_{35}$-*b*-PPP$_{15}$ unimer solution (THF, 1 mg/mL) to P3HT$_{35}$-*b*-PPP$_{15}$ seed micelles (*n*BuAc, 0.1 mg/mL) at 22 °C. Solutions were aged at 22 °C for 24 h followed by solvent evaporation prior to TEM imaging.

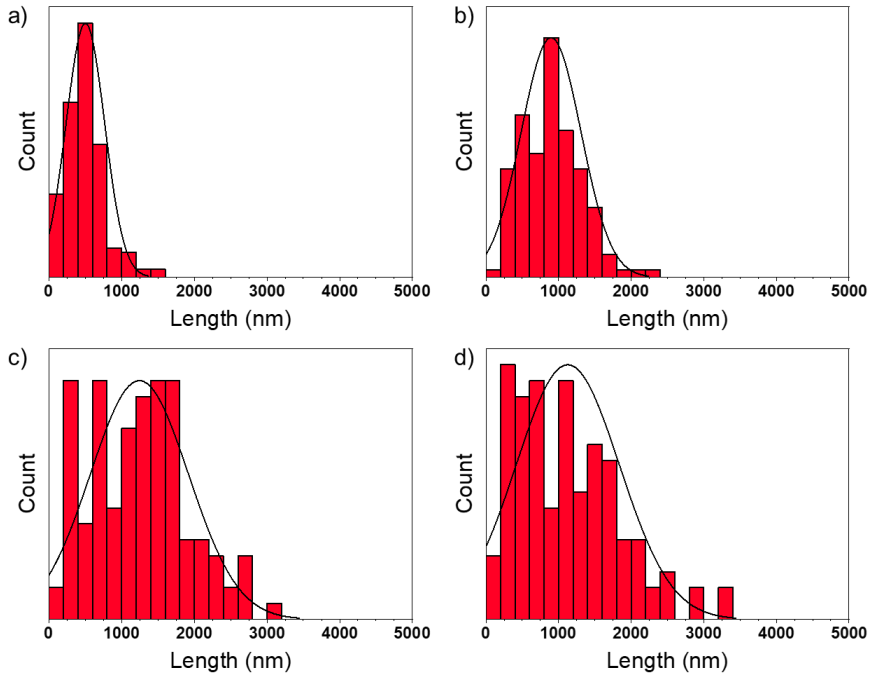

Figure S3.24. Histograms showing the nanofiber length distribution of P3HT$_{35}$-*b*-PPP$_{15}$ seed micelles (*n*BuAc, 0.1 mg/mL) that were treated with **(a)** 1, **(b)** 2, **(c)** 3, and **(d)** 4 equivalents of P3HT$_{35}$-*b*-PPP$_{15}$ unimer solution (1 mg/mL in THF) at 22 °C. Final concentrations were 0.05 mg/mL.

Table S3.1. Summary of data from seeded growth experiments of homogeneous P3HT$_{35}$-*b*-PPP$_{15}$ nanofibers at 22 °C. σ is standard deviation in L_n measurements.

m_{unimer}/m_{seed}	L_n	L_w	$Đ_L$	σ
Seeds	49	59	1.20	22
1	502	636	1.27	265
2	896	1084	1.21	411
3	1261	1677	1.33	731
4	1126	1565	1.39	708

Attempted self-nucleation suppressed seeded growth of P3HT$_{35}$-*b*-PPP$_{15}$ nanofibers at 50 °C

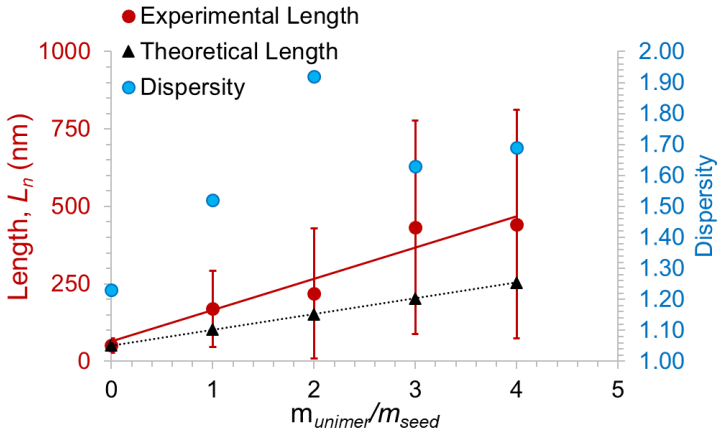

Figure S3.25. Plot showing the dependence of P3HT$_{35}$-*b*-PPP$_{15}$ nanofiber length (L_n) on unimer-to-seed ratio (m_{unimer}/m_{seed}) using self-nucleation suppressed seeded growth at 50 °C. Error bars represent standard deviation in L_n measurements.

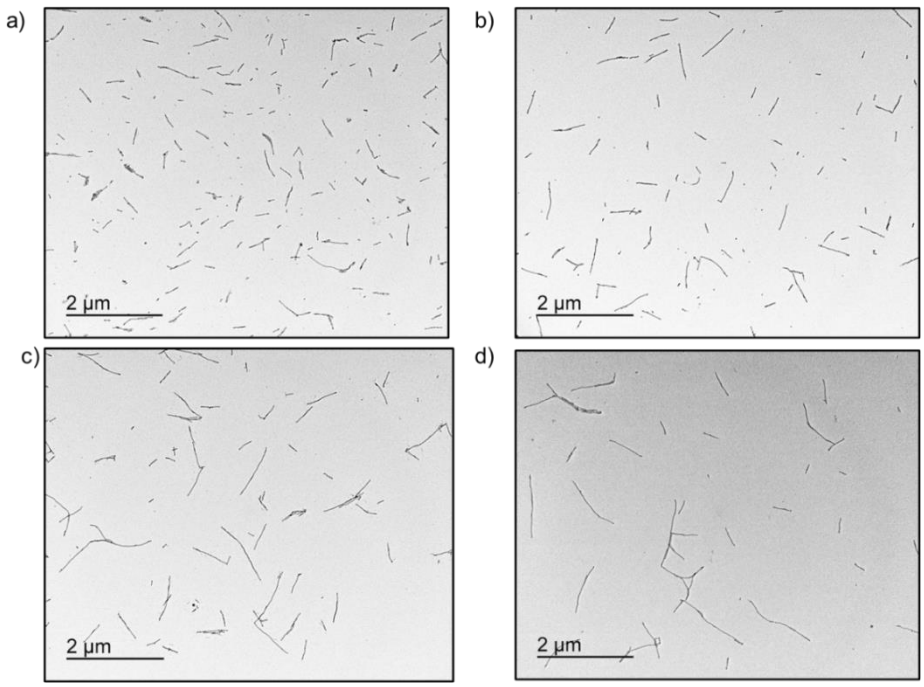

Figure S3.26. TEM images of P3HT$_{35}$-*b*-PPP$_{15}$ nanofibers in *n*BuAc (0.05 mg/mL) formed by self-nucleation suppressed seeded growth (50 °C) following solvent evaporation. Unimer-to-seed ratio m_{unimer}/m_{seed} = **(a)** 1, **(b)** 2, **(c)** 3, and **(d)** 4.

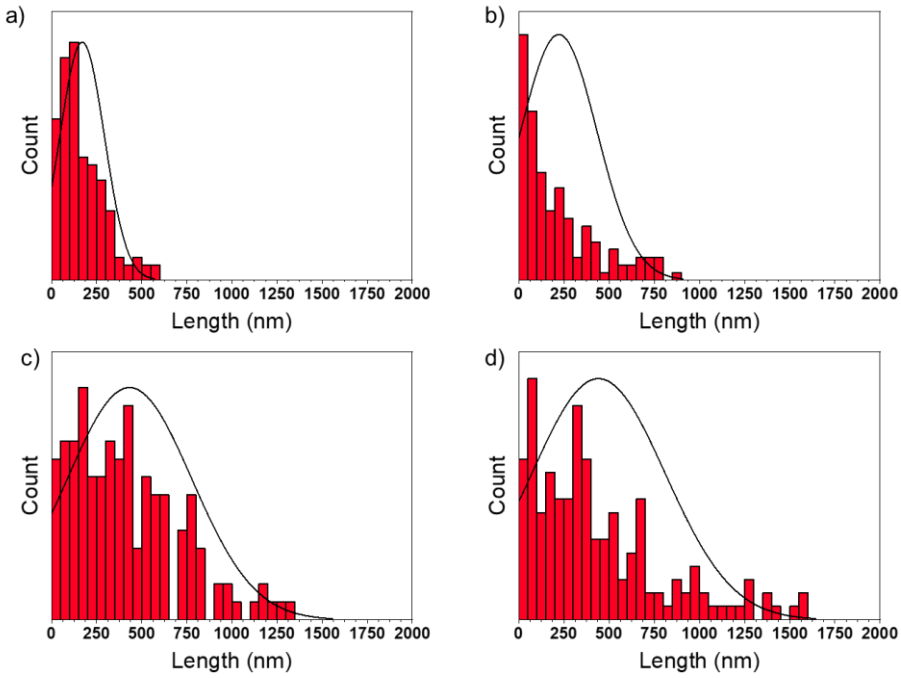

Figure S3.27. Histograms showing the nanofiber length distribution of $P3HT_{35}$-*b*-PPP_{15} nanofibers in *n*BuAc (0.05 mg/mL) formed by self-nucleation suppressed seeded growth (50 °C) following solvent evaporation. Unimer-to-seed ratio m_{unimer}/m_{seed} = **(a)** 1, **(b)** 2, **(c)** 3, and **(d)** 4. Final concentrations were 0.05 mg/mL.

Table S3.2. Summary of data from self-nucleation suppressed seeded growth experiments of homogeneous $P3HT_{35}$-*b*-PPP_{15} nanofibers (*n*BuAc, 0.1 mg/mL) at 50 °C. σ is standard deviation in L_n measurements.

m_{unimer}/m_{seed}	L_n	L_w	$Đ_L$	σ
Seeds	49	59	1.20	22
1	170	259	1.52	123
2	219	421	1.92	210
3	433	708	1.63	345
4	443	749	1.69	369

3.6 References

(1) MacFarlane, L. R.; Shaikh, H.; Garcia-Hernandez, J. D.; Vespa, M.; Fukui, T.; Manners, I. Functional Nanoparticles through π-Conjugated Polymer Self-Assembly. *Nat. Rev. Mater.* **2021**, *6* (1), 7–26. https://doi.org/10.1038/s41578-020-00233-4.

(2) Zhang, Y.; Tian, J.; Shaikh, H.; MacKenzie, H. K.; He, Y.; Zhao, C.; Lei, S.; Ren, Y.; Manners, I. Tailored Energy Funneling in Photocatalytic π-Conjugated Polymer Nanofibers for High-Performance Hydrogen Production. *J. Am. Chem. Soc.* **2023**, *145* (41), 22539–22547. https://doi.org/10.1021/jacs.3c07443.

(3) Li, X.; Wolanin, P. J.; MacFarlane, L. R.; Harniman, R. L.; Qian, J.; Gould, O. E. C. C.; Dane, T. G.; Rudin, J.; Cryan, M. J.; Schmaltz, T.; Frauenrath, H.; Winnik, M. A.; Faul, C. F. J. J.; Manners, I. Uniform Electroactive Fibre-like Micelle Nanowires for Organic Electronics. *Nat. Commun.* **2017**, *8* (1), 15909. https://doi.org/10.1038/ncomms15909.

(4) Jiang, Y.; McNeill, J. Light-Harvesting and Amplified Energy Transfer in Conjugated Polymer Nanoparticles. *Chem. Rev.* **2017**, *117* (2), 838–859. https://doi.org/10.1021/acs.chemrev.6b00419.

(5) Tuncel, D. π-Conjugated Nanostructured Materials: Preparation, Properties and Photonic Applications. *Nanoscale Adv.* **2019**, *1* (1), 19–33. https://doi.org/10.1039/c8na00108a.

(6) Sneyd, A. J.; Fukui, T.; Paleček, D.; Prodhan, S.; Wagner, I.; Zhang, Y.; Sung, J.; Collins, S. M.; Slater, T. J. A.; Andaji-Garmaroudi, Z.; MacFarlane, L. R.; Garcia-Hernandez, J. D.; Wang, L.; Whittell, G. R.; Hodgkiss, J. M.; Chen, K.; Beljonne, D.; Manners, I.; Friend, R. H.; Rao, A. Efficient Energy Transport in an Organic Semiconductor Mediated by Transient Exciton Delocalization. *Sci. Adv.* **2021**, *7* (32). https://doi.org/10.1126/sciadv.abh4232.

(7) Marszalek, T.; Li, M.; Pisula, W. Design Directed Self-Assembly of Donor-Acceptor Polymers. *Chem. Commun.* **2016**, *52* (73), 10938–10947. https://doi.org/10.1039/c6cc04523e.

(8) Ganda, S.; Stenzel, M. H. Concepts, Fabrication Methods and Applications of Living Crystallization-Driven Self-Assembly of Block Copolymers. *Prog. Polym. Sci.* **2020**, *101*, 101195. https://doi.org/10.1016/j.progpolymsci.2019.101195.

(9) MacFarlane, L.; Zhao, C.; Cai, J.; Qiu, H.; Manners, I. Emerging Applications for Living Crystallization-Driven Self-Assembly. *Chem. Sci.* **2021**, *12* (13), 4661–4682. https://doi.org/10.1039/d0sc06878k.

(10) Wang, X.; Guerin, G.; Wang, H.; Wang, Y.; Manners, I.; Winnik, M. A. Cylindrical Block Copolymer Micelles and Co-Micelles of Controlled Length and Architecture. *Science* **2007**, *317* (5838), 644–647. https://doi.org/10.1126/science.1141382.

(11) Shin, S.; Menk, F.; Kim, Y.; Lim, J.; Char, K.; Zentel, R.; Choi, T. L. Living Light-Induced Crystallization-Driven Self-Assembly for Rapid Preparation of Semiconducting Nanofibers. *J. Am. Chem. Soc.* **2018**, *140* (19), 6088–6094. https://doi.org/10.1021/jacs.8b01954.

(12) Zhu, Y.; Han, L.; Fan, H.; Wang, M.; Qi, R.; Zhao, Y.; He, F. Three-Dimensional Spirals of Conjugated Block Copolymers Driven by Screw Dislocation. *Macromolecules* **2020**, *53*,

3217–3223. https://doi.org/10.1021/acs.macromol.0c00071.

(13) Tao, D.; Feng, C.; Cui, Y.; Yang, X.; Manners, I.; Winnik, M. A.; Huang, X. Monodisperse Fiber-like Micelles of Controlled Length and Composition with an Oligo(p-Phenylenevinylene) Core via "Living" Crystallization-Driven Self-Assembly. *J. Am. Chem. Soc.* **2017**, *139* (21), 7136–7139. https://doi.org/10.1021/jacs.7b02208.

(14) Cui, Y.; Wang, Z.; Huang, X.; Lu, G.; Manners, I.; Winnik, M. A.; Feng, C. How a Small Change of Oligo(p-Phenylenevinylene) Chain Length Affects Self-Seeding of Oligo(p-Phenylenevinylene)-Containing Block Copolymers. *Macromolecules* **2020**, *53* (5), 1831–1841. https://doi.org/10.1021/acs.macromol.0c00068.

(15) Jin, S. M.; Kim, I.; Lim, J. A.; Ahn, H.; Lee, E. Interfacial Crystallization-Driven Assembly of Conjugated Polymers/Quantum Dots into Coaxial Hybrid Nanowires: Elucidation of Conjugated Polymer Arrangements by Electron Tomography. *Adv. Funct. Mater.* **2016**, *26* (19), 3226–3235. https://doi.org/10.1002/adfm.201504964.

(16) Kim, Y. J.; Cho, C. H.; Paek, K.; Jo, M.; Park, M. K.; Lee, N. E.; Kim, Y. J.; Kim, B. J.; Lee, E. Precise Control of Quantum Dot Location within the P3HT-b-P2VP/QD Nanowires Formed by Crystallization-Driven 1D Growth of Hybrid Dimeric Seeds. *J. Am. Chem. Soc.* **2014**, *136* (7), 2767–2774. https://doi.org/10.1021/ja410165f.

(17) Kamps, A. C.; Cativo, M. H. M.; Chen, X. J.; Park, S. J. Self-Assembly of DNA-Coupled Semiconducting Block Copolymers. *Macromolecules* **2014**, *47* (11), 3720–3726. https://doi.org/10.1021/ma500509u.

(18) Hicks, G. E. J.; Jarrett-Wilkins, C. N.; Panchuk, J. R.; Manion, J. G.; Seferos, D. S. Oxidation Promoted Self-Assembly of π-Conjugated Polymers. *Chem. Sci.* **2020**, *11* (25), 6383–6392. https://doi.org/10.1039/d0sc00806k.

(19) Xu, L.; Xu, X. H.; Liu, N.; Zou, H.; Wu, Z. Q. A Facile Synthetic Route to Multifunctional Poly(3-Hexylthiophene)-b-Poly(Phenyl Isocyanide) Copolymers: From Aggregation-Induced Emission to Controlled Helicity. *Macromolecules* **2018**, *51* (19), 7546–7555. https://doi.org/10.1021/acs.macromol.8b01478.

(20) Kynaston, E. L.; Gould, O. E. C.; Gwyther, J.; Whittell, G. R.; Winnik, M. A.; Manners, I. Fiber-Like Micelles from the Crystallization-Driven Self-Assembly of Poly(3-Heptylselenophene)-Block-Polystyrene. *Macromol. Chem. Phys.* **2015**, *216* (6), 685–695. https://doi.org/10.1002/macp.201400541.

(21) Zhang, Y.; Shaikh, H.; Sneyd, A. J.; Tian, J.; Xiao, J.; Blackburn, A.; Rao, A.; Friend, R. H.; Manners, I. Efficient Energy Funneling in Spatially Tailored Segmented Conjugated Block Copolymer Nanofiber-Quantum Dot or Rod Conjugates. *J. Am. Chem. Soc.* **2021**, *143* (18), 7032–7041. https://doi.org/10.1021/jacs.1c01571.

(22) Jin, X.-H.; Price, M. B.; Finnegan, J. R.; Boott, C. E.; Richter, J. M.; Rao, A.; Menke, S. M.; Friend, R. H.; Whittell, G. R.; Manners, I. Long-Range Exciton Transport in Conjugated Polymer Nanofibers Prepared by Seeded Growth. *Science* **2018**, *360* (3691), 897–900. https://doi.org/10.1126/science.aar8104.

(23) Han, L.; Fan, H.; Zhu, Y.; Wang, M.; Pan, F.; Yu, D.; Zhao, Y.; He, F. Precisely Controlled Two-Dimensional Rhombic Copolymer Micelles for Sensitive Flexible Tunneling Devices. *CCS Chem.* **2021**, *3* (5), 1399–1409. https://doi.org/10.31635/ccschem.020.202000297.

(24) Jin, S. M.; Hwang, J. H.; Lee, E. Crystallization-Driven Solution-State Assembly of Conjugated Block Copolymers in Materials Science. *Macromolecules* **2023**, *56* (10), 3474–3496. https://doi.org/10.1021/acs.macromol.3c00374.

(25) Kang, S.; Kim, G. H.; Park, S. J. Conjugated Block Copolymers for Functional Nanostructures. *Acc. Chem. Res.* **2022**, *55* (16), 2224–2234. https://doi.org/10.1021/acs.accounts.2c00244.

(26) Yu, W.; Foster, J. C.; Dove, A. P.; O'Reilly, R. K. Length Control of Biodegradable Fiber-Like Micelles via Tuning Solubility: A Self-Seeding Crystallization-Driven Self-Assembly of Poly(ϵ-Caprolactone)-Containing Triblock Copolymers. *Macromolecules* **2020**, *53* (4), 1514–1521. https://doi.org/10.1021/acs.macromol.9b02613.

(27) Gilroy, J. B.; Gädt, T.; Whittell, G. R.; Chabanne, L.; Mitchels, J. M.; Richardson, R. M.; Winnik, M. A.; Manners, I. Monodisperse Cylindrical Micelles by Crystallization-Driven Living Self-Assembly. *Nat. Chem.* **2010**, *2* (7), 566–570. https://doi.org/10.1038/nchem.664.

(28) Xu, L.; Wang, C.; Li, Y.-X.; Xu, X.; Zhou, L.; Liu, N.; Wu, Z.-Q. Crystallization-Driven Asymmetric Helical Assembly of Conjugated Block Copolymers and the Aggregation Induced White-Light Emission and Circularly Polarized Luminescence. *Angew. Chem. Int. Ed.* **2020**, *59* (38), 16675–16682. https://doi.org/10.1002/anie.202006561.

(29) Schmelz, J.; Schedl, A. E.; Steinlein, C.; Manners, I.; Schmalz, H. Length Control and Block-Type Architectures in Worm-like Micelles with Polyethylene Cores. *J. Am. Chem. Soc.* **2012**, *134* (34), 14217–14225. https://doi.org/10.1021/ja306264d.

(30) Mikhnenko, O. V.; Blom, P. W. M.; Nguyen, T. Q. Exciton Diffusion in Organic Semiconductors. *Energy Environ. Sci.* **2015**, *8* (7), 1867–1888. https://doi.org/10.1039/c5ee00925a.

(31) Sneyd, A. J.; Beljonne, D.; Rao, A. A New Frontier in Exciton Transport: Transient Delocalization. *J. Phys. Chem. Lett.* **2022**, *13* (29), 6820–6830. https://doi.org/10.1021/acs.jpclett.2c01133.

(32) Gwyther, J.; Gilroy, J. B.; Rupar, P. A.; Lunn, D. J.; Kynaston, E.; Patra, S. K.; Whittell, G. R.; Winnik, M. A.; Manners, I. Dimensional Control of Block Copolymer Nanofibers with a π-Conjugated Core: Crystallization-Driven Solution Self-Assembly of Amphiphilic Poly(3-Hexylthiophene)-b-Poly(2-Vinylpyridine). *Chem. Eur. J.* **2013**, *19* (28), 9186–9197. https://doi.org/10.1002/chem.201300463.

(33) Patra, S. K.; Ahmed, R.; Whittell, G. R.; Lunn, D. J.; Dunphy, E. L.; Winnik, M. A.; Manners, I. Cylindrical Micelles of Controlled Length with a π-Conjugated Polythiophene Core via Crystallization-Driven Self-Assembly. *J. Am. Chem. Soc.* **2011**, *133* (23), 8842–8845. https://doi.org/10.1021/ja202408w.

(34) Tritschler, U.; Gwyther, J.; Harniman, R. L.; Whittell, G. R.; Winnik, M. A.; Manners, I. Toward Uniform Nanofibers with a π-Conjugated Core: Optimizing the "Living" Crystallization-Driven Self-Assembly of Diblock Copolymers with a Poly(3-Octylthiophene) Core-Forming Block. *Macromolecules* **2018**, *51* (14), 5101–5113. https://doi.org/10.1021/acs.macromol.8b00488.

(35) Lee, I. H.; Amaladass, P.; Choi, T. L. One-Pot Synthesis of Nanocaterpillar Structures via

in Situ Nanoparticlization of Fully Conjugated Poly(p-Phenylene)-Block-Polythiophene. *Chem. Commun.* **2014**, *50* (59), 7945–7948. https://doi.org/10.1039/c4cc02787f.

(36) Zhu, Y.-Y.; Yin, T.-T.; Yin, J.; Liu, N.; Yu, Z.-P.; Zhu, Y.-W.; Ding, Y.-S.; Yin, J.; Wu, Z.-Q. Poly(3-Hexylthiophene)-Block-Poly(5,8-Di-p-Tolylquinoxaline-2,3-Diyl) Conjugated Rod-Rod Copolymers: One Pot Synthesis, Self-Assembly and Highly Selective Sensing of Cobalt. *RSC Adv.* **2014**, *4* (76), 40241–40250. https://doi.org/10.1039/c4ra06571a.

(37) Liu, N.; Qi, C. G.; Wang, Y.; Liu, D. F.; Yin, J.; Zhu, Y. Y.; Wu, Z. Q. Solvent-Induced White-Light Emission of Amphiphilic Rod-Rod Poly(3-Triethylene Glycol Thiophene)-Block-Poly(Phenyl Isocyanide) Copolymer. *Macromolecules* **2013**, *46* (19), 7753–7758. https://doi.org/10.1021/ma4016664.

(38) Yin, Y.; Chen, S.; Zhu, S.; Li, L.; Zhai, D.; Huang, D.; Peng, J. Tailoring Cocrystallization and Microphase Separation in Rod-Rod Block Copolymers for Field-Effect Transistors. *Macromolecules* **2021**, *54* (10), 4571–4581. https://doi.org/10.1021/acs.macromol.0c02788.

(39) Chen, J.; Wang, S.; Shi, G.; Wang, R.; Cai, S.; Zhang, J.; Wan, X. Amphiphilic Rod-Rod Block Copolymers Based on Phenylacetylene and 3,5-Disubstituted Phenylacetylene: Synthesis, Helical Conformation, and Self-Assembly. *Macromolecules* **2018**, *51* (19), 7500–7508. https://doi.org/10.1021/acs.macromol.8b01512.

(40) Kim, J.; Chung, W.; Kim, D.; Kang, J.; Grandes Reyes, C. F.; Jeong, J.; Kim, K. T. Semi-Conductive Micellar Networks of All-Conjugated Diblock and Triblock Copolymer Blends. *Chem. Commun.* **2023**, *59* (24), 3578–3581. https://doi.org/10.1039/d3cc00081h.

(41) Hwang, S.-H.; Kang, S.-Y.; Yang, S.; Lee, J.; Choi, T.-L. Synchronous Preparation of Length-Controllable 1D Nanoparticles via Crystallization-Driven in Situ Nanoparticlization of Conjugated Polymers. *J. Am. Chem. Soc.* **2022**, *144* (13), 5921–5929. https://doi.org/10.1021/jacs.1c13385.

(42) Bryan, Z. J.; McNeil, A. J. Conjugated Polymer Synthesis via Catalyst-Transfer Polycondensation (CTP): Mechanism, Scope, and Applications. *Macromolecules* **2013**, *46* (21), 8395–8405. https://doi.org/10.1021/ma401314x.

(43) Lee, I. H.; Amaladass, P.; Choi, I.; Bergmann, V. W.; Weber, S. A. L.; Choi, T. L. Preparing DNA-Mimicking Multi-Line Nanocaterpillars via in Situ Nanoparticlisation of Fully Conjugated Polymers. *Polym. Chem.* **2016**, *7* (7), 1422–1428. https://doi.org/10.1039/c5py01967b.

(44) Doubina, N.; Ho, A.; Jen, A. K. Y.; Luscombe, C. K. Effect of Initiators on the Kumada Catalyst Transfer Polycondensation Reaction. *Macromolecules* **2009**, *42* (20), 7670–7677. https://doi.org/10.1021/ma901410k.

(45) Miyakoshi, R.; Yokoyama, A.; Yokozawa, T. Importance of the Order of Successive Catalyst-Transfer Condensation Polymerization in the Synthesis of Block Copolymers of Polythiophene and Poly(p-Phenylene). *Chem. Lett.* **2008**, *37* (10), 1022–1023. https://doi.org/10.1246/cl.2008.1022.

(46) Wu, S.; Bu, L.; Huang, L.; Yu, X.; Han, Y.; Geng, Y.; Wang, F. Synthesis and Characterization of Phenylene-Thiophene All-Conjugated Diblock Copolymers. *Polymer.*

2009, *50* (26), 6245–6251. https://doi.org/10.1016/j.polymer.2009.11.001.

(47) Ceunen, W.; De Winter, J.; Gerbaux, P.; Koeckelberghs, G. Insights in the Ni-Thiophene Association in the Synthesis of Thiophene-Para-Phenylene Block Copolymers via Kumada Catalyst Transfer Condensative Polymerization. *Eur. Polym. J.* **2019**, *121* (September), 109311. https://doi.org/10.1016/j.eurpolymj.2019.109311.

(48) Liu, J.; Loewe, R. S.; McCullough, R. D. Employing MALDI-MS on Poly(Alkylthiophenes): Analysis of Molecular Weights, Molecular Weight Distributions, End-Group Structures, and End-Group Modifications. *Macromolecules* **1999**, *32* (18), 5777–5785. https://doi.org/10.1021/ma9905324.

(49) Tian, Y.; Kuzimenkova, M. V.; Halle, J.; Wojdyr, M.; Diaz De Zerio Mendaza, A.; Larsson, P. O.; Müller, C.; Scheblykin, I. G. Molecular Weight Determination by Counting Molecules. *J. Phys. Chem. Lett.* **2015**, *6* (6), 923–927. https://doi.org/10.1021/acs.jpclett.5b00296.

(50) Hayward, D. W.; Lunn, D. J.; Seddon, A.; Finnegan, J. R.; Gould, O. E. C.; Magdysyuk, O.; Manners, I.; Whittell, G. R.; Richardson, R. M. Structure of the Crystalline Core of Fiber-like Polythiophene Block Copolymer Micelles. *Macromolecules* **2018**, *51* (8), 3097–3106. https://doi.org/10.1021/acs.macromol.7b02552.

(51) Ge, J.; He, M.; Xie, N.; Yang, X.; Ye, Z.; Qiu, F. Microphase Separation and Crystallization in All-Conjugated Poly(3-Alkylthiophene) Diblock Copolymers. *Macromolecules* **2012**, *48* (1), 279–286. https://doi.org/10.1021/ma502321d.

(52) Shen, C.; Lee, Y.; Lee, Y.; Chiang, C.; Wei, F.; Wu, C.; Kau, K.; Liu, H.; Hsieh, C.; Wang, L.; Dai, C. Self-Organization and Phase Transformation of All π -Conjugated Diblock Copolymers and Its Applications in Organic Solar Cells. *React. Funct. Polym.* **2016**, *108*, 94–102. https://doi.org/10.1016/j.reactfunctpolym.2016.06.007.

(53) Ho, V.; Boudouris, B. W.; Segalman, R. A. Tuning Polythiophene Crystallization through Systematic Side Chain Functionalization. *Macromolecules* **2010**, *43* (19), 7895–7899. https://doi.org/10.1021/ma101697m.

(54) Himmelberger, S.; Duong, D. T.; Northrup, J. E.; Rivnay, J.; Koch, F. P. V.; Beckingham, B. S.; Stingelin, N.; Segalman, R. A.; Mannsfeld, S. C. B.; Salleo, A. Role of Side-Chain Branching on Thin-Film Structure and Electronic Properties of Polythiophenes. *Adv. Funct. Mater.* **2015**, *25* (17), 2616–2624. https://doi.org/10.1002/adfm.201500101.

(55) Kleinhenz, N.; Rosu, C.; Chatterjee, S.; Chang, M.; Nayani, K.; Xue, Z.; Kim, E.; Middlebrooks, J.; Russo, P. S.; Park, J. O.; Srinivasarao, M.; Reichmanis, E. Liquid Crystalline Poly(3-Hexylthiophene) Solutions Revisited: Role of Time-Dependent Self-Assembly. *Chem. Mater.* **2015**, *27* (7), 2687–2694. https://doi.org/10.1021/acs.chemmater.5b00635.

(56) Kleinhenz, N.; Persson, N.; Xue, Z.; Chu, P. H.; Wang, G.; Yuan, Z.; McBride, M. A.; Choi, D.; Grover, M. A.; Reichmanis, E. Ordering of Poly(3-Hexylthiophene) in Solutions and Films: Effects of Fiber Length and Grain Boundaries on Anisotropy and Mobility. *Chem. Mater.* **2016**, *28* (11), 3905–3913. https://doi.org/10.1021/acs.chemmater.6b01163.

(57) Jo, G.; Jung, J.; Chang, M. Controlled Self-Assembly of Conjugated Polymers via a Solvent Vapor Pre-Treatment for Use in Organic Field-Effect Transistors. *Polymers.* **2019**, *11* (2),

332. https://doi.org/10.3390/polym11020332.

(58) Chang, M.; Choi, D.; Wang, G.; Kleinhenz, N.; Persson, N.; Park, B.; Reichmanis, E. Photoinduced Anisotropic Assembly of Conjugated Polymers in Insulating Polymer Blends. *ACS Appl. Mater. Interfaces* **2015**, *7*, 14095−14103. https://doi.org/10.1021/acsami.5b03310.

(59) Rahimi, K.; Botiz, I.; Agumba, J. O.; Motamen, S.; Stingelin, N.; Reiter, G. Light Absorption of Poly(3-Hexylthiophene) Single Crystals. *RSC Adv.* **2014**, *4* (22), 11121–11123. https://doi.org/10.1039/c3ra47064d.

(60) Fukui, T.; Garcia-Hernandez, J. D.; MacFarlane, L. R.; Lei, S.; Whittell, G. R.; Manners, I. Seeded Self-Assembly of Charge-Terminated Poly(3-Hexylthiophene) Amphiphiles Based on the Energy Landscape. *J. Am. Chem. Soc.* **2020**, *142* (35), 15038–15048. https://doi.org/10.1021/jacs.0c06185.

(61) Davidson, E. C.; Beckingham, B. S.; Ho, V.; Segalman, R. A. Confined Crystallization in Lamellae Forming Poly(3-(2′-Ethyl)Hexylthiophene) (P3EHT) Block Copolymers. *J. Polym. Sci. Part B Polym. Phys.* **2016**, *54* (2), 205–215. https://doi.org/10.1002/polb.23904.

(62) Ji, E.; Pellerin, V.; Rubatat, L.; Grelet, E.; Bousquet, A.; Billon, L. Self-Assembly of Ionizable "Clicked" P3HT-b-PMMA Copolymers: Ionic Bonding Group/Counterion Effects on Morphology. *Macromolecules* **2017**, *50* (1), 235–243. https://doi.org/10.1021/acs.macromol.6b02101.

(63) Chen, W.; Lee, Y.; Chen, C.; Kau, K.; Lin, L.; Dai, C.; Wu, C.; Ho, K.; Wang, J.; Wang, L. Self-Assembled All-Conjugated Block Copolymer as an Effective Hole Conductor for Solid-State Dye-Sensitized Solar Cells. *ACS Nano* **2014**, *8* (2), 1254–1262. https://doi.org/10.1021/nn404346v.

(64) Erb, T.; Zhokhavets, U.; Gobsch, G.; Raleva, S.; Stühn, B.; Schilinsky, P.; Waldauf, C.; Brabec, C. J. Correlation between Structural and Optical Properties of Composite Polymer/Fullerene Films for Organic Solar Cells. *Adv. Funct. Mater.* **2005**, *15* (7), 1193–1196. https://doi.org/10.1002/adfm.200400521.

(65) Peng, R.; Zhu, J.; Pang, W.; Cui, Q.; Wu, F.; Liu, K.; Wang, M.; Pan, G. Thermal Annealing Effects on the Absorption and Structural Properties of Regioregular Poly(3-Hexylthiophene) Films. *J. Macromol. Sci. Part B* **2011**, *50* (3), 624–636. https://doi.org/10.1080/00222341003784741.

(66) Crassous, J.; Schurtenberger, P.; Ballauff, M.; Mihut, A. M. Design of Block Copolymer Micelles via Crystallization. *Polymer.* **2015**, *62*, A1–A13. https://doi.org/10.1016/j.polymer.2015.02.030.

(67) Qian, J.; Guerin, G.; Lu, Y.; Cambridge, G.; Manners, I.; Winnik, M. A. Self-Seeding in One Dimension: An Approach to Control the Length of Fiberlike Polyisoprene-Polyferrocenylsilane Block Copolymer Micelles. *Angew. Chem. Int. Ed.* **2011**, *50* (7), 1622–1625. https://doi.org/10.1002/anie.201006223.

(68) Tao, D.; Feng, C.; Lu, Y.; Cui, Y.; Yang, X.; Manners, I.; Winnik, M. A.; Huang, X. Self-Seeding of Block Copolymers with a π-Conjugated Oligo(p-Phenylenevinylene) Segment: A Versatile Route toward Monodisperse Fiber-like Nanostructures. *Macromolecules* **2018**, *51* (5), 2065–2075. https://doi.org/10.1021/acs.macromol.8b00046.

(69) Shaikh, H.; Jin, X. H.; Harniman, R. L.; Richardson, R. M.; Whittell, G. R.; Manners, I. Solid-State Donor-Acceptor Coaxial Heterojunction Nanowires via Living Crystallization-Driven Self-Assembly. *J. Am. Chem. Soc.* **2020**, *142* (31), 13469–13480. https://doi.org/10.1021/jacs.0c04975.

(70) MacFarlane, L. R.; Li, X.; Faul, C. F. J.; Manners, I. Efficient and Controlled Seeded Growth of Poly(3-Hexylthiophene) Block Copolymer Nanofibers through Suppression of Homogeneous Nucleation. *Macromolecules* **2021**, *54* (24), 11269–11280. https://doi.org/10.1021/acs.macromol.1c02005.

(71) Li, M.; Heng, Z.; Chen, Y.; Zou, H.; Liang, M. High Toughness Induced by Wormlike-Nanostructure in Epoxy Thermoset Containing Amphiphilic PDMS-PCL Block Copolymers. *Ind. Eng. Chem. Res.* **2018**, *57* (39), 13036–13047. https://doi.org/10.1021/acs.iecr.8b02336.

(72) Dean, J. M.; Verghese, N. E.; Pham, H. Q.; Bates, F. S. Nanostructure Toughened Epoxy Resins. *Macromolecules* **2003**, *36* (25), 9267–9674. https://doi.org/https://doi.org/10.1021/ma034807y.

(73) Liu, J.; Thompson, Z. J.; Sue, H. J.; Bates, F. S.; Hillmyer, M. A.; Dettloff, M.; Jacob, G.; Verghese, N.; Pham, H. Toughening of Epoxies with Block Copolymer Micelles of Wormlike Morphology. *Macromolecules* **2010**, *43* (17), 7238–7243. https://doi.org/10.1021/ma902471g.

(74) Gilroy, J. B.; Lunn, D. J.; Patra, S. K.; Whittell, G. R.; Winnik, M. A.; Manners, I. Fiber-like Micelles via the Crystallization-Driven Solution Self-Assembly of Poly(3-Hexylthiophene)-Block-Poly(Methyl Methacrylate) Copolymers. *Macromolecules* **2012**, *45* (14), 5806–5815. https://doi.org/10.1021/ma3008114.

(75) Kynaston, E. L.; Nazemi, A.; MacFarlane, L. R.; Whittell, G. R.; Faul, C. F. J. J.; Manners, I. Uniform Polyselenophene Block Copolymer Fiberlike Micelles and Block Co-Micelles via Living Crystallization-Driven Self-Assembly. *Macromolecules* **2018**, *51* (3), 1002–1010. https://doi.org/10.1021/acs.macromol.7b02317.

(76) Vespa, M.; Hudson, Z. M.; Manners, I. Homogeneous and Segmented Nanofibers with a Conjugated Poly[3-(2′-Ethylhexyl)Thiophene] Core via Living Crystallization-Driven Self-Assembly. *Macromolecules* **2024**, *57* (4), 1509–1520. https://doi.org/10.1021/acs.macromol.3c02357.

(77) Pangborn, A. B.; Giardello, M. A.; Grubbs, R. H.; Rosen, R. K.; Timmers, F. J. Safe and Convenient Procedure for Solvent Purification. *Organometallics* **1996**, *15* (5), 1518–1520. https://doi.org/10.1021/om9503712.

(78) Standley, E. A.; Smith, S. J.; Müller, P.; Jamison, T. F. A Broadly Applicable Strategy for Entry into Homogeneous Nickel(0) Catalysts from Air-Stable Nickel(II) Complexes. *Organometallics* **2014**, *33* (8), 2012–2018. https://doi.org/10.1021/om500156q.

(79) Schneider, C. A.; Rasband, W. S.; Eliceiri, K. W. NIH Image to ImageJ: 25 Years of Image Analysis. *Nat. Methods* **2012**, *9* (7), 671–675. https://doi.org/10.1038/nmeth.2089.

(80) Usta, H.; Alimli, D.; Ozdemir, R.; Tekin, E.; Alkan, F.; Kacar, R.; Altas, A. G.; Dabak, S.; Gürek, A. G.; Mutlugun, E.; Yazici, A. F.; Can, A. A Hybridized Local and Charge Transfer Excited State for Solution-Processed Non-Doped Green Electroluminescence Based on

Oligo(p-Phenyleneethynylene). *J. Mater. Chem. C* **2020**, *8* (24), 8047–8060. https://doi.org/10.1039/d0tc01266a.

Chapter 4

Exploring the self-assembly of amphiphilic poly(3-(2'-ethylhexyl)thiophene) (P3EHT) homopolymers with singly-charged termini

This chapter contains as of yet unpublished results.

Contributions:

Marcus Vespa, Dr. Tsz Shing Cheung, and Prof. Ian Manners conceived the project. Marcus Vespa and Dr. Tsz Shing Cheung synthesized the materials and jointly performed self-assembly experiments along with relevant characterization and data processing. Dr. Shixing Lei and Prof. Ian Manners contributed to data discussions. Marcus Vespa and Dr. Tsz Shing Cheung wrote the first draft of the manuscript.

4.1 Abstract

2-Dimensional (2D) semiconducting nanoparticles fabricated by π-conjugated polymer solution self-assembly have received intense interest due to their potential applications in optoelectronic devices arising from their novel electronic properties, but exerting control over their nanoscale morphology and size remains a major challenge. Previous research has shown that minimizing the corona-forming block volume fraction by functionalizing the core block termini with a positively charged functional group that acts as a solvophilic stabilizer is a promising method towards preferential formation of low interfacial curvature nanostructures such as 2D platelets. Herein, we describe the synthesis of a poly(3-(2'-ethylhexyl)thiophene) (P3EHT) homopolymer terminated with a positively charged phosphonium group ($[P3EHT_{23}\text{-}PPh_3]^+Br^-$) and discuss attempts to form area-controlled 2D nanoplatelets *via* living crystallization-driven self-assembly (CDSA). Large polydisperse 2D nanoribbons were successfully fabricated using various methodologies, marking the first example of 2D P3EHT nanostructures made by solution self-assembly; however, control over the platelet dimensionality was not achieved. Regardless, we found that we could exert excellent control over the dimensionality of 1D fibers and fabricated long (1-2 μm), length-controlled B-A-B and B-C-B triblock comicelles with low dispersity ($Đ_L \leq$ 1.1) by initiating growth using 1D seeds composed of $P3EHT_{23}$-*b*-PEG_{113} and $P3EHT_{19}$-*b*-$P2VP_{138}$, respectively. The modularity of these systems provides exciting opportunities for customizable nanostructure construction, as well as potential selective functionalization. Further, the ability of charged P3EHT homopolymers to form both 1D or 2D nanostructures dependent on the solvent system and growth initiator provides valuable insight into the self-assembly of π-conjugated charge-terminated polymeric amphiphiles.

4.2 Introduction

2-Dimensional (2D) semiconducting nanomaterials, such as graphene, have received enormous attention due to their electronic conductivity,[1] flat morphology,[2] and large surface area,[3] which make them particularly suited towards potential applications in organic photovoltaics. These features offer large domains to maximize light absorption, and the continuous nature of the conductive pathways presents fascinating possibilities for utilization in energy transfer applications. Their flat morphology makes them the able to fully cover the surface of a substrate, as opposed to 1D nanofiber films which often form an interwoven mat with gaps between fibers and inconsistent surface coverage. Recently, considerable progress has been made in fabricating 2D nanostructures using self-assembly of block copolymers (BCPs) with a π-conjugated core, with some examples achieving dimensional control.[1,4] Some notable cases of semiconducting conjugated polymer nanoparticles (CPNPs) include square,[5] rhombic/diamond,[1,6] ribbon-like,[7,8] and rectangular[2,4,9] assemblies. Despite these significant advances, reports on these materials are limited due to the relative infancy of the field and the lack of robust design principles presently available.

Crystallization-driven self-assembly (CDSA) of polymeric amphiphiles with a crystallizable core-forming block has been shown to produce morphologically uniform samples of 1D and 2D core-shell micelles. In particular, 2D assemblies are easily obtainable when using core-forming blocks such as poly(ferrocenyldimethylsilane) (PFS)[10–12] and poly(L-lactide) (PLLA);[12–14] however, fabrication of crystalline 2D architectures using polymeric amphiphiles with a π-conjugated core-forming block is considerably more challenging and has not produced similar results. Strong intermolecular π-π stacking dominates the self-assembly of π-conjugated BCPs leading to directional anisotropic growth primarily in the π-π stacking direction, causing a

preference to form 1D fibers over 2D platelets. To form a 2D structure, an additional driving force perpendicular to the π-π stacking direction, such as interchain packing of alkyl side chains, must be facilitated to promote lateral growth. The rate of crystallization in the alkyl chain packing direction must be comparable to the π-π stacking direction, although, the forces governing interdigitation of alkyl chains are typically comparatively weak relative to π-π stacking and can be easily interrupted by other factors, including conformation defects.[8] Another method that can be used to equalize both forces is inhibiting the rate of growth in the π-π stacking direction, thereby promoting formation of 2D nanostructures with equal length sides.

Living CDSA of BCPs with a crystallizable core-forming block is a convenient method to generate low length dispersity ($Đ_L$ < 1.1, where $Đ_L = L_w/L_n$) samples of 1D nanofibers and 2D platelets with controlled size and dimensions.[15–23] Living CDSA primarily consists of two self-assembly approaches: the seeded growth method and the self-seeding method. 1D fibers will be used in the following examples but the same methods apply to the fabrication of 2D structures. The seeded growth method uses addition of pre-existing seeds to initiate growth of length-controlled structures and begins with the formation of long polydisperse nanofibers by: 1) dissolving the BCP in a solvent that is suitable for both blocks (common solvent) and inducing crystallization of the insoluble core-forming block by adding solvent which selectively solvates the corona-forming block or 2) by heating the BCP in a temperature-dependent selective solvent that acts as a common solvent at high temperatures and a corona-selective solvent at ambient temperature.[16,24] The long fibers are subsequently fragmented using ultrasonication to generate "seed" micelle fragments with relatively low average lengths.[16,25] The seeds remain active towards the addition of molecularly dissolved BCP (unimer) in a good solvent for both blocks. This leads to epitaxial crystallization at the seed termini and creates nanostructures with final lengths that are

linearly correlated to the unimer-to-seed mass ratio (m_{unimer}/m_{seed}), allowing for variable and predictable nanofiber lengths to be achieved. This method also provides the ability to fabricate modular, segmented B-A-B triblock comicelles by adding unimer with the same core-forming block, but with a corona-forming block that is chemically distinct from that of the BCP used for the seed.

The second living CDSA method is termed thermal self-seeding. In this approach, the BCP is heated in a selective solvent to induce dissolution of the less crystalline regions of the seeds.[24,26–30] Seed dissolution generates free unimer which, upon cooling, crystallizes epitaxially *in situ* onto the termini of the surviving seeds resulting in length-controlled 1D structures. Higher self-seeding temperatures increases seed dissolution and release of unimer into solution, resulting in longer fibers upon cooling. There is an exponential relationship between the self-seeding temperature and the final nanofiber length, which makes accurate prediction of the final length and formation of short nanofibers difficult.[27,28] Furthermore, the temperature at which polymer crystals melt depends on their thermal history and sample crystallinity, so self-seeding temperatures are batch-dependent.[28,31–33]

One method that has previously been used to form 2D nanostructures involves minimization of the corona-forming block volume fraction by shortening coronal block length or introduction of a charged solubilizing group in place of the solvophilic corona-forming block, thereby reducing intercoronal chain repulsion and core-corona interfacial curvature.[12,13] Terminating PFS and PLLA crystalline homopolymers with a positively charged phosphonium group resulted in the formation of colloidally-stable 2D platelets of varying shapes;[12,13] however, when poly(3-hexylthiophene) (P3HT)[34] and poly(fluorenyltrimethylcarbonate) (PFTMC)[35] homopolymers were terminated using the same phosphonium end-group, the formation of 1D

nanofibers was preferred over 2D platelets. Even though self-assembly of charged-terminated P3HT did not result in 2D platelets, highly efficient seeded growth of 1D fibers was accomplished with lengths up to 2.8 μm and low dispersity ($Đ_L$ < 1.1).[34] Further studies revealed a notable stability of the P3HT-based fibers upon oxidation[34] and exceptionally high exciton diffusion lengths of ~350 nm,[36] suggesting that these structures are promising candidates for conductive nanowire and optoelectronic applications. P3EHT has been shown to have a slower crystallization rate compared to P3HT due to its enhanced solubility and the increased steric barrier towards crystallization associated with 2-ethylhexyl side chain inclusion.[37] As this slower crystallization rate may allow for a diminished face-to-face packing rate in the to π-π stacking direction, increased lateral growth and lamellar stacking could generate 2D platelets.[38] The reduced rate of unimer crystallization on the seed termini may also produce a micelle core with fewer crystalline defects, potentially eclipsing the impressive exciton diffusion lengths found in P3HT amphiphile-based fibers. Further to this, the lack of a bulky and electronically insulating corona-forming block such as poly(methyl methacrylate) (PMMA),[39] poly(dimethylsiloxane),[40] and poly(2-vinylpyridine) (P2VP)[41] could allow for closer association of the nanofiber cores once cast into a film, resulting in more efficient inter-fiber charge transfer and increased film conductivity.[24] The absence of a corona-forming block altogether prevents a "coronal poisoning" effect,[38,42] wherein the corona-forming block sterically obstructs the termini of the micelle core, which prevents micelle growth and changes the growth rate in both directions, leading to irregular structures. With all of this in mind, the following chapter explores the self-assembly of charge-terminated P3EHT species, $[P3EHT_{23}\text{-}PPh_3]^+Br^-$, and discusses attempts to form area-controlled 2D CPNPs. It also investigates the 1D growth capabilities of this polymer and its ability to form custom triblock comicelles of controlled lengths.

4.3 Results and Discussion

4.3.1 Synthesis of a charged polythiophene [P3EHT$_{23}$-PPh$_3$]$^+$Br$^-$

Previously, our group reported the synthesis of a phosphonium-terminated P3HT homopolymer by functionalization of the P3HT core-block with 4-(diphenyphosphino)phenylmagnesium chloride and subsequent quaternization of the phosphorus atom using iodomethane, but this method requires extensive purification to remove uncharged homopolymer and the phosphorus atom can potentially oxidize during the purification, making it unsusceptible to quaternization.[34] As a result, we explored an alternative synthetic pathway which directly appends a charged phosphonium group to the π-conjugated core block termini through a copper-catalyzed azide-alkyne cycloaddition (CuAAC) click reaction and doesn't require extensive purification. Firstly, the bromide functionality terminating the butyl chain in (4-bromobutyl)triphenylphosphonium bromide was converted to an azide group by treatment with sodium azide and the reaction success was determined by analysis using ^{1}H and ^{31}P NMR spectroscopy (Scheme 4.1, Figure S4.3, S4.5).

Scheme 4.1. Synthesis of (4-azidobutyl)triphenylphosphonium bromide. NaN_3 = sodium azide, H_2O = water, EtOH = ethanol.

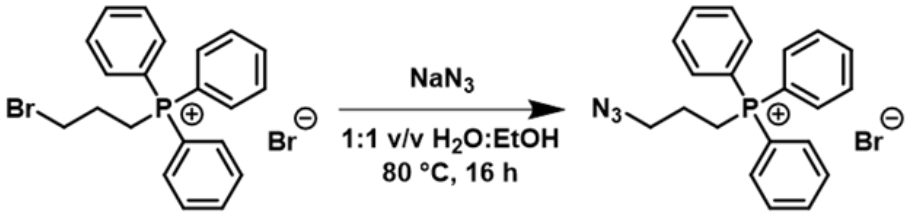

Following this, an alkyne terminated P3EHT$_{23}$ homopolymer was synthesized through GRIM polymerization of an *in situ* generated difunctional thiophene monomer using Ni(*o*-tolyl)(dppe)Cl as a catalyst followed by quenching with excess ethynylmagnesium bromide (M_n =

4,600 Da, $Đ_M = M_w/M_n$ = 1.08) where subscripts denote the polymer degree of polymerization (DP_n).[43] The DP_n of $P3EHT_{23}$ was determined by relative integration of ^1H NMR spectrum resonances (Figure S4.2) corresponding to the *ortho*-tolyl methyl group at 2.51 ppm and the proton in the 4-position on the thiophene rings at 6.94 ppm. Reaction of the azide-functionalized phosphonium species with the alkyne terminated $P3EHT_{23}$ *via* a CuAAC click reaction resulted in the desired $[P3EHT_{23}\text{-}PPh_3]^+Br^-$ material (M_n = 5,100 Da, $Đ_M$ = 1.07) (Scheme 4.2, S4.2) which was characterized by gel permeation chromatography (GPC) (Figure S4.1) and ^1H and ^{31}P NMR spectroscopy (Figure S4.4, S4.6). In the GPC chromatogram, the $[P3EHT_{23}\text{-}PPh_3]^+Br^-$ trace had a relatively lower retention volume compared to the $P3EHT_{23}$ homopolymer suggesting that the cycloaddition reaction formed a higher molecular mass species (Figure S4.1). ^1H NMR spectrometric analysis of the final product showed the presence of signals belonging to both the P3EHT block as well as the phosphonium group. Disappearance of the alkynyl singlet peak at 3.51 ppm in the ^1H NMR spectrum of the P3EHT homopolymer (Figure S4.2) indicates that this group no longer exists in the final structure following the cycloaddition reaction (Figure S4.4) and the peak representing the triazole ring proton appears at 8.25 ppm, confirming formation of this heterocycle.

Scheme 4.2. Synthesis of $[P3EHT_{23}\text{-}PPh_3]^+Br^-$ by the CuAAC reaction of alkyne-terminated P3EHT and (4-azidobutyl)triphenylphosphonium bromide. CuBr = copper(I) bromide, PMDETA = *N,N,N′,N″,N″*-pentamethyldiethylenetriamine, THF = tetrahydrofuran.

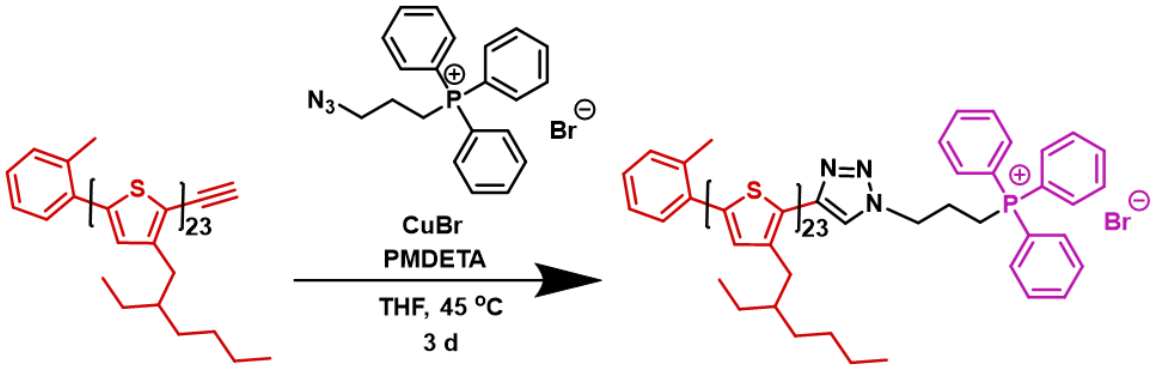

4.3.2 CDSA of [P3EHT$_{23}$-PPh$_3$]$^+$Br$^-$ into polydisperse 2D nanoribbons and attempts to form area-controlled structures from 2D seeds by seeded growth at 22 °C and self-seeding

Self-assembly was performed using two separate methods; the first method involved dissolving solid material in a common solvent (tetrahydrofuran, THF) and slowly adding a solvent selective for the positively charged phosphonium group (methanol, MeOH) while the second method involved a heating-cooling cycle in a temperature-dependant selective solvent, *n*-butanol (*n*BuOH) followed by addition of MeOH after cooling. Using the first self-assembly method, solid [P3EHT$_{23}$-PPh$_3$]$^+$Br$^-$ was dissolved in THF and MeOH was added dropwise with stirring to form a 1:3 v/v THF:MeOH mixture (0.1 mg/mL) followed by aging at 22 °C for 24 h which caused formation of an orange solution. Using the second self-assembly method, solid [P3EHT$_{23}$-PPh$_3$]$^+$Br$^-$ was heated to 90 °C for 30 min. in *n*BuOH (0.2 mg/mL), cooled to 22 °C slowly (ca. 4 h), and aged for 24 h at 22 °C which also formed an orange solution. After aging, an equivalent amount of deoxygenated MeOH was added to form a 1:1 v/v *n*BuOH:MeOH mixture (0.1 mg/mL) and enhance colloidal stability. The solutions were drop-cast onto a carbon-coated copper TEM grid and imaged using bright-field TEM following solvent evaporation. TEM analysis of both samples revealed the presence of polydisperse 2D [P3EHT$_{23}$-PPh$_3$]$^+$Br$^-$ nanoribbons that varied in length and width (Figure 4.1a, b), contrasting the solution self-assembly of an analogous phosphonium-terminated P3HT amphiphile of similar DP$_n$ that formed 1D nanofibers exclusively under self-nucleation conditions.[34] The ability of [P3EHT$_{23}$-PPh$_3$]$^+$Br$^-$ to preferentially form 2D ribbons over 1D fibers is proposed to be caused by the slower crystallization rate of P3EHT in the π-π stacking direction compared to P3HT. Reducing crystallization rate in the π-π stacking direction could be a guiding strategy towards fabrication of 2D CPNPs if the crystallization rate of the core forming block were lowered further by including a functional group with an even larger

steric barrier than a 2-ethylhexyl chain. Following nanoribbon formation, small platelet fragments that function as 2D seeds were produced by sonicating polydisperse $[P3EHT_{23}\text{-}PPh_3]^+Br^-$ nanoribbon solutions in 1:3 THF:MeOH (Figure 4.1a, c, S4.12a, b) (A_n = 8500 nm^2, $Đ_A$ = 1.81) ($Đ_A = A_w/A_n$) and 1:1 *n*BuOH:MeOH (Figure 4.1b, d, S4.14a, b) at 0 °C for 4 h, followed by annealing at 30 °C for 18 h (A_n = 7800 nm^2, $Đ_A$ = 2.07).

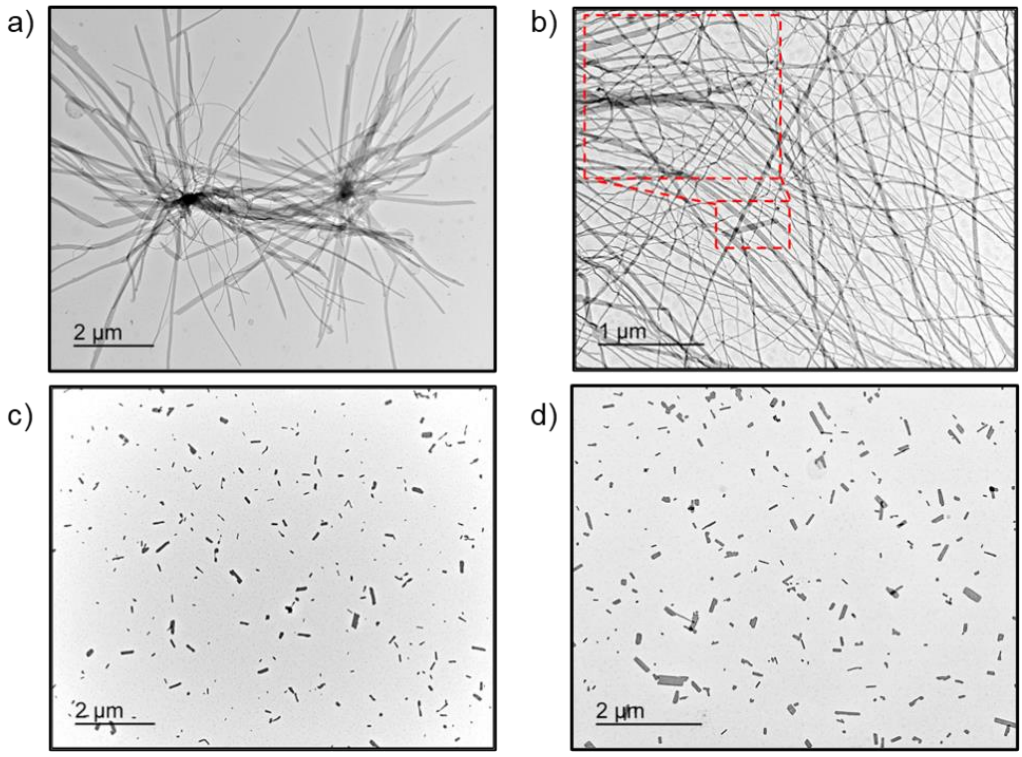

Figure 4.1. TEM images of polydisperse $[P3EHT_{23}\text{-}PPh_3]^+Br^-$ nanoribbons in **(a)** 1:3 THF:MeOH and **(b)** deoxygenated 1:1 *n*BuOH:MeOH following solvent evaporation. Inset in **(b)** shows 2D nature of fabricated nanostructures. 2D seed micelles formed by ultrasonication of polydisperse nanoribbons in **(c)** 1:3 THF:MeOH and **(d)** 1:1 *n*BuOH:MeOH.

To further characterize the nanoribbon dimensions, a 1:1 *n*BuOH:MeOH solution (0.05 mg/mL) of polydisperse $[P3EHT_{23}\text{-}PPh_3]^+Br^-$ nanoribbons prepared by self-nucleation (Figure 4.1b) was spin-cast onto a silicon substrate and analyzed using atomic force microscopy (AFM) (Figure S4.8a-c). Measurements were made perpendicular to the long axis of the ribbon and the

average height was found to be 13.0 nm ± 0.9 nm and the average width (W_n) was W_n = 167 nm ± 8.8 nm (Figure S4.8a-c). Unlike the packing in nanofibers wherein the long axis of the polymer chains is oriented parallel to the x-axis (Figure 4.2a) and the micelle height (y-axis) results from lamellar stacking through interdigitation, in 2D micelles the long axis of the polymer chains is oriented along the y-axis and the polymer DP_n constitutes the micelle height (y-axis) with lamellar stacking constituting the ribbon width (x-axis). Considering that the P3EHT unit cell contains a 3-(2'-ethylhexyl)thiophene dimer and the width of this unit along the polymer chain backbone is 7.72 Å,[44] a P3EHT polymer with a DP_n = 23 in its fully extended conformation would have a width of 8.9 nm, which is ~4 nm smaller than the measured platelet height here (13 nm). The phosphonium groups on the top and bottom of the platelet would also contribute to the height which may explain the discrepancy between the measurements. The distance between P3EHT chains in the alkyl chain stacking direction was found to be 1.51 nm in Chapter 2 and so the W_n = 167 nm measured here by AFM suggests that ~112 lamellae of P3EHT chains interdigitate in this direction to form the width of this ribbon (x-axis).

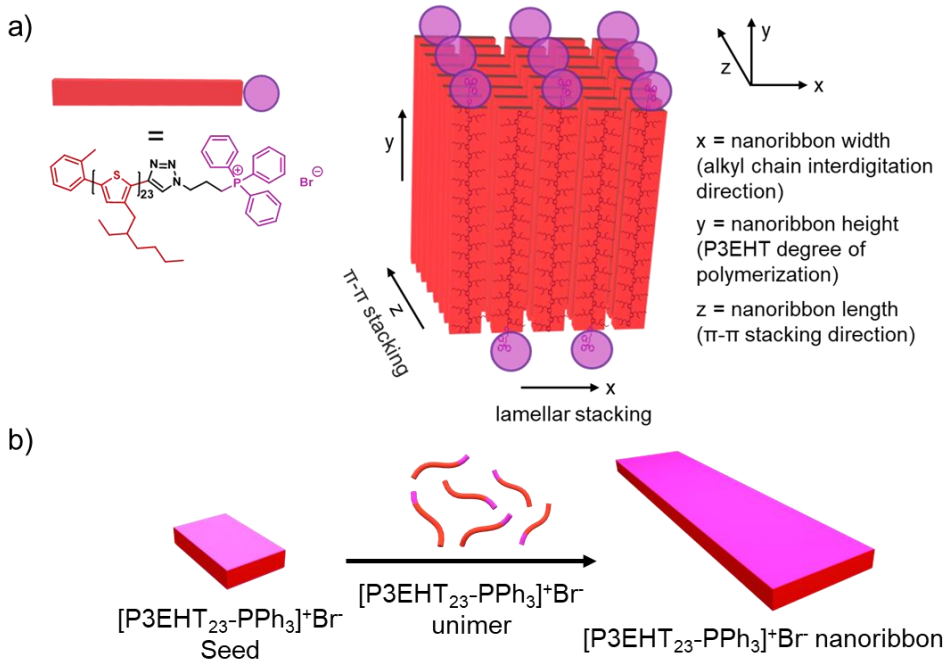

Figure 4.2. (a) Cartoon schematic showing the chain packing geometry (not drawn to scale and bromide anions excluded) and dimensions of a $[P3EHT_{23}\text{-}PPh_3]^+Br^-$ nanoribbon. **(b)** Cartoon schematic showing attempted seeded growth of nanoribbons upon addition of $[P3EHT_{23}\text{-}PPh_3]^+Br^-$ unimer to 2D $[P3EHT_{23}\text{-}PPh_3]^+Br^-$ seeds.

Next, seeded growth of area-controlled $[P3EHT_{23}\text{-}PPh_3]^+Br^-$ nanoplatelets in 1:3 THF:MeOH was attempted by adding increasing volumes of a stock solution of unimeric $[P3EHT_{23}\text{-}PPh_3]^+Br^-$ (THF, 1 mg/mL) to seed solutions in 1:3 THF:MeOH (Figure 4.1c) at 22 °C (Figure 4.2b). Unfortunately, at all unimer-to-seed ratios (m_{unimer}/m_{seed} = 5, 10, 15), no control over the dimensionality was achieved and TEM analysis of the resulting nanostructures revealed unpredictable growth as well as micelle aggregation and stacking, which is proposed to be a drying effect that occurs as solvent evaporates from the TEM grid following drop-casting (Figure S4.15a-f). Using the same seeded growth protocol with seeds in 1:1 *n*BuOH:MeOH (Figure 4.1d, S4.16a-f), similar results were observed but the micelles were found to be thinner and have more irregular edges compared to the trials carried out in 1:3 THF:MeOH suggesting that THF:MeOH mixture promotes more lamellar stacking compared to 1:1 *n*BuOH:MeOH.

Subsequently, experiments attempting to form uniform platelets *via* self-seeding were conducted by heating [P3EHT$_{23}$-PPh$_3$]$^+$Br$^-$ seeds in 1:1 *n*BuOH:MeOH (A_n = 7802 nm^2, $Đ_A$ = 2.07) (Figure S4.14) to self-seeding temperatures for 1 h before cooling directly to 22 °C over ca. 4 h. From 53 °C – 55 °C, no growth from the seeds was detected and dimensionally homogenous nanoplatelets were not observed (Figure S4.17a, b). When solutions were heated to 57 °C or 59 °C, branched micelles were observed along with a small fraction of large-area nanoplatelets (Figure S4.17c, d). Micelle branching may be caused by the exposure of core faces to the solvent due to the lack of steric protection provided by the phosphonium group, leading to a higher incidence of crystalline defects and screw dislocations. Heating to ≥61 °C led to full seed dissolution as only polydisperse nanoribbons were observed after cooling to 22 °C (Figure S4.17e).

Although control over the 2D platelet area was not achieved using these methods, formation of 2D nanostructures from π-conjugated materials in general is rare,[1,5,7,8,45,46] and the nanoribbons formed here are the first example of 2D P3EHT structures made by solution self-assembly. In-depth analysis of the CPNP photophysical and optoelectronic properties is necessary to evaluate the energy transfer processes which underly exciton diffusion and determine their suitability towards application in optoelectronic devices. As an example, 1D nanostructures formed by living CDSA display excellent exciton diffusion lengths;[23,36] however, in these cases, exciton diffusion is largely restricted to one bidirectional axis (the long axis of the fiber). Exciton diffusion mechanisms and directionality through 2D semiconductive nanostructures has just begun to be understood and many questions remain about the behaviour of charged quasiparticles in 2D materials.[47] It is not clear if excitons diffuse along the perpendicular directions of π–π stacking and lamellar stacking in these systems, nor is it clear if the increased potential pathways for excitons to diffuse creates materials with different energy transport capabilities compared to diffusion

through the core of a fiber. Investigation of these fundamental processes by using 1D and 2D CPNPs made from living CDSA as model systems could provide valuable insight to numerous physical and chemical fields, leading to a more complete understanding of their photophysical behaviour and better-informed material design. Additionally, this evidence suggests that inclusion of a more sterically demanding alkyl chain promotes 2D platelet formation and further exploring the extent of this strategy by modifying the polymer structure may lead to polymeric materials that improve access to semiconductive 2D CPNPs.

4.3.3 Fabrication of length-controlled B-A-B ($[P3EHT_{23}\text{-}PPh_3]^+Br^-$-*m*-$P3EHT_{23}$-*b*-$PEG_{113}$-*m*-$[P3EHT_{23}\text{-}PPh_3]^+Br^-$) and B-C-B ($[P3EHT_{23}\text{-}PPh_3]^+Br^-$-*m*-$P3EHT_{19}$-*b*-$P2VP_{138}$-*m*-$[P3EHT_{23}\text{-}PPh_3]^+Br^-$) triblock comicelles by seeded growth at 22 °C

Due to the difficulties obtaining uniform 2D platelets using seeded growth and self-seeding with 2D $[P3EHT_{23}\text{-}PPh_3]^+Br^-$ seeds, we attempted to use 1D seeds to seed growth of 2D area-controlled micelles, which has been successful previously with PFS-based materials.[12] To 1D $P3EHT_{23}$-*b*-PEG_{113} seeds in 1:1 *n*BuOH:MeOH (L_n = 77, $Đ_L$ = 1.19), increasing amounts of a stock $[P3EHT_{23}\text{-}PPh_3]^+Br^-$ unimer solution (THF, 1 mg/mL) was added at 22 °C and area-controlled 2D platelets were not recovered; however, we surprisingly formed 1D B-A-B triblock comicelles ($[P3EHT_{23}\text{-}PPh_3]^+Br^-$-*m*-$P3EHT_{23}$-*b*-$PEG_{113}$-*m*-$[P3EHT_{23}\text{-}PPh_3]^+Br^-$) (*m* = micelle segment) with a continuous P3EHT core and a PEG corona located in the central "A" block and $[P3EHT_{23}\text{-}PPh_3]^+Br^-$ terminal "B" regions (Figure 4.3). The B-A-B triblock comicelle lengths increased linearly with the unimer-to-seed ratio (m_{unimer}/m_{seed} = 5–40) with lengths ranging from L_n = 364 to L_n = 1715 nm and low $Đ_L \leq 1.07$ (Figure 4.3, 4.4, S4.18-S4.20, Table S4.2). The production of fibers with low dispersities, high lengths up to 1700 nm, and experimental lengths commensurate

with theoretical values demonstrates the substantial control exerted over the growth of [P3EHT$_{23}$-PPh$_3$]$^+$Br$^-$ from 1D P3EHT$_{23}$-*b*-PEG$_{113}$ seeds.

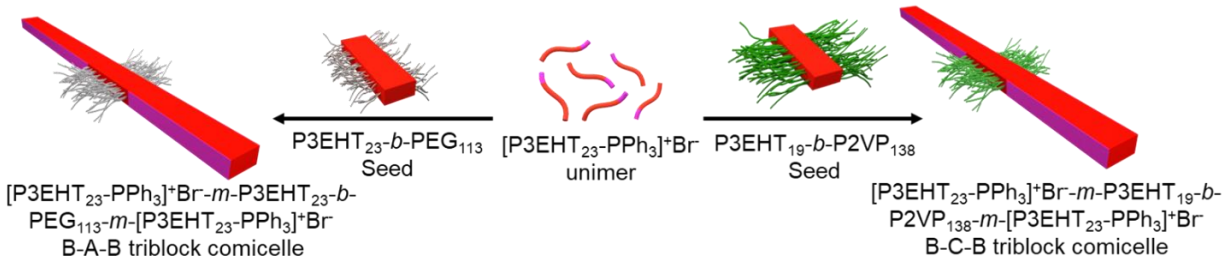

Figure 4.3. Formation of 1D B-A-B ([P3EHT$_{23}$-PPh$_3$]$^+$Br$^-$-*m*-P3EHT$_{23}$-*b*-PEG$_{113}$-*m*-[P3EHT$_{23}$-PPh$_3$]$^+$Br$^-$) comicelles (left) by addition of [P3EHT$_{23}$-PPh$_3$]$^+$Br$^-$ unimer to P3EHT$_{23}$-*b*-PEG$_{113}$ seeds and 1D B-C-B ([P3EHT$_{23}$-PPh$_3$]$^+$Br$^-$-*m*-P3EHT$_{19}$-*b*-P2VP$_{138}$-*m*-[P3EHT$_{23}$-PPh$_3$]$^+$Br$^-$) comicelles (right) by addition of [P3EHT$_{23}$-PPh$_3$]$^+$Br$^-$ unimer to P3EHT$_{19}$-*b*-P2VP$_{138}$ seeds.

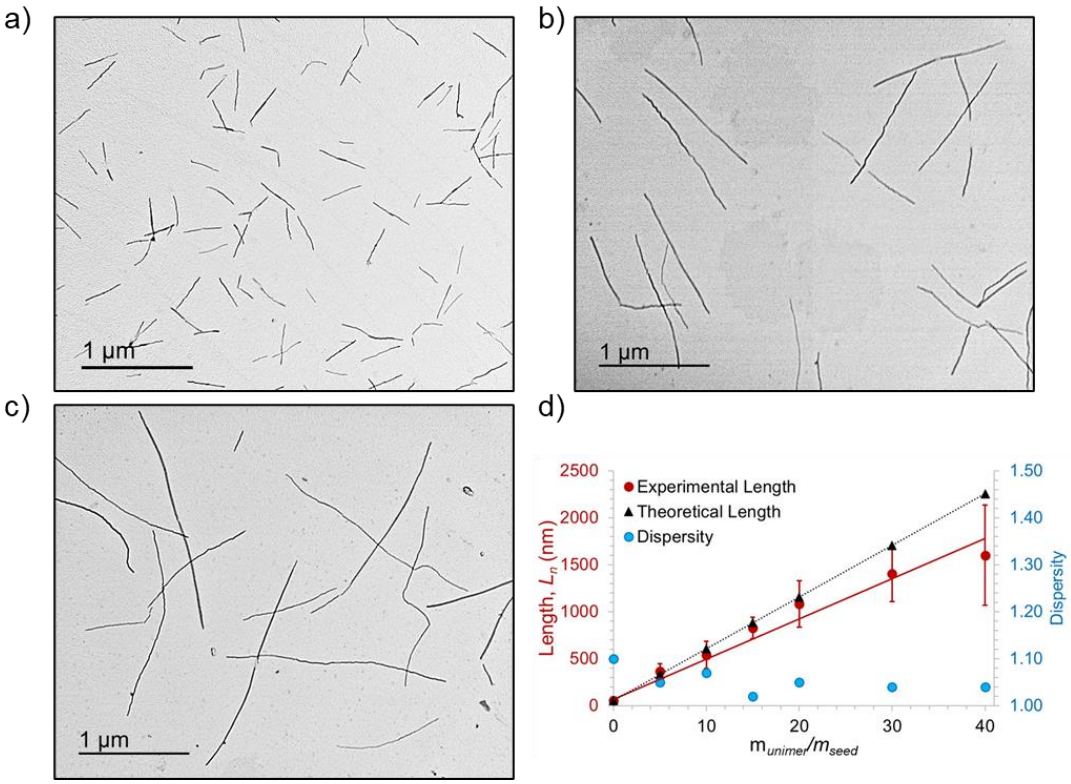

Figure 4.4. TEM images of length-controlled B-A-B ([P3EHT$_{23}$-PPh$_3$]$^+$Br$^-$-*m*-P3EHT$_{23}$-*b*-PEG$_{113}$-*m*-[P3EHT$_{23}$-PPh$_3$]$^+$Br$^-$) triblock comicelles prepared by the addition of [P3EHT$_{23}$-PPh$_3$]$^+$Br$^-$ unimer (THF, 1 mg/mL) to P3EHT$_{23}$-*b*-PEG$_{113}$ seeds solutions (L_n = 77 nm, 1:1 *n*BuOH:MeOH) at 22 °C with m_{unimer}/m_{seed} = **(a)** 5, **(b)** 20, and **(c)** 40. **(d)** Plot showing the linear dependence of B-A-B nanofiber length (L_n) on unimer-to-seed ratio (m_{unimer}/m_{seed}).

Finally, we expanded on the scope of the seeded growth experiments by fabricating B-C-B triblock comicelles ([P3EHT$_{23}$-PPh$_3$]$^+$Br$^-$-*m*-P3EHT$_{19}$-*b*-P2VP$_{138}$-*m*-[P3EHT$_{23}$-PPh$_3$]$^+$Br$^-$) with a continuous P3EHT core and a P2VP corona located in the central "C" block and [P3EHT$_{23}$-PPh$_3$]$^+$Br$^-$ terminal "B" regions. Increasing amounts of stock [P3EHT$_{23}$-PPh$_3$]$^+$Br$^-$ unimer solution (THF, 1 mg/mL) was added to 1D P3EHT$_{19}$-*b*-P2VP$_{138}$ seed solutions (*n*BuOH, 0.05 mg/mL, L_n = 38 nm, $Đ_L$ = 1.24) (Figure 4.5) at 22 °C resulting in the formation of triblock comicelles with lengths ranging from L_n = 293 to L_n = 1089 nm and $Đ_L \leq 1.13$ (Figure 4.3, 4.5, S4.21-23, Table S4.3) that increased linearly with the unimer-to-seed ratio (m_{unimer}/m_{seed} = 5–30). The segmented coronal structure of these nanofibers confers the ability to spatially localize different functionality on the nanofiber and the positively-charged terminal blocks provides exciting opportunities for tailored functionalization with inorganic quantum dots for energy transfer studies within hybrid organic-inorganic assembllies,[48] attachment to surfaces for surface-confined nanofiber growth,[49] as well as selective chemical detection.[7,50–52]

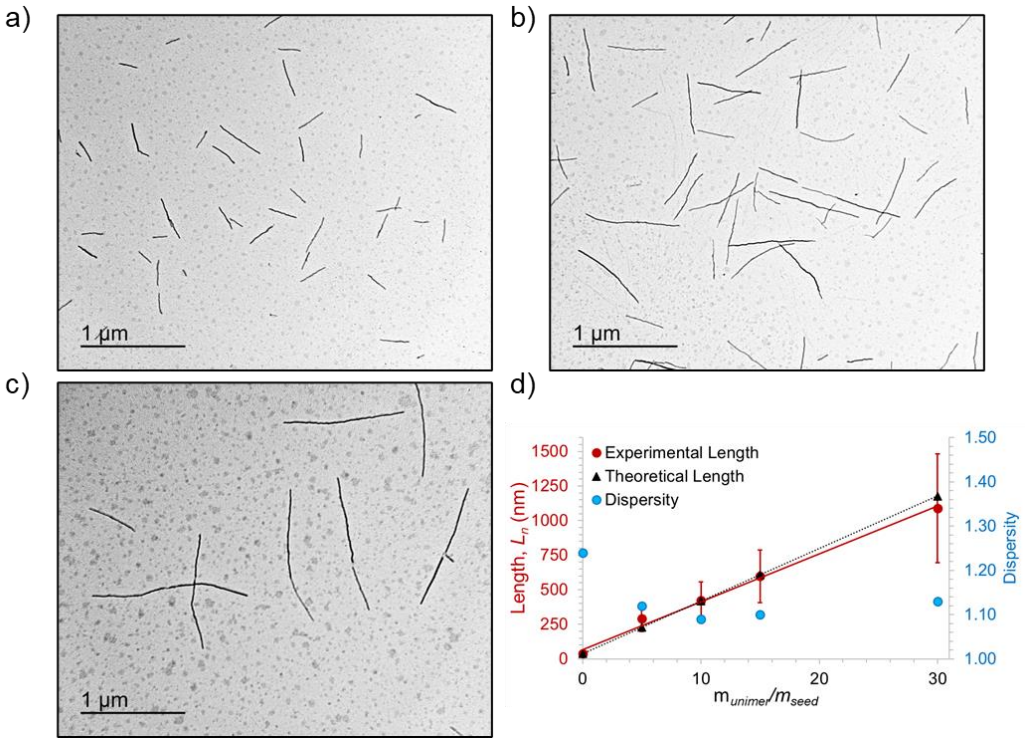

Figure 4.5. TEM images of length-controlled B-C-B ($[P3EHT_{23}\text{-}PPh_3]^+Br^-$-*m*-$P3EHT_{19}$-*b*-$P2VP_{138}$-*m*-$[P3EHT_{23}\text{-}PPh_3]^+Br^-$) triblock comicelles made by addition of $[P3EHT_{23}\text{-}PPh_3]^+Br^-$ unimer (THF, 1 mg/mL) to $P3EHT_{19}$-*b*-$P2VP_{138}$ seeds solutions (L_n = 38 nm, *n*BuOH) at 22 °C with m_{unimer}/m_{seed} = **(a)** 5, **(b)** 15, and **(c)** 30. **(d)** Plot showing the dependence of B-C-B nanofiber length (L_n) on unimer-to-seed ratio (m_{unimer}/m_{seed}).

4.4 Conclusions and Summary

This work investigates the self-assembly behaviour of charge terminated P3EHT species and illustrates that the nanostructural morphology of $[P3EHT_{23}\text{-}PPh_3]^+Br^-$ CPNPs can be tuned from a 2D to 1D architecture depending on the self-assembly conditions and growth initiator. Self-nucleation induced growth of 2D $[P3EHT_{23}\text{-}PPh_3]^+Br^-$ nanoribbons was achieved, marking the first example of 2D P3EHT nanostructures made by solution self-assembly. In striking contrast to a charge-terminated P3HT analogue, preferential formation of 2D nanostructures using charge-terminated P3EHT-based materials is proposed to be due to the slower crystallization of P3EHT compared to P3HT and the increased steric barrier associated with inclusion of a 2-ethylhexyl chain. The preferential formation of 2D CPNPs over 1D CPNPS when a P3EHT core-forming block was used instead of P3HT suggests that reducing the crystallization rate in the π-π stacking direction may be a practical methodology towards fabrication of 2D structures from π-conjugated polymeric amphiphiles. Length-controlled B-A-B and B-C-B triblock comicelles with low dispersity were also fabricated *via* seeded growth and the segmented and heterogeneous nature of the micelle provides opportunities for selective attachment of quantum dots and energy transfer studies. Further, the modularity of this nanofiber system provides promising opportunities for energy-funneling and selective surface attachment applications.

4.5 Supporting Information

4.5.1 Methods

Materials

All reagents used for polymers synthesis were of reagent grade and were used as received unless otherwise stated. All air-free chemistry was performed in a dinitrogen-filled (N_2) MBraun 200B glovebox equipped with a cold-well or using a dinitrogen Schlenk line using standard techniques. 3-bromothiophene (97%), (2-ethylhexyl)magnesium bromide (1.0M in diethyl ether), ethynylmagnesium bromide (0.5M in THF), 1,2-bis(diphenylphosphino)propane dichloronickel(II) (Ni(dppp)Cl_2), (3-bromopropyl)triphenylphosphonium bromide, sodium azide, and isopropylmagnesium chloride – lithium chloride (*i*PrMgCl•LiCl) (1.3M in THF) were purchased from Millipore Sigma. *N*-Bromosuccinimide (NBS) was recrystallized from boiling water prior to use[53] and Ni(*o*-tolyl)(dppe)Cl was synthesized as previously reported.[54] 3-(2'-ethylhexyl)thiophene and 2,5-dibromo-3-(2'-ethylhexyl)thiophene were synthesized as previously reported.[37] Copper(I) bromide (CuBr) was purified by suspending in glacial acetic acid, filtering and washing with copious amounts of absolute ethyl alcohol then anhydrous ethyl ether followed by drying in a vacuum oven at 80 °C for three days and stored under nitrogen.[55] *N,N,N′,N″,N‴*-pentamethyldiethylenetriamine (PMDETA) was degassed prior to use using 3 freeze-pump-thaw cycles and stored under an N_2 atmosphere. Solvents were dried and deoxygenated using a Solvent Purification System (SPS).[56] Self-assembly experiments were performed using HPLC grade solvents and the solvents were filtered through a 0.2 μm poly(tetrafluoroethylene) membrane.

Nuclear Magnetic Resonance (NMR)

^{1}H NMR spectra were obtained with a Bruker 500 MHz spectrometer; chemical shifts were referenced to the residual proteosolvent peak ($CHCl_3$, δ = 7.26 ppm).

Gel Permeation Chromatography (GPC)

GPC was conducted using a Malvern Omnisec Resolve/Reveal equipped with a triple detector array, automatic sampler, pump, injector, inline degasser column oven (set at 35 °C), elution columns consisting of styrene/divinylbenzene gels (of pore size 500–5,000 Å), refractometer, four capillary differential viscometer, UV/Vis detector (λ = 440 nm) and dual angle laser light scattering detector (7° and 90°). GPC grade THF with 1 wt% triethylamine was used as the eluent, with a set flow rate of 1 mL/min. Samples were dissolved in THF at 1 mg/mL and filtered through a 0.2 µm poly(tetrafluoroethylene) membrane prior to analysis.

Transmission Electron Microscopy (TEM)

Carbon films were deposited onto freshly cleaved mica sheets using a Leica EM ACE600 sputter/carbon coater instrument. Carbon films were deposited onto copper grids (500 mesh) purchased from Ted Pella, Inc. by floatation on water and allowed to dry over 24 h. Samples for electron microscopy were prepared by drop-casting 10 µL of colloidal nanofiber solution onto a TEM grid placed on filter paper to absorb the excess solution. Bright field TEM images were obtained using a JEOL JEM 1011 microscope operating at 80 kV, equipped with a Gatan Orius SC1000 CCD camera.

4.5.2 Statistical Analysis

Nanofiber lengths and widths were analysed using ImageJ, an open source software package developed at the US National Institute of Health.[57] Approximately 150 micelles were traced by hand to determine contour lengths that were then used to calculate the number-averaged length (L_n) and weight-average length (L_w) or the number-average micelle area (A_n) and weight-average micelle area (A_w) using supplementary equations S4.1–S4.4 from the measurements of the contour length/area (L_i/A_i) of individual micelles, where N_i is the number of the micelles of length L_i or area A_i, and n is the number of micelles examined in each sample.

$$(Equation\ S4.1)\ L_n = \frac{\sum_{i=1}^{n} N_i L_i}{\sum_{i=1}^{n} N_i} \qquad (Equation\ S4.2)\ \ L_w = \frac{\sum_{i=1}^{n} N_i L_i^2}{\sum_{i=1}^{n} N_i L_i}$$

$$(Equation\ S4.3)\ A_n = \frac{\sum_{i=1}^{n} N_i A_i}{\sum_{i=1}^{n} N_i} \qquad (Equation\ S4.4)\ \ A_w = \frac{\sum_{i=1}^{n} N_i A_i^2}{\sum_{i=1}^{n} N_i A_i}$$

The polydispersity index ($Đ_L$ *or* $Đ_A$) and standard deviations (σ) of the measured lengths/areas were related through the following expressions (Equations S4.5-S4.8).

$$(Equation\ S4.5)\ \ Đ_L = \frac{L_w}{L_n} \qquad (Equation\ S4.6)\ \ Đ_A = \frac{A_w}{A_n}$$

$$(Equation\ S4.7)\ \ \frac{L_w}{L_n} - 1 = \left(\frac{\sigma}{L_n}\right)^2 \quad (Equation\ S4.8)\ \ \frac{A_w}{A_n} - 1 = \left(\frac{\sigma}{A_n}\right)^2$$

Sonication

Nanofiber sonication was carried out using a Fisherbrand FB11203 sonication bath (37 kHz, 100% power) with the sweep function on and a bath temperature of 0 °C.

4.5.3 Synthesis and Characterization

Alkynyl-P3EHT, P3EHT$_{23}$-*b*-PEG$_{113}$, and P3EHT$_{19}$-*b*-P2VP$_{138}$ were synthesized as previously discussed in Chapter 2 by sequential GRIM polymerization and is not reported here. Molar mass and dispersity of polymers used in this chapter are found in the Table S4.1 below.

Table S4.1. Molar masses and dispersities of polymers used in Chapter 4.

Polymer	M_n (Da)	M_w (Da)	$Đ_M$[a]
[P3EHT$_{23}$-PPh$_3$]$^+$Br$^-$	5,100[a]; 5,000[b]	5,400[a]; 5,300[b]	1.07
P3EHT$_{23}$-*b*-PEG$_{113}$	11,900[a]; 9,600[b]	12,600[a], 10,200[b]	1.06
P3EHT$_{19}$-*b*-P2VP$_{138}$	18,300[a];18,800[b]	20,000[a], 22,100[b]	1.14

[a]Determined by GPC. [b]Determined by relative integration of ^{1}H NMR spectrum signals. M_w[b] values from ^{1}H NMR signals were estimated by using the $Đ_M$[a] obtained from GPC data and multiplying it by M_n[b] values obtained by ^{1}H NMR spectroscopy according to the equation $(Đ_M^a)(M_n^b) = M_w^b$.

Scheme S4.1. Synthesis of (3-azidopropyl)triphenylphosphonium bromide

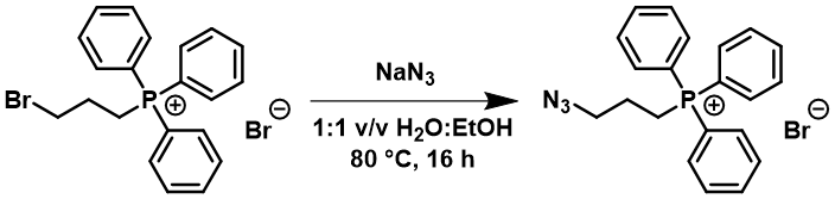

(3-Bromopropyl)triphenyl phosphonium bromide (2.0 g, 4.29 mmol, 1 equiv.) and sodium azide (0.56 g, 8.61 mmol, 2 equiv.) were dissolved in 10 mL of a water: ethanol mixture (1:1 v/v). The resulting mixture, while stirring, was heated to 80 °C for 16 h. After concentrating in vacuo to ~3 mL, the solution was cooled in an ice bath (0 °C) for 2 h. The solution was filtered, and the solids were washed with ice cold water to afford the product as a white solid. (1.55 g, 85 % yield) ^{1}H NMR ($CDCl_3$, 500 MHz): 7.94-7.65 (m, 15H, phenyl), 4.17-4.01 (m, 2H, CH_2P^+), 3.87 (t, 2H, J = 6.2 Hz, CH_2N_3), 1.92 (p, 2H, J = 7.2 Hz, $CH_2CH_2N_3$). ^{31}P NMR ($CDCl_3$, 203 MHz): 24.7.

Scheme S4.2. Synthesis of [P3EHT$_{23}$-PPh$_3$]$^+$Br$^-$

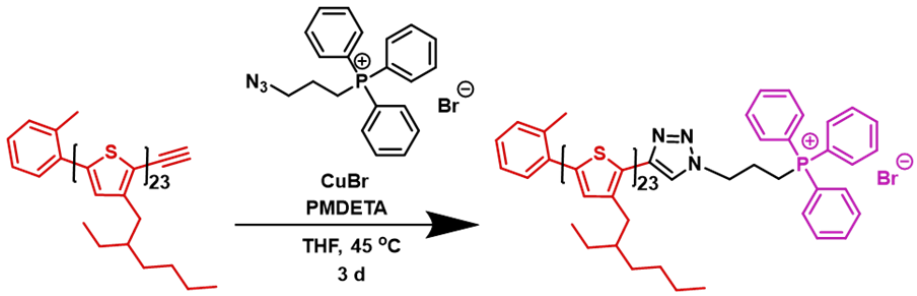

Alkynyl-P3EHT$_{23}$ (M_n = 4,600 Da, $Đ_M$ = 1.08, 200 mg, 0.04 mmol, 1.0 equiv.), (3-azidopropyl)triphenylphosphonium bromide (85 mg, 0.20 mmol, 5.0 equiv.), and CuBr (34 mg, 0.24 mmol, 6.0 equiv.) were added to a Schlenk flask equipped with a stir bar and attached to a Schlenk line. The flask was evacuated and backfilled three times with nitrogen gas before dry THF (200 mL) and PMDETA (42 mg, 50 µl, 0.24 mmol, 6.0 equiv.) were added to the flask with a syringe. The solution was degassed using 3 freeze-pump-thaw cycles, the flask was backfilled with nitrogen gas, and then stirred at 50 °C for 3 days. To the brown cloudy solution was added $CHCl_3$ (200 mL), and the solution was washed with deionized water (3 x 200 mL) and brine (1 x 200 mL), dried over magnesium sulfate, gravity filtered, and concentrated *in vacuo* using a rotary evaporator. The crude product was purified by column chromatography using a $CHCl_3$/MeOH mixture (97:3) as an eluent. The collected fractions were concentrated, $CHCl_3$ (min. amount) was added, and the solution was precipitated into hexanes, followed by collection with centrifugation which yielded the product as a red solid (168 mg, 82% yield, M_n = 5,100 Da, $Đ_M$ = 1.07). Purity was assayed using thin layer chromatography with $CHCl_3$/MeOH (97:3) as a mobile phase which showed no evidence of remaining homopolymers. ^{1}H NMR ($CDCl_3$, 500 MHz): 8.25 (s, 1H, triazole H), 7.83 – 7.65 (m, phenyl), 7.46 – 7.42 (m, tolyl), 7.25 – 7.22 (m, tolyl), 6.94 (s, 23H, thiophene), 2.74 (d, J = 7.3 Hz, thiophene-CH_2-), 2.51 (s, tolyl-CH_3), 1.71 (hept, J = 6.7 Hz, -CH-), 1.44 – 1.20 (m, -CH_2), 0.94 – 0.79 (m, -CH_3). ^{31}P NMR ($CDCl_3$, 203 MHz): 24.5.

4.5.4 Gel Permeation Chromatography

Alkynyl-P3EHT$_{23}$ and [P3EHT$_{23}$-PPh$_3$]$^+$Br$^-$

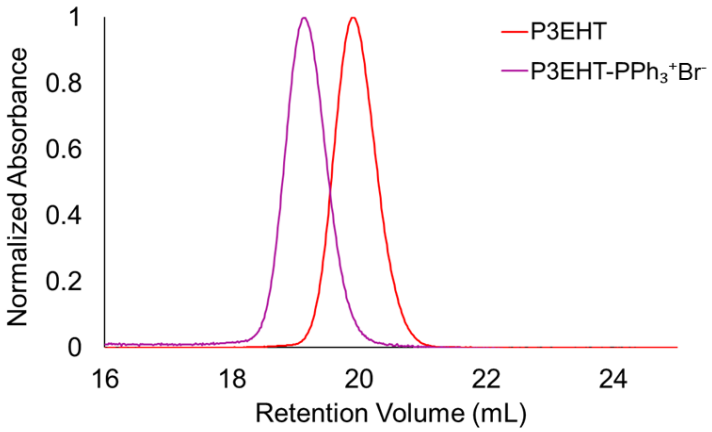

Figure S4.1. Overlaid GPC chromatograms of alkynyl-P3EHT$_{23}$ (red trace) and [P3EHT$_{23}$-PPh$_3$]$^+$Br$^-$ (purple trace). Sample concentrations were 1 mg/mL in THF.

4.5.5 ^{1}H NMR Spectroscopy

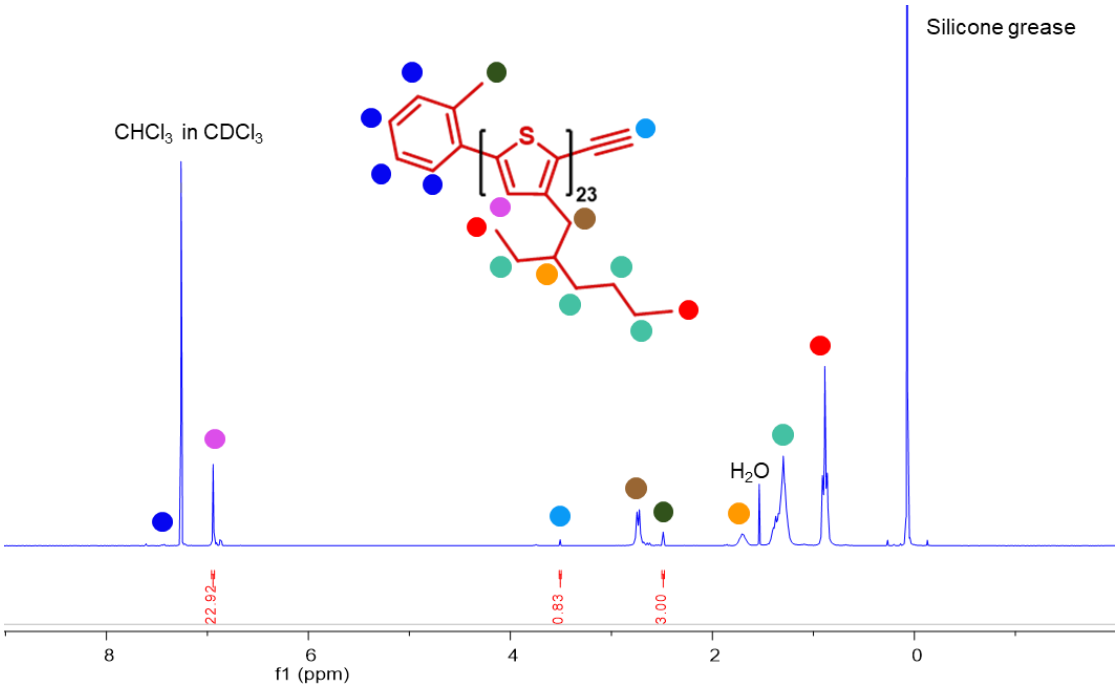

Figure S4.2. ^{1}H NMR spectrum of alkyne-terminated P3EHT$_{23}$ homopolymer (500 MHz, $CDCl_3$).

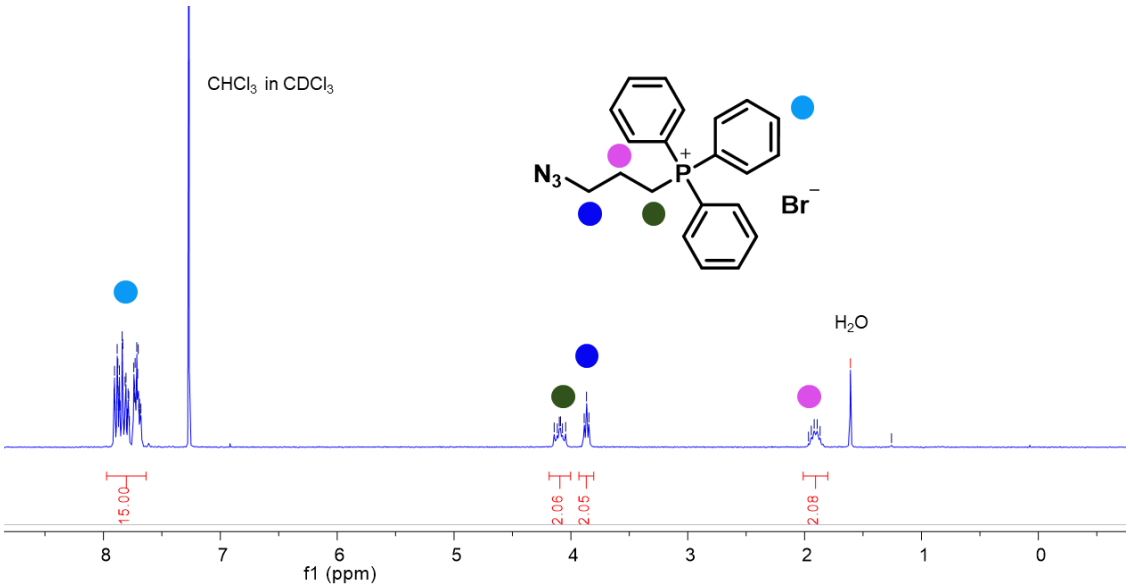

Figure S4.3. ^{1}H NMR spectrum of (3-azidopropyl)triphenylphosphonium bromide (500 MHz, $CDCl_3$).

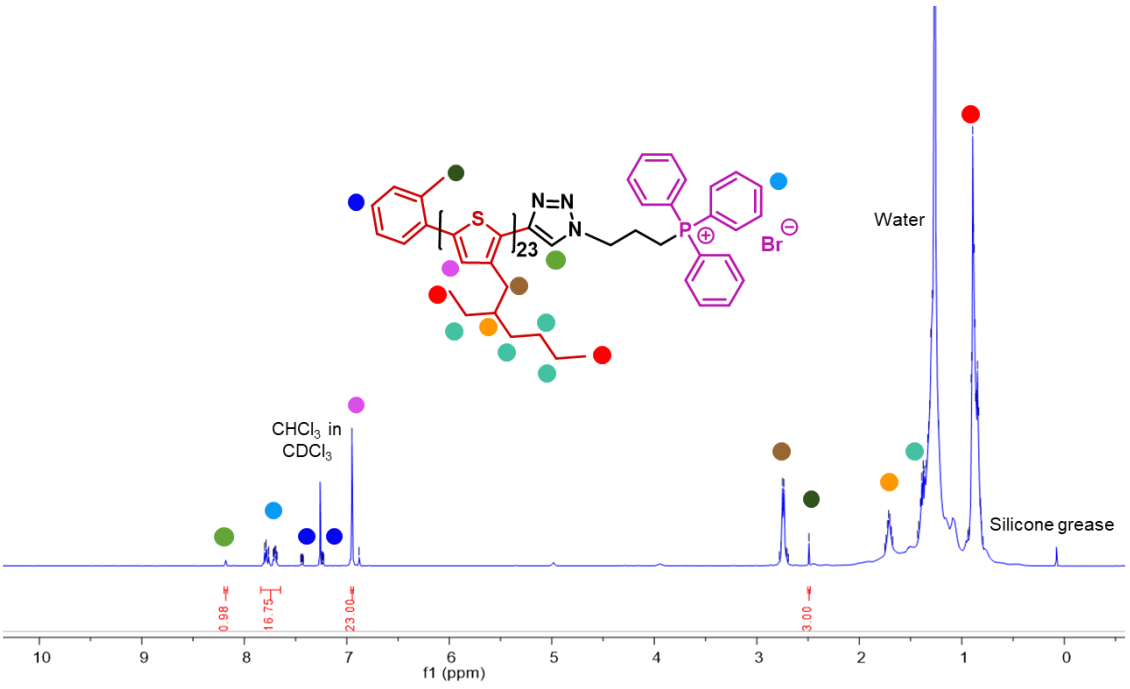

Figure S4.4. ^{1}H NMR spectrum of $[P3EHT_{23}\text{-}PPh_3]^{+}Br^{-}$ (500 MHz, $CDCl_3$).

4.5.6 ^{31}P NMR Spectroscopy

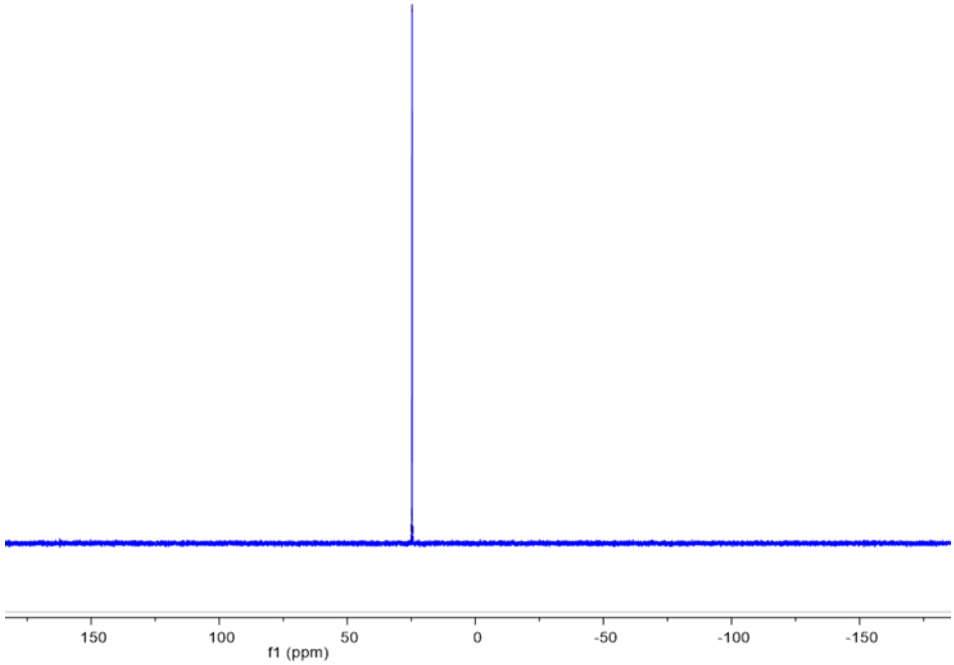

Figure S4.5. ^{31}P NMR spectrum of (3-azidopropyl)triphenylphosphonium bromide (202 MHz, $CDCl_3$). ^{31}P NMR: 24.7 ppm.

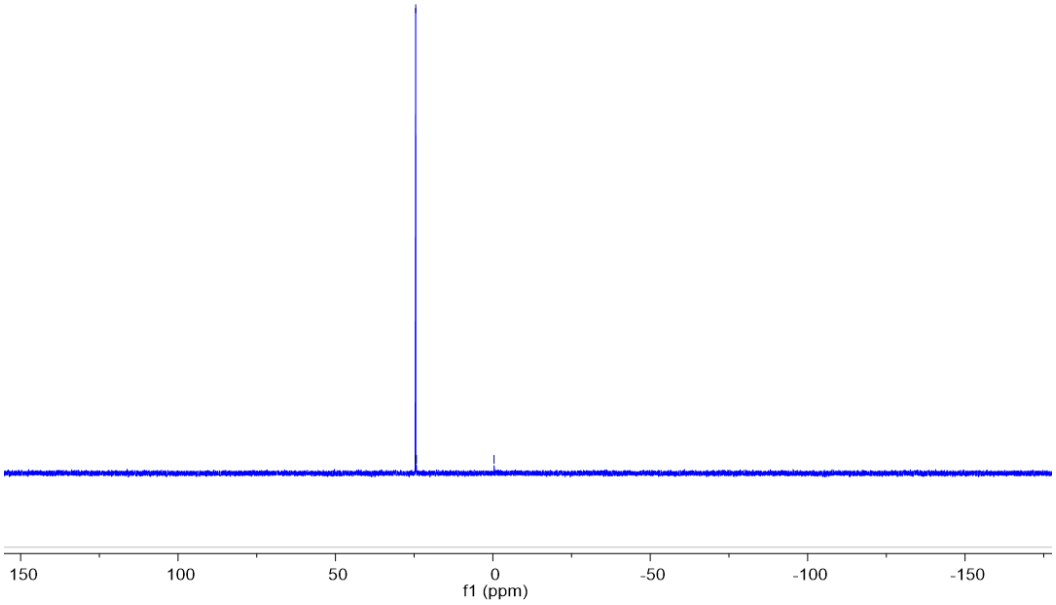

Figure S4.6. ^{31}P NMR spectrum of $[P3EHT_{23}\text{-}PPh_3]^+Br^-$ (202 MHz, $CDCl_3$). ^{31}P NMR: 24.5.

4.5.7 UV-Vis Spectroscopy

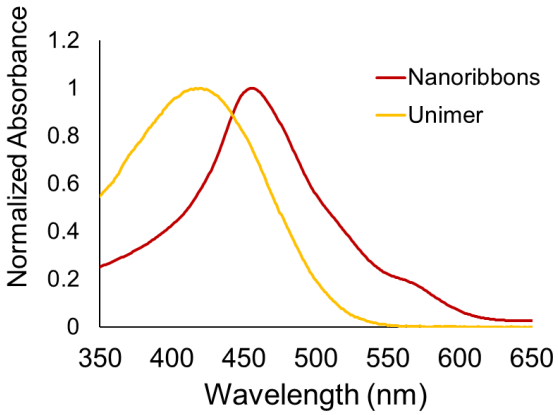

Figure S4.7. Overlayed solution-phase UV-Vis absorbance plots from polydisperse [P3EHT$_{23}$-PPh$_3$]$^+$Br$^-$ nanoribbon solution in 1:1 *n*BuOH:MeOH (0.05 mg/mL) (red trace) and [P3EHT$_{23}$-PPh$_3$]$^+$Br$^-$ unimer solution in THF (0.1 mg/mL) (orange trace) at 22 °C.

4.5.8 Atomic Force Microscopy

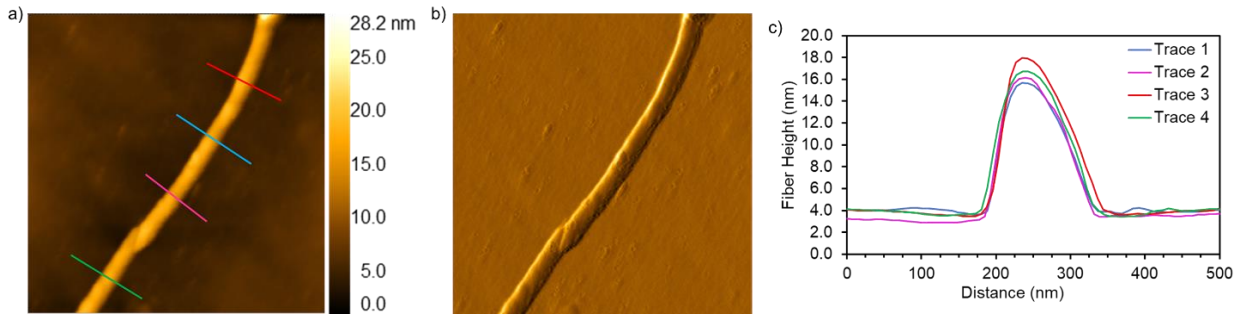

Figure S4.8. AFM **(a)** height and **(b)** amplitude images of polydisperse [P3EHT$_{23}$-PPh$_3$]$^+$Br$^-$ nanoribbons in 1:1 *n*BuOH:MeOH (0.05 mg/mL) spin-cast onto a silicon wafer. Coloured lines indicate the height profile shown in **(c)** drawn perpendicular to the long axis of the nanoribbons. Trace 1 - height: 11.7 nm, width: 157 nm; Trace 2 – height: 12.9 nm, width: 163 nm; Trace 3 - height: 14.1 nm, width: 168 nm; Trace 4 - height: 13.1 nm, width: 181 nm; Average height: 13 nm ± 0.9 nm, Average width: 167 nm ± 8.8 nm.

4.5.9 Crystallization-Driven Self-Assembly

General self-assembly procedure for polydisperse 2D nanoribbons of [P3EHT$_{23}$-PPh$_3$]$^+$Br$^-$ and seed production

Method 1: Solid [P3EHT$_{23}$-PPh$_3$]$^+$Br$^-$ was dissolved in THF to make a 0.4 mg/mL solution. MeOH was added to the vials dropwise with stirring to form a 1:3 THF:MeOH solution (0.1 mg/mL) and then aged at 22 °C for 24 h. The vial was then placed in a 0 °C ultrasonic cleaning bath and sonicated for 4 h to give seed micelles (37 kHz, 100% power). Seeds were annealed at 30 °C for 18 h prior to use.

Method 2: To a vial containing solid [P3EHT$_{23}$-PPh$_3$]$^+$Br$^-$ was added 500 uL of deoxygenated *n*BuOH to form a solution with a concentration of 0.2 mg/mL. The vial was sealed and heated to 80 °C using a metal heating block for 30 min. and then allowed to cool to 22 °C slowly (ca. 4 h) followed by aging for 24 h. After aging, 500 uL of deoxygenated MeOH was added to form a solution with a final concentration of 0.1 mg/mL. The vial was then placed in a 0 °C ultrasonic cleaning bath and sonicated for 4 h to give seed micelles (37 kHz, 100% power). Seeds were annealed at 30 °C for 18 h prior to use.

General self-assembly procedure for attempted seeded growth of area-controlled [P3EHT$_{23}$-PPh$_3$]$^+$Br$^-$ nanoribbons at 22 °C

[P3EHT$_{23}$-PPh$_3$]$^+$Br$^-$ seed micelle solutions in either 1:3 THF:MeOH or 1:1 *n*BuOH:MeOH (0.1 mg/mL) were added to vials and diluted with 1:3 THF:MeOH or 1:1 *n*BuOH:MeOH, respectively, such that the final concentration will be 0.05 mg/mL following unimer addition. [P3EHT$_{23}$-PPh$_3$]$^+$Br$^-$ unimer solution (deoxygenated THF, 1 mg/mL) correlating to m_{unimer}/m_{seed} = 5, 10, 15 was added quickly in one aliquot, the solutions were vortexed for 10 s, and then aged at 22 °C for 24 h prior to imaging by TEM.

General self-assembly procedure for self-seeding of length-controlled [P3EHT$_{23}$-PPh$_3$]$^+$Br$^-$ nanoribbons

[P3EHT$_{23}$-PPh$_3$]$^+$Br$^-$ seed micelle solution (1:1 *n*BuOH:MeOH, 0.05 mg/mL) was heated to self-seeding temperatures (53 - 61 °C) for 1 h and then cooled slowly (ca. 4 h) to 22 °C. After reaching 22 °C and aging for 24 h, the samples were imaged by TEM.

General self-assembly for formation of B-A-B segmented nanofibers (A = P3EHT$_{23}$-*b*-PEG$_{113}$, B = [P3EHT$_{23}$-PPh$_3$]$^+$ Br$^-$) by seeded growth at 22 °C

P3EHT$_{23}$-*b*-PEG$_{113}$ seed micelle solutions (1:1 *n*BuOH:MeOH, 0.1 mg/mL) were added to separate vials and diluted with a mixture of deoxygenated 1:1 *n*BuOH:MeOH such that the final concentration after unimer addition will be 0.05 mg/mL. [P3EHT$_{23}$-PPh$_3$]$^+$Br$^-$ unimer solution (deoxygenated THF, 1 mg/mL) correlating to m_{unimer}/m_{seed} = 5, 10, 15, 20, 30, 40 was added in one aliquot, the solutions were vortexed for 10 s, and then aged at 22 °C for 24 h prior to TEM imaging.

General self-assembly for formation of B-C-B segmented nanofibers (B = [P3EHT$_{23}$-PPh$_3$]$^+$ Br$^-$, C = P3EHT$_{19}$-*b*-P2VP$_{138}$) by seeded growth at 22 °C

P3EHT$_{19}$-*b*-P2VP$_{138}$ seed micelle solutions (*n*BuOH, 0.1 mg/mL) were added to separate vials and diluted with a deoxygenated *n*BuOH such that the final concentration after unimer addition will be 0.05 mg/mL. [P3EHT$_{23}$-PPh$_3$]$^+$Br$^-$ unimer solution (deoxygenated THF, 1 mg/mL) correlating to m_{unimer}/m_{seed} = 5, 10, 15, 30 was added quickly in one aliquot, the solutions were vortexed for 10 s, and then aged at 22 °C for 24 h prior to imaging by TEM.

4.5.10 Transmission Electron Microscopy

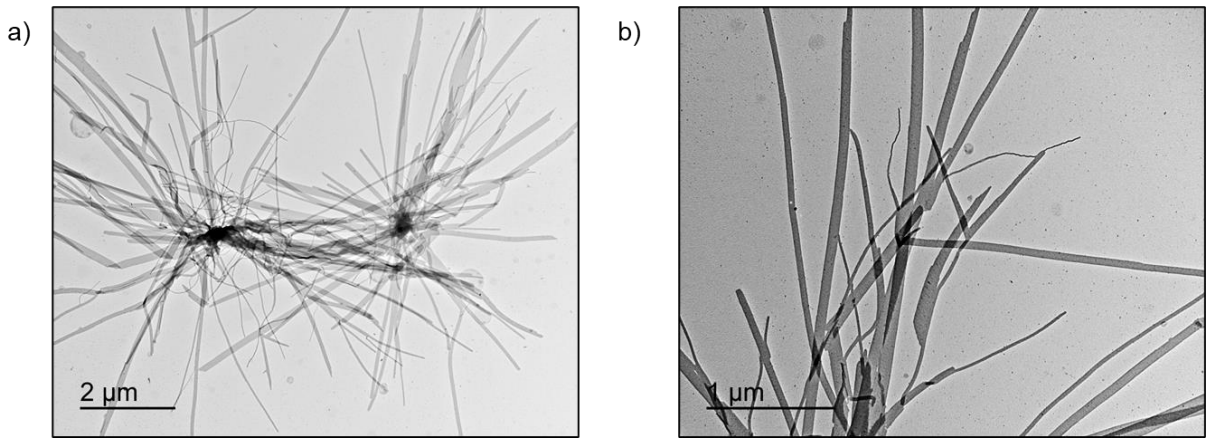

Figure S4.9. (a, b) TEM images of polydisperse $[P3EHT_{23}\text{-}PPh_3]^+Br^-$ nanoribbons made by dropwise addition of MeOH to $[P3EHT_{23}\text{-}PPh_3]^+Br^-$ THF solutions with stirring to make 1:3 v/v THF:MeOH solutions (0.1 mg/mL) followed by aging at 22 °C for 24 h. The samples were then drop-cast onto a carbon-coated copper TEM grid and imaged following solvent evaporation.

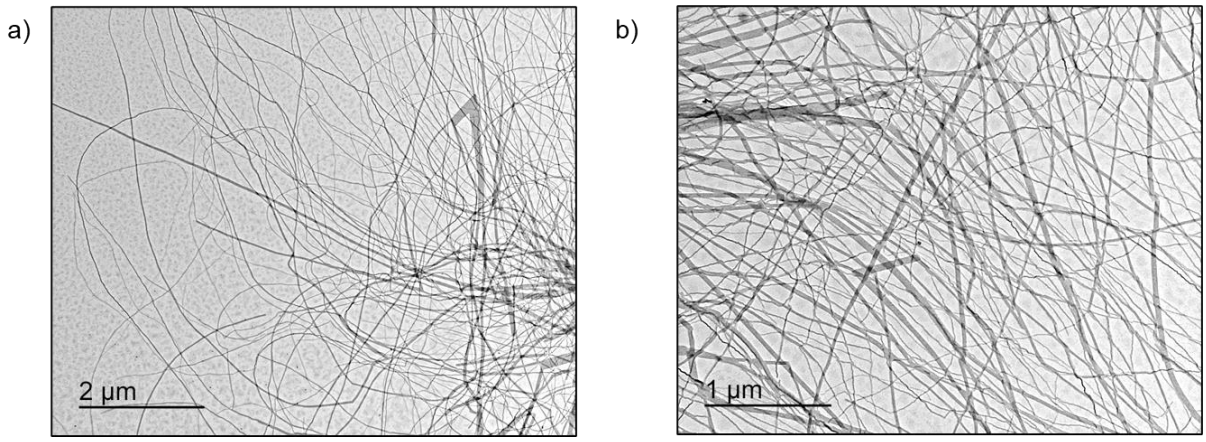

Figure S4.10. (a, b) TEM images of polydisperse $[P3EHT_{23}\text{-}PPh_3]^+Br^-$ nanoribbons made by heating solid $[P3EHT_{23}\text{-}PPh_3]^+Br^-$ in deoxygenated *n*BuOH to 80 °C for 30 min. and then cooling the 0.2 mg/mL solution to 22 °C and aging 24 h. After aging, an equivalent amount of deoxygenated MeOH was added to form a 1:1 v/v *n*BuOH:MeOH solution with a final concentration of 0.1 mg/mL. The samples were then drop-cast onto a carbon-coated copper TEM grid and imaged by TEM following solvent evaporation.

Seed Fabrication

1:3 THF:MeOH – Not Annealed

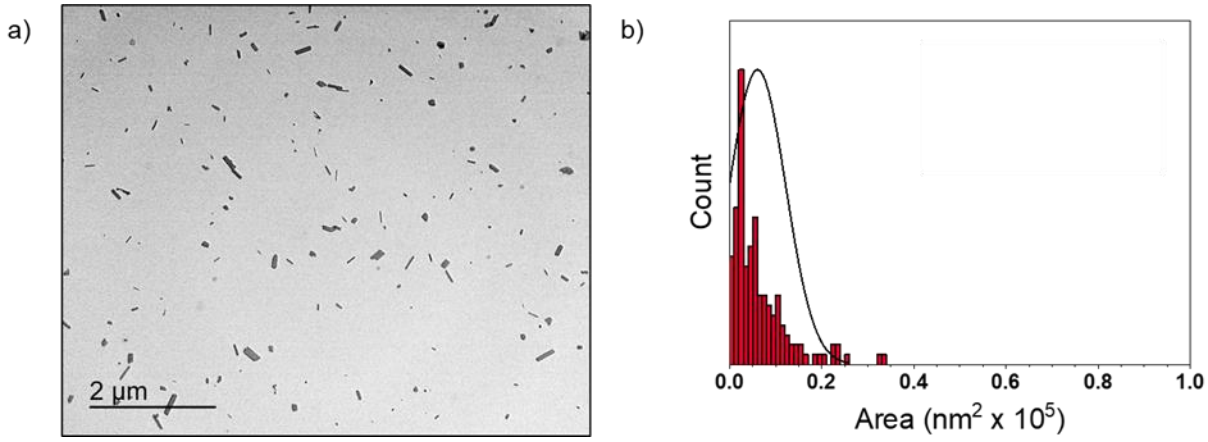

Figure S4.11. (a) TEM image of seeds formed by ultrasonication of a $[P3EHT_{23}\text{-}PPh_3]^+Br^-$ polydisperse nanoribbon solution (1:3 THF:MeOH, 0.1 mg/mL) at 0 °C for 4 h. **(b)** Histogram showing the area distribution of $[P3EHT_{23}\text{-}PPh_3]^+Br^-$ seeds (A_n = 6000 nm^2, A_w = 12200 nm^2, $Đ_A$ = 2.03, σ = ± 6100 nm^2, n = 151).

1:3 THF:MeOH - Annealed

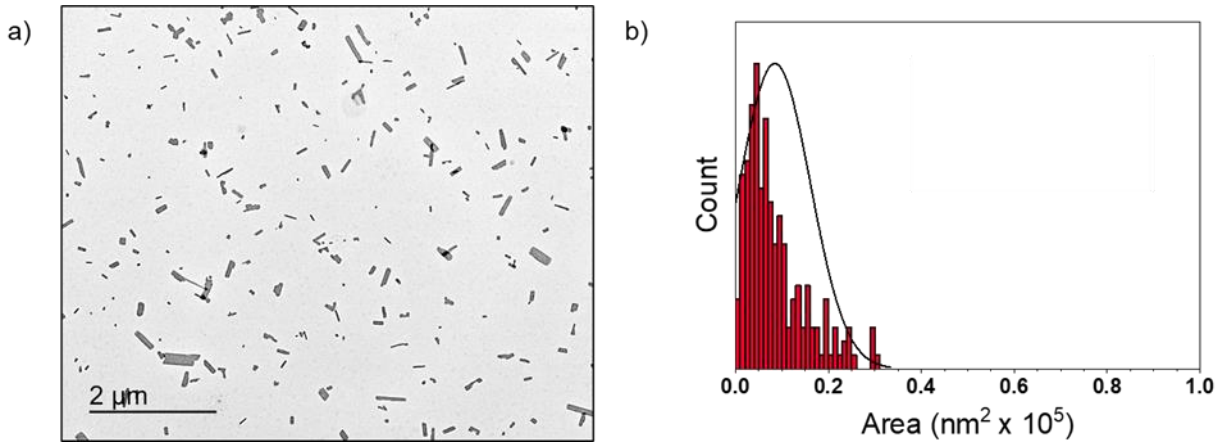

Figure S4.12. (a) TEM image of seeds formed by ultrasonication of a $[P3EHT_{23}\text{-}PPh_3]^+Br^-$ polydisperse nanoribbon solution (1:3 THF:MeOH, 0.1 mg/mL) at 0 °C for 4 h. Seeds were annealed at 30 °C for 18 h and then cooled to 22 °C and imaged following solvent evaporation. **(b)** Histogram showing the area distribution of $[P3EHT_{23}\text{-}PPh_3]^+Br^-$ seeds (A_n = 8500 nm^2, A_w = 15300 nm^2, $Đ_A$ = 1.81, σ = ± 7600 nm^2, n = 199).

1:1 *n*BuOH:MeOH - Not Annealed

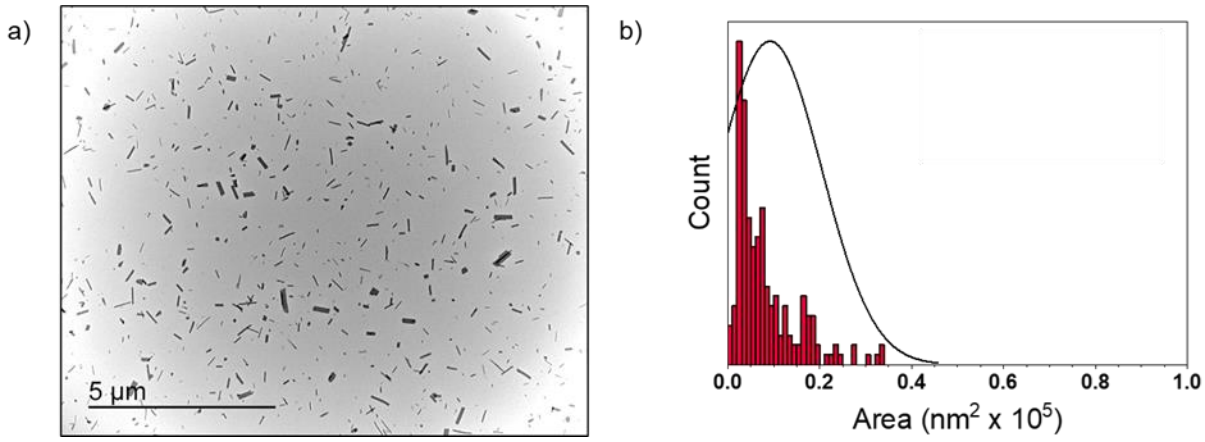

Figure S4.13. (a) TEM image of seeds formed by ultrasonication of a $[P3EHT_{23}\text{-}PPh_3]^+Br^-$ polydisperse nanoribbon solution (1:1 *n*BuOH:MeOH, 0.1 mg/mL) at 0 °C for 4 h. **(b)** Histogram showing the area distribution of $[P3EHT_{23}\text{-}PPh_3]^+Br^-$ seeds (A_n = 9200 nm^2, A_w = 22800 nm^2, $Đ_A$ = 2.48, σ = ± 11200 nm^2, n = 200).

1:1 *n*BuOH:MeOH - Annealed

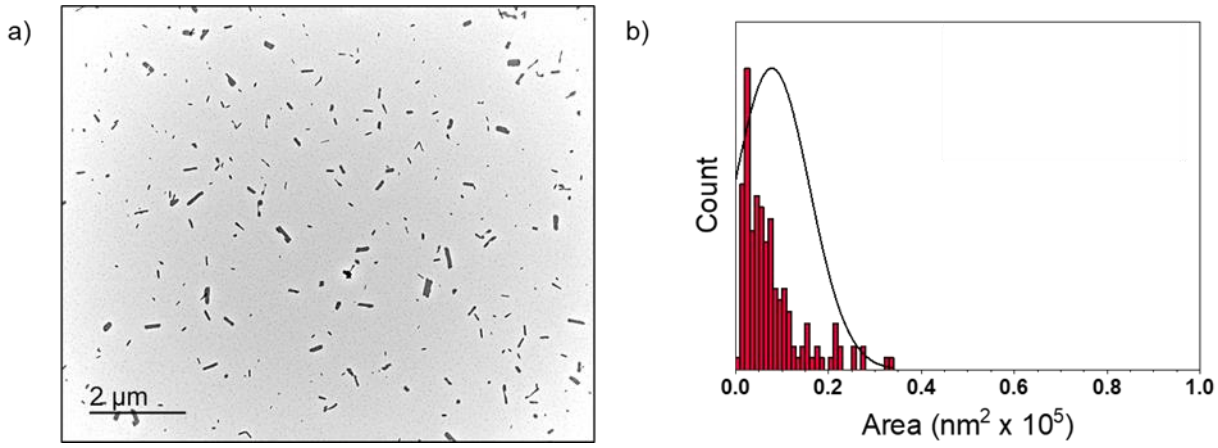

Figure S4.14. (a) TEM image of seeds formed by ultrasonication of a $[P3EHT_{23}\text{-}PPh_3]^+Br^-$ polydisperse nanoribbon solution (1:1 *n*BuOH:MeOH, 0.1 mg/mL) at 0 °C for 4 h. Seeds were annealed at 30 °C for 18 h and then cooled to 22 °C and imaged following solvent evaporation. **(b)** Histogram showing the area distribution of $[P3EHT_{23}\text{-}PPh_3]^+Br^-$ seeds (A_n = 7800 nm^2, A_w = 16200 nm^2, $Đ_A$ = 2.07, σ = ± 8100 nm^2, n = 162).

Attempted seeded growth of area-controlled 2D nanoplatelets at 22 °C using 2D seeds

Using [P3EHT$_{23}$-PPh$_3$]$^+$Br$^-$ Seeds in 1:3 THF:MeOH - Annealed

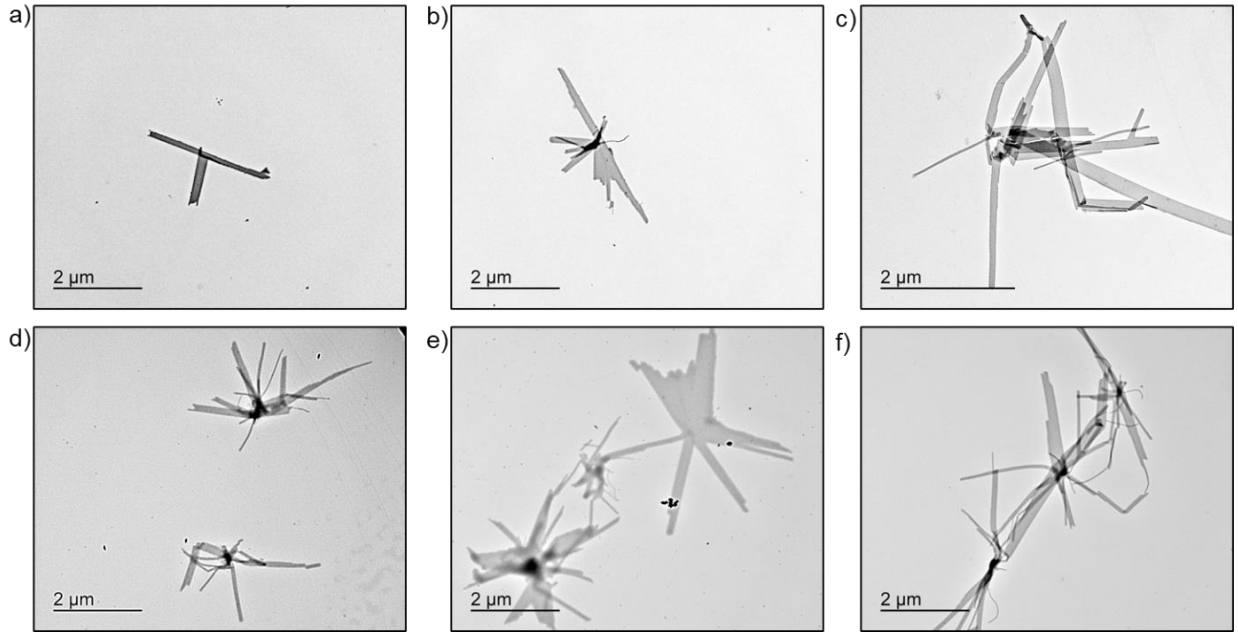

Figure S4.15. TEM images of [P3EHT$_{23}$-PPh$_3$]$^+$Br$^-$ assemblies (1:3 THF:MeOH, 0.05 mg/mL) formed by seeded growth using seed micelles (1:3 THF:MeOH, 0.1 mg/mL) which were annealed at 30 °C for 18 h prior to use. [P3EHT$_{23}$-PPh$_3$]$^+$Br$^-$ seed micelles were treated with **(a, b)** 5, **(c, d)** 10, and **(e, f)** 15 equivalents of [P3EHT$_{23}$-PPh$_3$]$^+$Br$^-$ unimer (THF, 1 mg/mL) at 22 °C. Solutions were aged at 22 °C for 24 h followed by solvent evaporation prior to TEM imaging.

Using [P3EHT$_{23}$-PPh$_3$]$^+$Br$^-$ seeds in 1:1 *n*BuOH:MeOH - Annealed

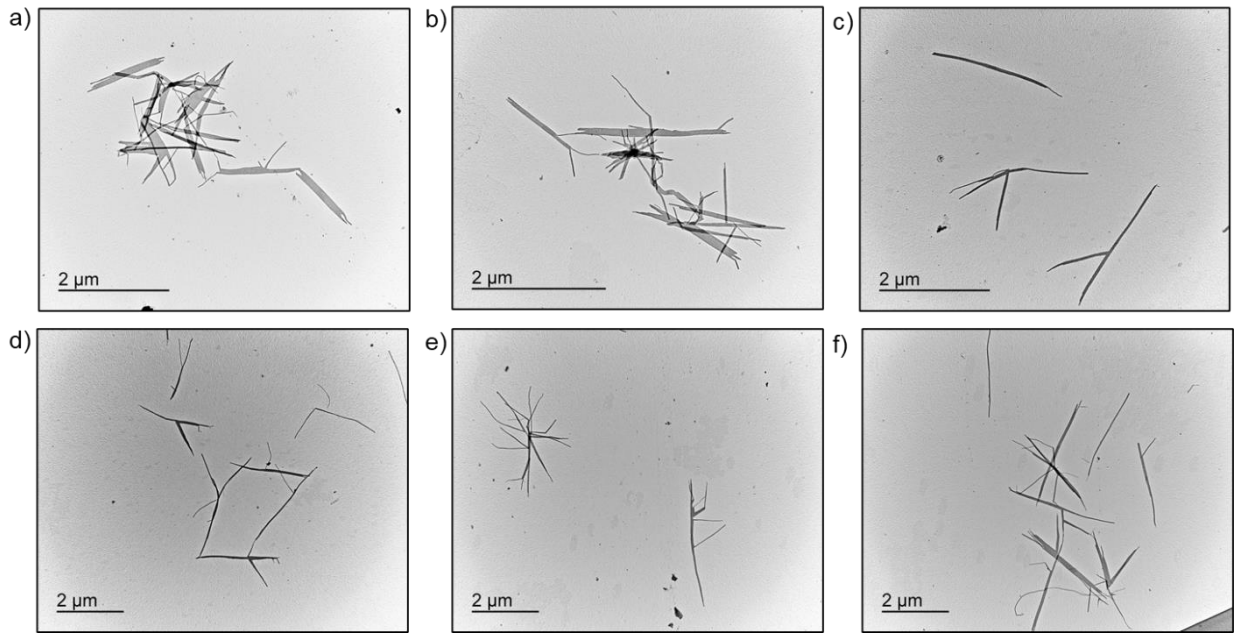

Figure S4.16. TEM images of [P3EHT$_{23}$-PPh$_3$]$^+$Br$^-$ assemblies (1:1 *n*BuOH:MeOH, 0.05 mg/mL) formed by seeded growth using seed micelles (1:1 *n*BuOH:MeOH, 0.1 mg/mL) which were annealed at 30 °C for 18 h prior to use. [P3EHT$_{23}$-PPh$_3$]$^+$Br$^-$ seed micelles were treated with **(a, b)** 5, **(c, d)** 10, and **(e, f)** 15 equivalents of [P3EHT$_{23}$-PPh$_3$]$^+$Br$^-$ unimer (THF, 1 mg/mL) at 22 °C. Solutions were aged at 22 °C for 24 h followed by solvent evaporation prior to TEM imaging.

Attempted self-seeding of area-controlled 2D nanoplatelets using 2D seeds

Using [P3EHT$_{23}$-PPh$_3$]$^+$Br$^-$ seeds in 1:1 *n*BuOH:MeOH – Annealed

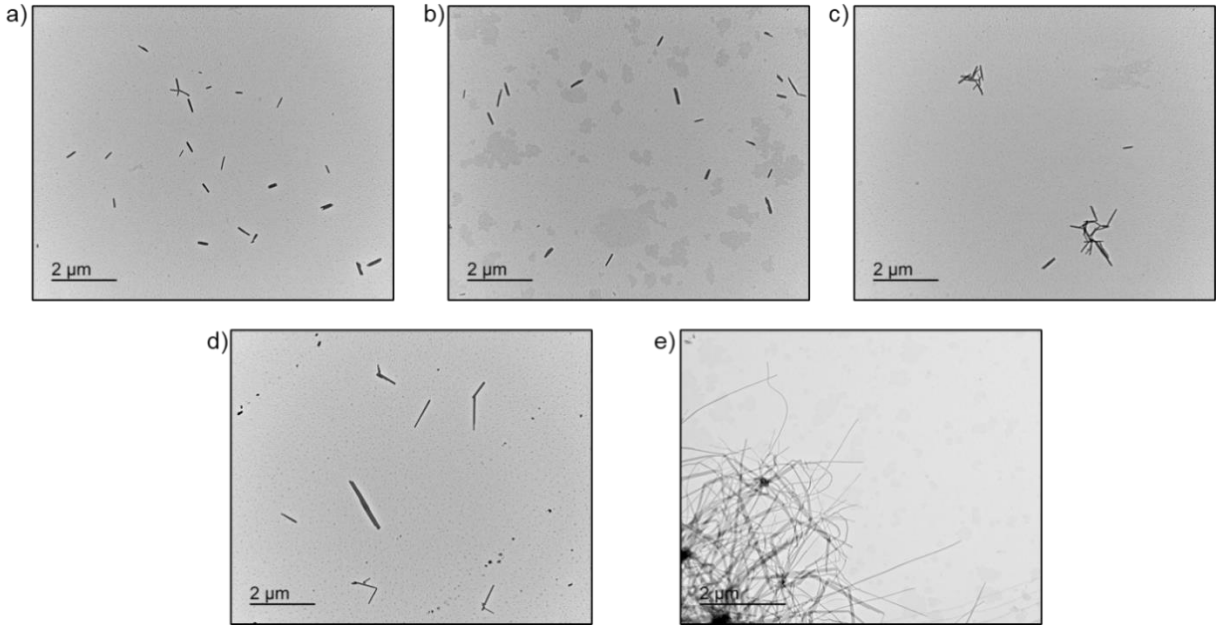

Figure S4.17. TEM images of [P3EHT$_{23}$-PPh$_3$]$^+$Br$^-$ nanoribbons (1:1 *n*BuOH:MeOH, 0.05 mg/mL) formed by heating annealed seed solutions (1:1 *n*BuOH:MeOH, 0.05 mg/mL) to **(a)** 53 °C, **(b)** 55°C, **(c)** 57 °C, **(d)** 59 °C, and **(e)** 61 °C for 1 h followed by cooling directly to 22 °C slowly (ca. 4 h) and aging 24 h. TEM images were obtained following drop-casting onto a carbon-coated copper grid and subsequent solvent evaporation.

Length-controlled B-A-B segmented triblock comicelles by seeded growth of [P3EHT$_{23}$-PPh$_3$]$^+$Br$^-$ from P3EHT$_{23}$-*b*-PEG$_{113}$ seeds at 22 °C

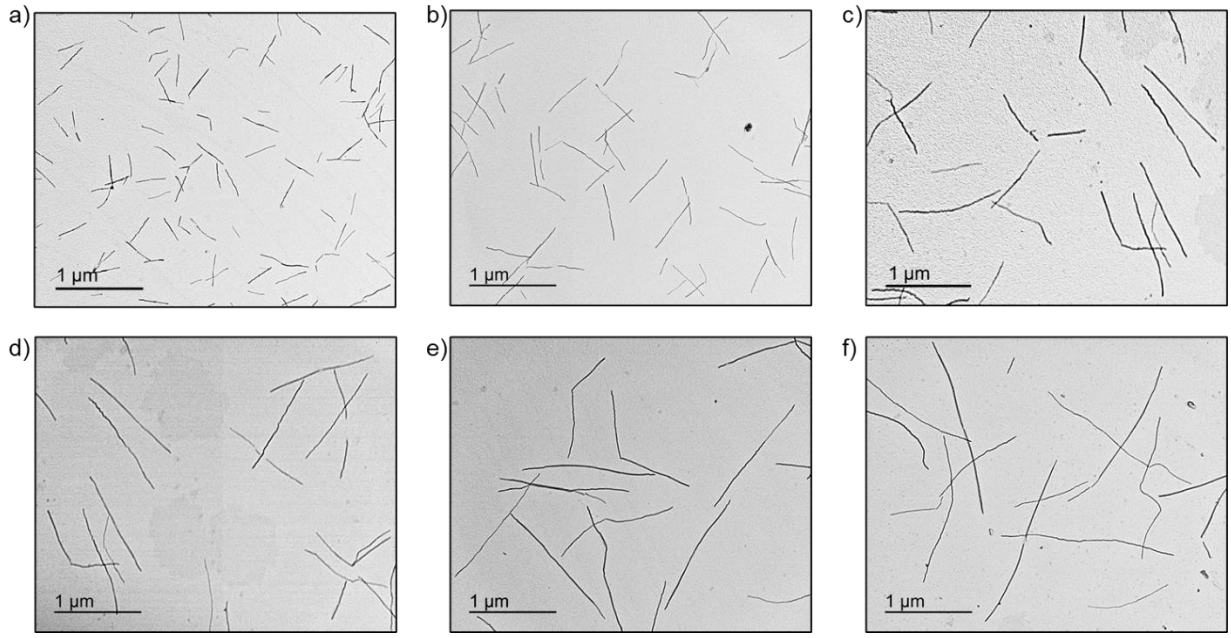

Figure S4.18. TEM images of length-controlled B-A-B nanofibers ([P3EHT$_{23}$-PPh$_3$]$^+$Br$^-$-*m*-P3EHT$_{23}$-*b*-PEG$_{113}$-*m*-[P3EHT$_{23}$-PPh$_3$]$^+$Br$^-$) (*m* = micelle segment) formed by living CDSA seeded growth (1:1 *n*BuOH:MeOH, 0.05 mg/mL) using P3EHT$_{23}$-*b*-PEG$_{113}$ seed micelles (1:1 *n*BuOH:MeOH, 0.1 mg/mL) which were annealed at 30 °C for 18 h prior to use. P3EHT$_{23}$-*b*-PEG$_{113}$ seed micelles were treated with **(a)** 5, **(b)** 10, **(c)** 15, **(d)** 20, **(e)** 30, and **(f)** 40 equivalents of [P3EHT$_{23}$-PPh$_3$]$^+$Br$^-$ unimer (THF, 1 mg/mL) at 22 °C. Solutions were aged at 22 °C for 24 h followed by drop-casting onto a carbon coated copper grid followed and solvent evaporation prior to TEM imaging.

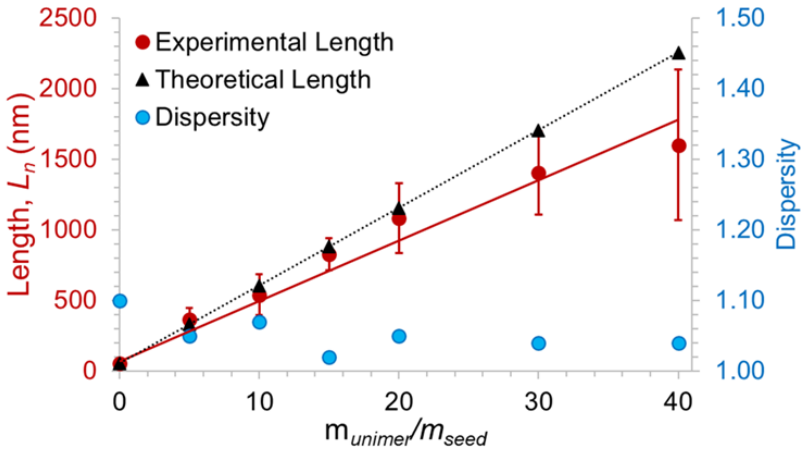

Figure S4.19. Plot showing the dependence of B-A-B triblock comicelle length (L_n) on unimer-to-seed mass ratio (m_{unimer}/m_{seed}) when using [P3EHT$_{23}$-PPh$_3$]$^+$Br$^-$ unimer and P3EHT$_{23}$-*b*-PEG$_{113}$ seeds (L_n = 77 nm, $Đ_L$ = 1.19) for seeded growth experiments at 22 °C. Error bars represent standard deviation.

Table S4.2. Summary of data from seeded growth experiments at 22 °C to form B-A-B ([P3EHT$_{23}$-PPh$_3$]$^+$Br$^-$-*m*-P3EHT$_{23}$-*b*-PEG$_{113}$-*m*-[P3EHT$_{23}$-PPh$_3$]$^+$Br$^-$) triblock comicelles with a central P3EHT$_{23}$-*b*-PEG$_{113}$ block and terminal [P3EHT$_{23}$-PPh$_3$]$^+$Br$^-$ blocks. σ is standard deviation in L_n measurements.

m_{unimer}/m_{seed}	L_n	L_w	$Đ_L$	σ
Seeds	77	92	1.19	33
5	364	382	1.05	80
10	538	577	1.07	145
15	826	842	1.02	115
20	1080	1138	1.05	249
30	1400	1463	1.04	296
40	1715	1792	1.04	362

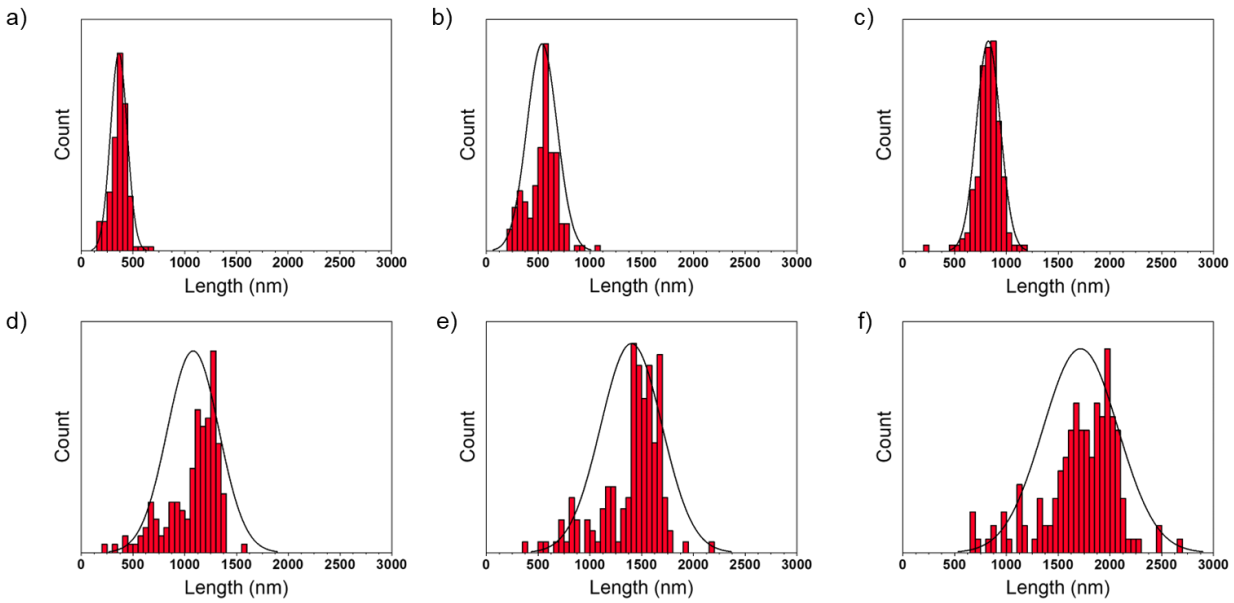

Figure S4.20. Histograms showing the triblock comicelle length distribution of B-A-B ($[P3EHT_{23}\text{-}PPh_3]^+Br^-$-*m*-$P3EHT_{23}$-*b*-$PEG_{113}$-*m*-$[P3EHT_{23}\text{-}PPh_3]^+Br^-$) nanofibers following seeded growth experiments at 22 °C. Annealed $P3EHT_{23}$-*b*-PEG_{113} seed micelles (1:1 *n*BuOH:MeOH, 0.1 mg/mL, 77 nm) were treated with **(a)** 5, **(b)** 10, **(c)** 15, **(d)** 20, **(e)** 30, and **(f)** 40 equivalents of $[P3EHT_{23}\text{-}PPh_3]^+Br^-$ unimer (THF, 1 mg/mL) at 22 °C. Final concentrations were 0.05 mg/mL.

Length-controlled B-C-B segmented triblock comicelles by seeded growth of [P3EHT$_{23}$-PPh$_3$]$^+$Br$^-$ from P3EHT$_{19}$-*b*-P2VP$_{138}$ seeds ([P3EHT$_{23}$-PPh$_3$]$^+$Br$^-$-*m*-P3EHT$_{19}$-*b*-P2VP$_{138}$-*m*-[P3EHT$_{23}$-PPh$_3$]$^+$Br$^-$) at 22 °C

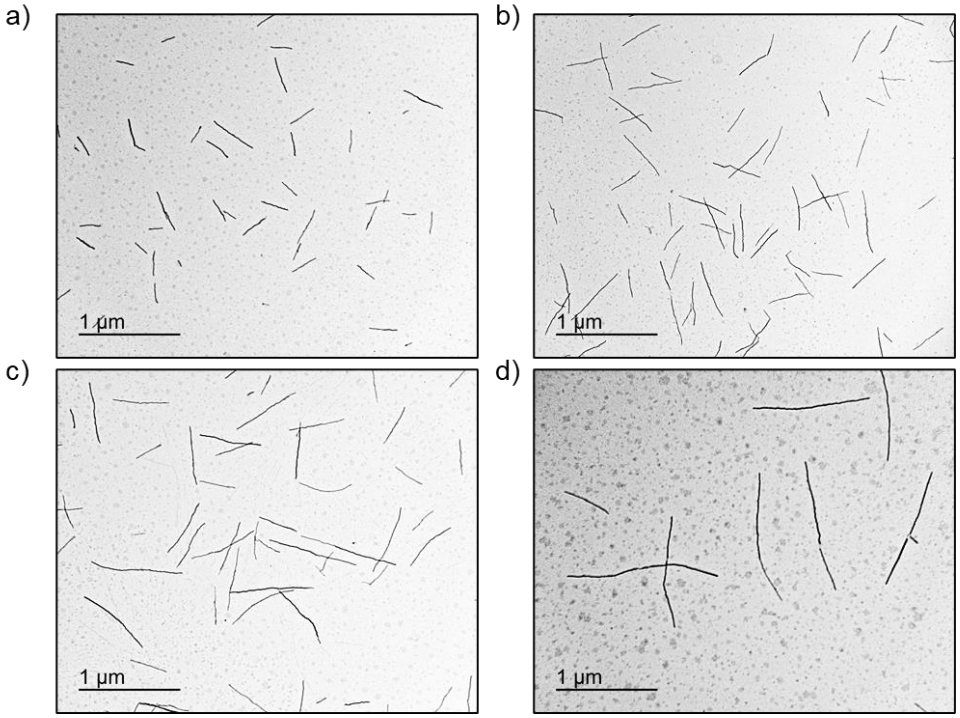

Figure S4.21. TEM images of length-controlled B-C-B ([P3EHT$_{23}$-PPh$_3$]$^+$Br$^-$-*m*-P3EHT$_{19}$-*b*-P2VP$_{138}$-*m*-[P3EHT$_{23}$-PPh$_3$]$^+$Br$^-$) (*m* = micelle segment) triblock comicelles (*n*BuOH, 0.05 mg/mL) formed by seeded growth at 22 °C. P3EHT$_{19}$-*b*-P2VP$_{138}$ seed micelles (L_n = 38 nm, $Đ_L$ = 1.24) were treated with **(a)** 5, **(b)** 10, **(c)** 15, and **(d)** 30 equivalents of [P3EHT$_{23}$-PPh$_3$]$^+$Br$^-$ unimer (THF, 1 mg/mL). Solutions (*n*BuOH, 0.05 mg/mL) were aged at 22 °C for 24 h followed by solvent evaporation prior to TEM imaging.

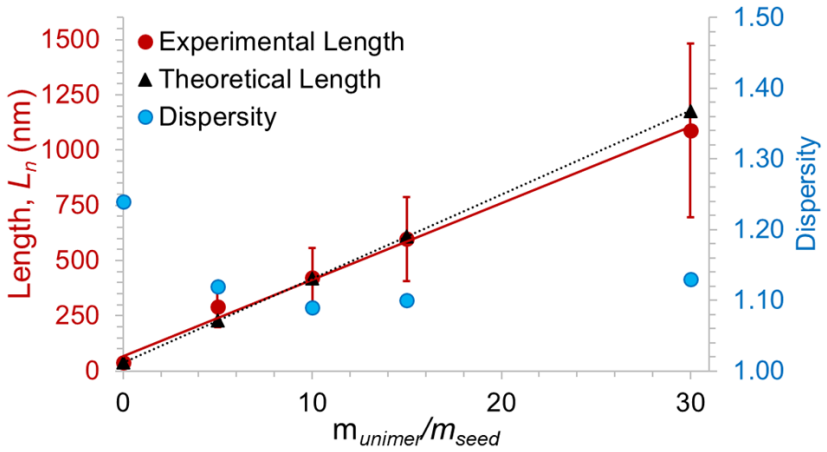

Figure S4.22. Plot showing the dependence of B-C-B nanofiber length (L_n) on unimer to seed mass ratio (m_{unimer}/m_{seed}) when using [P3EHT$_{23}$-PPh$_3$]$^+$Br$^-$ unimer and P3EHT$_{19}$-*b*-P2VP$_{138}$ seeds (L_n = 38 nm, $Đ_L$ = 1.24) for seeded growth experiments at 22 °C. Error bars represent standard deviation.

Table S4.3. Summary of data from seeded growth experiments at 22 °C to form B-C-B ([P3EHT$_{23}$-PPh$_3$]$^+$Br$^-$-*m*-P3EHT$_{19}$-*b*-P2VP$_{138}$-*m*-[P3EHT$_{23}$-PPh$_3$]$^+$Br$^-$) triblock comicelles with a central P3EHT$_{19}$-*b*-P2VP$_{138}$ block and terminal [P3EHT$_{23}$-PPh$_3$]$^+$Br$^-$ blocks. σ is standard deviation in L_n measurements.

m_{unimer}/m_{seed}	L_n	L_w	$Đ_L$	σ
Seeds	38	47	1.24	19
5	293	328	1.12	94
10	424	462	1.09	132
15	597	656	1.10	190
30	1088	1229	1.13	393

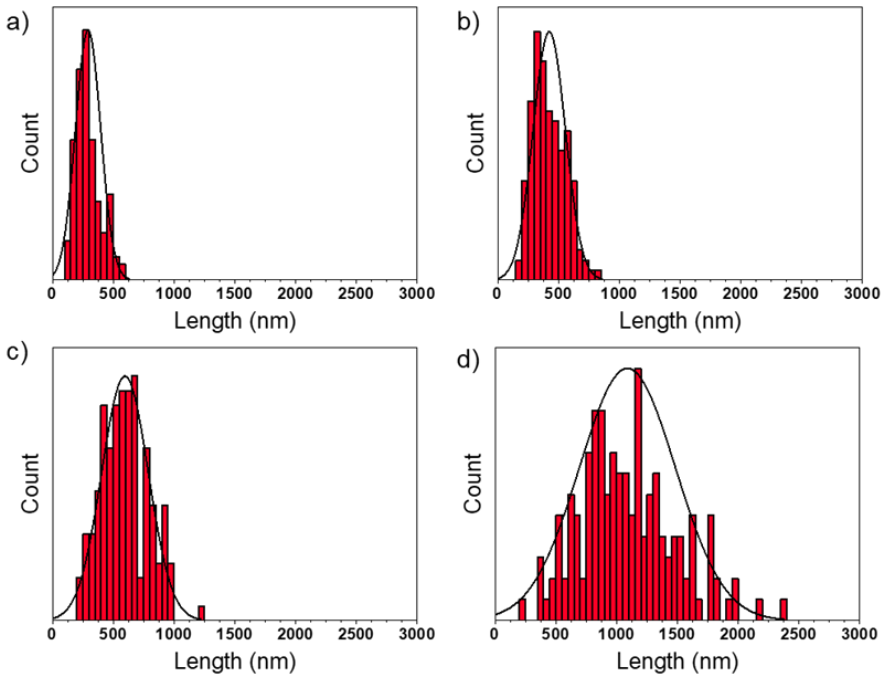

Figure S4.23. Histograms showing the triblock comicelle length distribution of B-C-B ([P3EHT$_{23}$-PPh$_3$]$^+$Br$^-$-*m*-P3EHT$_{19}$-*b*-P2VP$_{138}$-*m*-[P3EHT$_{23}$-PPh$_3$]$^+$Br$^-$) nanofibers following seeded growth experiments at 22 °C. Annealed P3EHT$_{19}$-*b*-P2VP$_{138}$ seed micelles (*n*BuOH, 0.1 mg/mL, 38 nm) were treated with **(a)** 5, **(b)** 10, **(c)** 15, and **(d)** 30 equivalents of [P3EHT$_{23}$-PPh$_3$]$^+$Br$^-$ unimer (THF, 1 mg/mL) at 22 °C Final concentrations were 0.05 mg/mL.

4.6 References

(1) Han, L.; Fan, H.; Zhu, Y.; Wang, M.; Pan, F.; Yu, D.; Zhao, Y.; He, F. Precisely Controlled Two-Dimensional Rhombic Copolymer Micelles for Sensitive Flexible Tunneling Devices. *CCS Chem.* **2021**, *3* (5), 1399–1409. https://doi.org/10.31635/ccschem.020.202000297.

(2) Yang, S.; Kang, S. Y.; Choi, T. L. Semi-Conducting 2D Rectangles with Tunable Length via Uniaxial Living Crystallization-Driven Self-Assembly of Homopolymer. *Nat. Commun.* **2021**, *12* (1), 6–13. https://doi.org/10.1038/s41467-021-22879-6.

(3) Xia, T.; Tong, Z.; Xie, Y.; Arno, M. C.; Lei, S.; Xiao, L.; Rho, J. Y.; Ferguson, C. T. J.; Manners, I.; Dove, A. P.; O'Reilly, R. K. Tuning the Functionality of Self-Assembled 2D Platelets in the Third Dimension. *J. Am. Chem. Soc.* **2023**, *145* (46), 25274–25282. https://doi.org/10.1021/jacs.3c08770.

(4) Qi, R.; Zhu, Y.; Han, L.; Wang, M.; He, F. Rectangular Platelet Micelles with Controlled Aspect Ratio by Hierarchical Self-Assembly of Poly(3-Hexylthiophene)-b-Poly(Ethylene Glycol). *Macromolecules* **2020**, *53* (15), 6555–6565. https://doi.org/10.1021/acs.macromol.0c01092.

(5) Han, L.; Wang, M.; Jia, X.; Chen, W.; Qian, H.; He, F. Uniform Two-Dimensional Square

Assemblies from Conjugated Block Copolymers Driven by π-π Interactions with Controllable Sizes. *Nat. Commun.* **2018**, *9* (1), 1–12. https://doi.org/10.1038/s41467-018-03195-y.

(6) Li, H.; Han, L.; Zhu, Y.; Fernández-Trillo, P.; He, F. Transformation from Rod-like to Diamond-like Micelles by Thermally Induced Nucleation Self-Assembly. *Macromolecules* **2021**, *54* (11), 5278–5285. https://doi.org/10.1021/acs.macromol.1c00744.

(7) Kamps, A. C.; Cativo, M. H. M.; Chen, X. J.; Park, S. J. Self-Assembly of DNA-Coupled Semiconducting Block Copolymers. *Macromolecules* **2014**, *47* (11), 3720–3726. https://doi.org/10.1021/ma500509u.

(8) Guo, X. S.; Zhang, Z. K.; Zhang, T. Y.; Tong, Z. Z.; Xu, J. T.; Fan, Z. Q. Interfacial Self-Assembly of Amphiphilic Conjugated Block Copolymer into 2D Nanotapes. *Soft Matter* **2019**, *15* (43), 8790–8799. https://doi.org/10.1039/c9sm01503e.

(9) Yun, N.; Kang, C.; Yang, S.; Hwang, S. H.; Park, J. M.; Choi, T. L. Size-Tunable Semiconducting 2D Nanorectangles from Conjugated Polyenyne Homopolymer Synthesized via Cascade Metathesis and Metallotropy Polymerization. *J. Am. Chem. Soc.* **2023**, 1–10. https://doi.org/10.1021/jacs.3c00357.

(10) Qiu, H.; Gao, Y.; Boott, C. E.; Gould, O. E. C.; Harniman, R. L.; Miles, M. J.; Webb, S. E. D.; Winnik, M. A.; Manners, I. Uniform Patchy and Hollow Rectangular Platelet Micelles from Crystallizable Polymer Blends. *Science* **2016**, *352* (6286), 697–702.

(11) Hudson, Z. M.; Boott, C. E.; Robinson, M. E.; Rupar, P. A.; Winnik, M. A.; Manners, I. Tailored Hierarchical Micelle Architectures Using Living Crystallization-Driven Self-Assembly in Two Dimensions. *Nat. Chem.* **2014**, *6* (10), 893–898. https://doi.org/10.1038/nchem.2038.

(12) He, X.; Hsiao, M. S.; Boott, C. E.; Harniman, R. L.; Nazemi, A.; Li, X.; Winnik, M. A.; Manners, I. Two-Dimensional Assemblies from Crystallizable Homopolymers with Charged Termini. *Nat. Mater.* **2017**, *16* (4), 481–488. https://doi.org/10.1038/NMAT4837.

(13) He, X.; He, Y.; Hsiao, M. S.; Harniman, R. L.; Pearce, S.; Winnik, M. A.; Manners, I. Complex and Hierarchical 2D Assemblies via Crystallization-Driven Self-Assembly of Poly(l -Lactide) Homopolymers with Charged Termini. *J. Am. Chem. Soc.* **2017**, *139* (27), 9221–9228. https://doi.org/10.1021/jacs.7b03172.

(14) Li, Z.; Zhang, Y.; Wu, L.; Yu, W.; Wilks, T. R.; Dove, A. P.; Ding, H. M.; O'Reilly, R. K.; Chen, G.; Jiang, M. Glyco-Platelets with Controlled Morphologies via Crystallization-Driven Self-Assembly and Their Shape-Dependent Interplay with Macrophages. *ACS Macro Lett.* **2019**, 596–602. https://doi.org/10.1021/acsmacrolett.9b00221.

(15) MacFarlane, L. R.; Shaikh, H.; Garcia-Hernandez, J. D.; Vespa, M.; Fukui, T.; Manners, I. Functional Nanoparticles through π-Conjugated Polymer Self-Assembly. *Nat. Rev. Mater.* **2021**, *6* (1), 7–26. https://doi.org/10.1038/s41578-020-00233-4.

(16) Gilroy, J. B.; Gädt, T.; Whittell, G. R.; Chabanne, L.; Mitchels, J. M.; Richardson, R. M.; Winnik, M. A.; Manners, I. Monodisperse Cylindrical Micelles by Crystallization-Driven Living Self-Assembly. *Nat. Chem.* **2010**, *2* (7), 566–570. https://doi.org/10.1038/nchem.664.

(17) Xu, L.; Wang, C.; Li, Y.-X.; Xu, X.; Zhou, L.; Liu, N.; Wu, Z.-Q. Crystallization-Driven Asymmetric Helical Assembly of Conjugated Block Copolymers and the Aggregation Induced White-Light Emission and Circularly Polarized Luminescence. *Angew. Chem. Int. Ed.* **2020**, *59* (38), 16675–16682. https://doi.org/10.1002/anie.202006561.

(18) Hwang, S.-H.; Kang, S.-Y.; Yang, S.; Lee, J.; Choi, T.-L. Synchronous Preparation of Length-Controllable 1D Nanoparticles via Crystallization-Driven in Situ Nanoparticlization of Conjugated Polymers. *J. Am. Chem. Soc.* **2022**, *144* (13), 5921–5929. https://doi.org/10.1021/jacs.1c13385.

(19) Shin, S.; Menk, F.; Kim, Y.; Lim, J.; Char, K.; Zentel, R.; Choi, T. L. Living Light-Induced Crystallization-Driven Self-Assembly for Rapid Preparation of Semiconducting Nanofibers. *J. Am. Chem. Soc.* **2018**, *140* (19), 6088–6094. https://doi.org/10.1021/jacs.8b01954.

(20) Ma, J.; Hao, B.; Zhang, S.; Huang, X.; Lu, G.; Feng, C. Uniform π-Conjugated-Co-Oligomer-Based Nanofibers of Controlled Length with Near-Infrared Emission, Photodynamic and Photothermal Activities. *Adv. Mater. Interfaces* **2022**, *9* (33), 2201823. https://doi.org/10.1002/admi.202201823.

(21) Ma, J.; Lu, G.; Huang, X.; Feng, C. π-Conjugated-Polymer-Based Nanofibers through Living Crystallization-Driven Self-Assembly: Preparation, Properties and Applications. *Chem. Commun.* **2021**, *57* (98), 13259–13274. https://doi.org/10.1039/d1cc04825b.

(22) Petzetakis, N.; Dove, A. P.; O'Reilly, R. K. Cylindrical Micelles from the Living Crystallization-Driven Self-Assembly of Poly(Lactide)-Containing Block Copolymers. *Chem. Sci.* **2011**, *2* (5), 955–960. https://doi.org/10.1039/c0sc00596g.

(23) Jin, X.-H.; Price, M. B.; Finnegan, J. R.; Boott, C. E.; Richter, J. M.; Rao, A.; Menke, S. M.; Friend, R. H.; Whittell, G. R.; Manners, I. Long-Range Exciton Transport in Conjugated Polymer Nanofibers Prepared by Seeded Growth. *Science* **2018**, *360* (3691), 897–900. https://doi.org/10.1126/science.aar8104.

(24) Li, X.; Wolanin, P. J.; MacFarlane, L. R.; Harniman, R. L.; Qian, J.; Gould, O. E. C. C.; Dane, T. G.; Rudin, J.; Cryan, M. J.; Schmaltz, T.; Frauenrath, H.; Winnik, M. A.; Faul, C. F. J. J.; Manners, I. Uniform Electroactive Fibre-like Micelle Nanowires for Organic Electronics. *Nat. Commun.* **2017**, *8* (1), 15909. https://doi.org/10.1038/ncomms15909.

(25) Wang, X.; Guerin, G.; Wang, H.; Wang, Y.; Manners, I.; Winnik, M. A. Cylindrical Block Copolymer Micelles and Co-Micelles of Controlled Length and Architecture. *Science* **2007**, *317* (5838), 644–647. https://doi.org/10.1126/science.1141382.

(26) Tao, D.; Feng, C.; Lu, Y.; Cui, Y.; Yang, X.; Manners, I.; Winnik, M. A.; Huang, X. Self-Seeding of Block Copolymers with a π-Conjugated Oligo(p-Phenylenevinylene) Segment: A Versatile Route toward Monodisperse Fiber-like Nanostructures. *Macromolecules* **2018**, *51* (5), 2065–2075. https://doi.org/10.1021/acs.macromol.8b00046.

(27) Qian, J.; Guerin, G.; Lu, Y.; Cambridge, G.; Manners, I.; Winnik, M. A. Self-Seeding in One Dimension: An Approach to Control the Length of Fiberlike Polyisoprene-Polyferrocenylsilane Block Copolymer Micelles. *Angew. Chem. Int. Ed.* **2011**, *50* (7), 1622–1625. https://doi.org/10.1002/anie.201006223.

(28) Qian, J.; Lu, Y.; Chia, A.; Zhang, M.; Rupar, P. A.; Gunari, N.; Walker, G. C.; Cambridge,

G.; He, F.; Guerin, G.; Manners, I.; Winnik, M. A. Self-Seeding in One Dimension: A Route to Uniform Fiber-like Nanostructures from Block Copolymers with a Crystallizable Core-Forming Block. *ACS Nano* **2013**, *7* (5), 3754–3766. https://doi.org/10.1021/nn400124x.

(29) Xu, J.; Ma, Y.; Hu, W.; Rehahn, M.; Reiter, G. Cloning Polymer Single Crystals through Self-Seeding. *Nat. Mater.* **2009**, *8* (4), 348–353. https://doi.org/10.1038/nmat2405.

(30) Nie, J.; Wang, Z.; Xia, L.; Huang, X.; Lu, G.; Feng, C. Co-Self-Seeding: A Facile Approach to Generate Heterogeneous π-Conjugated Fiber-Like Comicelles with Tunable Length, Composition and Morphology. *Eur. Polym. J.* **2023**, *197* (August), 112384. https://doi.org/10.1016/j.eurpolymj.2023.112384.

(31) Strobl, G. Crystallization and Melting of Bulk Polymers: New Observations, Conclusions and a Thermodynamic Scheme. *Prog. Polym. Sci.* **2006**, *31* (4), 398–442. https://doi.org/10.1016/j.progpolymsci.2006.01.001.

(32) MacFarlane, L.; Zhao, C.; Cai, J.; Qiu, H.; Manners, I. Emerging Applications for Living Crystallization-Driven Self-Assembly. *Chem. Sci.* **2021**, *12* (13), 4661–4682. https://doi.org/10.1039/d0sc06878k.

(33) MacFarlane, L. R.; Li, X.; Faul, C. F. J.; Manners, I. Efficient and Controlled Seeded Growth of Poly(3-Hexylthiophene) Block Copolymer Nanofibers through Suppression of Homogeneous Nucleation. *Macromolecules* **2021**, *54* (24), 11269–11280. https://doi.org/10.1021/acs.macromol.1c02005.

(34) Fukui, T.; Garcia-Hernandez, J. D.; MacFarlane, L. R.; Lei, S.; Whittell, G. R.; Manners, I. Seeded Self-Assembly of Charge-Terminated Poly(3-Hexylthiophene) Amphiphiles Based on the Energy Landscape. *J. Am. Chem. Soc.* **2020**, *142* (35), 15038–15048. https://doi.org/10.1021/jacs.0c06185.

(35) He, X.; Finnegan, J. R.; Hayward, D. W.; MacFarlane, L. R.; Harniman, R. L.; Manners, I. Living Crystallization-Driven Self-Assembly of Polymeric Amphiphiles: Low-Dispersity Fiber-like Micelles from Crystallizable Phosphonium-Capped Polycarbonate Homopolymers. *Macromolecules* **2020**, *53* (23), 10591–10600. https://doi.org/10.1021/acs.macromol.0c02075.

(36) Sneyd, A. J.; Fukui, T.; Paleček, D.; Prodhan, S.; Wagner, I.; Zhang, Y.; Sung, J.; Collins, S. M.; Slater, T. J. A.; Andaji-Garmaroudi, Z.; MacFarlane, L. R.; Garcia-Hernandez, J. D.; Wang, L.; Whittell, G. R.; Hodgkiss, J. M.; Chen, K.; Beljonne, D.; Manners, I.; Friend, R. H.; Rao, A. Efficient Energy Transport in an Organic Semiconductor Mediated by Transient Exciton Delocalization. *Sci. Adv.* **2021**, *7* (32). https://doi.org/10.1126/sciadv.abh4232.

(37) Ho, V.; Boudouris, B. W.; Segalman, R. A. Tuning Polythiophene Crystallization through Systematic Side Chain Functionalization. *Macromolecules* **2010**, *43* (19), 7895–7899. https://doi.org/10.1021/ma101697m.

(38) Hsiao, M. S.; Yusoff, S. F. M.; Winnik, M. A.; Manners, I. Crystallization-Driven Self-Assembly of Block Copolymers with a Short Crystallizable Core-Forming Segment: Controlling Micelle Morphology through the Influence of Molar Mass and Solvent Selectivity. *Macromolecules* **2014**, *47* (7), 2361–2372. https://doi.org/10.1021/ma402429d.

(39) Gilroy, J. B.; Lunn, D. J.; Patra, S. K.; Whittell, G. R.; Winnik, M. A.; Manners, I. Fiber-like Micelles via the Crystallization-Driven Solution Self-Assembly of Poly(3-

Hexylthiophene)-Block-Poly(Methyl Methacrylate) Copolymers. *Macromolecules* **2012**, *45* (14), 5806–5815. https://doi.org/10.1021/ma3008114.

(40) Patra, S. K.; Ahmed, R.; Whittell, G. R.; Lunn, D. J.; Dunphy, E. L.; Winnik, M. A.; Manners, I. Cylindrical Micelles of Controlled Length with a π-Conjugated Polythiophene Core via Crystallization-Driven Self-Assembly. *J. Am. Chem. Soc.* **2011**, *133* (23), 8842–8845. https://doi.org/10.1021/ja202408w.

(41) Gwyther, J.; Gilroy, J. B.; Rupar, P. A.; Lunn, D. J.; Kynaston, E.; Patra, S. K.; Whittell, G. R.; Winnik, M. A.; Manners, I. Dimensional Control of Block Copolymer Nanofibers with a π-Conjugated Core: Crystallization-Driven Solution Self-Assembly of Amphiphilic Poly(3-Hexylthiophene)-b-Poly(2-Vinylpyridine). *Chem. Eur. J.* **2013**, *19* (28), 9186–9197. https://doi.org/10.1002/chem.201300463.

(42) Yusoff, S. F. M.; Hsiao, M. S.; Schacher, F. H.; Winnik, M. A.; Manners, I. Formation of Lenticular Platelet Micelles via the Interplay of Crystallization and Chain Stretching: Solution Self-Assembly of Poly(Ferrocenyldimethylsilane)-Block-Poly(2-Vinylpyridine) with a Crystallizable Core-Forming Metalloblock. *Macromolecules* **2012**, *45* (9), 3883–3891. https://doi.org/10.1021/ma2027726.

(43) Vespa, M.; Hudson, Z. M.; Manners, I. Homogeneous and Segmented Nanofibers with a Conjugated Poly[3-(2′-Ethylhexyl)Thiophene] Core via Living Crystallization-Driven Self-Assembly. *Macromolecules* **2024**, *57* (4), 1509–1520. https://doi.org/10.1021/acs.macromol.3c02357.

(44) Himmelberger, S.; Duong, D. T.; Northrup, J. E.; Rivnay, J.; Koch, F. P. V.; Beckingham, B. S.; Stingelin, N.; Segalman, R. A.; Mannsfeld, S. C. B.; Salleo, A. Role of Side-Chain Branching on Thin-Film Structure and Electronic Properties of Polythiophenes. *Adv. Funct. Mater.* **2015**, *25* (17), 2616–2624. https://doi.org/10.1002/adfm.201500101.

(45) Kamps, A. C.; Cativo, M. H. M.; Fryd, M.; Park, S.-J. Self-Assembly of Amphiphilic Conjugated Diblock Copolymers into One-Dimensional Nanoribbons. *Macromolecules* **2014**, *47* (1), 161–164. https://doi.org/10.1021/ma4021483.

(46) Yu, Z.; Yan, H.; Lu, K.; Zhang, Y.; Wei, Z. Self-Assembly of Two-Dimensional Nanostructures of Linear Regioregular Poly(3-Hexylthiophene). *RSC Adv.* **2012**, *2* (1), 338–343. https://doi.org/10.1039/c1ra00833a.

(47) Lee, H.; Kim, Y. Bin; Ryu, J. W.; Kim, S.; Bae, J.; Koo, Y.; Jang, D.; Park, K. D. Recent Progress of Exciton Transport in Two-Dimensional Semiconductors. *Nano Converg.* **2023**, *10* (1). https://doi.org/10.1186/s40580-023-00404-3.

(48) Zhang, Y.; Shaikh, H.; Sneyd, A. J.; Tian, J.; Xiao, J.; Blackburn, A.; Rao, A.; Friend, R. H.; Manners, I. Efficient Energy Funneling in Spatially Tailored Segmented Conjugated Block Copolymer Nanofiber-Quantum Dot or Rod Conjugates. *J. Am. Chem. Soc.* **2021**, *143* (18), 7032–7041. https://doi.org/10.1021/jacs.1c01571.

(49) Cai, J.; Li, C.; Kong, N.; Lu, Y.; Lin, G.; Wang, X.; Yao, Y.; Manners, I.; Qiu, H. Tailored Multifunctional Micellar Brushes via Crystallization-Driven Growth from a Surface. *Science* **2019**, *366* (6469), 1095–1098. https://doi.org/10.1126/science.aax9075.

(50) Zhu, Q.; Xiong, W.; Gong, Y.; Zheng, Y.; Che, Y.; Zhao, J. Discrimination of Five Classes of Explosives by a Fluorescence Array Sensor Composed of Two Tricarbazole-

Nanostructures. *Anal. Chem.* **2017**, *89* (22), 11908–11912. https://doi.org/10.1021/acs.analchem.7b04083.

(51) Sun, C.; Xiong, W.; Ye, W.; Zheng, Y.; Duan, R.; Che, Y.; Zhao, J. Fast and Ultrasensitive Detection of a Nerve Agent Simulant Using Carbazole-Based Nanofibers with Amplified Ratiometric Fluorescence Responses. *Anal. Chem.* **2018**, *90* (12), 7131–7134. https://doi.org/10.1021/acs.analchem.8b01810.

(52) Zhang, Y.; Pearce, S.; Eloi, J. C.; Harniman, R. L.; Tian, J.; Cordoba, C.; Kang, Y.; Fukui, T.; Qiu, H.; Blackburn, A.; Richardson, R. M.; Manners, I. Dendritic Micelles with Controlled Branching and Sensor Applications. *J. Am. Chem. Soc.* **2021**, *143* (15), 5805–5814. https://doi.org/10.1021/jacs.1c00770.

(53) Dauben, B. H. J.; Mccoy, L. L. N-Bromosuccinimide. I. Allylic Bromination, a General Survey of Reaction Variables. *J. Am. Chem. Soc* **1959**, *81* (18), 4863–4873. https://doi.org/https://doi.org/10.1021/ja01527a027.

(54) Standley, E. A.; Smith, S. J.; Müller, P.; Jamison, T. F. A Broadly Applicable Strategy for Entry into Homogeneous Nickel(0) Catalysts from Air-Stable Nickel(II) Complexes. *Organometallics* **2014**, *33* (8), 2012–2018. https://doi.org/10.1021/om500156q.

(55) Azzam, T.; Eisenberg, A. Control of Vesicular Morphologies through Hydrophobic Block Length. *Angew. Chem. Int. Ed.* **2006**, *45* (44), 7443–7447. https://doi.org/10.1002/anie.200602897.

(56) Pangborn, A. B.; Giardello, M. A.; Grubbs, R. H.; Rosen, R. K.; Timmers, F. J. Safe and Convenient Procedure for Solvent Purification. *Organometallics* **1996**, *15* (5), 1518–1520. https://doi.org/10.1021/om9503712.

(57) Schneider, C. A.; Rasband, W. S.; Eliceiri, K. W. NIH Image to ImageJ: 25 Years of Image Analysis. *Nat. Methods* **2012**, *9* (7), 671–675. https://doi.org/10.1038/nmeth.2089.

Chapter 5

Surface-Confined Growth of Micellar Brushes with a Semiconductive Crystalline Core Towards Hybrid Organic-Inorganic Photodetectors

This chapter contains as of yet unpublished results.

Introductory Comments:

This chapter aims to fabricate a light-harvesting photodetector device using nanofibers grown from surface-confined seeds. The work presented herein consists only of investigations into surface-confined seeded growth and characterization of the resulting surfaces. Further work on device fabrication is needed to bring this project to completion.

Contributions:

This work was conceived by Prof. Ian Manners, Prof. Akshay Rao, and Prof. Huibin Qiu. Marcus Vespa performed the synthesis, solution self-assembly experiments, material characterization, and some seed attachment experiments. AFM imaging made use of the 4D LABS core facility at Simon Fraser University (SFU) and was performed by Ayesha Nadeem along with some surface nanofiber growth experiments. Prof. Ian Manners, Prof. Yifan Zhang, Prof. Makhsud Saidaminov, and Dr. Shixing Lei contributed to data discussions. Marcus Vespa wrote the manuscript along with input from Dr. Etienne LaPierre.

5.1 Abstract

Seeded growth of nanofibers from surface-confined seed micelles has emerged as a useful technique to specifically pattern surfaces with tailored functionality. Crystallization-driven self-assembly (CDSA) of diblock copolymers (BCPs) with a π-conjugated core-forming block has been demonstrated to produce 1D length-controlled nanofibers with desirable optoelectronic properties such as broad absorption over the UV-visible range and long exciton diffusion lengths of up to 350 nm. Herein, we report the immobilization of seed micelles on a crystalline silicon surface and investigate the surface-confined seeded growth of two poly(ethylene glycol) (PEG)-functionalized BCPs, PDHF$_{17}$-*b*-PEG$_{227}$ (PDHF = poly(di-*n*-hexylfluorene)) and P3EHT$_{23}$-*b*-PEG$_{113}$ (P3EHT = poly(3-(2'-ethylhexyl)thiophene)), towards the formation of hybrid organic-inorganic photodetection (PD) devices that utilize the nanofibers as light-harvesting antennae by funnelling photogenerated charges from the nanofiber termini to the silicon substrate. We report the surface topology following seed immobilization and nanofiber growth and reveal the superior ability of PEG corona-forming blocks to adhere to silicon surfaces compared to the currently used poly(2-vinylpyridine) (P2VP) corona-forming block. Following this, potential device architectures and experiments are proposed to test the ability of surface-confined π-conjugated polymer nanoparticles (CPNPs) to act as light harvesting antennae in silicon-based PDs.

5.2 Introduction

Photodetectors (PDs) are electronic devices that convert energy generated by light absorption into electrical signals that are utilized in the fields of night surveillance, secure communication, environmental monitoring, and light sensing/detection.[1–4] The most prevalent PDs

are based on inorganic semiconductors such as single crystalline or polycrystalline silicon, because they exhibit small exciton binding energies, high photonic sensitivity, charge carrier mobilities, and stability.[3,4] Despite these advantageous properties, silicon suffers from being brittle and requiring expensive and energy intensive manufacturing processes.[1,4] Silicon's ubiquity in PD devices is due to its natural abundance and the significant overlap between the bandgap of single crystalline and polycrystalline silicon (~1.1 eV) with the solar spectrum; however, low molar absorptivity, particularly from 800-1100 nm ($\varepsilon = 10^3$-10^0), means thick layers (~50 μm) are required to absorb broadband light sources, most notably, sunlight.[5] Further, ~40% of 500 nm light incident on bare silicon is reflected away and does not generate usable charges.[6,7]

Organic polymeric semiconductors mitigate these shortcomings as they are solution-processable, have tunable absorptions that can extend to the near IR range, and are printable on large-area flexible substrates.[8–11] Adding a polymeric layer onto silicon increases incident light absorption efficiency by reducing surface reflectivity, as a P3HT thin film reflects only 18% of 500 nm incident light and absorbs 95% of 450-600 nm light when deposited as a 240 nm thick film.[12,13] Unfortunately, exciton diffusion lengths in organic polymeric films are notoriously lower (~5-10 nm) than their inorganic counterparts, restricting the effective thickness of a photoactive layer to 20 nm, while a layer ~100 nm thick is necessary to absorb most incident sunlight.[14,15] A promising approach towards addressing these limitations is the formation of semiconducting fiber-like micelles with high exciton diffusion lengths by crystallization-driven self-assembly (CDSA) of π-conjugated BCPs. Generally, π-conjugated polymer nanoparticles (CPNPs) have large absorption cross sections, efficient energy transfer capabilities, and absorbed photons have a high chance to form mobile excitons, making them excellent candidates for light harvesting and PD applications.[16–18] For example, nanofibers self-assembled from a charged phosphonium-

terminated P3HT amphiphile, $P3HT_{30}$-[PPh_3Me][BPh_4], allowed for exciton diffusion lengths of 350 nm to be achieved through the fiber core.[19,20]

Living CDSA seeded growth of BCPs with a crystallizable, conjugated core-forming block is a powerful technique to generate uniform samples of 1D nanofibers with controlled size and dimensions.[21–30] The seeded growth method begins with the formation of long polydisperse nanofibers through spontaneous nucleation and crystallization of the core-forming block induced by dissolving the BCP in a solvent which is suitable for both blocks (common solvent) and adding solvent which selectively solvates the corona-forming block (selective solvent) or by heating the BCP in a temperature-dependent selective solvent which acts as a common solvent at high temperatures and a corona-selective solvent at room temperature.[22,31,32] Ultrasonication-induced fracturing of the polydisperse fibers generates "seed" micelle fragments with relatively low average lengths and length differences.[22,31,32] The seed termini remain active towards addition of dissolved BCP (unimer) in a good solvent for both blocks and upon unimer addition, BCP molecules epitaxially crystallize on the seed termini creating nanofibers with final lengths that are linearly correlated to the unimer-to-seed mass ratio (m_{unimer}/m_{seed}), allowing for exceptional control over nanofiber length.

By combining the broadband light absorption well-suited for the solar spectrum of silicon with the long-range exciton diffusion lengths and visible light harvesting capabilities of CPNPs, more efficient light absorption and subsequent charge generation is expected. Moreover, the optoelectronic properties of CPNPs are dependent on their size, chemical composition and dimensionality and living CDSA provides a convenient methodology to allow for control over the latter two factors, which is crucial to maximizing electronic performance.[29]

Seeded growth of nanofibers from a surface represents an attractive approach for fabrication of specifically patterned surfaces.[33] Hydrogen-bonding interactions between the corona-forming block in poly(ferrocenyldimethylsilane)-*b*-poly(2-vinylpyridine) (PFS-*b*-P2VP) and surface silanol (Si-OH) groups on a silicon wafer were used to immobilize PFS-*b*-P2VP seed micelles on the silicon surface, and the seeds were subsequently used as sites for seeded growth of length-controlled and modular micellar brushes.[33] Substitution of the functionally inert PFS core-forming block used by Qiu and coworkers[33] for a π-conjugated semiconductive core-forming block such as poly(3-(2'-ethylhexyl)thiophene) (P3EHT) or poly(di-*n*-hexylfluorene) (PDHF) unlocks exciting opportunities for fabrication of thin film organic-inorganic PDs capable of efficient Förster resonance energy transfer (FRET) to silicon. In addition, the directionality of the grown nanofibers, perpendicular to the surface, provides an efficient avenue to funnel energy generated at the fiber termini directly toward the silicon. Because the nanofibers are directly anchored and therefore in the immediate proximity to the substrate, efficient FRET from the nanofiber to the silicon is expected upon photoexcitation.

Recently, P3EHT-*b*-P2VP seed micelles were attached to a silicon surface and successfully used as sites for nanofiber growth; however, the authors did not analyze the nanofibers' ability to transmit photogenerated excitons.[34] To create a nanofiber-based PD device with maximized light absorption and optimal transfer of photogenerated charges to silicon, high density and homogeneous nanofiber layers are necessary for full and uniform coverage of the substrate. We hypothesize that PEG may serve as a more effective anchoring corona-forming block compared to P2VP corona-forming blocks used previously.[33–35] Per unit mass, PEG has a greater density of potential hydrogen bond acceptors (oxygen) compared to P2VP (nitrogen), because most of the atoms which comprise P2VP are non-hydrogen bonding atoms (carbon). Furthermore, in P2VP

the nitrogen atoms are in the 1- position of the pyridine rings which is sterically obstructed by the carbon chain composing the polymer backbone, thereby restricting access of the nitrogen atom to the silanol groups on the silicon surface and potentially preventing all of the nitrogen atoms from forming an effective hydrogen bond. Conversely, the sp^3 hybridization of all the atoms in PEG and lack of any planar aromatic system confers free rotational movement around every bond which may result in a comparatively higher number of oxygen atoms contacting the silicon surface and formation of more hydrogen bonds. We propose that seeds composed of PEG-functionalized BCPs will attach to silicon more robustly resulting in higher density nanofiber layers. Herein, we investigate the ability of CPNPs formed from two BCPs with PEG coronas of different degrees of polymerization (DP_n), $PDHF_{17}$-*b*-PEG_{227} and $P3EHT_{23}$-*b*-PEG_{113}, to hydrogen bond to a silicon surface and provide sites for nanofiber growth.

5.3 Results and Discussion

5.3.1 Block copolymer synthesis and characterization

Alkyne-terminated PDHF homopolymers were synthesized by Grignard Metathesis (GRIM) Polymerization beginning by generating an organomagnesium reagent through transmetallation of a C-I bond using turbo-Grignard addition to a dihalogenated fluorene monomer and subsequent polymerization using $Ni(dppp)Cl_2$ (dppp = 1,3-bis(diphenylphosphino)propane). *In situ* termination of the living $PDHF_{17}$ chain with an alkyne end group was achieved through the addition of excess ethynylmagnesium bromide and, after successive precipitation into methanol (MeOH) and acetone, the desired product was isolated as a yellow solid in a 58% yield (Scheme 5.1a) where subscripts denote the polymer degree of polymerization (DP_n).[36] The polymer number average molecular mass (M_n) and dispersity ($Đ_M$, where $Đ_M = M_w/M_n$) were determined by gel

permeation chromatography (GPC) which revealed a $PDHF_{17}$ homopolymer of $DP_n = 17$ (M_n = 5, 800 Da, $Đ_M$ = 1.09) (Figure S5.1). The product was analyzed using ^{1}H NMR spectroscopy, which showed a singlet resonance at 3.16 ppm consistent with a terminal ethynyl proton, indicating successful functionalization of the polymer chain end with an alkyne (Figure S5.4).[30] Next, azide-terminated PEG_{227}-N_3 (M_n = 10, 000 Da) was synthesized by conversion of the terminal hydroxy group on a PEG-methyl ether homopolymer to a tosyl group followed by introduction of an azide group by treatment with sodium azide (Scheme 5.1b). This material was synthesized in a yield of 72% and analyzed using ^{1}H NMR spectroscopy and GPC. Complete removal of the terminal tosyl group following reaction with sodium azide is indicated by the disappearance of the aromatic resonances in the ^{1}H NMR spectrum (~7-8 ppm) (Figure S5.5) and the GPC trace showed the presence of a polymeric material with a M_n = 10, 000 Da and $Đ_M$ = 1.11 (Figure S5.1).

Scheme 5.1. (a) Synthesis of alkynyl-$PDHF_{17}$ homopolymer. *i*PrMgCl•LiCl = isopropylmagnesium chloride–lithium chloride, THF = tetrahydrofuran. **(b)** Synthesis of azide-functionalized PEG_{113}-N_3 or PEG_{227}-N_3 homopolymers. DCM = dichloromethane, DMF = *N*,*N*-dimethylformamide.

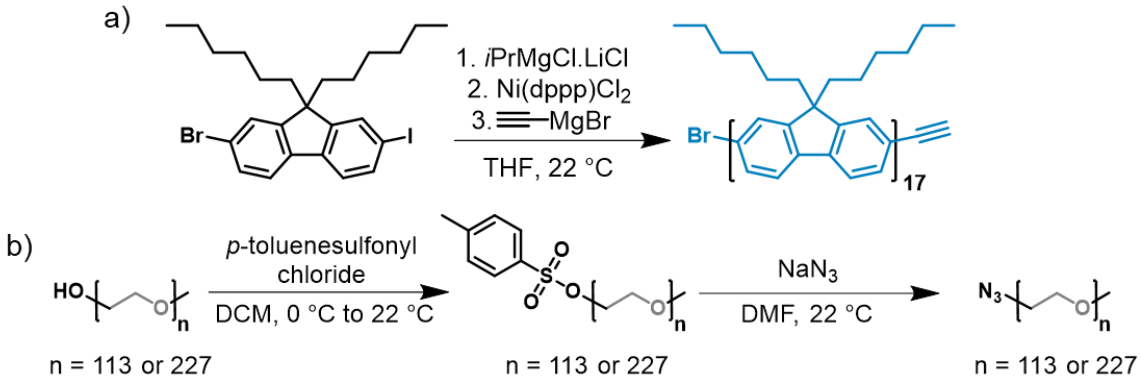

The azide-functionalized-PEG (PEG_{227}-N_3) was suitable for coupling with alkynyl-$PDHF_{17}$ using copper-mediated azide-alkyne cycloaddition click chemistry (CuAAC) to form $PDHF_{17}$-*b*-PEG_{227}. The crude $PDHF_{17}$-*b*-PEG_{227} BCP was purified using successive precipitation

into ethanol to remove excess PEG_{227}-N_3 followed by column chromatography with chloroform as a mobile phase to remove $PDHF_{17}$ homopolymer. The resulting product was a yellow solid isolated in an 18% yield that was subsequently analyzed using ^{1}H NMR spectroscopy and GPC. The ^{1}H NMR spectrum closely matched that reported in the literature and when analyzed by GPC, the product was found to have a number-average molar mass of M_n = 15,800 Da and $Đ_M$ = 1.19.[30] The $PDHF_{17}$-*b*-PEG_{227} GPC trace shows a maximum absorbance at a relatively lower retention volume than the constituent homopolymers suggesting formation of a higher molecular mass species when compared to alkynyl-$PDHF_{17}$ and PEG_{227}-N_3 (Figure S5.1). $P3EHT_{23}$-*b*-PEG_{113} and its homopolymer precursors were synthesized using the method described in Chapter 2.

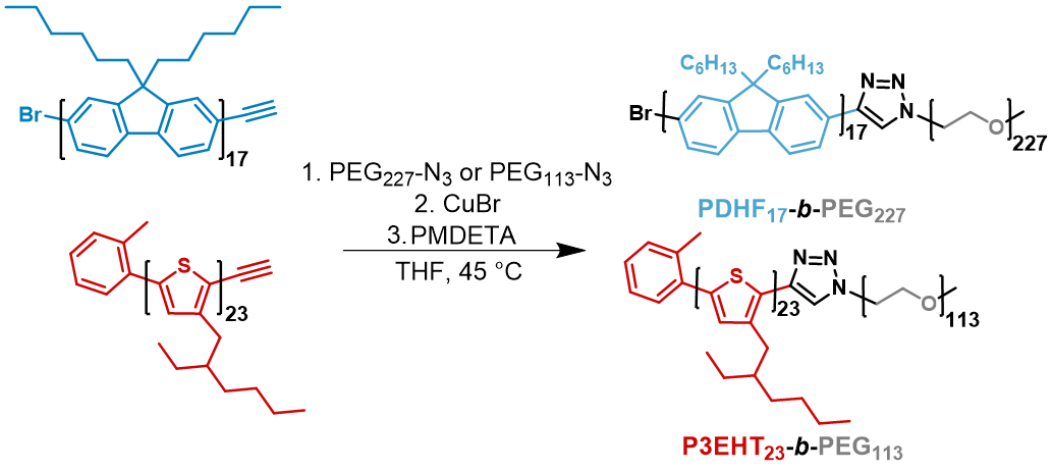

Polymer	M_n (Da)	M_w (Da)	$Đ_M$[a]
$PDHF_{17}$-*b*-PEG_{227}	15,800[a]	18,800[a]	1.19
$P3EHT_{23}$-*b*-PEG_{113}	11,900[a]; 9,600[b]	12,600[a], 10,200[b]	1.06

Figure 5.1. Chemical structures and molar mass characterization of the synthesized BCPs analyzed by GPC and by integration of proton nuclear magnetic resonance (^{1}H NMR) spectra. [a]Determined by GPC. [b]Determined by relative integration of ^{1}H NMR spectrum signals. For alkynyl-P3EHT, relative integration was performed between ^{1}H NMR signals at 2.51 ppm (s, *o*-tolyl CH_3 = 3H) and 6.97 ppm (s, thiophene CH = 1H). CuBr = copper(I) bromide, PMDETA = *N,N,N′,N″,N″*-pentamethyldiethylenetriamine, THF = tetrahydrofuran.

5.3.2 Preparation of polydisperse 1D nanofibers and seeds of $PDHF_{17}$-*b*-PEG_{227} and $P3EHT_{23}$-*b*-PEG_{113}

(a) $PDHF_{17}$-*b*-PEG_{227}

Polydisperse fiber-like 1D micelles (nanofibers) of $PDHF_{17}$-*b*-PEG_{227} were fabricated by first dissolving the BCP in tetrahydrofuran (THF, 0.2 mg/mL) which is a suitable solvent for both blocks, followed by dropwise addition of an equivalent volume of MeOH, a selective solvent for the PEG corona-forming block, to form a 1:1 v/v THF:MeOH solution (0.1 mg/mL). The nanofiber solution was annealed at 30 °C for 24 h before being cooled to 22 °C and aged for 24 h (Figure 5.2a, S5.18a, b). Small nanofiber fragments that function as seeds were produced by ultrasonication of a polydisperse $PDHF_{17}$-*b*-PEG_{227} nanofiber solution (Figure 5.2c) (1:1 THF:MeOH, 0.1 mg/mL) at 0 °C for 3 h (L_n = 47 nm, $Đ_L$ = 1.35) followed by annealing at 30 °C for 18 h prior to use (Figure S5.20a).

(b) $P3EHT_{23}$-*b*-PEG_{113}

Polydisperse $P3EHT_{23}$-*b*-PEG_{113} nanofibers were fabricated by heating solid $P3EHT_{23}$-*b*-PEG_{113} in *n*-butanol (*n*BuOH) to 90 °C for 30 min. then cooling to 22 °C slowly (over ca. 4 h) and aging for 24 h. After aging, MeOH was added to form a 1:1 v/v *n*BuOH:MeOH mixture (0.1 mg/mL) which was drop-cast onto a carbon-coated copper grid and imaged using bright-field transmission electron microscopy (TEM) (Figure 5.2b, S5.19a, b). Seeds (Figure 5.2d) were produced by ultrasonication of a polydisperse $P3EHT_{23}$-*b*-PEG_{113} nanofiber solution in 1:1 *n*BuOH:MeOH at 0 °C for 3 h (L_n = 44 nm, $Đ_L$ = 1.26) followed by annealing at 30 °C for 24 h (Figure S5.21a, b) prior to the following seeded growth experiments.

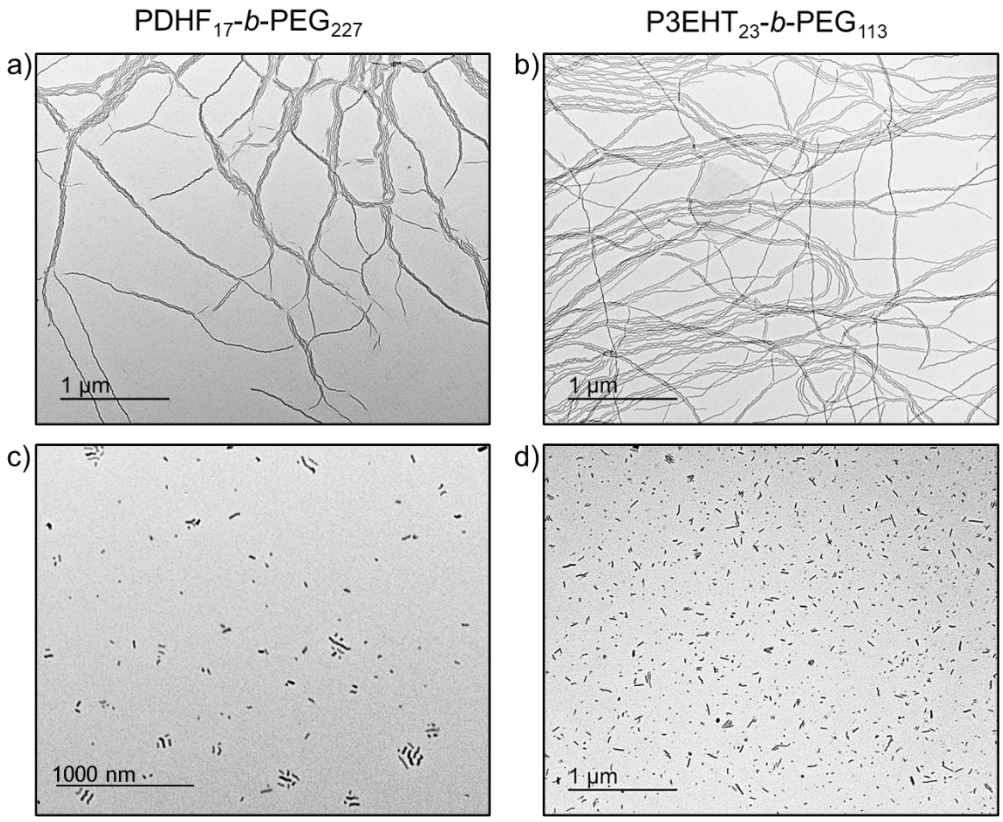

Figure 5.2. TEM images of polydisperse **(a)** $PDHF_{17}$-*b*-PEG_{227} and **(b)** $P3EHT_{23}$-*b*-PEG_{113} nanofiber solutions following solvent evaporation. TEM images of **(c)** $PDHF_{17}$-*b*-PEG_{227} seeds (L_n = 47 nm, $Đ_L$ = 1.35) and **(d)** $P3EHT_{23}$-*b*-PEG_{113} seeds (L_n = 44 nm, $Đ_L$ = 1.26) formed by ultrasonication of their respective polydisperse nanofiber solutions. TEM images were obtained following solvent evaporation.

5.3.3 Solution-phase seeded growth of length-controlled nanofibers using colloidal seeds

Before seeded growth using surface-immobilized seeds was attempted, solution-phase seeded growth from colloidal seeds was performed to ensure that nanofiber growth was controlled, and the experimental lengths matched theoretically predicted values. Theoretical lengths are based on the equation $L_{n(theory)} = L_{n(seed)} [(m_{unimer}/m_{seed}) +1]$.[32]

(a) $PDHF_{17}$-*b*-PEG_{227}

Seeded growth of length-controlled $PDHF_{17}$-*b*-PEG_{227} nanofibers at 22 °C was achieved

by adding increasing volumes of a stock solution of unimeric PDHF$_{17}$-*b*-PEG$_{227}$ (THF, 1 mg/mL) to seed solutions (47 nm) (1:1 THF:MeOH, 0.1 mg/mL). Nanofibers with lengths ranging from L_n = 224 nm (m_{unimer}/m_{seed} = 4) to L_n = 622 nm (m_{unimer}/m_{seed} = 17) and low dispersities from $Đ_L$ = 1.05-1.13 were fabricated (Figure 5.3a, S5.22-S5.24, Table S5.1). Using seeds with L_n = 47 nm, at m_{unimer}/m_{seed} = 8, $L_{n(theory)}$ is 423 nm and the experimental L_n found here is 381 nm. The experimental nanofiber lengths are within one standard deviation (σ) of the theoretically predicted lengths.

(b) P3EHT$_{23}$-*b*-PEG$_{113}$

Seeded growth of length-controlled P3EHT$_{23}$-*b*-PEG$_{113}$ nanofibers at 22 °C was achieved by adding increasing volumes of a stock solution of unimeric P3EHT$_{23}$-*b*-PEG$_{113}$ (THF, 2 mg/mL) to seed solutions (44 nm) (1:1 *n*BuOH:MeOH, 0.1 mg/mL). Nanofibers with lengths ranging from L_n = 131 nm (m_{unimer}/m_{seed} = 4) to L_n = 1528 nm (m_{unimer}/m_{seed} = 20) and dispersities of $Đ_L$ = ~1.30 were fabricated (Figure 5.3b, S5.25-S5.27, Table S5.2). Higher dispersity nanofibers were obtained during seeded growth of this material at 22 °C compared to fibers of PDHF$_{17}$-*b*-PEG$_{227}$ which is known to occur in this material as discussed in Chapter 2.

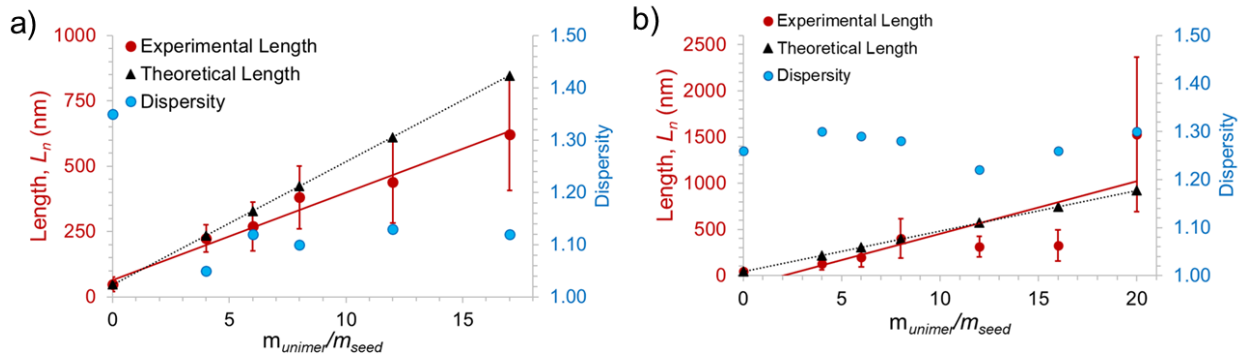

Figure 5.3. Plot showing the dependence of fiber length (L_n) on unimer-to-seed mass ratio when using solution-phase seeded growth at 22 °C from seeds of **(a)** PDHF$_{17}$-*b*-PEG$_{227}$ and **(b)** P3EHT$_{23}$-*b*-PEG$_{113}$. Error bars represent standard deviation in L_n values.

5.3.4 Seeded growth of π-conjugated core nanofibers using surface immobilized seeds

Seed attachment and seed density studies before and after washing with selective solvent mixture

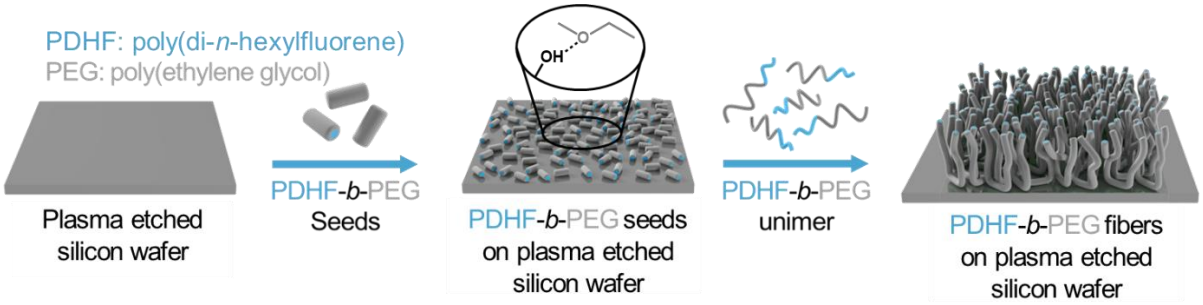

Figure 5.4. Surface-confined self-assembly of $PDHF_{17}$-*b*-PEG_{227} on a plasma etched silicon wafer. Cartoon schematic showing adherence of $PDHF_{17}$-*b*-PEG_{227} seeds to silicon wafer surface through hydrogen bonding to surface silanol groups and subsequent growth of nanofiber brush layers following unimer addition.

To determine if PEG-functionalized BCP seeds attach to a silicon wafer surface, polished boron-doped (*p*-type) silicon wafers (1 cm x 1 cm) were plasma etched by exposure to oxygen plasma for 600 s to remove contaminants adhered to the surface.

(a) $PDHF_{17}$-*b*-PEG_{227}

A film of $PDHF_{17}$-*b*-PEG_{227} seeds was deposited onto the plasma etched silicon surface by spin coating a $PDHF_{17}$-*b*-PEG_{227} seed solution (10 µl, 1:1 v/v THF:MeOH, 0.5 mg/mL, 3000 rpm). To remove non-adhered seeds, the nanofiber laden wafer was washed by submersion in 1:1 THF:MeOH three times and allowed to dry 16 h before AFM analysis. The average seed height was 3.6 ± 0.1 nm which is ~1 nm shorter than heights previously found when measuring $PDHF_{14}$-*b*-PEG_{227} CPNPs (4.5 nm) (Figure S5.6).[30] While this discrepancy is small, a potential reason for the lower height values in this case may be because the PEG corona is attached to the silicon wafer and therefore does not collapse on top of the micelle, which may be the case in previous

measurements wherein nanofibers were drop-cast onto a non-plasma etched substrate. Additionally, previous measurements were performed on fibers where steric crowding of the coronal chains causes them to be in a more extended conformation.

An analysis of the surface seed density prior to and after washing with 1:1 THF:MeOH was undertaken to evaluate the efficacy of washing and determine how many seeds detach during washing which is a measure of the anchoring robustness. Prior to washing, $PDHF_{17}$-*b*-PEG_{227} seeds tended to aggregate into distinct regions and unevenly coat the surface (Figure S5.8a-e) and following washing, the seeds appeared less densely packed but remained clustered into small groups (Figure S5.9a-j). We also investigated the number of seeds attached to the surface following deposition of seed solutions of varying concentration after washing. When casting from seed solutions with concentrations of 0.1-0.4 mg/mL, the number of seeds attached to the surface per μm^2 was approximately equivalent (~40), while use of a 0.5 mg/mL seed solution resulted in 135 seeds per μm^2 (3375 per 25 μm^2) (Figure 5.7, S5.10a, b). The seeds appeared less evenly distributed when 0.5 mg/mL seed solutions were used (Figure 5.5a) but casting using this solution concentration resulted in the highest seed attachment (Figure S5.10a, b) so this concentration was chosen to perform surface-confined nanofiber growth studies.

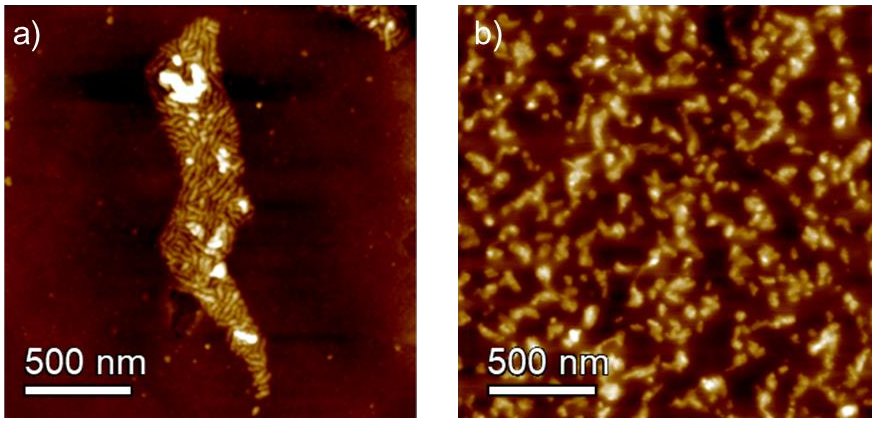

Figure 5.5. AFM height images of adhered **(a)** $PDHF_{17}$-*b*-PEG_{227} seeds (1:1 THF:MeOH, 0.5 mg/mL) and **(b)** $P3EHT_{23}$-*b*-PEG_{113} seeds (1:1 *n*BuOH:MeOH, 0.5 mg/mL) on a plasma etched silicon wafer surface after washing with 1:1 THF:MeOH or 1:1 *n*BuOH:MeOH, respectively.

Negative control experiments were performed wherein a blank, plasma etched silicon wafer surface was imaged using atomic force microscopy (AFM) showing no CPNPs and only irregular 2D structures (Figure 5.6a) that are proposed to be inherent height variations in the silicon surface topology as it is not manufactured as a perfectly smooth surface. Next, we investigated if $PDHF_{17}$-*b*-PEG_{227} self-assembles on the silicon surface if placed in 1:1 THF:MeOH with no seeds present. To a blank, plasma etched silicon wafer, a solution of $PDHF_{17}$-*b*-PEG_{227} unimer (10 µl, THF, 2 mg/mL) was applied by spin-coating onto the surface and then the wafer was fully submerged in 1:1 THF:MeOH, the solution was allowed to age at 22 °C while shaking on an automatic mixing table for 24 h, and then removed from the solvent and dried before AFM imaging. AFM revealed the presence of localized regions of ill-defined BCP aggregates (Figure 5.6b) with no CPNPs observable, reinforcing that added unimer does not form 1D CPNPs in the absence of seeds on the surface if the wafer is submerged in a 1:1 THF:MeOH solution alone.

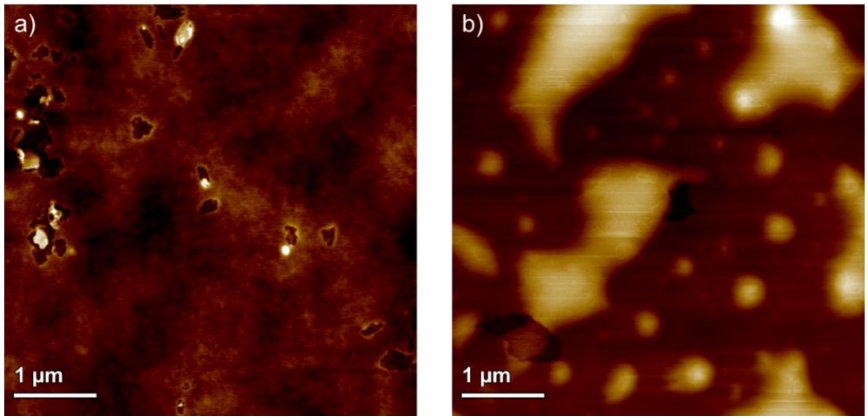

Figure 5.6. AFM height images of **(a)** a blank, plasma etched silicon surface and **(b)** $PDHF_{17}$-*b*-PEG_{227} unimer (10 µl, THF, 2 mg/mL) that was spin-coated (3000 rpm) onto a blank plasma etched silicon surface and placed in 1:1 v/v THF:MeOH with no seeds present. Only ill-defined BCP aggregates are observed on the surface.

(b) $P3EHT_{23}$-*b*-PEG_{113}

Next, we investigated attachment of $P3EHT_{23}$-*b*-PEG_{113} seeds to a plasma etched silicon surface. In contrast to $PDHF_{17}$-*b*-PEG_{227} seeds, casting a film of $P3EHT_{23}$-*b*-PEG_{113} seeds resulted in a significantly more even seed distribution across the surface with little localization or aggregation (Figure 5.5b) which may be caused by the slower evaporation of 1:1 v/v *n*BuOH:MeOH compared to 1:1 THF:MeOH. From 0.2 – 0.5 mg/mL, higher counts of $P3EHT_{23}$-*b*-PEG_{113} seeds were observed compared to $PDHF_{17}$-*b*-PEG_{227} seeds following washing (Figure 5.7, S5.13a, b). When casting from $P3EHT_{23}$-*b*-PEG_{113} seed solutions with concentrations of 0.1-0.4 mg/mL, ~90 seeds attached to the surface per μm^2 which is nearly double the amount of attached $PDHF_{17}$-*b*-PEG_{227} seeds at the same concentrations, with the highest attachment (110 seeds per μm^2) occurring when a 0.3 mg/mL $P3EHT_{23}$-*b*-PEG_{113} seed solution was used (Figure S5.13a, b). A higher incidence of $P3EHT_{23}$-*b*-PEG_{113} seeds attached to the surface is expected because the $P3EHT_{23}$-*b*-PEG_{113} seed solution has a higher molar concentration (2.5×10^{-4} mmol/mL) compared to the $PDHF_{17}$-*b*-PEG_{227} seed solution (1.89×10^{-4} mmol/mL); however,

double the comparative attachment is too large of a discrepancy to attribute to only concentration differences. For example, 10 µl of a 0.3 mg/mL P3EHT$_{23}$-*b*-PEG$_{113}$ seed solution was spin coated onto the silicon surface and contains 2.5 x 10^{-8} mmol of material while 10 µl of a 0.3 mg/mL PDHF$_{17}$-*b*-PEG$_{227}$ solution contains 1.89 x 10^{-8} mmol of material. Assuming the same amount of solvent and seeds is removed from the surface during spin-coating for both, P3EHT$_{23}$-*b*-PEG$_{113}$ should have 1.32 times the number of attached seeds (2.5 x 10^{-8}/1.89 x 10^{-8}) based on molarity alone. Further, the PDHF$_{17}$-*b*-PEG$_{227}$ seeds are slightly longer (L_n = 47 nm) than the P3EHT$_{23}$-*b*-PEG$_{113}$ seeds (L_n = 44 nm), but less BCP chains compose a 47 nm PDHF$_{17}$-*b*-PEG$_{227}$ seed than a 44 nm P3EHT$_{23}$-*b*-PEG$_{113}$ seed. This is based on previous reports that the PDHF π-π stacking distance in PDHF$_{14}$-*b*-PEG$_{227}$ fibers is 0.46 nm and has 4 interdigitated lamellae,[30] so a 47 nm seed has 409 BCP chains ([47 nm/0.46 nm] x 4 lamellae) while P3EHT chains have a π-π stacking distance of 0.49 nm in P3EHT$_{23}$-*b*-PEG$_{113}$ fibers and 6 interdigitated lamellae,[37] so a 44 nm seed has 539 BCP chains ([44 nm/0.49 nm] x 6 lamellae). Less BCP chains in PDHF-*b*-PEG seeds suggests that even though there is a lower molar concentration, the chains are distributed among more seeds compared to P3EHT-*b*-PEG seeds leading to the conclusion that the shorter PEG corona-forming block (PEG$_{113}$) causes higher seed attachment than the comparatively longer PEG$_{227}$ corona-forming block. This may be because the PEG$_{113}$-functionalized seeds occupy a smaller surface area, and therefore more seeds can attach in a given area compared to the longer PEG$_{227}$-functionalized seeds despite there being more potential hydrogen bond acceptors in PEG$_{227}$ than PEG$_{113}$. It is also possible that the higher attachment is caused by more individual PEG chains composing a P3EHT$_{23}$-*b*-PEG$_{113}$ seed than a PDHF$_{17}$-*b*-PEG$_{227}$ seed or because the long PEG$_{227}$ blocks have a higher preference to associate with PEG$_{227}$ chains on adjacent micelles rather than the silicon surface which could explain the observed seed localization in films cast from PDHF$_{17}$-

b-PEG$_{227}$ seed solutions. Regardless, both P3EHT$_{23}$-*b*-PEG$_{113}$ and PDHF$_{17}$-*b*-PEG$_{227}$ had higher seed attachment per 25 μm^2 than PFS$_{36}$-*b*-P2VP$_{502}$[33] at all tested concentrations (0.2 – 0.5 mg/mL) (Figure 5.7) even though the P2VP block DP$_n$ used by Qiu and coworkers is ~2-5 times higher than the DP$_n$ of both PEG blocks used here, supporting that PEG is a superior anchoring corona-forming block compared to P2VP. This finding could be used to design BCPs with a higher affinity for surfaces and allows tailoring of a substrate surface if higher or lower seed densities are required.

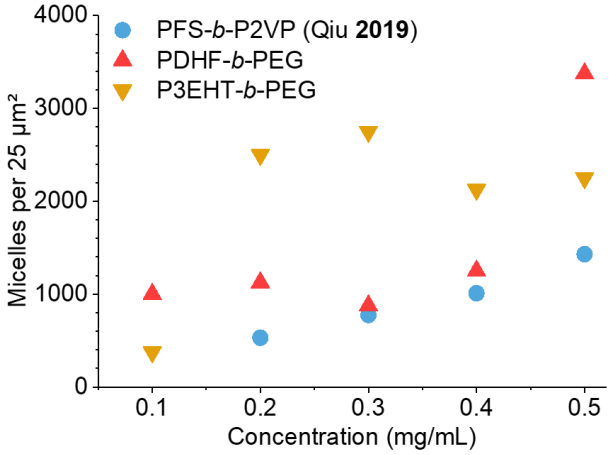

Figure 5.7. Graph showing the comparative seed densities per 25 μm^2 of PDHF$_{17}$-*b*-PEG$_{227}$ (red triangles) and P3EHT$_{23}$-*b*-PEG$_{113}$ (orange triangles) compared to PFS$_{36}$-*b*-P2VP$_{502}$ (blue circles) (Qiu et *al. Science*, 2019).[33] All samples were washed with their self-assembly solvents prior to seed density counts being obtained.

Seeded growth of 1D nanofibers from surface immobilized seeds

(a) PDHF$_{17}$-*b*-PEG$_{227}$

PDHF$_{17}$-*b*-PEG$_{227}$ seed-functionalized silicon wafers were placed in vials containing 1:1 THF:MeOH such that the final concentration will be 0.05 mg/mL following unimer addition. The vial was placed on an automatic mixing table and increasing amounts of stock PDHF$_{17}$-*b*-PEG$_{227}$ unimer solution (THF, 2 mg/mL) was added in one aliquot, the vial was sealed, and the solutions were allowed to mix for 24 h. After 24 h, the wafer was removed from the vial, washed three times

in 1:1 THF:MeOH, and allowed to dry 16 h before analysis by AFM. When unimer equivalents equaling m_{unimer}/m_{seed} = 0.2 were added, it was difficult to visualize growth from the seeds by AFM; however, nanofiber growth from the seeds was more apparent when higher equivalents were used (m_{unimer}/m_{seed} = 0.4, 0.8, and 1.2) (Figure 5.8a-d). Addition of 0.4 mass equivalents showed modest growth, likely due to the small amount of unimer added, but addition of 0.8 and 1.2 mass equivalents showed clear fiber elongation compared to the original seed length, with a relatively uniform nanofiber layer developing at 0.8 equivalents (Figure 5.8c). Addition of 1.2 mass equivalents formed longer nanofibers compared to 0.8 mass equivalents, but the surface is more sparsely populated which may be due to seed or fiber dislodgement (Figure 5.8d).

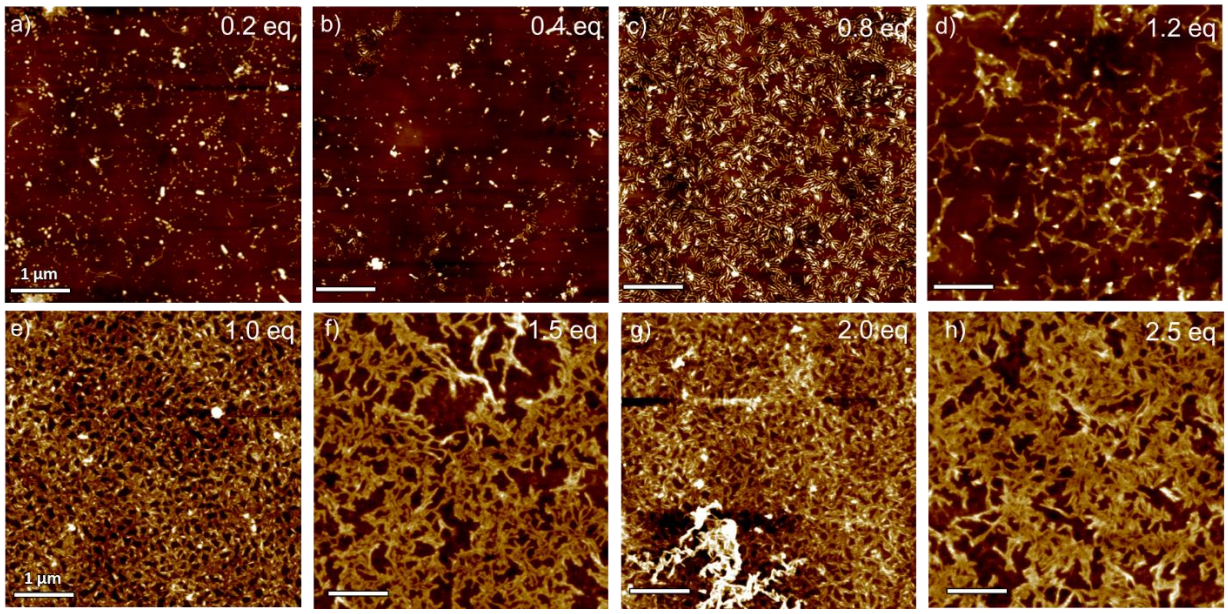

Figure 5.8. AFM height images of PDHF$_{17}$-*b*-PEG$_{227}$ fibers grown from surface immobilized seeds following washing upon addition of unimer equaling m_{unimer}/m_{seed} = **(a)** 0.2, **(b)** 0.4, **(c)** 0.8, and **(d)** 1.2 in 1:1 THF:MeOH (0.05 mg/mL). AFM height images of P3EHT$_{23}$-*b*-PEG$_{113}$ fibers grown from surface immobilized seeds following washing upon addition of unimer equaling m_{unimer}/m_{seed} = **(e)** 1.0, **(f)** 1.5, **(g)** 2.0, and **(h)** 2.5 in 1:1 *n*BuOH:MeOH (0.05 mg/mL). All scale bars represent 1 µm.

(b) P3EHT$_{23}$-*b*-PEG$_{113}$

The same protocol for nanofiber growth from P3EHT$_{23}$-*b*-PEG$_{113}$ seeded silicon surfaces was performed as described above for PDHF$_{17}$-*b*-PEG$_{227}$ seeded surfaces, but higher mass equivalents were used to make nanofiber growth more readily observable by AFM. Increasing volumes of stock P3EHT$_{23}$-*b*-PEG$_{113}$ unimer solution (THF, 2 mg/mL) was added equaling m_{unimer}/m_{seed} = 1.0, 1.5, 2.0, and 2.5 which all resulted in distinct growth of CPNP brush layers. The P3EHT$_{23}$-*b*-PEG$_{113}$ nanofibers made relatively consistent coverings of the silicon surface and were visually longer at m_{unimer}/m_{seed} = 2.5 compared to m_{unimer}/m_{seed} = 1.0, with the lengths increasing more regularly compared to growth from PDHF$_{17}$-*b*-PEG$_{227}$ seeds. A potential cause of this difference in self-assembly behaviour may be that the longer corona-forming block on PDHF$_{17}$-*b*-PEG$_{227}$ seeds may interfere with unimer adding to the seed termini, causing irregular nanofiber growth, a process known as coronal poisoning.[38,39]

Both materials made surface-confined brush layers successfully, and future work will involve adding higher unimer equivalents to make thicker nanofiber brush layers. Scanning electron microscopy and AFM could be used to analyze the brush layer thickness at different equivalents as it is proposed that increased nanofiber length causes surface crowding and the formation of erect structures.[33,34]

5.3.5 Proposed photodetector device design and testing

Surface-confined CPNP growth has been demonstrated here and results in nanofiber brush layers that cover the silicon wafer so the design and construction of PD devices must be considered next. Three silicon-based PD devices will be constructed by first thermally depositing gold onto the backside of the silicon wafer to form contact electrodes, which will be connected to a digital

multimeter for measurement of the photocurrent amperage and voltage (Figure 5.9). Following seed adherence and nanofiber growth, the devices will be exposed to 200-1000 nm light and the photocurrent will be measured as a function of the incident light wavelength. The first device will be a control device of bare polished silicon to obtain the baseline photocurrent generated by a silicon-based PD (Figure 5.9a), the second device (Figure 5.9b) will have a BCP layer spin-coated onto the surface to determine if non-assembled BCP increases photocurrent, and the third device (Figure 5.9c) will be covered with a CPNP brush layer grown from surface-immobilized seeds to determine if nanofibers efficiently funnel charges to the silicon substrate and increase photocurrent as proposed. This will be completed for both the BCP systems investigated herein and follow-up work will compare the performance of all 5 PDs to evaluate the capabilities of these CPNPs to act as light-harvesting antennae for hybrid organic-inorganic devices.

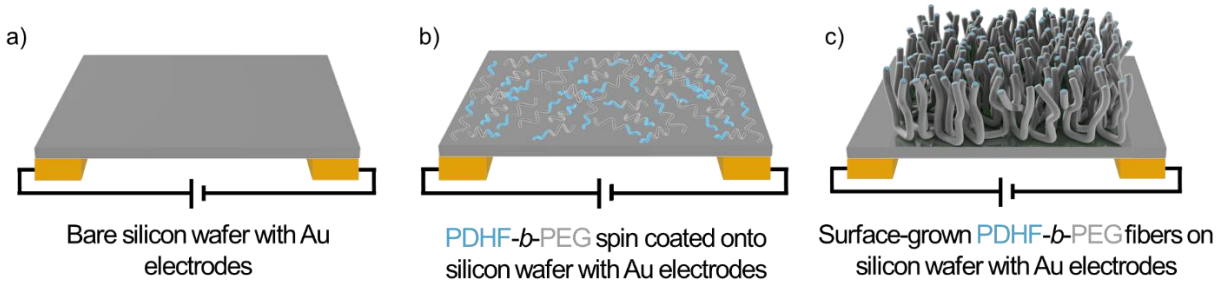

Figure 5.9. Cartoon schematic representations of three hybrid organic-inorganic photodetector devices. **(a)** Silicon wafer with gold (Au) electrodes thermally deposited onto the wafer backside that acts as a control device to get a baseline photocurrent generated by a silicon-based PD. **(b)** Silicon wafer with gold (Au) electrodes thermally deposited onto the wafer backside and a $PDHF_{17}$-*b*-PEG_{227} BCP layer spin cast onto the surface to determine if non-assembled BCP increases photocurrent. **(c)** Silicon wafer with gold (Au) electrodes thermally deposited onto the wafer backside and a $PDHF_{17}$-*b*-PEG_{227} nanofiber layer grown from surface-confined seeds. $PDHF_{17}$-*b*-PEG_{227} was used in this example but the same devices will be fabricated using $P3EHT_{23}$-*b*-PEG_{113} CPNPs to make 5 PDs total.

5.4 Conclusions and Summary

This chapter details an initial investigation into the application of CPNPs formed from two PEG-functionalized BCPs with a π-conjugated core, $PDHF_{17}$-*b*-PEG_{227} and $P3EHT_{23}$-*b*-PEG_{113}, to act as light harvesting antennae when silicon surface immobilized seed micelles serve as sites for seeded growth. Seeds composed of a BCP with a shorter PEG_{113} corona ($P3EHT_{23}$-*b*-PEG_{113}) were found to have increased attachment and a more regular distribution on the silicon surface compared to seeds composed of a BCP with a longer PEG_{227} corona ($PDHF_{17}$-*b*-PEG_{227}). Seeds consisting of PEG-functionalized BCPs in general attach more robustly to silicon surfaces following washing compared to previously used P2VP-containing BCPs even though the DP_n of the P2VP block was 2-5 times higher, illustrating the superior ability of PEG to anchor to a silicon surface. Surface-confined nanofibers of $PDHF_{17}$-*b*-PEG_{227} and $P3EHT_{23}$-*b*-PEG_{113} were fabricated by initiation from immobilized seeds, with the $P3EHT_{23}$-*b*-PEG_{113} material producing a more homogenous nanofiber layer. Finally, practical device and experiment designs were proposed to test the efficacy of these nanofibers to act as light-harvesting antennae and maximize photocurrent in a hybrid organic-inorganic PD. Further work is necessary to bring these proposals to fruition, along with comparative investigations between the light harvesting performance of $PDHF_{17}$-*b*-PEG_{227} and $P3EHT_{23}$-*b*-PEG_{113} nanofibers as well as structure-property studies to determine optimal nanofiber length for maximized light harvesting and photocurrent generation.

5.5 Supporting Information

5.5.1 Methods

Materials

All reagents used for polymer synthesis were of reagent grade and were used as received unless otherwise stated. All the air-free chemistry was performed in a dinitrogen-filled (N_2) MBraun 200B glovebox equipped with a cold-well or on a dinitrogen Schlenk line using standard techniques. 3-bromothiophene (97%), poly(ethylene glycol) methyl ether (PEG) (average M_n = 5000 and 10000 Da), (2-ethylhexyl)magnesium bromide (1.0 M in diethyl ether), ethynylmagnesium bromide (0.5M in THF), *p*-toluenesulfonyl chloride (99%), isopropylmagnesium chloride – lithium chloride (*i*PrMgCl•LiCl) (1.3 M in THF), sodium azide, and 1,2-bis(diphenylphosphino)propane dichloronickel(II) (Ni(dppp)Cl_2) were purchased from Millipore Sigma. 2-bromo-7-iodo-fluorene was purchased from Combiblocks. *N*-Bromosuccinimide (NBS) was recrystallized from boiling water prior to use[40] and Ni(*o*-tolyl)(dppe)Cl was synthesized as previously reported.[41] Copper(I) bromide (CuBr) was purified by suspending in glacial acetic acid, filtering and washing with copious amounts of absolute ethyl alcohol then anhydrous ethyl ether followed by drying in a vacuum oven at 80 °C for three days and stored under nitrogen.[42] *N,N,N′,N″,N″*-pentamethyldiethylenetriamine (PMDETA) was degassed prior to use using 3 freeze-pump-thaw cycles and stored under an N_2 atmosphere. Solvents were dried and deoxygenated using a Solvent Purification System (SPS).[43] Self-assembly experiments were performed using HPLC grade solvents and solvents were filtered through a 0.2 µm poly(tetrafluoroethylene) membrane.

Nuclear Magnetic Resonance (NMR)

^{1}H NMR spectra were taken with a Bruker 500 MHz spectrometer; chemical shifts were referenced to the residual proteosolvent peak ($CHCl_3$, δ = 7.26 ppm).

Gel Permeation Chromatography (GPC)

GPC was conducted using a Malvern Omnisec Resolve/Reveal equipped with an automatic sampler, pump, injector, inline degasser column oven (set at 35 °C), elution columns consisting of styrene/divinylbenzene gels (of pore size 500–5,000 Å), refractometer, four capillary differential viscometer, UV/Vis detector (λ = 440 nm) and dual angle laser light scattering detector (7° and 90°). GPC grade THF with 1 wt% triethylamine was used as the eluent, with a set flow rate of 1 mL/min. Samples were dissolved in THF at 1 mg/mL and filtered through a 0.2 μm poly(tetrafluoroethylene) membrane prior to analysis.

Preparatory GPC

Preparatory gel permeation chromatography was performed on a Shimadzu Prep GPC equipped with a CBM-20A communications bus module, LC-20AP solvent delivery unit, SIL-10AP autosampler, CTO-40C column oven, SPD-40 UV-Vis detector, RID-20A refractive index detector, and FRC-10A fraction collector. An initial injection of polymer in THF (1 mL, 10 mg/mL) at a flow rate of 3 mL/min using HPLC grade THF as eluent was used to gather the retention times of the species in solution. Using this data, the fraction collector was calibrated to separate the desired peaks into separate vials. Subsequent injections (3 mL, 10 mg/mL, 3 mL/min) were repeated until the desired volume was collected. The resulting solutions were concentrated *in vacuo* to yield the final polymers. Removal of homopolymers was assessed using UV-detection on the Malvern Omnisec GPC and thin layer chromatography.

Transmission Electron Microscopy (TEM)

Carbon films were deposited onto freshly cleaved mica sheets using a Leica EM ACE600 sputter/carbon coater instrument. Carbon films were deposited onto copper grids (500 mesh) purchased from Ted Pella, Inc. by floatation on water and allowed to dry over 24 h. Samples for electron microscopy were prepared by drop-casting 10 μL of a colloidal nanofiber solution onto a TEM grid placed on filter paper to absorb the excess solution. Bright field TEM images were obtained using a JEOL JEM 1011 microscope operating at 80 kV, equipped with a Gatan Orius SC1000 CCD camera.

Sonication

Nanofiber sonication was carried out using a Fisherbrand FB11203 sonication bath (37 kHz, 100% power) with the sweep function on and a bath temperature of 0 °C.

Variable-temperature UV/Vis absorption spectroscopy (VT-UV/Vis)

VT-UV/Vis data from 200 to 800 nm was obtained using a Cary 100 spectrometer equipped with a Peltier temperature controller employing quartz cells (1 cm x 0.1 cm). Experiments were conducted at a concentration of 0.05 mg/mL.

Wide-Angle X-ray Scattering (WAXS)

Reciprocal space maps were collected with a Pixcel 3D detector on an Empyrean diffractometer (Panalytical) equipped with a Cu Kα1 ($\lambda = 1.5406$ Å) source powered at 45 kV and 40 mA.

Atomic Force Microscopy (AFM)

Atomic-force microscopy (AFM) height images were taken at ambient temperature in air using a Bruker Multimode VIII atomic force microscope equipped with a ScanAsyst-HR fast

scanning module and ScanAsyst-Air-HR probe (tip radius of 2 nm), utilising peak force feedback control. Samples for AFM were drop-cast onto a plasma etched silicon wafer (1 x 1 cm) and allowed to dry in air before imaging. The spring constant for the AFM tip used was 5 N/m.

5.5.2 Statistical Analysis

Nanofiber lengths and widths were analysed using ImageJ, an open source software package developed at the US National Institute of Health.[44] Approximately 150 micelles were traced by hand to determine contour lengths that were then used to calculate the number-averaged length (L_n) and weight-average length (L_w) were calculated by using supplementary equations S5.1 and S5.2 from the measurements of the contour length (L_i) of individual micelles, where N_i is the number of the micelles of length L_i, and n is the number of micelles examined in each sample.

$$(Equation\ S5.1)\ L_n = \frac{\sum_{i=1}^{n} N_i L_i}{\sum_{i=1}^{n} N_i} \qquad (Equation\ S5.2)\quad L_w = \frac{\sum_{i=1}^{n} N_i L_i^2}{\sum_{i=1}^{n} N_i L_i}$$

Number-averaged width (W_n) was calculated according to equation S5.3 where W_i = object width and N_i = number of micelles of length W_i.

$$(Equation\ S5.3)\quad W_n = \frac{\sum_{i}^{n} N_i W_i}{\sum_{i}^{n} N_i}$$

The polydispersity index ($Đ_L$) and standard deviations (σ) of the measured lengths were related through the following expressions (Equations S5.4 and S5.5).

$$(Equation\ S5.4)\quad Đ_L = \frac{L_w}{L_n} \qquad (Equation\ S5.5)\quad \frac{L_w}{L_n} - 1 = \left(\frac{\sigma}{L_n}\right)^2$$

5.5.3 Synthesis and Characterization

Scheme S5.1. Synthesis of alkynyl-terminated $PDHF_{17}$

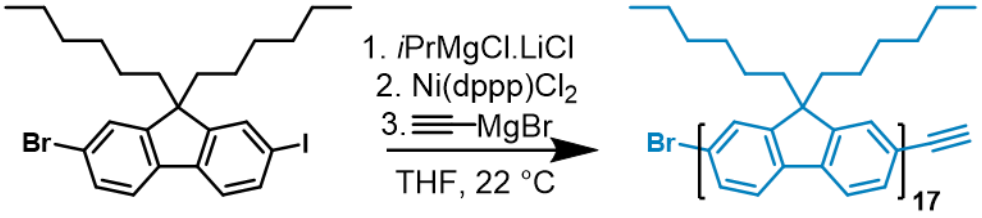

2-Bromo-7-iodo-9,9-bis-*n*-hexylfluorene was synthesized as previously reported. The ^{1}H NMR spectrum matches what was previously reported.[45] Alkynyl-$PDHF_{17}$ was synthesized according to the procedure from ref 30.[30] 150 mg, 58% yield, M_n = 5, 800 Da, $Đ_M$ = 1.09. ^{1}H NMR ($CDCl_3$, 500 MHz): 7.96-7.44 (m, 6H, aromatic CH), 3.16 (s, 1H, alkyne CH), 2.12 (bs, 4H, polyfluorene-(CH_2) x 2), 1.36-0.59 (m, 22H, polyfluorene-($CH_2(CH_2)_4$) x 2 and -CH_3 x 2).

Scheme S5.2. Synthesis of azide-terminated poly(ethylene glycol) (PEG_{113}-N_3 and PEG_{227}-N_3)

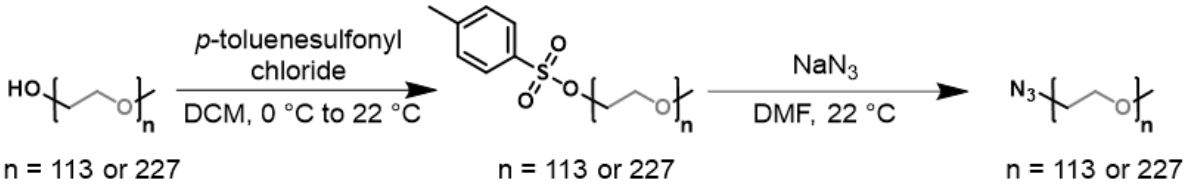

The title compound was synthesized using a previously published procedure.[46] Tosylation was performed under N_2 atmosphere employing Schlenk techniques. (5.45 g, 88% yield). Azidation was performed on a Schlenk line under N_2 atmosphere (2.02 g, 69% yield, M_n = 5, 000 Da, $Đ_M$ = 1.16). ^{1}H NMR spectra match what was previously reported in the literature.[46] PEG_{227}-N_3 was synthesized using the same procedure found in ref 46.[46] (1.56 g, 72% yield, M_n = 10, 000 Da, $Đ_M$ = 1.11).

Scheme S5.3. Synthesis of PDHF$_{17}$-*b*-PEG$_{227}$

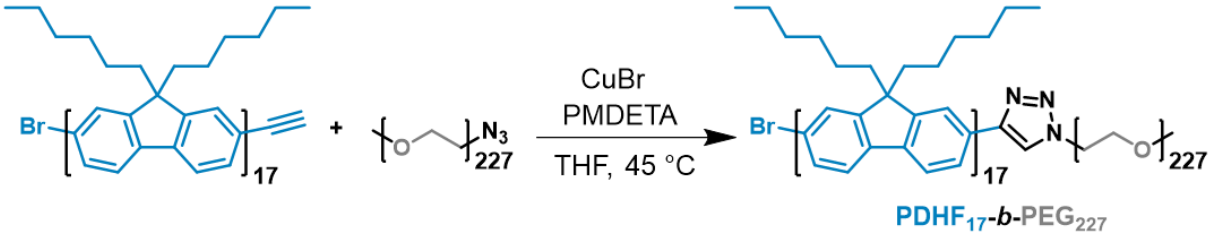

Synthesis of PDHF$_{17}$-*b*-PEG$_{227}$ was carried out according to a previously reported procedure.[30] ^{1}H NMR spectrum matches the previous report. 65 mg, 18% yield, M_n = 15, 800 Da, $Đ_M$ = 1.19.

Scheme S5.4. Synthesis of P3EHT$_{23}$-*b*-PEG$_{113}$

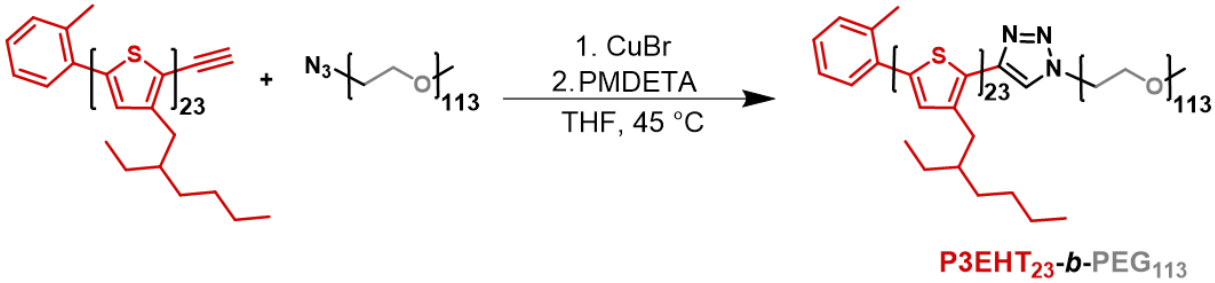

Alkynyl-P3EHT$_{23}$, PEG$_{113}$-N$_3$, and P3EHT$_{23}$-*b*-PEG$_{113}$ was synthesized as stated in Chapter 2 on page 86 and relevant characterization can be found there. GPC: M_n = 11, 900 Da, $Đ_M$ = 1.06.

5.5.4 Gel Permeation Chromatography

Ethynyl-PDHF$_{17}$, PEG$_{227}$-N$_3$, and PDHF$_{17}$-*b*-PEG$_{227}$

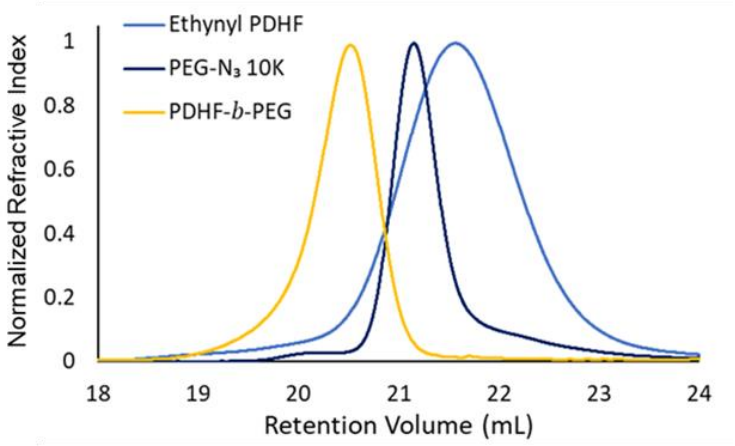

Figure S5.1. Overlaid GPC chromatograms of alkynyl-PDHF$_{17}$ (light blue trace), PEG$_{227}$-N$_3$ (dark blue trace), and PDHF$_{17}$-*b*-PEG$_{227}$ (yellow trace). Sample concentrations were 1 mg/mL in THF.

Alkynyl-P3EHT$_{23}$, PEG$_{113}$-N$_3$, and P3EHT$_{23}$-*b*-PEG$_{113}$

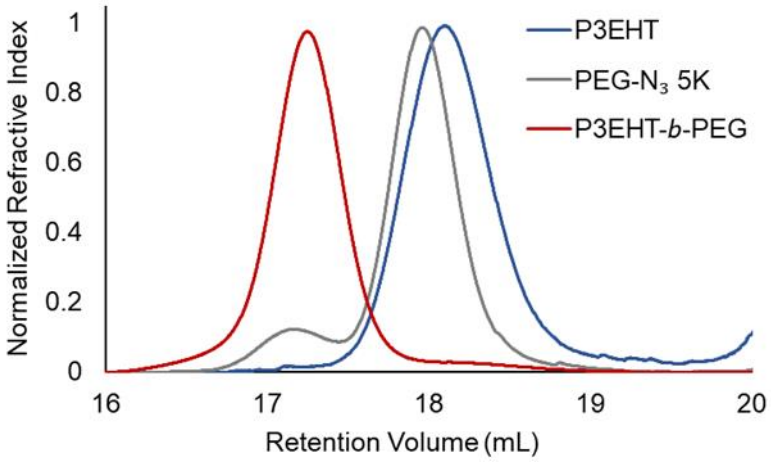

Figure S5.2. Overlaid GPC chromatograms of alkynyl-P3EHT$_{23}$ (blue trace), PEG$_{113}$-N$_3$ (grey trace), and P3EHT$_{23}$-*b*-PEG$_{113}$ (red trace). Sample concentrations were 1 mg/mL in THF.

5.5.5 ^{1}H NMR Spectroscopy

2-Bromo-7-iodo-9,9-bis-*n*-hexylfluorene

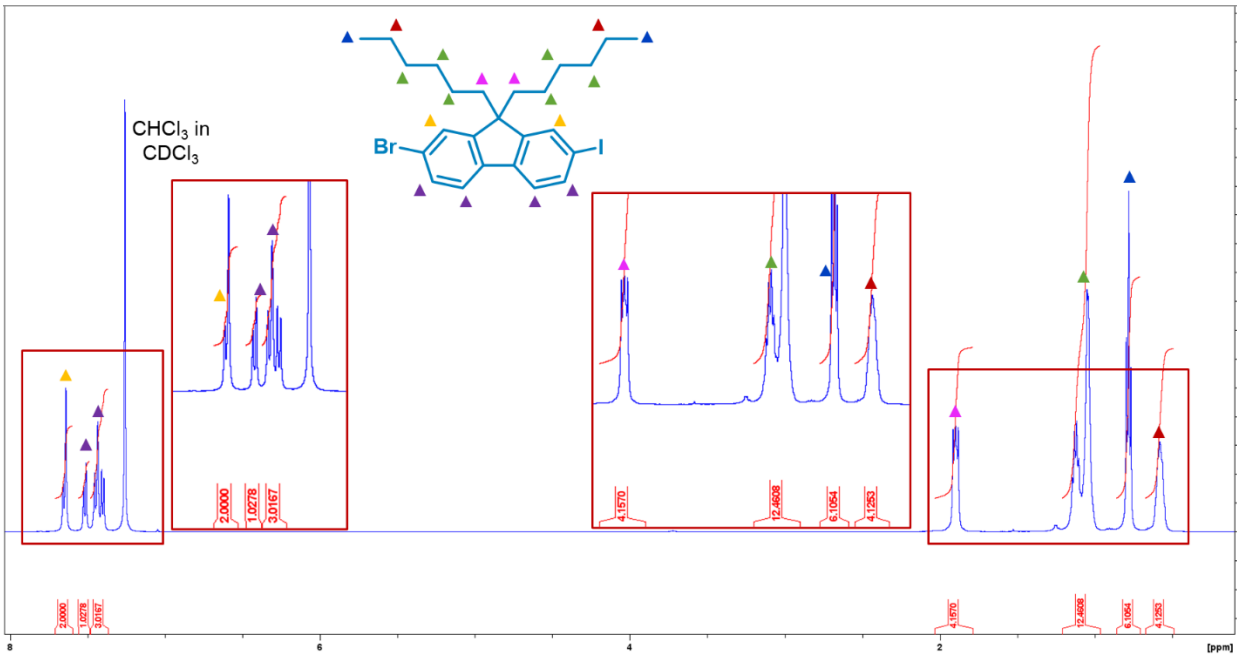

Figure S5.3. ^{1}H NMR spectrum of 2-bromo-7-iodo-9,9-bis-*n*-hexylfluorene (500 MHz, $CDCl_3$).

Alkynyl PDHF$_{17}$

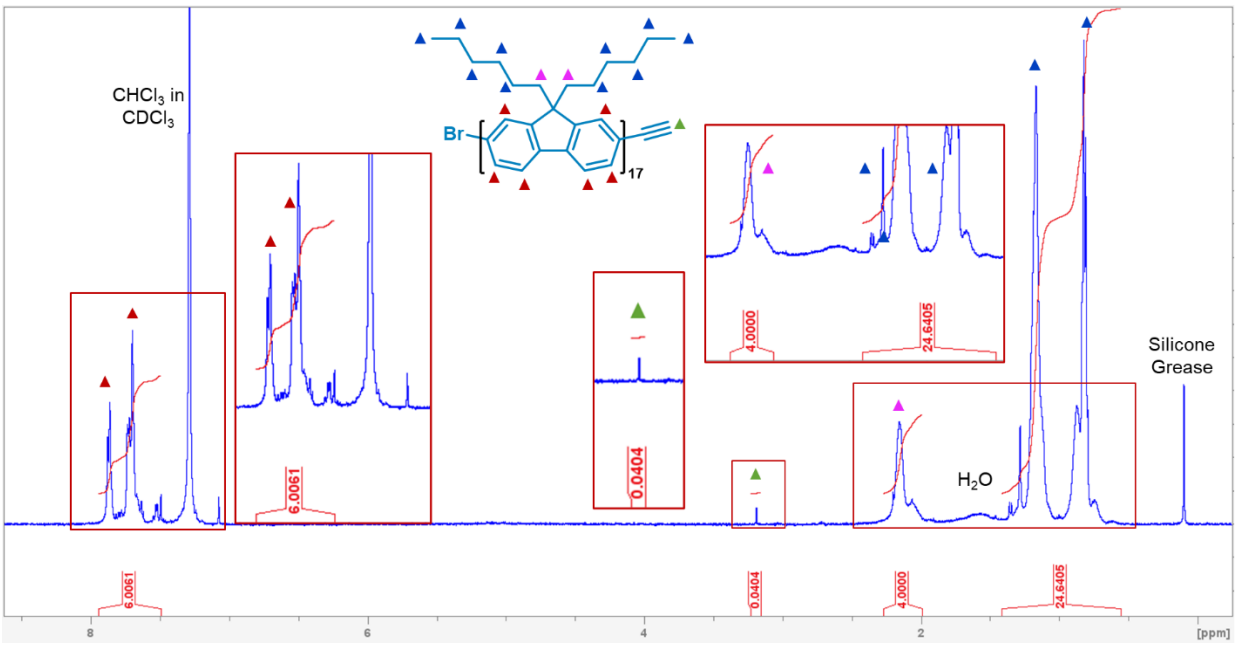

Figure S5.4. ^{1}H NMR spectrum of alkyne-terminated PDHF$_{17}$ homopolymer (500 MHz, $CDCl_3$).

PEG$_{227}$-N$_3$

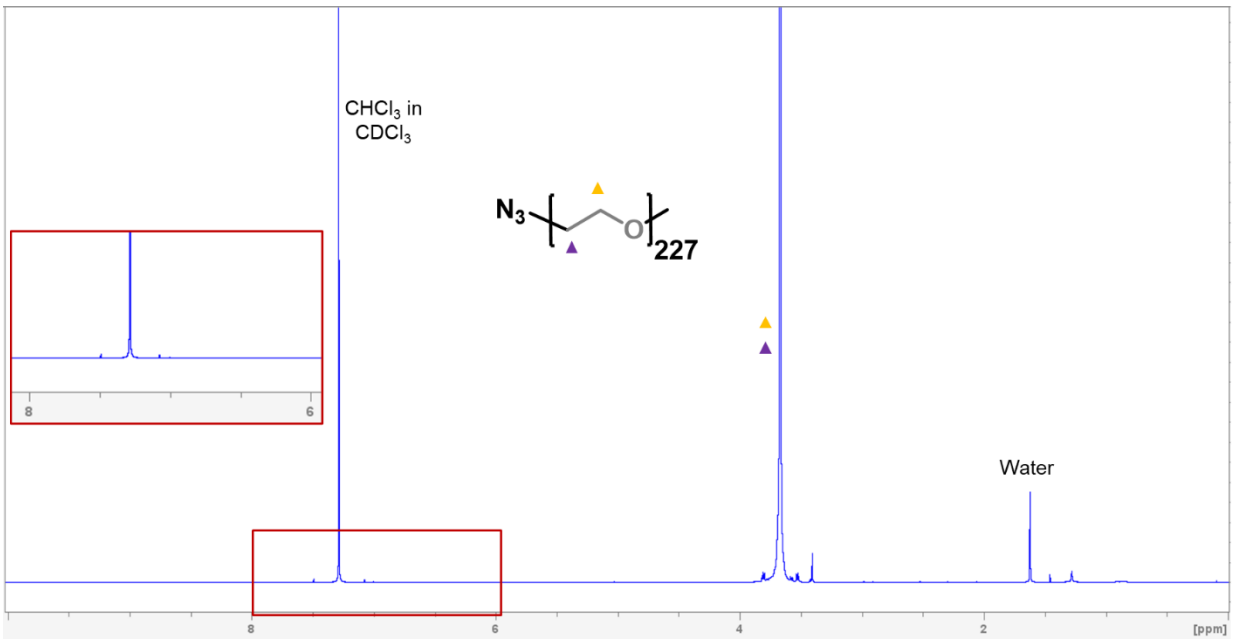

Figure S5.5. ^{1}H NMR spectrum of azide-functionalized PEG$_{227}$ homopolymer (500 MHz, $CDCl_3$). Inset (red box) shows aromatic region with no peaks correlated to remaining tosyl-PEG$_{227}$.

5.5.6 Crystallization-Driven Self-Assembly Procedures

General self-assembly procedure for polydisperse fibers and seed fabrication

PDHF$_{17}$-*b*-PEG$_{227}$

10 mL of THF was added to a vial containing 2 mg of solid PDHF$_{17}$-*b*-PEG$_{227}$. To the 0.2 mg/mL THF solution was added 10 mL of MeOH dropwise with continuous mixing followed by annealing at 30 °C for 24 h (final concentration = 0.1 mg/mL, 1:1 v/v THF:MeOH). The vial was then placed in a 0 °C ultrasonic cleaning bath and sonicated (37 kHz, 100% power) for 3 h to give seed micelles. Seeds were annealed at 30 °C for 18 h prior to use.

P3EHT$_{23}$-*b*-PEG$_{113}$

10 mL of deoxygenated *n*BuOH was added to a vial containing 2 mg of solid P3EHT$_{23}$-*b*-PEG$_{113}$ which was then heated to 90 °C in a metal heating block for 30 min. The 0.2 mg/mL solution was allowed to cool to 22 °C slowly (ca. 4 h) followed by aging for 24 h. After aging, 10 mL of deoxygenated MeOH was added to form a solution with a final concentration of 0.1 mg/mL. The vial was then placed in a 0 °C ultrasonic cleaning bath and sonicated (37 kHz, 100% power) for 3 h to give seed micelles. Seeds were annealed at 30 °C for 18 h prior to use.

General self-assembly procedure for solution-phase seeded growth of length-controlled nanofibers at 22 °C

PDHF$_{17}$-*b*-PEG$_{227}$

PDHF$_{17}$-*b*-PEG$_{227}$ seed micelle solutions (1:1 THF:MeOH, 0.1 mg/mL) were added to a vial and diluted with 1:1 THF:MeOH such that the final solution concentration will be 0.05 mg/mL following unimer addition. Increasing amounts of stock PDHF$_{17}$-*b*-PEG$_{227}$ unimer solution (THF, 1 mg/mL) was added quickly in one aliquot, the solutions were vortexed for 10 s, and then aged at

22 °C for 24 h prior to imaging by TEM.

P3EHT$_{23}$-*b*-PEG$_{113}$

P3EHT$_{23}$-*b*-PEG$_{113}$ seed micelle solution (1:1 *n*BuOH:MeOH, 0.1 mg/mL) was added to a vial and diluted with a deoxygenated 1:1 *n*BuOH:MeOH solution such that the final concentration will be 0.05 mg/mL following unimer addition. Increasing amounts of stock P3EHT$_{23}$-*b*-PEG$_{113}$ unimer solution (deoxygenated THF, 2 mg/mL) was added quickly in one aliquot, the solutions were vortexed for 10 s, and then aged at 22 °C for 24 h prior to imaging by TEM.

General procedure for adherence of seeds to silicon surface and washing with selective solvent mixture

A *p*-type silicon wafer (1 cm x 1 cm) was first cleaned by sonication (37 kHz, 100% power) in water (3 x 5 min), methanol (3 x 5 min), and acetone (3 x 5 min) followed by drying. The wafer was then plasma etched by exposing it to an oxygen plasma for 600 s. Following this, the wafer was placed on a spin-coater stage and seed solution (10 µl) was dropped onto the silicon and then the wafer was spun at 3000 rpm for 90 s. The wafer was allowed to dry at 22 °C for 1 h. Unwashed wafers were analyzed by AFM as-is while the washed wafers were washed by submerging three times into 1:1 THF:MeOH (for PDHF$_{17}$-*b*-PEG$_{227}$) or 1:1 *n*BuOH:MeOH (for P3EHT$_{23}$-*b*-PEG$_{113}$) and then placed on a filter paper and allowed to dry for at least 1 h at 22 °C before AFM analysis.

General procedure for seeded growth of nanofibers from silicon surface immobilized seeds

The seed-functionalized silicon wafer was placed in a vial which was filled with either 1:1 THF:MeOH for PDHF$_{17}$-*b*-PEG$_{227}$ or 1:1 *n*BuOH:MeOH for P3EHT$_{23}$-*b*-PEG$_{113}$ such that the final concentration will be 0.05 mg/mL following unimer addition and taking care that the silicon wafer is fully submerged. The vial was placed on an automatic mixing table and set to a speed that does

not cause the solvent to drop below the silicon wafer surface while mixing/shaking. Stock unimer solution (THF, 2 mg/mL) was quickly added in one aliquot, the vial was sealed, and the solutions were allowed to mix for 24 h. After 24 h, the wafer was removed from the vial, placed on a filter paper, and allowed to dry overnight before AFM analysis.

5.5.7 Atomic Force Microscopy

PDHF$_{17}$-*b*-PEG$_{227}$ Seeds

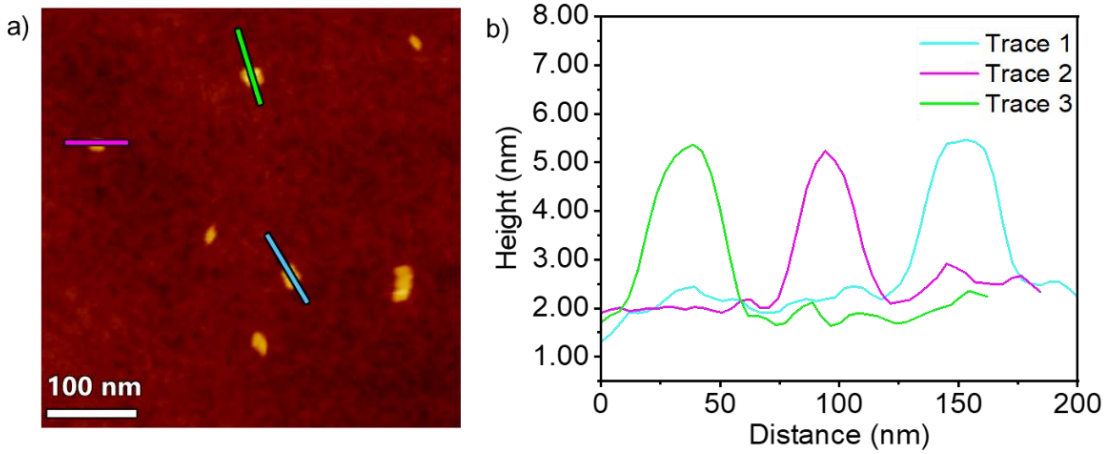

Figure S5.6. (a) AFM height image of PDHF$_{17}$-*b*-PEG$_{227}$ seeds (L_n = 47 nm) in 1:1 THF:MeOH (0.05 mg/mL) immobilized on a plasma etched silicon surface. Coloured lines indicate height profile shown in **(b)** Trace 1 - height: 3.4 nm; Trace 2 - height 3.2 nm; Trace 3 - height: 3.5 nm. Average height: 3.6 nm ± 0.1 nm.

P3EHT$_{23}$-*b*-PEG$_{113}$ Seeds

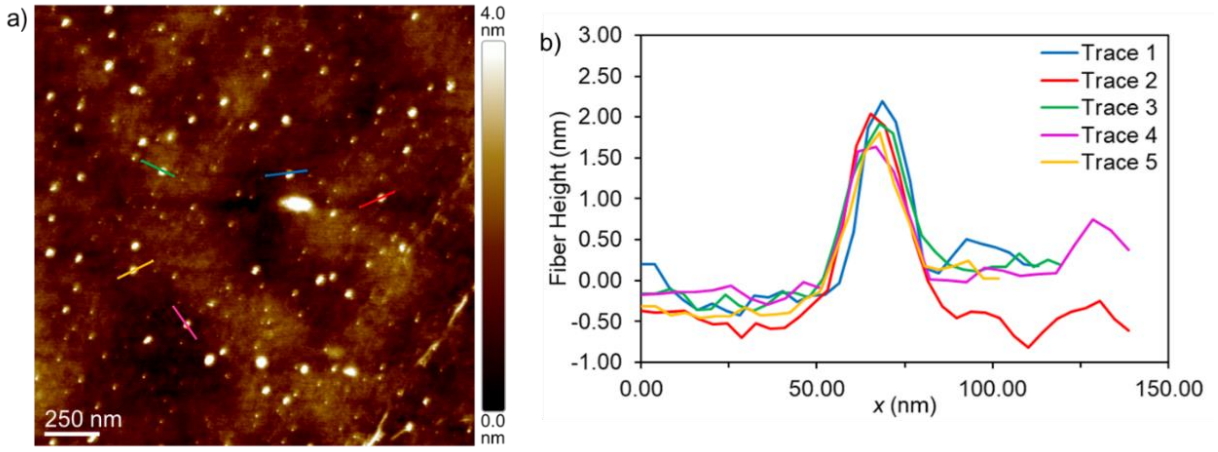

Figure S5.7. (a) AFM height image of P3EHT$_{23}$-*b*-PEG$_{113}$ seeds in 1:1 *n*BuOH:MeOH (0.05 mg/mL) (L_n = 44 nm) immobilized on a plasma etched silicon surface. Coloured lines indicate the height profile shown in **(b)** drawn perpendicular to the long axis of the nanofibers. Trace 1 - height: 4.4 nm; Trace 2 - height: 3.7 nm; Trace 3 - height: 3.4 nm; Trace 4 - height: 4.1 nm; Trace 5 - height: 3.5 nm. Average height: 3.8 nm ± 0.4 nm.

Seed immobilization on a silicon surface and seed density comparisons

PDHF$_{17}$-*b*-PEG$_{227}$ - Unwashed

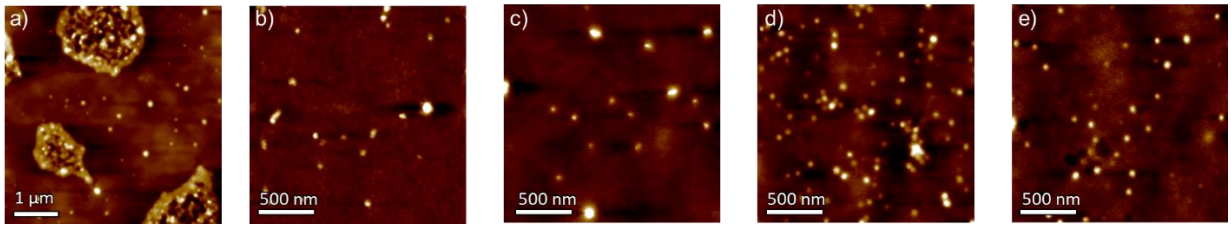

Figure S5.8. AFM height images after depositing 10 µl of **(a)** 0.5 mg/mL, **(b)** 0.4 mg/mL, **(c)** 0.3 mg/mL, **(d)** 0.2 mg/mL, and **(e)** 0.1 mg/mL PDHF$_{17}$-*b*-PEG$_{227}$ seed solutions onto plasma etched silicon wafers *via* spin coating imaged using AFM. Surfaces were not washed prior to imaging.

PDHF$_{17}$-*b*-PEG$_{227}$ - Washed

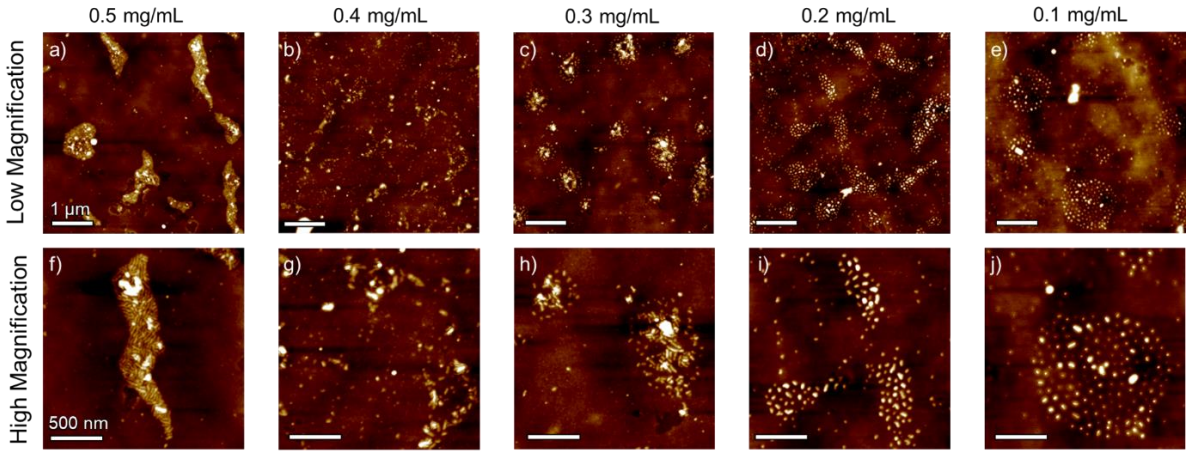

Figure S5.9. AFM height images after depositing 10 µl of **(a)** 0.5 mg/mL, **(b)** 0.4 mg/mL, **(c)** 0.3 mg/mL, **(d)** 0.2 mg/mL, and **(e)** 0.1 mg/mL PDHF$_{17}$-*b*-PEG$_{227}$ seed solutions onto plasma etched silicon wafers *via* spin coating and imaged at low magnification. AFM height images after depositing 10 µl of **(f)** 0.5 mg/mL, **(g)** 0.4 mg/mL, **(h)** 0.3 mg/mL, **(i)** 0.2 mg/mL, and **(j)** 0.1 mg/mL PDHF$_{17}$-*b*-PEG$_{227}$ seed solutions deposited on plasma etched silicon wafers *via* spin coating and imaged at high magnification. All samples were washed with 1:1 THF:MeOH following spin coating prior to imaging.

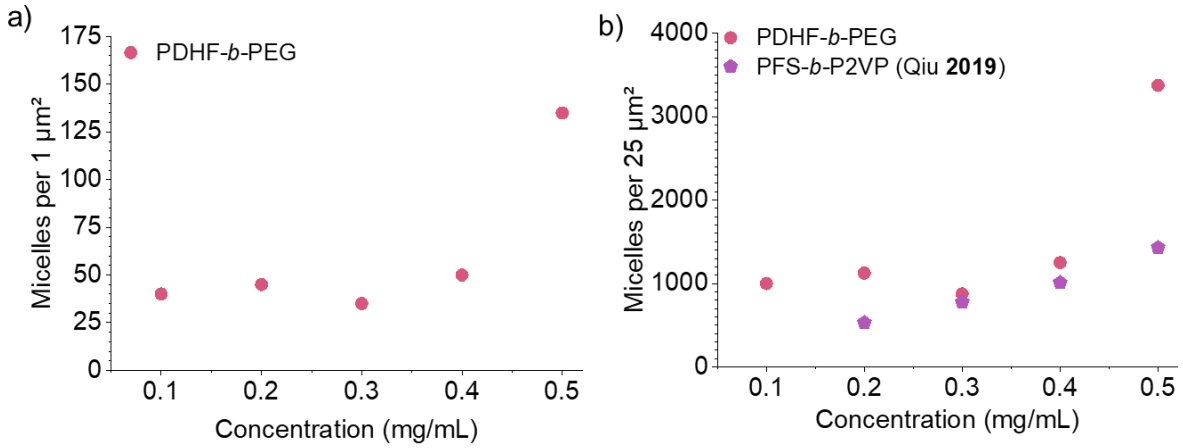

Figure S5.10. Graph showing the seed density of PDHF$_{17}$-*b*-PEG$_{227}$ seeds per **(a)** 1 µm^2 and **(b)** 25 µm^2 compared to PFS$_{36}$-*b*-P2VP$_{502}$ (Qiu et *al. Science*, 2019).[33] Density was approximated by counting immobilized seeds in 1 µm^2 and multiplying by 25 to get seed density across 25 µm^2. Seed distribution densities across 1 µm^2 - 0.1 mg/mL = 40; 0.2 mg/mL = 45; 0.3 mg/mL = 35; 0.4 mg/mL = 50; 0.5 mg/mL = 135. Seed distribution densities across 25 µm^2 - 0.1 mg/mL = 1000; 0.2 mg/mL = 1125; 0.3 mg/mL = 875; 0.4 mg/mL = 1250; 0.5 mg/mL = 3375.

P3EHT$_{23}$-*b*-PEG$_{113}$ - Unwashed

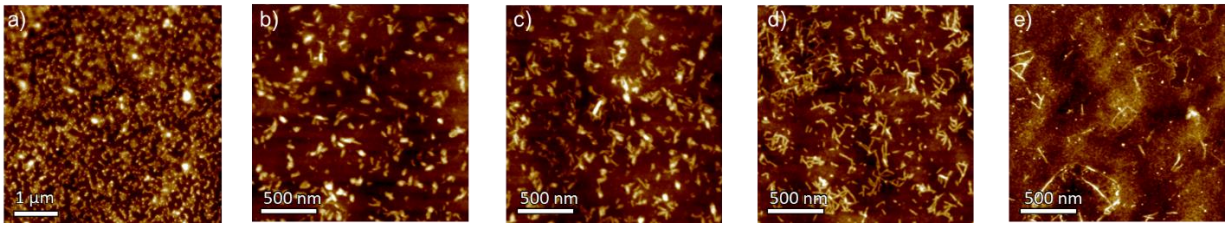

Figure S5.11. AFM height images of 10 µl of **(a)** 0.5 mg/mL, **(b)** 0.4 mg/mL, **(c)** 0.3 mg/mL, **(d)** 0.2 mg/mL, and **(e)** 0.1 mg/mL P3EHT$_{23}$-*b*-PEG$_{113}$ seed solutions (L_n = 44 nm) deposited onto plasma etched silicon wafers *via* spin coating imaged using AFM. Surfaces were not washed prior to imaging.

P3EHT$_{23}$-*b*-PEG$_{113}$ - Washed

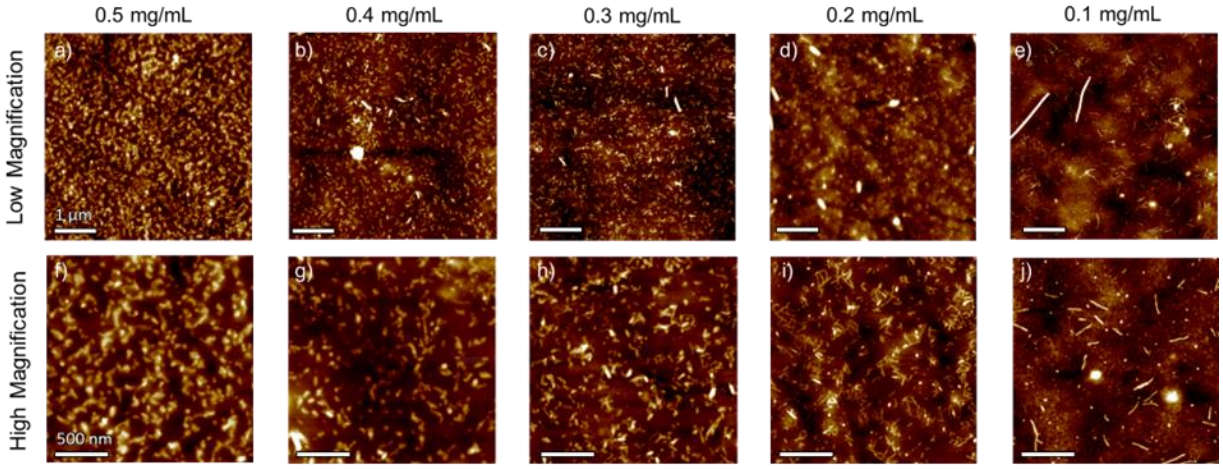

Figure S5.12. AFM height images of 10 µl of **(a)** 0.5 mg/mL, **(b)** 0.4 mg/mL, **(c)** 0.3 mg/mL, **(d)** 0.2 mg/mL, and **(e)** 0.1 mg/mL P3EHT$_{23}$-*b*-PEG$_{113}$ seed solutions deposited onto plasma etched silicon wafers *via* spin coating and imaged at low magnification. AFM height images of **(f)** 0.5 mg/mL, **(g)** 0.4 mg/mL, **(h)** 0.3 mg/mL, **(i)** 0.2 mg/mL, and **(j)** 0.1 mg/mL P3EHT$_{23}$-*b*-PEG$_{113}$ seed solutions deposited on plasma etched silicon wafers *via* spin coating and imaged at high magnification. All samples were washed prior to imaging.

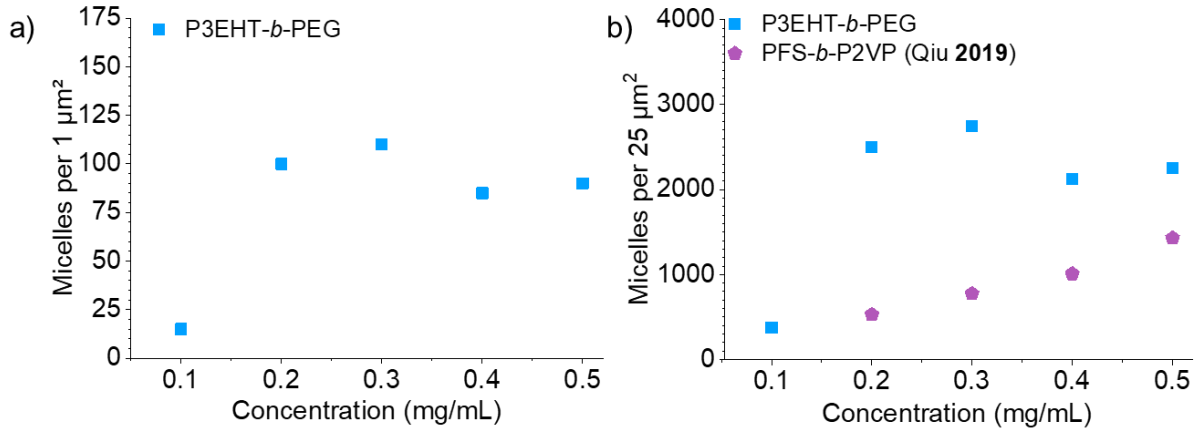

Figure S5.13. Graph showing the seed density of P3EHT$_{23}$-*b*-PEG$_{113}$ seeds per **(a)** 1 µm^2 and **(b)** 25 µm^2 compared to PFS$_{36}$-*b*-P2VP$_{502}$ (Qiu et *al. Science,* 2019).[33] Density was approximated by counting immobilized seeds in 1 µm^2 and multiplying by 25 to get seed density across 25 µm^2. Seed distribution densities across 1 µm^2 - 0.1 mg/mL = 15; 0.2 mg/mL = 100; 0.3 mg/mL = 110; 0.4 mg/mL = 85; 0.5 mg/mL = 90. Seed distribution densities across 25 µm^2 - 0.1 mg/mL = 375; 0.2 mg/mL = 2500; 0.3 mg/mL = 2750; 0.4 mg/mL = 2125; 0.5 mg/mL = 2250.

Nanofiber growth from surface immobilized seeds

PDHF$_{17}$-*b*-PEG$_{227}$

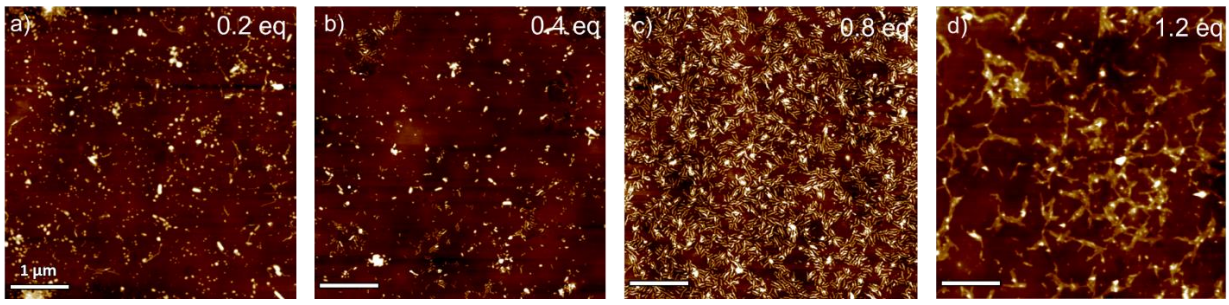

Figure S5.14. AFM height images of PDHF$_{17}$-*b*-PEG$_{227}$ fibers grown from surface-immobilized seeds (0.5 mg/mL) upon addition of unimer equaling m_{unimer}/m_{seed} = **(a)** 0.2, **(b)** 0.4, **(c)** 0.8, and **(d)** 1.2 in 1:1 THF:MeOH (0.05 mg/mL). Samples were washed before AFM imaging and all scale bars represent 1 µm.

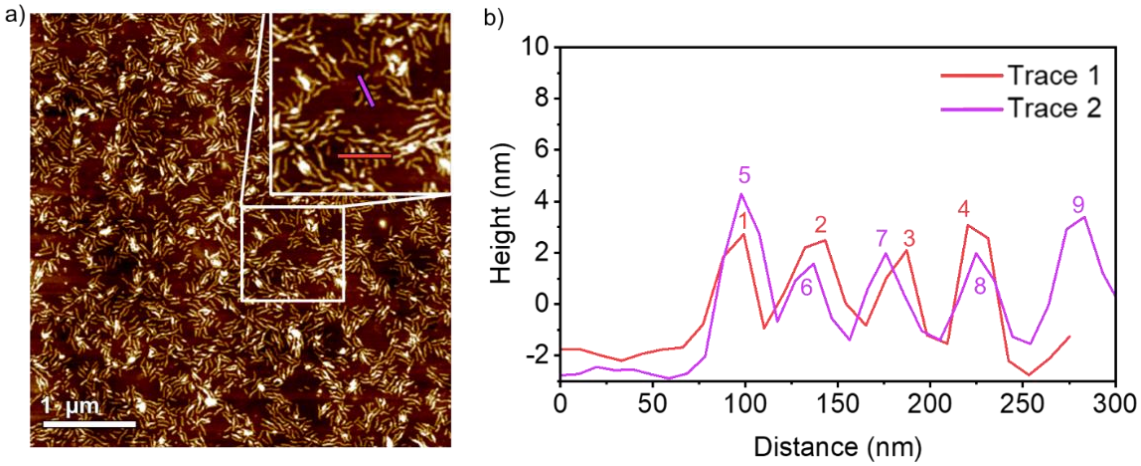

Figure S5.15. (a) AFM height image of $PDHF_{17}$-*b*-PEG_{227} fibers (m_{unimer}/m_{seed} = 1.2) in 1:1 THF:MeOH (0.05 mg/mL) grown from silicon wafer surface immobilized $PDHF_{17}$-*b*-PEG_{227} seeds. Coloured lines indicate height profile shown in **(b)** drawn perpendicular to the long axis of the nanofibers. Trace 1 – Peak 1 - height: 5.2 nm; Peak 2 - height 5.0 nm; Peak 3 - height: 4.6 nm; Peak 4 - height: 5.6 nm. Average height: 5.1 nm ± 0.4 nm. Trace 2 – Peak 5 - height: 7.2 nm; Peak 6 - height 4.5 nm; Peak 7 - height: 4.9 nm; Peak 8 - height: 4.9 nm; Peak 9 - height: 6.3 nm. Average height: 5.5 nm ± 1.2 nm.

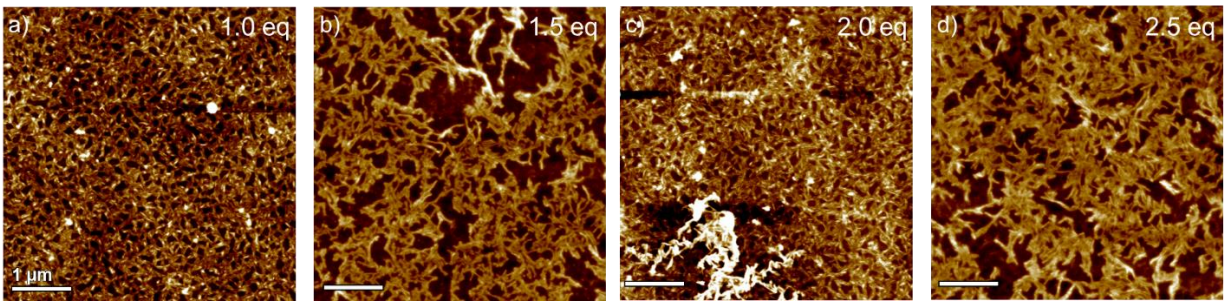

Figure S5.16. AFM height images of $P3EHT_{23}$-*b*-PEG_{113} fibers grown from surface-immobilized seeds following washing upon addition of unimer equaling m_{unimer}/m_{seed} = **(a)** 1.0, **(b)** 1.5, **(c)** 2.0, and **(d)** 2.5 in 1:1 *n*BuOH:MeOH (0.05 mg/mL). Samples were washed before AFM imaging and all scale bars represent 1 µm.

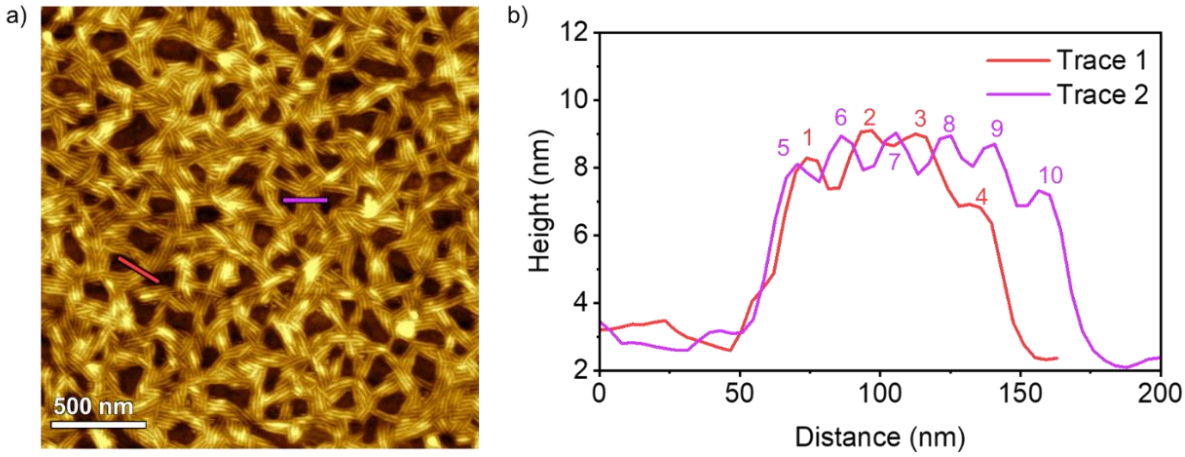

Figure S5.17. (a) AFM height image of P3EHT$_{23}$-*b*-PEG$_{113}$ fibers (m_{unimer}/m_{seed} = 1.5) in 1:1 *n*BuOH:MeOH (0.05 mg/mL) grown from silicon wafer surface immobilized P3EHT$_{23}$-*b*-PEG$_{113}$ seeds. Coloured lines indicate height profile shown in **(b)** drawn perpendicular to the long axis of the nanofibers. Trace 1 – Peak 1 - height: 5.2 nm; Peak 2 - height 6.0 nm; Peak 3 - height: 6.0 nm; Peak 4 - height: 3.9 nm. Average height: 5.3 nm ± 0.9 nm. Trace 2 – Peak 5 - height: 5.7 nm; Peak 6 - height 6.4 nm; Peak 7 - height: 6.7 nm; Peak 8 - height: 6.6 nm; Peak 9 - height: 6.3 nm; Peak 10 - height: 4.8 nm. Average height: 6.1 nm ± 0.6 nm.

5.5.8 Transmission Electron Microscopy

Polydisperse Micelles

PDHF$_{17}$-*b*-PEG$_{227}$

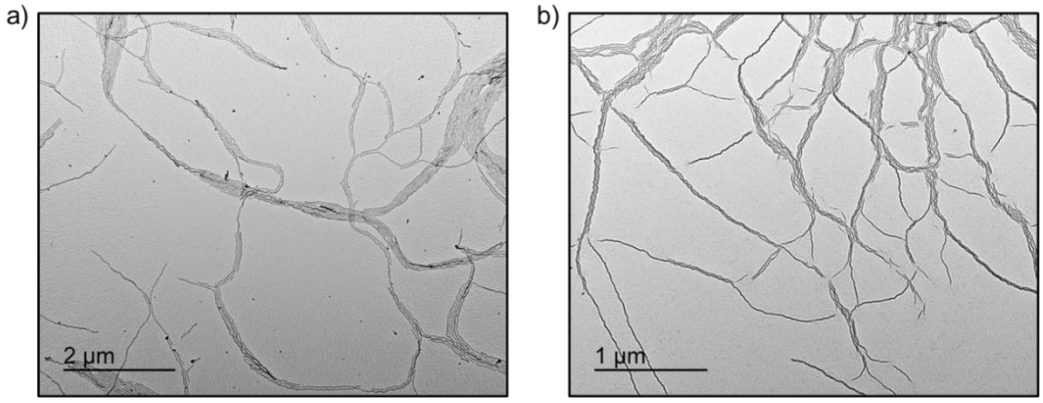

Figure S5.18. (a, b) TEM images of polydisperse PDHF$_{17}$-*b*-PEG$_{227}$ nanofibers made by dissolving the BCP in tetrahydrofuran (THF, 0.2 mg/mL) and subsequent dropwise addition of an equivalent amount of MeOH. The solution (0.1 mg/mL) was annealed at 30 °C for 24 h before being cooled to 22 °C and aged 24 h. Sample was drop-cast onto a carbon-coated copper TEM grid and imaged by TEM following solvent evaporation.

P3EHT$_{23}$-*b*-PEG$_{113}$

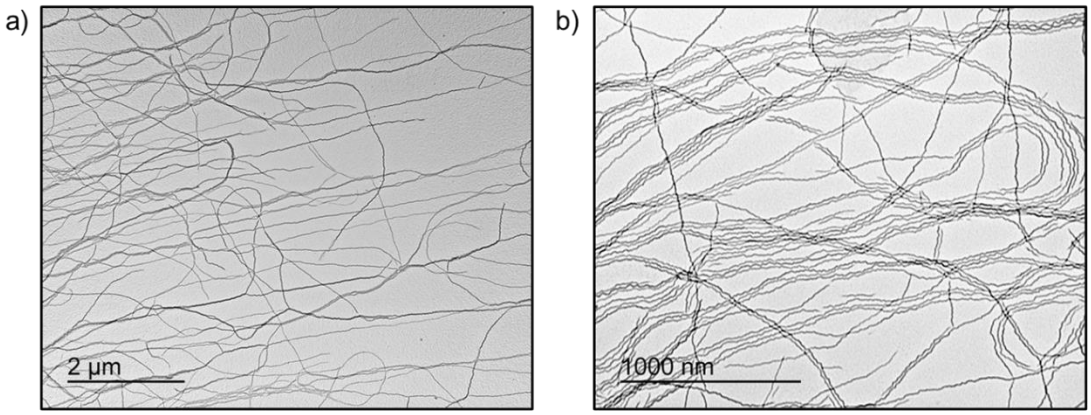

Figure S5.19. (a, b) TEM images of polydisperse P3EHT$_{23}$-*b*-PEG$_{113}$ nanofibers made by heating the BCP in deoxygenated *n*BuOH to 90 °C for 30 min. and then cooling the 0.2 mg/mL solution to 22 °C and aging 24 h. After aging, an equivalent amount of deoxygenated MeOH was added (0.1 mg/mL). Sample was drop-cast onto a carbon-coated copper TEM grid and imaged by TEM following solvent evaporation.

Seed Fabrication

PDHF$_{17}$-*b*-PEG$_{227}$ - Annealed

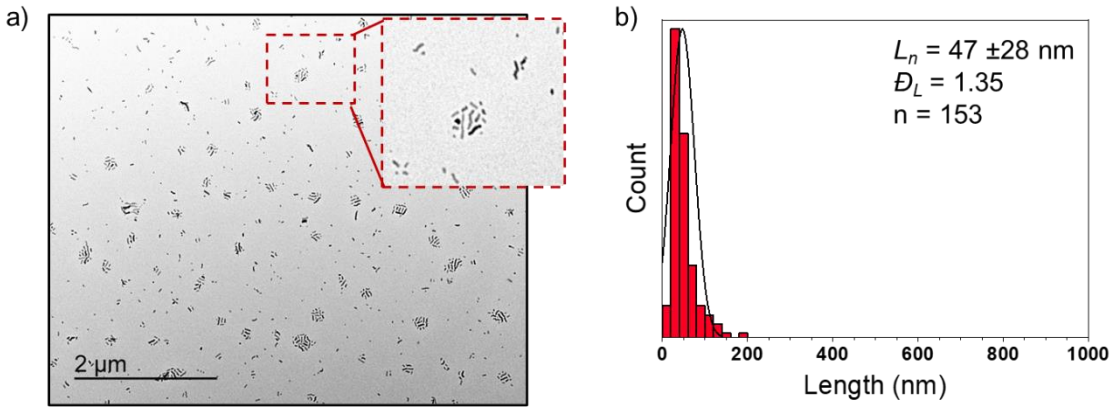

Figure S5.20. (a) TEM image of seeds formed by ultrasonication of a PDHF$_{17}$-*b*-PEG$_{227}$ polydisperse nanofiber solution (1:1 THF:MeOH, 0.1 mg/mL) at 0 °C for 3 h. Seeds were annealed at 30 °C for 18 h and then cooled to 22 °C and imaged following solvent evaporation. **(b)** Histogram showing the fiber length distribution of PDHF$_{17}$-*b*-PEG$_{227}$ seeds (L_n = 47 nm, L_w = 63 nm, $Đ_L$ = 1.35, σ = ± 28 nm, n = 153).

P3EHT$_{23}$-*b*-PEG$_{113}$ - Annealed

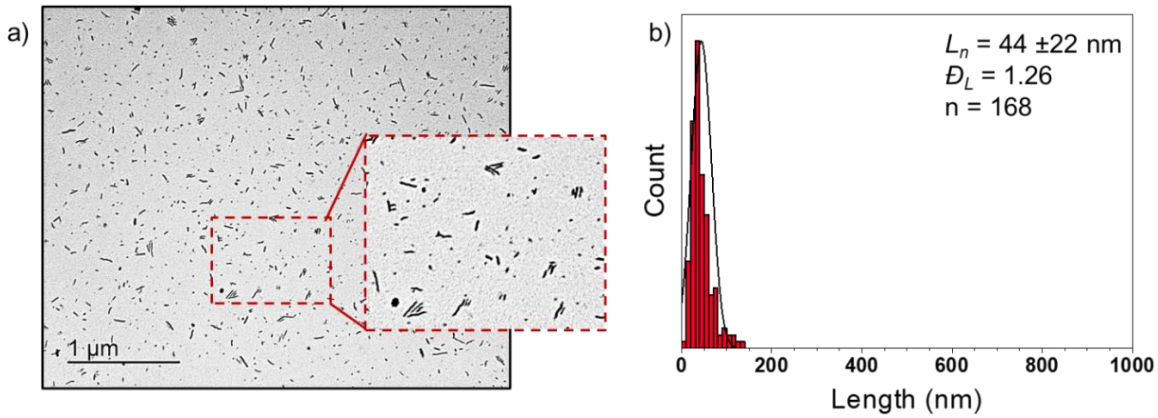

Figure S5.21. (a) TEM image of seeds formed by ultrasonication of a P3EHT$_{23}$-*b*-PEG$_{113}$ polydisperse nanofiber solution (1:1 *n*BuOH:MeOH, 0.1 mg/mL) at 0 °C for 3 h. Seeds were annealed at 30 °C for 18 h and then cooled to 22 °C and imaged following solvent evaporation. **(b)** Histogram showing the fiber length distribution of P3EHT$_{23}$-*b*-PEG$_{113}$ seeds (L_n = 44 nm, L_w = 55 nm, $Đ_L$ = 1.26, σ = ± 22 nm, n = 168).

Solution-phase seeded growth of length-controlled nanofibers at 22 °C

PDHF$_{17}$-*b*-PEG$_{227}$ seeds which were annealed at 30 °C for 18 h

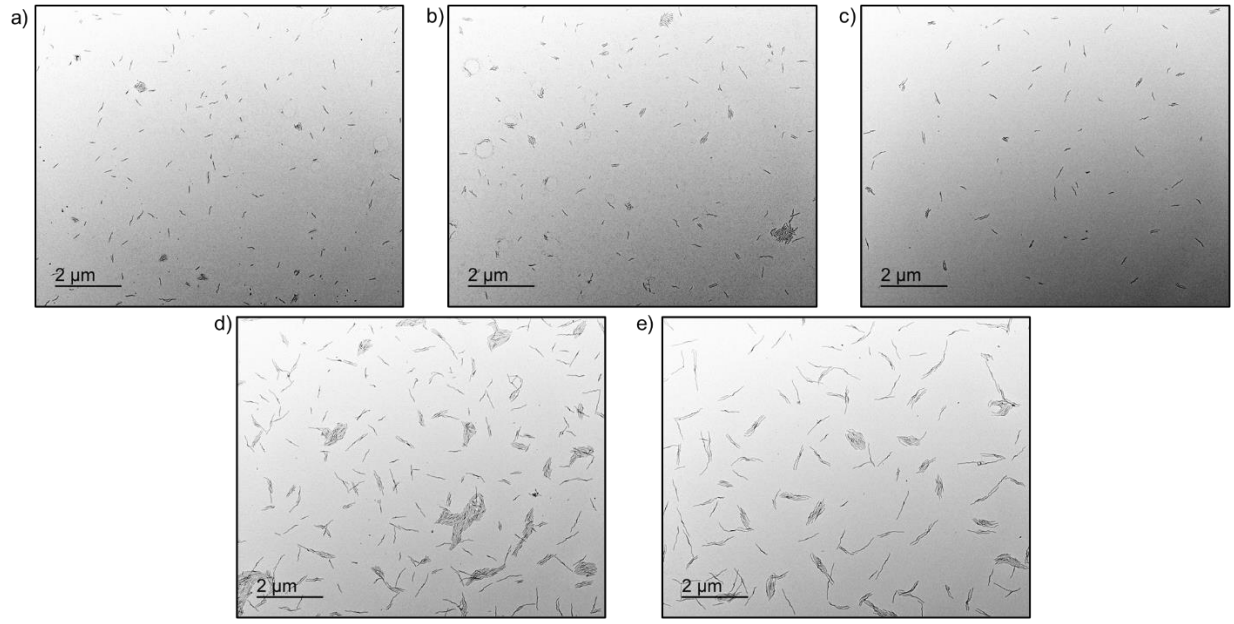

Figure S5.22. TEM images of PDHF$_{17}$-*b*-PEG$_{227}$ nanofibers in (1:1 THF:MeOH, 0.05 mg/mL) formed by living CDSA seeded growth using seed micelles (1:1 THF:MeOH, 0.1 mg/mL) which were annealed at 30 °C prior to use. PDHF$_{17}$-*b*-PEG$_{227}$ seed micelles (1:1 THF:MeOH, 0.1 mg/mL) were treated with **(a)** 4, **(b)** 6, **(c)** 8, **(d)** 12, and **(e)** 17 equivalents of PDHF$_{17}$-*b*-PEG$_{227}$ unimer (THF, 1 mg/mL) at 22 °C. Solutions were aged at 22 °C for 24 h followed by solvent evaporation prior to TEM imaging.

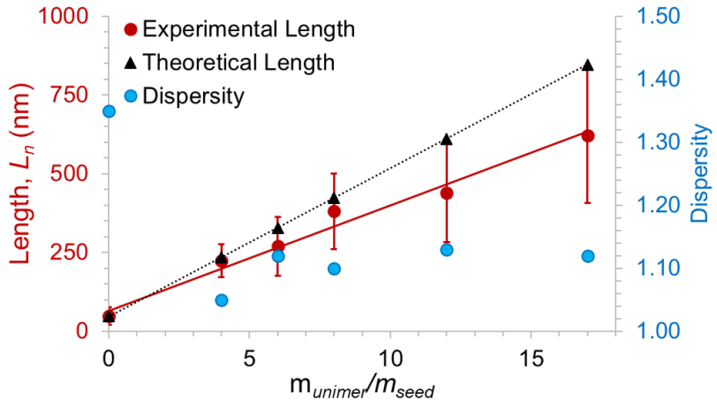

Figure S5.23. Plot showing the dependence of fiber length (L_n) on unimer to seed mass ratio when using PDHF$_{17}$-*b*-PEG$_{227}$ seeds (L_n = 47 nm, $Đ_L$ = 1.35) that were annealed at 30 °C for 18 h prior to seeded growth experiments at 22 °C. Error bars represent standard deviation.

Table S5.1. Summary of data from seeded growth experiments with $PDHF_{17}$-*b*-PEG_{227} seed micelles which were annealed. σ is standard deviation in L_n measurements.

m_{unimer}/m_{seed}	L_n	L_w	$Đ_L$	σ
Seeds	47	63	1.35	28
4	224	235	1.05	52
6	269	301	1.12	94
8	381	419	1.10	120
12	440	497	1.13	158
17	622	684	1.12	216

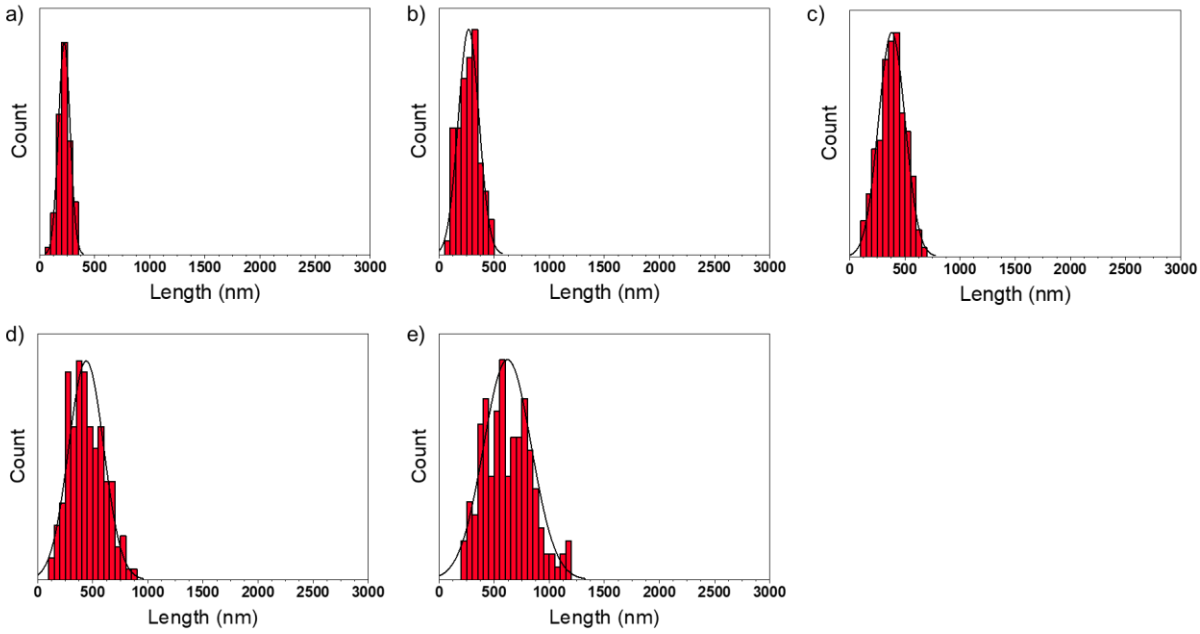

Figure S5.24. Histograms showing the nanofiber length distribution of $PDHF_{17}$-*b*-PEG_{227} seed micelles that were treated with **(a)** 4, **(b)** 6, **(c)** 8, **(d)** 12, and **(e)** 17 equivalents of $PDHF_{17}$-*b*-PEG_{227} unimer in THF at 22 °C.

P3EHT$_{23}$-*b*-PEG$_{113}$ seeds that were annealed at 30 °C for 18 h

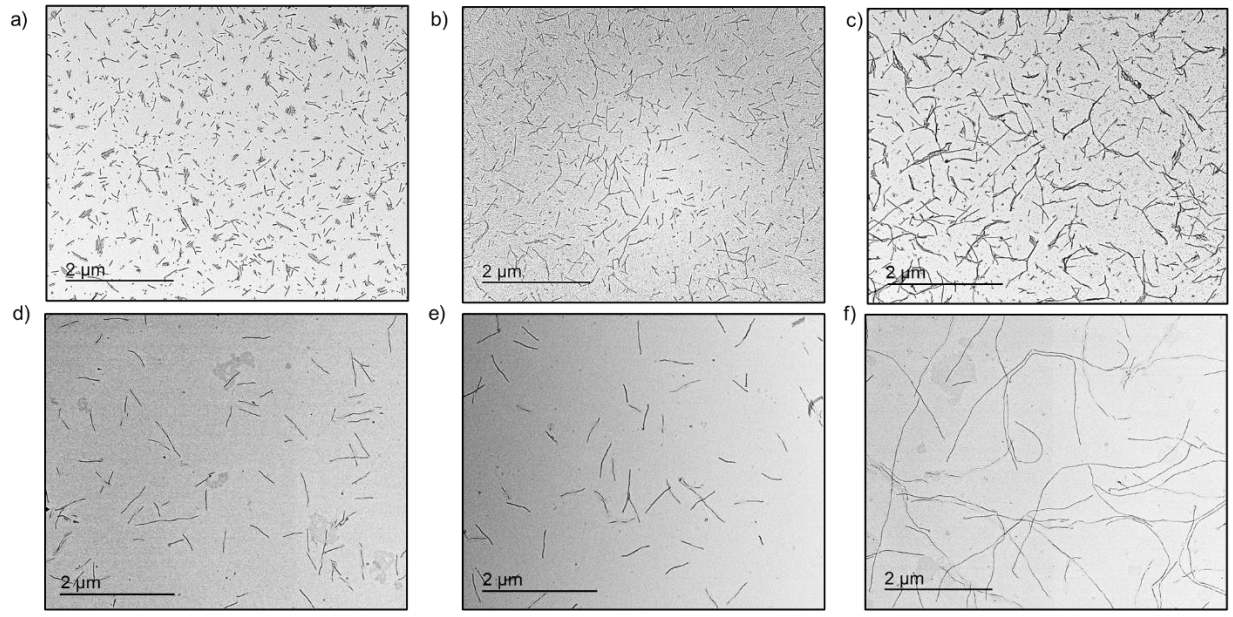

Figure S5.25. TEM images of P3EHT$_{23}$-*b*-PEG$_{113}$ nanofibers in 1:1 *n*BuOH:MeOH (0.05 mg/mL) formed by living CDSA seeded growth using seed micelles (1:1 *n*BuOH:MeOH, 0.1 mg/mL) that were annealed at 30 °C for 18 h prior to use. Annealed P3EHT$_{23}$-*b*-PEG$_{113}$ seed micelles (1:1 *n*BuOH:MeOH, 0.1 mg/mL) were treated with **(a)** 4, **(b)** 6, **(c)** 8, **(d)** 12, **(e)** 16, and **(f)** 20 equivalents of P3EHT$_{23}$-*b*-PEG$_{113}$ unimer (THF, 2 mg/mL) at 22 °C. Solutions were aged at 22 °C for 24 h followed by solvent evaporation prior to TEM imaging.

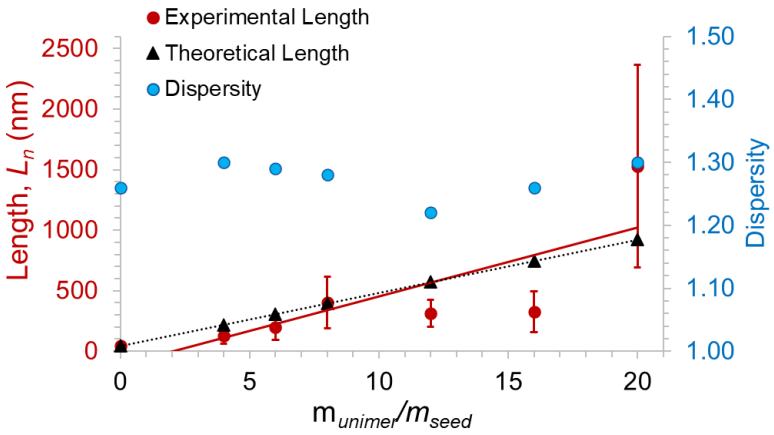

Figure S5.26. Plot showing the dependence of fiber length (L_n) on unimer to seed mass ratio when using seeds (L_n = 44 nm, $Đ_L$ = 1.26) that were annealed at 30 °C for 18 h prior to conducting seeded growth experiments at 22 °C. Error bars represent standard deviation.

Table S5.2. Summary of data from seeded growth experiments at 22 °C with P3EHT$_{23}$-*b*-PEG$_{113}$ seed micelles (1:1 *n*BuOH:MeOH, 0.1 mg/mL) which were annealed at 30 °C for 18 h. σ is standard deviation in L_n measurements.

m_{unimer}/m_{seed}	L_n	L_w	$Đ_L$	σ
Seeds	44	55	1.26	22
4	131	170	1.30	72
6	200	258	1.29	156
8	403	516	1.28	215
12	313	382	1.22	109
16	326	411	1.26	168
20	1528	1986	1.30	839

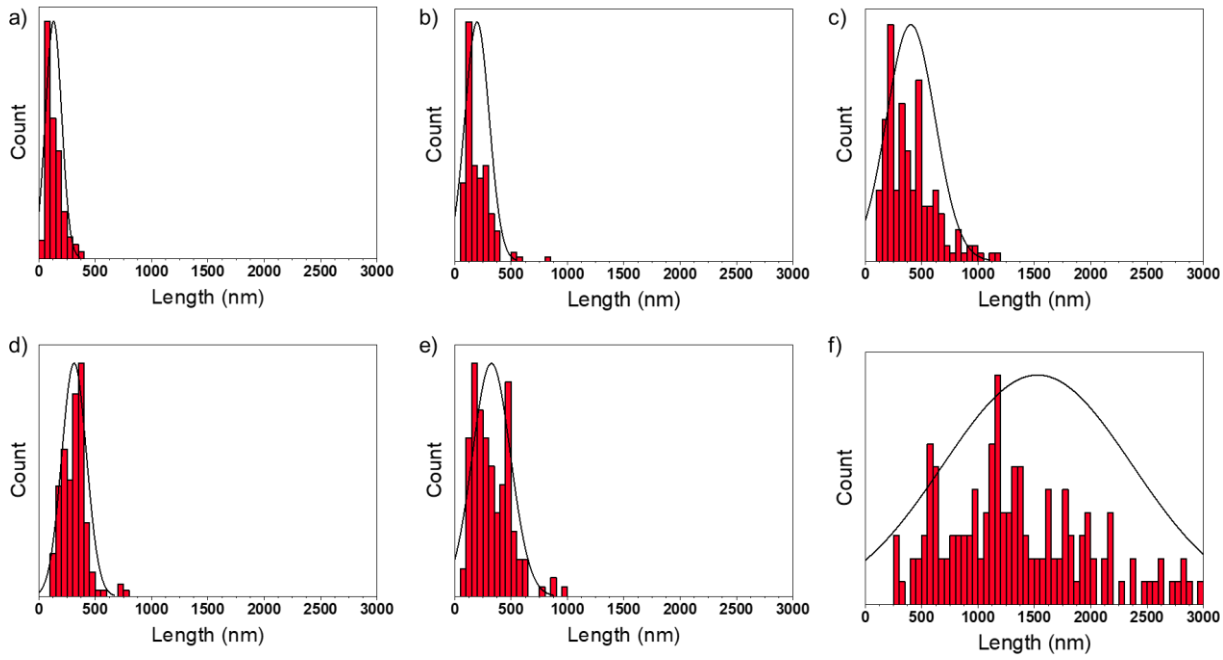

Figure S5.27. Histograms showing the nanofiber length distribution of annealed (30 °C, 18 h) P3EHT$_{23}$-*b*-PEG$_{113}$ seed micelles (1:1 *n*BuOH:MeOH, 0.1 mg/mL) that were treated with **(a)** 4, **(b)** 6, **(c)** 8, **(d)** 12, **(e)** 16, and **(f)** 20 equivalents of P3EHT$_{23}$-*b*-PEG$_{113}$ unimer (THF, 2 mg/mL) at 22 °C. Final concentrations were 0.05 mg/mL.

5.6 References

(1) Ren, H.; Chen, J. De; Li, Y. Q.; Tang, J. X. Recent Progress in Organic Photodetectors and Their Applications. *Adv. Sci.* **2021**, *8* (1), 1–23. https://doi.org/10.1002/advs.202002418.

(2) Zhao, Y.; Liu, T.; Wu, B.; Zhang, S.; Prine, N.; Zhang, L.; Pang, S.; Yin, B.; Ye, L.; Gu, X.; Yu, G.; Duan, C.; Huang, F.; Cao, Y. High-Performance All-Polymer Solar Cells and Photodetectors Enabled by a High-Mobility n-Type Polymer and Optimized Bulk-Heterojunction Morphology. *Chem. Mater.* **2021**, *33* (10), 3746–3756. https://doi.org/10.1021/acs.chemmater.1c00825.

(3) Yang, D.; Ma, D. Development of Organic Semiconductor Photodetectors: From Mechanism to Applications. *Adv. Opt. Mater.* **2019**, *7* (1), 1–23. https://doi.org/10.1002/adom.201800522.

(4) Xie, C.; Lu, X. T.; Tong, X. W.; Zhang, Z. X.; Liang, F. X.; Liang, L.; Luo, L. B.; Wu, Y. C. Recent Progress in Solar-Blind Deep-Ultraviolet Photodetectors Based on Inorganic Ultrawide Bandgap Semiconductors. *Adv. Funct. Mater.* **2019**, *29* (9), 1–40. https://doi.org/10.1002/adfm.201806006.

(5) Zhang, D.; Shi, J.; Zi, W.; Wang, P.; Liu, S. F. Recent Advances in Photoelectrochemical Applications of Silicon Materials for Solar-to-Chemicals Conversion. *ChemSusChem* **2017**, *10* (22), 4324–4341. https://doi.org/10.1002/cssc.201701674.

(6) Green, M. A.; Keevers, M. J. Optical Properties of Intrinsic Silicon at 300 K. *Prog. Photovoltaics Res. Appl.* **1995**, *3* (3), 189–192. https://doi.org/10.1002/pip.4670030303.

(7) Green, M. A. Self-Consistent Optical Parameters of Intrinsic Silicon at 300 K Including Temperature Coefficients. *Sol. Energy Mater. Sol. Cells* **2008**, *92* (11), 1305–1310. https://doi.org/10.1016/j.solmat.2008.06.009.

(8) Duan, L.; Hou, L.; Lee, T. W.; Qiao, J.; Zhang, D.; Dong, G.; Wang, L.; Qiu, Y. Solution Processable Small Molecules for Organic Light-Emitting Diodes. *J. Mater. Chem.* **2010**, *20* (31), 6392–6407. https://doi.org/10.1039/b926348a.

(9) Jiang, J. M.; Yuan, M. C.; Dinakaran, K.; Hariharan, A.; Wei, K. H. Crystalline Donor-Acceptor Conjugated Polymers for Bulk Heterojunction Photovoltaics. *J. Mater. Chem. A* **2013**, *1* (14), 4415–4422. https://doi.org/10.1039/c2ta00965j.

(10) Schmatz, B.; Yuan, Z.; Lang, A. W.; Hernandez, J. L.; Reichmanis, E.; Reynolds, J. R. Aqueous Processing for Printed Organic Electronics: Conjugated Polymers with Multistage Cleavable Side Chains. *ACS Cent. Sci.* **2017**, *3* (9), 961–967. https://doi.org/10.1021/acscentsci.7b00232.

(11) Stolar, M.; Baumgartner, T. Organic N-Type Materials for Charge Transport and Charge Storage Applications. *Phys. Chem. Chem. Phys.* **2013**, *15* (23), 9007–9024. https://doi.org/10.1039/c3cp51379c.

(12) Saini, V.; Abdulrazzaq, O.; Bourdo, S.; Dervishi, E.; Petre, A.; Bairi, V. G.; Mustafa, T.; Schnackenberg, L.; Viswanathan, T.; Biris, A. S. Structural and Optoelectronic Properties of P3HT-Graphene Composites Prepared by in Situ Oxidative Polymerization. *J. Appl. Phys.* **2012**, *112* (5). https://doi.org/10.1063/1.4751271.

(13) Benchaabane, A.; Ben Hamed, Z.; Lahmar, A.; Sanhoury, M. A.; Kouki, F.; Zellama, K.; Zeinert, A.; Bouchriha, H. Optical Properties of P3HT:Tributylphosphine Oxide-Capped CdSe Nanocomposites. *Appl. Phys. A Mater. Sci. Process.* **2016**, *122* (8), 1–8. https://doi.org/10.1007/s00339-016-0244-z.

(14) Mikhnenko, O. V.; Blom, P. W. M.; Nguyen, T. Q. Exciton Diffusion in Organic Semiconductors. *Energy Environ. Sci.* **2015**, *8* (7), 1867–1888. https://doi.org/10.1039/c5ee00925a.

(15) Janssen, R. Introduction to Polymer Solar Cells (3Y280). *Eng. Mater. Sci.* **2007**.

(16) Tuncel, D. π-Conjugated Nanostructured Materials: Preparation, Properties and Photonic Applications. *Nanoscale Adv.* **2019**, *1* (1), 19–33. https://doi.org/10.1039/c8na00108a.

(17) Jiang, Y.; McNeill, J. Light-Harvesting and Amplified Energy Transfer in Conjugated Polymer Nanoparticles. *Chem. Rev.* **2017**, *117* (2), 838–859. https://doi.org/10.1021/acs.chemrev.6b00419.

(18) Kundu, S.; Patra, A. Nanoscale Strategies for Light Harvesting. *Chem. Rev.* **2017**, *117* (2), 712–757. https://doi.org/10.1021/acs.chemrev.6b00036.

(19) Fukui, T.; Garcia-Hernandez, J. D.; MacFarlane, L. R.; Lei, S.; Whittell, G. R.; Manners, I. Seeded Self-Assembly of Charge-Terminated Poly(3-Hexylthiophene) Amphiphiles Based on the Energy Landscape. *J. Am. Chem. Soc.* **2020**, *142* (35), 15038–15048. https://doi.org/10.1021/jacs.0c06185.

(20) Sneyd, A. J.; Fukui, T.; Paleček, D.; Prodhan, S.; Wagner, I.; Zhang, Y.; Sung, J.; Collins, S. M.; Slater, T. J. A.; Andaji-Garmaroudi, Z.; MacFarlane, L. R.; Garcia-Hernandez, J. D.; Wang, L.; Whittell, G. R.; Hodgkiss, J. M.; Chen, K.; Beljonne, D.; Manners, I.; Friend, R. H.; Rao, A. Efficient Energy Transport in an Organic Semiconductor Mediated by Transient Exciton Delocalization. *Sci. Adv.* **2021**, *7* (32). https://doi.org/10.1126/sciadv.abh4232.

(21) MacFarlane, L. R.; Shaikh, H.; Garcia-Hernandez, J. D.; Vespa, M.; Fukui, T.; Manners, I. Functional Nanoparticles through π-Conjugated Polymer Self-Assembly. *Nat. Rev. Mater.* **2021**, *6* (1), 7–26. https://doi.org/10.1038/s41578-020-00233-4.

(22) Gilroy, J. B.; Gädt, T.; Whittell, G. R.; Chabanne, L.; Mitchels, J. M.; Richardson, R. M.; Winnik, M. A.; Manners, I. Monodisperse Cylindrical Micelles by Crystallization-Driven Living Self-Assembly. *Nat. Chem.* **2010**, *2* (7), 566–570. https://doi.org/10.1038/nchem.664.

(23) Xu, L.; Wang, C.; Li, Y.-X.; Xu, X.; Zhou, L.; Liu, N.; Wu, Z.-Q. Crystallization-Driven Asymmetric Helical Assembly of Conjugated Block Copolymers and the Aggregation Induced White-Light Emission and Circularly Polarized Luminescence. *Angew. Chem. Int. Ed.* **2020**, *59* (38), 16675–16682. https://doi.org/10.1002/anie.202006561.

(24) Schmelz, J.; Schedl, A. E.; Steinlein, C.; Manners, I.; Schmalz, H. Length Control and Block-Type Architectures in Worm-like Micelles with Polyethylene Cores. *J. Am. Chem. Soc.* **2012**, *134* (34), 14217–14225. https://doi.org/10.1021/ja306264d.

(25) Shin, S.; Menk, F.; Kim, Y.; Lim, J.; Char, K.; Zentel, R.; Choi, T. L. Living Light-Induced Crystallization-Driven Self-Assembly for Rapid Preparation of Semiconducting Nanofibers. *J. Am. Chem. Soc.* **2018**, *140* (19), 6088–6094.

https://doi.org/10.1021/jacs.8b01954.

(26) Tao, D.; Feng, C.; Lu, Y.; Cui, Y.; Yang, X.; Manners, I.; Winnik, M. A.; Huang, X. Self-Seeding of Block Copolymers with a π-Conjugated Oligo(p-Phenylenevinylene) Segment: A Versatile Route toward Monodisperse Fiber-like Nanostructures. *Macromolecules* **2018**, *51* (5), 2065–2075. https://doi.org/10.1021/acs.macromol.8b00046.

(27) Ma, J.; Lu, G.; Huang, X.; Feng, C. π-Conjugated-Polymer-Based Nanofibers through Living Crystallization-Driven Self-Assembly: Preparation, Properties and Applications. *Chem. Commun.* **2021**, *57* (98), 13259–13274. https://doi.org/10.1039/d1cc04825b.

(28) Shaikh, H.; Jin, X. H.; Harniman, R. L.; Richardson, R. M.; Whittell, G. R.; Manners, I. Solid-State Donor-Acceptor Coaxial Heterojunction Nanowires via Living Crystallization-Driven Self-Assembly. *J. Am. Chem. Soc.* **2020**, *142* (31), 13469–13480. https://doi.org/10.1021/jacs.0c04975.

(29) Li, X.; Wolanin, P. J.; MacFarlane, L. R.; Harniman, R. L.; Qian, J.; Gould, O. E. C. C.; Dane, T. G.; Rudin, J.; Cryan, M. J.; Schmaltz, T.; Frauenrath, H.; Winnik, M. A.; Faul, C. F. J. J.; Manners, I. Uniform Electroactive Fibre-like Micelle Nanowires for Organic Electronics. *Nat. Commun.* **2017**, *8* (1), 15909. https://doi.org/10.1038/ncomms15909.

(30) Jin, X.-H.; Price, M. B.; Finnegan, J. R.; Boott, C. E.; Richter, J. M.; Rao, A.; Menke, S. M.; Friend, R. H.; Whittell, G. R.; Manners, I. Long-Range Exciton Transport in Conjugated Polymer Nanofibers Prepared by Seeded Growth. *Science* **2018**, *360* (3691), 897–900. https://doi.org/10.1126/science.aar8104.

(31) Wang, X.; Guerin, G.; Wang, H.; Wang, Y.; Manners, I.; Winnik, M. A. Cylindrical Block Copolymer Micelles and Co-Micelles of Controlled Length and Architecture. *Science* **2007**, *317* (5838), 644–647. https://doi.org/10.1126/science.1141382.

(32) MacFarlane, L. R.; Li, X.; Faul, C. F. J.; Manners, I. Efficient and Controlled Seeded Growth of Poly(3-Hexylthiophene) Block Copolymer Nanofibers through Suppression of Homogeneous Nucleation. *Macromolecules* **2021**, *54* (24), 11269–11280. https://doi.org/10.1021/acs.macromol.1c02005.

(33) Cai, J.; Li, C.; Kong, N.; Lu, Y.; Lin, G.; Wang, X.; Yao, Y.; Manners, I.; Qiu, H. Tailored Multifunctional Micellar Brushes via Crystallization-Driven Growth from a Surface. *Science* **2019**, *366* (6469), 1095–1098. https://doi.org/10.1126/science.aax9075.

(34) Zhang, Y.; Yang, L.; Sun, Y.; Lin, G.; Manners, I.; Qiu, H. Surface-Initiated Living Self-Assembly of Polythiophene-Based Conjugated Block Copolymer into Erect Micellar Brushes. *Angew. Chem. Int. Ed.* **2024**, *2*, 1–8. https://doi.org/10.1002/anie.202315740.

(35) Lin, G.; Cai, J.; Sun, Y.; Cui, Y.; Liu, Q.; Manners, I.; Qiu, H. Capillary-Bound Dense Micelle Brush Supports for Continuous Flow Catalysis. *Angew. Chem. Int. Ed.* **2021**, *60* (46), 24637–24643. https://doi.org/10.1002/anie.202110206.

(36) Jeffries-El, M.; Sauvé, G.; McCullough, R. D. In-Situ End-Group Functionalization of Regioregular Poly(3-Alkylthiophene) Using the Grignard Metathesis Polymerization Method. *Adv. Mater.* **2004**, *16* (12), 1017–1019. https://doi.org/10.1002/adma.200400137.

(37) Vespa, M.; Hudson, Z. M.; Manners, I. Homogeneous and Segmented Nanofibers with a Conjugated Poly[3-(2′-Ethylhexyl)Thiophene] Core via Living Crystallization-Driven Self-

Assembly. *Macromolecules* **2024**, *57* (4), 1509–1520. https://doi.org/10.1021/acs.macromol.3c02357.

(38) Hsiao, M. S.; Yusoff, S. F. M.; Winnik, M. A.; Manners, I. Crystallization-Driven Self-Assembly of Block Copolymers with a Short Crystallizable Core-Forming Segment: Controlling Micelle Morphology through the Influence of Molar Mass and Solvent Selectivity. *Macromolecules* **2014**, *47* (7), 2361–2372. https://doi.org/10.1021/ma402429d.

(39) Yusoff, S. F. M.; Hsiao, M. S.; Schacher, F. H.; Winnik, M. A.; Manners, I. Formation of Lenticular Platelet Micelles via the Interplay of Crystallization and Chain Stretching: Solution Self-Assembly of Poly(Ferrocenyldimethylsilane)-Block-Poly(2-Vinylpyridine) with a Crystallizable Core-Forming Metalloblock. *Macromolecules* **2012**, *45* (9), 3883–3891. https://doi.org/10.1021/ma2027726.

(40) Dauben, B. H. J.; Mccoy, L. L. N-Bromosuccinimide. I. Allylic Bromination, a General Survey of Reaction Variables. *J. Am. Chem. Soc* **1959**, *81* (18), 4863–4873. https://doi.org/https://doi.org/10.1021/ja01527a027.

(41) Standley, E. A.; Smith, S. J.; Müller, P.; Jamison, T. F. A Broadly Applicable Strategy for Entry into Homogeneous Nickel(0) Catalysts from Air-Stable Nickel(II) Complexes. *Organometallics* **2014**, *33* (8), 2012–2018. https://doi.org/10.1021/om500156q.

(42) Azzam, T.; Eisenberg, A. Control of Vesicular Morphologies through Hydrophobic Block Length. *Angew. Chem. Int. Ed.* **2006**, *45* (44), 7443–7447. https://doi.org/10.1002/anie.200602897.

(43) Pangborn, A. B.; Giardello, M. A.; Grubbs, R. H.; Rosen, R. K.; Timmers, F. J. Safe and Convenient Procedure for Solvent Purification. *Organometallics* **1996**, *15* (5), 1518–1520. https://doi.org/10.1021/om9503712.

(44) Schneider, C. A.; Rasband, W. S.; Eliceiri, K. W. NIH Image to ImageJ: 25 Years of Image Analysis. *Nat. Methods* **2012**, *9* (7), 671–675. https://doi.org/10.1038/nmeth.2089.

(45) Peterson, J. J.; Werre, M.; Simon, Y. C.; Bryan Coughlin, E.; Carter, K. R. Carborane-Containing Polyfluorene: O-Carborane in the Main Chain. *Macromolecules* **2009**, *42* (22), 8594–8598. https://doi.org/10.1021/ma901703r.

(46) Deng, J.; Luo, Y.; Zhang, L. M. PEGylated Polyamidoamine Dendron-Assisted Encapsulation of Plasmid DNA into in Situ Forming Supramolecular Hydrogel. *Soft Matter* **2011**, *7* (13), 5944–5947. https://doi.org/10.1039/c1sm05259d.

Chapter 6

Outlook and Future Work

6.1 Thesis Summary and Future Work

The research presented in this thesis focused on establishing reliable polymer structure-property relationships, expanding the scope of π-conjugated block copolymers (BCPs) compatible with living crystallization-driven self-assembly (CDSA) (e.g. P3EHT-based materials), and exploring under-investigated areas of solution-phase BCP self-assembly (e.g. self-nucleation suppression, surface-confined nanofiber growth, and fully rigid BCP assembly). In particular, the work primarily focused on self-assembly of polythiophene based materials, with a strong emphasis on P3EHT as a crystallizable core-forming block in amphiphilic BCPs, resulting in optimized control over the length and morphology of CPNPs and the creation of novel nanostructures.

6.1.1 Homogenous and segmented nanofibers from P3EHT BCPs

The work presented on P3EHT BCP self-assembly (Chapter 2) to form length-controlled homogenous and heterogeneous nanofibers illustrates that small, facile modifications to the polymeric structure can result in large, beneficial self-assembly differences. This research lays the fundamental and experimental groundwork for rational modifications that could be done to the polythiophene structure to exert more control over the length of CPNPs and endow new material properties, thereby expanding the landscape of potential applications. For instance, the C_2 position of the 2-ethylhexyl chains on the thiophene rings is chiral, but the substituents used in this chapter were a racemic mixture. Use of a stereospecific chain may result in chiral helical supramolecular assemblies with selective handedness (Figure 6.1a), which have potential applications as optical

materials,[1,2] scaffolds for asymmetric synthesis,[3,4] and in separation science.[5,6] Because the improved control over the self-assembly is proposed to stem from the relative increased steric barrier and reduced crystallization rate of 2-ethylhexyl substituted polythiophene compared to linear *n*-hexyl functionalized polythiophene, further exploration of CPNP morphologies and properties can be achieved through alkyl chain tuning by increasing the number of branches,[7] changing branching position on the main alkyl chain,[8] changing main and branch chain lengths,[9,10] and inclusion of heteroatoms such as oxygen (Figure 6.1b).[11,12] In addition, the successful expansion of the self-nucleation suppression method from P3HT BCPs to P3EHT-based BCPs provides compelling evidence that this method may be generalized to other π-conjugated polymers, particularly ones where self-nucleation has been a persistent issue during living CDSA. Future work could involve exploring the applicability of this method to other BCP systems to determine if increased control over the self-assembly is achieved.

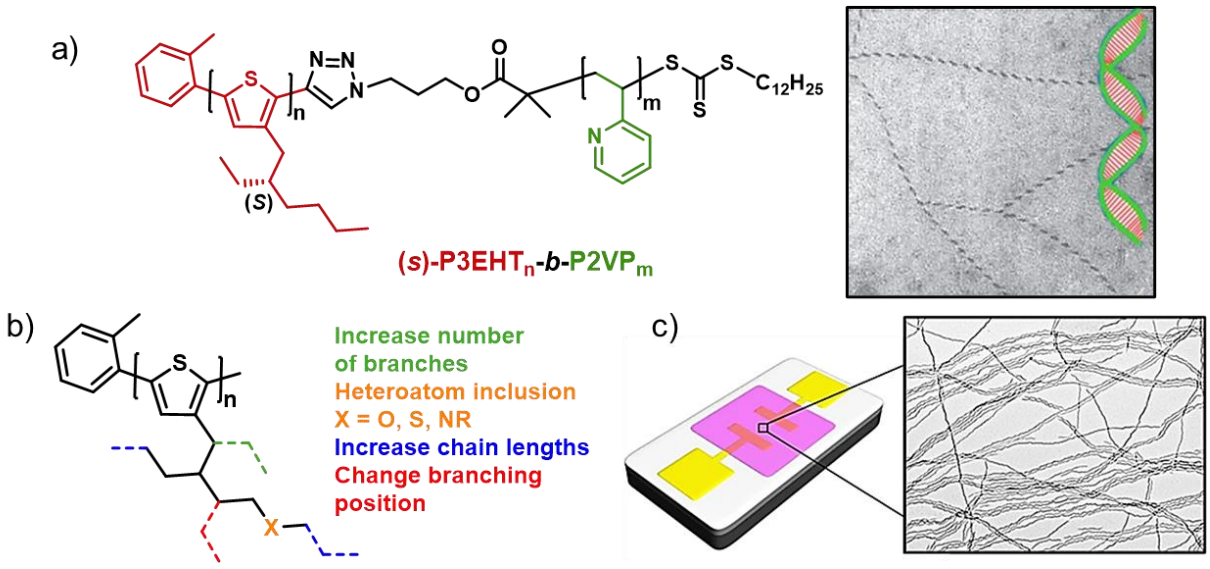

Figure 6.1. (a) Self-assembly of stereospecific poly(3-[(2'-*S*)-ethylhexyl]thiophene)-*b*-poly(2-vinylpyridine) ((*s*)-P3EHT-*b*-P2VP) which is proposed to result in chiral helical nanofibers. TEM image reproduced with permission from ref 13.[13] **(b)** Potential synthetic modifications to the alkyl chain that could be performed to modify the self-assembly. **(c)** Cartoon schematic of a P3EHT-nanofiber based organic field effect transistor (OFET) or organic electrochemical transistor.

Reducing the crystallization rate of π-conjugated BCPs is proposed to be a guiding strategy towards improving crystal packing within the micelle core which could drastically affect electronic conduction capabilities and exciton diffusion lengths. Charge carrier mobility measurements could be ascertained by fabrication of a P3EHT-nanofiber based organic electrochemical transistor or OFET device,[14] which is currently underway, while exciton diffusion lengths could be indirectly determined through the fabrication of length-controlled triblock comicelles capable of undergoing FRET from the core to the terminal coronal blocks,[15] or directly through transient absorption spectroscopy.[16] Currently, more advanced photophysical studies on the assemblies are required to reveal the capacity of such unique organic semiconductor materials to be used in electronics/optoelectronics.

6.1.2 Self-assembly of an all-conjugated BCP with a rigid corona-forming block

Chapter 3 outlines investigations into the solution-phase self-assembly of fully rigid rod-rod block copolymers and establishes that increasing the core:corona block ratio is a viable approach towards forming long nanofibers with well-connected core domains. P3HT-*b*-PPP nanofibers exhibited an impressive resilience towards the induction of shear stress compared to other conjugated polymer nanofibers, making them good candidates for reinforcing components of nanofiber-based composites.[17–20] Fracture prevention and brittleness reduction could be realized by incorporating these fibers into epoxy or siloxane thermosets, and studies evaluating optimal nanofiber length, weight percentage, and BCP block ratio could be undertaken (Figure 6.2a-c). Another potential application would be to determine if the well-connected fiber cores and long lengths provide improved electronic performance relative to neat P3HT films.

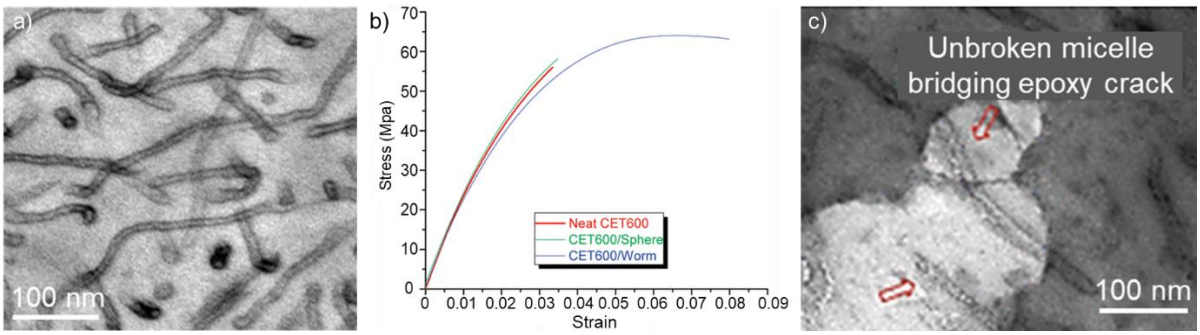

Figure 6.2. (a) TEM micrograph of RuO_4-stained PEP-*b*-PEO (PEP = poly(ethylene-*alt*-propylene), PEO = poly(ethylene oxide)) wormlike micelles dispersed in cured epoxy thermoset (CET). **(b)** Stress-strain curves of neat cured epoxy thermoset (neat CET600, red), cured epoxy thermoset modified with PEP-*b*-PEO spherical micelles (CET600/sphere, green), and cured epoxy thermoset modified with PEP-*b*-PEO wormlike micelles (CET600/worm, blue) showing superior tensile strength of CET/worm relative to neat CET600 and CET600/sphere thermosets. **(c)** TEM image showing wormlike micelle reinforcing epoxy thermoset in CET600/worm upon crack formation. Reproduced with permission from ref 20.[20]

6.1.3 Exploring the self-assembly of amphiphilic poly(3-(2'-ethylhexyl)thiophene) (P3EHT) homopolymers with singly-charged termini

Utilizing π-conjugated polymer amphiphiles with a crystallizable poly(3-(2'-ethylhexyl)thiophene (P3EHT) homopolymer core and a singly charged phosphonium terminus, 2D nanoribbon CPNPs with a continuous π-conjugated core have been prepared using CDSA (Chapter 4). In-depth analysis of their photophysical and optoelectronic properties is necessary to evaluate the energy transfer processes which underly exciton diffusion in organic semiconductors and determine their suitability towards application in devices, respectively. Exciton diffusion lengths through these 2D CPNPs could be evaluated and then incorporated into flexible pressure sensors.[21] Additionally, this evidence suggests that inclusion of a more sterically demanding alkyl chain promotes 2D platelet formation and further exploring the extent of this strategy by optimizing the polymer structure may lead to polymeric materials that provide enhanced access to semiconducting 2D CPNPs.

The research in this chapter also outlined the controlled self-assembly of well-defined coronally segmented triblock comicelles wherein charge-terminated P3EHT homopolymer ($[P3EHT_{23}\text{-}PPh_3]^+Br^-$) was grown from seeds of $P3EHT_{23}$-*b*-PEG_{113} and $P3EHT_{19}$-*b*-$P2VP_{138}$. The segmented coronal structure of these nanofibers confers the ability to spatially localize different functionality and the positively-charged terminal blocks provides exciting opportunities for tailored functionalization with inorganic quantum dots for energy transfer studies within hybrid organic-inorganic assemblies,[22] attachment to surfaces for surface-confined nanofiber growth,[23] as well as selective chemical detection.[12,24–26] As an example, perfluoroalkyl acids (PFAAs) and their salts are persistent, toxic environmental pollutants with a negatively-charged terminal functional group such as a carboxylate, sulfonate, or phosphonate.[27] The positively charged fiber termini could bond to the negative PFAA group electrostatically, causing bromide counterion displacement and inducing morphological or solubility changes which could be an indicator for the presence of PFAAs in drinking water. To date, only CDSA of positively charge-terminated homopolymers has been explored while negatively charge terminated homopolymers remain completely uninvestigated. Electron repulsion between these groups may lead to more exotic, higher curvature nanostructure morphologies, and offer possibilities to detect a broader range of analytes including hazardous environmental pollutants such as various metal cations.

Moreover, this chapter did not explore the growth of $P3EHT_{23}$-*b*-PEG_{113} or $P3EHT_{19}$-*b*-$P2VP_{138}$ from 2D seeds of $[P3EHT_{23}\text{-}PPh_3]^+Br^-$ which are proposed to result in "scarf-like" micelles with a central 2D platelet core and 1D "tassels" extending from it (Figure 6.3).[28] Adherence of the central platelet to a surface such as silicon could allow for energy funnelling from the tassels termini to the central 2D block, which may result in higher photocurrent generation than surface-confined nanofibers studied in Chapter 5.

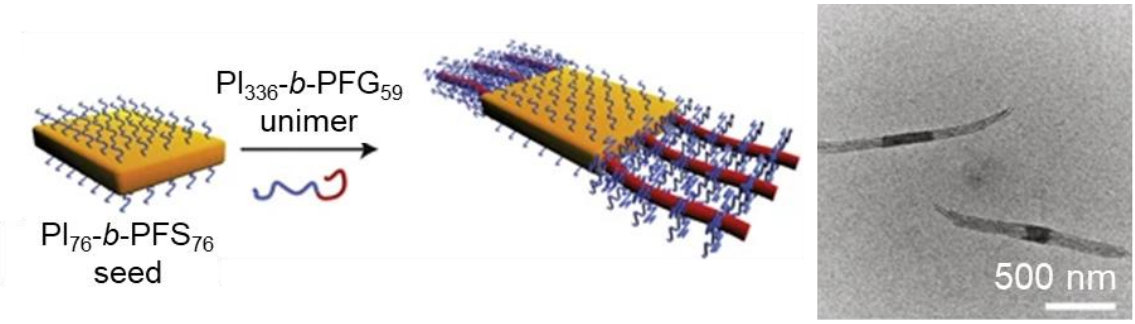

Figure 6.3. Scarf-shaped micelle obtained by heteroepitaxial growth of poly(isoprene)-*b*-poly(ferrocenyldimethylgermane) (PI_{336}-*b*-PFG_{59}) unimer from PI_{76}-*b*-PFS_{76} 2D seeds in xylene/decane (1:10 v/v). Reproduced and adapted with permission from ref 28.[28]

6.1.4 Surface-confined growth of π-conjugated nanofibers

The final chapter (Chapter 5) discussed the superior adherence of PEG-functionalized CPNP seeds to a silicon surface compared to P2VP-functionalized CPNP seeds, followed by nanofiber growth from the PEG-functionalized seeds toward hybrid light-harvesting photodetector (PD) devices. Future work will include determining what the optimal nanofiber length is for photocurrent generation. Additionally, the plasma etching used to remove surface contaminants also deprotonates the silanol groups, thereby removing their ability to be hydrogen bond donors. Following etching, it would be prudent to investigate if treatment of the silicon surface with additives such as weak acids protonates the oxides and further improves seed adherence. One attractive alternative would be to investigate if CPNPs composed of the positively-charged polymer $[P3EHT_{23}\text{-}PPh_3]^+Br^-$ attaches to the surface effectively through electrostatic interactions (Figure 6.4). Not only would this allow for high coverage of the silicon, but the lack of an insulating corona block such as PEG or P2VP would cause closer association of the micelle core to the surface. Since FRET is a through-space process, this could result in greater charge transfer from the core to the substrate.

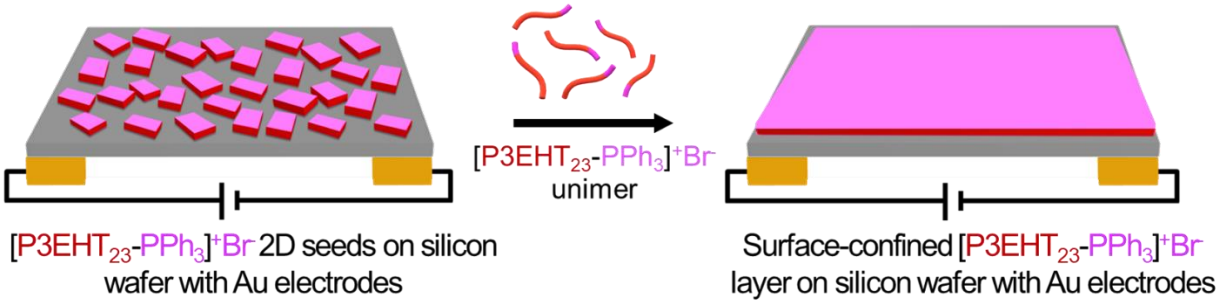

Figure 6.4. Schematic cartoon showing the adherence of $[P3EHT_{23}\text{-}PPh_3]^+Br^-$ 2D seeds to a plasma etched silicon wafer using electrostatic interactions and subsequent growth into a flat nanoplatelet layer following unimer addition.

6.2 Outlook

Living CDSA is a powerful methodology that allows for fabrication of low dispersity nanostructures with controlled size and dimension. The tunability of conjugated polymer properties along with the directed assembly of conjugated polymers into tailored, multifunctional CPNPs has enabled their application in fields such as photocatalysis, optoelectronics, nanomedicine, and material science. Further exploration of crystallizable core-forming blocks compatible with living CDSA is critical to fabricate new materials with undiscovered properties for advanced applications. “Push-pull” low bandgap crystalline polymers with alternating donor-acceptor monomeric units are excellent candidates for OPVs but their investigation as core-forming blocks amenable to living CDSA have not yet been investigated in this capacity.[8] Heteroepitaxial seeded growth of semiconductive π-conjugated BCPs could be used to create nanoscale heterojunctions which allow for effective charge separation upon exciton generation. Living CDSA is typically done in small batches that vary in crystal quality and nanoparticle size which has prevented industrial adoption of this process while the fabrication of CPNPs using continuous flow chemistry could remedy these shortcomings.[29] As well, the strong dependence of CPNP properties on morphology suggests that higher order assemblies such as dimensionally-

controlled 3D architectures[30] and conductive superlattices[31,32] may provide access to novel conductive properties, such as graphene has. The advancement towards increasingly smaller multifunctional materials has become a focal point of materials and energy research and CPNPs made by living CDSA represent an important class of materials in these promising and influential fields.

6.3 References

(1) Kim, Y. H.; Zhai, Y.; Lu, H.; Pan, X.; Xiao, C.; Gaulding, E. A.; Harvey, S. P.; Berry, J. J.; Vardeny, Z. V.; Luther, J. M.; Beard, M. C. Chiral-Induced Spin Selectivity Enables a Room-Temperature Spin Light-Emitting Diode. *Science* **2021**, *371* (6534), 1129–1133. https://doi.org/10.1126/science.abf5291.

(2) Sang, Y.; Han, J.; Zhao, T.; Duan, P.; Liu, M. Circularly Polarized Luminescence in Nanoassemblies: Generation, Amplification, and Application. *Adv. Mater.* **2020**, *32* (41), 1–33. https://doi.org/10.1002/adma.201900110.

(3) Jiang, J.; Ouyang, G.; Zhang, L.; Liu, M. Self-Assembled Chiral Nanostructures as Scaffolds for Asymmetric Reactions. *Chem. Eur. J.* **2017**, *23* (40), 9439–9450. https://doi.org/10.1002/chem.201700727.

(4) Han, X.; Yuan, C.; Hou, B.; Liu, L.; Li, H.; Liu, Y.; Cui, Y. Chiral Covalent Organic Frameworks: Design, Synthesis and Property. *Chem. Soc. Rev.* **2020**, *49* (17), 6248–6272. https://doi.org/10.1039/d0cs00009d.

(5) Qian, H. L.; Yang, C. X.; Yan, X. P. Bottom-up Synthesis of Chiral Covalent Organic Frameworks and Their Bound Capillaries for Chiral Separation. *Nat. Commun.* **2016**, *7* (May). https://doi.org/10.1038/ncomms12104.

(6) Liu, J.; Han, G.; Zhao, D.; Lu, K.; Gao, J.; Chung, T. S. Self-Standing and Flexible Covalent Organic Framework (Cof) Membranes for Molecular Separation. *Sci. Adv.* **2020**, *6* (41), 1–8. https://doi.org/10.1126/sciadv.abb1110.

(7) Kiriy, A.; Pötzsch, R.; Wei, Q.; Voit, B. High-Tech Functional Polymers Designed for Applications in Organic Electronics. *Polym. Degrad. Stab.* **2017**, *145*, 150–156. https://doi.org/10.1016/j.polymdegradstab.2017.06.009.

(8) Nübling, F.; Hopper, T. R.; Kuei, B.; Komber, H.; Untilova, V.; Schmidt, S. B.; Brinkmann, M.; Gomez, E. D.; Bakulin, A. A.; Sommer, M. Block Junction-Functionalized All-Conjugated Donor-Acceptor Block Copolymers. *ACS Appl. Mater. Interfaces* **2019**, *11* (1), 1143–1155. https://doi.org/10.1021/acsami.8b18608.

(9) Coote, J. P.; Kim, J. S.; Lee, B.; Han, J.; Kim, B. J.; Stein, G. E. Crystallization Modes of Poly(3-Dodecylthiophene)-Based Block Copolymers Depend on Regioregularity and Morphology. *Macromolecules* **2018**, *51* (22), 9276–9283. https://doi.org/10.1021/acs.macromol.8b01985.

(10) Yin, Y.; Chen, S.; Zhu, S.; Li, L.; Zhai, D.; Huang, D.; Peng, J. Tailoring Cocrystallization and Microphase Separation in Rod-Rod Block Copolymers for Field-Effect Transistors. *Macromolecules* **2021**, *54* (10), 4571–4581. https://doi.org/10.1021/acs.macromol.0c02788.

(11) Kamps, A. C.; Cativo, M. H. M.; Fryd, M.; Park, S.-J. Self-Assembly of Amphiphilic Conjugated Diblock Copolymers into One-Dimensional Nanoribbons. *Macromolecules* **2014**, *47* (1), 161–164. https://doi.org/10.1021/ma4021483.

(12) Kamps, A. C.; Cativo, M. H. M.; Chen, X. J.; Park, S. J. Self-Assembly of DNA-Coupled Semiconducting Block Copolymers. *Macromolecules* **2014**, *47* (11), 3720–3726. https://doi.org/10.1021/ma500509u.

(13) MacFarlane, L. R.; Shaikh, H.; Garcia-Hernandez, J. D.; Vespa, M.; Fukui, T.; Manners, I. Functional Nanoparticles through π-Conjugated Polymer Self-Assembly. *Nat. Rev. Mater.* **2021**, *6* (1), 7–26. https://doi.org/10.1038/s41578-020-00233-4.

(14) Li, X.; Wolanin, P. J.; MacFarlane, L. R.; Harniman, R. L.; Qian, J.; Gould, O. E. C. C.; Dane, T. G.; Rudin, J.; Cryan, M. J.; Schmaltz, T.; Frauenrath, H.; Winnik, M. A.; Faul, C. F. J. J.; Manners, I. Uniform Electroactive Fibre-like Micelle Nanowires for Organic Electronics. *Nat. Commun.* **2017**, *8* (1), 15909. https://doi.org/10.1038/ncomms15909.

(15) Jin, X.-H.; Price, M. B.; Finnegan, J. R.; Boott, C. E.; Richter, J. M.; Rao, A.; Menke, S. M.; Friend, R. H.; Whittell, G. R.; Manners, I. Long-Range Exciton Transport in Conjugated Polymer Nanofibers Prepared by Seeded Growth. *Science* **2018**, *360* (3691), 897–900. https://doi.org/10.1126/science.aar8104.

(16) Sneyd, A. J.; Fukui, T.; Paleček, D.; Prodhan, S.; Wagner, I.; Zhang, Y.; Sung, J.; Collins, S. M.; Slater, T. J. A.; Andaji-Garmaroudi, Z.; MacFarlane, L. R.; Garcia-Hernandez, J. D.; Wang, L.; Whittell, G. R.; Hodgkiss, J. M.; Chen, K.; Beljonne, D.; Manners, I.; Friend, R. H.; Rao, A. Efficient Energy Transport in an Organic Semiconductor Mediated by Transient Exciton Delocalization. *Sci. Adv.* **2021**, *7* (32). https://doi.org/10.1126/sciadv.abh4232.

(17) Dean, J. M.; Verghese, N. E.; Pham, H. Q.; Bates, F. S. Nanostructure Toughened Epoxy Resins. *Macromolecules* **2003**, *36* (25), 9267–9674. https://doi.org/https://doi.org/10.1021/ma034807y.

(18) Li, M.; Heng, Z.; Chen, Y.; Zou, H.; Liang, M. High Toughness Induced by Wormlike-Nanostructure in Epoxy Thermoset Containing Amphiphilic PDMS-PCL Block Copolymers. *Ind. Eng. Chem. Res.* **2018**, *57* (39), 13036–13047. https://doi.org/10.1021/acs.iecr.8b02336.

(19) Shen, L.; Wang, T. P.; Lin, F. Y.; Torres, S.; Robison, T.; Kalluru, S. H.; Hernández, N. B.; Cochran, E. W. Polystyrene-Block-Polydimethylsiloxane as a Potential Silica Substitute for Polysiloxane Reinforcement. *ACS Macro Lett.* **2020**, *9* (6), 781–787. https://doi.org/10.1021/acsmacrolett.0c00211.

(20) Liu, J.; Thompson, Z. J.; Sue, H. J.; Bates, F. S.; Hillmyer, M. A.; Dettloff, M.; Jacob, G.; Verghese, N.; Pham, H. Toughening of Epoxies with Block Copolymer Micelles of Wormlike Morphology. *Macromolecules* **2010**, *43* (17), 7238–7243. https://doi.org/10.1021/ma902471g.

(21) Han, L.; Fan, H.; Zhu, Y.; Wang, M.; Pan, F.; Yu, D.; Zhao, Y.; He, F. Precisely Controlled Two-Dimensional Rhombic Copolymer Micelles for Sensitive Flexible Tunneling Devices. *CCS Chem.* **2021**, *3* (5), 1399–1409. https://doi.org/10.31635/ccschem.020.202000297.

(22) Zhang, Y.; Shaikh, H.; Sneyd, A. J.; Tian, J.; Xiao, J.; Blackburn, A.; Rao, A.; Friend, R. H.; Manners, I. Efficient Energy Funneling in Spatially Tailored Segmented Conjugated Block Copolymer Nanofiber-Quantum Dot or Rod Conjugates. *J. Am. Chem. Soc.* **2021**, *143* (18), 7032–7041. https://doi.org/10.1021/jacs.1c01571.

(23) Cai, J.; Li, C.; Kong, N.; Lu, Y.; Lin, G.; Wang, X.; Yao, Y.; Manners, I.; Qiu, H. Tailored Multifunctional Micellar Brushes via Crystallization-Driven Growth from a Surface. *Science* **2019**, *366* (6469), 1095–1098. https://doi.org/10.1126/science.aax9075.

(24) Zhu, Q.; Xiong, W.; Gong, Y.; Zheng, Y.; Che, Y.; Zhao, J. Discrimination of Five Classes of Explosives by a Fluorescence Array Sensor Composed of Two Tricarbazole-Nanostructures. *Anal. Chem.* **2017**, *89* (22), 11908–11912. https://doi.org/10.1021/acs.analchem.7b04083.

(25) Sun, C.; Xiong, W.; Ye, W.; Zheng, Y.; Duan, R.; Che, Y.; Zhao, J. Fast and Ultrasensitive Detection of a Nerve Agent Simulant Using Carbazole-Based Nanofibers with Amplified Ratiometric Fluorescence Responses. *Anal. Chem.* **2018**, *90* (12), 7131–7134. https://doi.org/10.1021/acs.analchem.8b01810.

(26) Zhang, Y.; Pearce, S.; Eloi, J. C.; Harniman, R. L.; Tian, J.; Cordoba, C.; Kang, Y.; Fukui, T.; Qiu, H.; Blackburn, A.; Richardson, R. M.; Manners, I. Dendritic Micelles with Controlled Branching and Sensor Applications. *J. Am. Chem. Soc.* **2021**, *143* (15), 5805–5814. https://doi.org/10.1021/jacs.1c00770.

(27) Yang, S.; Li, X.; Jiang, Z. The Interaction of Perfluoroalkyl Acids and a Family History of Diabetes on Arthritis: Analyses of 2011–2018 NHANES. *BMC Public Health* **2024**, *24* (1), 1–10. https://doi.org/10.1186/s12889-024-17879-2.

(28) Gädt, T.; Ieong, N. S.; Cambridge, G.; Winnik, M. A.; Manners, I. Complex and Hierarchical Micelle Architectures from Diblock Copolymers Using Living, Crystallization-Driven Polymerizations. *Nat. Mater.* **2009**, *8* (2), 144–150. https://doi.org/10.1038/nmat2356.

(29) Xiao, L.; Parkinson, S. J.; Xia, T.; Edge, P.; O'Reilly, R. K. Enhancing the Scalability of Crystallization-Driven Self-Assembly Using Flow Reactors. *ACS Macro Lett.* **2023**, 1636–1641. https://doi.org/10.1021/acsmacrolett.3c00600.

(30) Xia, T.; Tong, Z.; Xie, Y.; Arno, M. C.; Lei, S.; Xiao, L.; Rho, J. Y.; Ferguson, C. T. J.; Manners, I.; Dove, A. P.; O'Reilly, R. K. Tuning the Functionality of Self-Assembled 2D Platelets in the Third Dimension. *J. Am. Chem. Soc.* **2023**, *145* (46), 25274–25282. https://doi.org/10.1021/jacs.3c08770.

(31) Qiu, H.; Hudson, Z. M.; Winnik, M. A.; Manners, I. Multidimensional Hierarchical Self-Assembly of Amphiphilic Cylindrical Block Comicelles. *Science* **2015**, *347* (6228), 1329–1332. https://doi.org/10.1126/science.1261816.

(32) Shim, J.; Bates, F. S.; Lodge, T. P. Superlattice by Charged Block Copolymer Self-Assembly. *Nat. Commun.* **2019**, *10* (1), 1–7. https://doi.org/10.1038/s41467-019-10141-z.